UNIVERSIDAD
DE GRANADA

FACULTAD DE FARMACIA

DEPARTAMENTO DE FARMACIA

Y TECNOLOGÍA FARMACÉUTICA

NANOHÍBRIDOS BASADOS EN MINERALES DE LA ARCILLA COMO TRANSPORTADORES DE FÁRMACOS ANTITUBERCULOSOS

CLAY MINERALS-BASED NANOHYBRIDS AS CARRIERS OF TUBERCULOSTATIC DRUGS

ESPERANZA CARAZO GIL

PROGRAMA DE DOCTORADO EN MEDICINA CLÍNICA Y SALUD PÚBLICA

TESIS DOCTORAL CON MENCIÓN INTERNACIONAL

Granada, 2019

Editor: Universidad de Granada. Tesis Doctorales
Autor: Esperanza Carazo Gil
ISBN: 978-84-1306-189-4
URI: http://hdl.handle.net/10481/55718

UNIVERSIDAD
DE GRANADA

Memoria de Tesis presentada por la Licenciada en Farmacia Esperanza Carazo Gil para optar al grado de Doctor por la Universidad de Granada, con mención de Doctorado Internacional.

Esta Tesis Doctoral ha sido dirigida por los Doctores Carola Aguzzi y César Viseras Iborra, Profesores del Departamento de Farmacia y Tecnología Farmacéutica de la Universidad de Granada.

Granada, 5 de marzo de 2019

VºBº de los Directores

Carola Aguzzi

César Viseras Iborra

La Doctoranda

Esperanza Carazo Gil

El doctorando ESPERANZA CARAZO GIL y los directores de la tesis CAROLA AGUZZI y CÉSAR VISERAS IBORRA garantizamos, al firmar esta tesis doctoral, que el trabajo ha sido realizado por el doctorando bajo la dirección de los directores de la tesis y hasta donde nuestro conocimiento alcanza, en la realización del trabajo, se han respetado los derechos de otros autores a ser citados, cuando se han utilizado sus resultados o publicaciones.

En GRANADA, 5 de marzo de 2019.

Director/es de la tesis

Doctorando

Fdo.: CAROLA AGUZZI

Fdo.: ESPERANZA CARAZO GIL

Fdo.: CÉSAR VISERAS IBORRA

La presente Tesis Doctoral ha sido financiada por el Proyecto de Excelencia RNM-1897 de la Junta de Andalucía, el Proyecto del Plan Nacional CGL2016-80833-R y por el Grupo de Investigación CTS-946 de la Junta de Andalucía. La doctoranda ha disfrutado de una ayuda para la Formación del Profesorado Universitario del Programa FPU del Ministerio de Educación, Cultura y Deporte (FPU 13/04765) y una ayuda para Estancias Breves y Traslados Temporales del mismo Programa (EST15/00225). El trabajo ha sido desarrollado en los laboratorios del Departamento de Farmacia y Tecnología Farmacéutica de la Facultad de Farmacia de la Universidad de Granada, del Instituto Andaluz de Ciencias de la Tierra (Consejo Superior de Investigaciones Científicas-Universidad de Granada) y del Dipartimento di Scienze del Farmaco, della Universitá degli Studi di Pavia (Italia).

ÍNDICE

RESUMEN/SUMMARY

RESUMEN

La tuberculosis es una enfermedad infecciosa causada por *Mycobacterium tuberculosis* y representa una de las diez principales causas de mortalidad en el mundo. Es una enfermedad curable, pero es necesario un tratamiento de larga duración (al menos seis meses) y la administración de cuatro fármacos antituberculosos de primera línea (isoniazida, rifampicina, pirazinamida y etambutol), dando lugar a un cumplimiento terapéutico bajo, lo que propicia la aparición de resistencias, que dificultan el tratamiento al aumentar su coste y duración. La Organización Mundial de la Salud recomienda la administración conjunta de los cuatro fármacos en una misma forma farmacéutica, en las denominadas "combinaciones a dosis fijas" (FDC: "Fixed-dose combinations"), con el objetivo de aumentar el cumplimiento del régimen terapéutico. Las FDC desarrolladas hasta ahora presentan problemas tecnológicos de inestabilidad física y química entre los fármacos, así como una elevada variabilidad interindividual en la biodisponibilidad de los fármacos incluidos. El fármaco más utilizado en la terapia antituberculosa es la isoniazida, por ser el de mayor actividad bactericida. Sin embargo, presenta una baja biodisponibilidad oral debida a su baja permeabilidad intestinal, que junto a su elevada solubilidad, determinan su inclusión en la clase III del Sistema de Clasificación Biofarmacéutica.

Entre los excipientes inorgánicos naturales, determinados materiales constituidos fundamentalmente por minerales de la arcilla son usados en formas farmacéuticas con distintos objetivos y han sido propuestos como nanomateriales de empleo en la elaboración de sistemas híbridos capaces de optimizar las características tecnológicas y/o biofarmacéuticas de fármacos de distinta naturaleza.

En esta Tesis Doctoral se han desarrollado sistemas nanohíbridos con dos excipientes naturales constituidos por minerales de la arcilla (halloysita y palygorskita) y el fármaco más usado para el tratamiento de la tuberculosis (isoniazida). El diseño y desarrollo de estos sistemas pretendía mejorar el perfil biofarmacéutico del fármaco y paralelamente aumentar su estabilidad en presencia de los otros fármacos tuberculostáticos con los que se administra. Los sistemas se han obtenido mediante la técnica de intercalación sólido-líquido. Las materias primas y los nanohíbridos obtenidos han sido caracterizados por diversas técnicas de caracterización al estado sólido. Asimismo se ha completado un estudio teórico y experimental de las propiedades cinéticas y termodinámicas del

proceso de adsorción de la isoniazida en las dos arcillas. En ambos casos, el proceso de adsorción global se produce en dos etapas: adsorción de moléculas de isoniazida en los sitios activos de los adsorbentes, seguida de la precipitación de moléculas de fármaco sobre la monocapa previamente adsorbida. Ambas etapas son espontáneas para ambos sistemas en las condiciones estudiadas. El nanohíbrido isoniazida-halloysita ha sido objeto de estudios complementarios: se han estudiado, mediante modelado computacional, las características del proceso de adsorción de moléculas de isoniazida en los nanotubos de halloysita, confirmando los resultados experimentales; se ha completado un estudio cinético y del mecanismo de liberación del fármaco desde dicho nanohíbrido, demostrando que la liberación del fármaco tiene lugar mediante un único proceso de desorción; se han realizado ensayos *in-vitro* de citotoxicidad y permeabilidad intestinal en la línea celular de adenocarcinoma de colon Caco-2, no obteniendo efectos citotóxicos, sino incluso resultados positivos de proliferación celular en algunos casos y un aumento significativo de la permeabilidad intestinal de la isoniazida en el nanohíbrido; por último, se ha estudiado la estabilidad de la isoniazida cargada en la halloysita en presencia de los otros tres fármacos antituberculosos de primera línea, observándose un efecto protector de los nanotubos y consiguiente disminución de la degradación de isoniazida. El doble propósito, tecnológico y biofarmacéutico, planteado se cumple de forma satisfactoria al utilizar halloysita como nanotransportador de la isoniazida.

SUMMARY

Tuberculosis is an infectious disease caused by the bacillus *Mycobacterium tuberculosis* and is one of the top ten causes of death worldwide. It is curable, but its treatment present severe difficulties as its long duration and need of polymedication (six- to nine month course of four drugs in combination: isoniazid, rifampicin, pyrazinamide and ethambutol) leading to poor adherence, lack of patient compliance and development of antibiotic resistances, which hamper the treatment by an increase of its length and cost. The World Health Organization recommends the administration of fixed-dose combinations (FDC) containing the four first-line tuberculostatic drugs as an attempt to increase the patient compliance. However, tuberculostatic drugs included in these FDC suffer not only from physical and chemical instability but also from high interindividual variability of bioavailability values of the drugs included. Isoniazid, which is the most widely used tuberculostatic drug, possesses high solubility and low intestinal permeability and is included in the class III of the Biopharmaceutical Classification System.

Among the natural inorganic excipients, certain materials consisting mainly of clay minerals are used in pharmaceutical forms with different objectives and have been proposed as nanomaterials for use in the development of hybrid systems capable of optimizing the technological and/or biopharmaceutical characteristics of drugs of different nature.

With these premises, in this Doctoral Thesis, two pharmaceutical-grade clay minerals (halloysite and palygorskite), were selected as inorganic nanocarriers of isoniazid. Clay minerals-isoniazid nanohybrids were prepared by the solid-liquid intercalation technique. Raw materials and the resulting nanohybrids were subjected to full and comprehensive solid state characterization studies. Besides, kinetic and thermodynamic assessment of the adsorption process of this drug onto the two sorbents was performed revealing that, in both cases, the global adsorption process was thermodynamically spontaneous and the sum of two steps: adsorption of isoniazid molecules onto the active sites of the clay minerals, and precipitation of drug molecules over the previously adsorbed monolayer. Halloysite-isoniazid nanohybrid was subjected to further complementary studies: a computational modeling study corroborated the experimental adsorption data; i*n-vitro* release tests of isoniazid from the nanohybrid were performed

revealing that drug release consisted on a simple desorption process; Caco-2 cell line was selected to performed *in-vitro* cytotoxicity and permeability tests; results showed that the nanohybrid did not exert any cytotoxic effect towards human Caco-2 cell line, and even in some cases proliferative effects were obtained; *in-vitro* intestinal permeability of the drug was enhanced when loaded onto the nanotubes; accelerated stability tests were carried out by means of binary and quaternary physical mixtures of pure INH or halloysite-isoniazid nanohybrid with the other first-line tuberculostatics. It was found that halloysite exerted a protective role in terms of decreasing the degradation rate of isoniazid. In basis of the results obtained, it could be stated that both technological and biopharmaceutical aims of the doctoral Thesis have been fulfilled by using halloysite nanotubes as isoniazid nanocarrier.

CAPÍTULO I

Introducción

I.1 TUBERCULOSIS

I.1.1 GENERALIDADES

La tuberculosis (TB) es una enfermedad infecciosa y transmisible. Está causada por el bacilo *Mycobacterium tuberculosis (Mtb)* (Figura I.1), una bacteria perteneciente al género *Mycobacterium*, también conocida como bacilo de Koch, en honor a su descubridor (Brock, 1988).

Figura I.1. *Mycobacterium tuberculosis* (https://www.flickr.com/photos/niaid/5149398656).

I.1.1.1 Antecedentes históricos

La TB es una de las enfermedades más antiguas que afectan al ser humano. El primer caso se remonta al Neolítico y fue descubierto en 1907 gracias al hallazgo de vértebras de un adulto joven con lesiones características de la enfermedad de Pott o TB ósteoarticular, una de las formas extrapulmonares de la enfermedad tuberculosa (Daniel, 2006). La TB ha sido conocida con diversos nombres a lo largo de la historia; de entre ellos destacan "tisis", del griego *phythysis*, que significa secar, y que se utilizaba con la idea de consumirse, y "peste blanca", por la TB endémica del siglo XVII que produjo una alta mortalidad en Europa. El término "tuberculosis" fue enunciado en 1839 por un médico alemán (Johann Lukas Schönlein), adaptado de la palabra tubérculo, por las lesiones características de la enfermedad (Daniel, 2006).

La naturaleza transmisible de la TB fue enunciada por Antoine Villemin (1869). Sin embargo, fue el microbiólogo alemán Robert Koch quien aisló el agente etiológico causante de la TB y demostró su naturaleza infecciosa (1882), valiéndole esos resultados para recibir el premio Nobel en 1905 (Koch, 1882; Kaufman y Schaible, 2005).

I.1.1.2 Aspectos microbiológicos y taxonomía del género Mycobacterium

El género *Mycobacterium* (bacteria fúngica) debe su nombre al crecimiento en forma de hongo del bacilo en medios líquidos. Dicho género pertenece al orden *Actinomycetales*, suborden *Corynebacteriaceae* y a la familia *Mycobacteriaceae* (Waksman y Henrici, 1943).

Las micobacterias son microorganismos aerobios estrictos, inmóviles, con morfología bacilar o cocoide, sin cápsula ni flagelos y no formadores de esporas (Cole et al., 1998). Tienen una pared celular gruesa y de alto contenido lipídico, destacando de entre sus componentes los ácidos micólicos. Debido a la estructura de la pared celular, ésta es poco permeable y es la responsable de la ineficacia de múltiples agentes antimicrobianos y tinciones de microscopía. En su estructura podrían diferenciarse tres capas con distinta composición y propiedades. La capa más interna le confiere rigidez por la presencia de péptidoglicanos; en la capa media se encuentran los ácidos micólicos, y en la capa más externa se encuentran glucolípidos y péptidos (Brennan, 2003).

I.1.2 PATOGENIA

La transmisión de *Mtb* se produce de forma habitual por vía respiratoria. *Mtb* entra en el organismo a través de las vías aéreas (Figura I.2). En los pulmones, *Mtb* puede ser completamente eliminado por el sistema inmune, permanecer en estado latente o dar lugar a la forma activa de la enfermedad (Cooper, 2009). La evolución dependerá del estado del sistema inmune de la persona infectada (Pai et al., 2016; Schnappinger y Ehrt, 2016).

La respuesta inmune generada por la infección es altamente eficaz y aproximadamente un 90 % de las personas infectadas mantienen controlados los bacilos en estado latente durante toda la vida. Cuando se produce la infección en pacientes que no han sido

previamente expuestos a *Mtb*; macrófagos, células dendríticas y células epiteliales interaccionan con ligandos del *Mtb*. Como resultado, se producen citoquinas y quimioquinas inflamatorias que reclutan células mononucleares de los tejidos adyacentes al sitio de infección e inician la formación del granuloma temprano por el sistema inmune innato. Este granuloma temprano es la característica primaria de la enfermedad y conforme éste madura, desarrolla una cápsula fibrosa. Los granulomas maduros pueden encapsularse y aíslan a la bacteria, la cual permanecería inactiva en condiciones anaerobias durante la vida del hospedador inmunocompetente. Esta etapa de los granulomas maduros se considera de infección. En el caso de una infección progresiva, el centro del granuloma se licúa y se diseminan los agentes infecciosos a las vías aéreas. El daño pulmonar provoca el desarrollo de tos productiva, que facilita la generación de aerosoles infecciosos y de esta forma finaliza el ciclo vital de la bacteria (Russel, 2007).

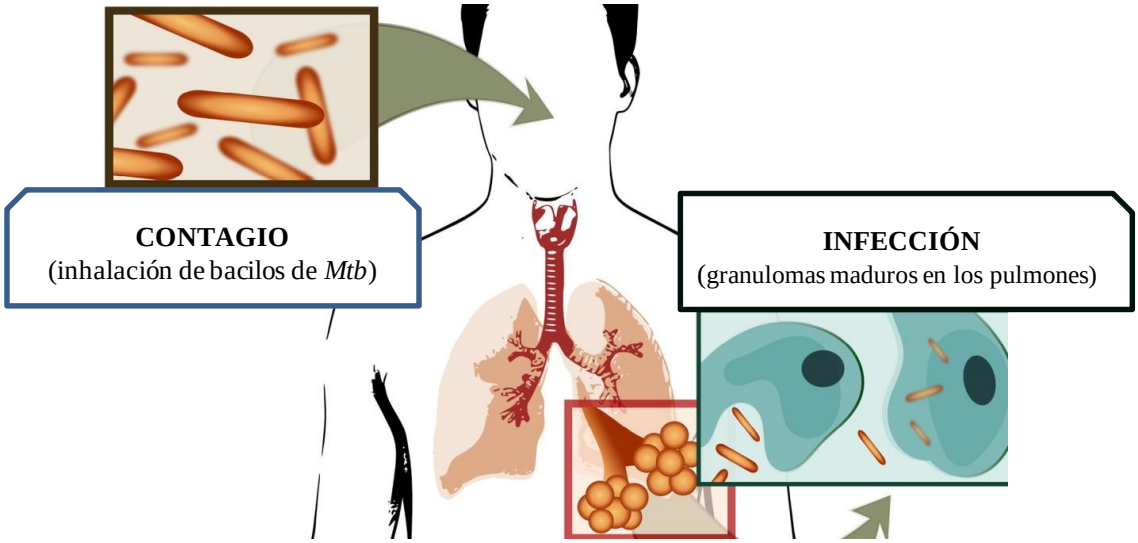

Figura. I.2. Evolución de la TB desde el contagio hasta la infección (modificada de Costa et al., 2016).

En algunas personas, los bacilos son capaces de salvar el sistema inmune y se multiplican rápidamente, resultando en la evolución desde infección a enfermedad, con mayor capacidad de diseminación de la enfermedad a otras personas. Dicha evolución puede ocurrir de forma inmediata o después de muchos años de infección (Ulrichs y Kaufmann, 2006).

I.1.2.1 Manifestaciones clínicas

Las manifestaciones de la forma activa de TB son muy variables. Puede llegar a ser asintomática, grave, como en el caso de la enfermedad de Pott, también conocida como TB vertebral o espondilitis tuberculosa, o incluso con riesgo de muerte, como es el caso de la meningitis tuberculosa (Glaziou et al., 2015). La enfermedad pulmonar (TB-P) está presente en casi todos los casos de TB, pero puede verse afectada también cualquier otra parte del cuerpo (TB extrapulmonar: TB-EP), la cual ocurre en aproximadamente un 20% de los casos, pudiendo superar el 50% en pacientes inmunodeprimidos. La diseminación puede realizarse mediante vías linfáticas, hematógenas (sanguíneas), o de forma directa desde un foco de infección (Sharma y Mohan, 2004; Gambhir et al., 2017).

I.1.2.1.1 TB pulmonar (TB-P)

La TB-P puede ser asintomática o cursar con sintomatología general (fiebre, sudoración, astenia, anorexia y pérdida de peso) y manifestaciones clínicas inespecíficas (tos, expectoración, dolor torácico). Los resultados de la exploración torácica pueden ser normales, o bien pueden detectarse estertores localizados. Si se sospecha que pueda existir la enfermedad, y en todo paciente con síntomas respiratorios y/o síntomas generales de más de 2–3 semanas de duración iniciar las pruebas diagnósticas.

I.1.2.1.2 TB extrapulmonar (TB-EP)

Como se ha descrito anteriormente, *Mtb* puede diseminarse e implantarse en cualquier otro lugar del organismo que no sean los pulmones, dando lugar a distintas manifestaciones clínicas (Golden y Vikram, 2005; Gambhir et al., 2017):

a) TB del sistema nervioso central: la meningitis tuberculosa es la forma más frecuente de presentación de TB en el sistema nervioso central (SNC). Su pronóstico es muy grave si no se administra el tratamiento. Otras formas graves de TB en el SNC son los tuberculomas, abscesos cerebrales, hidrocefalia con hipertensión intracraneal y los infartos isquémicos secundarios a vasculitis.

b) TB ósteoarticular: la localización vertebral es la más frecuente (Enfermedad de Pott). El paciente presenta dolor y molestias inespecíficas localizadas. Las localizaciones más frecuentes son la columna torácica en los pacientes jóvenes y la lumbar en los mayores.

c) TB urinaria: cursa con sintomatología inespecífica o incluso asintomática. Si la enfermedad se extiende por el uréter y la vejiga, los síntomas de inicio más frecuentes son disuria y hematuria, pudiendo llegar a producir fibrosis e incluso obstrucción del tracto urinario.

d) TB genital: frecuentemente se asocia a la TB urinaria. En varones pueden verse afectados la próstata, el epidídimo, los testículos y las vesículas seminales. En las mujeres, la trompa de Falopio y el endometrio. Es de escasa prevalencia en Europa pero supone una de las causas más frecuentes de infertilidad en el mundo.

e) TB ganglionar: los ganglios linfáticos cervicales y la región supraclavicular suponen las zonas más frecuentes de afectación ganglionar. La tumoración cervical es la forma de presentación más frecuente.

f) TB miliar: este tipo de TB-EP produce la aparición de pequeños nódulos en los órganos afectados. Es grave en cualquier persona, principalmente en pacientes con inmunodepresión, como los enfermos de sida.

g) TB laríngea: se suele asociar a TB pulmonar bacilífera, y por lo tanto es una forma altamente contagiosa. Se produce fundamentalmente por extensión local procedente del árbol bronquial. El signo más frecuente es la disfonía.

h) TB cutánea: las manifestaciones de la TB cutánea dependen de la situación inmunitaria del paciente. El *lupus vulgaris* es propio de pacientes inmudeprimidos y puede dar lugar a deformidades crónicas. Las tuberculides

(eritema indurado de Bazin, liquen escrofuloso y tuberculides papulonecróticas), son otras formas de presentación en pacientes inmunocompetentes.

i) TB gastrointestinal: puede comprometer cualquier parte del tracto digestivo, desde la boca hasta el ano. La localización íleocecal es la más frecuente seguida del páncreas, vías biliares e hígado.

I.1.3 FACTORES DE RIESGO

Determinadas circunstancias socioeconómicas y/o coinfecciones pueden determinar un mayor riesgo de desarrollar TB activa (Lönnroth et al., 2009; Narasinham et al., 2013; Ai et al., 2016; Silva et al., 2018). De entre todos los posibles factores que pueden intervenir en un mayor riesgo de desarrollo de la forma activa de la enfermedad, cabe destacar:

I.1.3.1 Virus de la Inmunodeficiencia Humana (VIH)

Las personas con VIH tienen entre 20 y 30 veces más probabilidades de desarrollar TB activa que las VIH-negativas (Amoakwa et al., 2015; www.tballiance.org). La combinación de la infección por el VIH con la TB es letal, ya que una acelera la evolución de la otra (Kasper, 2015). Los pacientes infectados por el VIH no sólo están predispuestos a la reactivación de una infección antigua en estado latente, sino también a la progresión rápida de una infección adquirida recientemente (Khan y Divangahi, 2018). Se estima que el riesgo de muerte en personas coinfectadas con *Mtb* y VIH es el doble con respecto a los pacientes solamente infectados por VIH. En 2017 aproximadamente un 40% de las muertes registradas en personas VIH-positivas se debieron a la TB (WHO, 2018a).

I.1.3.2 Diabetes

La relación diabetes-TB ha sido objeto de multitud de estudios a lo largo de la historia. La susceptibilidad a padecer la enfermedad tuberculosa aumenta con la hiperglucemia que sufren los pacientes diabéticos no controlados (Podell et al., 2014). Por otra parte, la insulinopenia así como la disminución de la función fagocítica y de los linfocitos T también interviene en la mayor susceptibilidad, al verse reducida la capacidad del

sistema inmunitario para detener la infección (Dooley y Chaisson, 2009). Además, los pacientes diabéticos tienen mayor riesgo de presentar reacciones adversas graves al tratamiento antituberculoso, tales como nefrotoxicidad e hipotiroidismo (Muñoz-Torrico et al., 2017).

I.1.3.3 Inmigración

Los inmigrantes reproducen en el país de destino la misma situación epidemiológica de sus lugares de origen, donde la TB aún es endémica y la mantienen dos o tres generaciones después de haberse establecido en el país, ya que tienden a vivir en comunidades relativamente cerradas (Pareek et al., 2016; Sánchez-Montalvá et al., 2018). Además, la situación de la mayoría de ellos es marginal, lo que dificulta el acceso al sistema sanitario y la posible detección y tratamiento; por éste mismo motivo el número de enfermos diagnosticados en los inmigrantes es siempre inferior al real (Lönnroth et al., 2017).

I.1.3.4 Transplantes

La TB es una de las infecciones oportunistas más importantes en los pacientes receptores de un trasplante de órgano sólido, debido normalmente a la reactivación de una infección latente tras el inicio del tratamiento inmunosupresor (Ai et al., 2016). Actualmente, la Organización Mundial de la Salud (OMS) recomienda a los países de ingresos altos o medianos con una baja tasa de incidencia de TB (<100 por cada 100.000 habitantes) que traten la infección latente de TB en pacientes que se preparan para ser transplantados (Ai et al., 2016).

I.1.3.5 Insuficiencia renal crónica y hemodiálisis

Además de la alta prevalencia de TB en la población sometida a diálisis, el diagnóstico de TB en pacientes con insuficiencia renal crónica (IRC) resulta difícil, ya que la sensibilidad de las pruebas diagnósticas está disminuída en estos casos, y la localización de la TB en pacientes con IRC suele ser extrapulmonar, presentándose principalmente como peritonitis tuberculosa y linfadenitis. Por dichos motivos, actualmente, en varias guías e informes, se sugieren pruebas y profilaxis de TB en pacientes con IRC (Ferguson et al., 2015; Campbell et al., 2016; Romanowski et al., 2016).

I.1.3.6 Silicosis

La relación entre silicosis y TB es conocida desde antiguo. En la actualidad hay estudios que reflejan que hasta un 25-30% de los pacientes con silicosis desarrollan TB, y el riesgo relativo de TB está multiplicado por 3 en pacientes con silicosis en comparación con la población general (Cheepsattayakorn y Cheepsattayakorn, 2018).

I.1.3.7 Otros factores de riesgo

Además de los factores de riesgo arriba citados, entre los que destaca el VIH, se debe destacar el mayor riesgo de desarrollar una forma activa de TB en pacientes cuyo consumo de alcohol diario sea elevado (más de 40 g al día), debido a su papel negativo en el estado del sistema inmune (Imtiaz et al., 2017). Otros hábitos como el tabaquismo también se asocian con un mayor riesgo de TB activa, sobretodo TB pulmonar (Zellweger et al., 2015). Posibles mecanismos que intervienen en esta mayor predisposición son una respuesta inmune debilitada, linfocitopenia T-CD4, defectos en la respuesta de los macrófagos y defectos en la movilidad de los cilios de las vías aéreas (Bates et al., 2007; Slama et al., 2007). Un déficit en la vitamina D (25-hidroxicolecalciferol) también supone un factor de riesgo para el desarrollo de la infección tuberculosa, ya que su metabolito activo, el 1,25-dihidroxicolecalciferol, ayuda a los fagocitos mononucleares a suprimir el crecimiento intracelular de *Mtb* (Wilkinson et al., 2000; Cegielski y McMurray, 2004; Autier et al., 2014).

I.1.4 TB RESISTENTE

La resistencia a *Mtb* puede ser primaria, en pacientes que nunca antes han recibido tratamiento antituberculoso, o secundaria, también llamada adquirida, debida a una quimioterapia incorrecta (incumplimiento terapéutico, esquema terapéutico inicial erróneo o indicación inadecuada de tratamiento de infección tuberculosa) o pacientes que abandonan el tratamiento antes de haber erradicado la enfermedad (Falzon et al., 2017). Por otra parte, debemos distinguir distintos tipos de resistencia en función del/los fármaco/s ante los cuales no sea susceptible la cepa de *Mtb*:

I.1.4.1 TB Resistente a la Rifampicina (TB-RR)

La TB-RR ocurre cuando se produce una infección por una cepa no susceptible a la rifampicina. Se puede tratar y curar mediante el uso de fármacos de segunda línea, los cuales tienen el inconveniente de ser de mayor coste, toxicidad y duración del tratamiento (WHO, 2016a).

I.1.4.2 TB Multirresistente (TB-MDR)

La TB-MDR es la causada por una cepa no susceptible a la acción bactericida de los dos fármacos antituberculosos de primera línea más eficaces de que se dispone (isoniazida y rifampicina). Como en el caso de la TB-RR, se puede tratar y curar mediante el uso de fármacos de segunda línea, con los inconvenientes que plantean (WHO, 2016a).

I.1.4.3 TB Extremadamente Resistente (TB-XDR)

La TB-XDR es un tipo de TB-MDR poco común. Sus pacientes mantienen la no susceptibilidad a isoniazida y rifampicina, a las cuales se suman todas las fluoroquinolonas y por lo menos uno de los tres fármacos inyectables de segunda línea (Falzon et al., 2017).

I.1.5 EPIDEMIOLOGÍA

I.1.5.1 Situación actual de la TB

La TB es la novena causa mundial de muerte y la primera de las causadas por una enfermedad infecciosa, superando al VIH. En el año 2017 se produjeron 1,3 (intervalo 1,2-1,4) millones de muertes en personas VIH-negativas, y 300.000 (intervalo 266.000-335.000) en personas VIH-positivas (WHO, 2018a). Ese mismo año se estima que contrajeron la enfermedad unos 10 (rango 9-11) millones de personas (Figura I.3), de las cuales, 5,8 millones eran del sexo masculino, 3,2 millones del sexo femenino y aproximadamente 1 millón eran niños. Se han registrado casos en todos los países y grupos de edad, pero el 90% de ellos son adultos (≥15 años de edad), el 9% VIH-positivos (el 72% de ellos en África) (Figura I.4) y dos tercios del total de casos se han producido en sólo 8 países: India (27%), China (9%), Indonesia (8%), Filipinas (6%), Pakistán (5%), Nigeria (4%), Bangladesh (4%) y Sudáfrica (3%) (WHO, 2018a).

Asimismo, sólo un 3% de los casos globales se han producido en Europa, y una cifra similar en América (WHO, 2018a).

A nivel mundial, la TB produce aproximadamente 5.000 muertes diariamente. Cada año contrae la enfermedad tuberculosa un millón de niños. Entorno a uno de cada cinco casos de TB no reciben el tratamiento adecuado, y para el año 2050 el tratamiento de las formas resistentes de TB supondrán un coste de 17 trillones de dólares (www.tballiance.org).

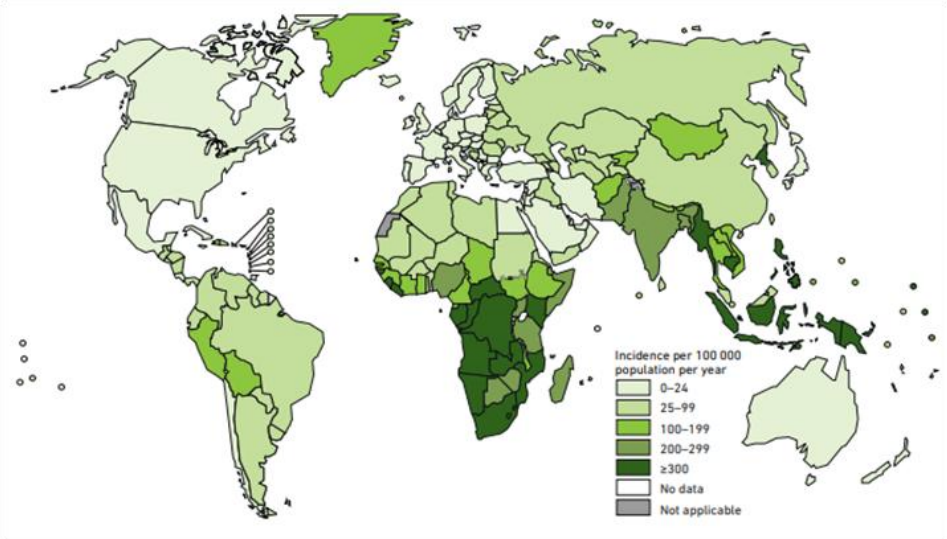

Figura I.3. Tasas de incidencia estimada de TB en el año 2017 (WHO, 2018a).

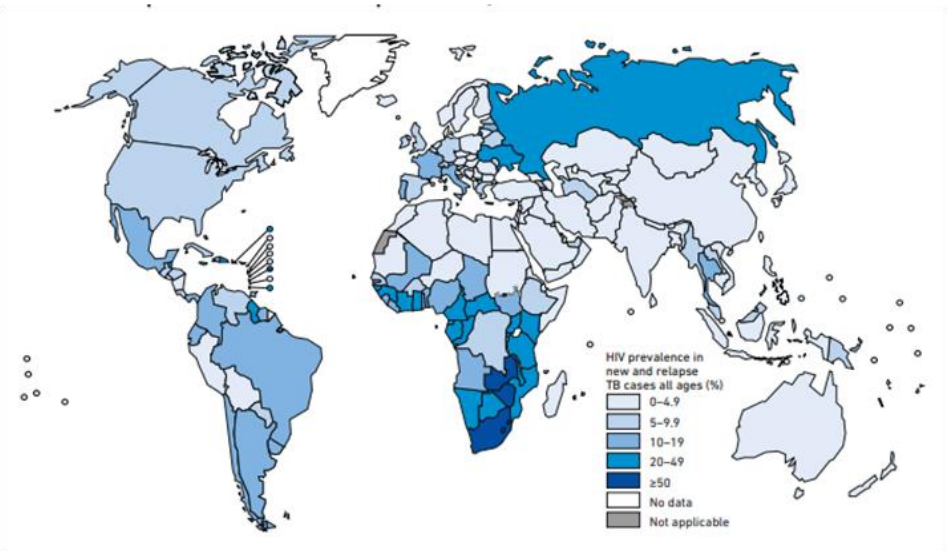

Figura I.4. Tasas de incidencia estimada de coinfección VIH-TB en el año 2017 (WHO, 2018a).

La TB es una enfermedad de declaración obligatoria en España. Las autoridades de salud pública de las Comunidades Autónomas notifican los casos al Centro Nacional de Epidemiología, a través de la Red Nacional de Vigilancia Epidemiológica (RENAVE). Una vez consolidada la información en el nivel estatal, esta se difunde a las Comunidades Autónomas, al Ministerio de Sanidad, Servicios Sociales e Igualdad, al Centro Europeo para la Prevención y Control de Enfermedades (ECDC) y a la OMS (Cano-Portero et al., 2018).

España es, desde hace años, uno de los países de Europa occidental con mayor número de casos y desde el año 2004 se dispone de información a nivel estatal sobre los casos de TB clasificados según TB-P, meningitis tuberculosa, y otras formas de TB. Los adultos jóvenes son los que presentan la tasa más elevada de TB respiratoria mientras que para la meningitis tuberculosa son los menores de 4 años los que tienen mayores tasas y en TB de otras localizaciones son los mayores de 65 años los que superan en incidencia a los demás grupos. La proporción de casos nacidos fuera de España varía mucho entre las distintas comunidades autónomas, siendo las Comunidades de Cataluña y Madrid las que presentan un porcentaje más elevado de casos extranjeros (46% cada una), mientras que Asturias es la que tiene menor proporción de casos nacidos fuera de España (3%) (Centro Nacional de Epidemiología. Instituto de Salud Carlos III. Informe epidemiológico sobre la situación de la tuberculosis en España. Año 2014. Madrid, 2015).

I.1.5.2 Estrategias de prevención y control de la enfermedad

I.1.5.2.1 Organización Mundial de la Salud (OMS)

La OMS desempeña cinco funciones básicas con respecto a la TB:

1. Elaborar políticas, estrategias y patrones con bases científicas para la prevención, atención y control de la enfermedad, y seguir de cerca su aplicación.
2. Prestar apoyo técnico a los Estados Miembros, ser agente catalizador del cambio y crear una capacidad sostenible.
3. Vigilar la situación mundial de la TB y cuantificar los progresos realizados en la atención, el control y la financiación.

4. Preparar el programa de investigaciones y estimular la producción, la traducción y la divulgación de conocimientos relevantes.
5. Facilitar las alianzas contra la TB y participar en ellas.

La estrategia "Alto a la Tuberculosis" de la OMS, adoptada por la Asamblea Mundial de la Salud en mayo de 2014, ofrece a los países un modelo para poner fin a la epidemia de TB, reduciendo la mortalidad y la incidencia de esta enfermedad y eliminando los costes asociados. Este instrumento incluye una serie de metas de impacto a nivel mundial que, por un lado prevén reducir las muertes por TB en un 90% y los nuevos casos en un 80% entre 2015 y 2030, y por otro lado evitar que ninguna familia tenga que hacer frente sin ayuda al coste económico de la enfermedad. Los tres pilares de dicha estrategia, que guía la respuesta mundial a la TB, hacen hincapié en los planteamientos específicos nacionales para alcanzar el acceso universal a la atención de alta calidad, apoyo al tratamiento y diagnóstico rápido y temprano de todas las formas de TB, incluidas la TB farmacorresistente, la coinfección con VIH, el tratamiento de comorbilidades, así como la terapia preventiva en personas de alto riesgo. Se necesitará intensificar las acciones a diferentes niveles de gobierno y al nivel de prestación de servicios. Los líderes gubernamentales deberán encargarse de la gestión general y de mantener el objetivo de terminar con la epidemia en un puesto prioritario de su agenda. El Plan Mundial 2016-2020 es un plan de inversión de 5 años que representa la hoja de ruta para acelerar el impacto sobre la epidemia de TB y llegar a los objetivos de la estrategia “Alto a la Tuberculosis” de la OMS (Stop TB Partnership, 2016).

Si bien ha habido avances significativos en la lucha contra la TB con 54 millones de vidas salvadas desde el 2000, el daño causado por dicha enfermedad sigue siendo inmenso. En 2017, 10 millones de personas enfermaron de TB y 1,6 millones de personas perdieron la vida. Aunque los países se han comprometido a poner fin a la epidemia mundial de TB para 2030 como parte de la estrategia “Alto a la Tuberculosis”, involucrar al sector privado y el despliegue de nuevas herramientas, junto con todas las demandas operativas de la prestación de servicios a gran escala puede contribuir a aliviar la pesada carga de los planes públicos nacionales de acción contra la TB. Evaluaciones de informes emitidos por diversos países y distintos proyectos han demostrado que enfoques mixtos público-privados supondrían un aumento en la

detección de casos y asegurarían mejores resultados en el tratamiento contra la TB (WHO, 2018b).

Por otra parte, en cuanto a los casos de TB que afectan a los sectores más jóvenes de la población mundial, en 2013 se publicó la primera hoja de ruta que comenzó a dar importancia a la epidemia de TB infantil después de décadas de abandono (WHO, 2013). Actualmente, estamos más cerca de una generación de niños libres de TB, ya que tenemos una visión más clara de lo que se necesita, cómo hacerlo, y las acciones prioritarias e inversiones que se requieren con urgencia. La hoja de ruta de 2018 incorpora una población crítica adicional: los adolescentes (WHO, 2018c). En el mundo, se ha pasado por alto en gran medida a los adolescentes, sin embargo, con edades comprendidas entre los 10 y los 19 años, los adolescentes corren riesgo de contraer TB y representan una población importante para el control de la TB, ya que a menudo presentan TB infecciosa y con frecuencia tienen múltiples contactos en entornos públicos, tales como escuelas y otras instituciones educativas. La nueva hoja de ruta para acabar con la TB en niños y adolescentes está destinada a una amplia audiencia, y se debe fomentar su adaptación por parte de los países de acuerdo con los contextos nacionales. Se anticipa que será utilizado por los responsables políticos mundiales, regionales y nacionales (WHO, 2018 c, d).

I.1.5.2.2 Alianza contra la TB ("TB Alliance")

La Alianza contra la TB es una organización sin ánimo de lucro que se dedica al descubrimiento y desarrollo de un tratamiento contra la TB que sea más eficaz, más rápido, asequible y que se encuentre a disposición de aquellos que lo necesiten. Estos nuevos tratamientos aportarían salud, esperanza y prosperidad a millones de personas en el mundo. Desde su fundación en el año 2000, la Alianza contra la TB ha liderado la búsqueda y desarrollo mundial de nuevos tratamientos contra la TB. La Figura I.5 recoge algunos datos de la situación actual y futura de la epidemia de TB (www.tballiance.org).

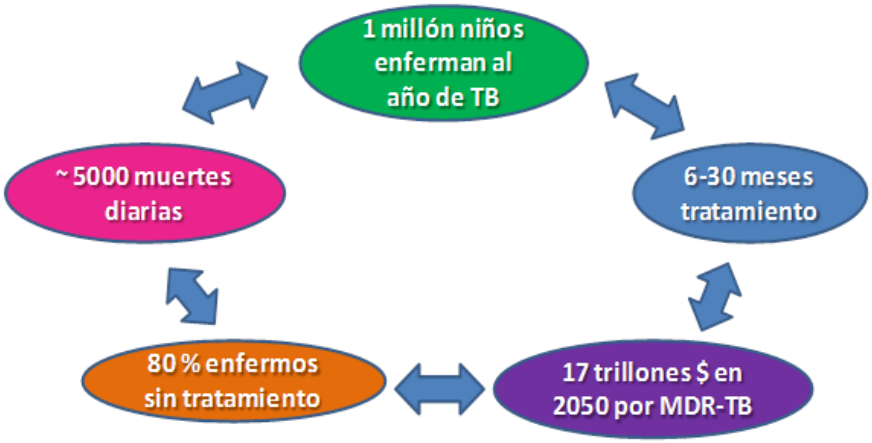

Figura I.5. Datos epidemiológicos de la TB, según datos de la Alianza contra la TB (www.tballiance.org).

I.1.5.2.3 Estrategias nacionales y regionales

Las Sociedades Científicas Sanitarias de la Comunidad Autónoma de Andalucía (Sociedad Andaluza de Salud Pública (SASPAS-Hipatia), Sociedad Andaluza de Epidemiología (SAE), Sociedad Andaluza de Medicina Preventiva y Salud Pública (SAMPSP), Sociedad Andaluza de Medicina de Familia y Comunitaria (SAMFyC), Asociación Andaluza de Enfermería Comunitaria (ASANEC), Sociedad Española de Médicos de Atención Primaria (SEMERGEN- Andalucía), Sociedad Andaluza de Medicina Interna (SADEMI), Asociación Española de Trabajo Social y Salud (AETS y S Andalucía), Sociedad Andaluza de Microbiología y Parasitología Clínica (SAMPAC), Sociedad Andaluza de Enfermedades Infecciosas (SAEI) y Asociación de Neumología y Cirugía Torácica del Sur (NEUMOSUR) juntos con los responsables de las políticas, la Organización Mundial de la Salud, las Administraciones Sanitarias y de Servicios Sociales, los proyectos de financiación y Entidades de Cooperación al Desarrollo, las ONGs y la Sociedad Civil, declaran:

"1. Que la TB es la enfermedad infecciosa que ha causado el mayor número de muertes en la historia de la humanidad y continúa siendo responsable de cerca de 1,5 millones de muertes al año, que a menudo afectan a los más vulnerables, y que debería ser considerada una prioridad política global.

2. Que el ritmo actual de progreso en la lucha contra la TB es demasiado lento, de manera que la enfermedad, de mantenerse el actual ritmo, seguirá siendo una amenaza para el bienestar social y económico de millones de ciudadanos de todo el mundo en los años venideros. Por ello es necesario incrementar los esfuerzos para conseguir que los avances consigan disminuir o enlentecer el actual progreso de la enfermedad. Los gobiernos tienen que implicarse aún más en el control de la enfermedad.

3. Que la TB resistente demuestra el fracaso colectivo en el abordaje correcto de la enfermedad; impone a menudo una insoportable carga de tratamiento en los pacientes; amenaza con generar el retroceso del progreso contra la enfermedad a través del grave costo de millones de vidas y debería ser el foco de acción inmediata.

4. Que los medicamentos actuales para el tratamiento, las vacunas y los diagnósticos resultan insuficientes y que el mercado comercial para el desarrollo farmacéutico ha fallado a los pacientes con TB. La industria farmacéutica debe aliarse con los gobiernos en la fabricación y suministro de los medicamentos, especialmente en los países pobres.

5. Que la TB impone a los pacientes una carga triple; combina el devastador impacto en la salud de la enfermedad en si misma, la dura carga del tratamiento, y el aislamiento de la exclusión social que es impulsada por el estigma y el miedo; y que estos problemas deben abordarse de manera integral por los programas nacionales de salud.

6. Que las coinfecciones de TB, como el VIH y la diabetes, componen los desafíos que enfrentan los pacientes durante el tratamiento, lo que dificulta los esfuerzos para reducir las tasas de enfermedad, el aumento de la mortalidad y la morbilidad asociada a la TB y que los sistemas de salud deben integrar los programas de coinfecciones clave.

7. Por lo tanto, se necesita compromiso a utilizar todos los medios para instar una acción sostenida, para asegurar los recursos necesarios para luchar contra la TB y conseguir la priorización de la enfermedad en las agendas políticas.

8. Exigir que todos los pacientes, independientemente de quiénes son, de dónde viven, o de su capacidad de pago, tengan acceso a un diagnóstico rápido, preciso y un tratamiento de alta calidad y que el diagnóstico y el tratamiento de la TB nunca dé como resultado el empobrecimiento de los pacientes o de sus familias.

9. Hacer un llamamiento para tener un modelo de investigación y desarrollo que esté impulsado por la necesidad de la Salud Pública y la voluntad de apoyar y mejorar los conductos existentes que desesperadamente necesitan los nuevos medicamentos, los diagnósticos y las vacunas, para garantizar que los nuevos tratamientos sean accesibles y asequibles para los pacientes que los necesitan.

10. Insistir en que los pacientes y los grupos vulnerables sean posicionados en el centro de la respuesta a la enfermedad, en el apoyo a la participación de las comunidades y grupos de la sociedad civil, en todos los aspectos de la prevención de la TB, detección y tratamiento, acabando con el estigma y dando a los pacientes una voz más fuerte en la respuesta a la epidemia".

Creo que merece destacar el punto cuarto que señala la responsabilidad de la industria farmacéutica en el desarrollo insuficiente de medicamentos y productos sanitarios para el tratamiento y diagnóstico de la TB. Sin embargo, la culpa de la investigación y desarrollo insuficiente en este sentido no puede hacerse caer solamente sobre la industria, que no lo olvidemos se mueve en un mundo en el que el mercado es el patrón, sino que también los centros de investigación públicos, nacionales e internacionales, deberían y deben hacer un esfuerzo por cubrir estas necesidades. Como se ha enunciado anteriormente, es necesario un enfoque mixto público-privado para aumentar la detección de casos y asegurar mejores resultados en el tratamiento contra la TB (WHO, 2018b).

I.1.6 DIAGNÓSTICO

I.1.6.1 Prueba de la Tuberculina (Test de Mantoux)

La prueba estándar para el diagnóstico de la infección tuberculosa es la prueba de la Tuberculina, en la que se utiliza un derivado proteico purificado de bacilos

tuberculosos. Se realiza una inyección intradérmica y se determina la hipersensibilidad mediante la medida del diámetro de la induración producida en caso de ser positiva la prueba (Huebner et al., 1993). Es el método más antiguo y continúa siendo de elección, sin embargo tiene múltiples limitaciones como son el riesgo de falsos negativos en personas inmunodeprimidas, dificultad para su correcta ejecución y subjetividad en la interpretación de los resultados (Scott et al., 2018).

I.1.6.2 Inmunoensayos

Con el objetivo de superar las limitaciones de la prueba de la Tuberculina se han desarrollado diferentes técnicas diagnósticas de laboratorio. Se basan en la detección en sangre de una citocina fundamental en el control de la infección, llamada interferon gamma. Éste se libera como respuesta a la estimulación *in vitro* de las células T sensibilizadas con antígenos específicos de *Mtb*. Dichas técnicas se conocen como IGRA (Interferon Gamma Release Assay) (Pai et al., 2014). Como principales ventajas con respecto a la prueba de la Tuberculina, las técnicas IGRA permiten discriminar a los individuos infectados por *Mtb* de los vacunados o infectados por otras micobacterias y pueden repetirse inmediatamente sin el riesgo de estimulación de la inmunidad. El principal inconveniente de las IGRA es su mayor coste económico respecto a la prueba de la tuberculina (Auguste et al., 2017; Gutiérrez et al., 2017).

I.1.6.3 Radiología y técnicas de imagen

a) Radiografía

Los hallazgos en la radiografía, aunque inespecíficos, nos informan de posibles alteraciones estructurales del pulmón y del resto del tórax que pueden hacer sospechar acerca de la existencia de TB pulmonar (Pande et al., 2016).

b) Técnicas isotópicas

Estiman la actividad inflamatoria, permitiendo una detección temprana de la enfermedad. Su principal inconveniente consiste en que los hallazgos resultantes son inespecíficos para el diagnóstico de la TB de localización extratorácica. De entre ellas destacan la gammagrafía y la tomografía por emisión de positrones (Allwood et al., 2015; Malherbe et al., 2016).

I.1.6.4 Diagnóstico microbiológico

a) Técnicas de microscopía

La técnica más rápida, sencilla y accesible para realizar el diagnóstico rápido de la TB es la tinción ácido-alcohol resistente. Su principal limitación es la baja sensibilidad, pues para que el diagnóstico sea positivo deben existir entre 5.000–10.000 bacilos/mL en la muestra, por lo que una baciloscopia negativa nunca descarta la enfermedad. Resulta también de gran utilidad para realizar un seguimiento de la eficacia del tratamiento ya que el número de bacterias presentes en la tinción disminuirá si el tratamiento es eficaz (Davis et al., 2013).

b) Técnicas de cultivo

El cultivo es la prueba de referencia debido a su alta sensibilidad (capaz de detectar entre 10–100 bacterias/mL de muestra) y capacidad de aislar e identificar la micobacteria presente en la muestra. Su principal inconveniente es la lentitud en la obtención de resultados positivos, ya que *Mtb* es una micobacteria de crecimiento lento (Rageade et al., 2014; Asmar et al., 2015).

c) Antibiograma

El estudio de sensibilidad de *Mtb* se basa en la detección en el cultivo de un porcentaje superior al 1% de bacterias resistentes en comparación con un control de crecimiento sin antibiótico (Kaul et al., 2015).

I.1.6.5 Métodos moleculares

Se basan en la amplificación de fragmentos genéticos específicos de *Mtb* directamente en las muestras clínicas. Actualmente su principal interés teórico es su potencialidad en el diagnóstico rápido de enfermedad tuberculosa con una sensibilidad superior a la baciloscopia, considerada la técnica rápida de referencia (Lin y Desmond, 2014).

I.1.6.6 Otros métodos de diagnóstico:

a) Histología

La lesión típica de TB en los tejidos es la inflamación granulomatosa con necrosis central. Se considera un hallazgo de elevada especificidad y justifica iniciar tratamiento

antituberculoso. También pueden observarse con frecuencia granulomas sin necrosis (Montenegro et al., 2015).

b) Determinación de Adenosina Desaminasa (ADA) y otros parámetros bioquímicos y citológicos

Cuando la TB se localiza en serosas se desarrolla una respuesta inflamatoria característica. Diversos parámetros citológicos y bioquímicos producto de esta reacción son útiles en el diagnóstico, siendo la determinación de adenosina desaminasa (ADA) el que mayor información aporta, ya que ésta es una enzima que interviene en el catabolismo de las purinas, producida por monocitos y macrófagos, y que se encuentra en concentración elevada en la TB (González-Martín et al., 2010).

I.1.6.7 Respuesta de la OMS

La OMS publicó en mayo de 2018 la primera edición de la Lista Modelo de Pruebas Esenciales para el Diagnóstico *in vitro* (EDL, siglas en inglés), en reconocimiento a que el diagnóstico *in vitro* es un componente esencial en el desarrollo de la cobertura universal de salud, en el enfrentamiento de las emergencias de salud, y en la promoción de poblaciones más saludables, todas prioridades estratégicas del XIII Programa General de Trabajo de la OMS (2019–2023) (WHO, 2018e). En dicha EDL se incluyen pruebas para diagnosticar enfermedades comunes, como la diabetes tipo 2, y aquellas que más muertes causan a nivel mundial, como es el caso de la TB. En el caso de la TB, la EDL incluye, entre otros, pruebas diagnósticas comerciales centradas en la detección de resistencias a fármacos antituberculosos de primera y segunda línea, inmunoensayos (IGRAs) y la prueba de la tuberculina para la detección de TB latente (Gilpin y Weyer, 2018).

I.1.7 TRATAMIENTO Y PREVENCIÓN DE LA ENFERMEDAD TUBERCULOSA

Para conseguir controlar la TB es necesario instaurar un tratamiento correcto, prolongado y supervisado, cuyos objetivos fundamentales pueden resumirse en (WHO, 2018a):

1. Eliminación rápida de los bacilos tuberculosos que están multiplicándose de forma activa. Se utilizan los fármacos más bactericidas: isoniazida (INH) y rifampicina (RIF).
2. Evitar la aparición de resistencias bacteriana con asociaciones de fármacos, especialmente INH, RIF y etambutol (ETB).
3. Esterilización de las lesiones tuberculosas utilizando RIF, pirazinamida (PIR) e INH.

Durante muchos siglos la TB fue una enfermedad devastadora hasta la inclusión de la estreptomicina en la terapéutica de la enfermedad tuberculosa en la década de los cuarenta, seguida de INH y posteriormente de RIF y ETB. Concretamente, la quimioterapia antituberculosa se inició en 1944 cuando se instauró el tratamiento con el recién descubierto agente antibiótico estreptomicina (Smith y McClosky, 1945). La administración de los antibióticos en forma de monoterapia daba lugar a resistencias. Sin embargo, la asociación de dos fármacos, estreptomicina y ácido para-aminosalicílico (p-aminosalicílico), retardaba o eliminaba el desarrollo de la temida resistencia bacteriana (Graessle y Pietrowski, 1949). Fue en 1952 cuando la introducción de la INH hizo curables la mayor parte de los casos de TB y supuso un enorme éxito (Albert, 1956). Posteriormente, la RIF (1970) acortó notablemente la duración del tratamiento, empleando INH y RIF de forma combinada. Con posterioridad se han incorporado otros fármacos al tratamiento de la enfermedad, dando lugar a una terapéutica que contempla el uso combinado de varios principios activos durante periodos más o menos prolongados.

I.1.7.1 Fármacos antituberculosos

I.1.7.1.1 Fármacos antituberculosos de primera línea

La Tabla I.I muestra las fórmulas de los cuatro fármacos antituberculosos de primera línea, así como sus intervalos de mínima concentración inhibitoria (MIC), expresada en (µg/mL) (Pham et al., 2015).

Tabla I.I. Fármacos antituberculosos de primera línea.

Fármaco	Fórmula	MIC (µg/mL)
Isoniazida (INH)	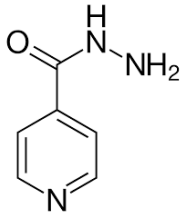	0,01 – 0,2
Rifampicina (RIF)	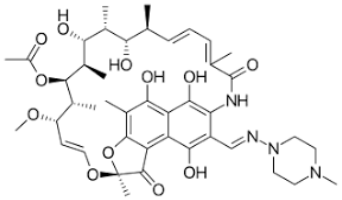	0,05 – 0,5
Etambutol (ETB)	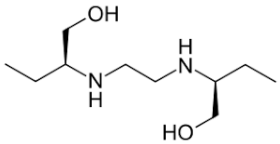	1 – 5
Pirazinamida (PIR)	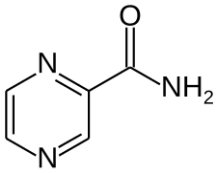	20 – 100 (pH 5,5 - 6)

En el anexo 6 del documento "Guidelines for treatment of drug-susceptible tuberculosis and patient care 2017 update", titulado "Essential first-line antituberculosis drugs", (WHO, 2017), se recoge la información clínica fundamental de los cuatro fármacos que aparecen en la Tabla I.I, que de forma resumida señala:

a) Isoniazida: hidracida del ácido isonicotínico o isonicotinilhidrazina.

- Actividad y mecanismo de acción: es un profármaco activado por la hemoproteína catalasa-peroxidasa KatG. Fármaco con actividad bactericida contra las micobacterias de crecimiento rápido y bacteriostática si las micobacterias son de crecimiento lento. Su mecanismo de acción se basa en la inhibición de la proteína InhA, una enoil-ACP-reductasa directamente relacionada con la síntesis de los ácidos grasos. Los mecanismos de resistencia aparecen asociados a mutaciones en los genes de la molécula diana (InhA) o la activadora (KatG). Es el fármaco antituberculoso más ampliamente utilizado debido a que es el que presenta un menor valor de MIC. Su acción es muy específica, siendo activa sólo contra determinadas especies del género *Mycobacterium*, siendo poco

eficaz cuando la especie bacteriana presenta baja actividad de la enzima KatG (WHO, 2017).

- Administración y características farmacocinéticas: su administración se realiza principalmente por vía oral, pudiéndose administrar también por vía intramuscular en casos muy graves (WHO, 2017). Debido a su elevada solubilidad y baja permeabilidad, se engloba dentro de la clase III del Sistema de Clasificación Biofarmacéutica (SCB) (Kasim et al., 2004). La dosis recomendada para adultos es de 5 mg/kg (4-6 mg/kg) al día. La vida media en plasma está genéticamente determinada y varía entre menos de 1 hora para acetiladores rápidos y más de 3 horas para acetiladores lentos, dependiendo del tipo de polimorfo de la enzima N-arilamina acetiltransferasa predominante en el paciente (Manning et al., 2017; WHO, 2017). Aproximadamente, el 50% de la población negra y el 100% de los europeos son acetiladores lentos, mientras que la mayoría de asiáticos son rápidos. La determinación de la velocidad de acetilación se emplea en el establecimiento de un régimen de dosificación (del orden de 3 mg/kg para los acetiladores lentos y del orden de 6 mg/kg para los acetiladores rápidos). Tras una administración oral se alcanza, entre 1-2 horas, la concentración plasmática máxima. Su distribución es amplia y difunde rápidamente en los fluidos orgánicos. Atraviesa la barrera placentaria y también se encuentra en la leche, permaneciendo a concentraciones similares a las plasmáticas. Se metaboliza, principalmente, a través de la acetilación y la deshidrazinación, con una elevada variabilidad interindividual (Florey, 1979). La metabolización cursa a través de la transformación en acetilisoniazida que posteriormente se hidroliza en acetilhidrazina para transformarse parcialmente en un metabolito inestable que es responsable de la hepatotoxicidad de la INH. Del 75 al 95% de la dosis de INH se excreta en la orina en las primeras 24 horas tras su administración, principalmente en forma de metabolitos inactivos. En pequeñas cantidades se excreta por las heces y saliva (Davies y Nuermberger, 2008; WHO, 2017).

- Precauciones y contraindicaciones: en cuanto a las precauciones a tener en cuenta, la monitorización clínica (y las pruebas de función hepática, si es posible) se deben realizar durante el tratamiento de personas con enfermedad hepática preexistente. Personas en riesgo de neuropatía periférica, como resultado de la desnutrición, la dependencia crónica del alcohol, la infección por el VIH, el embarazo, lactancia materna, insuficiencia renal o diabetes, deben recibir piridoxina (10 mg/día). Por

neuropatía periférica establecida, la piridoxina debe administrarse a una dosis de 50-75 mg/día (WHO, 2017). Está contraindicada la INH en casos de personas con hipersensibilidad conocida y pacientes con enfermedad hepática inestable y activa (con ictericia) (WHO, 2017). Los síntomas causados por una sobredosis (náuseas, vómitos, mareos, visión borrosa y dificultad para hablar) pueden manifestarse en un intervalo de tiempo de entre 30 minutos a 3 horas de producirse la sobredosis. La emesis y el lavado gástrico, el carbón activo, los antiepilépticos y el bicarbonato de sodio intravenoso son útiles para tratar las sobredosis transcurridas pocas horas de la ingestión. Posteriormente, se debe recurrir a hemodiálisis (WHO, 2017). No se conoce que la INH sea nociva en el embarazo. La suplementación con piridoxina está recomendada para todas las mujeres embarazadas o lactantes que tomen INH.

- Reacciones adversas: la INH generalmente se tolera bien a las dosis recomendadas, sin embargo, reacciones de hipersensibilidad sistémica o cutánea ocurren ocasionalmente durante las primeras semanas de tratamiento. El riesgo de neuropatía periférica se excluye si las personas vulnerables reciben suplementos diarios de piridoxina. Otras formas menos comunes de alteración del sistema nervioso, incluida la neuritis óptica, psicosis tóxica y convulsiones generalizadas, pueden desarrollarse en las últimas etapas del tratamiento. La hepatitis sintomática es una reacción poco común pero potencialmente grave que generalmente puede ser evitada retirando rápidamente el tratamiento. Más a menudo, sin embargo, un aumento asintomático en las concentraciones séricas de transaminasas hepáticas al inicio del tratamiento no son clínicamente significativas y generalmente se resuelven espontáneamente a medida que el tratamiento continúa. Síndromes similares al lupus, la pelagra, la anemia y la artralgia son otros efectos adversos raros (Madigan et al., 2015; Rang, 2016; WHO, 2017).
- Interacciones: la INH inhibe el metabolismo de ciertos fármacos, incluyendo carbamazepina, benzodiazepinas metabolizadas por oxidación (como triazolam), paracetamol, valproato, antidepresivos serotoninérgicos, disulfiram, warfarina y teofilina (WHO, 2017).
- Almacenamiento: los comprimidos deben mantenerse en recipientes bien cerrados, mientras que las soluciones para inyección deben almacenarse en ampollas, en ambos casos, protegidas de la luz (WHO, 2017).

b) Rifampicina:

- Actividad y mecanismo de acción: derivado semisintético de la rifamicina. Tiene acción bactericida y un potente efecto esterilizante contra los bacilos tuberculosos intra y extracelulares, ya que penetra en los fagocitos y puede destruir microorganismos intracelulares. Su mecanismo de acción se basa en su capacidad de unión e inhibición de la ARN polimerasa dependiente del ADN de las células procariotas, sin afectar a la de las eucariotas (WHO, 2017). Es uno de los fármacos anti-TB más activos que se conocen y es eficaz también frente a la mayoría de las bacterias Gram positivas, así como muchas Gram negativas.

- Administración y características farmacocinéticas: se administra por vía oral en forma de cápsulas y comprimidos. Es liposoluble y se engloba dentro de la clase II del SCB por su baja solubilidad y elevada permeabilidad (Kasim et al., 2004). También está disponible para administración intravenosa para personas en estado crítico. Después de la administración oral, se absorbe rápida y prácticamente completamente y se distribuye a través de los tejidos celulares y fluidos corporales. Si las meninges están inflamadas, cantidades significativas entran en el líquido cefalorraquídeo. Con una dosis de 600 mg (aconsejada por la OMS; WHO, 2018a), las concentraciones séricas máximas (del orden de 10 μg/mL) aparecen entre 1,5 y 3 horas después de la administración. La vida media de la RIF para la dosis de 600 mg es del orden de 2,5 horas. Aproximadamente el 80% de la RIF se transporta en sangre unida a proteínas plasmáticas, principalmente albúmina (Florey, 1979). Se metaboliza por desacetilación para dar desacetilrifampicina, más polar y microbiológicamente activa, que se excreta por orina sin ser reabsorbida (Florey, 1979). La RIF se excreta casi por igual en la bilis y la orina. La administración de RIF a los recién nacidos y niños es seguida por niveles sanguíneos generalmente más bajos que los encontrados en adultos con los mismos niveles de dosis (Davies y Nuernberger, 2008). La RIF compite con la bilirrubina y otras sustancias para la excreción biliar, dando lugar a valores de retención de bilirrubina transitorios y reversibles. Para adultos se recomienda una dosis de 10 mg/kg (8-12 mg/kg) al día.

- Precauciones y contraindicaciones: dado que la resistencia se desarrolla fácilmente, la RIF siempre debe administrarse en combinación con otros agentes antimicobacterianos efectivos. Se puede desarrollar resistencia de forma rápida mediante un proceso de un solo paso en el que una mutación cromosómica modifica su sitio de unión en la ARN

polimerasa dependiente de ADN bacteriana. La RIF debe administrarse preferiblemente al menos 30 minutos antes de las comidas, para evitar que disminuya su absorción (WHO, 2017). Está contraindicada en pacientes con hipersensibilidad conocida a las rifamicinas y enfermedad hepática inestable y activa (con ictericia). Las personas que reciben tratamiento deben ser advertidas de que el tratamiento puede causar una coloración rojiza de todas las secreciones corporales (orina, lágrimas, saliva, sudor, semen y esputo). Su uso durante el embarazo debe acompañarse de vitamina K1 debido al riesgo de hemorragia postnatal (WHO, 2017). En caso de sobredosis, el lavado gástrico puede ser valioso si se realiza dentro de unas pocas horas después de la ingestión. Dosis muy altas de RIF pueden deprimir el funcionamiento del sistema nervioso central. No hay un antídoto específico (WHO, 2017).

- Reacciones adversas: los efectos adversos son poco frecuentes, siendo en su mayoría erupciones cutáneas, fiebre y molestias gastrointestinales. Sin embargo, se han descrito lesiones hepáticas con ictericia, que resultaron ser de gravedad y que hacen imprescindible una evaluación previa de la función hepática antes de empezar el tratamiento con RIF. La mayoría de las personas tolera bien la RIF a las dosis actualmente recomendadas, pero puede causar reacciones gastrointestinales (dolor abdominal, náuseas y vómitos) y prurito con o sin erupción. Aumentos moderados en las concentraciones séricas de bilirrubina y transaminasas, que son comunes al comienzo del tratamiento, a menudo son transitorios y sin importancia clínica. Sin embargo, pueden aparecer hepatitis dosis-dependientes, potencialmente fatales (WHO, 2017).
- Interacciones: la RIF induce las enzimas hepáticas responsables del metabolismo de muchos fármacos incrementando la velocidad de degradación de numerosos fármacos (Madigan et al., 2015; Rang, 2016; WHO, 2017).
- Almacenamiento: las cápsulas y comprimidos deben mantenerse en recipientes bien cerrados, protegidos de la luz.

c) Etambutol:

- Actividad y mecanismo de acción: derivado sintético de la 1,2-etanodiamina, con efecto bacteriostático frente a *Mtb* y otras micobacterias. Se usa en combinación con otros fármacos anti-TB para prevenir o retrasar la aparición de resistencias. Su

mecanismo de acción se basa en su capacidad de penetración al interior de las micobacterias y su acción bacteriostática transcurre tras 24 horas, probablemente debida a la inhibición de la síntesis del arabinogalactano de la pared celular bacteriana. También se han observado efectos en el metabolismo del RNA, el transporte de ácidos micólicos a la pared celular y la síntesis fosfolipídica. No se puede administrar como monoterapia debido a que desarrolla resistencias rápidamente.

- Administración y características farmacocinéticas: se administra principalmente por vía oral. Debido a su elevada solubilidad y baja permeabilidad, se engloba dentro de la clase III del SCB (Kasim et al., 2004). También puede administrarse por vía intravenosa. Se absorbe fácilmente en el tracto gastrointestinal. Las concentraciones plasmáticas alcanzan su máximo en 2-4 horas y posee una vida media plasmática de 3-4 horas. Se metaboliza por la acción de la enzima alcohol deshidrogenasa que oxida los grupos alcohólicos presentes en la molécula de fármaco a aldehídos y posteriormente a ácidos dicarboxílicos, dando lugar a metabolitos muy polares, inactivos farmacológicamente y que se excretan por vía urinaria. Alrededor del 20% se elimina por las heces en forma no modificada (WHO, 2017). La dosis diaria recomendada vía oral para adultos es de 15 mg/kg (15-20 mg/kg) (WHO, 2017).
- Precauciones y contraindicaciones: está contraindicada su administración en casos de hipersensibilidad conocida y neuritis óptica preexistente. En cuanto a las precauciones, se recomienda examen ocular antes y durante el tratamiento. Siempre que sea posible, la función renal debe evaluarse antes del tratamiento. La concentración plasmática de ETB debe controlarse si el aclaramiento de creatinina es menor a 30 mL/min. El ETB no es dañino en el embarazo (WHO, 2017). En caso de sobredosis, la emesis y el lavado gástrico pueden ser eficaces si se realizan pocas horas después de la ingestión. Posteriormente, la diálisis puede ser útil. No hay un antídoto específico.
- Reacciones adversas: los efectos adversos son poco frecuentes y el más importante es la neuritis óptica, que es dosis dependiente y ocurre de forma más probable en pacientes con la función renal alterada. Se producen trastornos visuales que inician como una ceguera a los colores rojo y verde y que evolucionan finalmente hacia una disminución de la agudeza visual. Otros eventos adversos raros incluyen la reacción cutánea generalizada, la artralgia y, muy raramente, hepatitis (Madigan et al., 2015; Rang, 2016; WHO, 2017).

- Interacciones: la OMS no recoge interacciones de ETB con otros fármacos (WHO, 2017).
- Almacenamiento: los comprimidos deben almacenarse en contenedores herméticamente cerrados (WHO, 2017).

d) Pirazinamida:

- Actividad y mecanismo de acción: análogo sintético de la nicotinamida. Es un profármaco que se transforma en ácido pirazinoico por una enzima (pirazinamidasa). Es débilmente bactericida contra *Mtb*, pero tiene una potente actividad de esterilización, especialmente en el ambiente intracelular ácido de macrófagos y en áreas de inflamación aguda. Es altamente efectivo durante los primeros dos meses de tratamiento, cuando la inflamación es más aguda, y su uso ha acortado los regímenes de tratamiento y reducido el riesgo de recaída. Resulta inactiva a pH neutro, pero tuberculostática a pH ácido. Es eficaz frente a los microorganismos intracelulares alojados en los macrófagos, ya que una vez fagocitados, se acumulan en los fagolisosomas donde el pH es ácido. Su mecanismo de acción se basa en la inhibición de la síntesis de ácidos grasos bacterianos (WHO, 2017). La resistencia se desarrolla rápidamente, pero no existe resistencia cruzada con INH.
- Administración y características farmacocinéticas: se administra por vía oral, absorbiéndose rápidamente y distribuyéndose por todo el organismo, penetrando incluso en las meninges. Debido a su elevada solubilidad acuosa y baja permeabilidad, la PIR se engloba dentro de la clase III del SCB (Kasim et al., 2004). Las concentraciones séricas de PIR aumentan en proporción a la dosis y existe poca variación intraindividual en la absorción o la excreción (WHO, 2017). Las concentraciones plasmáticas máximas se alcanzan en dos horas, y la vida media plasmática es aproximadamente 10 horas. El metabolismo se produce en los hepatocitos. Los principales metabolitos de la PIR son el ácido pirazinoico, la 5-hidroxi-pirazinamida, el ácido 5-hidroxi-pirazinoico y el ácido pirazinúrico. Se excreta principalmente por vía renal y el porcentaje acumulado de fármaco excretado en orina después de 24 horas alcanza sólo el 40% (Florey, 1979). En adultos se administra generalmente durante los primeros 2-3 meses de tratamiento una dosis diaria de 25 mg/kg (20-30 mg/kg).

- Precauciones y contraindicaciones: las personas con diabetes y enfermedad hepática preexistente deben ser monitorizadas durante el tratamiento. Está contraindicado su uso en casos de hipersensibilidad conocida, enfermedad hepática inestable y activa (con ictericia) y porfiria. La PIR puede usarse de manera segura durante el embarazo (WHO, 2017). En caso de una sobredosis de PIR, han sido reportados daño hepático agudo e hiperuricemia. El tratamiento es esencialmente sintomático. En caso de sobredosis, la emesis y el lavado gástrico pueden ser eficaces si se realizan pocas horas después de la ingestión. No hay un antídoto específico (Madigan et al., 2015; Rang, 2016; WHO, 2017).
- Reacciones adversas: la PIR puede causar intolerancia gastrointestinal. Las reacciones de hipersensibilidad son raras, pero algunas personas se quejan de un leve enrojecimiento de la piel. Los aumentos moderados en las concentraciones de transaminasas son comunes durante las primeras fases de tratamiento, mientras que la hepatotoxicidad grave es rara. Como la secreción tubular renal está inhibida, puede producirse hiperuricemia, que a menudo es asintomática, pero ocasionalmente puede producirse gota que requiere tratamiento con alopurinol. Puede ocurrir artralgia, especialmente de los hombros, y responde a analgésicos simples (especialmente aspirina). Los eventos adversos raros incluyen anemia sideroblástica y dermatitis fotosensible (WHO, 2017).
- Interacciones: la OMS no recoge interacciones de PIR con otros fármacos (WHO, 2017).
- Almacenamiento: los comprimidos deben almacenarse en recipientes bien cerrados, protegidos de la luz (WHO, 2017).

I.1.7.1.2 Fármacos antituberculosos de segunda línea

En mayo de 2016 la OMS publicó una guía de fármacos anti-TB de segunda línea divididos en cuatros grupos (A, B, C, D) ordenados de mayor a menor eficacia (WHO, 2016a). La Tabla I.II recoge los distintos principios activos que se incluyen en cada grupo:

Tabla I.II. Clasificación fármacos antituberculosos de segunda línea (WHO, 2016a).

Grupo A: Fluoroquinolonas	Levofloxacina Moxifloxacina Gatifloxacina
Grupo B: Fármacos anti-TB de segunda línea inyectables	Amikacina Capreomicina Kanamicina Estreptomicina
Grupo C: Otros fármacos anti-TB de segunda línea incluidos en la Lista Principal de Medicamentos Esenciales	Etionamida/protionamida Cicloserina/terizidona Linezolid Clofacimina
Grupo D: Otros (no forman parte del tratamiento principal de la TB-MDR)	**D1:** PIR, ETB, INH a altas dosis
	D2: Bedaquilina Delamanid
	D3: Ácido p-aminosalicílico Imipenem-cilastatin Meropenem Amoxicilina-clavulanato Tioacetazona

- **Grupo A. Fluoroquinolonas**

El tratamiento con fluoroquinolonas de última generación (definidas para estas pautas como altas dosis de levofloxacina, moxifloxacina y gatifloxacina) mejora significativamente los resultados del tratamiento en adultos con TB-MDR. Este grupo de fármacos se considera el componente más importante del régimen contra la TB-MDR y los beneficios de su uso superan los riesgos potenciales. Por lo tanto, deberían siempre incluirse a menos que haya evidencia de contraindicación absoluta para su uso (WHO, 2016a).

- **Grupo B. Agentes inyectables de segunda línea**

Se recomienda que los adultos con TB-MDR siempre reciban un agente inyectable de segunda línea como parte de su régimen a menos que haya una contraindicación

importante. En niños con formas leves de enfermedad, sin embargo, los daños asociados con este grupo de fármacos pueden ser mayores que los beneficios potenciales y por lo tanto, los agentes inyectables pueden excluirse para los niños. Amikacina, capreomicina o kanamicina se emplearan preferentemente, y cuando no sea posible se sustituirán por estreptomicina. La pérdida de audición y la nefrotoxicidad son las reacciones adversas más frecuentes y graves de estos fármacos (WHO, 2016a).

- **Grupo C. Otros agentes de segunda línea**

El régimen de tratamiento de TB-MDR incluye, asimismo, dos o más de los siguientes cuatro principios activos: etionamida (o protionamida), cicloserina (o terizidona), linezolid y clofazimina. La etionamida puede usarse indistintamente con protionamida, y la terizidona puede utilizarse en lugar de cicloserina. La elección de cuáles incluir está determinado por el equilibrio de efectos deseables a indeseables. La etionamida y la protionamida causan trastornos gastrointestinales, en particular vómitos, y puede producir también hipotiroidismo, especialmente cuando se administran en combinación con ácido p-aminosalicílico. La cicloserina puede causar reacciones adversas neuropsiquiátricas. Las reacciones adversas de linezolid incluyen acidosis láctica, trombocitopenia y anemia. Dada la posible gravedad de las reacciones adversas asociadas con linezolid, su uso debe ir acompañado de una estrecha vigilancia de los eventos adversos. Cuando esto no sea posible, linezolid sería mejor reservarlo para pacientes con TB-MDR que tienen resistencia a otros fármacos, o pacientes con TB-XDR. La clofazimina probablemente contribuye a la función de esterilización en sustitución de la PIR, cuando esta no es efectiva. Uno de los principales efectos adversos de la clofazimina es la decoloración de la piel. La clofazimina puede prolongar el intervalo QT, por lo que se recomienda precaución cuando se usa este fármaco en combinación con otros principios activos con igual efecto (WHO, 2016a).

- **Grupo D. Agentes complementarios**:

a) El grupo D1 consiste en PIR, ETB y altas dosis de INH. Se añaden a la terapia con principios activos centrales de segunda línea, a menos que se confirme la resistencia, intolerancia o que la interacción fármaco-fármaco supere sus beneficios potenciales.

b) El grupo D2 está formado por dos nuevos principios activos lanzados en los últimos años: bedaquilina y delamanid. Cuando los resultados de los estudios en curso y los ensayos de fase III estén disponibles, la evidencia de la eficacia de estos dos nuevos principios activos serán reevaluados con respecto a los otros agentes que componen el régimen de TB-MDR.

c) El grupo D3 consiste en: ácido p-aminosalicílico, imipenem-cilastatina, meropenem, clavulanato y tioacetazona. Sólo se deben usar cuando se administre un régimen de TB-MDR con al menos cinco fármacos efectivos en la fase intensiva (es decir, cuatro fármacos básicos de segunda línea más PIR) que no se pueda componer de otro modo. El uso de ácido p-aminosalicílico está asociado con alta frecuencia a reacciones adversas y, por lo tanto, está reservado para situaciones en las que no existe la opción de usar otros fármacos. Las reacciones adversas relacionadas con ácido p-aminosalicílico incluyen trastornos gastrointestinales e hipotiroidismo (en particular cuando se administra en combinación con etionamida/protionamida). Los carbapenémicos (imipenem-cilastina o meropenem) parecen hidrolizarse más lentamente. La OMS recomienda que cuando amoxicilina-clavulánico y los carbapenémicos estén incluidos en los regímenes, siempre deben usarse juntos. La tioacetazona, que se empleaba en el pasado como fármaco de primera línea para TB se usará solamente como agente complementario, debido a las graves reacciones cutáneas que causa, y bajo una estrecha vigilancia de las reacciones cutáneas graves. Los macrólidos están asociados con la prolongación del intervalo QT, lo que sería especialmente preocupante si los pacientes reciben otros medicamentos con un riesgo similar, como moxifloxacina, clofazimina, bedaquilina o delamanid (WHO, 2016a).

I.1.7.2 Esquemas de tratamiento actuales y formas de administración

I.1.7.2.1 Nuevos enfermos de TB

Se debe utilizar una combinación de fármacos antituberculosos de primera línea durante un tiempo suficiente y administrados simultáneamente. La asociación ideal sería: dos meses de INH, RIF y PIR, seguida de cuatro meses en los que la PIR se elimina del tratamiento y se mantienen INH y RIF (WHO, 2018a). Las ventajas de este régimen son su alto nivel bactericida y esterilizante, el escaso número de fracasos y recaídas y sus mínimos efectos adversos. Sin embargo, debido al incumplimiento terapéutico es

necesario incluir otro fármaco para prevenir el desarrollo de resistencia a RIF, sobre todo en presencia de INH. Este nuevo fármaco a incluir es el ETB, que ha demostrado tener poca resistencia primaria. El esquema que recomienda la OMS para nuevos enfermos de TB incluye ETB como cuarto fármaco en la primera fase y en casos de zonas con alto nivel de resistencia inicial a INH continuar con ETB también durante la segunda fase (Tabla I.III) (WHO, 2018a).

Tabla I.III. Dosis recomendadas para nuevos enfermos de TB adultos (WHO, 2018a).

DOSIS RECOMENDADAS				
	DIARIAMENTE		3 VECES A LA SEMANA	
Fármaco	Dosis e intervalo (mg/kg de peso)	Máximo (mg)	Dosis e intervalo (mg/kg de peso)	Máximo (mg)
INH	5 (4-6)	300	10 (8-12)	900
RIF	10 (8-12)	600	10 (8-12)	600
PIR	25 (20-30)	-	35 (30-40)	-
ETB	15 (15-20)	-	30 (25-35)	-

Asimismo, se recomienda la administración conjunta en una misma forma farmacéutica en las denominadas combinaciones de dosis fijas (FDCs, por sus siglas en inglés) (WHO, 2018a).

I.1.7.2.1.1 "Fixed-dose combinations" (FDCs)

Las FDCs son formas farmacéuticas que incluyen dos o más fármacos antituberculosos de primera línea combinados en dosis fijas. En 1994, la OMS recomendó seis combinaciones de dosis con dos fármacos y dos combinaciones de dosis con tres fármacos. En 1999 se incluyó en la Lista Modelo de Medicamentos Esenciales (LMME) de la OMS una FDC que incluía los cuatro fármacos antituberculosos de primera línea (INH, RIF, ETB, PIR) de administración diaria vía oral para adultos y tres FDCs de uso pediátrico. Desde 1999 hasta la actualidad, numerosas FDCs han sido incluidas en la LMME. La última actualización, llevada a cabo en 2017 (WHO, 2017), introduce una versión revisada de las FDCs pediátricas de fármacos antituberculosos. Las FDCs actualmente disponibles para la TB pediátrica son (WHO, 2018f):

- Fase intensiva: RIF (75 mg) + INH (50 mg) + PIR (150 mg).
- Fase de continuación: RIF (75 mg) + INH (50 mg).

El tratamiento debe además incluir separadamente ETB en la fase intensiva para niños con enfermedad grave o que vivan en entornos donde la prevalencia de la resistencia a INH es alta.

En el caso de adultos, en la actualidad, la OMS recomienda para el tratamiento de pacientes tuberculosos no resistentes, una FDC que contiene RIF (150 mg), INH (75 mg), PIR (400 mg) y ETB (275 mg) (WHO, 2017, 2018a). La pauta de tratamiento estándar de todas las formas de TB (TB-P y TB-EP), salvo la meningitis tuberculosa, consiste en una combinación de INH, RIF y PIR durante 2 meses, seguida de INH y RIF 4 meses más. La adición de ETB depende de las tasas de resistencia. En España las tasas de resistencias son bajas y no sería necesario un cuarto fármaco. Sin embargo, el aumento de la población inmigrante está suponiendo un problema por las tasas de resistencias superiores, obligando a añadir un cuarto fármaco. Existen además otras FDCs binarias y ternarias de fármacos antituberculosos de segunda línea que se incluyen en la última edición de la lista de medicamentos esenciales para la TB (WHO, 2017) cuya composición y dosis aparecen en una tabla de un apartado posterior de esta memoria (I.1.7.3).

a) Ventajas ofrecidas por las FDCs:

Aunque no existen evidencias de la superioridad de las asociaciones antituberculosas a dosis fijas frente a su administración en formas farmacéuticas separadas, la totalidad de expertos y organismos coinciden promover el uso de las mismas por las ventajas de reducir el riesgo de selección de cepas resistentes, evitar errores de cálculo de dosis y sobre todo mejorar el cumplimiento y la adherencia, al pasar de tomar entre 10-14 a 3-5 comprimidos diarios (www.cadime.es). Podría decirse que las ventajas que justifican el tratamiento con FDCs incluyen: la mayor facilidad para el cálculo de dosis, la prevención de errores de prescripción debido a la simplificación y normalización de los regímenes terapéuticos y, fundamentalmente, el aumento en la adherencia y cumplimiento terapéuticos. Por último, también disminuye el coste de un tratamiento completo en comparación con la administración separada de los fármacos (Blomberg y Fourie, 2003; Monedero y Caminero, 2011).

b) Problemas relacionados con las FDCs:

Las FDCs presentan, no obstante las ventajas citadas, serios problemas relacionados con incompatibilidades entre los fármacos antituberculosos de primera línea cuando se encuentran juntos (Battini et al., 2018). En particular, la RIF se degrada rápidamente en presencia de INH en el ambiente ácido del estómago dando lugar a una amplia variabilidad en la biodisponibilidad de RIF después de una administración oral de una FDC (Singh et al., 2001; Moretton et al., 2014). Más concretamente, en medio ácido RIF se descompone en 3-Formil rifamicina, la cual, en presencia de INH reacciona con ésta formando isonicotinil hidrazona mediante una reacción muy rápida de segundo orden. Esta hidrazona que se forma es muy inestable en medio ácido y vuelve a convertirse en INH y 3-Formil rifamicina mediante una reacción lenta de pseudo primer orden (Figura I.6). Debido las características de la reacción de formación de hidrazona (rápida y de segundo orden), el equilibrio se desplaza hacia este sentido, dando lugar a una mayor y más rápida degradación de RIF a 3-Formil rifamicina (Singh et al., 2001; Freire et al., 2014; Moretton et al., 2014). Además otros problemas de inestabilidad dan lugar a la degradación de INH: la naturaleza higroscópica del ETB cataliza la degradación de INH debido al ambiente ácido y húmedo creado por la presencia de ETB (Singh et al., 2001; Bhutani et al., 2004; 2005 a, b) y, por otro lado, la interacción directa de RIF con INH, cuyo mecanismo implica la interacción del grupo imina de la RIF con el grupo amino de INH para producir isonicotinil hidrazona, el producto de degradación principal de la INH. Esta última reacción aumenta en presencia de ETB y PIR, que actúan como catalizadores (Singh et al., 2001; Bhutani et al., 2004; 2005 a, b).

Por otro lado, se ha demostrado que el ácido ascórbico por su acción antioxidante reduce la degradación de RIF en presencia de INH (Subashini et al., 2017), así como se reduce la degradación de INH al incluirla en las FDC en forma de cocristales con ácido cafeico y ácido vanílico (Battini et al., 2018)

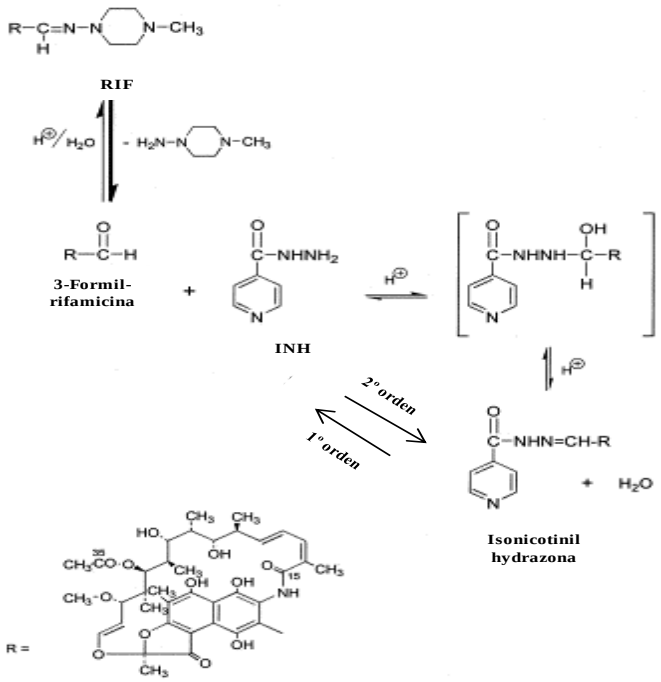

Figura I.6. Mecanismo de degradación de RIF en presencia de INH (modificada de Singh et al., 2001).

Además de los serios problemas de estabilidad, se ha demostrado que existe una alta variabilidad interindividual en la farmacocinética de los cuatro agentes antituberculosos de primera línea que dan lugar a que una proporción significativa de pacientes con TB tratados con FDC de cuatro fármacos estándar presente niveles plasmáticos de uno o varios de los fármacos por debajo de lo previsto (Verbeeck et al., 2016). Las FDC se evalúan antes de su empleo mediante estudios de bioequivalencia *in vivo* y son sometidas a pruebas continuas de control de calidad después del registro (Verbeeck et al., 2016). No obstante, este es un problema que dista de estar resuelto.

I.1.7.2.2 Enfermos de TB VIH-positivos

En el caso de pacientes coinfectados con VIH, el tratamiento antirretroviral debe administrarse en todos los casos, independientemente del nivel de inmunodepresión (WHO, 2018a). El tratamiento antituberculoso debe iniciarse primero, seguido del tratamiento antirretroviral lo antes posible, siempre durante las 8 primeras semanas de tratamiento. En el caso de pacientes VIH-positivos con un grado profundo de inmunosupresión (<50 linfocitos T CD-4/mm^3), deben iniciar el tratamiento antirretroviral durante las dos primeras semanas de haber iniciado el tratamiento antituberculoso (WHO, 2018a). En cuanto a la duración del tratamiento en pacientes

coinfectados por TB y VIH, se recomienda la duración estándar de 6 meses en lugar del tratamiento extendido de 8 meses (WHO, 2018a).

I.1.7.2.3 Enfermos de TB Resistente

A nivel mundial, apenas el 54% de los enfermos con TB-MDR y el 30% de los enfermos con TB-XDR reciben actualmente un tratamiento eficaz. La OMS aprobó en 2016 (WHO, 2016a) el uso de un régimen normalizado de corta duración para enfermos con TB-MDR en los que no se han detectado cepas resistentes a los fármacos antituberculosos de segunda línea (punto I.I.7.1.2 de esta memoria). Este régimen terapéutico, que varía entre los 9 y 12 meses, está estandarizado y supone un coste muy inferior a los tratamientos convencionales contra la TB-MDR que pueden durar hasta 2 años. La estructura básica del régimen terapéutico de corta duración para tratar TB-RR y TB-MDR es la siguiente (WHO, 2016a):

- Primeros 4-6 meses: kanamicina ó amikacina + moxifloxacino + protionamida ó etionamida + clofazimina + PIR + INH (altas dosis) + ETB
- 5 meses posteriores: moxifloxacino + clofazimina + PIR + ETB

Los pacientes con TB-XDR o fármaco-resistencia a los antituberculosos de segunda línea, sin embargo, no pueden utilizar este régimen y deberán seguir tratamientos más largos. Dichos tratamientos tienen una duración de entre 18-20 meses y pueden ser estándar o individualizados. Están diseñados para incluir al menos 5 fármacos que se consideren eficaces. La Tabla I.IV recoge los fármacos recomendados para el tratamiento largo de TB-MDR o TB-XDR (WHO, 2018g). Supone una reagrupación en 3 categorías de los fármacos que en 2016 se propusieron para el régimen terapéutico de corta duración (punto I.I.7.1.2 de esta memoria; WHO, 2016a). La reagrupación de los fármacos se basa en los últimos datos de eficacia y seguridad obtenidos y se encuentran ordenados según prioridad de inclusión en la terapia (A>B>C). Los fármacos que se han eliminado del tratamiento de larga duración son la kanamicina y capreomicina, debido al mayor riesgo que suponen por la mayor duración del tratamiento; no ocurre con la amikacina, la cual sí se incluye en la lista. Por otro lado, la asociación amoxicilina-ácido clavulánico sólo se recomienda para acompañar el tratamiento con carbapenems (WHO, 2018g). La inclusión de delamanid en el tratamiento de TB-MDR y TB-XDR ha sido de

las que más controversia ha despertado debido a la falta de datos clínicos (WHO, 2018h). La decisión de usar delamanid en tales regímenes debe ser tomada basándose en una evaluación individual del paciente (WHO, 2018h).

Tabla I.IV. Fármacos empleados en el tratamiento de larga duración de TB-MDR y TB-XDR (WHO, 2018g).

Grupo A (mayor prioridad)	Levofloxacino/moxifloxacino
	Bedaquilina
	Linezolid
Grupo B (fármacos para ser añadidos después)	Clofazimina
	Cicloserina/terizidona
Grupo C (recomendados para completar el tratamiento y cuando no se puedan utilizar los fármacos de los grupos A y B)	ETB
	Delamanid
	PIR
	Imipenem-cilastatina
	Meropenem
	Amikacina (estreptomicina)
	Etionamida/protionamida
	Ácido p-aminosalicílico

I.1.7.2.4 Tratamiento pediátrico TB

Al menos 1 millón de niños enferman de TB cada año. Los niños representan sobre el 10-11% de todos los casos de TB. En 2017, más de 250.000 niños murieron de TB, entre los cuales unos 50000 VIH positivos (WHO, 2018a). La mayoría de los niños tolera el tratamiento muy bien. El tratamiento preventivo es altamente efectivo en niños expuestos a la TB (WHO, 2018c,d).

El tratamiento para niños enfermos de TB consiste en una fase intensiva de dos meses con INH, RIF, PIR (y, dependiendo del entorno y del tipo de TB, ETB), seguido de la fase de continuación con INH y RIF durante al menos 4 meses. Las siguientes dosis e intervalos de fármacos tuberculostáticos de primera línea deben ser utilizadas diariamente para el tratamiento de la TB pediátrica (WHO, 2018a,c,d).

- INH: 10 mg/kg (intervalo 7–15 mg/kg)
- RIF: 15 mg/kg (intervalo 10–20 mg/kg)
- PIR: 35 mg/kg (intervalo 30–40 mg/kg)

- ETB: 20 mg/kg (intervalo 15–25 mg/kg)

Como adelantamos antes, existen también FDCs pediátricas (WHO, 2018c,d,e):

- Fase intensiva: RIF (75 mg) + INH (50 mg) + PIR (150 mg).
- Fase de continuación: RIF (75 mg) + INH (50 mg).

I.1.7.3 Medicamentos esenciales TB

La vigésima edición de la lista de la OMS de medicamentos esenciales se encuentra dividida en dos sublistas: principal y complementaria (WHO, 2017). La lista principal recopila las necesidades mínimas de medicamentos para un sistema de atención básico de salud, enumerando los medicamentos más eficaces, seguros y rentables para las condiciones prioritarias. Las condiciones prioritarias se seleccionan sobre la base de la relevancia futura actual y estimada de la salud pública, y la posibilidad de un tratamiento seguro y rentable. La lista complementaria presenta los medicamentos esenciales para las enfermedades prioritarias, para lo cual se necesitan instalaciones especializadas de diagnóstico o monitoreo, y/o atención médica especializada, y/o capacitación especializada. En caso de duda, los medicamentos también pueden enumerarse como complementarios sobre la base de costos más altos consistentes o una relación costo-efectividad menos positiva. En el caso particular de la TB, en dicho documento (WHO, 2017), se recomienda el uso de las FDCs existentes, así como el ***desarrollo de nuevas FDCs que incluyan formas farmacéuticas de liberación modificada,*** productos no refrigerados y formulaciones pediátricas de calidad. En la sección 6.2.4 "Antituberculosis medicines" del citado documento (WHO, 2017), se incluye la clofazimina como nueva indicación para el tratamiento de TB-MDR en la lista complementaria de la Lista de Medicamentos Esenciales. Además también incluye el delamanid para el tratamiento de TB-MDR en niños de entre 6 y 17 años. Dos formulaciones FDCs pediátricas (INH + PIR + RIF y INH + RIF) fueron recomendadas para incluirlas en la lista. Por el contrario, la inclusión de gatifloxacin no se recomendó debido a que no estaba demostrado que tuviera mejor perfil daño-beneficio que los medicamentos que ya estaban incluidos en la lista. El uso de la ofloxacina como alternativa a levofloxacina se eliminó en la versión actualizada de la guía de tratamiento de la TB-MDR, mientras que el moxifloxacino, la otra alternativa al levofloxacino, se

mantiene en la lista. La estreptomicina desapareció de la lista principal de medicamentos esenciales, pero permanece dentro de la lista complementaria (WHO, 2017). A continuación, en las tablas quedan recogidos los fármacos y FDCs esenciales, así como su dosificación, para el tratamiento de la TB susceptible a fármacos (Tabla I.V) y la TB-MDR (Tabla I.VI).

Tabla I.V. Medicamentos esenciales recomendados para el tratamiento de la TB susceptible a fármacos (WHO, 2017).

ETB	**Forma farmacéutica líquida oral:** 25 mg/mL. **Comprimidos:** 100 - 400 mg (ETB clorhidrato).
ETB + INH	**Comprimidos FDC:** 400 mg + 150 mg.
ETB + INH + PIR + RIF	**Comprimidos FDC:** 275 mg + 75 mg + 400 mg + 150 mg.
ETB + INH + RIF	**Comprimidos FDC:** 275 mg + 75 mg + 150 mg.
INH	**Forma farmacéutica líquida oral:** 50 mg/5 mL. **Comprimidos:** 100 mg - 300 mg. **Comprimido ranurado:** 50 mg.
INH + PIR + RIF	**Comprimidos FDC:** 75 mg + 400 mg + 150 mg. 150 mg + 500 mg + 150 mg (uso intermitente tres veces a la semana). **Comprimidos dispersables FDC:** 50 mg + 150 mg + 75 mg.
INH + RIF	**Comprimidos FDC:** 75 mg + 150 mg. 150 mg + 300 mg. 60 mg + 60 mg (uso intermitente tres veces a la semana). 150 mg + 150 mg (uso intermitente tres veces a la semana). **Comprimidos dispersables FDC:** 50 mg + 75 mg**.**
PIR	**Forma farmacéutica líquida oral:** 30 mg/mL. **Comprimidos:** 400 mg. **Comprimido dispersable:** 150 mg. **Comprimido ranurado:** 150 mg.
Rifabutina	**Cápsulas gelatinosas duras:** 150 mg.* * Para pacientes con VIH que estén en tratamiento con fármacos inhibidores de proteasas.
RIF	**Forma farmacéutica líquida oral**: 20 mg/mL. **Comprimidos:** 150 mg - 300 mg.
Rifapentina	**Comprimidos:** 150 mg.* *Sólo para tratamiento de TB latente.

Tabla I.VI. Medicamentos esenciales recomendados para el tratamiento de la TB-RR, TB-MDR y TB-XDR (WHO, 2017).

Amikacina	**Polvo para inyectables:** 100 mg; 500 mg; 1 g (sulfato) en vial.
Bedaquilina	**Comprimidos:** 100 mg.
Capreomicina	**Polvo para inyectables:** 1 g (sulfato) en vial.
Clofazimina	**Cápsulas:** 50 mg; 100 mg
Cicloserina*	**Comprimidos:** 250 mg. *Terizidona como alternativa.
Delamanid [a]	**Comprimidos:** 50 mg. [a] > 6 años.
Etionamida*	**Comprimidos:** 125 mg; 250 mg. *Protionamida como alternativa.
Kanamicina	**Polvo para inyectables:** 1 g (sulfato) en vial.
Levofloxacina	**Comprimidos:** 250mg; 500 mg; 750 mg.
Linezolid	**Inyección para administración intravenosa:** 2 mg/mL en bolsa de 300 mL. **Polvo para forma farmacéutica líquida administración oral**: 100 mg/5 mL. **Comprimidos:** 400 mg; 600 mg
Moxifloxacino	**Comprimidos:** 400 mg.
Ácido p-aminosalicílico	**Granulados:** 4 g en paquetes. **Comprimidos:** 500 mg.
Estreptomicina	**Polvo para inyectables:** 1 g (sulfato) en vial.

I.I.7.4 Terapia preventiva antituberculosa

La infección tuberculosa latente (TB-L) se define como un estado de respuesta inmune persistente a la estimulación mediante antígenos de *Mtb* sin evidencia de TB activa clínicamente manifiesta. La carga global de TB-L no se conoce con certeza; sin embargo, se estima que hasta un tercio de la población mundial está infectada con *Mtb* y, aunque la gran mayoría no desarrolle sintomatología, aproximadamente el 5-10% de los infectados desarrollarán la enfermedad de TB activa, mayoritariamente en los primeros 5 años tras la infección inicial (WHO, 2018i). El riesgo de desarrollar TB activa depende de múltiples factores, destacando entre ellos el estado del sistema inmunitario (WHO, 2018a, i).

La terapia preventiva se administra con el fin de reducir el riesgo de progresión de TB-L hacia enfermedad activa y es uno de los pilares de la estrategia "Alto a la Tuberculosis" (Stop TB Partnership, 2016). La eficacia de la terapia preventiva oscila entre un 60-90%

(WHO, 2018i). Sin embargo, las consideraciones son diferentes en entornos de alta y baja incidencia. En entornos de alta incidencia, el efecto protector de la terapia preventiva es transitorio, dada la alta probabilidad de futura reinfección, pero tiene un valor particular para cubrir los períodos de alta vulnerabilidad, como la infección en niños pequeños o adultos infectados por el VIH. Por otro lado, en entornos de baja incidencia con transmisión mínima de TB, la protección proporcionada por la terapia preventiva es más duradera (dado el riesgo limitado de reinfección), pero el beneficio poblacional se reduce debido al bajo riesgo de transmisión que presentan los casos de TB. En ambos casos, la decisión de utilizarse la terapia preventiva contra la TB debe ponderar esencialmente los beneficios personales potenciales contra el riesgo de toxicidad de los fármacos (Fox et al., 2017; WHO, 2018i).

I.1.7.4.1 Tipos de terapia preventiva antituberculosa:

a) Terapia preventiva con INH:

La terapia diaria con INH, durante entre 6 y 12 meses, ha sido el pilar de la terapia preventiva antituberculosa. La OMS recomienda la administración diaria de INH durante 6 meses como el estándar para el tratamiento preventivo de la TB en adultos y niños en zonas de baja y alta incidencia de TB. Para las pacientes coinfectados por VIH, generalmente se recomiendan alargar la duración de la monoterapia con INH (≥36 meses) (WHO, 2018a, i).

b) Regímenes basados en rifamicinas:

Las rifamicinas son una clase de antibióticos orales que incluyen RIF, rifabutina y rifapentina, que actúan inhibiendo la síntesis de ARN bacteriano mediante unión a la ARN polimerasa dependiente del ADN (Fox et al., 2017). Dentro de este régimen, la OMS recomienda dos posibilidades como alternativa a la terapia preventiva con INH como monoterapia (WHO, 2018i):

- Rifapentina/INH semanal durante 3 meses para adultos y niños en países con alta incidencia de TB.
- RIF/INH semanal durante 3-4 meses para niños y adolescentes <15 años en países con alta incidencia de TB.

En caso de pacientes con VIH que estén recibiendo terapia antirretroviral, ambos regímenes, (Rifapentina/INH y RIF/INH), deben ser prescritos siguiendo una atención especial debido al posible riesgo de interacciones fármaco-fármaco (WHO, 2018i).

c) Vacuna BCG (Bacilo Calmette-Guerin)

La vacuna BCG se utilizó por primera vez para inmunizar a seres humanos en 1921. Debe su nombre a Calmette y Guérin, quienes consiguieron aislar y atenuar una cepa de *Mycobacterium bovis*, de la cual derivan todas las cepas vacunales actuales (Calmette et al., 1926). Actualmente, se administra la vacuna BCG a unos 100 millones de niños cada año. Se ha documentado el efecto protector en niños de la vacuna BCG contra la meningitis tuberculosa y la TB miliar, sin embargo, no evita la infección primaria ni evita la reactivación de la infección pulmonar latente (Trunz et al., 2006; Kelekçi et al., 2014). Según la OMS, la vacuna BCG está indicada para todos los lactantes que viven en zonas con alta endemicidad de TB, con riesgo particular de exposición a la TB o personas expuestas a *Mtb* multirresistente (WHO, 2018j). Sin embargo, la vacuna BCG está contraindicada para personas con inmunodeficiencias, enfermos que reciben tratamiento inmunodepresor (corticoesteroides, agentes alquilantes, antimetabolitos, radiación) y durante el embarazo (WHO, 2018j).

I.1.7.5 Novedades en la terapia antituberculosa

I.1.7.5.1 Fármacos

La aparición de resistencias al tratamiento convencional (TB-MDR y TB-XDR) ha detonado la urgente necesidad de nuevos fármacos antituberculosos. A fecha de agosto de 2018 la lista de nuevos fármacos antituberculosos incluía 20 moléculas en ensayos de Fase I, II o III (WHO, 2018a). Once de estas moléculas son nuevas: contezolid, delpazolid, GSK-3036656, macozinone, OPC-167832, pretomanid, Q203, SQ109, TBA-7371, TBI-166 y sutezolid. Otras dos, bedaquilina y delamanid, ya tienen aprobación regulatoria basada en los resultados de la Fase IIb y siete de ellas son fármacos usados a los que se pretende ampliar el uso: clofazimina, linezolid, levofloxacina, moxifloxacina, nitazoxanida, rifampicina (dosis alta) y rifapentina (WHO, 2018a).

- **Nuevos compuestos:**
    - Contezolid: MRX4, un profármaco del contezolid (MRX-I), está en Fase I en EEUU. MRX-I es un potente antibiótico contra bacterias Gram positivas. Tras una administración oral, ha demostrado una eficacia igual o superior que linezolid en infecciones locales o sistémicas en ratones.

    - Bedaquilina: la OMS publicó una guía de política provisional sobre el uso de bedaquilina para el tratamiento de pacientes con TB-MDR en 2013. Hubo una recomendación condicional para usar bedaquilina para fortalecer los regímenes de tratamiento más largos para TB-MDR recomendados por la OMS. La OMS convocó un Grupo de Desarrollo de Directrices en 2016 cuyo principal resultado fue mantener la misma recomendación condicional.

    - Delamanid: la etapa de seguimiento de un ensayo de Fase III de seguridad y eficacia de delamanid como adición para el tratamiento de adultos con TB-MDR ha terminado recientemente.

    - Delpazolid (LCB01-0371): es una nueva oxazolidinona desarrollada por LegoChem BioSciences. Entró en un ensayo de Fase II en la República de Corea en 2017.

    - GSK-3036656: es un nuevo compuesto de oxaborol desarrollado por GlaxoSmithKline. Un ensayo de Fase I comenzó en marzo de 2017.

    - Macozinona (PBTZ169): es una benzotiacinona desarrollada por Nearmedic Plus. Se ha completado la fase I y ha empezado una Fase II en Rusia.

    - OPC-167832: es una 2-quinolona desarrollada por Otsuka que es bactericida contra bacilos crecientes e intracelulares.

- Pretomanid: es un nitroimidazol que está siendo desarrollado por la Alianza contra la TB (www.tballiance.org). Actualmente se está probando como parte de los regímenes de combinación para el tratamiento de la TB susceptible como fármacorresistente, incluyendo TB-XDR.

- Q203: es una imidazopiridina que ha sido desarrollada por Qurient (República de Corea). Está siendo probada en dos ensayos de Fase I.

- SQ109: es un fármaco descubierto por científicos de Sequella Inc. (EE. UU.) y los Institutos Nacionales de Salud de EE. UU. Un ensayo de Fase IIb/III en el cual el principio activo fue agregado a un régimen estándar para TB-MDR, se ha completado en siete centros clínicos en Rusia, con resultados positivos en términos de seguridad, eficacia y tolerabilidad. La fase II de prueba se está implementando en los EE. UU.

- TBA-7371: es un inhibidor de la enzima DprE1, esencial en la síntesis de los componentes de la pared celular de las micobacterias. Ha demostrado ser eficaz contra cepas de *Mtb* resistentes a fármacos antituberculosos conocidos. La Alianza contra la TB está implementando un ensayo de Fase I en EE. UU.

- TBI-166: es un antibiótico de la familia de las riminofenacinas que ha mejorado las propiedades físicoquímicas y farmacocinéticas de la clofazimina, obteniendo una eficacia similar. Un ensayo de Fase I se inició en enero de 2018 en China.

- Sutezolid (PNU-100480): es una oxazolidinona y un análogo de linezolid. En el Día Mundial de la TB de 2017, la Alianza contra la TB y la Medicines Patent Pool anunció un acuerdo de licencia para el desarrollo clínico de sutezolid.

- **Fármacos ya aprobados para otras indicaciones:**
  - Clofazimina: es una riminofenacina que se usa para tratar la lepra al ser eficaz contra el *Mycobacterium leprae*. Su uso en el tratamiento de TB-MDR está en fase preclínica en modelos de *Mtb*, para comprender mejor sus efectos anti-TB.

  - Levofloxacina: se está probando en el estudio Fase II Opti-Q. Se está investigando la mejor dosis de levofloxacina para usar en el tratamiento de TB-MDR.

  - Linezolid: es una oxazolidinona con potente actividad contra *Mtb*. Ha sido ampliamente utilizado en el tratamiento de TB-MDR. Debido a su estrecha ventana terapéutica, y a que la estrategia de dosificación óptima sigue siendo desconocida, la Alianza contra la TB está implementando un ensayo de Fase II para evaluar actividad micobactericida, seguridad, tolerabilidad y farmacocinética de 5 dosis de linezolid en adultos enfermos de TB-P.

  - Moxifloxacina: está incluida en varios ensayos de nuevos regímenes para tratamiento de la TB susceptible a fármacos y TB-MDR.

  - Nitazoxanida: es un fármaco antiparasitario. Su actividad contra *Mtb* se está probando en un ensayo de Fase II en Haití.

  - RIF (altas dosis): el ensayo sugiere que dosis de 35 mg/kg de RIF administrada durante 12 semanas mejora los resultados del tratamiento.

  - Rifapentina: la efectividad de rifapentina en el tratamiento de la TB susceptible a fármacos se está estudiando en tres ensayos.

I.1.7.5.2 Regímenes terapéuticos

Nuevas combinaciones de fármacos para el tratamiento de TB susceptible y resistente se están probando en ensayos de Fase II y III:

- ACTG A5343 DELIBERATE: este ensayo está probando la posible cardiotoxicidad de regímenes terapéuticos consistentes en delamanid y bedaquilina de forma individual y en combinación, mediante estudios farmacocinéticos y de interacción fármaco-fármaco.

- endTB: este ensayo comenzó en 2017. Se basa en una comparación de diversos regímenes terapéuticos para TB-MDR y TB-XDR (bedaquilina y/o delamanid; moxifloxacino o levofloxacino y PIR + linezolid y/o clofazimina, en distintas combinaciones) frente al tratamiento de mayor duración recomendado por la OMS para los casos de TB-MDR.

- MDR-END: este ensayo está probando un régimen de 9 a 12 meses basado en delamanid, linezolid, levofloxacina y PIR para el tratamiento de TB-MDR en pacientes que no sean resistentes a fluoroquinolonas.

- NeXT: consiste en probar la eficacia de un régimen de 6 a 9 meses de duración sin administración de inyectables basado en bedaquilina, etionamida o INH (altas dosis), linezolid, levofloxacino y PIR para pacientes con TB-MDR, en comparación con el régimen recomendado de 21 a 24 meses de duración.

- NiX-TB, ZeNix y BPaMZ: el ensayo NiX-TB investiga la seguridad y eficacia de un régimen de 6 meses de exclusiva administración oral que combina bedaquilina, pretomanid y linezolid en pacientes con TB-XDR y en pacientes con TB-MDR que no puedan tolerar el tratamiento recomendado por la OMS o que no les haya funcionado. Los resultados de los primeros 15 pacientes obtuvieron una tasa de curación del 87%. De forma complementaria, el ensayo ZeNix estudia el efecto de disminuir dosis y duración de la administración de linezolid, para minimizar la posible toxicidad y ensayos en Fase IIc/III (SimpliciTB) de

bedaquilina, pretomanid, moxifloxacino y PIR (BPaMZ) se está realizando entre pacientes con TB susceptible a fármacos o TB-MDR.

- STREAM: compara un régimen de 9 meses para TB-MDR con las terapias más largas, de 18-24 meses. Los resultados finales fueron utilizados para actualizar el tratamiento de larga duración de TB-MDR y TB-XDR (WHO, 2018g).

- TB-PRACTECAL: es un ensayo que se encuentra en las fases II/III y evalúa la eficacia de un régimen de 6 meses que consiste en bedaquilina, pretomanid y linezolid, con o sin moxifloxacina y clofazimina, para el tratamiento de adultos con TB-MDR o TB-XDR.

I.1.7.5.3 Vacunas

La vacuna BCG, utilizada por primera vez en la década de 1920 (Calmette et al., 1926), sigue siendo la única vacuna autorizada como terapia preventiva de la TB (WHO, 2018c). Sin embargo, a pesar de la alta cobertura que supone la vacuna BCG a la población infantil, la lenta disminución de la incidencia de TB a nivel mundial destaca la necesidad de una vacuna que brinde protección contra todas las formas de TB en todos los grupos de edades. En la actualidad, 12 vacunas se encuentran en ensayos de Fase I, II o III (WHO, 2018a):

- **Fase I :**
  - Ad5 Ag85A: es un vector de adenovirus de serotipo 5 que expresa el antígeno 85A. Su administración intramuscular resultó ser segura, bien tolerada e inmunogénica.

  - AEC/BC02: es una vacuna recombinante que expresa el antígeno Ag85B y la proteína de fusión ESAT6-CFP10. Se está realizando un ensayo de Fase I en China para demostrar su seguridad e inmunogenicidad.

  - ChAdOx185A - MVA85A: ChAdOx185A es un adenovirus de simio y MVA85A es un virus recombinante de la viruela. Ambos expresan el

antígeno 85A. Estos candidatos se están desarrollando con el objetivo general de generar un régimen conjunto-heterólogo de estimulación-refuerzo.

- MTBVAC: es una cepa viva de *Mtb*, atenuada mediante deleciones de los genes phoP y fadD26. La población objetiva principal son los recién nacidos (como una vacuna de reemplazo de BCG); y adolescentes y adultos (como vacuna de refuerzo).

- **Fases II y III:**
  - Amplificador DAR-901: es una vacuna micobacteriana no tuberculosa de célula completa, inactivada por calor. Se encuentra en una Fase IIb entre adolescentes pretratados con BCG.

  - H4: IC31: es una vacuna de refuerzo BCG que contiene una proteína de fusión de Ag85B y TB, formulada con adyuvante IC31. Está siendo probada en un ensayo de Fase II entre adolescentes con alto riesgo de adquirir infección por *Mtb* con IGRA negativo y VIH negativo. También se encuentra en una Fase I/II en bebés.

  - H56: IC31: es una vacuna de subunidad que combina tres antígenos de *Mtb* (Ag85B, ESAT-6 y Rv2660c) con el adyuvante IC31. Se han completado pruebas de seguridad trifásicas I o I/IIa.

  - ID93 + GLA-SE: comprende cuatro antígenos asociados de *Mtb* y el adyuvante GLA-SE. Se ha terminado recientemente un ensayo de Fase IIa en pacientes con TB VIH-negativos.

  - M72/AS01E: es una vacuna de subunidad que combina dos antígenos de *Mtb* con un adyuvante (AS01E). Está siendo probada en un ensayo de eficacia de Fase IIb en adultos VIH negativos infectados con *Mtb* en Kenia, Sudáfrica y Zambia.

- RUTI®: es una vacuna polivalente no viva basada en el revestimiento celular de bacteria fragmentada de *Mtb*. Está enfocada como una vacuna terapéutica, que se utilizará junto con un breve tratamiento antibiótico intensivo. Un estudio de Fase I en voluntarios sanos y un estudio de Fase II en personas con TB latente demostró un buen perfil de seguridad y resultó ser inmunogénico en todas las dosis estudiadas.

- TB/FLU-04L: es una vacuna vectorizada basada en un vector atenuado del virus de la gripe. Fue diseñada como vacuna de refuerzo profiláctico para bebés, adolescentes y adultos. Se está implementando un ensayo de Fase IIa en personas con TB latente.

- Vaccae™: es un lisado específico que ha sido autorizado por la Administración de Alimentos y Medicamentos de China como un agente inmunoterapéutico para ayudar a acortar el tratamiento de TB para pacientes con TB sensible a los medicamentos. Se está implementando un ensayo de Fase III para evaluar su eficacia y seguridad en la prevención de la enfermedad de TB en personas con TB-L.

- VPM1002: es una vacuna recombinante viva. Un ensayo de Fase II se está implementando en Sudáfrica para evaluar la seguridad e inmunogenicidad de la vacuna en personas expuestas al VIH y recién nacidos no expuestos. Los preparativos para la posterior prueba de Fase III están en marcha.

I.2. FILOSILICATOS COMO NANOMATERIALES PARA EL TRATAMIENTO DE LA TUBERCULOSIS

I.2.1 NANOMATERIALES PARA EL TRATAMIENTO DE LA TUBERCULOSIS

"La nanotecnología puede definirse como la investigación y desarrollo tecnológico a escala atómica, molecular o macromolecular (1-100 nm) con el objetivo de proporcionar

un conocimiento fundamental de los fenómenos y materiales a esta escala (nanoescala) así como de crear y utilizar estructuras, dispositivos y sistemas con propiedades y funcionalidades novedosas que aparecen asociadas a estos tamaños. La nanomedicina es la rama de la nanotecnología centrada en las aplicaciones en salud, incluyendo nanodiagnóstico, nanoterapéutica y nanomateriales para aplicaciones farmacéuticas" (www.nih.gov).

El uso de nanomateriales en el tratamiento de la TB se considera una nueva estrategia con el fin de paliar las dificultades derivadas del tratamiento (Costa-Gouveia et al., 2017), siendo posible el diseño de nanosistemas capaces de actuar en los fagocitos infectados por patógenos intracelulares como las micobacterias (Kaur y Singh, 2014).

La Figura I.7 representa las principales ventajas que aporta la nanotecnología al tratamiento de la TB, entre las cuales destaca la mejora de la calidad de vida de los pacientes, al reducirse la frecuencia de administración y la duración del tratamiento (Kaur y Singh, 2014).

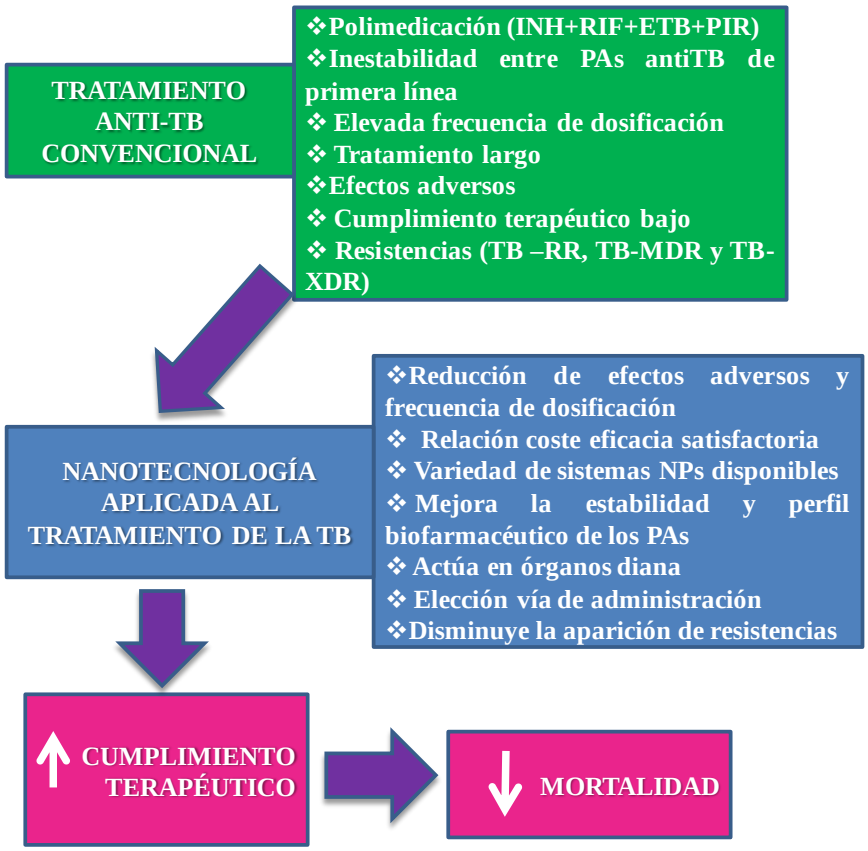

Figura I.7. Ventajas derivadas del uso de nanomateriales en el tratamiento de la TB.

El diseño y desarrollo de sistemas nanotecnológicos para la administración por vía oral de fármacos anti-TB persigue aumentar la biodisponibilidad, modulando la liberación, aumentando la solubilidad de fármacos poco solubles y protegiendo los principios activos frente a la degradación (Costa-Gouveia et al., 2017).

Por otra parte, la administración por vía pulmonar de sistemas nanoparticulares cargados con fármacos anti-TB ha sido planteado en razón de los buenos resultados obtenidos en la administración pulmonar de diversos antibióticos para otras enfermedades infecciosas pulmonares, que reduce los efectos secundarios de la administración sistémica y mejora la eficacia terapéutica al hacer llegar el fármaco directamente al lugar de acción. Asimismo la administración local consigue una alta concentración de fármaco localizada en el pulmón, lo que podría reducir la duración del tratamiento y prevenir la aparición de resistencias (Pham et al., 2015). Múltiples estudios han demostrado que la vía pulmonar para la administración de fármacos antituberculosos es una estrategia prometedora para combatir esta enfermedad (Pham et al., 2015; Costa et al., 2016; Goyal et al., 2017; Magalhães et al., 2018).

Por último, la administración de fármacos antituberculosos a través de la piel, por vía tópica o transdérmica, con el objetivo de tratar la TB cutánea podría ser una estrategia ventajosa, ya que promovería un aumento de concentración de los fármacos en el tejido cutáneo infectado, con menores efectos secundarios. Sin embargo, debido a la baja incidencia de la TB cutánea, esta ruta no invasiva aún se explora poco (Costa et al., 2016).

Son numerosos los estudios que recogen el empleo de nanomateriales de diversa naturaleza para ser empleados en el tratamiento de la TB (Choudhary y Devi, 2015; Costa et al., 2016; Gilani et al., 2017; Nasiruddin et al., 2017; Gupta y Kakkar, 2018; Kerry et al., 2018). El éxito de estos nanosistemas dependerá del diseño de formulaciones rentables que aborden las diferentes limitaciones de la farmacoterapia, haciendo que el tratamiento sea más práctico y asequible para todos los pacientes (Costa et al., 2016). Dentro del amplio grupo de excipientes disponibles para el diseño y desarrollo de sistemas nanotecnológicos de interés en el tratamiento de la TB,

centraremos nuestra atención en los que son objeto de estudio en esta tesis, los "minerales de la arcilla" o filosilicatos.

I.2.2 FILOSILICATOS COMO NANOMATERIALES

I.2.2.1 Generalidades de los filosilicatos

El silicio, con número atómico 14 y situado en el grupo 14 de la tabla periódica (IUPAC), antiguamente grupo IV, es el segundo elemento más abundante en la litosfera (27,7 % en peso) después del oxígeno (47,5 % en peso). Sus similitudes con el carbono, con el que comparte el grupo 14, y en particular, que posea los mismos cuatro enlaces básicos, le confiere la capacidad de formar numerosos compuestos, de forma que se estima que el 60 % de los compuestos de la litosfera contienen silicio y oxígeno. La mayoría de estos compuestos son silicatos, cuya estructura unidad está formada por 4 átomos de oxígeno en los vértices de un tetraedro regular, cuyo centro lo ocupa un átomo de silicio. La interacción entre estos dos elementos y la estabilidad de las estructuras que resultan se deben a un tipo especial de enlace que hay entre los átomos de silicio y oxígeno. Este enlace es 50% iónico y 50% covalente. Dado que el oxígeno tiene valencia -2 y el silicio +4, el tetraedro tiene carga -4 por lo que los oxígenos de los vértices son compartidos con otros tetraedros adyacentes, formando estructuras mayores. Puesto que las arcillas están compuestas principalmente por un grupo de minerales denominados filosilicatos, está muy extendida la denominación de "minerales de la arcilla" para referirse a los filosilicatos. El glosario de la Sociedad de Minerales de la Arcilla ("Clay Minerals Society") con fecha de abril de 2018 (Clay Minerals Society, 2018) define "minerales de la arcilla" como aquellos filosilicatos y/u otros minerales que aportan plasticidad a las arcillas y que se endurecen después de secado o cocción. El término arcilla, por su parte, viene definido en dicho glosario (Clay Minerals Society, 2018), como aquel material natural compuesto principalmente de minerales de grano fino, que es generalmente plástico cuando el contenido de agua es apropiado y se endurecerá tras secado o cocción.

El 90% de los minerales son silicatos. Cuando los tetraedros se unen por tres de los vértices a otros tetraedros dan como resultado capas tetraédricas. Las capas tetraédricas se asocian a capas formadas por octaedros de aluminio o magnesio con oxígenos en los

vértices; capas octaédricas (Figura I.8). Esta disposición de los tetraedros que da lugar a una red plana es la característica propia de los filosilicatos, un subgrupo de los silicatos. El término filosilicato deriva de la palabra griega *phyllon* (hoja) y la latina *silex* (sílice).

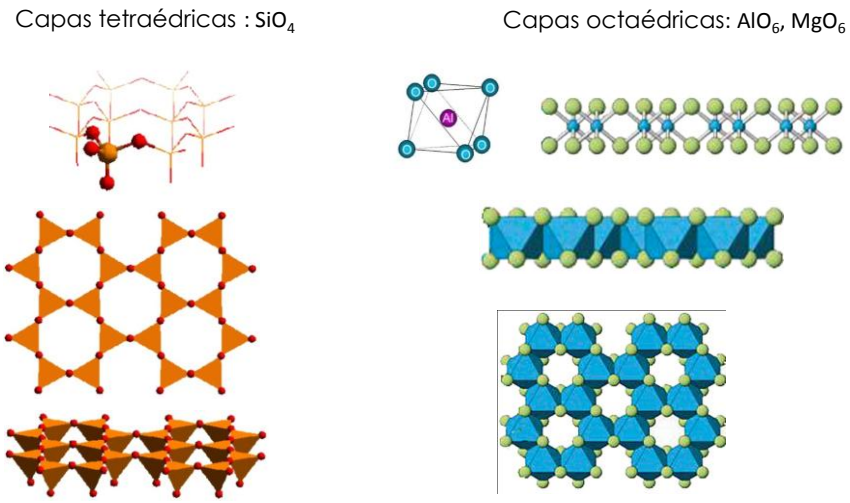

Figura I.8. Estructura de las capas fundamentales de la estructura de los filosilicatos.

En las capas octaédricas pueden darse dos situaciones: si todos los huecos octaédricos están ocupados, la capa se denomina trioctaédrica (Mg^{2+} dominante en la capa octaédrica). Si sólo están ocupadas dos tercios de las posiciones octaédricas y el tercio restante está vacante, se denomina dioctaédrica (el Al^{3+} es el catión octaédrico dominante) (Figura I.9).

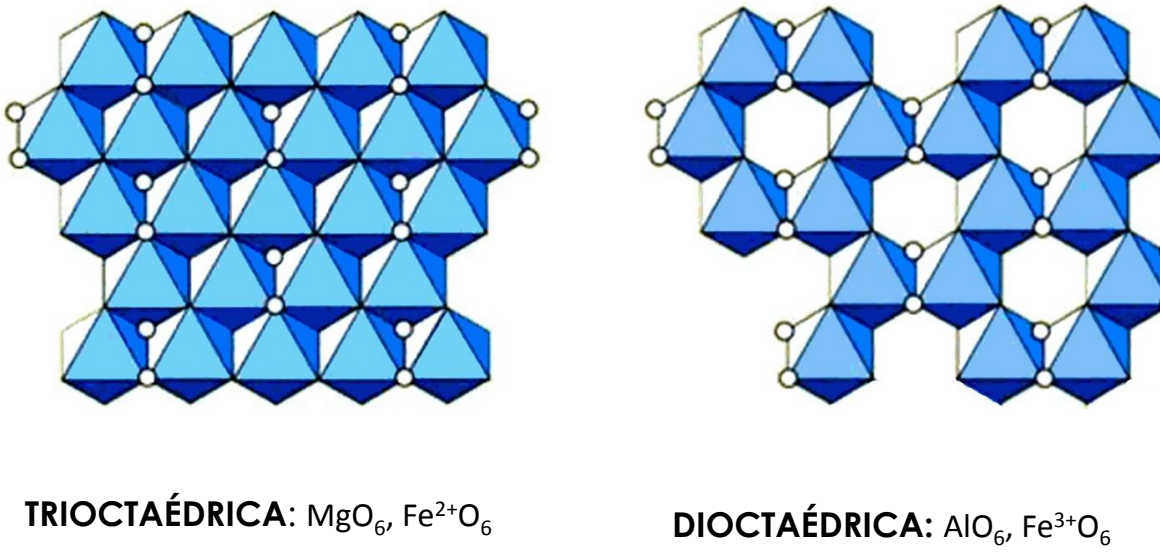

Figura I.9. Estructuras tri y dioctaédrica de las capas octaédricas.

A la unidad formada por la unión de una capa octaédrica más una o dos tetraédricas se le denomina lámina. Existen dos posibilidades (Figura I.10):

- Dos capas: 1 tetraédrica + 1 octaédrica → 1:1, T-O.
- Tres capas: 1 octaédrica + 2 tetraédricas → 2:1, T-O-T.

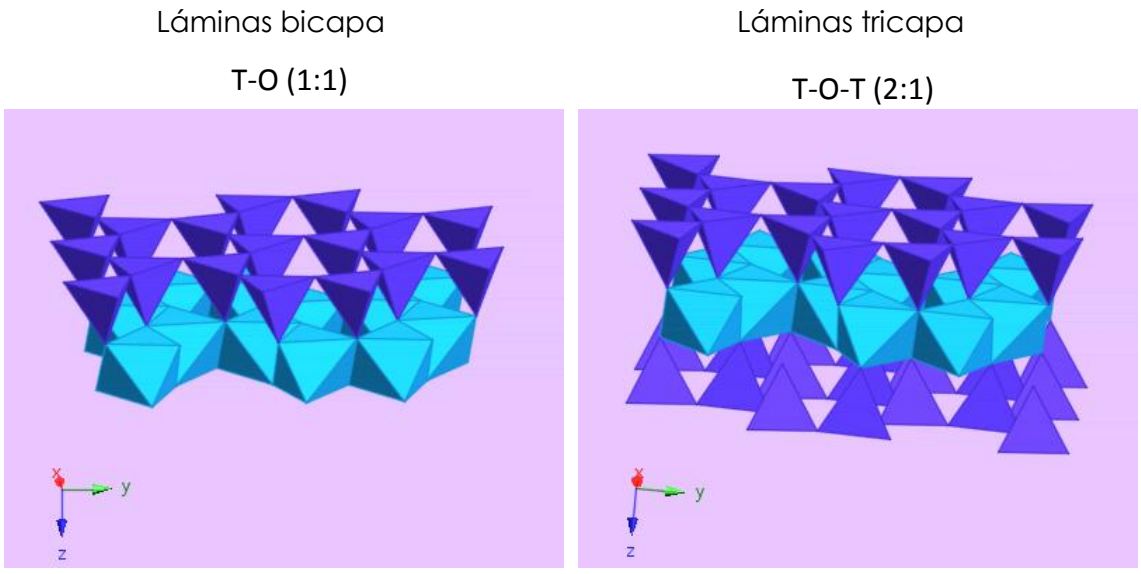

Figura I.10. Láminas bi y tricapa.

Según el tipo de apilamiento, el tipo de catión en el estrato octaédrico, la carga neta del paquete estructural y el tipo de catión (moléculas o agua) en el espacio interlaminar pueden distinguirse diferentes filosilicatos (Tabla I.VII).

Tabla I.VII. Clasificación de los filosilicatos de acuerdo con la AIPEA.

Tipo de apilamiento	Material Interlaminar	Grupo (x = carga neta)	Subgrupo	Ejemplos
1:1	Ninguno o H_2O	Serpentina-Kaolinita (x ≡ 0)	❖ Serpentina ❖ Kaolinita	Crisotilo Kaolinita Halloysita
	Ninguno	Talco-Pirofilita (x ≡ 0)	❖ Talco ❖ Pirofilita	Talco Pirofilita
2:1	Cationes hidratados intercambiables	Esmectita (x ≡ 0.2-0.6)	❖ Saponita ❖ Montmorillonita	Saponita Hectorita Montmorillonita Nontronita
		Vermiculita (x ≡ 0.6-0.9)	❖ Vermiculitas dioctaédricas	Vermiculitas dioctaédricas
			❖ Vermiculitas trioctaédricas	Vermiculitas trioctaédricas
	Cationes no hidratados	Mica (x ≡ 0.5-1)	❖ Micas dioctaédricas ❖ Micas trioctaédricas	Moscovita, Paragonita Biotita, Lepiolita
		Mica frágil (x ≡ 2)	❖ Micas frágiles dioctaédricas ❖ Micas frágiles trioctaédricas	Margarita Clintonita
	Hidróxidos	Clorita x ≡ variable	❖ Cloritas Dioctaédricas ❖ Cloritas Di, Trioctaedricas ❖ Cloritas Trioctaedricas	Donbassita Cookeita Clinochloro
	Ninguno	Sepiolita-Palygorskita (x variable)	❖ Sepiolitas	Sepiolita
			❖ Palygorskitas	Palygorskita

Algunos de estos minerales tienen un amplio uso farmacéutico, como sucede con los minerales del grupo del talco, de la caolinita, de las esmectitas (bentonitas) y de la palygorskita (atapulgita) y sepiolita. Todos estos minerales son excipientes de uso común en la formulación de formas farmacéuticas (sólidas, líquidas y semisólidas) para uso tópico y sistémico (Cerezo et al., 2001; López-Galindo et al., 2007; Aguzzi et al., 2007, 2010, 2013, 2014a, b, 2016; Viseras et al., 2007, 2008a, b, 2009, 2010, 2015; Salcedo et al., 2012, 2014; Sandri et al., 2014, 2016, 2017; Borrego-Sánchez 2016, 2017, 2018; García-Villén et al., 2019).

I.2.2.2 Propiedades de los filosilicatos

Los minerales de la arcilla presentan algunas propiedades esenciales que dependen de factores relacionados a su composición (mineralógica y química) y estructura. En particular, se distinguen:

a) Capacidad de Intercambio Catiónico (CEC).
b) Formación de Coloides Estructurados.
c) Hinchamiento (esmectitas).
d) Propiedades Reológicas.
e) Área Superficial Específica.

a) Capacidad de Intercambio Catiónico (CEC): se define intercambio iónico como un intercambio reversible de iones o cargas entre una fase líquida y una fase sólida, sin que se produzcan modificaciones radicales en la estructura y en las propiedades del sólido (Mantell, 1951). Dependiendo de la carga positiva o negativa de las especies iónicas que se intercambien, se diferencia a su vez entre intercambio catiónico o aniónico. La capacidad de intercambio catiónico (CEC) se define como la cantidad total de cationes intercambiables que pueden ser adsorbidos por un material determinado a un valor alto de pH. Se mide como miliequivalentes (meq) de carga por g (o más frecuentemente 100 g) de material adsorbente. Los valores más elevados (80-200 meq/100 g) se observan cuando el valor de CEC se debe esencialmente a las sustituciones isomórficas del retículo cristalino, lo cual ocurre en el grupo de las esmectitas. Por otro lado, las arcillas con un grado de sustituciones isomórficas bajo tienen actividad química escasa, se conocen como "arcillas inertes". Dentro de este último grupo se encuentran el caolín, el

talco y las arcillas fibrosas (sepiolita-palygorskita), cuya CEC es generalmente inferior a 15-20 meq/100 g.

La CEC de los minerales de la arcilla puede ser útil para la adsorción de moléculas orgánicas de carácter básico biológicamente activas, como es el caso de fármacos que sean bases débiles y cuya liberación se vea prolongada después de ser adsorbidos en arcillas. La capacidad de una molécula básica de sustituir a los cationes de la arcilla depende de su grado de protonación o basicidad, que a su vez depende del pH del medio (Bergaya y Lagaly, 2001).

b) Propiedades Eléctricas Superficiales: el tamaño de partícula de las arcillas (inferior a 2 μm), origina que en un medio acuoso las partículas sólidas den lugar a dispersiones coloidales caracterizadas por sus propiedades superficiales. Las partículas dispersas desarrollan cargas superficiales que generan una doble capa eléctrica que es también responsable de la estabilidad del sistema.

c) Formación de Coloides Estructurados: en los sistemas dispersos sólido/líquido (coloidales y no coloidales) pueden intervenir factores hidrodinámicos (todas las interacciones entre el medio dispersante y las partículas sólidas dispersas), y no hidrodinámicas (interacciones entre las partículas).

1. Factores hidrodinámicos: dependen de la concentración de las partículas, su forma, sus dimensiones y distribución granulométrica y de la viscosidad del medio.
2. Factores no hidrodinámicos: son responsables de la formación y de la estabilidad de los sistemas coloidales estructurados de las arcillas laminares (esmectitas) donde pueden establecerse interacciones cara-borde (formadoras) o cara-cara (desestabilizadoras) entre las partículas.

d) Capacidad de Hinchamiento (Esmectitas): el hinchamiento es una propiedad común de las dispersiones de las esmectitas y es consecuencia directa del mecanismo de hidratación de sus partículas.

e) Propiedades Reológicas:

- ***Tixotropía:*** las dispersiones de esmectitas y de arcillas fibrosas se comportan como sistemas tixotrópicos o tiempo-dependientes: en reposo, su viscosidad aumenta en el tiempo y tras aplicar agitación la viscosidad disminuye en el tiempo.

- ***Viscoplasticidad:*** las dispersiones de esmectitas son también sistemas viscoplásticos; presentan un valor de carga de deformación o límite elástico a partir del cual la viscosidad del sistema disminuye al aumentar el gradiente aplicado. Dicha carga de deformación o límite elástico es un índice de la resistencia del sistema a perder su estructura y como todas las propiedades ya descritas resulta muy útil para la formulación y estabilidad de sistemas farmacéuticos dispersos, como suspensiones y emulsiones.

f) Superficie Específica: algunas de las características estructurales (granulometría, presencia de canales zeolíticos) de los minerales de la arcilla hacen que el área superficial específica (m^2/g) de estos materiales sea alta.

I.2.2.3 Esmectitas

El término esmectitas se refiere a un grupo de filosilicatos laminares con elevada capacidad de intercambio catiónico. En el ámbito farmacéutico destacan dos minerales del grupo; la montmorillonita y la saponita, que se corresponden con monografías de las principales Farmacopeas (Ph. Eur., 2016; USP-NF, 2018); "bentonita" y "silicato de Al y Mg o de Mg y Al", respectivamente. En el paquete estructural de las esmectitas (tipo T-O-T electronegativo), los vértices de todos los tetraedros se orientan al centro, donde se unen a los grupos oxígenos del estrato octaédrico; los grupos OH compartidos por el estrato tetraédrico y octaédrico se convierten en O. En la interlámina se localizan cationes, débilmente retenidos, para neutralizar la carga negativa, así como moléculas de agua (Figura I.11).

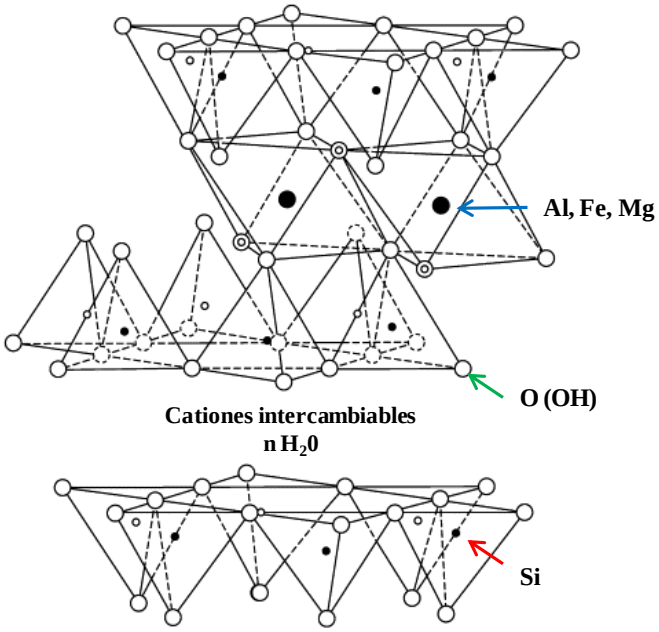

Figura. I.11. Estructura de las esmectitas (modificada de Murray, 2006).

Una característica común de todas las esmectitas son las sustituciones isomórficas (cambio de un átomo por otro de similares dimensiones sin modificar la estructura cristalina) de los átomos de Si y Al en los estratos tetraédricos y octaédricos. En particular, el Si^{4+} de los estratos tetraédricos, puede sustituirse por Al^{3+} o más raramente por P^{3+}, mientras que el Al^{3+} de los estratos octaédricos puede cambiarse por Mg^{2+}, y/o Fe^{3+}, Zn^{2+}, Ni^{2+}, Li^{+}, etc., dando lugar a minerales de composición y propiedades diversas (Tabla I.VIII). La Tabla I.VIII recoge los minerales del grupo de las esmectitas más usados como excipientes.

Tabla I.VIII. Esmectitas más utilizadas en la industria farmacéutica.

Dioctaédricas	
Montmorillonita	$(OH)_4Si_8(Al_{3.34}Mg_{0.66})O_{20}$
Beidellita	$(OH)_4Si_8(Al_{6.34}Mg_{1.66})Al_{4.34}O_{20}$
Nontronita	$(OH)_4(Si_{7.34}Al_{0.66})Fe^{3+}_{4.34}O_{20}$
Trioctaédricas	
Hectorita	$(OH)_4Si_8(Mg_{5.34}Li_{0.66})O_{20}$
Saponita	$(OH)_4(Si_{7.34}Al_{0.66})Mg_6O_{20}$

Hay que señalar que bajo la monografía de farmacopeas denominada "silicato de Al y Mg o de Mg y Al", quedarían incluidos todos los materiales constituidos principalmente por minerales del grupo distintos de la montmorillonita.

El diagrama representado en la Figura I.12 muestra un resumen de las propiedades características del grupo de las esmectitas derivadas de su estructura y composición que las hacen interesantes en el mundo de la industria farmacéutica.

Figura I.12. Propiedades de las esmectitas.

I.2.2.4 Caolín

La caolinita es el mineral más común del grupo del caolín (Murray, 2006). Su estructura 1:1 o T-O con inexistentes o pocas sustituciones isomórficas en los estratos T y O, dando lugar a que sean un grupo de minerales con carga mínima, de la cual derivan sus características. La caolinita (Figura I.13) es un aluminosilicato de composición $Al_2Si_2O_5(OH)_4$. Constituye el mineral representativo de este subgrupo y su uso en el

campo farmacéutico está consolidado. Morfológicamente se caracteriza por su aspecto planar y forma hexagonal de sus partículas.

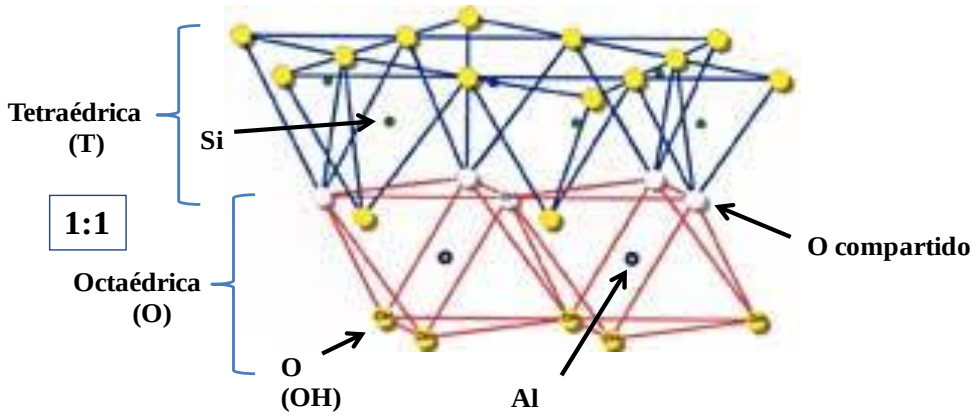

Figura I.13. Estructura de la caolinita (modificada de Grim, 1962).

La halloysita (Figura I.14) es un polimorfo del caolín que se forma a partir de la caolinita en dos posibles situaciones:

- ✓ Presencia de un exceso de agua entre los estratos estructurales (por procesos hidrotermales o por la acción de agentes atmosféricos) en dos etapas sucesivas: la primera parte del proceso se caracteriza por una delaminación del paquete T-O y consiguiente desorden estructural en los cristales de caolinita; en una segunda etapa, se produce un aumento del espaciado interlámina debido a que se hacen más débiles los enlaces de H entre los estratos.
- ✓ Sustituciones Si^{4+} con iones Al^{3+}, que pueden ocurrir en los estratos tetraédricos dando lugar una deformación estructural responsable de la estructura tubular característica de esta especie explicada por Bates y col. (1950).

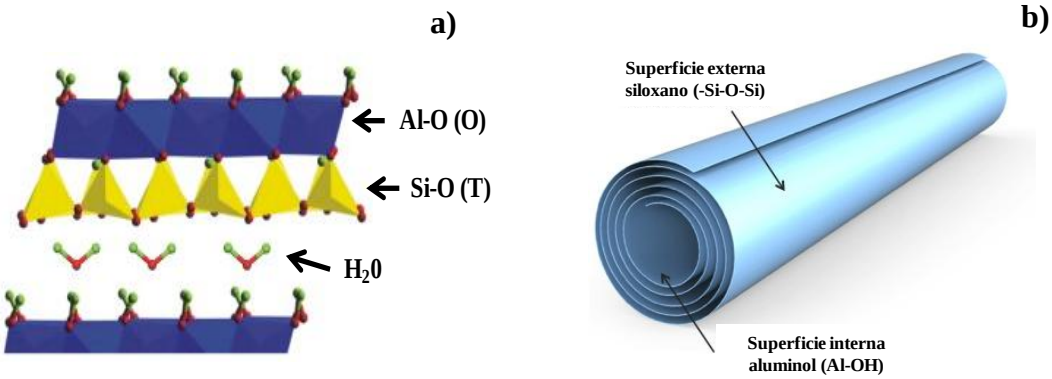

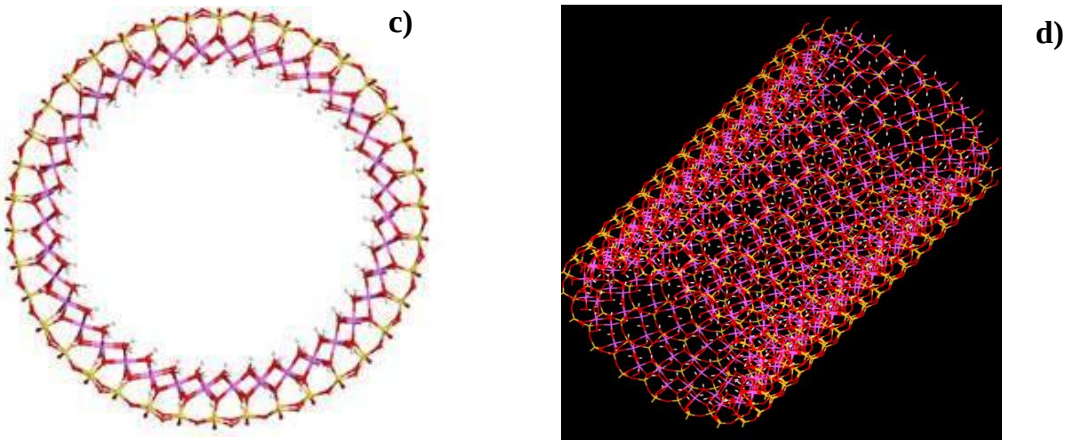

Figura I.14. Estructura de la halloysita: a) modificado de Yuan et al., 2015; b) modificado de http://phantomplastics.com/functional-fillers/halloysite/; c) d) modificado de Carazo et al., 2017b.

I.2.2.5 Sepiolita-Palygorskita

La red cristalina de estos minerales aparece como consecuencia de la inversión periódica de 180º cada 4 tetraedros en el caso de la palygorskita, y 6 tetraedros en el caso de la sepiolita de las capas tetraédricas, lo que origina canales zeolíticos que incluyen moléculas de agua y cationes intercambiables (Figura I.15). Las dimensiones medias de estos canales son de 4 x 6 Å en el caso de la palygorskita, y un poco más amplios (4 x 9.5 Å) para la sepiolita (Figura I.15).

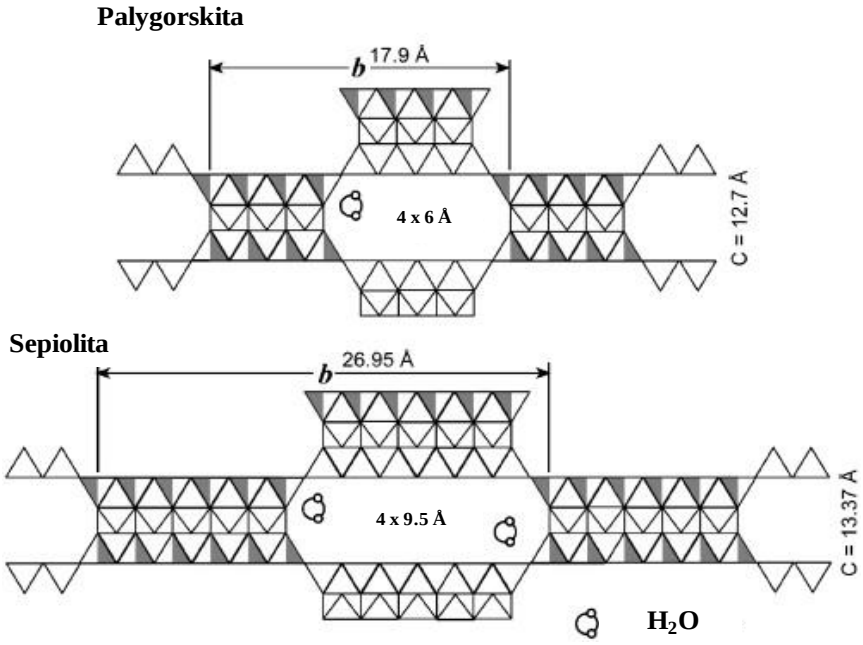

Figura I.15. Estructura palygorskita y sepiolita (modificada de Murray, 2006).

En el caso de la sepiolita, en las posiciones octaédricas el Al se sustituye por Mg, Fe y Fe, mientras que en las posiciones tetraédricas las sustituciones del Si con Al son muy escasas, de tal forma que en la mayor parte de las sepiolitas el contenido de Al es prácticamente nulo. La sepiolita contiene una cantidad de agua zeolítica superior a la palygorskita porque los canales zeolíticos son más grandes. La palygorskita presenta por lo general una composición octaédrica intermedia entre los filosilicatos dioctaédricos y trioctaédricos. De cada cinco posiciones octaédricas, los cationes ocupan de media cuatro. La Figura I.16 resume las propiedades de las arcillas del grupo sepiolita-palygorskita que las convierten en excipientes muy interesantes para el desarrollo de sistemas de liberación de fármacos.

Figura I.16. Propiedades de los minerales de la arcilla del grupo sepiolita-palygorskita.

I.2.3 FILOSILICATOS PARA EL TRATAMIENTO DE LA TB

No obstante hayan sido numerosos los estudios que han puesto de manifiesto el potencial de determinados filosilicatos en nanomedicina (Aguzzi et al., 2007; Viseras et al., 2008a, 2010, 2015; Sandri et al., 2016; Carazo et al., 2018a), son escasos hasta la fecha los estudios orientados a su empleo en terapéutica de la TB. La mayoría de ellos se limita a estudiar la interacción fármaco/filosilicato desde un punto de vista fisicoquímico. Así, la interacción de PIR y 4-aminopirimidina en sepiolita y montmorillonita puso de manifiesto que ambos fármacos interaccionan con montmorillonita, aumentando el espaciado interlaminar, por coordinación directa o indirecta (a través de moléculas de agua) con los cationes intercambiables, mientras que con la sepiolita se producen interacciones de tipo enlaces de hidrógeno a través de uno de los pares monovalentes de nitrógeno de la pirimidina (en el caso de 4-aminopiridina)

o el grupo carbonilo (en el caso de la pirazinamida) con los centros ácidos de Lewis o hidroxilos superficiales del filosilicato (Akyuz y Akyuz, 2004). La adsorción de INH en montmorillonita y saponita aumenta el espacio interlaminar de los filosilicatos y se produce por coordinación de las moléculas del fármaco a los cationes intercambiables presentes en el espaciado interlaminar de forma directa o indirectamente a través de puentes de hidrógeno (Akyuz y Akyuz, 2008). El mismo grupo estudió también la interacción entre sepiolita y palygorskita con INH, encontrando que se produce por coordinación del fármaco a hidroxilos superficiales mediante la interacción de enlaces H a través de los pares solitarios de nitrógeno del anillo de piridina. Además, algunas de las moléculas de fármaco adsorbidas podrían encontrarse en el interior de los canales zeolíticos de la estructura sepiolita-palygorskita mediante puentes de H con el agua zeolítica (Akyuz et al., 2010). Dos Santos Soares y col. (2013) realizaron un estudio de la interacción de una palygorskita brasileña con INH y RIF.

Un hidrogel a base de sepiolita y polivinilalcohol fue usado para modificar la liberación de RIF, demostrando que al aumentar la cantidad de sepiolita disminuía la velocidad de liberación (Vicosa et al., 2009). Banik y col. (2012) desarrollaron nanopartículas montmorillonita-quitosano mediante gelificación iónica para vehiculizar INH que fueron sometidas a estudios de caracterización al estado sólido, así como ensayos de disolución *in-vitro*, tests de citotoxicidad y mucoadhesión. Los resultados obtenidos (liberación modificada, mucoadhesión y no citotoxicidad) pusieron de manifiesto la posibilidad de usar los nanocomposites como transportadores del fármaco. Posteriormente, los mismos autores (Banik et al., 2013) prepararon nanopartículas de montmorillonita-soja mediante reticulación con glutaraldehído para ser cargadas con INH. Banik y col. (2014) demostraron que al aumentar la cantidad de agente de reticulación (glutaraldehído) usado en la formación de nanopartículas de carboximetil quitosano y montmorillonita cargadas con INH, la cantidad posteriormente liberada del fármaco disminuía, al verse dificultada su difusión. Otra línea del mismo grupo desarrolló un sistema basado en montmorillonita unida a nanopartículas de óxido de hierro recubiertas con almidón (Saikia et al., 2014) o carboximetil almidón (Saikia et al., 2015) como nanotransportadores de INH. Los resultados obtenidos pusieron de manifiesto que la adición del filosilicato mejoraba las propiedades de viabilidad celular,

mucoadhesión y retardaba la liberación del fármaco. La adición de tensioactivo (Tween® 80) en la preparación de las nanopartículas permitía disminuir el tamaño de estas y aumentar la cantidad de fármaco cargado, así como las propiedades mucoadhesivas (Saikia et al., 2015). Paralelamente, Sarmah y col. (2015) desarrollaron nanopartículas de gelatina-montmorillonita cargadas con INH, comprobando que al aumentar el contenido de montmorillonita, disminuía el porcentaje de fármaco liberado y aumentaba la mucoadhesión. Más recientemente, la RIF ha sido vehiculizada en montmorillonita modificada con poli (o-toluidina), obteniendo una liberación controlada del fármaco (Verma y Riaz, 2018). En el pasado año, una bentonita ha sido modificada con glicina con el objetivo de actuar como nanotransportador de INH, se ha estudiado el proceso de adsorción-desorción en medio acuoso y se ha concluido que el tiempo óptimo para alcanzar el equilibrio de adsorción es 20 minutos y que las moléculas de INH se adsorben sobre la superficie de la bentonita modificada mediante enlaces débiles de tipo Π (Çalışkan Salihi et al., 2018).

Estos estudios, la mayoría muy recientes, ponen de manifiesto que el empleo de filosilicatos en la mejora del tratamiento de la TB es un área de trabajo con intensa actividad, de cuyos resultados cabe esperar avances significativos en los próximos años.

CAPÍTULO II

Objetivos y Plan de Trabajo

II.1 Objetivos

La tuberculosis (TB) es una enfermedad infecciosa causada por el *Mycobacterium tuberculosis*. Es una de las diez principales causas de mortalidad en el mundo. En 2017, unos 10 millones de personas enfermaron de TB y 1,3 millones murieron por esta enfermedad (entre ellos, 0,3 millones de enfermos del virus de inmunodeficiencia humana). Más del 95% de las muertes por TB se producen en países subdesarrollados o en vías de desarrollo (WHO, 2018a). Es una enfermedad curable, pero es necesario un tratamiento de larga duración (al menos seis meses) y la administración conjunta de los cuatro fármacos antituberculosos de primera línea (isoniazida, rifampicina, pirazinamida y etambutol), dando lugar a un cumplimiento terapéutico bajo, lo que propicia la aparición de resistencias, que dificultan el tratamiento al aumentar su coste y duración (WHO, 2018a). Existen formas farmacéuticas que incluyen los cuatro fármacos antituberculosos de primera línea (FDC: "Fixed-dose combinations"), recomendadas por la Organización Mundial de la Salud por facilitar el cumplimiento terapéutico al reducir el número de formas farmacéuticas necesarias (WHO, 2018a). Sin embargo, dichas FDC presentan problemas de inestabilidad física y química entre los fármacos (Singh et al., 2001; Bhutani et al., 2004, 2005a, b; Tostmann et al., 2008; Battini et al., 2018), así como una elevada variabilidad interindividual en la biodisponibilidad de los fármacos incluidos (Verbeeck et al., 2016). El fármaco más utilizado en la terapia antituberculosa es la isoniazida, por ser el de mayor actividad bactericida (Cordes et al., 2016). Sin embargo, presenta una baja biodisponibilidad oral debida a su baja permeabilidad intestinal, que junto a su elevada solubilidad determina su inclusión en la clase III del Sistema de Clasificación Biofarmacéutica (Kasim et al., 2004; Ramirez et al., 2010).

Los minerales de la arcilla tienen la capacidad de modificar la liberación, aumentar la solubilidad y mejorar la estabilidad de los principios activos (Aguzzi et al., 2007). La elección adecuada del mineral de la arcilla a utilizar es el primer paso para lograr sistemas híbridos terapéuticamente eficaces. Otro aspecto de importancia crucial es el proceso de adsorción de los fármacos en las arcillas, así como los mecanismos de liberación. Las distintas posibilidades que puedan ofrecer estos sistemas híbridos

fármaco-arcillas dependerán de la cantidad de fármaco retenido por la arcilla, así como de la cinética de liberación y la cantidad total de fármaco liberado. Las ventajas terapéuticas ofrecidas por estos sistemas avanzados de liberación de fármacos los convierten en un área de especial interés en ciencias de la salud (Viseras et al., 2010).

El grupo de investigación CTS-946 ha desarrollado numerosos sistemas nanohíbridos basados en minerales de la arcilla para ser utilizados como nanotransportadores de fármacos. Distintas arcillas han sido empleadas como soportes de múltiples fármacos con diversos fines. Las Tesis Doctorales de las profesoras Cerezo (2003) y Aguzzi (2005), ya se centraban en el desarrollo de sistemas fármaco/arcilla. De los conocimientos adquiridos a través de esos trabajos, han surgido numerosas líneas de investigación que actualmente se llevan a cabo. Entre ellas, a manera de ejemplo, se ha mejorado recientemente la solubilidad del antihelmíntico praziquantel, objetivo de la Tesis Doctoral defendida recientemente por la Dra. Borrego-Sánchez (2018). Anteriormente, el polimorfo tubular del caolín conocido como halloysita fue elegido como soporte del antiinflamatorio ácido 5-aminosalicílico (5-ASA) y fueron estudiados de forma detallada los aspectos cinéticos y termodinámicos de los procesos de adsorción (Viseras et al., 2008b) y liberación (Aguzzi et al., 2013). En ocasiones la arcilla se ha conjugado con otros excipientes para optimizar las propiedades. Así, el uso de un sistema que incluía sepiolita y una ciclodextrina se ha utilizado para mejorar la solubilidad del fármaco oxaprocin (Mura et al., 2016) o se han elaborado nanocomposites de arcillas con quitosano para la liberación modificada de 5-ASA (Aguzzi et al., 2010) o para aumentar la permeabilidad intestinal *in-vitro* del antibiótico oxitetraciclina (Salcedo et al., 2014), previo estudio de su mucoadhesión y citocompatibilidad *in-vitro* en dicha línea celular (Salcedo et al., 2012). Similares nanosistemas montmorillonita-quitosano han sido usados como vehículos de sulfadiazina de plata para su administración vía tópica para mejorar la cicatrización de heridas “wound healing” (Aguzzi et al., 2014a; Sandri et al., 2014). Otras arcillas, como la palygorskita han sido objeto de formulaciones tópicas (López-Galindo et al., 2011; Tenci et al., 2017) y orales (Mura et al., 2016). Todos estos estudios constituyen la base de conocimiento sobre la que se sostienen las hipótesis y objetivos de esta Tesis.

Con las premisas establecidas hasta aquí, esta Tesis comprende el uso sostenible de determinadas arcillas como excipientes destinados a la preparación de nanosistemas

híbridos inorgánicos-orgánicos con fármacos antituberculosos. Dichos sistemas se han preparado con dos arcillas mediante la técnica de intercalación sólido/líquido utilizando siempre como fármaco de elección la isoniazida. Estos sistemas se plantean con un doble propósito: un propósito tecnológico, enfocado a la protección del fármaco isoniazida, minimizando interacciones cuando se administren en formas farmacéuticas combinadas con los otros antituberculosos de primera línea y un propósito biofarmacéutico, orientado al aumento de la biodisponibilidad oral de dicho fármaco.

Los objetivos específicos de la Tesis son:

1. Estudio de las posibilidades presentes y futuras ofrecidas por las arcillas de grado farmacéutico como nanotransportadores de los fármacos antituberculosos de primera línea.

2. Estudio experimental y teórico del fundamento termodinámico y cinético de la adsorción de isoniazida en minerales de las arcillas de distinta estructura y morfología (halloysita y palygorskita). Caracterización del estado sólido de las materias primas y nanohíbridos fármacos-arcillas obtenidos.

3. Estudio cinético de disolución *in-vitro* de la isoniazida desde el nanohíbrido halloysita-isoniazida obtenido. Estudios de citotoxicidad de las materias primas y el nanohíbrido y permeabilidad intestinal *in-vitro* del fármaco desde el nanohíbrido y sólo como control. Ensayo de estabilidad acelerada de la isoniazida pura y transportada en los nanotubos frente a los otros fármacos tuberculostáticos de primera línea (etambutol, pirazinamida y rifampicina).

II.2 Plan de trabajo

Este proyecto se basa en la investigación sobre los aspectos cinéticos y termodinámicos del proceso de adsorción-desorción del fármaco antituberculoso de primera línea isoniazida en la superficie de arcillas de grado farmacéutico nanotubulares (halloysita) o fibrosas (palygorskita) con el objeto de diseñar y desarrollar nuevos materiales

nanofuncionales de origen natural (nanohíbridos isoniazida-minerales de la arcilla) que permitan paliar las dificultades derivadas de la inestabilidad entre los fármacos antituberculosos y la baja biodisponibilidad oral del fármaco líder en la terapia. Los datos experimentales de los estudios de adsorción con las arcillas mencionadas, así como de liberación desde el nanohíbrido isoniazida-halloysita han sido ajustados a modelos teóricos no lineales con un coeficiente de correlación próximo a uno en todos los casos. Se ha realizado un estudio computacional del proceso de adsorción isoniazida-halloysita mediante modelado molecular, cuyos resultados corroboran los resultados experimentales obtenidos anteriormente. Durante una estancia en la Universidad de Pavía (Italia) en el año 2016 se estudió la permeabilidad intestinal *in-vitro* de la isoniazida sola y desde el nanohíbrido isoniazida-halloysita mediante el empleo de células de adenocarcinoma de Caco-2, que permiten diferenciarse en forma de monocapa y reproducir las condiciones de la barrera intestinal. Asimismo, se realizaron estudios de citotoxicidad *in-vitro* con los productos puros así como el nuevo nanohíbrido sintetizado. Por último, con el fin de comprobar si la inclusión del fármaco en los nanotubos de halloysita tenía algún efecto positivo en la compatibilidad de la isoniazida con el resto de fármacos antituberculosos de primera línea, se han llevado a cabo estudios de estabilidad acelerada de formulaciones binarias y cuaternarias conteniendo isoniazida (sola y como nanohíbrido halloysita-isoniazida) y uno (formulaciones binarias) o tres (formulaciones cuaternarias) de los principios activos antituberculosos de primera línea (etambutol, pirazinamida y rifampicina).

De acuerdo con los objetivos citados con anterioridad, el plan de trabajo de la Tesis Doctoral se organizó en los siguientes apartados, correspondientes a capítulos en esta memoria de Tesis:

Capítulo III. En este capítulo se aborda el objetivo 1 de la Tesis. Se concreta en dos publicaciones; un capítulo de libro en el que se revisa en profundidad el empleo de halloysita en nanomedicina y un "Opinion Paper" en el que se plantea la posibilidad de empleo de los filosilicatos como nanomateriales de interés en la terapéutica de la tuberculosis. Los otros minerales tienen una abundante bibliografía de empleo farmacéutico, pero entendimos que era necesario hacer un estudio específico de la halloysita, dadas sus especiales propiedades y estructura.

- **Aguzzi, C., Sandri, G., Cerezo, P., Carazo, E., Viseras, C. (2016). Health and medical applications of tubular clay minerals. En: Nanosized Tubular Clay Minerals. Halloysite and Imogolite. Peng Yuan, Antoine Thill y Faïza Bergaya (Eds). Serie: Developments in Clay Science, Elsevier. Vol. 7, capítulo 26, pp. 708-725.**

- **Carazo, E., Borrego-Sanchez, A., Aguzzi, C., Cerezo, P., Viseras, C. (2017). Use of clays as nanocarriers of first-line tuberculostatic drugs. Current Drug Delivery, 14(7), 902-903.**

Capítulos IV y V. Una vez hecha la necesaria revisión bibliográfica específica y orientada a los objetivos planteados, en estos capítulos se abordan los ensayos y resultados relativos a los aspectos termodinámicos y cinéticos de la adsorción de isoniazida en halloysita (Capítulo IV) y palygorskita (Capítulo V). Se cumple así con el objetivo 2 de la Tesis Doctoral mediante dos publicaciones de primer cuartil JCR, en las que se presentan los resultados del estudio separados por cada uno de los excipientes inorgánicos.

- **Carazo, E., Borrego-Sánchez, A., García-Villén, F., Sánchez-Espejo, R., Aguzzi, C., Viseras, C., Sainz-Díaz, C.I., Cerezo, P. (2017). Assessment of halloysite nanotubes as vehicles of isoniazid. Colloids and Surfaces B: Biointerfaces, 160, 337-344.**

- **Carazo, E., Borrego-Sánchez, A., García-Villén, F., Sánchez-Espejo, R., Viseras, C., Cerezo, P., Aguzzi, C. (2018). Adsorption and characterization of palygorskite-isoniazid nanohybrids. Applied Clay Science, 160, 180-185.**

Capítulo VI. Este capítulo se centra en el objetivo 3 de la Tesis Doctoral. Los resultados obtenidos en el capítulo anterior permitían seleccionar cualquiera de los híbridos obtenidos para dar continuidad al estudio. No obstante, el híbrido con halloysita presentaba valores de capacidad de retención en forma de monocapa (n^s_m)

superiores y requiere menores temperaturas para ser preparado de forma eficiente (30ºC) que en el caso de palygorskita (40ºC), siendo las constantes de adsorción similares en ambos casos, por lo que se decidió seleccionar el híbrido con halloysita para continuar el estudio. En este capítulo se recogen, por tanto, los estudios *in-vitro* de liberación, de citotoxicidad y de permeabilidad intestinal, destinados a establecer las posibilidades reales de empleo terapéutico de los híbridos con halloysita. Asimismo, se incluyen los estudios de estabilidad acelerada del fármaco soportado en la arcilla en presencia de los otros fármacos de empleo en la terapéutica de la tuberculosis, para establecer las ventajas tecnológicas de la interacción, y dado que se pretende desarrollar sistemas mejorados de empleo real. Todos los resultados obtenidos han sido recogidos en un artículo que ha sido aceptado para su publicación en una revista del primer cuartil JCR.

- **Carazo, E., Sandri, G., Cerezo, P., Ianni, C., Ferrari, F., Bonferoni, C., Viseras, C., Aguzzi, C. Halloysite Nanotubes as Tools to Improve the Actual Challenge of Fixed Doses Combinations in Tuberculosis Treatment. Journal of Biomedical Materials Research Part A (doi: 10.1002/jbm.a.36664).**

CAPÍTULO IIIa

Health and medical applications of tubular clay minerals

RESUMEN

Este capítulo publicado como capítulo de libro en 2016 reúne una amplia revisión biblográfica acerca del uso de minerales de la arcilla tubulares como nanomateriales de elección en tecnología farmacéutica.

Las nanoarcillas tubulares, halloysita e imogolita las más conocidas, son desde hace años muy utilizadas en multitud de aplicaciones biomédicas avanzadas. Pueden emplearse de forma natural, es decir, sin modificar, o previa funcionalización combinándolos con polímeros para dar lugar a nanocomposites polímero-arcilla, muy útiles como sistemas de liberación modificada de fármacos, y más actualmente, genes. Asimismo, se ha demostrado su potencial uso en ingeniería tisular y medicina regenerativa como transportadores de proteínas, factores de crecimiento y material genético; en sistemas de diagnóstico no invasivo capaces de detectar enfermedades como el cáncer y enfermedades degenerativas y en el desarrollo de productos sanitarios avanzados. El capítulo recoge una detallada revisión bibliográfica de los trabajos publicados enfocados al empleo de las nanoarcillas tubulares naturales y en forma de nanocomposites polímero-arcilla en cada uno de los aspectos biomédicos citados anteriormente.

Como reto final se postula la posible aplicación en un futuro próximo de las nanoarcillas tubulares como materiales teragnósticos, es decir, la integración de diagnóstico y terapia usando una misma plataforma.

IIIa.1 INTRODUCTION

This chapter aims to review the possible applications of halloysite and imogolite, two nanosized clay minerals with a hollow tubular structure, in nanopharmaceutics (ie, the use of nanotechnology in pharmaceutics). Pharmaceutics is concerned with the scientific and technological aspects of the design and manufacture of medicinal products and medical devices (Aulton and Taylor, 2013). Medicinal products are defined as "(i) Any substance or combination of substances presented as having properties for treating or preventing disease in human beings; or (ii) Any substance or combination of substances which may be used in or administered to human beings either with a view to restoring, correcting or modifying physiological functions by exerting a pharmacological, immunological or metabolic action, or to making a medical diagnosis" (European Directive, 2001). Medical devices are defined as "Any instrument, apparatus, appliance, software, material or other article, whether used alone or in combination, together with any accessories, …, for the purpose of diagnosis, prevention, monitoring, treatment or alleviation of disease,…, which does not achieve its principal intended action in or on the human body by pharmacological, immunological or metabolic means,…" (European Directive, 2007).

Medicinal products and medical devices are regulated throughout their entire life cycle, including basic and preclinical research, clinical trials, marketing authorisation and ongoing postauthorisation surveillance. It must be remembered that for every 10,000 new drug candidates studied in basic research, only 250 proceed to the next stage. In preclinical research, the safety of drug molecules and their efficacy expectations are studied before starting trials on humans, and in the end only five molecules reach the clinical trial stage. Clinical trials establish the efficacy of the medicinal product in humans (or animals, in the case of veterinary medicinal products) in the treatment of the disease for which it is intended to treat with an acceptable profile of adverse reactions. At the end of the process, only one molecule of the 10,000 initially investigated arrives to marketing authorisation. Similar proportions would be expected with nanotechnology materials and their applications in marketed medicinal products (Figure IIIa.1). Academic research plays a key role in this process, driving research and industrial development, as well as through numerous preclinical studies. Still, the market of nanopharmaceuticals could be estimated to be over 25 billion euros in 2020. What are the reasons that explain the success of nanopharmaceuticals in such a hostile

environment? First, the scientific push associated with the knowledge of molecular processes linked to diseases, as well as the advances in nanotechnology and subsequent new nanomaterials, increase the number of offerings. On the other hand, there is a strong demand for innovative solutions to early diagnosis of cancer and other pathologies, transport of drugs across the blood–brain barrier, as well as targeting of diseased tissue and organs or development of implant materials with longer lifespans. The strong demand and the increased number of offerings explain the success of nanopharmaceutics.

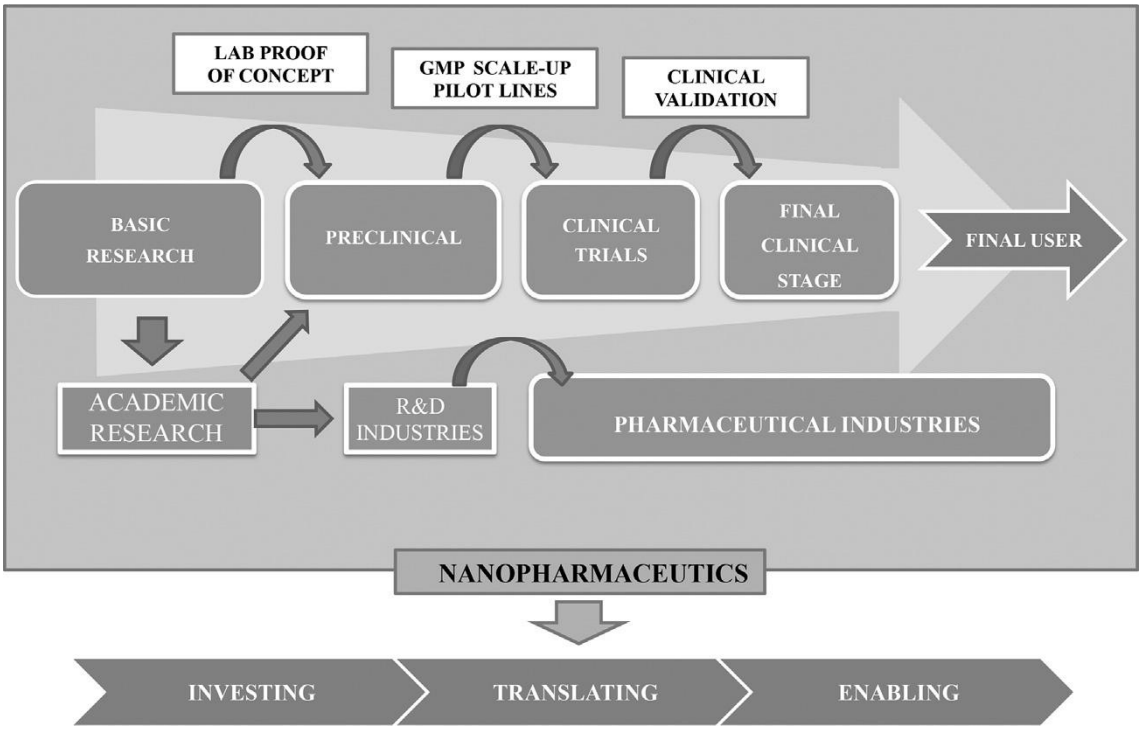

Figure IIIa1. Nanopharmaceuticals value chain, team members and network devoted to the successful fulfilment of nanopharmacy to human health care.

Both medicinal products and medical devices are materials that, once manipulated and controlled, are used to achieve some health objectives, including therapeutics (drug delivery), regenerative medicine and diagnostics (Figure IIIa.2). The development and application of "materials" at the nanoscale plays a relevant role in the design and manufacture of medicines and medical devices, and pharmaceutical nanotechnology (or nanopharmaceutics) is becoming an emerging academic and industrial area (Wagner et al., 2006). In particular, two nanosized tubular clay minerals, halloysite and imogolite, have been proposed as possible nanovectors for drug encapsulation based on their nanotubular structures, as well as in the restoring, maintaining and repairing of tissues

and organ functions, on behalf of their demonstrated biocompatibility (safety) and efficacy. Halloysite is a polymorph of kaolinite in which the sheets curl up to form empty cylinders, and imogolite nanotubes are curved gibbsitelike sheets ($Al(OH)_3$) forming tubes in which the inner hydroxyls are replaced by $SiO_3(OH)$ groups. Typical halloysite nanotubes show internal diameters ranging from 20 to 100 nm, whereas imogolite nanotubes are significantly smaller (~1 nm). These dimensions are high enough to allow most of the drug molecules to be loaded.

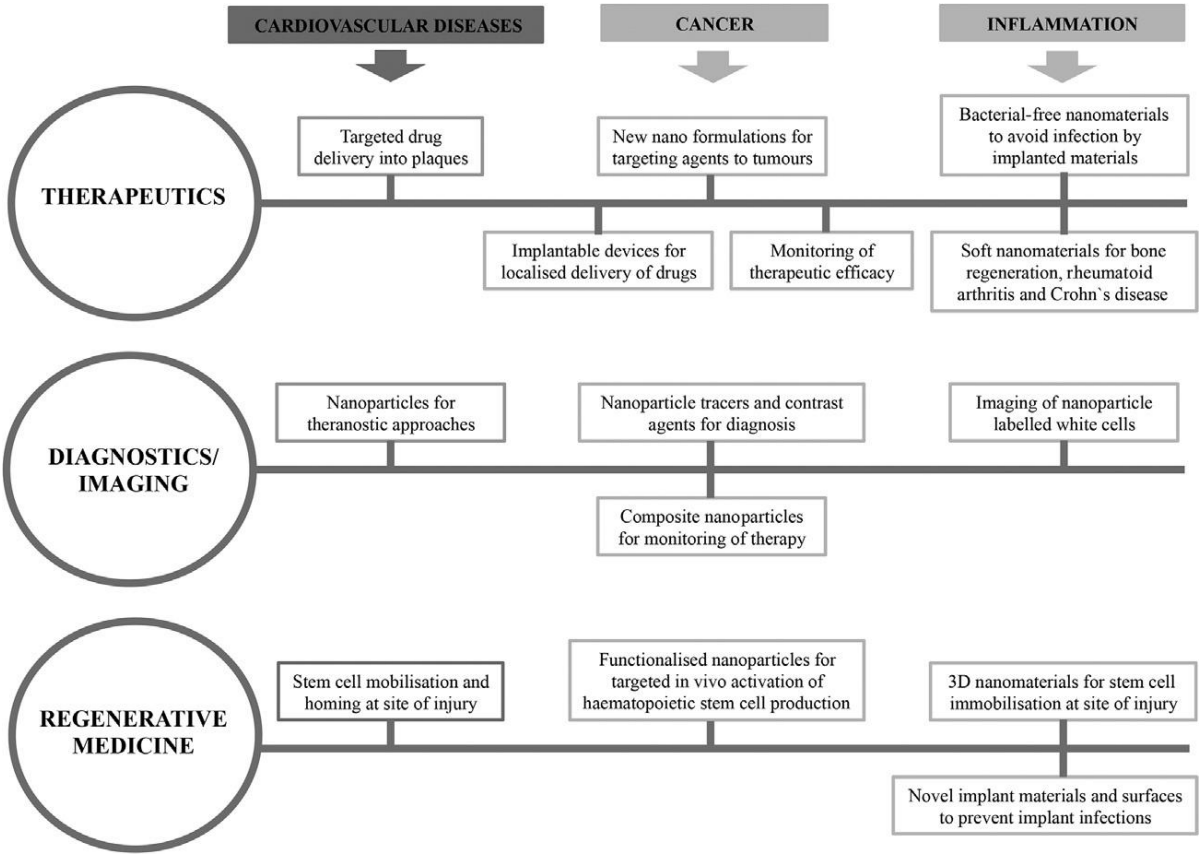

Figure IIIa2. Prospective uses of nanosized tubular clay minerals in nanopharmaceutics.

In the last several years, nanosized tubular clay minerals have been proposed in diagnostic scenarios as well, opening a new interesting application for these nanomaterials. Together with these uses in the manufacture of medicinal products, nanosized tubular clay minerals have been used in the development of medical devices. All these applications are reviewed in this chapter.

IIIa.2 USE OF NANOSIZED TUBULAR CLAY MINERALS IN DRUG DELIVERY

Drug delivery (particularly drug targeting) allows the selective attack of organs or cells, while saving healthy organs or tissues from nonspecific drug toxicity. Entrapping of drugs into the lumen of nanosized tubular clay minerals is a good strategy not only to modify drug release, but also to protect drugs against chemical and enzymatic degradation.

IIIa.2.1 Natural Nanosized Tubular Clay Minerals

Natural nanosized tubular clay minerals provide well-documented support for drug encapsulation and delivery (Lvov et al., 2014; Viseras et al., 2015; Yuan et al., 2015). Several drug molecules have been loaded onto halloysite nanotubes (Price et al., 2001; Levis and Deasy, 2003; Kelly et al., 2004; Veerabadran et al., 2007; Lvov and Price, 2008; Lvov et al., 2008; Forsgren et al., 2010; Abdullayev and Lvov, 2011; Zhang et al., 2013). The kind of interactions between the functional groups of the drug and the active sites of halloysite outer and inner surfaces are key factors in kinetics and thermodynamic features of drug/halloysite systems (Viseras et al., 2008a, 2009).

In particular, the loading process of halloysite nanotubes with an anti-inflammatory drug (5-aminosalicylic acid) was successfully explained as a combination of two separate processes: a rapid adsorption of the drug at the external surface of the clay mineral particles, and a slower adsorption occurring inside the halloysite lumen and aggregates (Fig. IIIa.3) (Viseras et al., 2008a). Recently, Elumalai et al. (2015) used Monte Carlo simulations to point out the importance of the diameter and length, together with particle charge, of halloysite nanotubes on the loading and release of some model drugs. Drug release from halloysite nanotubes is often characterised by biphasic profiles with an initial burst followed by a slower release phase, making it difficult to fit the experimental data and to explain the underlying release mechanism using a single mathematical model.

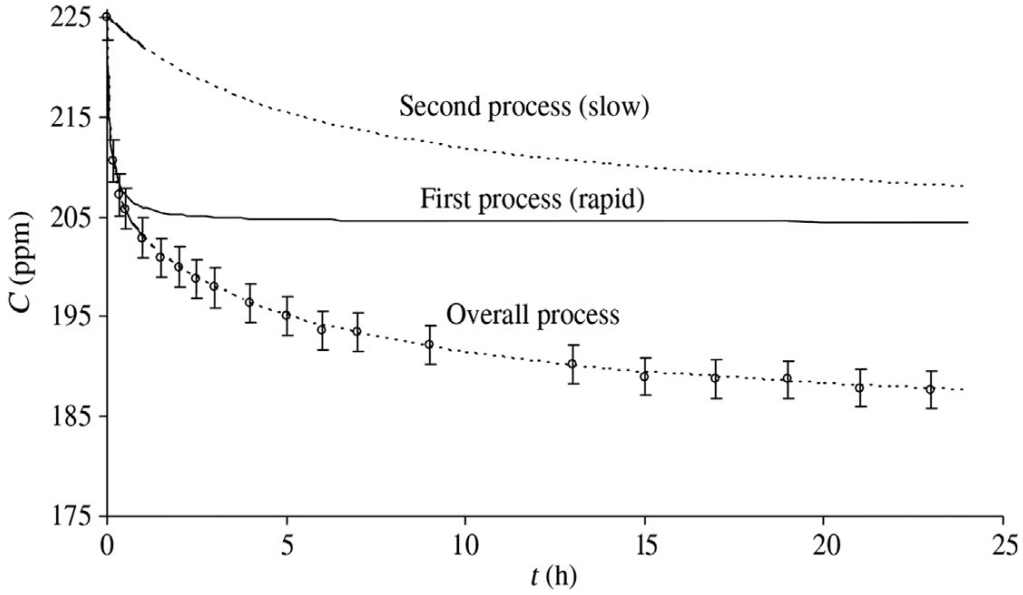

Figure IIIa.3. Individual and overall kinetic adsorption isotherms of 5-aminosalicylic acid onto halloysite at 30°C. Reprinted with permission from Viseras et al. (2008a). Copyright 2008 Elsevier.

A newer model based on kinetic laws able to describe biphasic release curves and provide information about kinetic order and specific release rate from these supports has been successfully postulated by Aguzzi et al. (2013). Briefly, the release of 5-aminosalicylic acid retained onto halloysite nanotubes was explained as an overall desorption process resulting from the contribution of individual simple processes governed by diffusion that included desorption of the drug adsorbed on the external clay mineral surfaces, interparticle spaces or both (fast process) and desorption of drug molecules adsorbed into the halloysite lumen (slow process) (Figure IIIa.4). This model provides real hypotheses about mechanisms implicated in drug release from nanosized tubular clay minerals and is able to satisfactorily fit all the experimental data with a simple equation. More examples concerning the use of halloysite as a drug carrier canbe found in Chapter 22.

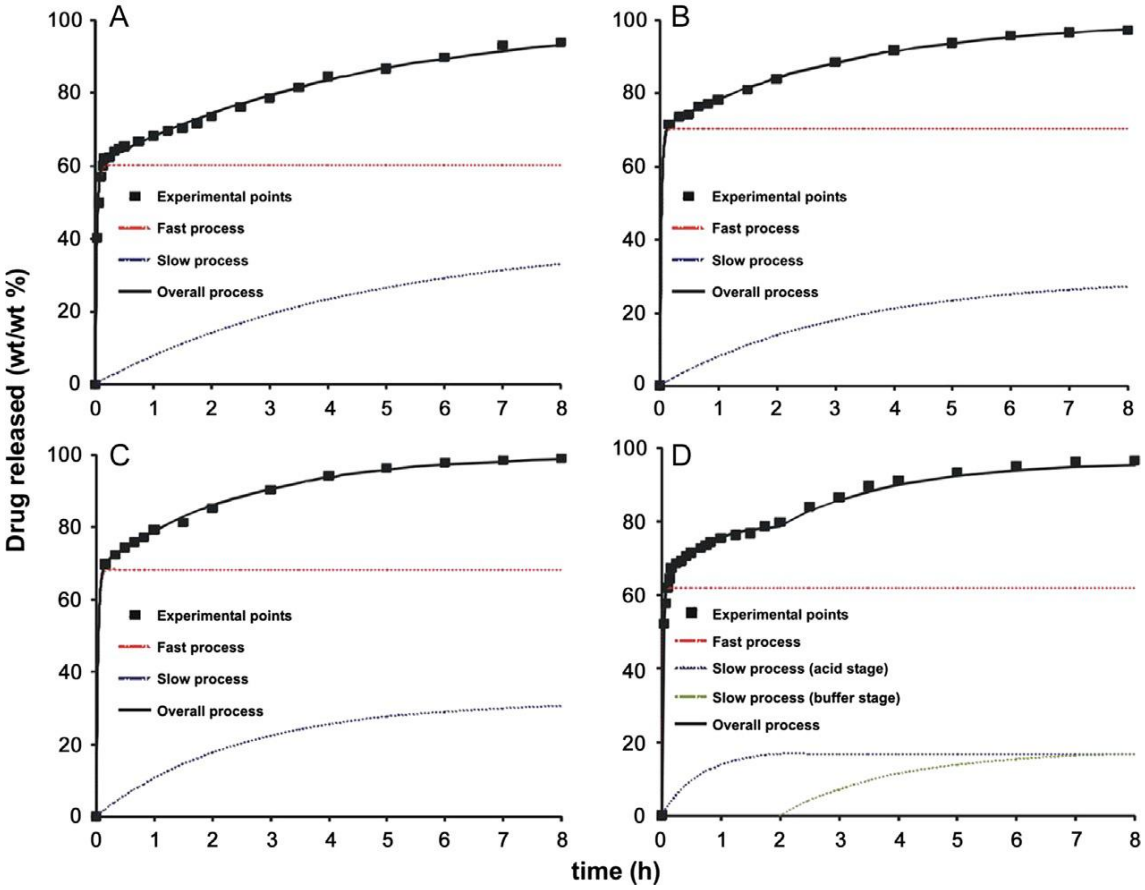

Figure IIIa.4. Amount of drug released (mean values ±s.d.; n=6) of 5-aminosalycilic acid from halloysite in three dissolution media (A); theoretical dissolution curves (lines) of overall and simple release processes in purified water (B), 0.1 M HCl (C) and pH 6.8 buffer (D). Reprinted with permission from Aguzzi et al. (2013). Copyright 2013 Elsevier.

IIIa.2.2 Functionalised Nanosized Tubular Clay Minerals

Halloysite nanotubes can be modified by interactions with specific functional groups or thermal processing in order to improve their performance as drug carriers (Yah et al., 2012; Yuan et al., 2012a,b; Joo et al., 2013; Tan et al., 2013). See more details concerning the modification of nanosized tubular clay minerals in Chapters 8 and 12. Functionalised nanotubes find several applications in both conventional and advanced (ie, gene delivery) therapies. Natural halloysite nanotubes modified with 3-aminopropyltriethoxysilane were successfully used as carriers for aspirin (Lun et al., 2014) and ibuprofen (Tan et al., 2014), showing a higher loading capacity and enhanced drug dissolution rate than unmodified halloysite. Functionalisation with carboxyl acid (Zargarian et al., 2015) or poly (N,N-dimethylaminoethylmethacrylate) (Hemmatpour et al., 2015) also provided halloysite nanotubes with improved loading capacities for drugs as diphenhydramine and diclofenac. Coating with polyorganosilanes was exploited to

change halloysite surface from hydrophilic to superhydrophobic, providing a slow release rate of diclofenac (Fan et al., 2014). Release of antiseptic agents was also greatly reduced by coating halloysite with a benzotriazole-Cu^{2+} chelate film (Wei et al., 2014). The obtained systems showed antibacterial activity against Staphylococcus aureus cell cultures for up to 72 h, which means that they look promising to be administered as bandages for wound healing. Halloysite loaded with tetracycline has been coated with polyvinyl alcohol and polymethyl methacrylate films to reduce the initial burst effect that was observed in the release of the drug from the natural nanotubes alone (Ward et al., 2010). Other studies showed that halloysite nanotubes modified with tetrazolium salts were able to enhance the in vitro activity of the antitumour drugs curcumin (Riela et al., 2014) and cardanol (Massaro et al., 2015a) against several tumour cell lines. Curcumin was also loaded on thermoresponsive poly(N-isopropylacrylamide)-halloysite nanotubes in order to prevent drug degradation (Cavallaro et al., 2015). Massaro et al. (2014) prepared functionalised halloysite with both cyclodextrins and thiosaccharide units. The obtained modified nanotubes were aimed to act as drug delivery systems and to mimic the binding occurring between cell proteins (lectins) and sugars during cellular recognition events. Layerby-layer adsorption of oppositely charged polyelectrolytes is another strategy to obtain novel nanovectors for anticancer agents (Guo et al., 2012; Mitchell et al., 2012a,b; Vergaro et al., 2012; Shutava et al., 2014). Cyclodextrinmodified halloysite nanotubes can offer the possibility for simultaneous encapsulation of different drugs in multiagent therapies, as demonstrated with two natural antitumoural agents (silibinin and quercetin) (Massaro et al., 2015b). Advanced therapy based on administration of genetic matter is also greatly attractive as a treatment for cancer disorders. Halloysite nanotubes could efficiently improve intracellular delivery and enhance the antitumour activity of antisense oligodeoxynucleotides (Shi et al., 2011). The clay mineral also has been proposed as a transgene transmission reagent (Campos et al., 2011) because of its cellular uptake and cytocompatibility properties (Kommireddy et al., 2005; Vergaro et al., 2010; Verma et al., 2012).

Imogolite nanotubes present a positive alumina surface and negative inner silica surface, combined with significantly smaller lumen diameter in comparison with halloysite, provoking a decrease in the efficacy of adsorption of biological macromolecules and drugs (Gustafsson, 2001). However, imogolite nanotubes have been successfully

exploited for DNA encapsulation in order to protect it from degradation by nucleases but maintain its biological activity (Jiravanichanun et al., 2012).

IIIa.2.3 Nanosized Tubular Clay Minerals/Biopolymer Nanocomposites

In addition with the abovementioned functionalisation strategies, clay mineral/biopolymer nanocomposites are designed to obtain hybrid materials with enhanced properties compared to the pure components (Viseras et al., 2008b, 2010). Natural mineral nanotubes can be assembled with a large variety of polymers yielding nanostructured hybrid materials used to design nanoscale drug delivery systems (Viseras et al., 2008b, 2010; Ghebaur et al., 2012; Abdullayev and Lvov, 2013). Diphenhydramine hydrochloride has been loaded into halloysite/polyvinyl alcohol nanocomposites to control drug delivery (Ghebaur et al., 2012). Biocompatible chitosan and gelatine multilayers were used for the encapsulation of halloysite tubes loaded with dexamethasone by means of layer-by-layer methodology (Veerabadran et al., 2009). Encapsulation of the drug in the mineral nanotubes, accomplished by the assembly of natural polymer shells, resulted in controlled release of the drug molecule. Halloysite/hyaluronate nanocomposites intended for colon target delivery of 5-fluorouracil were recently developed, showing promising pH-dependent drug release profiles (Rao et al., 2014).

IIIa.3 USE OF NANOSIZED TUBULAR CLAY MINERALS IN TISSUE ENGINEERING AND REPARATIVE MEDICINE

Biocompatibility is essential for the potential application of nanosized tubular clay minerals in tissue engineering and regenerative medicine. Halloysite nanotubes interactions with cells and the subsequent intracellular uptake have been studied in different cell lines (Kommireddy et al., 2005; Veerabadran et al., 2009; Vergaro et al., 2010; Lai et al., 2013). Cell adhesion and proliferation on biomaterials is a crucial point in tissue engineering and biotechnology.

Specific interactions between cells and substrates are important to regulate cell function, tissue homeostasis and matrix remodeling. The presence of divalent cations, such as Ca^{2+} and Mg^{2+}, associated with clay minerals, significantly influences cellular adhesion. Clay mineral/cell interactions depend on the shape, size and surface charge of the particles. It is well known that the cell membrane surface is negatively charged and that

positively charged nanoparticles can penetrate deep into cell membranes, while negatively charged particles cannot enter the cell wall. Charge density modulates the biocompatibility and antimicrobial properties of clay minerals, and this is related to the aspect ratio (ie, the relation between structure sizes) (Rawat et al., 2014). Halloysite improved fibroblast cell attachment and spreading and allowed cells to maintain cell phenotypes (Kommireddy et al., 2005). In vitro cell toxicity of halloysite has been studied using human dermal fibroblast and breast cancer cells, and a low inherent toxicity of the pure mineral has been found (Veerabadran et al., 2009). Vergaro et al. (2010) performed in vitro cytotoxicity testing that demonstrated good biocompatibility of halloysite at a concentration of 0.1 mg/mL. It was observed that halloysite was nontoxic towards cervical adenocarcinoma cells (HeLa) and breast cancer cells (MCF-7), as well as the fact that halloysite accumulated in cells without preventing their proliferation. The process of cellular uptake was based on both nanotube concentration around cells and their penetration into cells. Studies with other cellular lines (Caco-2 and HT29-MTX) have also shown a high degree of biocompatibility of halloysite nanotubes below 0.2 mg/mL (Lai et al., 2013). Cell viability and membrane integrity were preserved for middle-term exposure in vitro (6 h) and appeared unlikely to have toxic effects at moderate levels of exposure. At high concentrations (100 mg/L), a significant exposure change in protein expression was observed: this seemed related to the stimulation of the processes of cell growth and proliferation, which is similar to the response to cell infection, irritation and injury and enhanced antioxidant activity, all of which are characteristic of an overall adaptive response to exposure.

With regard to imogolite, its morphology (high length-to-diameter ratio) and expected persistence could suggest potential toxicity; however, the high hydrophilicity and external alumina layer contribute to the relative inertness of this mineral (Rotoli et al., 2014, Ishikawa et al., 2010a,b) declared that the amount of normalised protein per osteoblastlike cell cultured on imogolite was twice as much than when it was cultured on a culture dish, and they also pointed out that the cell-imogolite bindings was stronger than the cell-culture dish ones. These results make evident the good biocompatibility between cells and imogolite.

IIIa.3.1 Tissue Engineering

Tissue engineering offers a means to provide biocompatible replacement tissue with mechanical and functional integrity. A critical step in tissue engineering is the designing

of scaffolds with structure, composition, physicochemical, mechanical and biological features analogous to natural tissues. Scaffolds provide a three-dimensional (3D) environment that supports cell attachment, proliferation and differentiation, as well as enabling the transportation of nutrients and cell metabolites in tissue engineering (Patterson et al., 2010; Chrzanowski et al., 2013; Gaharwar et al., 2013; Song et al., 2014).

Hydrogel (Gaharwar et al., 2013; Song et al., 2014) has been studied as a scaffolding material, especially for soft tissue regeneration, even if it usually has inferior mechanical properties as well as lacking adequate functionality, which hinders its wide application in regenerative medicine (Biondi et al., 2008). The incorporation of clay mineral nanoparticles improved the mechanical properties and functionalities of these systems, fulfiling the requirements of tissue engineering. The 3D geometry is related to pore size, porosity and interpore connectivity that represent key issues for accelerated tissue engineering application. With these premises, different clay minerals have been proposed as innovative platforms for tissue regeneration and biomaterial design because of their capacity to enhance stem and progenitor cell proliferation and differentiation (Dawson and Oreffo, 2013). Polymer electrospun with halloysite showed potential applications in the fields of tissue engineering, wound dressing and drug delivery (Wang et al., 2012). Halloysite and polyvinyl alcohol were used to prepare clay polymer nanocomposites (CPN) with improved osteoblast adhesion (Zhou et al., 2010). Electrospun CPN with tissue engineering (and drug delivery of tetracycline) applications were prepared with halloysite and polylactic-co-glycolic acid (Qi et al., 2010, 2012, 2013). According to its haemocompatibility, halloysite polymer nanocomposites were considered suitable as artificial tissue/organ substitutes (Zhao et al., 2013). Halloysite polymethylmethacrylate nanocomposites have been used as bone cements doped with gentamicin, providing slow release of the drug without compromising the CPN mechanical strength while enhancing bone adhesiveness (Wei et al., 2012). Halloysite polycaprolactone nanocomposite scaffolds showed improved mechanical properties, substantial protein adsorption, enhanced mineralisation and osteogenic differentiation compared to the polymer scaffold without the clay mineral (Nitya et al., 2012). Polyglycerol sebacate was filled with halloysite nanotubes to obtain elastomeric nanocomposites with optimal combination of compliance and a degradable profile compared with the pure counterpart, showing excellentresilience and satisfactory biocompatibility in vitro to be used as a soft tissue engineering material (Chen et al.,

2011). Halloysite chitosan nanotubes nanocomposite scaffolds were prepared by combining solution-mixing and freeze drying techniques exhibiting a high porous structure and cytocompatibility with great potential for tissue engineering (Liu et al., 2013).

Imogolite is also receiving considerable attention in tissue engineering for its excellent adsorption properties and nanotubular shape. Reinforcement of polymeric materials with imogolite nanotubes has recently been described in the research literature (Yamamoto et al., 2005a,b; Yah et al., 2010; Shikinaka et al., 2011). These findings have been exploited to obtain collagen- (Nakano et al., 2010) and gelatine-based (Teramoto et al., 2012) nanocomposite hydrogels, showing improved properties and promising potential in pharmaceutical and tissue engineering development. Imogolite nanocomposite scaffolds exhibited good biocompatibility and enhancement effects of proliferation over mouse osteoblastlike cells (Ishikawa et al., 2010a). With regard to safety requirements, imogolite nanotubes must demonstrate no potential toxicological effects on humans. The possible cytotoxic and genotoxic effects of synthetic imogolite-like nanotubes have been evaluated, revealing no cytotoxic activity in human fibroblast cells up to 0.1 mg/mL of nanoparticles, whereas DNA damage depended on the cell uptake and aspect ratio of the nanotubes (Liu et al., 2012). Imogolite nanotubes offer a wide range of positive characteristics as scaffolds for osteoblastic proliferation and differentiation and are a both suitable and interesting alternative in bone tissue engineering (Ishikawa et al., 2010b). Imogolite nanotubes were applied to cell cultures to compare their properties as scaffolds with a conventional culture dish and a carbon nanotube scaffold. The scaffold containing more imogolite presented the best roughness, wettability and protein adsorption ability. In addition to these advances, modification and functionalisation of imogolite nanotubes (Kang et al., 2010, 2011) will probably offer new perspectives on biomedical field in the next several years.

IIIa.3.2 Reparative Medicine

A particular interesting use of nanosized tubular clay minerals in regenerative medicine is their use in design of wound-healing treatments. Wound healing involves multiple cell populations, extracellular matrix bioactive molecules as soluble mediators and particularly cytokines and growth factors (Velnar et al., 2009). Chronic wounds are the results of different causes and pathological states, such as burns, vasculitis, arterial and venous insufficiency, malignancies, diabetes and neuropathic and pressure ulcers. In

these cases, the normal stages of healing fail, indicating incomplete tissue reparation. Various factors could disturb the normal process, prolonging one or more stages, such as haemostasis, inflammation, proliferation and remodelling. In particular, tissue infections and hypoxia, necrosis and the presence of excessive levels of exudates and inflammatory cytokines could prolong a nonhealing state. A continuous state of wound inflammation causes a negative cascade of tissue responses, and the healing process results in poor functional and anatomical outcomes and frequent relapsing. Generally chronic wounds are often subjected to infections and result in complicated wounds. Different medical approaches and therapeutic choice could affect wound healing and the subsequent steps involved in tissue repairing. The loading and the localization of bioactive molecules in clay minerals, having a role in cell growth and proliferation, may induce cell differentiation (Salcedo et al., 2012). However a more interesting aspect is the possibility of stimulating cell differentiation per se due to the signals produced by charge density and ion concentration. Moreover, it was reported that the elasticity or the structure of the matrix environment regulated stem cell differentiation that depends not only on chemical differentiation factors in the culture medium, but also on characteristics of the matrix environment, such as the materials, the surface type and the mechanical properties of the culture substrates (Engler et al., 2006; Miyahara et al., 2006; Reilly and Engler, 2010; Kotobuki et al., 2013). The presence of silicon and magnesium elements has been described as being able to promote the osteogenic differentiation of mesenchymal stem cells. A biomimetic scaffold should be an artificially designed scaffold that enhance neotissue genesis via cell recruiting, adhesion and proliferation (Ma, 2008). The potential application of halloysite nanotubes for wound-healing purposes was pointed out by Lvov and Abdullayev (2013), showing that halloysite polycaprolactone nanocomposite scaffolds loaded with antiseptic agents were effective materials for skin regeneration. Halloysite has been shown to enhance the haemostatic and wound-healing properties of chitosan sponges in rats (Liu et al., 2014). The inclusion of the nanosized tubular clay minerals promotes in vivo epithelialisation and collagen deposition after 1 week, in comparison with pure chitosan. As for future trends, mineral coating of biological cells can be used to obtain surface-functionalised 3D structures (whole cells) with biomimetic properties. Yeast cells have been used to obtain hollow halloysite-based microcapsules (so-called cyborg cells) by layer-bylayer assembly of nanosized tubular clay minerals and subsequent thermal decomposition of

the cells (Konnova et al., 2013). These new assemblies may find applications in controllable cell growth.

IIIa.4 USE OF NANOSIZED TUBULAR CLAY MINERALS IN DIAGNOSTIC AND MEDICAL DEVICES

At the moment, the use of nanosized tubular clay minerals in diagnosis has not been explicitly raised by any research group. However, some recent articles allow to venture that this will be one of the most interesting research areas of application of nanosized tubular clay minerals in the near future. In cancer therapy, the count of circulating tumour cancer cells in blood can be a diagnostic tool to monitor the progression of the disease and detect possible metastasis. It was demonstrated that halloysite is effective to enhance cell adhesion of circulating cancer cells (Hughes and King, 2010; Hughes et al., 2012). Similar hybrid systems have been also used to detect DNA damage, and these systems could have many biological and medical applications (Rawtani et al., 2013).

The frontier between medicinal products (European Directive, 2001) and medical devices (European Directive, 2007) is not always clear, particularly with those systems based in nanotechnology. For example, an active implantable medical device may be intended to administer a medicinal product. Obviously, the consideration of this system as a medical device or medicinal product will greatly affect the possibilities of marketing. In any case, without going into a final consideration, some authors have proposed the use of halloysite specifically in the design of such devices. Recently, modified halloysite nanotubes have been used for capturing circulating tumour cells from the bloodstream (Mitchell et al., 2015). Functionalisation with surfactants alters the charge of naturally occurring halloysite nanotubes and induces differential adhesion of tumour cells and blood cells to nanotube-coated surfaces under flow. It is not clear at this point whether these systems are medical devices, but the significance of the basic research in this area is obvious.

IIIa.5 CONCLUDING REMARKS

Nanosized tubular clay minerals have attracted a great deal interest in recent years as materials for new, advanced biomedical applications. They are used as they naturally occur or after functionalisation, including clay mineral biopolymer nanohybrids, both in drug and gene delivery. Together with their possibilities in drug delivery, nanosized tubular clay minerals show good features in the development of scaffolds for tissue

engineering, medical devices and diagnostics. Clay minerals and clay biopolymer nanocomposites have been used as carriers of matrix proteins, growth factors and genes in tissue regeneration. The interaction of nanosized tubular clay minerals with biological structures open up opportunities for tissue engineering and offer a range of possibility to develop systems able to facilitate cell adhesion, proliferation and neotissue formation. CPN are characterised by porous network structure, swelling/deswelling behaviour and mechanical properties, which provide physical support for cell adhesion and proliferation as well as excellent biocompatibility.

Moreover, cells could interact with clay minerals, suggesting new opportunities in the functionalisation of surfaces for enhanced reparative response. An important aspect is the capability of clay minerals to induce cell differentiation without the employment of other inductors avoiding problems related to uncontrolled cell proliferation in other regions far from the application site. Nanosized tubular clay minerals could be also potentially used in the design of new noninvasive systems to diagnostic of disorders such as cancer and degenerative diseases.

Of the challenges for the medical application of nanosized tubular clay minerals, a particularly important one is the very moderate interest of the pharmaceutical and medical device industry in nanotechnology. Even though recent research includes many innovative studies based on the application of clay minerals in drug delivery and tissue regeneration/reparation, hard work will be needed to transfer the acquired knowledge to clinical practice, requiring high implications of the academic research. The first step to accomplish will be to create spinoffs that can develop current ideas and results to find major pharmaceutical or medical device companies that licence their technologies or partner with the spinoffs to bring their novel approaches through the regulatory approval process. The second challenge will be to develop nanopharmaceutical products with adequate cost-effectiveness in comparison to conventional alternatives, as health-care systems increasingly face cost pressures.

Nanosized tubular clay minerals have demonstrated their potential in both target delivery and diagnostics, and it is expected that in the near future, they will be used in theranostic platforms that can comprehensively carry out in situ diagnostics, then deliver drugs, genes or both to the diseased tissue or cell and monitor the resultant therapeutic response. These are the new frontiers of using natural mineral nanotubes in health-care applications.

CAPÍTULO IIIb

Use of clays as nanocarriers of first-line tuberculostatic drugs

RESUMEN

Completando la revisión bibliográfica de la Tesis Doctoral, se hizo un estudio específico de empleo de filosilicatos como excipientes en formulaciones con fármacos tuberculostáticos. Concretamente, en un "Opinion Paper" publicado en "Current Drug Delivery" se describen las dificultades que plantea el tratamiento de la tuberculosis (larga duración, necesidad de polimedicación, desarrollo de resistencias bacterianas, toxicidad por altas dosis requeridas y problemas de inestabilidad entre los principios activos antituberculosos de primera línea) y se postula el empleo de los minerales de la arcilla como nanotransportadores de fármacos capaces de mejorar la biodisponibilidad y estabilidad de los fármacos tuberculostáticos de elección.

Tuberculosis (TB) is an infectious disease caused by the bacillus *Mycobacterium tuberculosis (Mtb)*. TB ranks as the second leading cause of death from an infectious disease worldwide, particularly in development countries, only surpassed by the human immunodeficiency virus (HIV) (Zhang et al., 2012; Kaewphinit et al., 2013; WHO, 2015). Causing infection in one third of the world's population, TB might affect not only the lungs (pulmonary TB) but also other sites (extrapulmonary TB) (WHO, 2015). Owing to its rapid spread, high morbidity and mortality rate, the development of an effective treatment for tuberculosis (TB) represents an important global health priority. "The limited effectiveness of current therapy stems largely from the lengthy and complicated nature of first-line treatment for active TB: a six- to nine month course of four drugs in combination (two months of isoniazid, rifampin, pyrazinamide and ethambutol, followed by four to seven months of isoniazid and rifampin)" (Gingsberg et al., 2007). On top of that, in developed nations there is likelihood to achieve a poor adherence in long-term therapies. This lack of patient compliance increases the necessity of the development of prolonged release systems in order to reduce the frequency of drug administration (Traverso and Langer, 2015). As if it were not enough, tuberculostatic drugs exhibit a poor/variable bioavailability and their stability might be decreased when administered in anti-tubercular fixed-dose combination (FDC) (Saranjit et al., 2001). "In particular, the main stability concern with anti-TB FDC products is the interaction between rifampicin and isoniazid. Therefore, the observation of greater instability in three- or four-drug combinations lead to the conclusion that pyrazinamide and ethambutol hydrochloride are catalytic towards the reaction between rifampicin and isoniazid" (Bhutani et al., 2005b). Another limitation in the TB treatment is its toxicity. "A 2-month prophylactic regimen with rifampicin and pyrazinamide led to serious and fatal cases of hepatotoxicity" (American Thoracic Society and the Centers for Disease Control, 2001). Likewise "combined pyrazinamide and ethambutol for latent tuberculosis infection may be associated with a high risk of hepatic toxicity, and warrants close monitoring" (Younossian et al., 2005).

As previously mentioned, "patient non-compliance is the major drawback associated with the long duration chemotherapy of tuberculosis (TB); hence, reduction in dosing frequency forms an important therapeutic strategy" (Pandey et al., 2003). The information of the causes opens a few solutions that are discussed in this commentary.

As it is well documented in literature, clay minerals play a crucial role in modulating drug delivery and increasing drug stability (Aguzzi et al., 2007; Viseras et al., 2008, 2010). Our group has a wide and long experience in the use of clays and clay-polymer nanocomposites as drug carriers not only for oral but topical and periodontal administration (Aguzzi et al., 2010, 2013, 2014a,b; Salcedo et al., 2012, 2014; Sandri et al., 2014; Viseras et al., 2015) as well.

The final aim of our research work in this field is to take advantage of the endless possibilities that clay minerals offer for the development of modified drug delivery systems (MDDS) of the four first-line tuberculostatic drugs (isoniazid, etambuthol, pyrazynamide and rifampicin) in order to obtain a one and only dosage form with improved stability and bioavailability and reduced adverse clinical effects.

Should we succeed in fulfilling this enormous challenge, we will contribute greatly to the improvement of patient compliance, leading to increase the survival of TB patients.

Figure IIIb.1 represents a possible model of the adsorption of the first-line tuberculostatic drugs in the interlayer of the laminar clay montmorillonite as an example of drug-clay interaction.

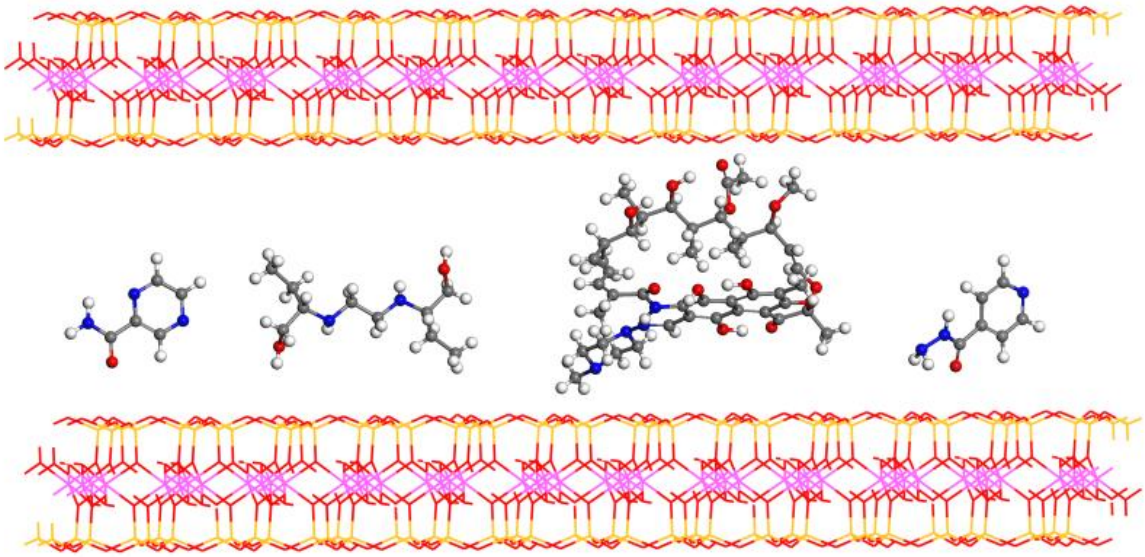

Figure IIIb.1. Idealization of the interaction between first-line tuberculostatic drugs and montmorillonite. From left to right: isoniazid, ethambutol, rifampicin and pyrazinamide.

CAPÍTULO IV

Assessment of halloysite nanotubes as vehicles of isoniazid

RESUMEN

En este capítulo se evalúan las características termodinámicas y cinéticas del proceso de adsorción de isoniazida como fármaco antituberculoso de elección en nanotubos de halloysita. Además se recoge una detallada caracterización al estado sólido de las materias primas y el nanohíbrido, así como un estudio computacional del proceso de adsorción que corrobora los resultados obtenidos experimentalmente.

Se realizaron experimentos de adsorción a distintas temperaturas, tiempos de contacto y concentración de fármaco. El proceso global de adsorción se explicó como la suma de dos procesos simples: adsorción de moléculas de isoniazida en los sitios activos de la halloysita, seguida de una ligera precipitación de moléculas de fármaco sobre la monocapa previamente adsorbida. La formación del nanohíbrido halloysita-isoniazida resultó ser espontánea, endotérmica y endoentrópica, con un aumento de la estabilidad termodinámica del sistema (ΔH = 70.40 kJ/mol; ΔS = 0.2519 kJ/molK). Las diferentes técnicas empleadas en la caracterización al estado sólido corroboraron la efectiva interacción entre el adsorbato (isoniazida) y el adsorbente (halloysita), confirmada también por la modelización computacional. La microscopía electrónica y el microanálisis asociado pusieron de manifiesto la doble localización de moléculas de isoniazida (interior del lumen y superficie externa de la halloysita), así como la distribución homogénea del fármaco en los nanohíbridos. La espectroscopia infrarroja determinó que la interacción ocurría principalmente por puentes de hidrógeno entre los grupos hidroxilo de la halloysita con los átomos de nitrógeno de las moléculas de isoniazida. Los resultados termodinámicamente favorables y la efectiva interacción fármaco-halloysita suponen que los nanohíbridos obtenidos sean la base para posteriores estudios con el fin último de mejorar la terapia antituberculosa.

ABSTRACT

Equilibrium and thermodynamic aspects of the adsorption of isoniazid (INH) onto halloysite nanotubes (HLNTs) and characteristics of the resultant drug/nanocarrier systems are investigated. Equilibrium studies were performed in aqueous medium at different times, temperatures and drug concentrations. The overall adsorption process was explained as the result of two simple processes: adsorption on the activated sites of HLNTs and precipitation of INH on HLNTs surface. Formation of the INH-loaded HLNTs was spontaneous, endothermic and endoentropic, increasing the thermodynamic stability of the system (ΔH = 70.40 kJ/mol; ΔS = 0.2519 kJ/molK). Solid state characterization corroborated the effective interaction between the components that was also described by modeling at molecular level by quantum mechanics calculations along with empirical interatomic potentials. Transmission electron microphotographs confirmed the double allocation and homogeneous distribution of INH in the nanohybrids. FTIR spectra revealed the interaction via hydrogen bonds between the inner hydroxyl groups of HLNTs and N in INH molecules. Loading of INH in the nanohybrids was approximately 20% w/w. Effective loading of INH and activation energies of the interactions enable to propose the designed nanohybrids in the development of modified drug delivery systems.

IV.1 INTRODUCTION

Tuberculosis (TB) ranks as the second leading cause of death worldwide from an infectious disease, particularly in develop-ment countries, only surpassed by the human immunodeficiency virus (WHO, 2016b). It is estimated that one third of the world's population is infected with Mycobacterium tuberculosis, with over 10 million new patients in 2015 and almost half a million of new cases of multidrug-resistant TB (WHO, 2016b). High morbidity and mortality rates make also the development of effective TB treatments an important global health priority (Ginsberg et al., 2007). The currently recommended treatment for new cases of TB consists on a six-month regimen of four first-line drugs (isoniazid, rifampicin, ethambutol and pyrazinamide), with a relatively low cost of about US$ 40 per person (WHO, 2016b). However, two factors determine a poor adherence to the therapy, especially indeveloped nations: its long-term duration and polymedication (Traverso and Langer, 2015). As a result of the low patient

compliance, multidrug-resistant TB increases globally, requiring longer and more expensive treatments (WHO, 2016b).

The design and development of new modified drug delivery systems arises as a good strategy to reduce the frequency of drug administration, increasing compliance and reducing resistant TB incidence (Ginsberg et al., 2007; Carazo et al., 2017a). A wide range of nanoparticulated systems have been proposed to modify drug delivery (Irvine, 2011; Ju et al., 2014; Adhikary et al., 2015; Blanco et al., 2015; Dai et al., 2015; Miller et al., 2015; Zhan et al., 2015) even if most of them are based on expensive materials and/or technologies. The use of clay minerals as carriers for these systems appears as a low cost and biocompatible alternative (Viseras et al., 2008a, 2010; Sandri et al., 2016). In particular, halloysite is a multilayer nanotubular material resulting from the wrapping of 1:1 layers of kaolinite (Bates et al., 1950; Singh and Makinnon, 1996; Yuan et al., 2015). Halloysite nanotubes (HLNTs) have been proposed as a natural vehicle for encapsulation and modified release of several drugs (Abduyallev and Lvov 2011, 2013; Viseras et al., 2015; Aguzzi et al., 2016; Fizir et al., 2017; Yendluri et al., 2017).

With these premises, the aim of this work was to design INH/HLNTs hybrids useful in modified drug delivery treatment of TB. Equilibrium and thermodynamics aspects of the adsorption process between INH and HLNTs were fully investigated and the hybrid systems were then characterized by solid state techniques in order to determine the nature and degree of the interactions between the clay surfaces and the drug molecules. Complementary molecular modeling of the INH/HLNTs adsorption process was carried out in terms of quantum mechanics calculations along with empirical interatomic potentials devoted to determine the most important interaction sites and to investigate mechanisms involved in the adsorption process.

IV.2 MATERIALS AND METHODS

IV.2.1 Materials

INH (Figure IV.1) and HLNTs were purchased from Sigma Aldrich (Spain).

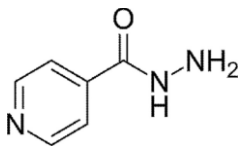

Figure IV.1. INH structure

IV.2.2. Adsorption studies

Adsorption experiments were carried out via intercalation solution technique to obtain equilibrium isotherms at different times and temperatures. 0.1 g of HLNTs were added to 20 mL of INH aqueous solutions with initial concentration (C_0) ranging from 0.05 to 0.5 mol/L, in 25 mL Pyrex TM glass flasks and stirred (150 rpm) in a thermostated bath for different times (24 h, 48 h, one week and two weeks) at 30 ± 0.1ºC. The resulting suspensions were then centrifuged and the equilibrium concentration (C_e) of the drug in the supernatant was determined by UV spectroscopy (UV–vis spectrophotometer Lambda 25, Perkin Elmer, S) at 262 nm. The difference between the initial and equilibrium drug concentration was assumed to be due to drug adsorption onto HLNTs and the amount of INH retained per gram of clay was calculated. One week experiments were also done at different temperatures (35, 40 ± 0.1ºC), once confirmed that this time was long enough to ensure that equilibrium was reached between INH adsorbed and INH in solution. Mathematical treatment of the data was performed (Viseras et al., 2008b), using the software packaging TableCurve 2D® (SystatSoftware Inc., UK) and the relevant adsorption parameters were obtained including monolayer adsorption capacity and equilibrium rate.

IV.2.3. Solid state characterization

Hybrid systems prepared at 30 ºC and initial concentration (C_0 = 0,25 mol/L) to achieve the monolayer adsorption capacity of HLNTs were characterized to determine the effective drug loading, the chemical groups involved in the adsorption process, as well as the presence and distribution of the drug in the internal lumen and/or external surface of HLNTs.

IV.2.3.1. X-ray powder diffraction

X-Ray powder diffraction (XRPD) was done by using a Philips® X-Pert diffractometer with Cu Kα radiation, 40 kV, 40 mA, 3–70º 2Θ exploration range, 6º 2Θ min^{-1}scanning speed, 1 × 10^3 sensitivity and 2 s time constant. The diffraction data were analysed using the XPOWDER® software (Martín-Ramos, 2004). The experiments were run in triplicate (experimental error ± 5%).

IV.2.3.2. Electron microscopy studies

Samples were stained by drop deposition with uranyl acetate 2% (w/v) aqueous solution to achieve selective fixation of uranyl to the amino groups of the drug molecules (Viseras et al., 2009). Briefly, dehydrated samples were embedded for 2 h in a mixture of ethanol and epoxy resin for microscopy (EMbed 812, EMS Ltd., U.K.) and then included for 24 h in pure resin. Subsequently, polymerization was performed by heating the samples at 37 ºC for 24 h and then at 70 ºC for 24 h. The polymerized blocks, cut into ultrathin slices (900 Å thickness) and placed on 300-mesh TEM copper grids (Neyco, France) were stained by deposition of uranyl acetate 2% (w/v) aqueous solution. The excess of the staining agent was absorbed onto filter paper and then grids were covered with a carbon film. The uranyl-stained samples were examined using a FEI Titan G2 60–300 ultra-high resolution transmission electron microscope (UHRTEM), coupled with analytical electron microscopy performed with a SUPER-X silicon-drift windowless energy-dispersive X-ray spectroscopy (EDX) detector. The AEM spectra were collected in STEM (Scaning TransmissionElectron Microscopy) mode using a HAADF (High Angle AnnularDark Field) detector. X-ray chemical element maps were also collected.

IV.2.3.3. Fourier transform infrared spectroscopy

Fourier Transform Infrared (FTIR) spectra were recorded on a FTIR spectrophotometer (JASCO 6200, with software SPECTRAMANAGER v2 and with an attenuated total reflectance (ATR) accessory). Measurements were carried out from 400 to 4000 cm^{-1} at 0.25 cm^{-1} resolution.

IV.2.3.4. Thermal analysis

Differential scanning calorimetry (DSC) and thermogravimetric analysis (TGA) were carried out by using a METTLER TOLEDO mod.TGA/DSC1 with FRS5 sensor and a microbalance (precision 0.1 µg) (Mettler-Toledo GMBH). Samples were heated in air atmosphere at 10ºC/min. Analyses were done in triplicate.

IV.2.4. Molecular modeling methodology and models

The INH molecule was taken from the crystallographic data of crystal form (Rajalakshmi et al., 2014). Our solid models were generated from the atomic

coordinates of a slide of an HLNT from previous works (BIOVIA, 2016) with the stoichiometry $Al_2Si_2O_5(OH)_4$. Periodic boundary conditions were applied to create a periodical crystal structure with the a and b cell parameters crossing the tube forming a cylinder section and the c cell parameter along the HLNT length. We established a = 50 Å, b = 50 Å large enough values for crystal lattice parameters in order to avoid interactions between vicinal tubes. However, the c cell parameter should be optimized point by point in order to connect the original slide to the next one forming a bridging O-Si distance similar of the others O-Si bonds. Then, this optimization yielded a value of c = 9.05 Å with the d (O-Si) = 1.67 Å. Hence, our unit cell of HLNT was a cylinder with an internal diameter of 27 Å formed with an external layer of Si oxide tetrahedra joined to an internal layer of aluminium hydroxide octahedral. The structure is neutral and the multilayer cylindrical structure was possible enlarging the AlOAl and OSiO angles to form the cylinder curvature. Hence, our unit cell of HLNT has the formula $Al_{76}Si_{76}O_{190}(OH)_{152}$ with 646 atoms. In some cases to avoid intermolecular interactions between adsorbates of vicinal cells a 1 × 1 × 2 supercell was generated of HLNT, $Al_{152}Si_{152}O_{380}(OH)_{304}$, with 1292 atoms. In natural HLNTs the internal diameter is around 15–50 nm, nevertheless our models can represent a good scenario to reproduce the interactions at molecular level of the adsorption process. The optimization of HLNT structure was performed with quantum mechanical calculations by using Density Functional Theory (DFT) with CASTEP code, within the generalized gradient approx imation (GGA), the Perdew–Burke–Ernzerhof (PBE) correlation exchange functional and the cut off energy of 300 eV. The adsorbate was placed over the internal surface of the nanotube with the heterocycle ring in a parallel disposition with respect to surface at an average distance of 3 Å to the hydroxyl groups of the mineral surface. The adsorbed complexes were optimized maintaining the mineral structure fixed by using empirical interatomic potentials with the Compass force field that has provided good results in previous studies (Guimarães et al., 2010; Borrego-Sánchez et al., 2016, 2017). For non-bonding interactions, the coulomb and van de Waals interactions were calculated by the Ewald method with a cut-off of 12 Å.

IV.3 RESULTS AND DISCUSSION

IV.3.1 Equilibrium studies

The experimental equilibrium isotherms obtained at different adsorption times as n^s (moles of solute retained per gram of adsorbent) vs C_e are plotted in Figure IV.2. The curves showed initial convex shapes, typical of L-class of Giles classification (Hinz, 2001). The behavior at higher concentrations allowed further classifying the curves as L3 class, characterized by an inflection point from a plateau phase to concave profiles. This behaviour suggested possible precipitation of drug molecules on HLNTs surface. In comparison with short times (one day and two days), an enhanced delineation of the plateau phase was observed after one week, with no further improvement in equilibrium profiles at longer times. Consequently, one week was chosen as the optimal time to suitably define the adsorption curves.

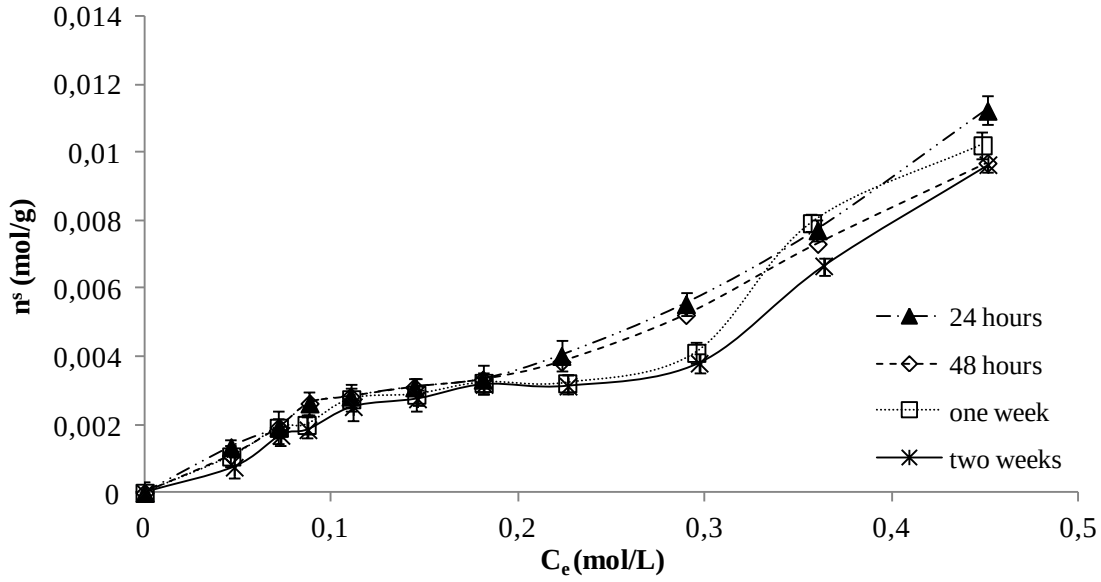

Figure IV.2. Equilibrium isotherms of INH onto HLNTs at different times (mean values ± s.d.; n = 3).

Data obtained from one-week experiments were fitted to the following continuous function (Eq. IV.1):

$$n^s = n_1^s + n_2^s = \sum_{i=1}^{i=2} \frac{K_i . n_{m(i)}^s . C}{K_i . C + 1} + k_f \, C^m \qquad \text{(IV.1)}$$

where n^s= mol of sorbate adsorbed per gram of sorbent, n^s_m = monolayer retention capacity, C = equilibrium concentration, k_i = kinetic equilibrium constant, k_f = kinetic precipitation constantand m = constant.

Equation (IV.1) suggests that the overall adsorption was the sum of two single processes: adsorption at the active surface sites of the sorbent (n^s_1) followed by precipitation of drug molecules (n^s_2) over the adsorbed monolayer (Viseras et al., 2008b). The theoretical overall adsorption curves and contribution of single adsorption processes (n^s_1, n^s_2) resulting from data fitting are shown in Figure IV.3.

At the studied temperatures, the initial contribution at lower drug concentrations was the n^s_1 process, whereas precipitation process (n^s_2) was significant only once the plateau phase was reached (C_e approximately 0.15 mol/L), becoming predominant at higher concentrations.

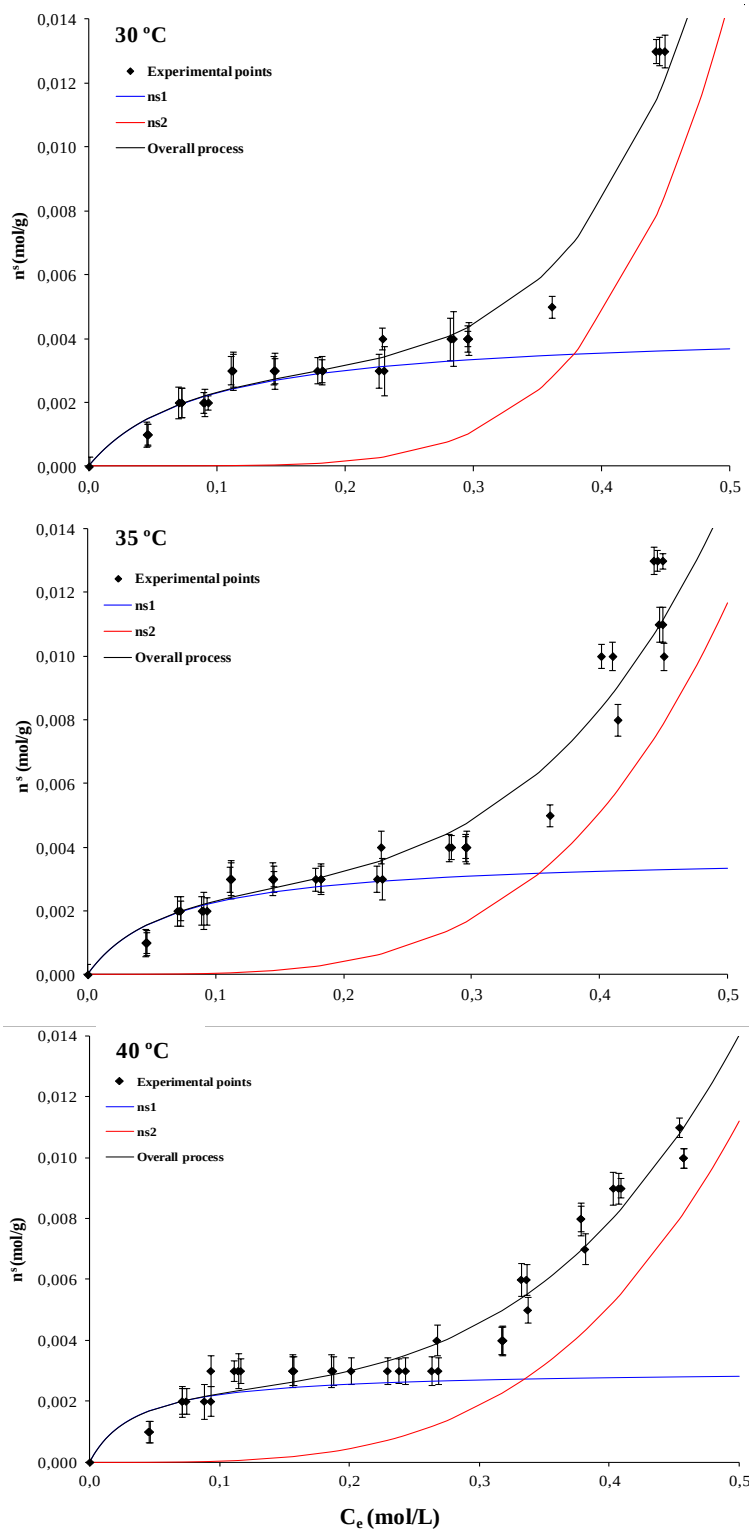

Figure IV.3. Average experimental and theoretical equilibrium isotherms of INH onto HLNTs obtained at one week and three different temperatures (30ºC, 35ºC and 40ºC).

The calculated parameters of Eq. (IV.1) are shown in Table IV.I. The monolayer adsorption capacity (n^s_m) increased with decreasing temperature, apparently suggesting

that adsorption took place as an exothermic process. However, the trending of k_i values was compatible with an endothermic process.

To elucidate the energetic behaviour of the system, k_i values were used to derive the thermodynamic activation functions by means of the following Eq. (IV.2) (Valenzuela-Calahorro et al., 2004):

$$ln\frac{k_i}{T} = ln\frac{R}{Nh} + \frac{\Delta S°}{R} - \frac{\Delta H°}{R} \times \frac{1}{T} \qquad \text{(IV.2)}$$

The calculated values are given in Table IV.I, which also includes ΔG (activation energy) values (calculated from the expression ΔG = ΔH-TΔS). The ΔH and ΔS values indicated that the adsorption of INH onto HLNTs was an endothermic and endoentropic process. The endothermic behaviour reflects that loss of solvation molecules (INH) is required for the incorporation of the adsorbable solute in the adsorbed phase. Otherwise, the positive ΔS value is due to the lower mobility of the adsorbed INH molecules, increasing the order of the system. Finally, the negative ΔG values revealed that at the studied conditions the adsorption process is thermodynamically spontaneous.

Table IV.I. Fitting parameters of Eqs. (IV.1) and (IV.2) for the adsorption of INH onto HLNTs at different temperatures and ΔG (activation energy) for the INH/HLNTs interaction.

Eq. (IV.1)					**Eq. (IV.2)**		
T (ºC)	**n^s_m (mol/g)**	**k_i**	**k_f**	**m**	**ΔH° (kJ/mol)**	**ΔS° (kJ/molK)**	**ΔG (kJ/mol)**
30	0.0025 ± 0.0002	11.271 ± 0.4865	0.508 ± 0.0245	5.116 ± 0.2147			-5.9257 ± 0.00021
35	0.0023 ± 0.0001	15.001 ± 0.3587	0.155 ± 0.0155	3.732 ± 0.1234	70.40 ± 1.244	0.2519 ± 0.00127	-7.1852 ± 0.00015
40	0.0021 ± 0.0001	27.575 ± 0.2111	0.128 ± 0.0872	3.513 ± 0.6547			-8.4447 ± 0.00071

IV.3.2 Solid state characterization

IV.3.2.1 X-ray powder diffraction

The powder X-ray diffraction patterns of the hybrid systems (INH-loaded HLNTs) and their individual components are given in Figure IV.4. INH showed a crystalline pattern, with main reflections at around 10º, 14º, 16º and 20º 2Θ, characteristic of the drug crystals (Angadi et al., 2010), whereas HLNTs showed the typical pattern of natural dehydrated halloysite, with a diffraction peak at 12.25º 2Θ, corresponding to a d001-spacing of 7.24 Å (Rooj et al., 2010). The dehydrated state was further confirmed by the presence of the 002 basal reflection at 24.55º 2Θ (Levis and Deasy, 2003). INH-loaded HLNTs pattern was similar to that of HLNTs, including weak reflections coherent with the presence of crystalline INH over the adsorbed drug monolayer. This finding is in line with the beginning of the precipitation process at the plateau phase, as discussed previously (Figure IV.3).

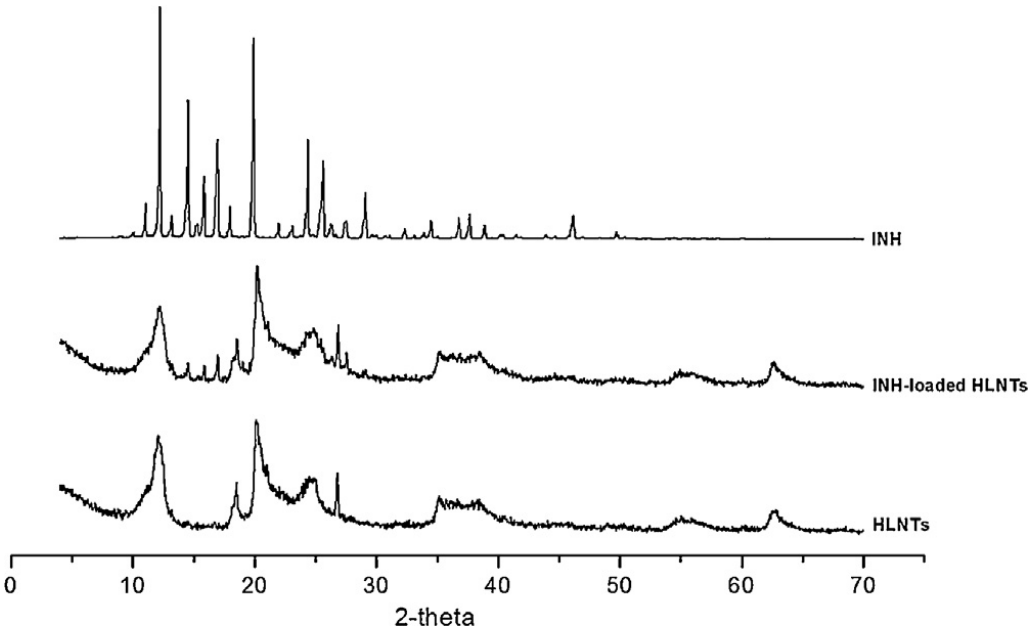

Figure IV.4. XRPD patterns of INH-loaded HLNTs and their pure components (INH and HLNTs).

IV.3.2.2 Electron microscopy studies

Ultra-high resolution transmission electron microphotographs of the uranyl stained samples (Figure IV.5) revealed the characteristic hollow tubular structure of the clay mineral both in native HLNTs (Figure IV.5A1) and the hybrid system (Figure IV.5B1). XEDS spectra of selected areas are also included in both cases, showing peaks of the

nanotube components (O, Al and Si) and a weak Cu peak from the grids used to support the samples. The presence of uranium peaks in the nanohybrid XEDS (Figure IV5B1) allows us to confirm the effective loading of the drug. Uranyl was detected both in the interior (1) and edge (2) of halloysite tubules, which indicates the double allocation of INH molecules. X-ray maps of Si (Figure IV.5A2 and IV.B2), Al (Figure IV.5A3 and IV.B3) and U (Figure IV.5A4 and IV.B4) evidenced the elemental composition of the nanotubes as well as the homogeneous distribution of INH in the hybrid systems.

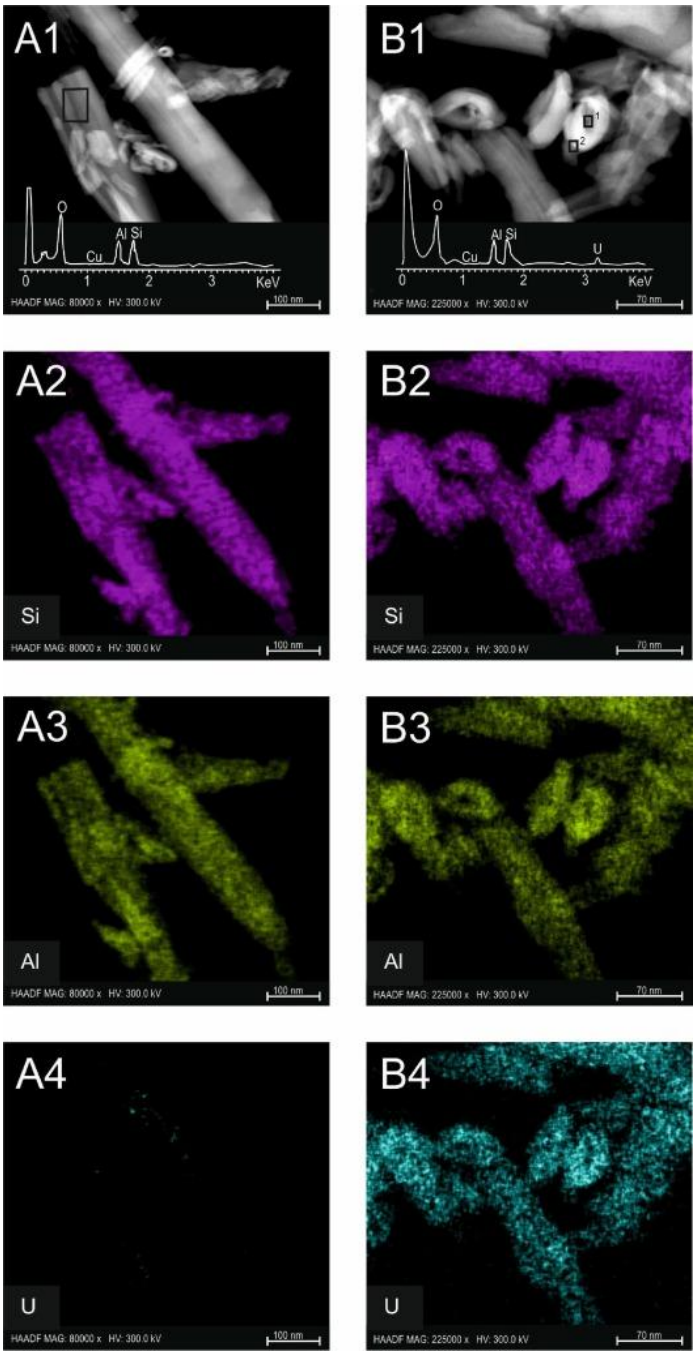

Figure IV.5. UHRTEM microphotographs, XEDS analysis and elemental X-Ray maps of HLNTs (left) and INH-loaded HLNTs (right).

IV.3.2.3 Fourier transform infrared spectroscopy

FTIR spectra of the loaded nanotubes were compared to those of individual components to describe the probable interaction mechanisms (Figure IV.6). INH showed a band at 3303 cm^{-1}, due to N H stretching vibrations. Bands at 1552 cm^{-1} and 1410 cm^{-1}corresponded to the ring C N stretching (amide II) and the ring C C symmetric stretching, respectively. Ring asymmetric bending were noticed twice by both bands at 1193 cm^{-1}stating for a ring C C H asymmetric bending and a ring C C C asymmetric bending with band at 745 cm^{-1}. The band observed at 886 cm^{-1}confirmed a C N C ring bending. The band at 1661 $cm^{-1}$was due to carbonyl of amide group stretching vibrations, while the one at 1631 cm^{-1}owed to the NH_2 deformation. Another band at 1331 $cm^{-1}$was attributed to C N stretching vibrations, while a band at 1556 cm^{-1} was assigned to N H bending vibrations (Brewer, 1977; Gunasekaran et al., 2009; Angadi et al., 2010). The infrared spectrum of HLNTs showed bands at 3692 $cm^{-1}$and 3621 cm^{-1}, assigned to two Al_2OH-stretching bands. Band at 3670 cm^{-1}, detected under a noise level of 0.1, was attributed to the O H stretching of inner-surface hydroxyl groups, while the one at 3545 $cm^{-1}$was referred to the out-of-phase vibration of the inner surface hydroxyls. The band at 1647 cm^{-1} revealed bending vibrations of the physically adsorbed water. The band at 1098 cm^{-1} was assigned to apical Si-O. Perpendicular stretching Si-O-Si vibrations were registered at 679 cm^{-1}. The peaks at 749 cm^{-1} and 796 cm^{-1} were assigned to OH translation vibration of halloysite OH units (Frost, 1995; Sun et al., 2010; Szczepanik et al., 2015). The INH-loaded HLNTs showed the above mentioned HLNTsAl2OH-stretching bands at 3693 $cm^{-1}$and 3622 cm^{-1}, as well as those corresponding to the perpendicular Si-O-Si stretching vibrations (673 cm^{-1}), OH translation vibration of halloysite units(747 cm^{-1} and 793 cm^{-1}) and bending vibrations of the physically adsorbed water (1654 cm^{-1}). The band attributed to INH ring C C H asymmetric bending (1119 cm^{-1}), appeared in the INH-loaded HLNTs spectra at 1193 cm−1. NH2deformation band which in INH spectra appeared at 1631 cm^{-1}, was also present in the spec-tra of the INH-loaded HLNTs but at a wavelength of 1654 cm^{-1}.However, the band at 3545 cm^{-1}, caused by the out of phase vibration of the inner surface hydroxyl in HLNTs was not observed in the spectrum of the INH-loaded HLNTs. Moreover, the little band noticeable at 3670 cm^{-1} in HLNTs spectrum, attributed to the O H stretching of inner-surface hydroxyl groups, also disappeared in the INH-loaded HLNTs spectrum. These changes are clearly related with the interaction

via hydrogen bonds between the inner hydroxyl groups of HLNTs and N in INH molecules.

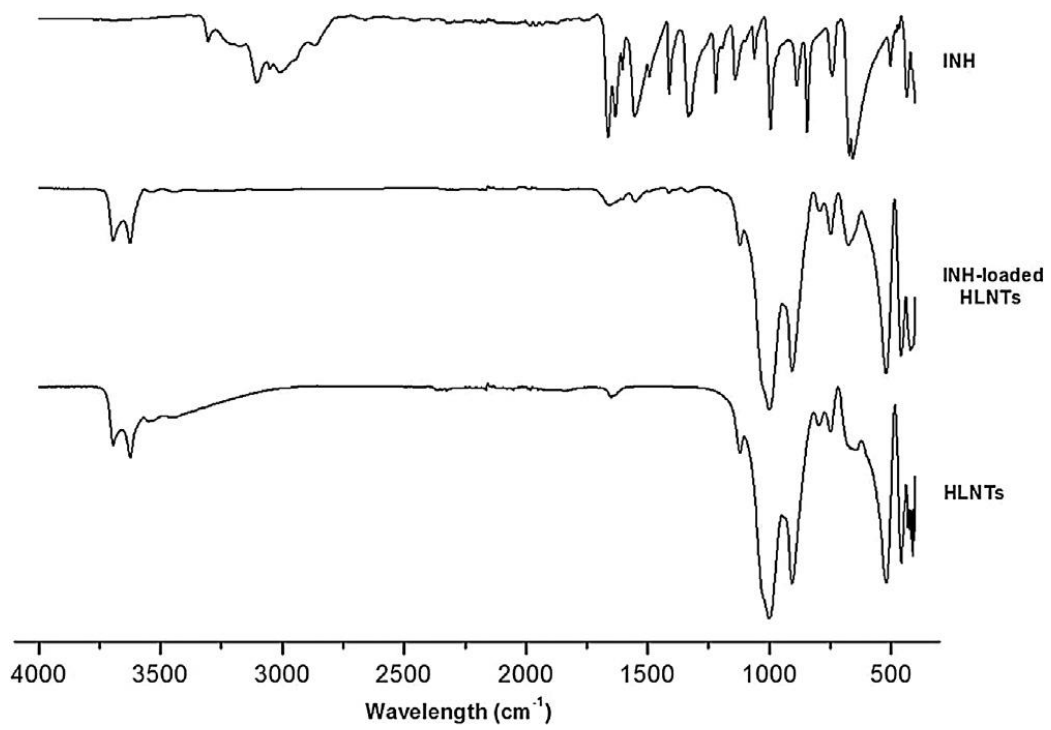

Figure IV.6. FTIR spectra of INH-loaded HLNTs and their pure components (INH and HLNTs).

IV.3.2.4 Thermal analysis

DSC curve of INH showed an endothermic peak at 175ºC, corresponding to the melting of the drug, followed by an exothermic process beginning at 250ºC, due to decomposition (Figure IV.7). DSC curves of HLNTs and INH-loaded HLNTs did not show any significant enthalpy changes at the studied temperature interval and conditions. TGA analysis allowed a more detailed comprehension of the thermal behaviour of the samples (Figure IV.7). TGA curve of INH showed a complete loss of mass in the interval 150°C − 350°C, corresponding to the decomposition of the drug, and associated to the exothermic process observed in the DSC curve (Figure IV.7). HLNTs exhibited two major mass losses at 100°C approximately, attributed to dehydration of the physically adsorbed water (Brindley and Robinson, 1946) and a second loss in the interval 400°C − 600°C, ascribed to dehydroxylation of the structural aluminol groups (AlOH) (Joussein et al., 2005). HLNTs is an extremely thermostable material, with a solid residue of 85.2 ± 0.09% w/w% of the initial mass at 1000 °C. TGA curve of INH-loaded HLNTs showed the decomposition of the drug as well as the dehydroxylation of the clay. Weight loss ascribed to INH decomposition was calculated

according to the rule of mixtures for the residual masses at 1000 °C and taking into account the water content (weight loss between 25 and 150 °C) (Cavallaro et al., 2011). The calculated value (18.9 ± 0.12% w/w) was in line with the theoretical amount of INH retained by the nanotubes calculated from the n^{S}_{m} at 30 °C (25.5% w/w).

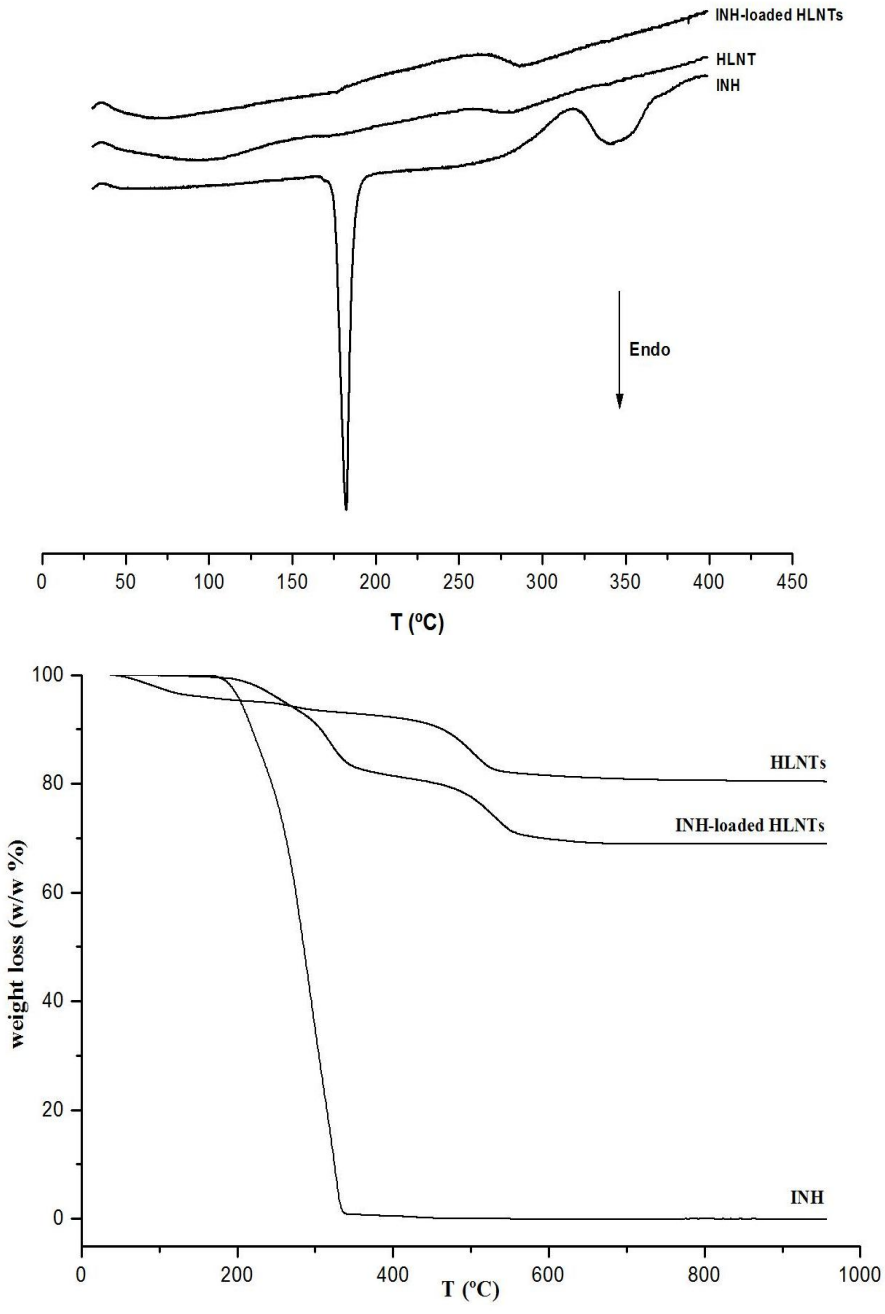

Figure IV.7. DSC and TGA curves of INH-loaded HLNTs and their pure components (INH and HLNTs).

IV.3.3 Molecular modeling

The adsorption of the INH molecule in the space of HLNTs was studied to determine the most important interaction sites with the mineral. This adsorption was simulated in both of two halloysite models and one INH molecule was placed over the internal surface of HLNTs. Dry conditions without presence of water molecules were used to avoid additional interactions that can hide the actual adsorbate-surface interactions. In the Al76Si76O190(OH)152 model the INH molecule was orientated along the cylinder section (H1) and in the Al152Si152O380(OH)304 model the INH molecule was orientated along the nanotube (H2) (Figure IV.8).

After the optimization, INH had similar behaviour in the adsorption of halloysite surface for both models. A conformational change was produced in the INH molecule where the carbonyl group was oriented in a perpendicular direction with respect to the heterocyclic ring. The carbonyl group and the heterocyclic N atom were approached to be coordinated with the H atoms of the OH group of HLNT surface, whereas the hydrazine moiety was oriented towards the centre of the nanotube. In both adsorption complexes the adsorbate maintained a similar orientation with respect to the HLNT with the heterocyclic ring in a parallel disposition with respect to the mineral surface. In H1 the main adsorbate-surface interactions were strong H bonds between the hydroxyl groups of mineral surface and the carbonyl and heterocyclic N atom of adsorbate with d(CO···HO) = 1.94 Å and d(N···HO) = 1.56 Å distances. Additional electrostatic interactions were detected between the N atom of the NH2 group of INH with the H of OH groups of HLNT surface with d(HN···HO) = 3.05 Å. In H2, similar interactions were observed with d(CO···HO) = 1.69 Å, and d(N···HO) = 1.59 Å distances. Also, the N of the aromatic ring had interactions with the H of the OH group of HLNT surface, the distance is 1.59 Å. Additional electrostatic interactions were detected between the N atom of the NH group of INH with the hydroxyl H atoms of HLNT surface with d(HN···HO) = 2.89 Å.

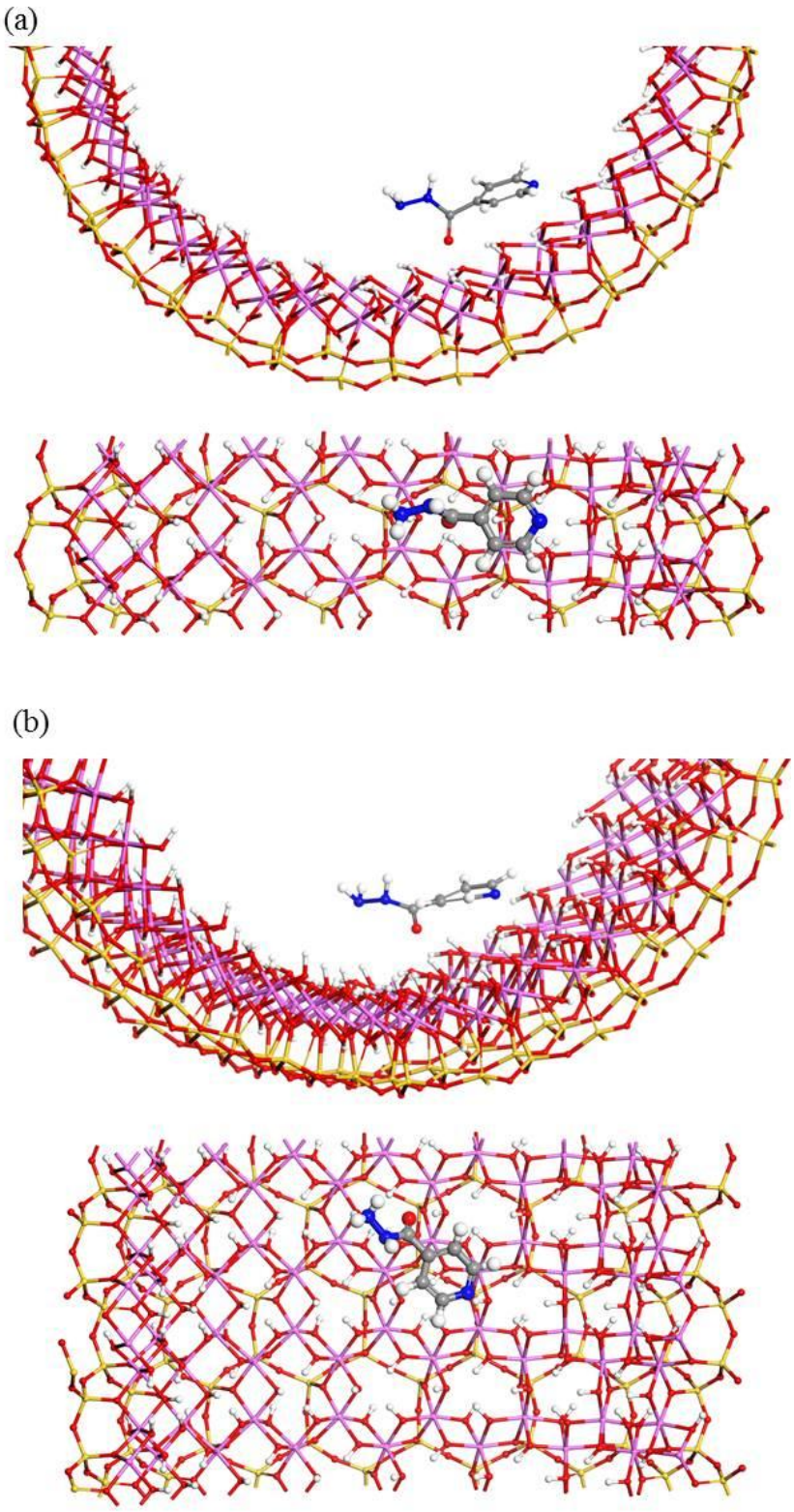

Figure IV.8. Adsorption complexes H1 (a) and H2 (b) of the INH molecule adsorbed on the internal surface of HLNTs optimized with Compass FF, views from (001) and (100) planes. The atoms of silicon, aluminium, hydrogen, carbon, nitrogen and oxygen are described in yellow, pink, white, grey, blue and red, respectively.

IV.4 Conclusions

Interaction of INH with HLNTs occurs according to two simple processes: adsorption and precipitation of drug molecules onto the nanoclay inner and outer surfaces. Formation of the INH-loaded HLNTs is a spontaneous process, endothermic and endoentropic that increases the thermodynamic stability of the system. Solid state characterization corroborates the effective interaction between the components. The adsorption of INH on the internal surface of HLNTs was possible to be modelled at molecular level with molecular modeling methods finding conformational changes in the molecule and strong hydrogen bond between the carbonyl group and heterocyclic N atom with the hydroxyl H atoms of the mineral surface. Effective loading of INH and the total amount adsorbed by the clay nanotubes as well as the measured activation energies of the interactions are promising features for the design of modified delivery systems able to promote the patient compliance in the treatment of tuberculosis. Complementary studies will be performed to assess biocompatibility and delivery release patterns of the drug from the nanotubes.

SUPPLEMENTARY MATERIAL

Structure of the halloysite nanotube optimized with CASTEP. The atoms of silicon, aluminium, hydrogen and oxygen are described in yellow, pink, white and red, respectively.

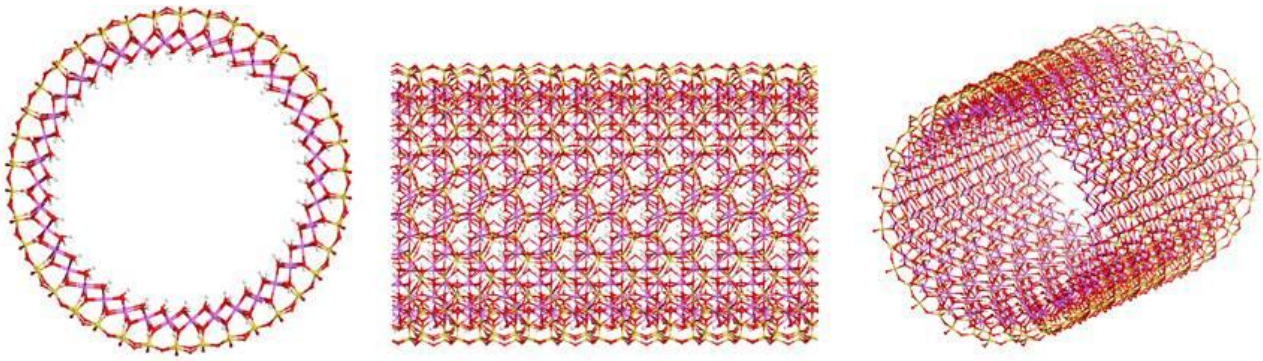

CAPÍTULO V

Adsorption and characterization of palygorskite-isoniazid nanohybrids

RESUMEN

En este capítulo de la memoria de Tesis Doctoral se incluye el estudio del proceso de adsorción de isoniazida en palygorskita, así como una completa caracterización al estado sólido de las materias primas y el nanohíbrido obtenido.
Los experimentos de adsorción fueron realizados en medio acuoso y a distintas temperaturas, tiempos de contacto y concentración de fármaco. El proceso de adsorción global era la suma de dos procesos: adsorción de isoniazida en los sitios activos de la palygorskita y precipitación posterior sobre la monocapa adsorbida. La obtención del nanohíbrido isoniazida-palygorskita resultó ser espontánea, exotérmica y exoentrópica ($\Delta H = -48.82$ kJ/mol; $\Delta S = -0.14$ kJ/molK). La efectiva interacción fármaco-arcilla se confirmó mediante una amplia caracterización al estado sólido, de la que cabe destacar que la interacción es de naturaleza no electrostática y se produce principalmente por puentes de hidrógeno entre el nitrógeno endocíclico de la isoniazida y los grupos hidroxilo de la superficie de la palygorskita y/o moléculas de agua presente en los canales zeolíticos de la arcilla. La carga efectiva de isoniazida en la palygorskita y los resultados favorables en la interacción isoniazida-palygorskita, así como la facilidad de la técnica de preparación de los nanohíbridos y el bajo coste de los excipientes empleados, suponen aspectos fundamentales a tener en cuenta para el desarrollo de sistemas capaces de paliar las dificultades del tratamiento antituberculoso. No obstante, la temperatura a la que se producía la máxima adsorción (40ºC) supone un coste que podría limitar el cambio de escala, por lo que sin menoscabo del interés científico de estos híbridos, desde un punto de vista eminentemente práctico se decidió continuar los estudios de desarrollo galénico con los híbridos obtenidos con halloysita a 30ºC.

ABSTRACT

Studies of the equilibrium and thermodynamic aspects of the adsorption of isoniazid onto a pharmaceutical-grade palygorskite and features of the resultant clay drug nanohybrid systems were carried out. Equilibrium studies were performed in aqueous medium at different times and temperatures. The overall adsorption process was explained as the result of two simple processes: drug adsorption on the activated sites of palygorskite and a slight precipitation phase of drug molecules over the adsorbed monolayer. Formation of the nanohybrid was spontaneous, exothermic and exoentropic, obtaining an increase in the thermodynamic stability of the system ($\Delta H = -48.82$ kJ/mol; $\Delta S = -0.14$ kJ/molK). A full and comprehensive study of the solid state characterization corroborated the effective interaction between the components. Total amount of INH loaded was about 20% w/w. FTIR spectra revealed the interaction via water bridges between the endocyclic N of the drug and surface OH groups of palygorskite. Surface charge studies confirmed the non-electrostatic nature of the interactions.

V.1 INTRODUCTION

Nanotechnology offers numerous possibilities in the treatment of global concern diseases as tuberculosis, the second cause of death from an infectious illness worldwide (WHO, 2015). Design of nanoparticulate drug delivery systems with the current tuberculostatic agents appears as an interesting strategy for improvement of therapy, as a result of the increase in patient compliance and decrease of drug adverse effects (Sharma et al., 2017). The use of clay minerals as nanocarriers for tuberculostatic drugs is a current matter of growing interest (Carazo et al., 2017a). In particular, halloysite nanotubes (Carazo et al., 2017b) and montmorillonite-polymer nanocomposites (Verma and Riaz, 2018) have been proposed as effective drug platforms in tuberculosis treatment.

Palygorskite is a fibrous clay mineral with several industrial applications (Galan, 1996) and considered a suitable candidate to vehicle bioactive molecules due to its large surface area (López-Galindo et al., 2011; Mura et al., 2016; Tenci et al., 2017). Palygorskite structure was described as a 2:1 clay mineral with tetrahedral silica sheets periodically inverted with respect to the tetrahedral bases leading to a periodically interruption in the octahedral sheets and cations occupying terminal positions must

complete their coordination sphere with water molecules (Bradley, 1940). The most intense absorption sites of palygorskite with organic molecules are surface hydroxyls and Lewis acidic centers (Serratosa, 1979). Isoniazid ($C_6H_7N_3O$; 137.14 g/mol), also known as isonicotinyl hydrazine, is a first-line drug in the prevention and treatment of tuberculosis (WHO, 2015). Akyuz et al. (2010) reported changes in infrared spectrum of palygorskite after interaction with isoniazid. Nevertheless, it has not been suggested until now the potential use of this mineral in the design of modified drug delivery systems of isoniazid.

With these premises, aim of this work was the study of the thermodynamics and equilibrium features of the adsorption of the first-line tuberculostatic drug isoniazid onto palygorskite as a prior step in the development of a modified release system based on the drug-clay mineral interactions. Solid state characterization of the pure materials and the resulting hybrid system was carried out in order to confirm the effectively loading of the drug, to assess qualitative and quantitatively the different interactions involved.

V.2 MATERIALS AND METHODS

V.2.1 Materials

Isoniazid (INH) from Sigma Aldrich (Spain) and a pharmaceutical grade palygorskite (Pharmasorb® Colloidal) (Pal) from Basf (Germany) were used as received. Pal had been fully characterized and used in previous studies (Viseras and López-Galindo, 1999, 2000; Viseras et al., 2000, 2001; Cerezo et al., 2001; Mura et al., 2016; Tenci et al., 2017).

All the reagents used were of analytical grade.

V.2.2 Adsorption studies

Adsorption experiments were performed following Carazo et al. (2017b) to obtain equilibrium isotherms at different times and temperatures. Briefly, known amounts of Pal were dispersed into INH aqueous solutions with initial concentration (C_0) ranging from 0.05 to 0.5 mol/L, for different times (24 h, 48 h and one week) and temperatures (20, 30, 40 ± 0.1 °C). The resulting dispersions were centrifuged and the equilibrium concentration (C_e) of the drug in the supernatant was determined by UV spectroscopy

(UV–Vis spectrophotometer Lambda 25, Perkin Elmer, S) at 262 nm. The difference between C_0 and C_e was used to calculate the amount of drug retained per gram of clay (expressed as n^s: mol of INH/g of Pal). Non-linear fitting of the data was performed using the software packaging TableCurve 2D® (Systat Software Inc., UK) and kinetic and thermodynamic parameters were determined.

V.2.3 Solid state characterization

V.2.3.1 Preparation of the drug-clay nanohybrids

Hybrid systems corresponding to the monolayer adsorption capacity of the clay mineral (48 h, C_0 = 0.2 mol/L) were prepared following the same procedure described above and then characterized.

V.2.3.2 Fourier transform infrared spectroscopy

Fourier transform infrared (FTIR) spectra were recorded on a FTIR spectrophotometer (JASCO 6200, with software SPECTRA MANAGER v2 and with an attenuated total reflectance (ATR) accessory). Measurements were carried out from 400 to 4000 cm^{-1} at 0.25 cm^{-1} resolution.

V.2.3.3 Thermal analysis

Thermogravimetric analysis (TGA) and Differential scanning calorimetry (DSC) were carried out by using a METTLER TOLEDO mod. TGA/DSC1 with FRS5 sensor and a microbalance (precision 0.1 μg) (Mettler-Toledo GMBH). Samples were heated in air atmosphere at 10 °C/min in the ranges 30–950 °C (TGA) and 30–400 °C (DSC).

V.2.3.4 X-ray powder diffraction

X-ray powder diffraction (XRPD) was done by using a Philips® X-Pert diffractometer with Cu Kα radiation. The diffraction data were analyzed using the XPOWDER® software (Martín-Ramos, 2004).

V.2.3.5 Surface charge

Surface charge properties of clay and drug-clay nanohybrid were determined from their zeta potential (ζ) values in aqueous suspension (0.05% w/v) on a Malvern Zetasizer Nano instrument (Malvern Instruments, USA).

V.3. RESULTS AND DISCUSSION

V.3.1 Equilibrium studies

Experimental equilibrium isotherms are plotted in Figure V.1 as n^s (moles of INH retained per gram of Pal; mol/g) vs Ce (mol/L).

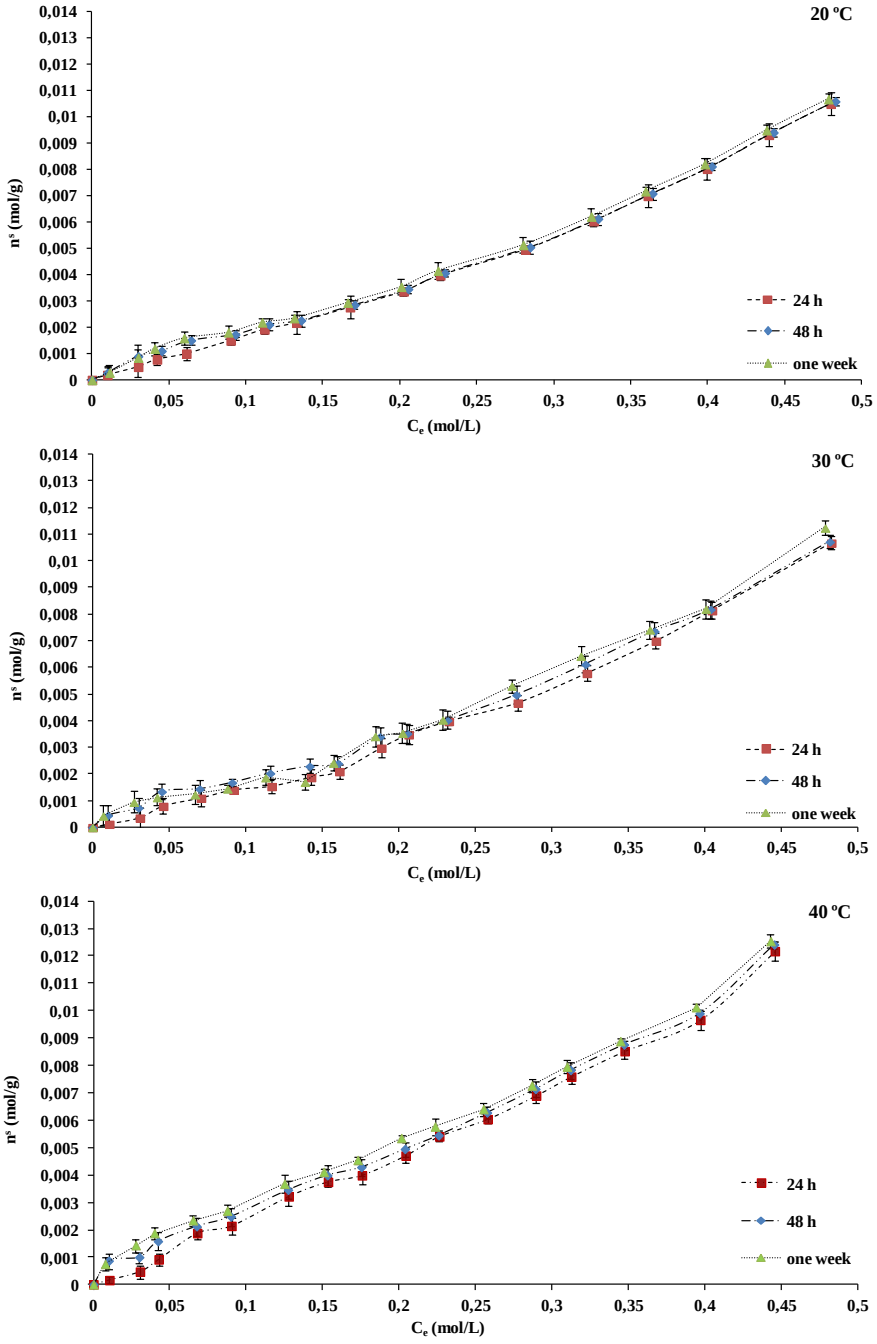

Figure V.1. Experimental adsorption isotherms of INH by Pal at different times and temperatures (mean values ± s.d.; n = 3).

The effect of time was almost negligible in the range of temperatures studied. Only a better outline of the plateau after 48 h in comparison with 24 h was observed, with no further improvement after one week of contact time. Replicates of the 48 h experiments were performed and the experimental data were collected to be mathematically treated. The isotherms fit the following equation, previously proposed to describe the adsorption of drugs to inorganic solid sorbents (Carazo et al., 2017b) (Eq. V.1):

$$n^s = n_1^s + n_2^s = \sum_{i=1}^{i=2} \frac{K_i . n_{m(i)}^s . C}{K_i . C + 1} + k_f C^m \qquad \text{(V.1)}$$

Where n^s = moles of adsorbate adsorbed per gram of sorbent, n^s_1 = adsorption at the active surface sites of the sorbent, n^s_2 = precipitation of drug molecules over the adsorbed monolayer, n^s_m = monolayer retention capacity, C = equilibrium concentration, k_i = kinetic equilibrium constant, k_f = kinetic precipitation constant, n = partial order of the process respect to the concentration (C) and m = constant.

Average experimental data and theoretical calculated curves (adsorption, precipitation and the sum of both processes) are shown in Fig. V.2. The global adsorption process is composed by the sum of two simple processes (adsorption of INH on the activated sites of Pal (n^s_1) followed by a slight precipitation of INH over the adsorbed monolayer (n^s_2)). The calculated fitting parameters (Table V.I) described adequately the experimental results with correlation coefficient ≥ 0.998. Monolayer retention capacity (n^s_m) slightly increased with temperature, whereas kinetic equilibrium constant (k_i) significantly decreased. The increase in temperature makes easier the dehydration of the drug molecules previous to their adsorption but concomitantly increase their mobility. K_f values are very low, suggesting a slight precipitation over the adsorbed drug monolayer.

Table V.I. Fitting parameters of Equation V.1 for the retention of INH by Pal at different temperatures and corresponding correlation coefficients (mean values ± s.d.; n = 3).

T° (C)	n^s_m (mmol/g)	k_i	k_f	m	r^2
20	1.205 ± 0.0011	23.991 ± 0.3431	0.032 ± 0.0112	1.783 ± 0.1234	0.997
30	1.411 ± 0.0012	13.212 ± 0.4122	0.033 ± 0.0234	1.863 ± 0.2454	0.999
40	1.801 ± 0.0015	6.651 ± 0.4751	0.048 ± 0.0346	2.362 ± 0.2987	0.998

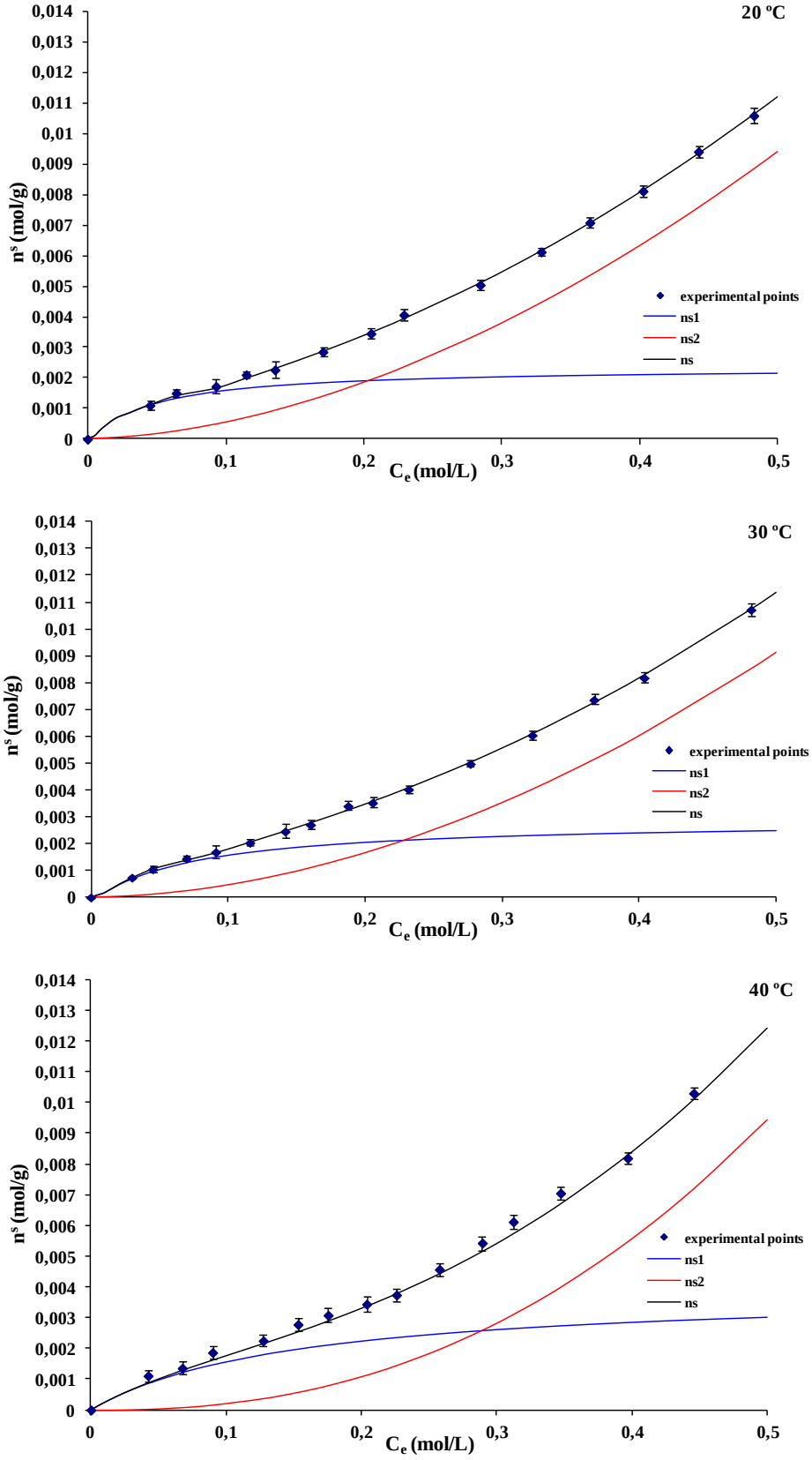

Figure V.2. Equilibrium isotherms of INH by Pal at different temperatures (mean values ± s.d.; n = 3).

K_i values obtained from Eq. (V.1) were used to determine the differential adsorption enthalpy ΔH° (kJ/mol) and the differential adsorption entropy ΔS° (kJ/molK) values using the linearization of the Eyring equation (Eq. V.2) by plotting ln (k/T) vs (1/T):

$$ln\frac{k_i}{T} = ln\frac{R}{Nh} + \frac{\Delta S°}{R} - \frac{\Delta H°}{R} \times \frac{1}{T} \quad \text{(V.2)}$$

(k = kinetic equilibrium constant (k_i), R = gas constant, N = Avogadro's number, h = Planck's constant, T = temp (K)).

The calculated values are given in Table V.II, which also includes the differential activation energy ΔG° (kJ/mol) calculated via the expression: ΔG° = ΔH° − TΔS°.

Table V.II. Thermodynamic functions for the Pal/INH interaction

T (K)	ΔH° (kJ/mol)	ΔS° (kJ/molK)	ΔG° (kJ/mol)
293	-48.821 ± 1.7780	-0.142 ± 0.0011	-2.812 ± 0.0014
303			-2.393 ± 0.0012
313			-1.664 ± 0.0021

The previous mentioned decrease of ki values with the increase of temperature suggested an exoenergetic process that was corroborated by negative values of enthalpy (ΔH°) and activation energy (ΔG°). Adsorption of isoniazid over palygorskite was therefore an exothermic process. The thermodynamic probability of adsorption (ΔG°) revealed that the reversible adsorption-desorption process moved towards the net adsorption. Negative values of ΔS° corresponded to the reduced degree of freedom of the INH adsorbed molecules with respect to those in dissolution.

V.3.2 Solid state characterization

V.3.2.1. Fourier transform infrared spectroscopy

FTIR spectra of INH, Pal and the clay–drug nanohybrid were carried out to determine the nature of the interactions involved in the adsorption process (Figure V.3). The stretching mode of the Si–OH bond in Pal spectrum was observed as a sharp band around 3700 cm^{-1}. Some intensity and frequency changes in the OH stretching band of surface hydroxyls (Si–OH) of the Pal-INH were observed, in line with previously reported results (Akyuz et al., 2010). The band at 3612 cm^{-1}, well documented in all

bibliographic references on FTIR of palygorskite (Mendelovici, 1973; Frost et al., 2001; Chahi et al., 2002; Chang et al., 2009) was related with the OH-stretching mode of structural hydroxyl groups. In the drug-clay nanohybrid, that band was detected at 3615 cm^{-1} and was assigned to coordination of INH molecules on the surface silanol (Si–OH) groups, directly or indirectly through water bridges. Bands appearing at 3543, 3400 and 3370 cm^{-1} were assigned to water molecules at terminal positions of the octahedral sheets (coordinated water) and water inside palygorskite channels (zeolitic water). Band at 3543 cm^{-1} was also ascribed to OH-stretching in AlMg OH, Fe–Mg–OH and Fe_2–OH groups. Band at 1652 cm^{-1} was ascribed as bending modes of absorbed and zeolitic water (Mendelovici, 1973; Mendelovici and Portillo, 1976). This band was shifted to 1661 cm^{-1} in the nanohybrids due to the H-bonding of INH molecules with water present in the clay mineral. In the range between 1200 and 400 cm^{-1} characteristic bands of silicate was observed. Bands at 644 cm^{-1} in Pal moved to 638 cm^{-1} in the nanohybrid.

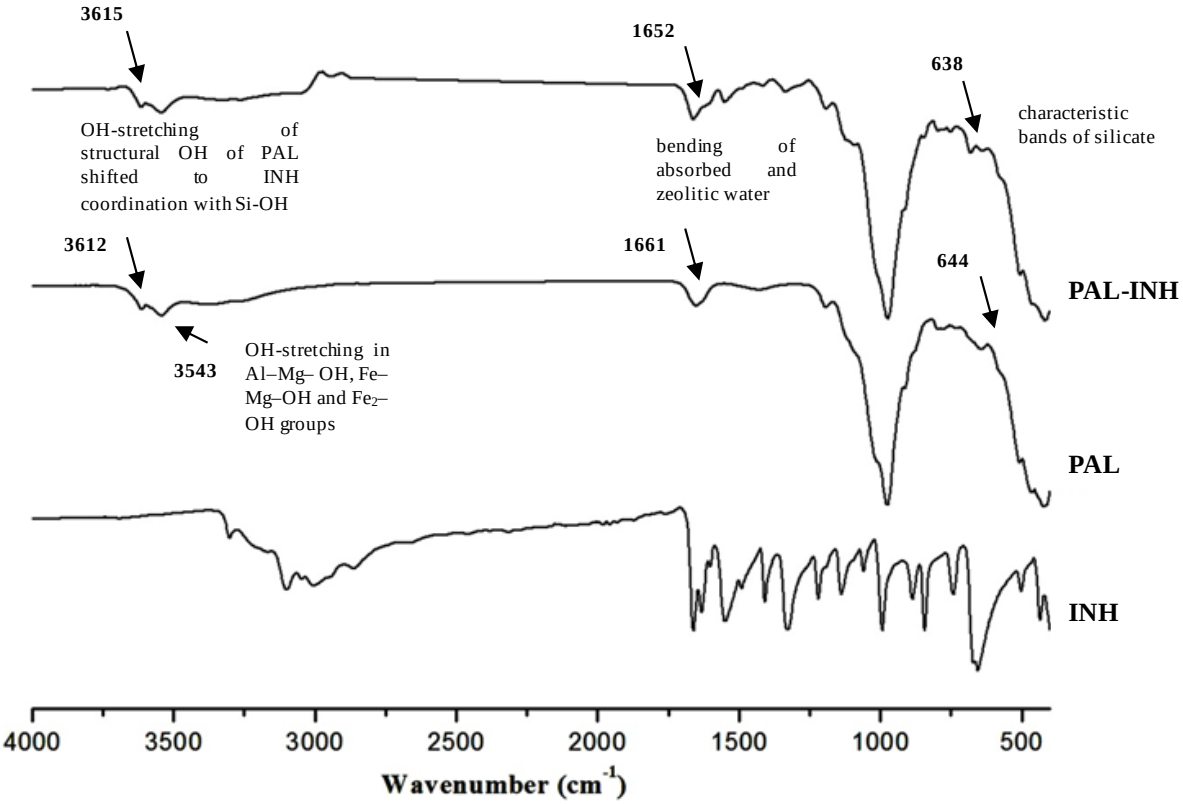

Figure V.3. FTIR spectra of Pal-INH nanohybrid and raw components.

V.3.2.2. Thermal analysis

TGA and DSC curves of the studied samples are shown in Figures V.4 and V.5. As described by Carazo et al. (2017b), INH melted at ~ 177 °C and decomposed in the interval 250 °C–350 °C. Pal showed the previously described four stages of mass loss of this sample (Viseras and López-Galindo, 1999). The same four steps (adsorbed and zeolitic water; bound water I; bound water II; dehydroxylation) have been also discussed by other authors in palygorskite-rich samples (González et al., 1990; Frost and Ding, 2003; Ogorodova et al., 2015; Xavier et al., 2016). According to the drug clay interaction, TGA curve of the nanohybrid showed the partial removal of the water molecules placed in the structural channels or bound to the external surface of the clay mineral. Slope of drug decomposition was lower indicating a protecting effect of the clay mineral on the thermal degradation of the drug. Weight losses corresponding to water in the folded channels of the clay mineral as well as dehydroxylation were not modified in the nanohydrid TGA. According to the measured weight losses, INH in the nanohybrid was ~ 20% w/w.

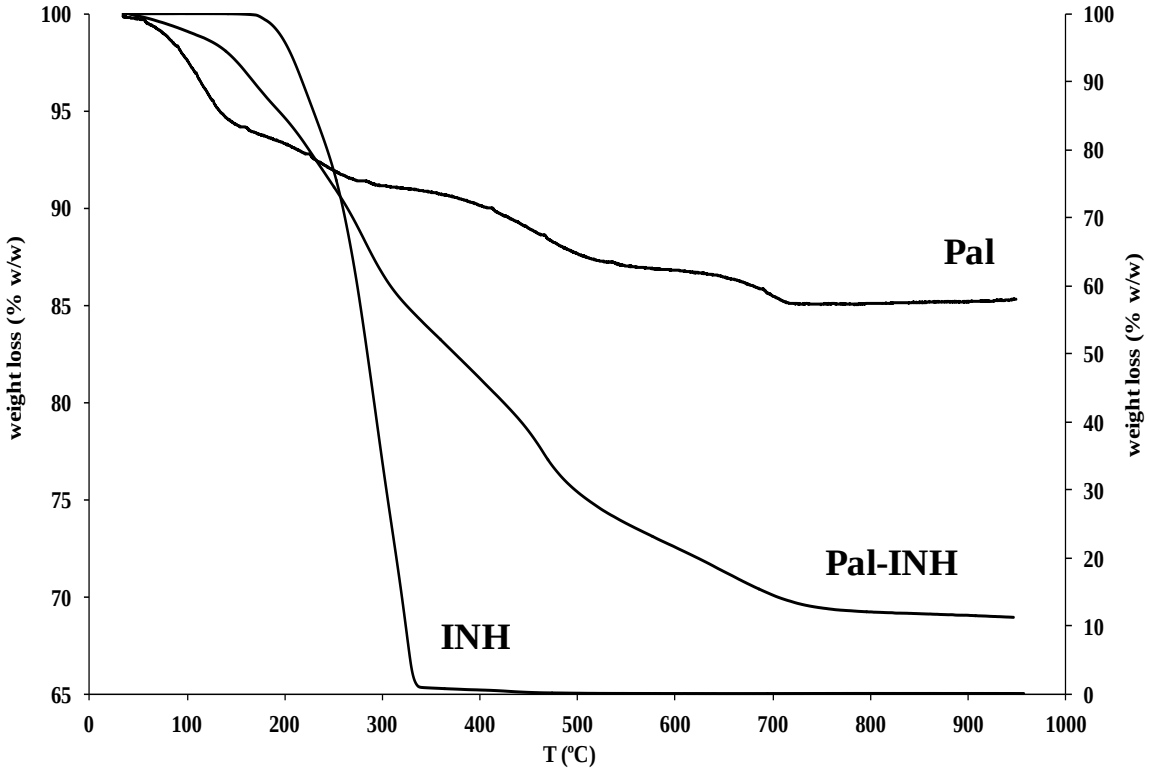

Figure V.4. TGA curves of Pal-INH nanohybrid and raw components.

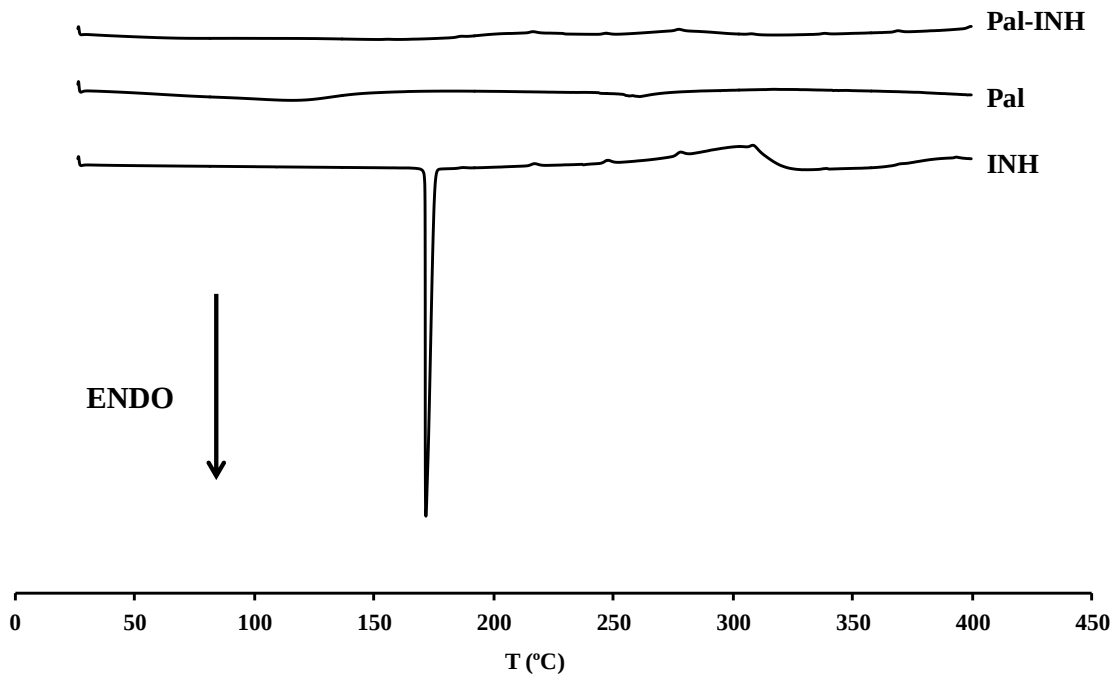

Figure V.5. DSC curves of Pal-INH nanohybrid and raw components.

V.3.2.3. X-ray powder diffraction

INH showed a crystalline pattern (Figure V.6), with main reflections at around 10°, 14°, 16° and 20° 2θ (Angadi et al., 2010). Pal diffraction pattern showed peaks corresponding to the mineral phases (mainly palygorskite with presence of minor quantities of quartz, Al-smectite, calcite and illite) presented in the material and quantified by Viseras and Lopez-Galindo (1999). The nanohybrid exhibited a similar diffraction pattern to the clay mineral. Disappearance of calcite and absence of INH peaks were the main differences, indicating the absence or negligible presence of precipitated crystals of the drug and the dissolution of the carbonate during the preparation of the hybrid.

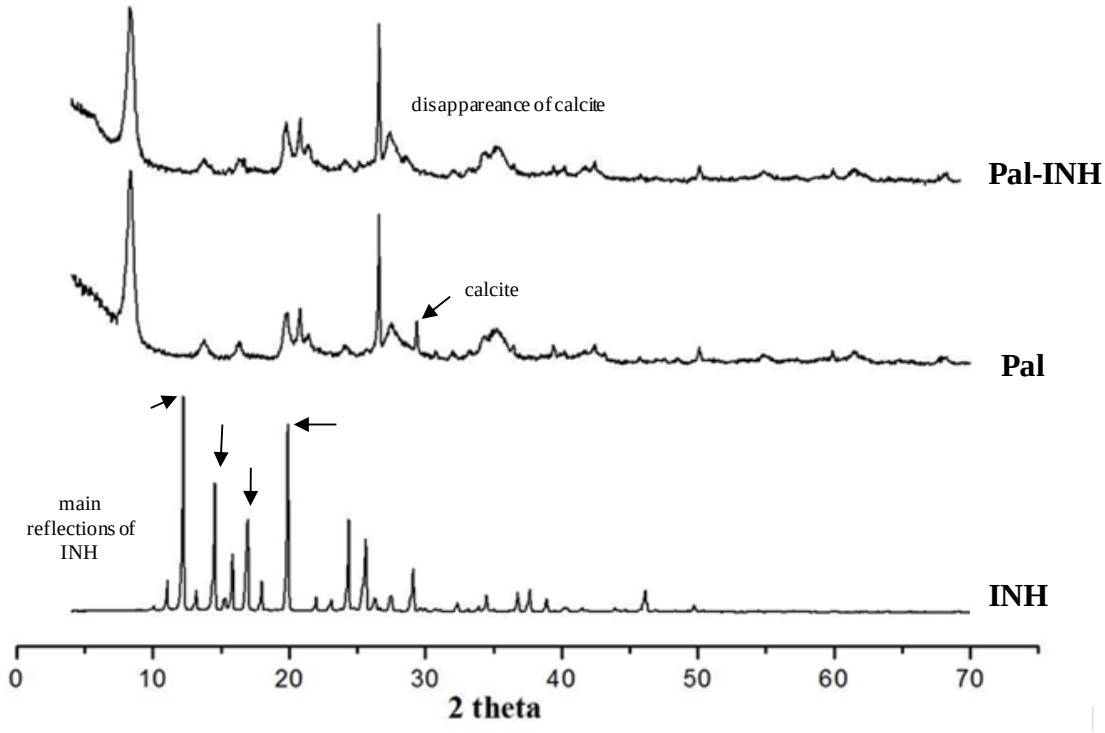

Figure V.6. XRPD patterns of Pal-INH nanohybrid and raw components.

V.3.2.4. Surface charge

Zeta potential of the raw clay mineral (− 15.5 ± 0.121 mV) almost remained unchanged after interaction with the drug molecules, being the ζ value of the nanohybrid – 14.9 ± 0.036 mV. The small difference was attributed to compression of the electrical double layer as a result of the coordination of the endocyclic nitrogen of INH molecules with the surface silanol (Si–OH) groups through water bridges. Similar effect with other organic molecules and palygorskite was also observed by Zeng et al. (2017). In practice, the almost absence of surface charge changes is confirming the non-electrostatic nature of the interaction.

V.4. CONCLUSIONS

Equilibrium isotherms fit to two simple processes: adsorption of INH on the activated sites of Pal followed by a slight precipitation of the drug on the clay mineral surface. Calculation of the fitting parameters of the equation that defines the processes and the thermodynamic functions reveals that: the INH retention capacity by the nanoclay increases with increasing temperature; the precipitation step is of low intensity and the formation of the Pal-INH nanohybrid fits to an exothermic, exoentropic and

thermodynamically spontaneous process. Total amount of INH adsorbed was about 20% w/w. FTIR spectroscopy indicated that INH molecules were coordinated to surface OH groups, directly or indirectly through water bridges. It was concluded that the endocyclic nitrogen is mainly involved in the coordination. Besides, some of the adsorbed INH molecules may enter the interior channels of the Pal and involve H–bonding interaction with zeolitic water. Effectively loading of INH onto Pal and a comprehensive study of the drug-clay nanohybrids structure and interactions involved in the adsorption process provided encouraging aspects to the design of modified drug delivery systems able to alleviate the struggles of the tuberculosis treatment. In particular, the low-cost of the excipients and the ease of the technique to prepare the nanosystems are important features in the development of tuberculostatic dosage forms.

CAPÍTULO VI

Halloysite nanotubes as tools to improve the actual challenge of fixed doses combinations in tuberculosis treatment

RESUMEN

Para dar cumplimiento al objetivo final de la Tesis Doctoral, esto es, el desarrollo de sistemas híbridos con excipientes inorgánicos de bajo coste, capaces de mejorar las características biofarmacéuticas y/o tecnológicas de las formulaciones para el tratamiento de la tuberculosis, en la fase que este capítulo recoge se plantearon y resolvieron los ensayos relativos a los estudios *in vitro* de liberación, citotoxicidad, permeabilidad intestinal, así como de estabilidad de isoniazida transportada en halloysita. Estos estudios establecen las posibilidades reales de empleo terapéutico de los nanohíbridos desarrollados en la tesis doctoral.

Los nanohíbridos halloysita-isoniazida obtenidos por intercalación sólido-líquido aumentan la permeabilidad intestinal del fármaco sin modificar la cinética de liberación (mejora biofarmacéutica) y, paralelamente, reducen significativamente la degradación en presencia de los otros principios activos antituberculosos de primera línea (etambutol, pirazinamida y rifampicina) (mejora tecnológica). Estos resultados auguran un avance fundamental en la terapia oral antituberculosa, sin incremento del coste del tratamiento.

ABSTRACT

Halloysite nanotubes (HLNTs) were used as nanocarriers of the tuberculostatic agent isoniazid (INH), a BCS (Biopharmaceutics Classification System) class III drug. Self-assembling nanohybrids (INH-loaded HLNTs) with an average outer diameter of 90 nm and polydispersity index of 0.7 approximately, were obtained by spontaneous adsorption of INH molecules to HLNTs powder in aqueous medium. The nanohybrids were aimed to improve oral drug bioavailability and reduce physicochemical incompatibility of INH with other concomitantly administered tuberculostatic agents. In vitro drug release from INH-loaded HLNTs was successfully fitted to a diffusive kinetic law founded on the adsorption-desorption equilibrium between drug molecules in solution and solid inorganic excipients. INH-loaded HLNTs showed good in vitro biocompatibility towards Caco-2 cells at the concentrations studied (up to 1233 μg/mL), with improved cell proliferation. Permeability tests showed that INH transport across Caco-2 cellular membranes was greatly enhanced and fluorescent microscopy confirmed that the drug encapsulated into nanohybrid was effectively internalized by the cells. INH-loaded HLNTs enhanced stability of the drug in presence of other tuberculostatic agents, both in binary and quaternary combinations. It has been demonstrated that simple interaction between INH with HLNTs leads to drug permeability and stability improvements that could greatly facilitate the design of multiple drug dosage forms, an actual challenge in oral treatment of tuberculosis.

VI.1 INTRODUCTION

Tuberculosis (TB) is a global health priority with almost 10 million of new cases worldwide every year and first cause of death from a single infectious agent (WHO, 2018a). TB treatment is based on a combination of four first-line tuberculostatic drugs and among them, INH is the most widely used and plays a crucial role based on its numerous advantages, as high early bactericidal activity, high selectivity to *Mycobacterium tuberculosis* and excellent bacteriostatic capacity with a minimum inhibitory concentration (MIC) of about 0.05 – 0.1 μg/mL (Huang et al., 2015; Cordes et al., 2016). Despite its crucial importance (INH is included in the WHO Model List of Essential Medicines (Kasim et al., 2004)), only low levels of INH gain access into plasma via oral route, due to its poor intestinal permeability, rapid and extensive hepatic metabolism and short plasma half-life (1–4 hours) (Bhandari and Kaur, 2013). To achieve therapeutic effects, repetitive and high doses are therefore required, leading to

severe adverse effects, such as hepatotoxicity and neuropathy (Goldman and Braman, 1972; Tostmann et al., 2008; Maryam et al., 2010; Metushi et al., 2011). INH possesses high aqueous solubility (140 mg/mL at 25 ºC) (Del Río-Estrada and Dougherty, 1970) and low permeability ((log P −0.402 at 25 ºC) (Mariappan and Singh, 2003), being considered as a class III drug of the BCS (Kasim et al., 2004; Ramirez et al., 2010). Oral bioavailability of this class of drugs mainly depends on their permeability pattern across the enterocyte membranes (Blume and Schug, 1999). Any carrier which can improve the permeability of class III drugs will therefore result in improved effectiveness at lower dose with less side effects leading to improved compliance with lowered health costs (Kaur and Singh, 2014). The WHO Model List of Essential Drugs includes fixed-dose-combinations (FDCs) of the first-line tuberculostatic drugs (INH, Rifampicin (RIF), Pyrazinamide (PYR), and Ethambutol dihydrochloride (ETB)) (WHO, 2017a) with numerous advantages, as the minor risk of acquisition of drug resistance due to monotherapy and the improved patient adherence derived from the smaller number of solid dosage forms to ingest. However, the commercialized 4-FDC dosage forms exhibit severe technological problems including extensive physical changes (color fading, red bleeding) and, particularly important for therapy efficacy, significant decomposition of RIF and INH in presence of the other drug molecules (Bhutani et al., 2004,2005a; Battini et al., 2018). The use of nanoparticles as vehicles for effective drug delivery in TB treatment have been proposed to increase drug bioavailability, protect from degradation and control release (Kaur and Singh, 2014; Costa-Gouveia et al., 2017). A particular type of inorganic low cost nanoparticles is being proposed as potential excipients in the improvement of TB (Carazo et al., 2017a), and in particular some interesting hybrids have been recently designed (Carazo et al., 2017b, 2018b,c). Halloysite is a two-layered aluminosilicate chemically similar to kaolin, with prevailing hollow tubular structure in the nanometer range (Lvov et al., 2008; Yuang et al., 2015; Yendluri et al., 2017). Essential features, as hollow tubular morphology and outer and inner surface charges, have made halloysite nanotubes (HLNTs) well documented carriers for encapsulation and release of drug molecules (Aguzzi et al., 2013, 2016; Bertolino et al., 2018; Lvov et al., 2016; Massaro et al., 2015a, 2018; Viseras et al., 2008, 2015; Wu et al., 2018). In a previous work, it was shown that INH is spontaneously adsorbed by HLNTs, giving a self-assembled and thermodynamic stable (ΔH = 70.40 kJ/mol; ΔS = 0.2519 kJ/molK) nanohybrid (INH-

loaded HNLTs), in which drug molecules were adsorbed both onto the inner and at the outer surface of the nanotubes (Carazo et al., 2017b). Given these premises, aim of this work was to assess biological compatibility as well as biopharmaceutical and technological performances of INH-loaded HNLTs to effectively improve the oral bioavailability of the drug and enhance INH compatibility in presence of the other tuberculostatic drugs. Cellular biocompatibility and drug permeability were evaluated using in vitro approaches, in which Caco-2 cell lines were used as established models for both cytotoxicity studies and in vitro prediction of drug absorption through the gastrointestinal wall (Artursson et al., 2001; Hubatsch et al., 2007). Complementary fluorescent microscopy was performed to confirm cellular uptake, visualizing the presence of the nanohybrid eventually entrapped in the cells. Accelerated stability tests of pure INH and INH-loaded HLNTs were carried out to assess the possible protective role of the nanotubes regarding INH stability as a first step aimed to design stable 4-FDC.

VI.2 MATERIALS AND METHODS

Pharmaceutical-grade halloysite nanotubes (HLNTs) and isoniazid (INH) were purchased from Sigma Aldrich, (Spain). Etambuthol hydrochloride (ETB) was purchased from Hildose (India), pyrazinamide (PYR) from Calyx Chemicals and Pharmaceuticals (India) and rifampicin (RIF) from Luohe Nanjiecun (China). The purity of all drugs was >99%.

VI.2.1 Preparation of the nanohybrid

Hybrid systems (INH-loaded HLNTs) were prepared dispersing HLNTs powder (100 mg) in 20 mL of INH aqueous solution (0.25 M) (initial drug/HLNTs ratio corresponding with the calculated monolayer adsorption capacity of the nanotubes), resulting in a drug content of 18.9 ± 0.12 % w/w (Carazo et al., 2017b). Drug entrapment was calculated according both to the thermogravimetry results and by the experimental and theoretical adsorption data (Carazo et al., 2017b). A complete physicochemical characterization of raw materials (INH and HLNTs) and the resulting nanohybrid (INH-loaded HLNTs) has been performed (Carazo et al., 2017b).

VII.2.2 Photon correlation spectroscopy (PCS)

Photon correlation spectroscopy (PCS) with low angle laser light scattering was used to

determine the size distribution profile of the nanohybrid and corresponding free components. The intensity weighted mean diameter and the polydispersity index were determined using a Particle Sizer BI-90 (Brookhaven, Holtsville, USA) at 25°C under an angle of 30°. All samples were diluted with demineralized particle-free water to an adequate scattering intensity prior to the measurement. PCS run settings parameters were: diluent viscosity (0.0089 poise), diluent refractive index (1.333), tested angle (30.1461º), run time (1200 s), equilibration time (1 min). The results were average of three analyses.

VI.2.3 Surface charge

Surface charge properties of clay mineral and drug-clay nanohybrid were determined from their zeta potential (ζ) values in aqueous suspensions (0.05% w/v) on a Malvern Zetasizer Nanoinstrument (Malvern Instruments, USA).

VI.2.4 *In vitro* release studies

Release of INH from 150 mg of INH-loaded HLNTs was tested in the USP dissolution apparatus II (SOTAX AG, Switzerland) at 100 rpm, 37 °C and 500 mL of dissolution media: i) HCl 0.001 M (pH 3); and ii) simulated intestinal fluid (SIF) without enzymes (pH = 6.8). pH 3 was chosen as gastric environment to avoid INH degradation in more acidic conditions (Bhutani et al., 2007). At established time intervals, samples of dissolution medium (5 mL) were withdrawn and renewed with a fresh medium each time, filtered through 0.45 μm Millipore® (S) membranes and the amount of drug dissolved was measured by HPLC. A mean of six determinations were recorded. Total amounts of drug released (Q_t) were calculated as follows (Eq. VI.1) (Aguzzi et al., 2013):

$$Q_t = V_m C_t + \sum_{i=0}^{t-1} V_a C_i \quad \text{(VI.1)}$$

where V_m and C_t are volume and concentration of the drug at time t, V_a is the volume of the sample withdrawn and C_i is drug concentration at time i (i < t).

VI.2.4.1 Drug assay

All the dissolution samples were analysed using an HPLC system (Infinity II 1260, Agilent, Spain) equipped with an autosampler and a UV detector. The stationary phase

was a column Agilent InfinityLab Poroshell 120 (4.6 mm × 150 mm, 4µm) (Agilent, Spain) and the mobile phase was a water and acetonitrile mixture (H_2O/CH_3CN) (95/5, v/v). The flow rate was set at 0.8 mL/min, the injection volume was 50 µL, the detector wavelength 264 nm and the run time 5 minutes. Data were recorded using Agilent Open LAB CDS ChemStation software package. Methods were linear in the range from 12 to 120 mg/L.

VI.2.5 Cell cultures

Caco-2 human colorectal adenocarcinoma cell lines were obtained from the American Type Culture Collection (ATCC, USA). Cells were grown at 37°C, 5% CO_2 atmosphere (PBI international, Italy) in pH 7.4 Dulbecco's Modified Eagle's Medium (DMEM) (Lonza, Italy) containing 10 % v/v heat inactivated Fetal Bovine Serum (FBS) (Euroclone, Italy), penicillin (100 IU/mL), streptomycin sulphate (100 µg/mL) and 1% v/v non essential aminoacids (Sigma Aldrich, Italy). The culture medium was changed three times a week during maintenance.

VI.2.5.1 Cytotoxicity measurements

Caco-2 cells were seeded in 96-well plates of area 0.35 cm^2 at density of 10^5 cells per square centimeter, resulting in approximately 35000 cells/plate. Cells were incubated at 37ºC, 5% CO_2 for 24 h. 100 µL of six suspensions of INH-loaded HLNTs containing HLNTs concentrations ranging from 1000 to 1 µg/mL (Table 1) in culture medium were kept in contact with the cells in the incubator for 24 h and then removed and washed with 100 µL/well of HBSS (Hank's Balanced Salt Solution), previously heated at 37ºC. For comparison, experiments were also done on pristine clay mineral (HLNTs 1-6) and drug (INH 1-6), according to their concentrations in the nanohybrid (Table VI.I). The HBSS was subsequently removed and replaced by 100 µL of HBSS and 50 µL of MTT (3-(4,5-dimethylthiazol-2-yl)-2,5-diphenyltetrazolium bromide) solution (2.5 mg/mL) in HBSS, previously sterilized via filtration. MTT was incubated for 3 hours at 37ºC and 5% CO_2. After incubation, MTT was aspirated and 100 µL of dimethyl sulfoxide (DMSO) were added. DMSO plays an important role in this test, as it breaks the cell membrane with the subsequent release of the formazan crystals. The absorbance of formazan solutions were assessed by ELISA plate reader (570 nm to 690 nm) after vigorously shaking for one minute (Microplate Absorbance Reader MARKTM, Bio-Rad Laboratories Srl, Italy).

Table VI.I. Samples tested for cytotoxicity measurements.

Sample	Concentration (μg/mL)
HLNTs 1	1
HLNTs 2	1.25
HLNTs 3	2
HLNTs 4	10
HLNTs 5	100
HLNTs 6	1000
INH-loaded HLNTs 1	1.23
INH-loaded HLNTs 2	1.54
INH-loaded HLNTs 3	2.46
INH-loaded HLNTs 4	12.3
INH-loaded HLNTs 5	123
INH-loaded HLNTs 6	1233
INH 1	0.23
INH 2	0.29
INH 3	0.46
INH 4	2.33
INH 5	23.3
INH 6	233

VI.2.5.2 Permeability studies

Cells were seeded on tissue-culture-treated polycarbonate filters (area 113.1 mm^2; inner diameter 13.85 mm) in 12-well plates (Greiner Bio-one, PBI international, Italy) at a seeding density of 10^5 cells/cm^2. Cell cultures were kept at 37ºC in an atmosphere of 95% air and 5% CO2. The test was carried out as follows: 500 μL of the samples

suspensions were diluted 1:1 in HBSS at pH 7.4 and were used as the apical (donor) phase of the monolayers. The basolateral (receptor) phase was 1 mL of HBSS at pH 7.4. At fixed times (0.5; 1.5; 3 and 6 h) the whole basolateral phase was collected to dose INH and fresh basolateral phase was added to the cell substrates. Drug content was assessed by HPLC as described above and the method was linear in the range from 1 to 100 mg/L. During the experiments, the integrity of the monolayers was tested by means of Transepithelial Electrical Resistance (TEER) measurements at the same times than the permeability test and after 24 h by means of a Millicell ERS-meter (Millipore Corp., Bedford, MA, USA). INH at the same concentration than that of the nanohybrid was subjected to the same assay and used as control.

VI.2.5.3 Fluorescent microscopy

Caco-2 cells grown on filters in 12-well plates and subjected to in vitro permeability tests were analyzed by using Fluorescent Microscopy to visualize INH-loaded HLNTs nanohybrids eventually entrapped in the cells. The cell substrates were fixed in ethanol by dipping for 1 h and dried overnight. Cell nuclei were stained by dipping the biological substrates into a solution (100 μg/mL) of Propidium Iodide (Sigma, Italy). A fluorescent microscope (BX51 Olympus microscope) was used to observe the cellular uptake of drug encapsulated into nanocomposites (Propidium Iodide excitation wavelength of 535 nm and an emission wavelength of 617 nm; INH excitation wavelength of 380 nm and an emission wavelength of 400 nm). The acquired images were processed by means of specific software (Olympus Image Analysis Software).

VI.2.6 Stability tests

Degradation of INH, loaded and unloaded in the nanohybrid, in presence of the other tuberculostatic drugs (ETB, PYR and RIF) was assessed following the ICH (International Conference on Harmonisation) guidelines for accelerated stability conditions (ICH Guideline Q1A(R), 2000) storing samples at 40°C and 75% relative humidity (RH) (climatic chamber CC/HR 0/100, Uniclima, Spain). Binary physical mixtures of pure INH or INH-loaded HLNTs with each one of the other tuberculostatics as well as quaternary physical mixtures including all the drugs were assayed. Individual components were weighed in a 1:1 drug:drug ratio and gently mixed in a small glass mortar. Stability was considered in terms of % of INH remaining after 15, 30 and 90 days. INH was subjected to the same test and use as control of non self-degradation of

the drug in the conditions tested. INH content was analyzed by HPLC as described above. Measurements were done in triplicate.

VI.2.7 Statistical analysis

Statistical differences were evaluated by means of a non-parametric test: Mann Whitney (Wilcolxon) W test, using the SPSS software version 21.0 of developed by Statistical Software Package (SPSS Inc. Chicago, USA). Differences were considered significant at $P<0.05$; only significant differences are reported in the captions of the relevant figures.

VI.3. RESULTS

VI.3.1 Photon correlation spectroscopy (PCS)

The intensity weighted mean diameter and the polydispersity index obtained for both HLNTs and INH-loaded HLNTs are presented in Table VI.II. Calculated mean diameter size of HLNTs was about 75 nm and agrees with that found in bibliography with external diameter varying from 30 to 190 nm (Yuan et al., 2015). Both external diameter and polydispersity index increased in the nanohybrid in comparison with pristine HLNTs.

Table VI.II. Average intensity weighted mean diameter (nm) and polydispersity index for both HLNTs and INH-loaded HLNTs (mean values ± s.d.; n = 3).

Sample	Mean diameter (nm)	Polydispersity Index (PI)
HLNTs	74.864 ±0.0004	0.370 ±0.0021
INH-loaded HLNTs	89.937 ±0.0001	0.703 ± 0.0054

VI.3.2. Surface charge

HLNTs suspension was characterized by negative zeta potential of -18.7 ± 0.21 mV, derived from the presence of hydroxyl groups in the external surface of the clay mineral (Yuan et al., 2015). This value increased after loading with INH molecules, being the ζ value of the INH-HLNTs nanohybrid -14.6 ± 0.04 mV.

VI.3.3 *In vitro* release studies

Drug release profiles of INH from the INH-loaded HLNTs nanohybrid in pH 3.0 and pH 6.8 are plotted in Figure VI.1 as w/w % of drug released vs time. In line with the high drug aqueous solubility, dissolution curves showed burst release and short drug delivery duration (95 w/w % of drug released in the early 15 min). A kinetic law was defined to describe the release process, following previous studies with similar inorganic carriers (Aguzzi et al., 2013).

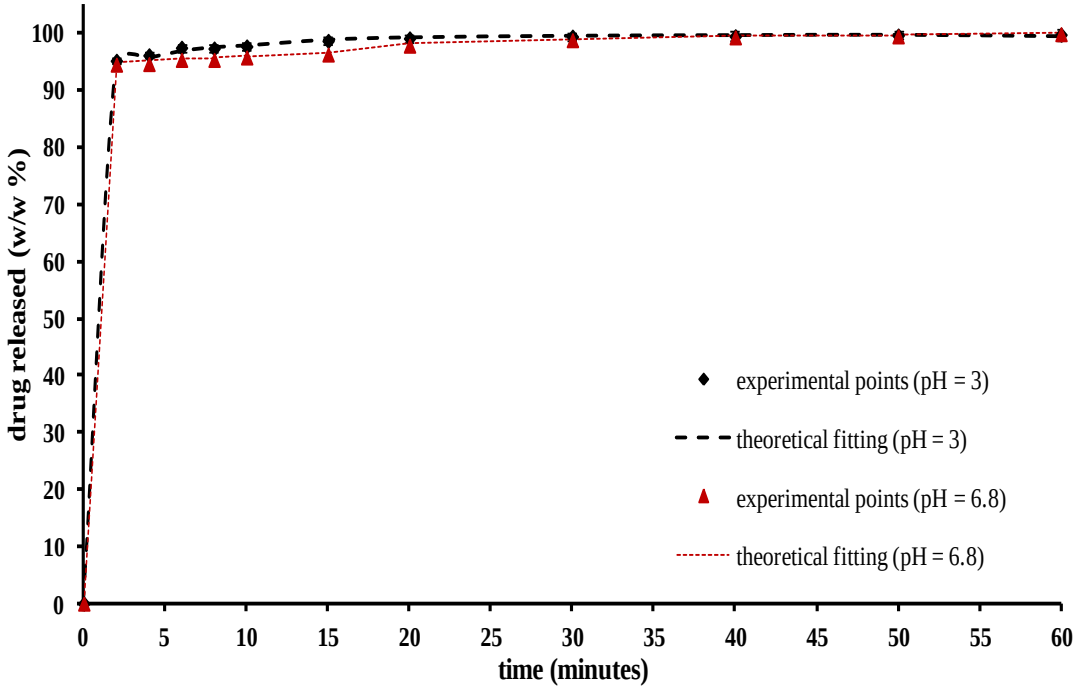

Figure VI.1. Amount of drug released (mean values ± s.d.; n = 6) from INH-loaded HLNTs nanohybrid and theoretical dissolution curves in the studied media.

The calculated release parameters (Table VI.III), obtained using the software packaging TableCurve 2D® (Systat Software Inc., U.K.), were discussed on the basis of adsorption-desorption equilibrium between INH molecules and the nanotubular carrier. Theoretical release curves are displayed in Figure VI.1 (dotted lines), where the almost overlapping with experimental points, suggests high suitability of the model to fit release data. Correlation coefficients (R^2>0.99) confirmed that the kinetic law adequately fitted the release pattern for INH from the nanohybrid in both media. Calculated release rates were very high and similar in acidic and neutral pH (kd ≈ 2000 h^{-1}) (Table VI.III).

Table VI.III. Values of kinetic parameters obtained from the proposed equation.

Parameters	0.001 M HCl (pH = 3)	SIF (pH = 6.8)
k_d (h^{-1})	1953	2167
C_e (%)	95.53	94.45
R^2	0.9929	0.9934

VI.3.4 Cytotoxicity measurements

Cytotoxicity was assessed for the pure materials (HLNTs and INH) and the nanohybrid (INH-loaded HLNTs) based on the percentage of viable cells in comparison with that of untreated cells grown in complete medium (positive control) (Figure VI.2).

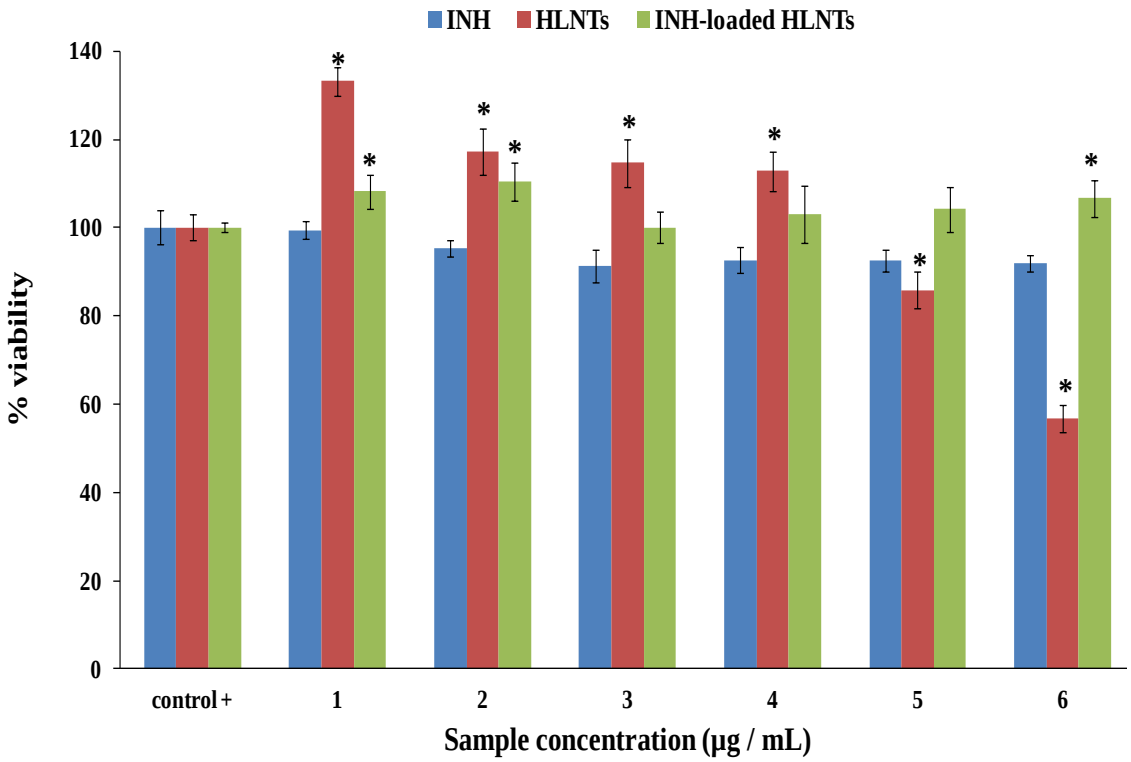

Figure VI.2. Cell viability from the studied samples after 24 h of incubation. (Positive control: untreated cells in complete medium) (mean values ± s.e.; n = 8) ($^*P< 0.05$).

VI.3.5 Permeability studies

Permeability assays were performed on the highest concentration of INH-loaded HLNTs tested which exhibited no cytotoxic behavior on the basis of cell viability measurements (INH-loaded HLNTs 6; 1233 µg/mL). INH at the same concentration as

in the nanohybrid (INH 6; 233 μg/mL) was used as control. In Figure 3, it is plotted the percentage of INH permeated to the basolateral phase vs time during the permeability experiments. First measured values (30 minutes) revealed no differences in % of drug permeated from the nanohybrid in comparison with pristine INH. The amount of INH permeated from the INH-loaded HLNTs tend to increase starting from 90 min., being significantly higher after 180 and 360 min., with almost 90 % of the total amount at the end of the test in comparison with the 58 % of INH alone.

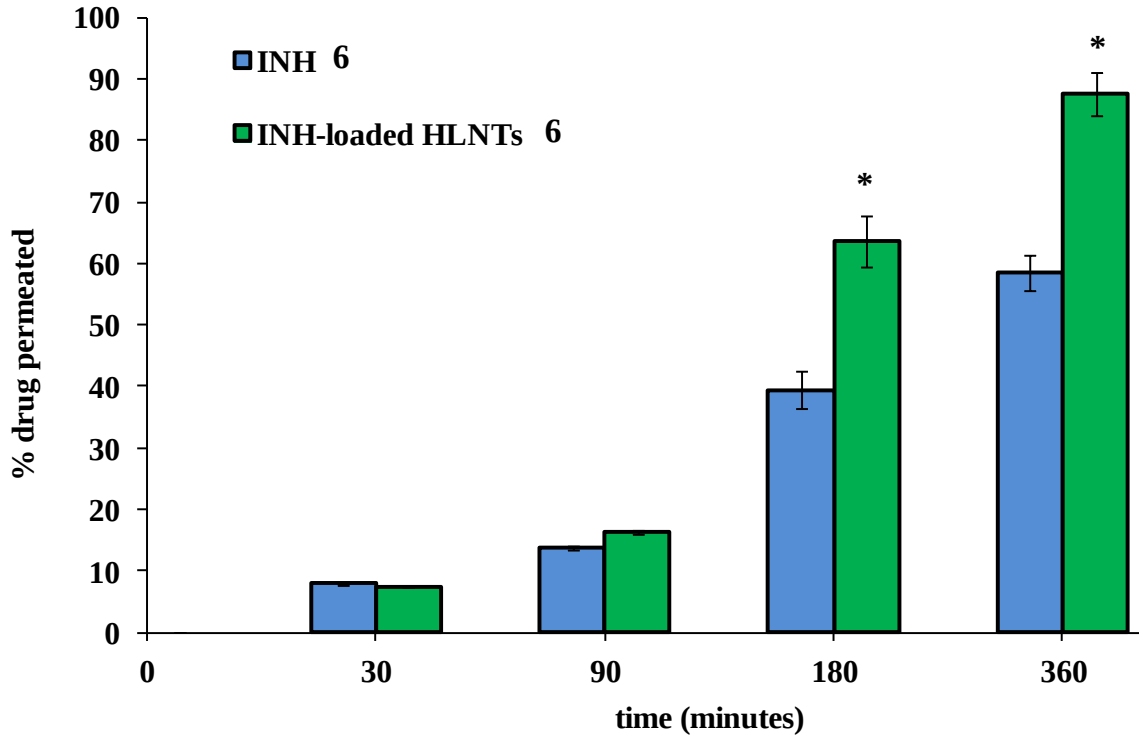

Figure VI.3. % of INH permeated across Caco-2 monolayers from samples INH-loaded HLNTs 6 and INH 6 (mean values ± s.d.; n = 3) (*P < 0.05).

Figure VI.4 shows the TEER profiles as a function of time for INH-loaded HLNTs nanohybrid and the same concentration of INH alone as control. The TEER profile of INH was close to the 100% during all the experiment time. As for the INH-loaded HLNTs nanohybrid there was a reversible decrease of the TEER which becomes significant after 90 minutes. After 24 hours of the beginning of the test, TEER profile of both INH alone and INH-loaded HLNTs, returned to its primitive values assuring that the total integrity of the monolayer was recovered.

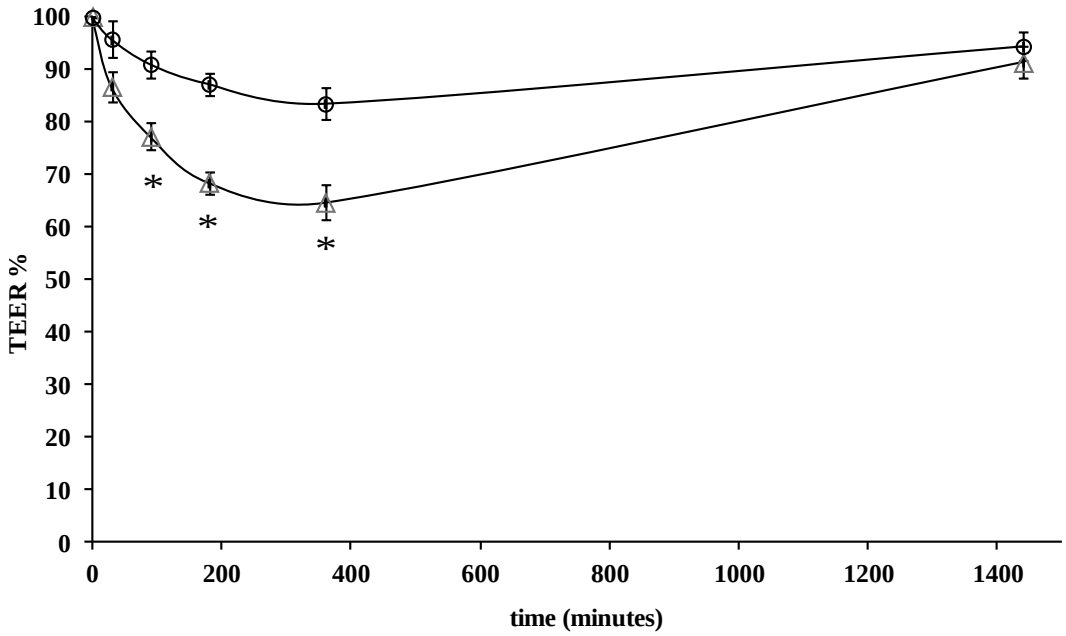

Figure VI.4. TEER% profiles (solid line: INH-loaded HLNTs 6; dotted line: INH 6 as control) (mean values ± s.d.; n = 3) ($^{*}P < 0.05$).

VI.3.6 Fluorescent Microscopy

To investigate the fate of INH and the interaction with Caco-2 cell monolayers, fluorescent microscopy was performed on the substrates subjected to the permeability experiments. Microphotographs obtained after 6h of contact time (at the end of the permeability experiment) between Caco-2 substrates and either INH-loaded HLNTs nanohybrid or drug alone INH (Figure VI.5) showed cell nuclei (red) and INH (light blue) as free drug or loaded in nanotubes.

Sample	Propidium Iodide (PI)	Isoniazid (INH)	PI + INH
INH-loaded HLNTs	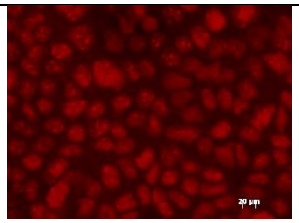	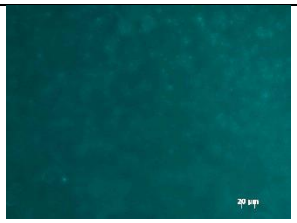	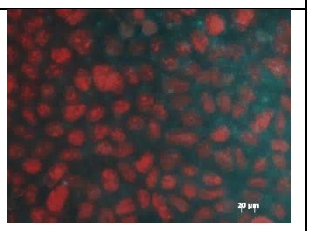
INH	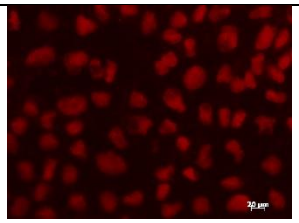	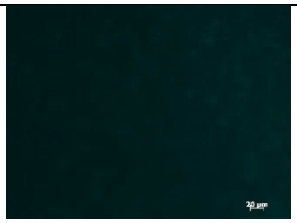	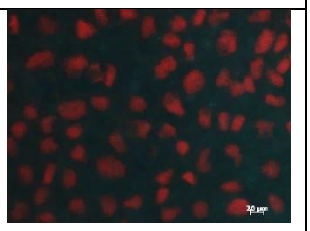

Figure VI.5 Fluorescent microphotographs of Caco-2 substrates treated with INH-loaded HLNTs and INH.

VI.3.7 Stability tests

Stability results showed that only mixtures containing ETB showed significant degradation of INH compared to the pristine drug (Figure VI.6), whereas binary combinations of PYR and RIF with INH or INH-loaded HLNTs did not modify INH content (data not shown). Amount of INH decreased to 60 % and 25 % of the initial content after 15 and 90 days, respectively, in the binary mixtures of INH and ETB.

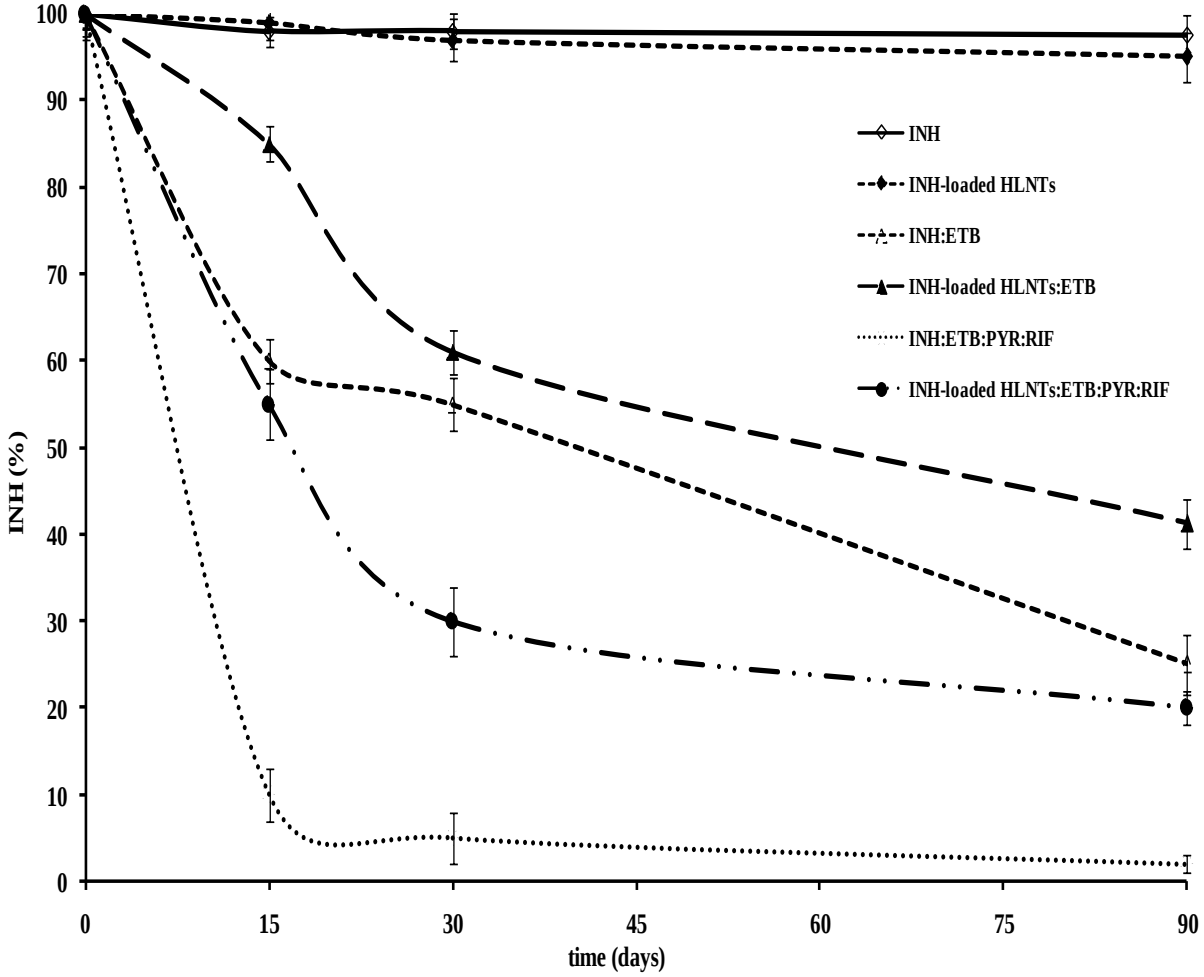

Figure VI.6. Amount of INH recovered after fixed times from binary and quaternary physical mixtures during compatibility test (mean values ± s.d.; n = 3).

VI.4. DISCUSSION

The increase of the polydispersity index of the nanohybrid revealed a wider variety of particle sizes after contact with INH, whereas the increase of external diameters of the hybrid was coherent with the presence of drug molecules on the outer surface of the nanotubes, as previously assessed by electron microscopy studies and theoretical computational modeling of the adsorption process (Carazo et al., 2017b). Moreover, the surface charge change of the nanohybrid in comparison with unloaded HLNTs, was ascribed to the adsorption of INH molecules by HLNTs, which occurred mainly by strong H bonds between the hydroxyl groups of HLNTs surfaces and the carbonyl and heterocyclic N atom of INH, as well as via electrostatic interactions between different groups of INH (-NH2,-NH and N of the aromatic ring) with the OH groups of HLNTs surfaces (Carazo et al., 2017b).

Drug release profiles of INH from the INH-loaded HLNTs nanohybrid in pH 3.0 and pH 6.8 suggested that drug release was not hindered by interaction between drug molecules and HNLTs. The kinetic law governing the release process can be expressed by the following equation (Equation VI.2), specifically designed to describe drug release from hybrid systems based on adsorption-desorption equilibrium between drug molecules and inorganic carriers (Aguzzi et al., 2013):

$$\frac{dC}{dt} = -k_a\, C\, (1-\theta) + k_d\, \theta \qquad \text{(VI.2)}$$

where C is the drug concentration in solution, k_a the specific adsorption rate, k_d the specific release rate, and θ the fraction of surface active sites in the HLNTs occupied by the drug molecules.

Integration of Eq. (VI.2) yields to:

$$F = \frac{C_t}{C_e} = 1 - e^{\left(\frac{-k_d \cdot t}{C_e}\right)} \qquad \text{(VI.3)}$$

where F is the fraction of drug released, C_t is the drug concentration in solution at time t, C_e is the drug concentration in solution at the equilibrium (maximum drug released) and k_d the specific release rate.

Eq. (VI.3) was used to fit in vitro release experimental data. Theoretical release curves calculated according to Eq. (VI.3) were assigned to desorption of INH molecules, described by the model as a solid/liquid interface process governed by diffusive transport of INH molecules from the active adsorption sites (inner and outer surfaces) of HLNTs to the surrounding liquid medium. Release rates (Table VI.3) suggest a strong affinity of drug molecules for the surrounding media (causing very easy and quickly release process), as well as a negligible influence of pH on drug dissolution. From a practical point of view, to prevent early release of INH from HLNTs and ensure that the drug remained associated to the HLNTs at the absorption site, use of enteric coated capsules seems to be a possible strategy for oral administration.

In vitro cytotoxicity tests towards Caco-2 cell line results revealed that, except for samples 5 (100 μg/mL) and 6 (1000 μg/mL), all the HLNTs concentrations tested were biocompatible towards Caco-2 cell lines (providing viability values not lower than the positive control). These results are in agreement with previously reported literature data (Vergaro et al., 2010; Han et al., 2011; Sandri et al., 2017). In addition, proliferative effects were found for concentrations 1-4, since the obtained viability values were significantly higher than the positive control. This effect was in line with previous

works in which HLNTs were found to have a positive influx on cell attachment and spreading, even higher than other similar inorganic carriers due to the higher roughness of its surface in comparison with the smooth of silica or montmorillonite (Kommireddy et al., 2005; Lai et al., 2013). In case of the drug alone, none of the concentrations assayed resulted in viability values significantly lower than the untreated cells (control). Similar results were found for the nanohybrid, whose biocompatibility in the whole range of concentrations was assessed and a positive trend on cell growth was observed, being also significant in some cases (1, 2 and 6). It is remarkable that INH-loaded HLNTs possess biocompatible behaviour even when HLNTs exhibited cytotoxic activity, so the interaction between HLNTs and INH turned to have a positive effect regarding cell viability. Permeability tests results showed that incorporation of HLNTs significantly improved the permeation of the drug across the cellular membrane. Similar findings were observed in previous studies with similar inorganic excipients and explained as a consequence of electrostatic interactions between silanol groups in the surface of inorganic carriers and positively charged constituents of cell membranes (Salcedo et al., 2014).

Regarding the TEER results, the value of the INH-loaded HLNTs nanohybrid suffered a reversible decrease that becomes significant after 90 minutes. This behaviour suggests that the presence of nanohybrid suspension interfered with the junctional proteins, probably via H bond and/or Van der Waals interactions, causing widen of the paracellular route, in agreement with permeability results, where increased of drug permeation was observed starting from 90 minutes. After 24 hours of the beginning of the test, TEER profiles of both samples were restored to primitive values meaning the recovery of the integrity of the cell monolayer. These results supported the protective effect of silicate-based carriers in restoring the epithelial barrier of Caco-2 cells by means of TEER measurements (Romero et al., 2016).

Fluorescent microphotographs revealed the internalization of INH when loaded in the nanohybrid which was non observable in the case of free INH. In the cell substrate treated with INH-loaded HLNTs, it can be noticed that there was a blue signal due to INH present in the cell substrate, to indicate an actual internalization of the drug (no blue signal was present in the control). Moreover there were some blue spots conceivably due to INH loaded nanohydrid to indicate the uptake of the system from cell substrate. In the substrate treated with INH no blue signal was visible to indicate the

low propensity of the drug to be internalized by Caco-2 cells. In all cases the staining of the nuclei demonstrated that no nuclear damage occurred during the experiments and no apoptotic cell could be identified confirming the lack of cytotoxicity of the INH-loaded HLNTs nanohybrid.

Degradation of INH in presence of ETB has been explained as a result of the hygroscopic nature of ETB, which attracts moisture and creates acidic environment increasing the rate of decomposition of INH (Bhutani et al., 2005b). Inclusion of INH onto HLNTs not only did not induce INH degradation, but also protected INH from ETB-induced degradation; the amounts of INH recovered from INH-loaded HLNTs after 15 and 90 days in presence of ETB were ~80 % and 40 % (Figure VI.6). Regarding the quaternary mixtures, results showed that the four first-line tuberculostatic drugs interact with each other in a multiple and complex manner leading to a significant loss of INH % in the samples, with a residual content of only ~10 % (15 days) and ~ 2 % (90 days) in case of the quaternary combinations containing unloaded INH (Figure VI.6). In line with previous studies, isonicotinylhydrazone could be stated as the major degradation product of INH, which is formed by the interaction of the imino group of 3-formyl rifampicin of RIF with the hydrazine group of INH under acidic conditions provided by the presence of ETB (Singh et al., 2001; Bhutani et al., 2005a). In the presence of the nanohybrid, compatibility of quaternary mixtures was enhanced, achieving residual INH contents from five to ten times higher than that found in absence of HLNTs at the same time. Assuming that INH degradation follows first order kinetics, plot of log (INH %) vs time allowed to calculate from the resulting straight lines the degradation rate constants (6.2×10^{-3} days−1 for INH:ETB and 4.6×10^{-3} $days^{-1}$ for INH-loaded:HLNTs) and $t_{1/2}$ values of 38 and 65 days, respectively.

Regarding the quaternary mixtures, rate constants of 15.4×10^{-3} and 7×10^{-3} $days^{-1}$ and $t_{1/2}$ of 11 and 22 days were calculated for mixtures containing unloaded and loaded INH, respectively. These findings prove that HLNTs strongly increased stability (in terms of decreasing the degradation rate) of INH in presence of the other first line tuberculostatic agents, suggesting promising application of INH-loaded HLNTs in 4-FDC treatment.

VI.5 CONCLUSIONS

Major challenges of TB treatment are related with compatibility problems between first-line tuberculostatic drugs when administered together in FDC dosage forms and, in particular, in the case of INH, with its low intestinal permeability requiring the

administration of high doses leading to severe toxic effects. Over the past few years, it has been shown that natural inorganic excipients as halloysite may play a leading role as affordable nanocarriers to be used in the design of advanced drug delivery systems. In this work, a novel drug-halloysite nanohybrid with significant enhancement of *in vitro* INH permeability and stability has been studied. *In vitro* release measurements revealed that adsorption of INH onto HLNTs did not hinder drug dissolution, drug release being complete in the early minutes of the test both in acidic and neutral environment. The mechanism of drug release was explained on the basis of a mechanistic adsorption-desorption model, as a diffusive mass transport across the solid/liquid interface. Cell cultures experiments confirmed that the nanohybrid was biocompatible on Caco-2 cells in the whole concentration range studied. Significant positive effects on cells proliferation were also found. In-vitro permeability tests showed a significant increase of the drug permeation across the Caco-2 monolayer. Complementary TEER measurements suggested widen of the paracellular route. The uptake of the nanohybrid by the cells was confirmed by fluorescent microscopy. Stability tests showed higher stability of INH-loaded HLNTs in binary and quaternary physical mixtures containing ETB, which is the principal responsible of the physical and chemical degradation of INH in 4-FDC.

CAPÍTULO VII

Conclusiones/Conclusions

En esta Tesis Doctoral se han desarrollado sistemas nanohíbridos orgánicos-inorgánicos con dos arcillas de grado farmacéutico de distinta estructura y composición (halloysita, y paligorskita) e isoniazida, el fármaco más utilizado en el tratamiento de la tuberculosis. Los sistemas se han obtenido mediante la técnica de intercalación sólido-líquido. Las materias primas y los distintos nanohíbridos obtenidos han sido caracterizados por diversas técnicas de caracterización al estado sólido. Asimismo se ha completado un estudio teórico y experimental de las propiedades cinéticas y termodinámicas del proceso de adsorción de la isoniazida en las arcillas. El nanohíbrido isoniazida-halloysita ha sido objeto de estudios complementarios. En particular, se ha estudiado mediante modelado computacional las características del proceso de adsorción de moléculas de isoniazida en los nanotubos de halloysita, se ha efectuado un estudio cinético y del mecanismo de liberación del fármaco desde dicho nanohíbrido, se han realizado ensayos *in-vitro* de citotoxicidad y permeabilidad intestinal en la línea celular de adenocarcinoma de colon Caco-2 y, por último, se han realizado ensayos de estabilidad acelerada de la isoniazida pura y cargada en la halloysita con combinaciones binarias y cuaternarias con los otros tres fármacos antituberculosos de primera línea (etambutol, pirazinamida y rifampicina).

Fruto del trabajo desarrollado durante estos años se han publicado 4 artículos JCR situados entre los primeros de su categoría y un capítulo de libro publicado por la editorial Elsevier, todos ellos directamente relacionados con el plan de trabajo de la Tesis Doctoral. En cada aportación se recogen conclusiones parciales que han quedado plasmadas en los capítulos anteriores. En el presente capítulo de conclusiones de esta memoria de Tesis Doctoral se señalan aquellas que consideramos conclusiones generales a las que cabe llegar, que son las siguientes:

1. Los datos de adsorción experimentales han sido ajustados mediante una ecuación desarrollada a partir de un modelo propuesto para este tipo de interacciones. Con la citada ecuación matemática no lineal se han conseguido ajustes de los datos experimentales con un elevado coeficiente de correlación en todos los casos.
2. Los estudios cinéticos y termodinámicos del proceso de adsorción de isoniazida en las arcillas estudiadas han revelado que dicho proceso se produce en dos etapas: la adsorción propiamente dicha de moléculas de isoniazida en los sitios activos de los adsorbentes, seguida de la precipitación de moléculas de fármaco

sobre la monocapa previamente adsorbida. Ambas etapas son espontáneas para todos los sistemas en las condiciones estudiadas.

3. El proceso de adsorción de isoniazida en halloysita era endotérmico y endoentrópico. El proceso de adsorción de isoniazida en palygorskita era exotérmico y exoentrópico.
4. El estudio de modelado computacional confirmó los resultados experimentales de la interacción entre la halloysita y la isoniazida. Se detectaron cambios conformacionales en la molécula de fármaco y se postuló que la interacción entre la isoniazida y la halloysita se producía mediante puentes de hidrógeno entre el átomo de nitrógeno del heterociclo de la molécula de isoniazida y los hidrógenos de los grupos hidroxilo de la halloysita.
5. La caracterización de los nanohíbridos ha permitido concluir que el fármaco se encuentra homogéneamente distribuido en las muestras y que se produce una interacción efectiva entre los soportes inorgánicos y las moléculas de fármaco. La unión se produce mediante puentes de hidrógeno.
6. La liberación del fármaco intercalado en los nanotubos de halloysita no se ve alterada y cursa siguiendo un proceso sencillo de desorción.
7. Los nanohíbridos de halloysita con isoniazida no son citotóxicos para la línea celular Caco-2 y en determinadas condiciones presentan efectos significativamente beneficiosos para la proliferación celular.
8. La permeabilidad intestinal de la isoniazida mejora significativamente cuando se incorpora a la halloysita, obteniendo aproximadamente un 90% del total de isoniazida permeada a través de la membrana en el nanohíbrido halloysita-isoniazida, frente a un 58% del total en el caso de la isoniazida pura.
9. La incorporación de la isoniazida en los nanotubos de halloysita mejora la compatibilidad de dicho fármaco en condiciones de estabilidad acelerada en mezclas binarias y cuaternarias con los fármacos antituberculosos de primera línea.

Como corolario de la Tesis Doctoral puede inferirse que:

Las arcillas deben ser consideradas materias primas susceptibles de empleo en el desarrollo de formas farmacéuticas de administración oral para ser empleadas en el tratamiento de la tuberculosis. En el caso particular de la isoniazida, hemos demostrado que la incorporación de forma sencilla a un excipiente de bajo coste como la halloysita mejora la permeabilidad intestinal y paralelamente la estabilidad del fármaco en presencia de los otros fármacos antituberculosos de primera línea.

In this doctoral Thesis, organic-inorganic nanohybrid systems have been developed with two pharmaceutical-grade clays of different structure and composition (halloysite and palygorskite) and isoniazid, the most commonly used drug in the treatment of tuberculosis. The nanohybrid systems have been prepared by the solid-liquid intercalation technique. Raw materials and the different nanohybrids obtained have been characterized by diverse solid state characterization techniques. Likewise, a theoretical and experimental study of the kinetic and thermodynamic properties of the adsorption process of isoniazid on the clays has been completed. The nanohybrid isoniazid-halloysite has been subjected to further complementary studies. In particular, the characteristics of the process of adsorption of isoniazid molecules in halloysite nanotubes have been studied through computational modeling, a study of the kinetics and mechanism involved in drug release from these nanohybrid has been fulfilled, *in-vitro* cytotoxicity and intestinal permeability assays have been performed in the Caco-2 colon adenocarcinoma cell line and, finally, compatibility trials have been carried out at accelerated stability conditions involving isoniazid (alone and loaded in halloysite) as part of binary and quaternary mixtures with the other three first-line tuberculostatic drugs (ethambutol, pyrazinamide and rifampicin).

As a result of the above detailed research carried out, 4 JCR articles among the first of their category and a book chapter edited by Elsevier have been published in which the objectives set out in the Thesis are addressed. In each of them, partial conclusions are given that have been fully explained in the previous chapters. In the present chapter of conclusions are indicated those that we consider general conclusions that can be reached, which are the following:

1. Adsorption experimental data have been fitted to a nonlinear mathematical equation developed in basis of a model proposed for this kind of interactions obtaining a correlation coefficient close to one in all cases.
2. Kinetic and thermodynamic studies of the isoniazid-clay minerals adsorption processes have revealed that, in all cases, this process follows two stages: adsorption of isoniazid molecules on the active sites of the adsorbents and precipitation of molecules of the drug over the previously adsorbed monolayer. These processes have been found to be spontaneous for the two systems prepared at the studied conditions.

3. Adsorption process of isoniazid onto halloysite was endothermic and endoentropic, while in case of palygorskite-isoniazid it was exothermic and exoentropic.
4. Computational modeling studies confirmed the results obtained for the halloysite-isoniazid system. Conformational changes in the molecule and strong hydrogen bonds between the carbonyl group and heterocyclic nitrogen atom with the hydroxyl hydrogen atoms of the mineral surface were found.
5. The results obtained from the different techniques used to complete the solid state characterization of the raw materials and nanohybrids showed that the drug was homogeneously distributed in the samples and that an effective interaction takes place between the inorganic carriers and the drug molecules. Mechanisms involved in the interaction were mainly hydrogen bonds.
6. Drug release was not hindered by interaction between drug molecules and halloysite nanotubes. Release consisted on a simple desorption process.
7. Halloysite-isoniazid nanohybrid exerted no cytotoxic effects towards Caco-2 cell line. In addition, in some cases, proliferative effects were found.
8. Intestinal permeability of isoniazid was greatly increased when incorporated onto halloysite nanotubes, reaching isoniazid permeated values at the end of the test of approximately 90% in case of the halloyite-isoniazid nanohybrid and 58% in case of the drug alone.
9. The incorporation of isoniazid in halloysite nanotubes improved the compatibility of this drug under conditions of accelerated stability in binary and quaternary mixtures containing the other first-line tuberculostatic drugs.

As a corollary of the Doctoral Thesis it can be inferred that:

Clay minerals must be considered raw materials to be employed in the development of advanced delivery systems for the oral treatment of tuberculosis. In the particular case of isoniazid, we have been able to demonstrate that by simple incorporation to a low-cost excipient as halloysite, not only its intestinal permeability but its stability in the presence of the other first-line tuberculostatic drugs greatly improve.

CAPÍTULO VIII

Bibliografía

Abdullayev, E. y Lvov, Y. (2011). Halloysite clay nanotubes for controlled release of protective agents. J. Nanosci. Nanotechnol. 11(11), 10007-10026.

Abdullayev, E. y Lvov, Y. (2013). Halloysite clay nanotubes as a ceramic skeleton forfunctional biopolymer composites with sustained drug release. J. Mater. Chem. B 1, 2894-2903.

Adhikary, R.R., More, P., Banerjee, R. (2015). Smart nanoparticles as targeting platforms for HIV infections. Nanoscale 7, 7520-7534.

Aguzzi, C., Cerezo, P., Viseras, C., Caramella, C. (2007). Use of clays as drug delivery systems: Possibilities and limitations. Appl. Clay Sci. 36(1), 22-36.

Aguzzi, C., Capra, P., Bonferoni, C., Cerezo, P., Salcedo, I., Sanchez, R., Caramella, C., Viseras, C. (2010). Chitosan-Silicate biocomposites to be used in modified drug release of 5-ASA. Appl. Clay Sci. 50(1), 106-111.

Aguzzi, C., Viseras, C., Cerezo, P., Salcedo, I., Sánchez, R., Valenzuela, C. (2013). Release kinetics of 5-aminosalicylic acid from halloysite. Colloids Surf. B Bionterfaces 105, 75-80.

Aguzzi, C., Sandri, G., Bonferoni, C., Cerezo, P., Rossi, S., Ferrari, F., Caramella, C., Viseras, C. (2014a). Solid state characterisation of silver sulfadiazine loaded on montmorillonite/chitosan nanocomposite for wound healing. Colloids Surf. B Biointerfaces, 113, 152-157.

Aguzzi, C., Sandri, G., Cerezo, P., Ferrari, F., Rossi, S., Bonferoni, C., Caramella, C., Viseras, C. (2014b). A novel bioadhesive semisolid formulation containing chitosan and tetracycline/layered clay complexes for local delivery into periodontal pockets. Mater. Technol. 29 (B2), B108-B113.

Aguzzi, C., Sandri, G., Cerezo, P., Carazo, E., Viseras, C. (2016). Health and medical applications of tubular clay minerals. En: Nanosized Tubular Clay Minerals. Halloysite

and Imogolite. Peng Yuan, Antoine Thill y Faïza Bergaya (Eds.) Serie: Developments in Clay Science, Elsevier. Vol. 7, capítulo 26, pp. 708-725.

Ai, J.W., Ruan, Q.L., Liu, Q.H., Zhang, W.H. (2016). Updates on the risk factors for latent tuberculosis reactivation and their managements. Emerg. Microbes Infect. 5(2), e10.

Akyuz, S. y Akyuz, T. (2004). FT-IR spectroscopic investigations adsorption of pyrazinamide and 4-aminopyrimidine by clays. J. Incl. Phenom. Macrocycl. Chem. 48(1-2), 75-80.

Akyuz, S. y Akyuz, T. (2008). FT-IR and FT-Raman spectroscopic studies of adsorption of isoniazid by montmorillonite and saponite. Vib. Spectrosc. 48(2), 229-232.

Akyuz, S., Akyuz, T., Akalin, E. (2010). Adsorption of isoniazid onto sepiolite–palygorskite group of clays: an IR study. Spectrochim. Acta A Mol. Biomol. Spectrosc. 75(4), 1304-1307.

Albert, A. (1956). Mode of action of isoniazid. Nature 177(4507), 525-526.

Allwood, B.W., Goldin, J., Said-Hartley, Q., van Zyl-Smit, R.N., Calligaro, G., Esmail, A., Bateman, E.D. (2015). Assessment of previous tuberculosis status using questionnaires, chest X-rays and computed tomography scans. Int. J. Tuberc. Lung Dis. 19(12), 1435-1440.

American Thoracic Society (ATS) and the Centers for Disease Control (CDC). (2001). Update: Fatal and severe liver injuries associated with rifampin and pyrazinamide for latent tuberculosis infection, and revisions in American Thoracic Society/CDC Recommendations- United States, 2001. Am. J. Respir. Crit. Care Med., 164, 1319-1320.

Amoakwa, K., Martinson, N.A., Moulton, L.H., Barnes, G.L., Msandiwa, R., Chaisson, R. E. (2015). Risk factors for developing active tuberculosis after the treatment of latent

tuberculosis in adults infected with human immunodeficiency virus. Open Forum Infect. Dis. 2(1), 1-4.

Angadi, S.C., Manjeshwar, L.S., Aminabhavi, T.M., (2010). Interpenetrating polymer network blend microspheres of chitosan and hydroxyethyl cellulose for controlled release of isoniazid. Int. J. Biol. Macromol. 47(2), 171-179.

Artursson, P., Palm, K., Luthman, K. (2001). Caco-2 monolayers in experimental and theoretical predictions of drug transport. Adv. Drug Deliv. Rev. 46(1-3), 27-43.

Arya, V. y Philip, L. (2016). Adsorption of pharmaceuticals in water using Fe_3O_4 coated polymer clay composite. Microporous Mesoporous Mat. 232, 273-280.

Asmar, S., Chatellier, S., Mirande, C., van Belkum, A., Canard, I., Raoult, D., Drancourt, M. (2015). A novel solid medium for culturing *Mycobacterium tuberculosis* isolates from clinical specimens. J. Clin. Microbiol. 53(8), 2566-2569.

Auguste, P., Tsertsvadze, A., Pink, J., McCarthy, N., Sutcliffe, P., Clarke, A. (2017). Comparing interferon-gamma release assays with tuberculin skin test for identifying latent tuberculosis infection that progresses to active tuberculosis: systematic review and meta-analysis. BMC Infect. Dis. 17(1), 200.

Aulton, M.E. y Taylor, K.M.G. (2013). Aulton's Pharmaceutics. The Design and Manufacture of Medicines, fourth ed. Churchill Livingstone-Elsevier, Edinburgh.

Autier, P., Boniol, M., Pizot, C., Mullie, P. (2014). Vitamin D status and ill health: a systematic review. Lancet Diabetes Endocrinol. 2(1), 76-89.

Banik, N., Hussain, A., Ramteke, A., Sharma, H.K., Maji, T.K. (2012). Preparation and evaluation of the effect of particle size on the properties of chitosan-montmorillonite nanoparticles loaded with isoniazid. RSC Adv. 2(28), 10519-10528.

Banik, N., Iman, M., Hussain, A., Ramteke, A., Boruah, R., Maji, T.K. (2013). Soy flour nanoparticles for controlled drug delivery: effect of crosslinker and montmorillonite (MMT). New J. Chem. 37(12), 3981-3990.

Banik, N., Ramteke, A., Maji, T.K. (2014). Carboxymethyl chitosan-montmorillonite nanoparticles for controlled delivery of isoniazid: evaluation of the effect of the glutaraldehyde and montmorillonite. Polym. Adv. Technol. 25(12), 1580-1589.

Bates, T.F., Hildebrand, F.A., Swineford, A. (1950). Morphology and structure of endellite and halloysite. Am. Mineral. 35(7-8), 463-484.

Bates, M.N., Khalakdina, A., Pai, M., Chang, L., Lessa, F., Smith, K.R. (2007). Risk of tuberculosis from exposure to tobacco smoke: a systematic review and meta-analysis. Arch. Inter. Med. 167(4), 335-342.

Battini, S., Mannava, M.C., Nangia, A. (2018). Improved stability of tuberculosis drug fixed-dose combination using isoniazid-caffeic acid and vanillic acid cocrystal. J. Pharm. Sci. 107(6), 1667-1679.

Bergaya, F. y Lagaly, G. (2001). Surface modification of clay minerals. Appl. Clay Sci. 1(19), 1-3.

Bertolino, V., Cavallaro, G., Lazzara, G., Milioto, S., Parisi, F. (2018). Halloysite nanotubes sandwiched between chitosan layers: a novel bionanocomposite with multilayer structure. New J. Chem. 42(11), 8384-8390.

Bhandari, R. y Kaur, I.P. (2013). Pharmacokinetics, tissue distribution and relative bioavailability of isoniazid-solid lipid nanoparticles. Int. J. Pharm. 441(1-2), 202-212.

Bhutani, H., Mariappan, T.T., Singh, S. (2004). An explanation for the physical instability of a marketed fixed dose combination (FDC) formulation containing isoniazid and ethambutol and proposed solutions. Drug Dev. Ind. Pharm. 30(6), 667-672.

Bhutani, H., Singh, S., Jindal, K.C. (2005a). Drug-drug interaction studies on first-line anti-tuberculosis drugs. Pharm. Dev. Technol. 10(4), 517-524.

Bhutani, H., Singh, S. Jindal, K.C. Chakraborti, A.K. (2005b). Mechanistic explanation to the catalysis by pyrazinamide and ethambutol of reaction between rifampicin and isoniazid in anti-TB FDCs. J. Pharm. Biomed. Anal., 39, 892-899.

Bhutani, H., Singh, S., Vir, S., Bhutani, K.K., Kumar, R., Chakraborti, A.K., Jindal, K. C. (2007). LC and LC-MS study of stress decomposition behaviour of isoniazid and establishment of validated stability-indicating assay method. J. Pharm. Biomed. Anal. 43(4), 1213-1220.

Biondi, M., Ungaro, F., Quaglia, F., Netti, P.A. (2008). Controlled drug delivery in tissue engineering. Adv. Drug Deliv. Rev. 60, 229-242.

BIOVIA Materials Studio, version 2016 (2016). Dassault Systemes.

Blanco, E., Shen, H., Ferrari, M. (2015). Principles of nanoparticle design for overcoming biological barriers to drug delivery. Nat. Biotechnol. 33, 941-951.

Blomberg, B. y Fourie, B. (2003). Fixed-dose combination drugs for tuberculosis. Drugs, 63(6), 535-553.

Blume, H.H. y Schug, B.S. (1999). The biopharmaceutics classification system (BCS): Class III drugs—Better candidates for BA/BE waiver? Eur. J. Pharm. Sci. 9(2), 117-121.

Borrego-Sánchez, A., Viseras, C., Aguzzi, C., Sainz-Díaz, C.I. (2016). Molecular andcrystal structure of praziquantel: spectroscopic properties and crystal polymorphism, Eur. J. Pharm. Sci. 92, 266-275.

Borrego-Sánchez, A., Hernández-Laguna, A., Sainz-Díaz, C.I. (2017). Molecular modeling and infrared and Raman spectroscopy of the crystal structure of the chiral antiparasitic drug Praziquantel. J. Mol. Model. 23(4), 106.

Borrego-Sánchez, A., Carazo, E., Aguzzi, C., Viseras, C., Sainz-Díaz, C.I. (2018). Biopharmaceutical improvement of praziquantel by interaction with montmorillonite and sepiolite. Appl. Clay Sci. 160, 173-179.

Bradley, W. (1940). The structural scheme of attapulgite. Am. Mineral. 25(6), 405-410.

Brennan, P.J. (2003). Structure, function, and biogenesis of the cell wall of Mycobacterium tuberculosis. Tuberculosis 83(1), 91-97.

Brewer, G.A. (1977). Isoniazid. Anal. Profiles Drug Subst. 6, 183-258.

Brindley, G.W. y Robinson, K. (1946). Randomness in the structures of kaolinitic clay minerals. Trans. Faraday Soc. 42, 198-205.

Brock, T.D. (1988). Robert Koch: a life in medicine and bacteriology. Madison, WI: Science Tech Publishers, pp. 96-104.

www.cadime.es. Centro Andaluz de Información y Documentación de Medicamentos.

Çalışkan Salihi, E., Gündüz, Z., Baştuğ, A.S. (2018). Fast retention of isoniazid on organobentonite prepared using green chemistry approach: contribution of the π interactions. Sep. Sci. Technol. 1-11.

Calmette, A., Guérin, C., Nègre, L., Boquet, A. (1926). Prémunition des nouveaux-nés contre la tuberculose par le vaccin BCG, 1921-1926. Ann. Inst. Pasteur 2, 89-120.

Campbell, J. R., Krot, J., Marra, F. (2016). Latent tuberculosis diagnostic tests to predict longitudinal tuberculosis during dialysis: a meta-analysis. Int. J. Tuberc. Lung Dis. 20(6), 764-770.

Campos, V.F., de Leon, P.M.M., Komninou, E.R., Dellagostin, O.A., Deschamps, J.C., Seixas, F.K., Collares, T., (2011). NanoSMGT: transgene transmission into bovine embryos using halloysite clay nanotubes or nanopolymer to improve transfection efficiency. Theriogenology 76, 1552-1560.

Cano-Portero, R., Amillategui-dos Santos, R., Boix-Martínez, R., Larrauri-Cámara, A. (2018). Epidemiología de la tuberculosis en España. Resultados obtenidos por la Red Nacional de Vigilancia Epidemiológica en el año 2015. Enferm. Infec. Microbiol. Clin. 36(3), 179-186.

Carazo, E., Borrego-Sánchez, A., Aguzzi, C., Cerezo, P., Viseras, C. (2017a). Use of clays as nanocarriers of tuberculostatic drugs. Curr. Drug Deliv. 14(7), 902-903.

Carazo, E., Borrego-Sánchez, A., García-Villén, F., Sánchez-Espejo, R., Aguzzi, C., Viseras, C., Sainz-Diaz, C.I., Cerezo, P. (2017b). Assessment of halloysite nanotubes as vehicles of isoniazid. Colloids Surf. B Biointerfaces 160, 337-344.

Carazo, E., Borrego-Sánchez, A., García-Villén, F., Sánchez-Espejo, R., Cerezo, P., Aguzzi, C., Viseras, C. (2018a). Advanced Inorganic Nanosystems for Skin Drug Delivery. Chem. Rec. 18, 1-10.

Carazo, E., Borrego-Sánchez, A., García-Villén, F., Sánchez-Espejo, R., Viseras, C., Cerezo, P., Aguzzi, C. (2018b). Adsorption and characterization of palygorskite-isoniazid nanohybrids. Appl. Clay Sci. 160, 180-185.

Carazo, E., Borrego-Sánchez, A., Sánchez-Espejo, R., García-Villén, F., Cerezo, P., Aguzzi, C., Viseras, C. (2018c). Kinetic and thermodynamic assessment on isoniazid/montmorillonite adsorption. Appl. Clay Sci. 165, 82-90.

Cavallaro, G., Lazzara, G., Milioto, S. (2011). Dispersions of nanoclays of differentshapes into aqueous and solid biopolymeric matrices. Extended physicochemical study. Langmuir 27(3), 1158-1167.

Cavallaro, G., Lazzara, G., Massaro, M., Milioto, S., Noto, R., Parisi, F., Riela, S., (2015). Biocompatible poly (N-isopropylacrylamide)-halloysite nanotubes for thermoresponsive curcumin release. J. Phys. Chem. C 119, 8944-8951.

Cegielski, J.P. y McMurray, D.N. (2004). The relationship between malnutrition and tuberculosis: evidence from studies in humans and experimental animals. Int. J. Tuberc. Lung Dis. 8(3), 286-298.

Centro Nacional de Epidemiología. Instituto de Salud Carlos III. Informe epidemiológico sobre la situación de la tuberculosis en España. Año 2014. Madrid, 2015.

Cerezo, P., Viseras, C., Lopez-Galindo, A., Ferrari, F., Caramella, C. (2001). Use of water uptake and capillary suction time measures for evaluation of the anti-diarrhoeic properties of fibrous clays. Appl. Clay Sci. 20(1), 81-86.

Chahi, A., Petit, S., Decarreau, A. (2002). Infrared evidence of dioctahedral-trioctahedral site occupancy in palygorskite. Clay Clay Miner. 50(3), 306-313.

Chang, P.H., Li, Z., Yu, T.L., Munkhbayer, S., Kuo, T.H., Hung, Y.C., Lin, K.H. (2009). Sorptive removal of tetracycline from water by palygorskite. J. Hazard. Mater. 165(1), 148-155.

Chen, Q.Z., Liang, S.L., Wang, J., Simon, G.P.J. (2011). Manipulation of mechanical compliance of elastomeric PGS by incorporation of halloysite nanotubes for soft tissue engineering applications. J. Mech. Behav. Biomed. Mater. 4, 1805-1818.

Cheepsattayakorn, A. y Cheepsattayakorn, R. (2018). Silicosis-associated tuberculosis: management and control. American J. Public Health 6(2), 125-129.

Choudhary, S. y Devi, V.K. (2015). Potential of nanotechnology as a delivery platform against tuberculosis: current research review. J. Control. Release 202, 65-75.

Chrzanowski, W., Kim, S.Y., Neel, E.A.A. (2013). Biomedical applications of clay. Aust. J. Chem. 66, 1315-1322.

Clay Minerals Society (2018). The Clay Minerals Society Glossary of Clay Science, 2018 version.

Cole, S., Brosch, R., Parkhill, J., Garnier, T., Churcher, C., Harris, D., Tekaia, F. (1998). Deciphering the biology of *Mycobacterium tuberculosis* from the complete genome sequence. Nature 393(6685), 537.

Cooper A.M. (2009). Cell mediated immune responses in tuberculosis. Annu. Rev. Immunol. 27, 393-422,

Cordes, H., Thiel, C., Aschmann, H.E., Baier, V., Blank, L.M., Kuepfer, L. (2016). A physiologically based pharmacokinetic model of isoniazid and its application in individualizing tuberculosis chemotherapy. Antimicrob. Agents Chemother. 60(10), 6134-6145.

Costa, A., Pinheiro, M., Magalhães, J., Ribeiro, R., Seabra, V., Reis, S., Sarmento, B. (2016). The formulation of nanomedicines for treating tuberculosis. Adv. Drug Deliv. Rev. 102, 102-115.

Costa-Gouveia, J., Aínsa, J.A., Brodin, P., Lucía, A. (2017). How can nanoparticles contribute to antituberculosis therapy? Drug Discov. Today 22(3), 600-607.

Dai, L., Cao, X., Liu, K.F., Li, C.X., Zhang, G.F., Deng, L.H., Si, C.L., He, J., Lei, J.D. (2015). Self-assembled targeted folate-conjugated eight-arm-polyethyleneglycol–betulinic acid nanoparticles for co-delivery of anticancer drugs. J.Mater. Chem. B 3, 3754-3766.

Daniel, T.M. (2006). The history of tuberculosis. Respir. Med. 100(11), 1862-1870.

Davies, G.R. y Nuermberger, E.L. (2008). Pharmacokinetics and pharmacodynamics in the development of anti-tuberculosis drugs. Tuberculosis 88, S65-S74.

Davis, J.L., Cattamanchi, A., Cuevas, L.E., Hopewell, P.C., Steingart, K.R. (2013). Diagnostic accuracy of same-day microscopy versus standard microscopy for pulmonary tuberculosis: a systematic review and meta-analysis. Lancet Infect. Dis. 13(2), 147-154.

Dawson, J.I. y Oreffo, R.O.C. (2013). Clay: new opportunities for tissue regeneration and biomaterial design. Adv. Mater. 25, 4069-4086.

Del Río-Estrada, C. y Dougherty, H.W. (1970). Profiles of Drug Substances, Excipients and Related Methodology. Britain, H. (Eds.) John Wiley and Sons. Vol. 21, pp. 528–533.

Dooley, K.E. y Chaisson, R.E. (2009). Tuberculosis and diabetes mellitus: convergence of two epidemics. Lancet Infect. Dis. 9(12), 737-746.

Dos Santos Soares, D., Fernandes, C.S., da Costa, A.C.S., Raffin, F.N., Acchar, W., Moura, T.F.D.L. (2013). Characterization of palygorskite clay from Piauí, Brazil and its potential use as excipient for solid dosage forms containing anti-tuberculosis drugs. J. Therm. Anal. Calorim. 113(2), 551-558.

Elumalai, D.N., Lvov, Y., Derosa, P. (2015). Implementation of a simulation model of the controlled release of molecular species from halloysite nanotubes. J. Encapsulation Adsorpt. Sci. 5, 74-92.

Engler, A.J., Sen, S., Sweeney, H.L., Discher, D.E. (2006). Matrix elasticity directs stem cell lineage specification. Cell 126, 677–689.

European Directive (2001). Directive 2001/83/EC of the European Parliament and of the Council of 6 November 2001 on the Community code relating to medicinal products for human use. Off. J. Eur. Union 311, 67. 28.11.2001.

European Directive (2007). Directive 2007/47/EC of the European Parliament and of the Council of 5 September 2007 amending Council Directive 90/385/EEC on the approximation of the laws of the Member States relating to active implantable medical devices, Council Directive 93/42/EEC concerning medical devices and Directive 98/8/EC concerning the placing of biocidal products on the market. Off. J. Eur. Union 247, 21-55. 21.9.2007.

Falzon, D., Schünemann, H.J., Harausz, E., González-Angulo, L., Lienhardt, C., Jaramillo, E., Weyer, K. (2017). World Health Organization treatment guidelines for drug-resistant tuberculosis, 2016 update. Eur. Respir. J. 49(3), 1602308.

Fan, L., Li, B., Wang, Q., Wang, A., Zhang, J. (2014). Superhydrophobic gated polyorganosilanes/halloysite nanocontainers for sustained drug release. Adv. Mater. Inter. 1, 130-136.

Ferguson, T.W., Tangri, N., Macdonald, K., Hiebert, B., Rigatto, C., Sood, M. M., Komenda, P. (2015). The diagnostic accuracy of tests for latent tuberculosis infection in hemodialysis patients: a systematic review and meta-analysis. Transplantation 99(5), 1084-1091.

Ferrari, M. (2008) Nanogeometry beyond drug delivery, Nat. Nanotechnol. 3, 131-132.

Fizir, M., Dramou, P., Zhang, K., Sun, C., Pham-Huy, C., He, H. (2017). Polymergrafted-magnetic halloysite nanotube for controlled and sustained release of cationic drug. J. Colloid Interface Sci. 505, 476-488.

https://www.flickr.com/photos/niaid/5149398656

Florey, K. (1979). Profiles of drug substances, excipients and related methodology. Volumen 8. Academic press.

Forsgren, J., Jamstorp, E., Bredenberg, S., Engqvist, H., Stromme, M. (2010). A ceramic drug delivery vehicle for oral administration of highly potent opioids. J. Pharm. Sci. U.S. 99(1), 219-226.

Fox, G.J., Dobler, C.C., Marais, B.J., Denholm, J.T. (2017). Preventive therapy for latent tuberculosis infection-the promise and the challenges. Int. J. Infect. Dis. 56, 68-76.

Freire, F.D., Câmara, M.B., Dantas, M.G., Aragão, C.F.S., e Moura, L., Raffin, F.N. (2014). Gastric-resistant isoniazid pellets reduced degradation of rifampicin in acidic medium. Braz. J. Pharm. Sci. 50(4), 749-755.

Frost, R.L. (1995). Fourier transform Raman spectroscopy of kaolinite: dickite and halloysite. Clay Clay Miner. 43(2) 191-195.

Frost, R.L., Locos, O.B., Ruan, H., Kloprogge, J.T. (2001). Near-infrared and mid-infrared spectroscopic study of sepiolites and palygorskites. Vib. Spectrosc. 27(1), 1-13.

Frost, R.L. y Ding, Z. (2003). Controlled rate thermal analysis and differential scanning calorimetry of sepiolites and palygorskites. Thermochim. Acta 397(1), 119-128.

Gaharwar, A.K., Peppas, N.A., Khademhosseini, A. (2013). Nanocomposite hydrogels for biomedical applications. Biotechnol. Bioeng. 111, 441-453.

Gambhir, S., Ravina, M., Rangan, K., Dixit, M., Barai, S., Bomanji, J. (2017). Imaging in extrapulmonary tuberculosis. Int. J. Infect. Dis. 56, 237-247.

Galan, E. (1996). Properties and applications of palygorskite-sepiolite clays. Clay Miner. 31(4), 443-453.

García-Villén, F., Carazo, E., Borrego-Sánchez, A., Sánchez-Espejo, R., Cerezo, P., Viseras, C., Aguzzi, C. (2019). Clay minerals in drug delivery systems. En: Modified Clay and Zeolite Nanocomposite Materials: Environmental and Pharmaceutical Applications . Mercurio, M., Sarkar, B., Langella, A. (Eds). Serie: Micro and Nano Technologies, Elsevier. Capítulo 6, pp. 129-166.

Ghebaur, A., Garea, S.A., Iovu, H. (2012). New polymer–halloysite hybrid materials-potential controlled drug release system. Int. J. Pharm. 436, 568-573.

Gilani, S.J., Zafar, A., Jafar, M., Shakil, K., Imam, S.S. (2017). Nano-carriers for the treatment of tuberculosis. Recent Pat. Antiinfect. Drug Discov. 12(2), 95-106.

Gilpin, C. y Weyer, K. (2018). Inclusion of TB diagnostics on the WHO Essential Diagnostics List. Int. J. Tuberc.Lung Dis. 22(8), 827-828.

Ginsberg, A.M. y Spigelman, M. (2007). Challenges in tuberculosis drug research and development. Nature Med. 13(3), 290-294.

Glaziou, P., Sismanidis, C., Floyd, K., Raviglione, M. (2015). Global epidemiology of tuberculosis. Cold Spring Harb. Perspect. Med. 5(2), a017798.

Golden, M.P. y Vikram, H.R. (2005). Extrapulmonary tuberculosis: an overview. Am. Fam. Physician 72(9), 1761-1768.

Goldman, A.L. y Braman, S.S. (1972). Isoniazid: a review with emphasis on adverse effects. Chest 62(1), 71-77.

Gonzalez, F., Pesquera, C., Blanco, C., Benito, I., Mendioroz, S., Pajares, J.A. (1990). Structural and textural evolution under thermal treatment of natural and acid-activated Al-rich and Mg-rich palygorskites. Appl. Clay Sci. 5(1), 23-36.

González-Martín, J., García-García, J.M., Anibarro, L., Vidal, R., Esteban, J., Blanquer, R., Ruiz-Manzano, J. (2010). Consensus document on the diagnosis, treatment and prevention of tuberculosis. Arch. Bronconeumol. 46(5), 255-274.

Goyal, A. K., Garg, T., Bhandari, S., Rath, G. (2017). Advancement in pulmonary drug delivery systems for treatment of tuberculosis. En: Nanostructures for Drug Delivery. Andronescu, E. y Grumezescu, A. (Eds.). Elsevier. Capítulo 22, pp. 669-695.

Graessle, O.E. y Pietrowski, J.J. (1949). The *in vitro* effect of para-aminosalicylic acid (PAS) in preventing acquired resistance to streptomycin by Mycobacterium tuberculosis. J. Bacteriol. 57(4), 459-464.

Grim, R.E. (1962). Applied clay mineralogy. Serie: International series in the Earth Sciences. Mc Graw Hill, 422 pp.

Guimarães, L., Enyashin, A.N., Seifert G., Duarte, H.A. (2010). Structural, electronic, and mechanical properties of single-Walled halloysite nanotube models, J. Phys.Chem. C 114, 11358-11363.

Gunasekaran, S., Sailatha, E., Seshadri, S., Kumaresan, S. (2009). FTIR, FT Raman spectra and molecular structural confirmation of isoniazid. Indian J. Pure Appl. Phys. 47, 12-18.

Guo, M., Wang, A., Muhammad, F., Qi, W., Ren, H., Guo, Y., Zhu, G. (2012). Halloysite nanotubes, a multifunctional nanovehicle for anticancer drug delivery. Chin. J. Chem. 30, 2115-2120.

Gupta, S., y Kakkar, V. (2018). Recent technological advancements in tuberculosis diagnostics-a review. Biosens. Bioelectron. 115, 14-29.

Gustafsson, J.P. (2001). The surface chemistry of imogolite. Clays Clay Miner. 49, 73-80.

Gutierrez, A.C., Zamora, D.S., Elorza, A.B., Ortiz, D.P., Hanabergh, C., Pedraza, J.G., Verastegui, M.C. (2017). Comparison Of Tuberculin Skin Test With Interferon Gamma Release Assay (Quantiferon®) For Detection Of Latent Tuberculosis Infection In Cancer Patients. Am. J. Respir. Crit. Care Med. 195, A4003.

Han, H.K., Lee, Y.C., Lee, M.Y., Patil, A.J., Shin, H.J. (2011). Magnesium and calcium organophyllosilicates: synthesis and *in vitro* cytotoxicity study. ACS Appl. Mater. Interfaces 3(7), 2564-2572.

Hemmatpour, H., Haddadi-Asl, V., Roghani-Mamaqani, H. (2015). Synthesis of pH-sensitive poly (N,N-dimethylaminoethyl methacrylate)-grafted halloysite nanotubes for adsorption and controlled release of DPH and DS drugs. Polymer 65, 143-153.

Hinz, C. (2001). Description of sorption data with isotherm equations, Geoderma 99 (3-4), 225-243.

Hu, C.M.J., Fang, R.F.H., Luk, B.T., Zhang, Z. (2014). Polymeric nanotherapeutics: clinicaldevelopment and advances in stealth functionalization strategies. Nanoscale 6, 65-75.

Huang, D., Li, D., Wang, T., Shen, H., Zhao, P., Liu, B., Wang, S. (2015). Isoniazid conjugated poly (lactide-co-glycolide): Long-term controlled drug release and tissue regeneration for bone tuberculosis therapy. Biomaterials 52, 417-425.

Hubatsch, I., Ragnarsson, E.G., Artursson, P. (2007). Determination of drug permeability and prediction of drug absorption in Caco-2 monolayers. Nat. Protoc. 2(9), 2111-2119.

Huebner, R.E., Schein, M.F., Bass, J.B. (1993). The tuberculin skin test. Clin. Infect. Dis., 968-975.

Hughes, A.D. y King, M.R. (2010). Use of naturally occurring halloysite nanotubes for enhanced capture of flowing cells. Langmuir 26, 12155-12164.

Hughes, A.D., Mattison, J., Western, L.T., Powderly, J.D., Greene, B.T., King, M.R. (2012). Microtube device for selectin-mediated capture of viable circulating tumour cells from blood. Clin. Chem. 58, 846-853.

ICH Guideline Q1A(R), 2000.

Imtiaz, S., Shield, K.D., Roerecke, M., Samokhvalov, A.V., Lönnroth, K., Rehm, J. (2017). Alcohol consumption as a risk factor for tuberculosis: meta-analyses and burden of disease. Eur. Respir. J. 50(1), 1700216.

Irvine, D.J. (2011). Drug delivery: one nanoparticle, one kill. Nat. Mater. 10, 342-343.

Ishikawa, K., Akasaka, T., Yawaka, Y., Watari, F. (2010a). High functional expression of osteoblasts on imogolite, aluminosilicate nanotubes. J. Biomed. Nanotechnol. 6, 59-65.

Ishikawa, K., Akasaka, T., Abe, S., Yawaka, Y., Suzuki, M., Watari, F. (2010b). Application of imogolite, almino-silicate nanotube, as scaffold for the mineralization of osteoblasts. Bioceram. Dev. Appl. 1, 1-3.

Jiravanichanun, N., Yamamoto, K., Kato, K., Kim, J., Horiuchi, S., Yah, W.O., Otsuka, H., Takahara, A. (2012). Preparation and characterization of imogolite/DNA hybrid hydrogels. Biomacromolecules 13, 276-281.

Joo, Y., Sim, J.H., Jeon, Y., Lee, S.U., Sohn, D. (2013). Opening and blocking the inner-pores of halloysite. Chem. Commun. 49, 4519-4521.

Joussein, E., Petit, S., Churchman, J., Theng, B., Righi, D., Delvaux, B. (2005). Halloysite clay minerals–a review. Clay Miner. 40(4), 383-426.

Kaewphinit, T., Arunrut, N., Kiatpathomchai, W., Santiwatanakul, S., Jaratsing, P., Chansiri, K. (2013). Detection of Mycobacterium tuberculosis by Using Loop-Mediated Isothermal Amplification Combined with a Lateral Flow Dipstick in Clinical Samples. BioMed. Res. Int. 2013, 1-6.

Kang, D.Y., Zang, J., Wright, E.R., McCanna, A.L., Jones, C.W., Nair, S. (2010). Dehydration, dehydroxylation, and rehydroxylation of single-walled aluminosilicate nanotubes. ACS Nano 4, 4897-4907.

Kang, D.Y., Zang, J., Jones, C.W., Nair, S. (2011). Single-walled aluminosilicate nanotubes with organic-modified interiors. J. Phys. Chem. C 115, 7676-7685.

Kasim, N.A., Whitehouse, M., Ramachandran, C., Bermejo, M., Lennernäs, H., Hussain, A S., Amidon, G.L. (2004). Molecular properties of WHO essential drugs and provisional biopharmaceutical classification. Mol. Pharm. 1(1), 85-96.

Kasper, D.L. (2015). Harrison's principles of internal medicine. Kasper, D.L. y Channing, W.E. (Eds.). New York: McGraw Hill Education, Vol. 1.

Kaufmann, S.H. y Schaible, U.E. (2005). 100th anniversary of Robert Koch's Nobel Prize for the discovery of the tubercle bacillus. Trends Microbiol. 13(10), 469-475.

Kaul, V., Zeyaullah, M., Alalyani, M. (2015). Latest laboratory diagnostic techniques and antibiogram testing of tuberculosis infection. J. Adv. Biotechnol. 5(1), 591-603.

Kaur, I.P. y Singh, H. (2014). Nanostructured drug delivery for better management of tuberculosis. J. Control. Release 184, 36-50.

Kelekçi, S., Karabel, M., Karabel, D., Hamidi, C., Hoşoğlu, S., Gürkan, M. F., Taş, M. A. (2014). Bacillus Calmette–Guérin is a preventive factor in mortality of childhood tuberculous meningitis. Int. J. Infect. Dis. 21, 1-4.

Kelly, H.M., Deasy, P.B., Ziaka, E., Claffey, N. (2004). Formulation and preliminary in vivo dog studies of a novel drug delivery system for the treatment of periodontitis. Int. J. Pharm. 274, 167–183.

Kerry, R.G., Gouda, S., Sil, B., Das, G., Shin, H.S., Ghodake, G., Patra, J.K. (2018). Cure of tuberculosis using nanotechnology: An overview. J. Microbiol. 56(5), 287-299.

Khan, N. y Divangahi, M. (2018). *Mycobacterium tuberculosis* and HIV coinfection brings fire and fury to macrophages. J. Infect. Dis. 217(12), 1851-1853.

Koch, R. (1882). The etiology of tuberculosis. Rev. Infect. Dis. 4(6), 1270-1274.

Kommireddy, D.S., Ichinose, I., Lvov, Y.M., Mills, D.K. (2005). Nanoparticle multilayers: surface modification for cell attachment and growth. J. Biomed. Nanotechnol. 1, 1-5.

Konnova, S.A., Sharipova, I.I., Demina, T.A., Osin, Y.N., Yarullina, D.R., Ilinskaya, O.N., Lvov, Y.M., Fakhrullin, R.F. (2013). Biomimetic cell-mediated three-dimensional assembly of halloysite nanotubes. Chem. Commun. 49, 4208-4210.

Kotobuki, N., Murata, K., Haraguchi, K. (2013). Proliferation and harvest of human mesenchymal stem cells using new thermoresponsive nanocomposite gels. J. Biomed. Mater. Res. 101, 537-546.

Lai, X., Agarwal, M., Lvov, Y.M., Pachpande, C., Varahramyan, K., Witzmann, F.A. (2013). Proteomic profiling of halloysite clay nanotube exposure in intestinal cell co-culture. J. Appl. Toxicol. 33, 1316-1329.

Levis, S.R. y Deasy, P.B. (2003). Use of coated microtubular halloysite for the sustained release of diltiazem hydrochloride and propranolol hydrochloride. Int. J. Pharm. 253, 145-157.

Lin, S.Y.G. y Desmond, E.P. (2014). Molecular diagnosis of tuberculosis and drug resistance. Clin. Lab. Med. 34(2), 297-314.

Liu, W., Chaurand, P., Di Giorgio, C., De Meo, M., Thill, A., Auffan, M., Masion, A., Borschneck, D., Chaspoul, F., Gallice, P., Botta, A., Bottero, J.Y., Rose, J. (2012). Influence of the length of imogolite-like nanotubes on their cytotoxicity and genotoxicity toward human dermal cells. Chem. Res. Toxicol. 25, 2513-2522.

Liu, M., Wu, C., Jiao, Y., Xiong, S., Zhou, C. (2013). Chitosan–halloysite nanotubes nanocomposite scaffolds for tissue engineering. J. Mater. Chem. B1, 2078-2089.

Liu, M., Shen, Y., Ao, P., Dai, L., Liu, Z., Zhou, C. (2014). The improvement of hemostatic and wound healing property of chitosan by halloysite nanotubes. RSC Adv. 4, 23540-23553.

Lönnroth, K., Jaramillo, E., Williams, B.G., Dye, C., Raviglione, M. (2009). Drivers of tuberculosis epidemics: the role of risk factors and social determinants. Soc. Sci. Med. 68(12), 2240-2246.

Lönnroth, K., Mor, Z., Erkens, C., Bruchfeld, J., Nathavitharana, R.R., van der Werf, M.J., Lange, C. (2017). Tuberculosis in migrants in low-incidence countries: Epidemiology and intervention entry points. Int. J. Tuberc. Lung Dis. 21(6), 624-636.

López-Galindo, A., Viseras, C., Cerezo, P. (2007). Compositional, technical and safety specifications of clays to be used as pharmaceutical and cosmetic products. Appl. Clay Sci. 36(1-3), 51-63.

López-Galindo, A., Viseras, C., Aguzzi, C., Cerezo, P. (2011). Pharmaceutical and cosmetic uses of fibrous clays. En: Developments in Palygorskite–Sepiolite Research. Galán, E. y Singer, A. (Eds.). Serie: Developments in Clay Science, Elsevier. Vol. 3, capítulo 13, pp. 290-324.

Lun, H., Ouyang, J., Yang, H. (2014). Natural halloysite nanotubes modified as an aspirin carrier. RSC Adv. 4, 44197-44202.

Lvov, Y. y Abdullayev, E. (2013). Functional polymer clay nanotube composites with sustained release of chemical agents. Prog. Polym. Sci. 38, 1690-1719.

Lvov, Y. y Price, R. (2008). Halloysite nanotubules a noble substrate for the controlled delivery of bioactive molecules. En: Bio-Inorganic Hybrid Nanomaterials. Ruiz-Hitzky, E., Ariga, K., Lvov, Y. (Eds.). Wiley, Berlin, London, pp. 440-478.

Lvov, Y., Shchukin, D.G., Mohwald, H., Price, R.R. (2008). Halloysite clay nanotubes for controlled release of protective agents. ACS Nano 2, 814-820.

Lvov, Y., Aerov, A., Fakhrullin, R. (2014). Clay nanotube encapsulation for functional biocomposites. Adv. Colloid Interf. Sci. 207, 189-198.

Lvov, Y., Wang, W., Zhang, L., Fakhrullin, R. (2016). Halloysite clay nanotubes for loading and sustained release of functional compounds. Adv. Mater. 28(6), 1227-1250.

Ma, P.X. (2008). Biomimetic materials for tissue engineering. Adv. Drug Deliv. Rev. 60, 184-198.

Madigan, M.T., Martinko, J.M., Bender, K.S., BucKley, D.H., Stahl, D.A. (2015). Brock Biología de los microorganismos. Madigan, M.T. (Ed.). Pearson Education, Madrid, Spain. 14ª Edición.

Magalhães, J., Vieira, A. C., Pinto, S., Pinheiro, S., Granja, A., Santos, S., Reis, S. (2018). New Approaches from Nanomedicine and Pulmonary Drug Delivery for the Treatment of Tuberculosis. En: Nanoparticles in Life Sciences and Biomedicine. Rute Neves, A. y Reis, S. (Eds.). Taylor and Francis. Capítulo 8, pp. 197-234.

Malherbe, S.T., Shenai, S., Ronacher, K., Loxton, A.G., Dolganov, G., Kriel, M., Song, T. (2016). Persisting positron emission tomography lesion activity and Mycobacterium tuberculosis mRNA after tuberculosis cure. Nat. Med. 22(10), 1094.

Manning, T.J., Wilkerson, K., Holder, T., Bartley, A.C., Jackson, C., Plummer, S., Wylie, G. (2017). Pharmacokinetic studies of a three-component complex that repurposes the front line antibiotic isoniazid against *Mycobacterium tuberculosis*. Tuberculosis 107, 149-155.

Mantell, C.L. (1951). Ion exchangers. En: Adsorption. McGraw-Hill, New York. pp. 185-216.

Mariappan, T.T. y Singh, S. (2003). Regional gastrointestinal permeability of rifampicin and isoniazid (alone and their combination) in the rat. Int. J.Tuberc. Lung Dis. 7(8), 797-803.

Martín-Ramos, J.D. (2004). X-Powder, a software package for powder X-ray diffractionanalysis, in: Legal Deposit G.R.1001/04, http://www.xpowder.com.

Maryam, S., Bhatti, A.S.A., Shahzad, A.W. (2010). Protective effects of silymarin in isoniazid induced hepatotoxicity in rabbits. Ann. King Edw. Med. Univ. 16(1), 417-443.

Massaro, M., Riela, S., Lo Meo, P., Noto, R., Cavallaro, G., Milioto, S., Lazzara, G. (2014). Functionalized halloysite multivalent glycocluster as a new drug delivery system. J. Mater. Chem. B 2, 7732-7738.

Massaro, M., Colletti, C.G., Noto, R., Riela, S., Poma, P., Guernelli, S., Parisi, F., Milioto, S., Lazzara, G. (2015a). Pharmaceutical properties of supramolecular assembly of co-loaded cardanol/triazole-halloysite systems. Int. J. Pharm. 478, 476-485.

Massaro, M., Piana, S., Colletti, C.G., Noto, R., Riela, S., Baiamonte, C., Giordano, C., Pizzolanti, G., Cavallaro, G., Milioto, S., Lazzara, G. (2015b). Multicavity halloysite–amphiphilic cyclodextrin hybrids for co-delivery of natural drugs into thyroid cancer cells. J. Mater. Chem. B 3, 4074-4081.

Massaro, M., Cavallaro, G., Colletti, C.G., Lazzara, G., Milioto, S., Noto, R., Riela, S. (2018). Chemical modification of halloysite nanotubes for controlled loading and release. J. Mater. Chem. B 6(21), 3415-3433.

Mendelovici, E. (1973). Infrared study of attapulgite and HCl treated attapulgite. Clays Clay Miner. 21(2), 115-119.

Mendelovici, E. y Portillo, D.C. (1976). Organic derivatives of attapulgite; I, Infrared spectroscopy and X-ray diffraction studies. Clays Clay Miner. 24(4), 177-182.

Metushi, I.G., Cai, P., Zhu, X., Nakagawa, T., Uetrecht, J.P. (2011). A fresh look at the mechanism of isoniazid induced hepatotoxicity. Clin. Pharmacol. Ther. 89(6), 911-914.

Miller, K.P., Wang, L., Benicewicz, B.C., Decho, A.W. (2015). Inorganic nanoparticles engineered to attack bacteria. Chem. Soc. Rev. 44, 7787-7807.

Mitchell, M.J., Chen, C.S., Ponmudi, V., Hughes, A.D., King, M.R. (2012a). E-selectin liposomal and nanotube-targeted delivery of doxorubicin to circulating tumour cells. J. Control. Release 160, 609-617.

Mitchell, M.J., Castellanos, C.A., King, M.R. (2012b). Nanostructured surfaces to target and kill circulating tumour cells while repelling leukocytes. J. Nanomater. 831263.

Mitchell, M.J., Castellanos, C.A., King, M.R. (2015). Surfactant functionalization induces robust, differential adhesion of tumour cells and blood cells to charged nanotube-coated biomaterials under flow. Biomaterials 56, 179-186.

Miyahara, Y., Nagaya, N., Kataoka, M., Yanagawa, B., Tanaka, K., Hao, H., Ishino, K., Ishida, H., Shimizu, T., Kangawa, K., Sano, S., Okano, T., Kitamura, S., Mori, H.

(2006). Monolayered mesenchymal stem cells repair scarred myocardium after myocardial infarction. Nat. Med. 12, 459-465.

Monedero, I. y Caminero, J.A. (2011). Evidence for promoting fixed-dose combination drugs in tuberculosis treatment and control: a review. Int. J. Tuberc. Lung Dis. 15(4), 433-439.

Montenegro, S., Delgado, C., Pineda, S., Reyes, C., de la Barra, T., Cabezas, C., Mucientes, F. (2015). Diagnóstico diferencial de tuberculosis en base a PCR en lesiones granulomatosas clasificadas histopatológicamente. Rev. Esp. Patol. 48(3), 145-153.

Moretton, M.A., Hocht, C., Taira, C., Sosnik, A. (2014). Rifampicin-loaded 'flower-like'polymeric micelles for enhanced oral bioavailability in an extemporaneous liquid fixed-dose combination with isoniazid. Nanomedicine 9(11), 1635-1650.

Muñoz-Torrico, M., Caminero-Luna, J., Migliori, G.B., D'Ambrosio, L., Carrillo-Alduenda, J.L., Villareal-Velarde, H., Centis, R. (2017). La diabetes se asocia con reacciones adversas graves en la tuberculosis multirresistente. Arch. Bronconeumol. 53(5), 245-250.

Mura, P., Maestrelli, F., Aguzzi, C., Viseras, C. (2016). Hybrid systems based on "drug–in cyclodextrin–in nanoclays" for improving oxaprozin dissolution properties. Int. J. Pharm. 509(1), 8-15.

Murray, H.H. (2006). Structure and composition of the clay minerals and their physical and chemical properties. En: Applied Clay Mineralogy: Occurrences, Processing and Application of Kaolins, Bentonites, Palygorskite-Sepiolite and Common Clays. Murray, H. H. (Eds.). Serie: Developments in Clay Science, Elsevier. Volumen 2, capítulo 2, pp. 7-31.

Nakano, A., Teramoto, N., Chen, G., Miura, Y., Shibata, M. (2010). Preparation and characterization of complex gel of Type I collagen and aluminosilicate containing imogolite nanofibers. J. Appl. Polym. Sci. 118, 2284-2290.

Narasimhan, P., Wood, J., MacIntyre, C.R., Mathai, D. (2013). Risk factors for tuberculosis. Pulm. Med. 2013, 828-839.

Nasiruddin, M., Neyaz, M., Das, S. (2017). Nanotechnology-Based approach in tuberculosis treatment. Tuberc. Res. Treat. 2017, 1-13.

www.nih.gov. National Institute of Health

Nitya, G., Nair, G. T., Mony, U., Chennazhi, K.P., Nair, S.V. (2012). "*In vitro*" evaluation of electrospun PCL/nanoclay composite scaffold for bone tissue engineering. J. Mater. Sci. Mater. Med. 23, 1749-1761.

Ogorodova, L., Vigasina, M., Melchakova, L., Krupskaya, V., Kiseleva, I. (2015). Thermochemical study of natural magnesium aluminum phyllosilicate: palygorskite. J. Chem. Thermodynamics 89, 205-211.

Pai, M., Denkinger, C.M., Kik, S.V., Rangaka, M.X., Zwerling, A., Oxlade, O., Banaei, N. (2014). Gamma interferon release assays for detection of *Mycobacterium tuberculosis* infection. Clin. Microbiol. Rev. 27(1), 3-20.

Pai, M., Behr, M. A., Dowdy, D., Dheda, K., Divangahi, M., Boehme, C. C., Ginsberg, A., Swaminathan, S., Spigelman, M., Getahun, H., Menzies, D., Raviglione, M. (2016). Tuberculosis. Nat. Rev. Dis. Primers 2, 16076, 1-23.

Pande, T., Cohen, C., Pai, M., Ahmad Khan, F. (2016). Computer-aided detection of pulmonary tuberculosis on digital chest radiographs: a systematic review. Int. J. Tuberc. Lung Dis. 20(9), 1226-1230.

Pandey, R., Zahoor, A., Sharma, S., Khuller, J.K. (2003). Nanoparticle encapsulated antitubercular drugs as a potential oral drug delivery system against murine tuberculosis. Tuberculosis 83, 373-378.

Pareek, M., Greenaway, C., Noori, T., Munoz, J., Zenner, D. (2016). The impact of migration on tuberculosis epidemiology and control in high-income countries: a review. BMC Med. 14(1), 48.

Patterson, J., Martino, M.M., Hubbell, J.A. (2010). Electrospun poly(lactic-co-glycolic acid)/ halloysite nanotube composite nanofibers for drug encapsulation and sustained release biomimetic materials in tissue engineering. Mater. Today 13, 15-22.

Pham, D.D., Fattal, E., Tsapis, N. (2015). Pulmonary drug delivery systems for tuberculosis treatment. Int. J. Pharm. 478(2), 517-529.

http://phantomplastics.com/functional-fillers/halloysite/

Ph. Eur. European Pharmacopoeia 9th Edition. (2016) European Directorate for the Quality of Medicines and HealthCare (EDQM Council of Europe).

Podell, B.K., Ackart, D.F., Obregon-Henao, A., Eck, S.P., Henao-Tamayo, M., Richardson, M., Basaraba, R.J. (2014). Increased severity of tuberculosis in Guinea pigs with type 2 diabetes: a model of diabetes-tuberculosis comorbidity. Am. J. Pathol. 184(4), 1104-1118.

Price, R.R., Gaber, B.P., Lvov, Y. (2001). *In-vitro* release characteristics of tetracycline HCl, khellin and nicotinamide adenine dineculeotide from halloysite; a cylindrical mineral. J. Microencapsul. 18, 713-722.

Qi, R., Guo, R., Shen, M., Cao, X., Zhang, L., Xu, J., Yu, J., Shi, X. (2010). Electrospun poly(lactic-co-glycolic acid)/halloysite nanotube composite nanofibers for drug encapsulation and sustained release. J. Mater. Chem. 20, 10622-10629.

Qi, R., Cao, X., Shen, M., Guo, R., Yu, J., Shi, X. (2012). Biocompatibility of electrospun halloysite nanotube-doped poly(lactic-co-glycolic acid) composite nanofibers. J. Biomater. Sci. Polym. Ed. 23, 299-313.

Qi, R., Guo, R., Zheng, F., Liu, H., Yu, J., Shi, X. (2013). Controlled release and antibacterial activity of antibiotic-loaded electrospun halloysite/poly(lactic-co-glycolic acid) composite nanofibers. Colloids Surf. B Biointerfaces 110, 148-155.

Rageade, F., Picot, N., Blanc-Michaud, A., Chatellier, S., Mirande, C., Fortin, E., van Belkum, A. (2014). Performance of solid and liquid culture media for the detection of *Mycobacterium tuberculosis* in clinical materials: meta-analysis of recent studies. Eur. J. Clin. Microbiol. Infect. Dis. 33(6), 867-870.

Rajalakshmi, G., Hathwar, V.R., Kumaradhas, P. (2014) Topological analysis of electrondensity and the electrostatic properties of isoniazid: an experimental and theoretical study. Acta Crystallogr. 70, 331-341.

Ramirez, E., Laosa, O., Guerra, P., Duque, B., Mosquera, B., Borobia, A.M., Lei, S.H., Carcas, A.J., Frias, J. (2010). Acceptability and characteristics of 124 human bioequivalence studies with active substances classified according to the Biopharmaceutic Classification System. Br. J. Clin. Pharmacol. 70, 694-702.

Rao, K.M., Nagappan, S., Seo, D.J., Ha, C.S. (2014). pH sensitive halloysite-sodium hyaluronate/poly(hydroxyethyl methacrylate) nanocomposites for colon cancer drug delivery. Appl. Clay Sci. 97, 33-42.

Rang, H., Ritter, J., Flower, R., Henderson, G. (2016). Farmacología: Rang y Dale. 8ª Edición. Elsevier, Barcelona, Spain. 776 pp.

Rawat, K., Agarwal, S., Tyagi, A., Verma, A.K., Bohidar, H.B. (2014). Aspect ratio dependent cytotoxicity and antimicrobial properties of nanoclay. Appl. Biochem. Biotechnol. 174, 936-944.

Rawtani, D., Agrawal, Y.K., Prajapati, P. (2013). Interaction behavior of DNA with halloysite nanotube-silver nanoparticle-based composite. BioNanoScience 3, 73-78.

Reilly, G.C. y Engler, A.J. (2010). Intrinsic extracellular matrix properties regulate stem cell differentiation. J. Biomech. 43, 55-62.

Riela, S., Massaro, M., Colletti, C.G., Bommarito, A., Giordano, C., Milioto, S., Noto, R., Poma, P., Lazzara, G. (2014). Development and characterization of co-loaded curcumin/ triazole-halloysite systems and evaluation of their potential anticancer activity. Int. J. Pharm. 475, 613-623.

Romanowski, K., Clark, E.G., Levin, A., Cook, V.J., Johnston, J.C. (2016). Tuberculosis and chronic kidney disease: an emerging global syndemic. Kidney Int. 90(1), 34-40.

Romero, A., Ares, I., Ramos, E., Castellano, V., Martínez, M., Martínez-Larrañaga, M. R., Martínez, M.A. (2016). Mycotoxins modify the barrier function of Caco-2 cells through differential gene expression of specific claudin isoforms: Protective effect of illite mineral clay. Toxicology 353, 21-33.

Rooj, S., Das, A., Thakur, V., Mahaling, R.N., Bhowmick, A.K., Heinrich, G. (2010) Preparation and properties of natural nanocomposites based on natural rubber and naturally occurring halloysite nanotubes. Mater. Des. 31(4), 2151-2156.

Rotoli, B.M., Guidi, P., Bonelli, B., Bernardeschi, M., Bianchi, M.G., Esposito, S., Frenzilli, G., Lucchesi, P., Nigro, M., Scarcelli, V., Tomatis, M., Zanello, P.P., Fubini, B., Bussolati, O., Bergamaschi, E. (2014). Imogolite: an aluminosilicate nanotube endowed with low cytotoxicity and genotoxicity. Chem. Res. Toxicol. 27, 1142-1154.

Russell, D.G. (2007). Who puts the tubercle in tuberculosis? Nat. Rev. Microbiol. 5(1), 39-47.

Saikia, C., Hussain, A., Ramteke, A., Sharma, H.K., Maji, T.K. (2014). Crosslinked thiolated starch coated Fe_3O_4 magnetic nanoparticles: effect of montmorillonite and crosslinking density on drug delivery properties. Starch-Stärke 66(7-8), 760-771.

Saikia, C., Hussain, A., Ramteke, A., Sharma, H.K., Maji, T.K. (2015). Carboxymethyl starch-chitosan-coated iron oxide magnetic nanoparticles for controlled delivery of isoniazid. J. Microencapsul. 32(1), 29-39.

Salcedo, I., Aguzzi, C., Sandri, G., Bonferoni, M.C., Mori, M., Cerezo, P., Sánchez, R., Viseras, C., Caramella, C. (2012). "*In vitro*" biocompatibility and mucoadhesion of montmorillonite chitosan nanocomposite: a new drug delivery. Appl. Clay Sci. 55, 131-137.

Salcedo, I., Sandri, G., Aguzzi, C., Bonferoni, C., Cerezo, P., Sánchez, R., Viseras, C. (2014). Intestinal permeability of oxytetracycline from chitosan-montmorillonite nanocomposites. Colloids Surf. B Biointerfaces 117, 441-448.

Sánchez-Montalvá, A., Salvador, F., Molina-Morant, D., Molina, I. (2017). Tuberculosis e inmigración. Enferm. Infecc. Microbiol. Clin. 36(7), 446-455.

Sandri, G., Bonferoni, M.C., Ferrari, F., Rossi, S., Aguzzi, C., Mori, M., Grisoli, P., Cerezo, P., Tenci, M., Viseras, C., Caramella, C. (2014). Montmorillonite-chitosan-silver sulfadiazine nanocomposites for topical treatment of chronic skin lesions: In vitro biocompatibility, antibacterial efficacy and gap closure cell motility properties. Carbohyd. Polym. 102(1), 970-977.

Sandri, S., Bonferoni, M.C., Rossi, S., Ferrari, F., Aguzzi, C., Viseras, C., Caramella, C. (2016). Clay minerals for tissue regeneration, repair, and engineering, En: Wound Healing Biomaterials. Ågren, M.S. (Eds.). Serie: Functional Biomaterials, Elsevier. Vol. 2, capítulo 19, pp. 385-402.

Sandri, G., Aguzzi, C., Rossi, S., Bonferoni, M.C., Bruni, G., Boselli, C., Ferrari, F. (2017). Halloysite and chitosan oligosaccharide nanocomposite for wound healing. Acta Biomater. 57, 216-224.

Saranjit, S., Mariappan, T.T., Sankar, R., Sarda, N., Baljinder, S. (2001). A critical review of the probable reasons for the poor/variable bioavailability of rifampicin from anti-tubercular fixed-dose combination (FDC) products, and the likely solutions to the problem. Int J. Pharm. 228, 5-17.

Saraogi, G.K., Sharma, B., Joshi, B., Gupta, P., Gupta, U.D., Jain, N.K., Agrawal, G.P. (2011). Mannosylated gelatin nanoparticles bearing isoniazid for effective management of tuberculosis. J. Drug Target. 19(3), 219-227.

Sarmah, M., Banik, N., Hussain, A., Ramteke, A., Sharma, H.K., Maji, T.K. (2015). Study on crosslinked gelatin–montmorillonite nanoparticles for controlled drug delivery applications. J. Mater. Sci. 50(22), 7303-7313.

Schnappinger, D. y Ehrt, S. (2016). A broader spectrum of tuberculosis. Nat. Med. 22, 1076-1077.

Scott, S., Hanna, D., Zebian, B., Ruiz, G., Das, S. (2018). The Silent Tuberculosis: A case study to highlight awareness of a global health disease and difficulties in diagnosis. World Academy of Science, Engineering and Technology, Int. J. Med. Health Sci. 5(1).

Serratosa, J.M. (1979). Surface properties of fibrous clay minerals (palygorskite and sepiolite). Dev. Sedimentol. 27, 99-109.

Sharma, R., Kaur, A., Sharma, A., Dilbaghi, N. (2017). Nano-based anti-tubercular drug delivery and therapeutic interventions in tuberculosis. Curr. Drug Targets 18(1), 72-86.

Sharma S.K. y Mohan, A. (2004). Extrapulmonary tuberculosis. Indian J. Med. Res. 120, 316-353.

Shi, Y.F., Tian, Z., Zhang, Y., Shen, H.B., Jia, N.Q. (2011). Functionalized halloysite nanotube-based carrier for intracellular delivery of antisense oligonucleotides. Nanoscale Res. Lett. 6(1), 608.

Shikinaka, K., Koizumi, Y., Osada, Y., Shigehara, K. (2011). Reinforcement of hydrogel by addition of fiber-like nanofiller. Polym. Adv. Technol. 22, 1212-1215.

Shutava, T.G., Fakhrullin, R.F., Lvov, Y.M. (2014). Spherical and tubule nanocarriers for sustained drug release. Curr. Opin. Pharmacol. 18, 141-148.

Silva, D.R., Muñoz-Torrico, M., Duarte, R., Galvão, T., Bonini, E.H., Arbex, F.F., Mello, F.C.D.Q. (2018). Risk factors for tuberculosis: diabetes, smoking, alcohol use, and the use of other drugs. J. Bras. Pneumol. 44(2), 145-152.

Singh, B. y Mackinnon, I.D.R. (1996). Experimental transformation of kaolinite to halloysite. Clays Clay Miner. 44(6), 825-834.

Singh, S., Mariappan, T.T., Shankar, R., Sarda, N., Singh, B. (2001). A critical review of the probable reasons for the poor variable bioavailability of rifampicin from anti-tubercular fixed-dose combination (FDC) products, and the likely solutions to the problem. Int. J. Pharm. 228(1-2), 5-17.

Slama, K., Chiang, C.Y., Enarson, D.A., Hassmiller, K., Fanning, A., Gupta, P., Ray, C. (2007). Tobacco and tuberculosis: a qualitative systematic review and meta-analysis. Int. J. Tuberc. Lung Dis. 11(10), 1049-1061.

Smith, M.I. y McClosky, W.T. (1945). The chemotherapeutic action of streptomycin and promin in experimental tuberculosis. Pub. Health Rep. 60, 1129-1138.

Song, F., Li, X., Wang, Q., Liao, L., Zhang, C. (2014). Nanocomposite hydrogels and their applications in drug delivery and tissue engineering. J. Biomed. Nanotechnol. 10, 1-13.

Stop TB Partnership, 2016. Plan Mundial para Detener la Tuberculosis: El Cambio de Paradigma 2016-2020.

Subashini, R., Murugan, A., Nidhina, R.C.M. (2017). Effect of ascorbic acid on dissolution stability of rifampicin in market fixed dose combination products for Tuberculosis. PharmaTutor, 5(1), 48-53.

Sun, X., Zhang, Y., Shen, H.G., Jia, N. (2010). Direct electrochemistry and electrocatalysisof horseradish peroxidase based on halloysite nanotubes/chitosannanocomposite film. Electrochim. Acta 56(2), 700-705.

Szczepanik, B., Słomkiewicza, P., Garnuszeka, M., Czecha, K., Bana´sc, D., Kubala-Kuku´sc, A., Stabrawac, I. (2015) The effect of chemical modification on the physico-chemical characteristics of halloysite: FTIR, XRF, and XRD studies. J.Mol. Struct. 1084, 16-22.

Tan, D., Yuan, P., Bergaya, F., Yu, H., Liu, D., Liu, H., He, H. (2013). Natural halloysite nanotubes as mesoporous carriers for the loading of ibuprofen. Micropor. Mesopor. Mater. 179, 89-98.

Tan, D., Yuan, P., Bergaya, F., Liu, D., Wang, L., Liu, H., He, H. (2014). Loading and in vitro release of ibuprofen in tubular halloysite. Appl. Clay Sci. 96, 50-55.

https://www.tballiance.org. Alianza contra la Tuberculosis ("TB Alliance").

Tenci, M., Rossi, S., Aguzzi, C., Carazo, E., Sandri, G., Bonferoni, M.C., Ferrari, F., Grisoli, P., Viseras, C., Caramella, C.M., Ferrari, F. (2017). Carvacrol/clay hybrids loaded into in situ gelling films. Int. J. Pharm. 531(2), 676-688.

Teramoto, N., Hayashi, A., Yamanaka, K., Sakiyama, A., Nakano, A., Shibata, M. (2012). Preparation and mechanical properties of photo-crosslinked fish gelatin/imogolite nanofiber composite hydrogel. Materials 5, 2573-2585.

Tierney, T., Bodnár, K., Rasmuson, Å., Hudson, S. (2017). Carrier particle design for stabilization and isolation of drug nanoparticles. Int. J. Pharm. 518(1), 111-118.

Tostmann, A., Boeree, M.J., Peters, W.H., Roelofs, H.M., Aarnoutse, R.E., van der Ven, A.J., Dekhuijzen, P.R. (2008). Isoniazid and its toxic metabolite hydrazine induce in vitro pyrazinamide toxicity. Int. J. Antimicrob. Agents 31(6), 577-580.

Traverso, G. y Langer, R. (2015). Special delivery for the gut. Nature, 519.

Trunz, B.B., Fine, P.E.M., Dye, C. (2006). Effect of BCG vaccination on childhood tuberculous meningitis and miliary tuberculosis worldwide: a meta-analysis and assessment of cost-effectiveness. Lancet 367(9517), 1173-1180.

Ulrichs, T., y Kaufmann, S.H. (2006). New insights into the function of granulomas in human tuberculosis. J. Pathol. 208(2), 261-269.

USP 41–NF 36. (2018). The United States Pharmacopoeia and National Formulary, The United States Pharmacopoeial Convention, Inc.: Rockville, MD, 2018.

Valenzuela-Calahorro, C., Navarrete-Guijosa, A., Stitou, M., Cuerda-Correa, E.M. (2004). Retention of progesterone by an activated carbon: study of the adsorption kinetics. Adsorption 10(1), 19-28.

Veerabadran, N.G., Price, R.R., Lvov, Y.M. (2007). Clay nanotubes for encapsulation and sustained release of drugs. Nano 2, 115-120.

Veerabadran, N.G., Mongayt, D., Torchilin, V., Price, R.R., Lvov, Y.M. (2009). Organized shells on clay nanotubes for controlled release of macromolecules. Macromol. Rapid Commun. 30, 99-103.

Velnar, T., Bailey, T., Smrkolj, V. (2009). The wound healing process: an overview of the cellular and molecular mechanisms. J. Int. Med. Res. 37, 1528-1542.

Verbeeck, R.K., Günther, G., Kibuule, D., Hunter, C., Rennie, T.W. (2016). Optimizing treatment outcome of first-line anti-tuberculosis drugs: the role of therapeutic drug monitoring. Eur. J. Clin. Pharmacol. 72(8), 905-916.

Vergaro, V., Abdullayev, E., Lvov, Y.M., Zeitoun, A., Cingolani, R., Rinaldi, R., Leporatti, S. (2010). Cytocompatibility and uptake of halloysite clay nanotubes. Biomacromolecules 11, 820-826.

Vergaro, V., Lvov, Y.M., Leporatti, S. (2012). Halloysite clay nanotubes for resveratroldelivery to cancer cells. Macromol. Biosci. 12, 1265-1271.

Verma, N.K., Moore, E., Blau, W., Volkov, Y., Babu, P.R. (2012). Cytotoxicity evaluation of nanoclays in human epithelial cell line A549 using high content screening and real-time impedance analysis. J. Nanopart. Res. 14, 1137-1147.

Verma, A. y Riaz, U. (2018). Mechanochemically synthesized poly (o-toluidine)-intercalated montmorillonite nanocomposites as antituberculosis drug carriers. Int. J. Polym. Mater. Polym. Biomater. 67(4), 221-228.

Vicosa, A.L., Gomes, A.C.O., Soares, B.G., Paranhos, C.M. (2009). Effect of sepiolite on the physical properties and swelling behavior of rifampicin-loaded nanocomposite hydrogels. Express Polym. Lett. 3, 518-524.

Viseras, C. y López-Galindo, A. (1999). Pharmaceutical applications of some Spanish clays (sepiolite, palygorskite, bentonite): some preformulation studies. Appl. Clay Sci. 14(1), 69-82.

Viseras, C. y López-Galindo, A. (2000). Characteristics of pharmaceutical grade phyllosilicate powders. Pharm. Dev. Technol. 5(1), 47-52.

Viseras, C., Yebra, A., López-Galindo, A. (2000). Characteristics of pharmaceutical grade phyllosilicate compacts. Pharm. Dev. Technol. 5(1), 53-58.

Viseras, C., Ferrari, F., Yebra, A., Rossi, S., Caramella, C., López-Galindo, A. (2001). Disintegrant efficiency of special phyllosilicates: Smectite, palygorskite, sepiolite. S.T.P. Pharma Sci. 11(2), 137-143.

Viseras, C., Aguzzi, C., Cerezo, P., López-Galindo, A. (2007). Uses of clay minerals in semisolid health care and therapeutic products. Appl. Clay Sci. 36(1-3), 37-50.

Viseras, C., Aguzzi, C., Cerezo, P., Bedmar, M.C. (2008a). Biopolymer clay nanocomposites for controlled drug delivery. Mater. Technol. 24(9), 1020-1026.

Viseras, M.T., Aguzzi, C., Cerezo, P., Viseras, C., Valenzuela-Calahorro, C. (2008b). Equilibrium and kinetics of 5-aminosalicylic acid adsorption by halloysite, Micropor. Mesopor. Mat. 108(1–3), 112-116.

Viseras, M.T., Aguzzi, C., Cerezo, P., Cultrone, G., Viseras, C. (2009) Supramolecular structure of 5-aminosalycilic acid/halloysite composites. J. Microencapsul. 26(3), 279-286.

Viseras, C., Cerezo, P., Sanchez, R., Salcedo, I., Aguzzi, C. (2010). Current challenges in clay minerals for drug delivery. Appl. Clay Sci. 48(3), 291-295.

Viseras, C., Aguzzi, C., Cerezo, P. (2015). Medical and health applications of natural mineral nanotubes. En: Natural Mineral Nanotubes: Properties and Applications. Pasbakhsh, P. y Churchman, G.J. (Eds.). Apple Academic Press, Oakville, Canada; Waretown NJ, pp. 437-448.

Wagner, V., Dullaart, A., Bock, A.K., Zweck, A. (2006). The emerging nanomedicine landscape. Nat. Biotechnol. 24, 1211-1217.

Waksman, S. A. y Henrici, A.T. (1943). The nomenclature and classification of the actinomycetes. J. Bacteriol. 46(4), 337.

Wang, S., Zhao, Y., Shen, M., Shi, X. (2012). Electrospun hybrid nanofibers doped with nanoparticles or nanotubes for biomedical applications. Ther. Deliv. 3, 1155-1169.

Ward, C.J., Song, S., Davis, E.W. (2010). Controlled release of tetracycline–HCl from halloysite– polymer composite films. J. Nanosci. Nanotechnol. 10, 6641-6649.

Wei, W., Abdullayev, E., Hollister, A., Mills, D., Lvov, Y.M., (2012). Clay nanotube/poly(methyl methacrylate) bone cement composites with sustained antibiotic release. Macromol. Mater. Eng. 297, 645-653.

Wei, W., Minullina, R., Abdullayev, E., Fakhrullin, R., Mills, D., Lvov, Y. (2014). Enhanced efficiency of antiseptics with sustained release from clay nanotubes. RSC Adv. 4, 488-494.

Wilkinson, R.J., Llewelyn, M., Toossi, Z., Patel, P., Pasvol, G., Lalvani, A., Wright, D., Latif, M., Davidson, R.N. (2000). Influence of vitamin D deficiency and vitamin D

receptor polymorphisms on tuberculosis among Gujarati Asians in west London: a case-control study. Lancet 355(9204), 618-621.

World Health Organization. (2013). Roadmap for childhood tuberculosis: towards zero deaths. Geneva: World Health Organization; 2013 (http:// apps.who.int/iris/handle/10665/89506, accessed 4 October 2018).

World Health Organization. (2015). Global Tuberculosis Report 2015.

World Health Organization. (2016a). WHO treatment guidelines for drug-resistant tuberculosis 2016 update.

World Health Organization. (2016b). Global Tuberculosis Report 2016.

World Health Organization. (2017). The selection and use of essential medicines: report of the WHO Expert Committee, 2017 (including the 20th WHO Model List of Essential Medicines and the 6th Model List of Essential Medicines for Children). World Health Organization.

World Health Organization. (2018a). Global Tuberculosis Report 2018. Geneva: World Health Organization; 2018. Licence: CC BY-NC-SA 3.0 IGO.

World Health Organization. (2018b). Public–private mix for TB prevention and care: a roadmap. Geneva: World Health Organization; 2018. Licence: CC BY-NC-SA 3.0 IGO.

World Health Organization. (2018c). Roadmap towards ending TB in children and adolescents, second edition. Geneva: World Health Organization; 2018. Licence: CC BY-NC-SA 3.0 IGO.

World Health Organization. (2018d). Best practices in child and adolescent tuberculosis. Geneva: World Health Organization; 2018. Licence: CC BY-NC-SA 3.0 IGO.

World Health Organization. (2018e). European Centre for Disease Prevention and Control/WHO Regional Office for Europe. Tuberculosis surveillance and monitoring in Europe 2018-2016 data.

World Health Organization (2018f). Factsheet. Fixed-dose combinations for the treatment of TB in children.

World Health Organization. (2018g). Rapid communication: key changes to treatment of multidrug- and rifampicin-resistant tuberculosis (MDR/RR-TB).

World Health Organization. (2018h). WHO position statement on the use of delamanid for MDR-TB. Licence: CC BY-NC-SA 3.0 IGO.

World Health Organization. (2018i). Latent tuberculosis infection: updated and consolidated guidelines for programmatic management. Geneva: World Health Organization; 2018. Licence: CC BY-NC-SA 3.0 IGO.

World Health Organization. (2018j). World Health Organization, Position paper: BCG vaccine 2018.

Wu, Y., Yang, J., Gao, H., Shen, Y., Jiang, L., Zhou, C., Liu, M. (2018). Folate conjugated halloysite nanotubes, an efficient drug carrier, deliver doxorubicin for targeted therapy of breast cancer. ACS Appl. Nano Mater. 1(2), 595-608.

Xavier, K.C., Santos, M.S., Osajima, J.A., Luz, A.B., Fonseca, M.G., Silva Filho, E.C. (2016). Thermally activated palygorskites as agents to clarify soybean oil. Appl. Clay Sci. 119, 338-347.

Yah, W.O., Yamamoto, K., Jiravanichanun, N., Otsuka, H., Takahara, A. (2010). Imogolite reinforced nanocomposites: multifaceted green materials. Materials 3, 1709-1745.

Yah, W.O., Takahara, A., Lvov, Y.M. (2012). Selective modification of halloysite lumen with octadecylphosphonic acid: new inorganic tubular micelle. J. Am. Chem. Soc. 134, 1853-1859.

Yamamoto, K., Otsuka, H., Wada, S.I., Sohn, D., Takahara, A. (2005a). Preparation and properties of [poly(methylmethacrylate)/imogolite] hybrid via surface modification using phosphoric acid ester. Polymer. 46, 12386-12392.

Yamamoto, K., Otsuka, H., Wada, S.I., Sohn, D., Takahara, A. (2005b). Transparent polymer nanohybrid prepared by in situ synthesis of aluminosilicate nanofibers in poly(vinilalcohol) solution. Soft Matter 1, 372-377.

Yendluri, R., Otto, D.P., De Villiers, M.M., Vinokurov, V., Lvov, Y.M. (2017). Application of halloysite clay nanotubes as a pharmaceutical excipient. Int. J. Pharm. 521, 267–273.

Younossian, A.B. Rochat, T. Ketterer, J.P. Wacker, J. Janssens, J.P. (2005). High hepatotoxicity of pyrazinamide and ethambutol for treatment of latent tuberculosis. Eur. Respir. J. 26(3), 462-464.

Yuan, P., Tan, D.Y., Bergaya, F., Yan, W.C., Fan, M.D., Liu, D., He, H.P. (2012a). Changes in structure, morphology, porosity, and surface activity of mesoporous halloysite nanotubes under heating. Clays Clay Miner. 60, 561-573.

Yuan, P., Southon, P.D., Liu, Z.W., Kepert, C.J. (2012b). Organosilane functionalization of halloysite nanotubes for enhanced loading and controlled release. Nanotechnology 23(37), 375705 (5pp).

Yuan, P., Tan, D., Bergaya, F. (2015). Properties and applications of halloysite nanotubes: recent research advances and future prospects. Appl. Clay Sci. 112, 75-93.

Zargarian, S., Haddadi-Asl, V., Hematpour, H. (2015). Carboxylic acid functionalization of halloysite nanotubes for sustained release of diphenhydramine hydrochloride. J. Nanopart. Res. 17, 218-231.

Zellweger, J.P., Cattamanchi, A., Sotgiu, G. (2015). Tobacco and tuberculosis: could we improve tuberculosis outcomes by helping patients to stop smoking? Eur. Respir. J. 45, 583-585.

Zeng, H.F., Lin, L.J., Xi, Y.M., Han, Z.Y. (2017). Effects of raw and heated palygorskite on rumen fermentation in vitro. Appl. Clay Sci. 138, 125-130.

Zhan, X. y Guan, Y.Q. (2015). Design of magnetic nanoparticles for hepatocellularcarcinoma treatment using the control mechanisms of the cell internalnucleus and external membrane, J. Mater. Chem. B 3, 4191-4204.

Zhang, J., Ligu, M., Yuanzhi, W., Peizhi, L., Haiyan, L., Yi, H., Bing, L., Li, Y. (2012). Genotypes and drug susceptibility of Mycobacterium tuberculosis Isolates in Shihezi, Xinjiang Province, China. BMC Res. Notes 5(309), 1-7.

Zhang, Y., Chen, Y., Zhang, H., Zhang, B., Liu, J. (2013). Potent antibacterial activity of a novel silver nanoparticle-halloysite nanotube nanocomposite powder. J. Inorg. Biochem. 118, 59-64.

Zhao, Y., Wang, S., Guo, Q., Shen, M., Shi, X.J. (2013). Hemocompatibility of electrospun halloysite nanotube- and carbon nanotube-doped composite poly(lactic-co-glycolic acid) nanofibers. J. Appl. Polym. Sci. 127, 4825-4832.

Zhou, W.Y., Guo, B., Liu, M., Liao, R., Rabie, A.B.M., Jia, D.J. (2010). Poly(vinyl alcohol)/halloysite nanotubes bionanocomposite films: properties and *in vitro* osteoblasts and fibroblasts response. J. Biomed. Mater. Res. A 93, 1574-1587.

ANEXO I

Publicaciones incluidas en la Tesis Doctoral

Chapter 26

Health and Medical Applications of Tubular Clay Minerals

C. Aguzzi[a], G. Sandri[b], P. Cerezo[a], E. Carazo[a] and C. Viseras[a,*]
[a]*University of Granada, Granada, Spain*
[b]*University of Pavia, Pavia, Italy*
[*]*Corresponding author: e-mail: cviseras@ugr.es*

26.1 INTRODUCTION

This chapter aims to review the possible applications of halloysite and imogolite, two nanosized clay minerals with a hollow tubular structure, in nanopharmaceutics (ie, the use of nanotechnology in pharmaceutics). Pharmaceutics is concerned with the scientific and technological aspects of the design and manufacture of medicinal products and medical devices (Aulton and Taylor, 2013). Medicinal products are defined as "(i) Any substance or combination of substances presented as having properties for treating or preventing disease in human beings; or (ii) Any substance or combination of substances which may be used in or administered to human beings either with a view to restoring, correcting or modifying physiological functions by exerting a pharmacological, immunological or metabolic action, or to making a medical diagnosis" (European Directive, 2001). Medical devices are defined as "Any instrument, apparatus, appliance, software, material or other article, whether used alone or in combination, together with any accessories, …, for the purpose of diagnosis, prevention, monitoring, treatment or alleviation of disease,…, which does not achieve its principal intended action in or on the human body by pharmacological, immunological or metabolic means,…" (European Directive, 2007).

Medicinal products and medical devices are regulated throughout their entire life cycle, including basic and preclinical research, clinical trials, marketing authorisation and ongoing postauthorisation surveillance. It must be remembered that for every 10,000 new drug candidates studied in basic research, only 250 proceed to the next stage. In preclinical research, the safety of drug molecules and their efficacy expectations are studied before starting trials on humans, and in the end only five molecules reach the clinical trial stage. Clinical trials establish the efficacy of the medicinal product in humans

Developments in Clay Science, Vol. 7. http://dx.doi.org/10.1016/B978-0-08-100293-3.00026-1

(or animals, in the case of veterinary medicinal products) in the treatment of the disease for which it is intended to treat with an acceptable profile of adverse reactions. At the end of the process, only one molecule of the 10,000 initially investigated arrives to marketing authorisation. Similar proportions would be expected with nanotechnology materials and their applications in marketed medicinal products (Fig. 26.1). Academic research plays a key role in this process, driving research and industrial development, as well as through numerous preclinical studies. Still, the market of nanopharmaceuticals could be estimated to be over 25 billion euros in 2020. What are the reasons that explain the success of nanopharmaceuticals in such a hostile environment? First, the scientific push associated with the knowledge of molecular processes linked to diseases, as well as the advances in nanotechnology and subsequent new nanomaterials, increase the number of offerings. On the other hand, there is a strong demand for innovative solutions to early diagnosis of cancer and other pathologies, transport of drugs across the blood–brain barrier, as well as targeting of diseased tissue and organs or development of implant materials with longer lifespans. The strong demand and the increased number of offerings explain the success of nanopharmaceutics.

Both medicinal products and medical devices are materials that, once manipulated and controlled, are used to achieve some health objectives, including therapeutics (drug delivery), regenerative medicine and diagnostics (Fig. 26.2). The development and application of "materials" at the nanoscale plays a relevant role in the design and manufacture of medicines and medical devices, and pharmaceutical nanotechnology (or nanopharmaceutics) is

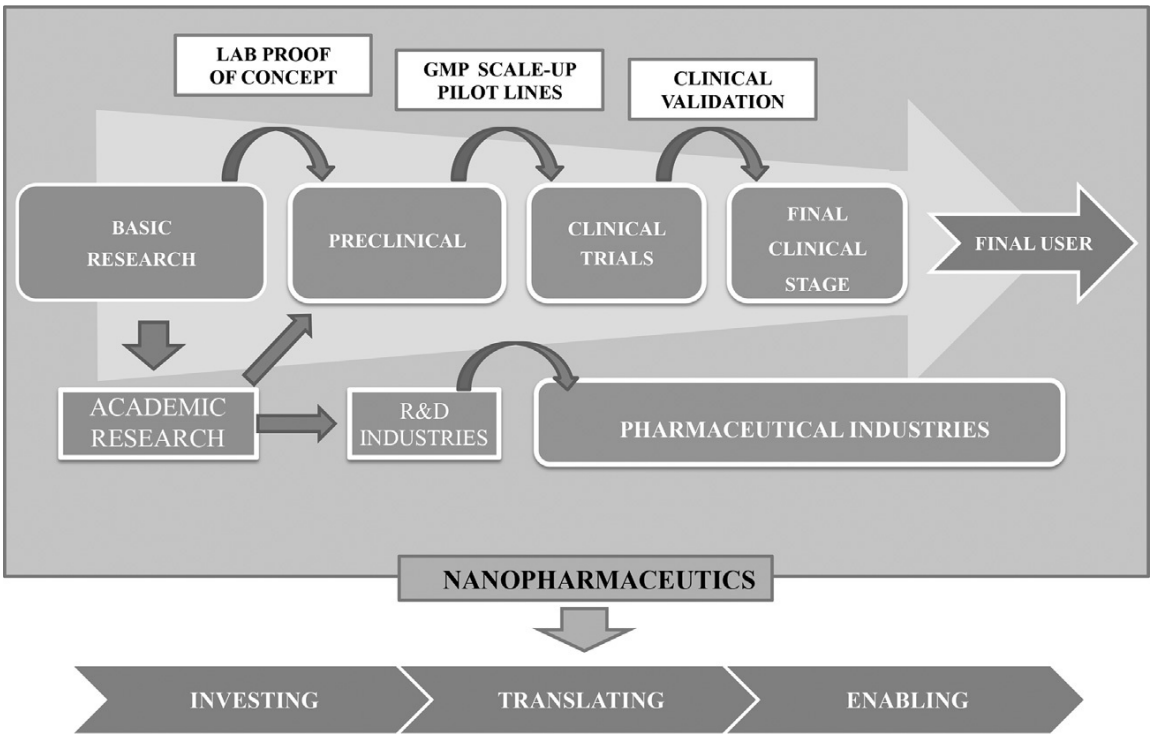

FIG. 26.1 Nanopharmaceuticals value chain, team members and network devoted to the successful fulfilment of nanopharmacy to human health care.

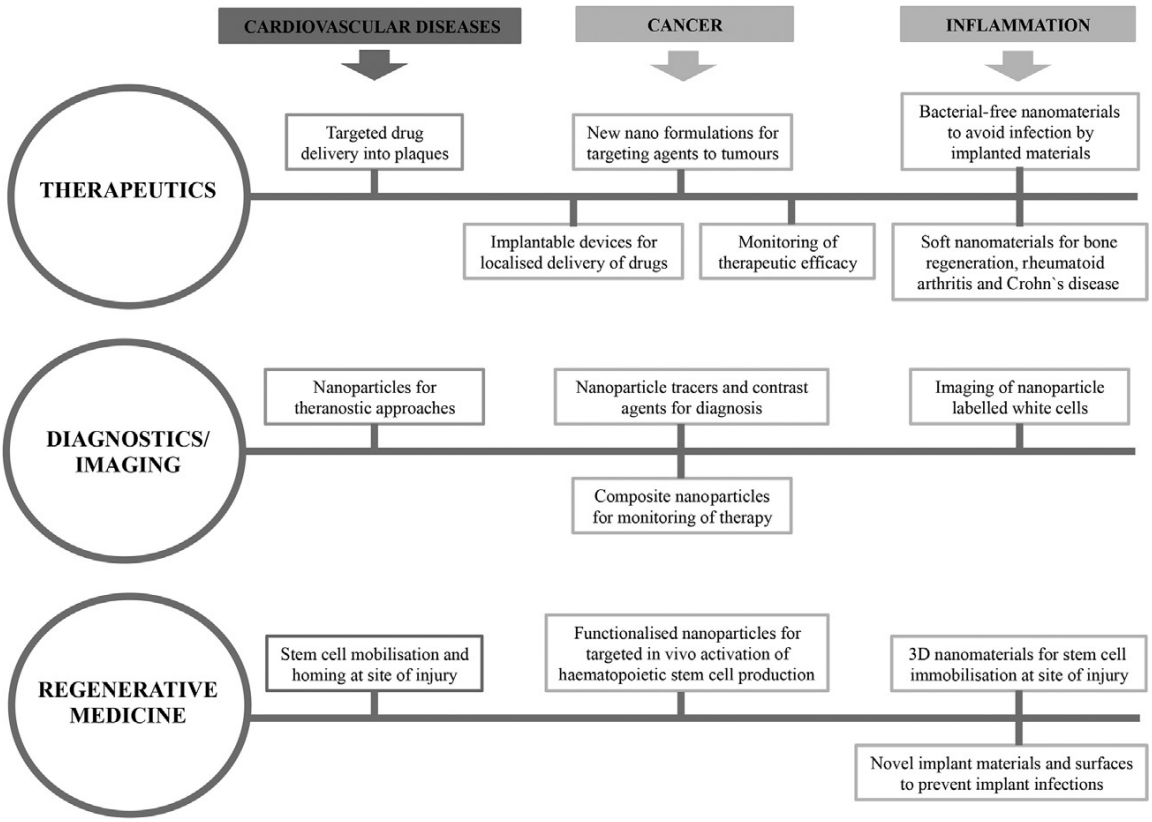

FIG. 26.2 Prospective uses of nanosized tubular clay minerals in nanopharmaceutics.

becoming an emerging academic and industrial area (Wagner et al., 2006). In particular, two nanosized tubular clay minerals, halloysite and imogolite, have been proposed as possible nanovectors for drug encapsulation based on their nanotubular structures, as well as in the restoring, maintaining and repairing of tissues and organ functions, on behalf of their demonstrated biocompatibility (safety) and efficacy. Halloysite is a polymorph of kaolinite in which the sheets curl up to form empty cylinders, and imogolite nanotubes are curved gibbsitelike sheets ($Al(OH)_3$) forming tubes in which the inner hydroxyls are replaced by $SiO_3(OH)$ groups. Typical halloysite nanotubes show internal diameters ranging from 20 to 100 nm, whereas imogolite nanotubes are significantly smaller ($\sim$1 nm). These dimensions are high enough to allow most of the drug molecules to be loaded.

In the last several years, nanosized tubular clay minerals have been proposed in diagnostic scenarios as well, opening a new interesting application for these nanomaterials. Together with these uses in the manufacture of medicinal products, nanosized tubular clay minerals have been used in the development of medical devices. All these applications are reviewed in this chapter.

26.2 USE OF NANOSIZED TUBULAR CLAY MINERALS IN DRUG DELIVERY

Drug delivery (particularly drug targeting) allows the selective attack of organs or cells, while saving healthy organs or tissues from nonspecific drug toxicity. Entrapping of drugs into the lumen of nanosized tubular clay

minerals is a good strategy not only to modify drug release, but also to protect drugs against chemical and enzymatic degradation.

26.2.1 Natural Nanosized Tubular Clay Minerals

Natural nanosized tubular clay minerals provide well-documented support for drug encapsulation and delivery (Lvov et al., 2014; Viseras et al., 2015; Yuan et al., 2015). Several drug molecules have been loaded onto halloysite nanotubes (Price et al., 2001; Levis and Deasy, 2003; Kelly et al., 2004; Veerabadran et al., 2007; Lvov and Price, 2008; Lvov et al., 2008; Forsgren et al., 2010; Abdullayev and Lvov, 2011; Zhang et al., 2013). The kind of interactions between the functional groups of the drug and the active sites of halloysite outer and inner surfaces are key factors in kinetics and thermodynamic features of drug/halloysite systems (Viseras et al., 2008a, 2009). In particular, the loading process of halloysite nanotubes with an antiinflammatory drug (5-aminosalicylic acid) was successfully explained as a combination of two separate processes: a rapid adsorption of the drug at the external surface of the clay mineral particles, and a slower adsorption occurring inside the halloysite lumen and aggregates (Fig. 26.3) (Viseras et al., 2008a). Recently, Elumalai et al. (2015) used Monte Carlo simulations to point out the importance of the diameter and length, together with particle charge, of halloysite nanotubes on the loading and release of some model drugs. Drug release from halloysite nanotubes is often characterised by biphasic profiles with an initial burst followed by a slower release phase,

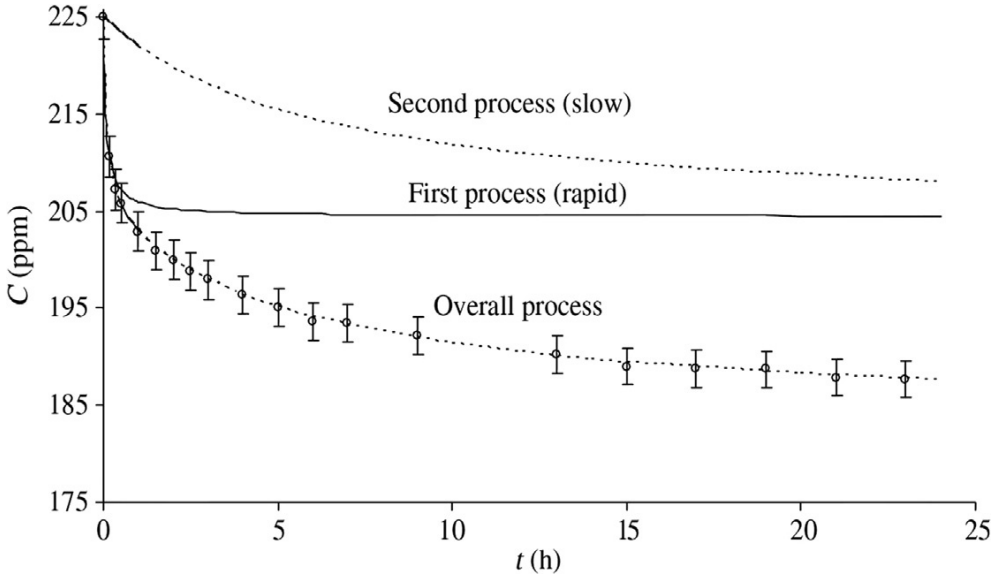

FIG. 26.3 Individual and overall kinetic adsorption isotherms of 5-aminosalicylic acid onto halloysite at 30°C. *Reprinted with permission from Viseras et al. (2008a). Copyright 2008 Elsevier.*

making it difficult to fit the experimental data and to explain the underlying release mechanism using a single mathematical model. A newer model based on kinetic laws able to describe biphasic release curves and provide information about kinetic order and specific release rate from these supports has been successfully postulated by Aguzzi et al. (2013). Briefly, the release of 5-aminosalicylic acid retained onto halloysite nanotubes was explained as an overall desorption process resulting from the contribution of individual simple processes governed by diffusion that included desorption of the drug adsorbed on the external clay mineral surfaces, interparticle spaces or both (fast process) and desorption of drug molecules adsorbed into the halloysite lumen (slow process) (Fig. 26.4). This model provides real hypotheses about mechanisms implicated in drug release from nanosized tubular clay minerals and is able to satisfactorily fit all the experimental data with a simple equation. More examples concerning the use of halloysite as a drug carrier can be found in Chapter 22.

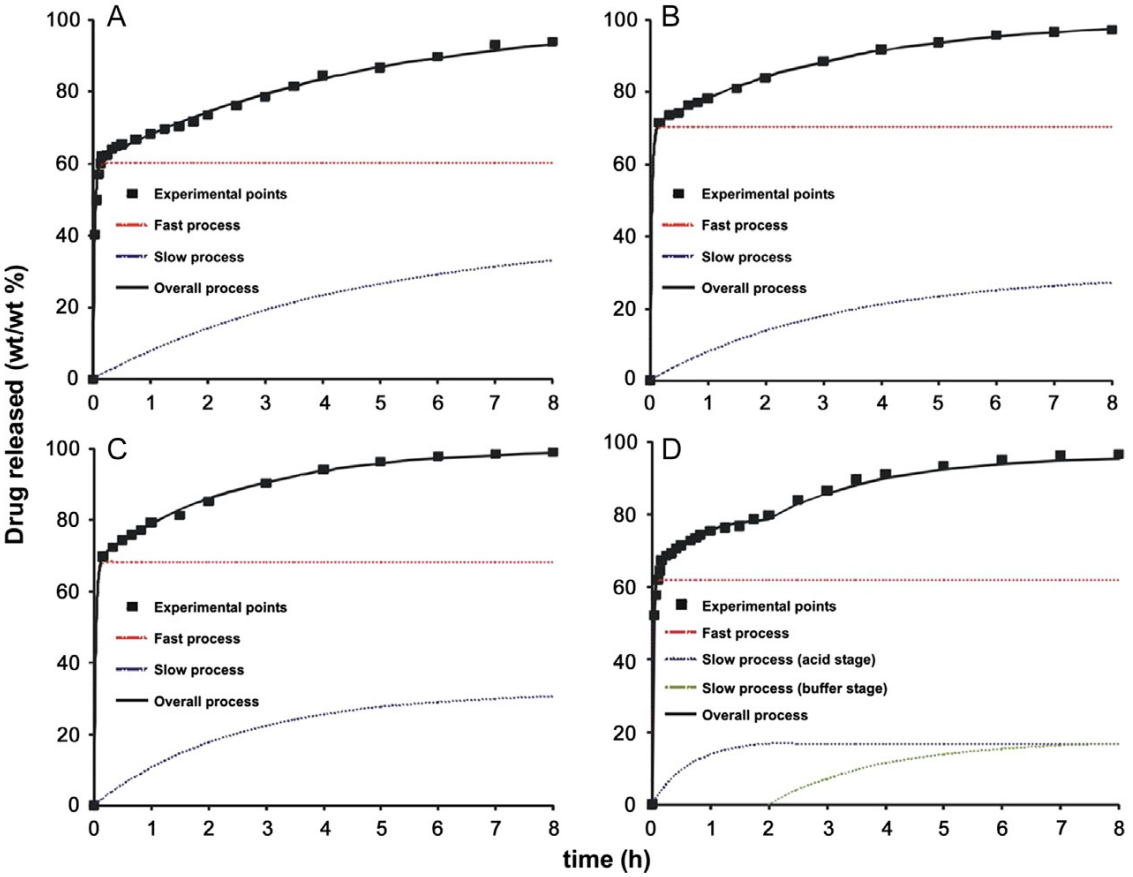

FIG. 26.4 Amount of drug released (mean values ± s.d.; $n = 6$) of 5-aminosalycilic acid from halloysite in three dissolution media (A); theoretical dissolution curves (*lines*) of overall and simple release processes in purified water (B), 0.1 M HCl (C) and pH 6.8 buffer (D). *Reprinted with permission from Aguzzi et al. (2013). Copyright 2013 Elsevier.*

26.2.2 Functionalised Nanosized Tubular Clay Minerals

Halloysite nanotubes can be modified by interactions with specific functional groups or thermal processing in order to improve their performance as drug carriers (Yah et al., 2012; Yuan et al., 2012a,b; Joo et al., 2013; Tan et al., 2013). See more details concerning the modification of nanosized tubular clay minerals in Chapters 8 and 12. Functionalised nanotubes find several applications in both conventional and advanced (ie, gene delivery) therapies. Natural halloysite nanotubes modified with 3-aminopropyltriethoxysilane were successfully used as carriers for aspirin (Lun et al., 2014) and ibuprofen (Tan et al., 2014), showing a higher loading capacity and enhanced drug dissolution rate than unmodified halloysite. Functionalisation with carboxyl acid (Zargarian et al., 2015) or poly (*N*,*N*-dimethylaminoethylmethacrylate) (Hemmatpour et al., 2015) also provided halloysite nanotubes with improved loading capacities for drugs as diphenhydramine and diclofenac. Coating with polyorganosilanes was exploited to change halloysite surface from hydrophilic to superhydrophobic, providing a slow release rate of diclofenac (Fan et al., 2014). Release of antiseptic agents was also greatly reduced by coating halloysite with a benzotriazole-Cu^{2+} chelate film (Wei et al., 2014). The obtained systems showed antibacterial activity against *Staphylococcus aureus* cell cultures for up to 72 h, which means that they look promising to be administered as bandages for wound healing. Halloysite loaded with tetracycline has been coated with polyvinyl alcohol and polymethyl methacrylate films to reduce the initial burst effect that was observed in the release of the drug from the natural nanotubes alone (Ward et al., 2010). Other studies showed that halloysite nanotubes modified with tetrazolium salts were able to enhance the in vitro activity of the antitumour drugs curcumin (Riela et al., 2014) and cardanol (Massaro et al., 2015a) against several tumour cell lines. Curcumin was also loaded on thermoresponsive poly(*N*-isopropylacrylamide)-halloysite nanotubes in order to prevent drug degradation (Cavallaro et al., 2015). Massaro et al. (2014) prepared functionalised halloysite with both cyclodextrins and thiosaccharide units. The obtained modified nanotubes were aimed to act as drug delivery systems and to mimic the binding occurring between cell proteins (lectins) and sugars during cellular recognition events. Layer-by-layer adsorption of oppositely charged polyelectrolytes is another strategy to obtain novel nanovectors for anticancer agents (Guo et al., 2012; Mitchell et al., 2012a,b; Vergaro et al., 2012; Shutava et al., 2014). Cyclodextrin-modified halloysite nanotubes can offer the possibility for simultaneous encapsulation of different drugs in multiagent therapies, as demonstrated with two natural antitumoural agents (silibinin and quercetin) (Massaro et al., 2015b). Advanced therapy based on administration of genetic matter is also greatly attractive as a treatment for cancer disorders. Halloysite nanotubes could efficiently improve intracellular delivery and enhance the antitumour activity of antisense oligodeoxynucleotides (Shi et al., 2011). The clay

mineral also has been proposed as a transgene transmission reagent (Campos et al., 2011) because of its cellular uptake and cytocompatibility properties (Kommireddy et al., 2005; Vergaro et al., 2010; Verma et al., 2012).

Imogolite nanotubes present a positive alumina surface and negative inner silica surface, combined with significantly smaller lumen diameter in comparison with halloysite, provoking a decrease in the efficacy of adsorption of biological macromolecules and drugs (Gustafsson, 2001). However, imogolite nanotubes have been successfully exploited for DNA encapsulation in order to protect it from degradation by nucleases but maintain its biological activity (Jiravanichanun et al., 2012).

26.2.3 Nanosized Tubular Clay Minerals/Biopolymer Nanocomposites

In addition with the abovementioned functionalisation strategies, clay mineral/biopolymer nanocomposites are designed to obtain hybrid materials with enhanced properties compared to the pure components (Viseras et al., 2008b, 2010). Natural mineral nanotubes can be assembled with a large variety of polymers yielding nanostructured hybrid materials used to design nanoscale drug delivery systems (Viseras et al., 2008b, 2010; Ghebaur et al., 2012; Abdullayev and Lvov, 2013). Diphenhydramine hydrochloride has been loaded into halloysite/polyvinyl alcohol nanocomposites to control drug delivery (Ghebaur et al., 2012). Biocompatible chitosan and gelatine multilayers were used for the encapsulation of halloysite tubes loaded with dexamethasone by means of layer-by-layer methodology (Veerabadran et al., 2009). Encapsulation of the drug in the mineral nanotubes, accomplished by the assembly of natural polymer shells, resulted in controlled release of the drug molecule. Halloysite/hyaluronate nanocomposites intended for colon target delivery of 5-fluorouracil were recently developed, showing promising pH-dependent drug release profiles (Rao et al., 2014).

26.3 USE OF NANOSIZED TUBULAR CLAY MINERALS IN TISSUE ENGINEERING AND REPARATIVE MEDICINE

Biocompatibility is essential for the potential application of nanosized tubular clay minerals in tissue engineering and regenerative medicine. Halloysite nanotube interactions with cells and the subsequent intracellular uptake have been studied in different cell lines (Kommireddy et al., 2005; Veerabadran et al., 2009; Vergaro et al., 2010; Lai et al., 2013). Cell adhesion and proliferation on biomaterials is a crucial point in tissue engineering and biotechnology. Specific interactions between cells and substrates are important to regulate cell function, tissue homeostasis and matrix remodelling. The presence of divalent cations, such as Ca^{2+} and Mg^{2+}, associated with clay minerals, significantly influences cellular adhesion. Clay mineral/cell interactions

depend on the shape, size and surface charge of the particles. It is well known that the cell membrane surface is negatively charged and that positively charged nanoparticles can penetrate deep into cell membranes, while negatively charged particles cannot enter the cell wall. Charge density modulates the biocompatibility and antimicrobial properties of clay minerals, and this is related to the aspect ratio (ie, the relation between structure sizes) (Rawat et al., 2014). Halloysite improved fibroblast cell attachment and spreading and allowed cells to maintain cell phenotypes (Kommireddy et al., 2005). In vitro cell toxicity of halloysite has been studied using human dermal fibroblast and breast cancer cells, and a low inherent toxicity of the pure mineral has been found (Veerabadran et al., 2009). Vergaro et al. (2010) performed in vitro cytotoxicity testing that demonstrated good biocompatibility of halloysite at a concentration of 0.1 mg/mL. It was observed that halloysite was nontoxic towards cervical adenocarcinoma cells (HeLa) and breast cancer cells (MCF-7), as well as the fact that halloysite accumulated in cells without preventing their proliferation. The process of cellular uptake was based on both nanotube concentration around cells and their penetration into cells. Studies with other cellular lines (Caco-2 and HT29-MTX) have also shown a high degree of biocompatibility of halloysite nanotubes below 0.2 mg/mL (Lai et al., 2013). Cell viability and membrane integrity were preserved for middle-term exposure in vitro (6 h) and appeared unlikely to have toxic effects at moderate levels of exposure. At high concentrations (100 mg/l), a significant exposure change in protein expression was observed: this seemed related to the stimulation of the processes of cell growth and proliferation, which is similar to the response to cell infection, irritation and injury and enhanced antioxidant activity, all of which are characteristic of an overall adaptive response to exposure.

With regard to imogolite, its morphology (high length-to-diameter ratio) and expected persistence could suggest potential toxicity; however, the high hydrophilicity and external alumina layer contribute to the relative inertness of this mineral (Rotoli et al., 2014). Ishikawa et al. (2010a,b) declared that the amount of normalised protein per osteoblastlike cell cultured on imogolite was twice as much than when it was cultured on a culture dish, and they also pointed out that the cell-imogolite bindings was stronger than the cell-culture dish ones. These results make evident the good biocompatibility between cells and imogolite.

26.3.1 Tissue Engineering

Tissue engineering offers a means to provide biocompatible replacement tissue with mechanical and functional integrity. A critical step in tissue engineering is the designing of scaffolds with structure, composition, physicochemical, mechanical and biological features analogous to natural tissues. Scaffolds provide a three-dimensional (3D) environment that supports cell

attachment, proliferation and differentiation, as well as enabling the transportation of nutrients and cell metabolites in tissue engineering (Patterson et al., 2010; Chrzanowski et al., 2013; Gaharwar et al., 2013; Song et al., 2014). Hydrogel (Gaharwar et al., 2013; Song et al., 2014) has been studied as a scaffolding material, especially for soft tissue regeneration, even if it usually has inferior mechanical properties as well as lacking adequate functionality, which hinders its wide application in regenerative medicine (Biondi et al., 2008). The incorporation of clay mineral nanoparticles improved the mechanical properties and functionalities of these systems, fulfiling the requirements of tissue engineering. The 3D geometry is related to pore size, porosity and interpore connectivity that represent key issues for accelerated tissue engineering application. With these premises, different clay minerals have been proposed as innovative platforms for tissue regeneration and biomaterial design because of their capacity to enhance stem and progenitor cell proliferation and differentiation (Dawson and Oreffo, 2013). Polymer electrospun with halloysite showed potential applications in the fields of tissue engineering, wound dressing and drug delivery (Wang et al., 2012). Halloysite and polyvinyl alcohol were used to prepare clay polymer nanocomposites (CPN) with improved osteoblast adhesion (Zhou et al., 2010). Electrospun CPN with tissue engineering (and drug delivery of tetracycline) applications were prepared with halloysite and polylactic-co-glycolic acid (Qi et al., 2010, 2012, 2013). According to its haemocompatibility, halloysite polymer nanocomposites were considered suitable as artificial tissue/organ substitutes (Zhao et al., 2013). Halloysite polymethylmethacrylate nanocomposites have been used as bone cements doped with gentamicin, providing slow release of the drug without compromising the CPN mechanical strength while enhancing bone adhesiveness (Wei et al., 2012). Halloysite polycaprolactone nanocomposite scaffolds showed improved mechanical properties, substantial protein adsorption, enhanced mineralisation and osteogenic differentiation compared to the polymer scaffold without the clay mineral (Nitya et al., 2012). Polyglycerol sebacate was filled with halloysite nanotubes to obtain elastomeric nanocomposites with optimal combination of compliance and a degradable profile compared with the pure counterpart, showing excellent resilience and satisfactory biocompatibility in vitro to be used as a soft tissue engineering material (Chen et al., 2011). Halloysite chitosan nanotubes nanocomposite scaffolds were prepared by combining solution-mixing and freeze-drying techniques exhibiting a high porous structure and cytocompatibility with great potential for tissue engineering (Liu et al., 2013).

Imogolite is also receiving considerable attention in tissue engineering for its excellent adsorption properties and nanotubular shape. Reinforcement of polymeric materials with imogolite nanotubes has recently been described in the research literature (Yamamoto et al., 2005a,b; Yah et al., 2010; Shikinaka et al., 2011). These findings have been exploited to obtain collagen- (Nakano et al., 2010) and gelatine-based (Teramoto et al., 2012)

nanocomposite hydrogels, showing improved properties and promising potential in pharmaceutical and tissue engineering development. Imogolite nanocomposite scaffolds exhibited good biocompatibility and enhancement effects of proliferation over mouse osteoblastlike cells (Ishikawa et al., 2010a). With regard to safety requirements, imogolite nanotubes must demonstrate no potential toxicological effects on humans. The possible cytotoxic and genotoxic effects of synthetic imogolite-like nanotubes have been evaluated, revealing no cytotoxic activity in human fibroblast cells up to 0.1 mg/mL of nanoparticles, whereas DNA damage depended on the cell uptake and aspect ratio of the nanotubes (Liu et al., 2012). Imogolite nanotubes offer a wide range of positive characteristics as scaffolds for osteoblastic proliferation and differentiation and are a both suitable and interesting alternative in bone tissue engineering (Ishikawa et al., 2010b). Imogolite nanotubes were applied to cell cultures to compare their properties as scaffolds with a conventional culture dish and a carbon nanotube scaffold. The scaffold containing more imogolite presented the best roughness, wettability and protein adsorption ability. In addition to these advances, modification and functionalisation of imogolite nanotubes (Kang et al., 2010, 2011) will probably offer new perspectives on biomedical field in the next several years.

26.3.2 Reparative Medicine

A particular interesting use of nanosized tubular clay minerals in regenerative medicine is their use in design of wound-healing treatments. Wound healing involves multiple cell populations, extracellular matrix bioactive molecules as soluble mediators and particularly cytokines and growth factors (Velnar et al., 2009). Chronic wounds are the results of different causes and pathological states, such as burns, vasculitis, arterial and venous insufficiency, malignancies, diabetes and neuropathic and pressure ulcers. In these cases, the normal stages of healing fail, indicating incomplete tissue reparation. Various factors could disturb the normal process, prolonging one or more stages, such as haemostasis, inflammation, proliferation and remodelling. In particular, tissue infections and hypoxia, necrosis and the presence of excessive levels of exudates and inflammatory cytokines could prolong a nonhealing state. A continuous state of wound inflammation causes a negative cascade of tissue responses, and the healing process results in poor functional and anatomical outcomes and frequent relapsing. Generally chronic wounds are often subjected to infections and result in complicated wounds. Different medical approaches and therapeutic choice could affect wound healing and the subsequent steps involved in tissue repairing. The loading and the localisation of bioactive molecules in clay minerals, having a role in cell growth and proliferation, may induce cell differentiation (Salcedo et al., 2012). However a more interesting aspect is the possibility of stimulating cell differentiation per se due to the signals produced by charge density and ion concentration.

Moreover, it was reported that the elasticity or the structure of the matrix environment regulated stem cell differentiation that depends not only on chemical differentiation factors in the culture medium, but also on characteristics of the matrix environment, such as the materials, the surface type and the mechanical properties of the culture substrates (Engler et al., 2006; Miyahara et al., 2006; Reilly and Engler, 2010; Kotobuki et al., 2013). The presence of silicon and magnesium elements has been described as being able to promote the osteogenic differentiation of mesenchymal stem cells. A biomimetic scaffold should be an artificially designed scaffold that enhance neotissue genesis via cell recruiting, adhesion and proliferation (Ma, 2008). The potential application of halloysite nanotubes for wound-healing purposes was pointed out by Lvov and Abdullayev (2013), showing that halloysite polycaprolactone nanocomposite scaffolds loaded with antiseptic agents were effective materials for skin regeneration. Halloysite has been shown to enhance the haemostatic and wound-healing properties of chitosan sponges in rats (Liu et al., 2014). The inclusion of the nanosized tubular clay minerals promotes in vivo epithelialisation and collagen deposition after 1 week, in comparison with pure chitosan. As for future trends, mineral coating of biological cells can be used to obtain surface-functionalised 3D structures (whole cells) with biomimetic properties. Yeast cells have been used to obtain hollow halloysite-based microcapsules (so-called cyborg cells) by layer-by-layer assembly of nanosized tubular clay minerals and subsequent thermal decomposition of the cells (Konnova et al., 2013). These new assemblies may find applications in controllable cell growth.

26.4 USE OF NANOSIZED TUBULAR CLAY MINERALS IN DIAGNOSTIC AND MEDICAL DEVICES

At the moment, the use of nanosized tubular clay minerals in diagnosis has not been explicitly raised by any research group. However, some recent articles allow to venture that this will be one of the most interesting research areas of application of nanosized tubular clay minerals in the near future. In cancer therapy, the count of circulating tumour cancer cells in blood can be a diagnostic tool to monitor the progression of the disease and detect possible metastasis. It was demonstrated that halloysite is effective to enhance cell adhesion of circulating cancer cells (Hughes and King, 2010; Hughes et al., 2012). Similar hybrid systems have been also used to detect DNA damage, and these systems could have many biological and medical applications (Rawtani et al., 2013).

The frontier between medicinal products (European Directive, 2001) and medical devices (European Directive, 2007) is not always clear, particularly with those systems based in nanotechnology. For example, an active implantable medical device may be intended to administer a medicinal product. Obviously, the consideration of this system as a medical device or medicinal

product will greatly affect the possibilities of marketing. In any case, without going into a final consideration, some authors have proposed the use of halloysite specifically in the design of such devices. Recently, modified halloysite nanotubes have been used for capturing circulating tumour cells from the bloodstream (Mitchell et al., 2015). Functionalisation with surfactants alters the charge of naturally occurring halloysite nanotubes and induces differential adhesion of tumour cells and blood cells to nanotube-coated surfaces under flow. It is not clear at this point whether these systems are medical devices, but the significance of the basic research in this area is obvious.

26.5 CONCLUDING REMARKS

Nanosized tubular clay minerals have attracted a great deal interest in recent years as materials for new, advanced biomedical applications. They are used as they naturally occur or after functionalisation, including clay mineral biopolymer nanohybrids, both in drug and gene delivery. Together with their possibilities in drug delivery, nanosized tubular clay minerals show good features in the development of scaffolds for tissue engineering, medical devices and diagnostics. Clay minerals and clay biopolymer nanocomposites have been used as carriers of matrix proteins, growth factors and genes in tissue regeneration. The interaction of nanosized tubular clay minerals with biological structures open up opportunities for tissue engineering and offer a range of possibility to develop systems able to facilitate cell adhesion, proliferation and neotissue formation. CPN are characterised by porous network structure, swelling/deswelling behaviour and mechanical properties, which provide physical support for cell adhesion and proliferation as well as excellent biocompatibility. Moreover, cells could interact with clay minerals, suggesting new opportunities in the functionalisation of surfaces for enhanced reparative response. An important aspect is the capability of clay minerals to induce cell differentiation without the employment of other inductors avoiding problems related to uncontrolled cell proliferation in other regions far from the application site. Nanosized tubular clay minerals could be also potentially used in the design of new noninvasive systems to diagnostic of disorders such as cancer and degenerative diseases.

Of the challenges for the medical application of nanosized tubular clay minerals, a particularly important one is the very moderate interest of the pharmaceutical and medical device industry in nanotechnology. Even though recent research includes many innovative studies based on the application of clay minerals in drug delivery and tissue regeneration/reparation, hard work will be needed to transfer the acquired knowledge to clinical practice, requiring high implications of the academic research. The first step to accomplish will be to create spinoffs that can develop current ideas and results to find major pharmaceutical or medical device companies that licence their technologies or partner with the spinoffs to bring their novel approaches through the

regulatory approval process. The second challenge will be to develop nanopharmaceutical products with adequate cost-effectiveness in comparison to conventional alternatives, as health-care systems increasingly face cost pressures.

Nanosized tubular clay minerals have demonstrated their potential in both target delivery and diagnostics, and it is expected that in the near future, they will be used in theranostic platforms that can comprehensively carry out in situ diagnostics, then deliver drugs, genes or both to the diseased tissue or cell and monitor the resultant therapeutic response. These are the new frontiers of using natural mineral nanotubes in health-care applications.

REFERENCES

Abdullayev, E., Lvov, Y., 2011. Halloysite clay nanotubes for controlled release of protective agents. J. Nanosci. Nanotechnol. 11, 10007–10026.

Abdullayev, E., Lvov, Y., 2013. Halloysite clay nanotubes as a ceramic "skeleton" for functional biopolymer composites with sustained drug release. J. Mater. Chem. B 1, 2894–2903.

Aguzzi, C., Viseras, C., Cerezo, P., Salcedo, I., Sánchez-Espejo, R., Valenzuela, C., 2013. Release kinetics of 5-aminosalicylic acid from halloysite. Colloids Surf. B 105, 75–80.

Aulton, M.E., Taylor, K.M.G., 2013. Aulton's Pharmaceutics. The Design and Manufacture of Medicines, fourth ed. Churchill Livingstone-Elsevier, Edinburgh.

Biondi, M., Ungaro, F., Quaglia, F., Netti, P.A., 2008. Controlled drug delivery in tissue engineering. Adv. Drug Deliv. Rev. 60, 229–242.

Campos, V.F., de Leon, P.M.M., Komninou, E.R., Dellagostin, O.A., Deschamps, J.C., Seixas, F.K., Collares, T., 2011. NanoSMGT: transgene transmission into bovine embryos using halloysite clay nanotubes or nanopolymer to improve transfection efficiency. Theriogenology 76, 1552–1560.

Cavallaro, G., Lazzara, G., Massaro, M., Milioto, S., Noto, R., Parisi, F., Riela, S., 2015. Biocompatible poly(N-isopropylacrylamide)-halloysite nanotubes for thermoresponsive curcumin release. J. Phys. Chem. C 119, 8944–8951.

Chen, Q.Z., Liang, S.L., Wang, J., Simon, G.P.J., 2011. Manipulation of mechanical compliance of elastomeric PGS by incorporation of halloysite nanotubes for soft tissue engineering applications. J. Mech. Behav. Biomed. Mater. 4, 1805–1818.

Chrzanowski, W., Kim, S.Y., Neel, E.A.A., 2013. Biomedical applications of clay. Aust. J. Chem. 66, 1315–1322.

Dawson, J.I., Oreffo, R.O.C., 2013. Clay: new opportunities for tissue regeneration and biomaterial design. Adv. Mater. 25, 4069–4086.

Elumalai, D.N., Lvov, Y., Derosa, P., 2015. Implementation of a simulation model of the controlled release of molecular species from halloysite nanotubes. J. Encapsulation Adsorpt. Sci. 5, 74–92.

Engler, A.J., Sen, S., Sweeney, H.L., Discher, D.E., 2006. Matrix elasticity directs stem cell lineage specification. Cell 126, 677–689.

European Directive, 2001. Directive 2001/83/EC of the European Parliament and of the Council of 6 November 2001 on the Community code relating to medicinal products for human use. Off. J. Eur. Union 311, 67. 28.11.2001.

European Directive, 2007. Directive 2007/47/EC of the European Parliament and of the Council of 5 September 2007 amending Council Directive 90/385/EEC on the approximation of the

laws of the Member States relating to active implantable medical devices, Council Directive 93/42/EEC concerning medical devices and Directive 98/8/EC concerning the placing of biocidal products on the market. Off. J. Eur. Union 247, 21–55. 21.9.2007.

Fan, L., Li, B., Wang, Q., Wang, A., Zhang, J., 2014. Superhydrophobic gated polyorganosilanes/halloysite nanocontainers for sustained drug release. Adv. Mater. Inter. 1, 1300136. 7 pp.

Forsgren, J., Jamstorp, E., Bredenberg, S., Engqvist, H., Stromme, M., 2010. A ceramic drug delivery vehicle for oral administration of highly potent opioids. J. Pharm. Sci. U.S. 99 (1), 219–226.

Gaharwar, A.K., Peppas, N.A., Khademhosseini, A., 2013. Nanocomposite hydrogels for biomedical applications. Biotechnol. Bioeng. 111, 441–453.

Ghebaur, A., Garea, S.A., Iovu, H., 2012. New polymer–halloysite hybrid materials-potential controlled drug release system. Int. J. Pharm. 436, 568–573.

Guo, M., Wang, A., Muhammad, F., Qi, W., Ren, H., Guo, Y., Zhu, G., 2012. Halloysite nanotubes, a multifunctional nanovehicle for anticancer drug delivery. Chin. J. Chem. 30, 2115–2120.

Gustafsson, J.P., 2001. The surface chemistry of imogolite. Clay Clay Miner. 49, 73–80.

Hemmatpour, H., Haddadi-Asl, V., Roghani-Mamaqani, H., 2015. Synthesis of pH-sensitive poly (N,N-dimethylaminoethyl methacrylate)-grafted halloysite nanotubes for adsorption and controlled release of DPH and DS drugs. Polymer 65, 143–153.

Hughes, A.D., King, M.R., 2010. Use of naturally occurring halloysite nanotubes for enhanced capture of flowing cells. Langmuir 26, 12155–12164.

Hughes, A.D., Mattison, J., Western, L.T., Powderly, J.D., Greene, B.T., King, M.R., 2012. Microtube device for selectin-mediated capture of viable circulating tumour cells from blood. Clin. Chem. 58, 846–853.

Ishikawa, K., Akasaka, T., Yawaka, Y., Watari, F., 2010a. High functional expression of osteoblasts on imogolite, aluminosilicate nanotubes. J. Biomed. Nanotechnol. 6, 59–65.

Ishikawa, K., Akasaka, T., Abe, S., Yawaka, Y., Suzuki, M., Watari, F., 2010b. Application of imogolite, almino-silicate nanotube, as scaffold for the mineralization of osteoblasts. Bioceram. Dev. Appl. 1, 1–3.

Jiravanichanun, N., Yamamoto, K., Kato, K., Kim, J., Horiuchi, S., Yah, W.-O., Otsuka, H., Takahara, A., 2012. Preparation and characterization of imogolite/DNA hybrid hydrogels. Biomacromolecules 13, 276–281.

Joo, Y., Sim, J.H., Jeon, Y., Lee, S.U., Sohn, D., 2013. Opening and blocking the inner-pores of halloysite. Chem. Commun. 49, 4519–4521.

Kang, D.Y., Zang, J., Wright, E.R., McCanna, A.L., Jones, C.W., Nair, S., 2010. Dehydration, dehydroxylation, and rehydroxylation of single-walled aluminosilicate nanotubes. ACS Nano 4, 4897–4907.

Kang, D.Y., Zang, J., Jones, C.W., Nair, S., 2011. Single-walled aluminosilicate nanotubes with organic-modified interiors. J. Phys. Chem. C 115, 7676–7685.

Kelly, H.M., Deasy, P.B., Ziaka, E., Claffey, N., 2004. Formulation and preliminary in vivo dog studies of a novel drug delivery system for the treatment of periodontitis. Int. J. Pharm. 274, 167–183.

Kommireddy, D.S., Ichinose, I., Lvov, Y.M., Mills, D.K., 2005. Nanoparticle multilayers: surface modification for cell attachment and growth. J. Biomed. Nanotechnol. 1, 1–5.

Konnova, S.A., Sharipova, I.I., Demina, T.A., Osin, Y.N., Yarullina, D.R., Ilinskaya, O.N., Lvov, Y.M., Fakhrullin, R.F., 2013. Biomimetic cell-mediated three-dimensional assembly of halloysite nanotubes. Chem. Commun. 49, 4208–4210.

Kotobuki, N., Murata, K., Haraguchi, K., 2013. Proliferation and harvest of human mesenchymal stem cells using new thermoresponsive nanocomposite gels. J. Biomed. Mater. Res. 101, 537–546.

Lai, X., Agarwal, M., Lvov, Y.M., Pachpande, C., Varahramyan, K., Witzmann, F.A., 2013. Proteomic profiling of halloysite clay nanotube exposure in intestinal cell co-culture. J. Appl. Toxicol. 33, 1316–1329.

Levis, S.R., Deasy, P.B., 2003. Use of coated microtubular halloysite for the sustained release of diltiazem hydrochloride and propranolol hydrochloride. Int. J. Pharm. 253, 145–157.

Liu, W., Chaurand, P., Di Giorgio, C., De Méo, M., Thill, A., Auffan, M., Masion, A., Borschneck, D., Chaspoul, F., Gallice, P., Botta, A., Bottero, J.Y., Rose, J., 2012. Influence of the length of imogolite-like nanotubes on their cytotoxicity and genotoxicity toward human dermal cells. Chem. Res. Toxicol. 25, 2513–2522.

Liu, M., Wu, C., Jiao, Y., Xiong, S., Zhou, C., 2013. Chitosan–halloysite nanotubes nanocomposite scaffolds for tissue engineering. J. Mater. Chem. B 1, 2078–2089.

Liu, M., Shen, Y., Ao, P., Dai, L., Liu, Z., Zhou, C., 2014. The improvement of hemostatic and wound healing property of chitosan by halloysite nanotubes. RSC Adv. 4, 23540–23553.

Lun, H., Ouyang, J., Yang, H., 2014. Natural halloysite nanotubes modified as an aspirin carrier. RSC Adv. 4, 44197–44202.

Lvov, Y., Abdullayev, E., 2013. Functional polymer clay nanotube composites with sustained release of chemical agents. Prog. Polym. Sci. 38, 1690–1719.

Lvov, Y., Price, R., 2008. Halloysite nanotubules a noble substrate for the controlled delivery of bioactive molecules. In: Ruiz-Hitzky, E., Ariga, K., Lvov, Y. (Eds.), Bio-Inorganic Hybrid Nanomaterials. Wiley, Berlin, London, pp. 440–478.

Lvov, Y.M., Shchukin, D.G., Mohwald, H., Price, R.R., 2008. Halloysite clay nanotubes for controlled release of protective agents. ACS Nano 2, 814–820.

Lvov, Y., Aerov, A., Fakhrullin, R., 2014. Clay nanotube encapsulation for functional biocomposites. Adv. Colloid Interf. Sci. 207, 189–198.

Ma, P.X., 2008. Biomimetic materials for tissue engineering. Adv. Drug Deliv. Rev. 60, 184–198.

Massaro, M., Riela, S., Lo Meo, P., Noto, R., Cavallaro, G., Milioto, S., Lazzara, G., 2014. Functionalized halloysite multivalent glycocluster as a new drug delivery system. J. Mater. Chem. B 2, 7732–7738.

Massaro, M., Colletti, C.G., Noto, R., Riela, S., Poma, P., Guernelli, S., Parisi, F., Milioto, S., Lazzara, G., 2015a. Pharmaceutical properties of supramolecular assembly of co-loaded cardanol/triazole-halloysite systems. Int. J. Pharm. 478, 476–485.

Massaro, M., Piana, S., Colletti, C.G., Noto, R., Riela, S., Baiamonte, C., Giordano, C., Pizzolanti, G., Cavallaro, G., Milioto, S., Lazzara, G., 2015b. Multicavity halloysite–amphiphilic cyclodextrin hybrids for co-delivery of natural drugs into thyroid cancer cells. J. Mater. Chem. B 3, 4074–4081.

Mitchell, M.J., Chen, C.S., Ponmudi, V., Hughes, A.D., King, M.R., 2012a. E-selectin liposomal and nanotube-targeted delivery of doxorubicin to circulating tumour cells. J. Control. Release 160, 609–617.

Mitchell, M.J., Castellanos, C.A., King, M.R., 2012b. Nanostructured surfaces to target and kill circulating tumour cells while repelling leukocytes. J. Nanomater. 831263 (10 pp).

Mitchell, M.J., Castellanos, C.A., King, M.R., 2015. Surfactant functionalization induces robust, differential adhesion of tumour cells and blood cells to charged nanotube-coated biomaterials under flow. Biomaterials 56, 179–186.

Miyahara, Y., Nagaya, N., Kataoka, M., Yanagawa, B., Tanaka, K., Hao, H., Ishino, K., Ishida, H., Shimizu, T., Kangawa, K., Sano, S., Okano, T., Kitamura, S., Mori, H., 2006.

Monolayered mesenchymal stem cells repair scarred myocardium after myocardial infarction. Nat. Med. 12, 459–465.

Nakano, A., Teramoto, N., Chen, G., Miura, Y., Shibata, M., 2010. Preparation and characterization of complex gel of Type I collagen and aluminosilicate containing imogolite nanofibers. J. Appl. Polym. Sci. 118, 2284–2290.

Nitya, G., Nair, G.T., Mony, U., Chennazhi, K.P., Nair, S.V., 2012. "In vitro" evaluation of electrospun PCL/nanoclay composite scaffold for bone tissue engineering. J. Mater. Sci. Mater. Med. 23, 1749–1761.

Patterson, J., Martino, M.M., Hubbell, J.A., 2010. Electrospun poly(lactic-co-glycolic acid)/halloysite nanotube composite nanofibers for drug encapsulation and sustained release biomimetic materials in tissue engineering. Mater. Today 13, 15–22.

Price, R.R., Gaber, B.P., Lvov, Y., 2001. In-vitro release characteristics of tetracycline HCl, khellin and nicotinamide adenine dineculeotide from halloysite; a cylindrical mineral. J. Microencapsul. 18, 713–722.

Qi, R., Guo, R., Shen, M., Cao, X., Zhang, L., Xu, J., Yu, J., Shi, X., 2010. Electrospun poly(lactic-co-glycolic acid)/halloysite nanotube composite nanofibers for drug encapsulation and sustained release. J. Mater. Chem. 20, 10622–10629.

Qi, R., Cao, X., Shen, M., Guo, R., Yu, J., Shi, X., 2012. Biocompatibility of electrospun halloysite nanotube-doped poly(lactic-co-glycolic acid) composite nanofibers. J. Biomater. Sci. Polym. Ed. 23, 299–313.

Qi, R., Guo, R., Zheng, F., Liu, H., Yu, J., Shi, X., 2013. Controlled release and antibacterial activity of antibiotic-loaded electrospun halloysite/poly(lactic-co-glycolic acid) composite nanofibers. Colloids Surf. B Biointerfaces 110, 148–155.

Rao, K.M., Nagappan, S., Seo, D.J., Ha, C.S., 2014. pH sensitive halloysite-sodium hyaluronate/poly(hydroxyethyl methacrylate) nanocomposites for colon cancer drug delivery. Appl. Clay Sci. 97–98, 33–42.

Rawat, K., Agarwal, S., Tyagi, A., Verma, A.K., Bohidar, H.B., 2014. Aspect ratio dependent cytotoxicity and antimicrobial properties of nanoclay. Appl. Biochem. Biotechnol. 174, 936–944.

Rawtani, D., Agrawal, Y.K., Prajapati, P., 2013. Interaction behavior of DNA with halloysite nanotube-silver nanoparticle-based composite. BioNanoScience 3, 73–78.

Reilly, G.C., Engler, A.J., 2010. Intrinsic extracellular matrix properties regulate stem cell differentiation. J. Biomech. 43, 55–62.

Riela, S., Massaro, M., Colletti, C.G., Bommarito, A., Giordano, C., Milioto, S., Noto, R., Poma, P., Lazzara, G., 2014. Development and characterization of co-loaded curcumin/triazole-halloysite systems and evaluation of their potential anticancer activity. Int. J. Pharm. 475, 613–623.

Rotoli, B.M., Guidi, P., Bonelli, B., Bernardeschi, M., Bianchi, M.G., Esposito, S., Frenzilli, G., Lucchesi, P., Nigro, M., Scarcelli, V., Tomatis, M., Zanello, P.P., Fubini, B., Bussolati, O., Bergamaschi, E., 2014. Imogolite: an aluminosilicate nanotube endowed with low cytotoxicity and genotoxicity. Chem. Res. Toxicol. 27, 1142–1154.

Salcedo, I., Aguzzi, C., Sandri, G., Bonferoni, M.C., Mori, M., Cerezo, P., Sánchez, R., Viseras, C., Caramella, C., 2012. "In vitro" biocompatibility and mucoadhesion of montmorillonite chitosan nanocomposite: a new drug delivery. Appl. Clay Sci. 55, 131–137.

Shi, Y.F., Tian, Z., Zhang, Y., Shen, H.B., Jia, N.Q., 2011. Functionalized halloysite nanotube-based carrier for intracellular delivery of antisense oligonucleotides. Nanoscale Res. Lett. 6, 1–7.

Shikinaka, K., Koizumi, Y., Osada, Y., Shigehara, K., 2011. Reinforcement of hydrogel by addition of fiber-like nanofiller. Polym. Adv. Technol. 22, 1212–1215.

Shutava, T.G., Fakhrullin, R.F., Lvov, Y.M., 2014. Spherical and tubule nanocarriers for sustained drug release. Curr. Opin. Pharmacol. 18, 141–148.

Song, F., Li, X., Wang, Q., Liao, L., Zhang, C., 2014. Nanocomposite hydrogels and their applications in drug delivery and tissue engineering. J. Biomed. Nanotechnol. 10, 1–13.

Tan, D., Yuan, P., Bergaya, F., Yu, H., Liu, D., Liu, H., He, H., 2013. Natural halloysite nanotubes as mesoporous carriers for the loading of ibuprofen. Microporous Mesoporous Mater. 179, 89–98.

Tan, D., Yuan, P., Bergaya, F., Liu, D., Wang, L., Liu, H., He, H., 2014. Loading and in vitro release of ibuprofen in tubular halloysite. Appl. Clay Sci. 96, 50–55.

Teramoto, N., Hayashi, A., Yamanaka, K., Sakiyama, A., Nakano, A., Shibata, M., 2012. Preparation and mechanical properties of photo-crosslinked fish gelatin/imogolite nanofiber composite hydrogel. Materials 5, 2573–2585.

Veerabadran, N.G., Price, R.R., Lvov, Y.M., 2007. Clay nanotubes for encapsulation and sustained release of drugs. Nano 2, 115–120.

Veerabadran, N.G., Mongayt, D., Torchilin, V., Price, R.R., Lvov, Y.M., 2009. Organized shells on clay nanotubes for controlled release of macromolecules. Macromol. Rapid Commun. 30, 99–103.

Velnar, T., Bailey, T., Smrkolj, V., 2009. The wound healing process: an overview of the cellular and molecular mechanisms. J. Int. Med. Res. 37, 1528–1542.

Vergaro, V., Abdullayev, E., Lvov, Y.M., Zeitoun, A., Cingolani, R., Rinaldi, R., Leporatti, S., 2010. Cytocompatibility and uptake of halloysite clay nanotubes. Biomacromolecules 11, 820–826.

Vergaro, V., Lvov, Y.M., Leporatti, S., 2012. Halloysite clay nanotubes for resveratroldelivery to cancer cells. Macromol. Biosci. 12, 1265–1271.

Verma, N.K., Moore, E., Blau, W., Volkov, Y., Babu, P.R., 2012. Cytotoxicity evaluation of nanoclays in human epithelial cell line A549 using high content screening and real-time impedance analysis. J. Nanopart. Res. 14, 1137–1147.

Viseras, M.T., Aguzzi, C., Cerezo, P., Viseras, C., Valenzuela, C., 2008a. Equilibrium and kinetics of 5-aminosalicylic acid adsorption by halloysite. Microporous Mesoporous Mater. 108, 112–116.

Viseras, C., Aguzzi, C., Cerezo, P., Bedmar, M.C., 2008b. Biopolymer–clay nanocomposites for controlled drug delivery. Mater. Sci. Technol. 24, 1020–1026.

Viseras, M.T., Aguzzi, C., Cerezo, P., Cultrone, G., Viseras, C., 2009. Supramolecularstructure of 5-aminosalycilic acid/halloysite composites. J. Microencapsul. 26, 279–286.

Viseras, C., Cerezo, P., Sanchez, R., Salcedo, I., Aguzzi, C., 2010. Current challenges in clay minerals for drug delivery. Appl. Clay Sci. 48, 291–295.

Viseras, C., Aguzzi, C., Cerezo, P., 2015. Medical and health applications of natural mineral nanotubes. In: Pasbakhsh, P., Churchman, G.-J. (Eds.), Natural Mineral Nanotubes: Properties and Applications. Apple Academic Press, Oakville, Canada; Waretown NJ, pp. 437–448.

Wagner, V., Dullaart, A., Bock, A.K., Zweck, A., 2006. The emerging nanomedicine landscape. Nat. Biotechnol. 24, 1211–1217.

Wang, S., Zhao, Y., Shen, M., Shi, X., 2012. Electrospun hybrid nanofibers doped with nanoparticles or nanotubes for biomedical applications. Ther. Deliv. 3, 1155–1169.

Ward, C.J., Song, S., Davis, E.W., 2010. Controlled release of tetracycline–HCl from halloysite–polymer composite films. J. Nanosci. Nanotechnol. 10, 6641–6649.

Wei, W., Abdullayev, E., Hollister, A., Mills, D., Lvov, Y.M., 2012. Clay nanotube/poly(methyl methacrylate) bone cement composites with sustained antibiotic release. Macromol. Mater. Eng. 297, 645–653.

Wei, W., Minullina, R., Abdullayev, E., Fakhrullin, R., Mills, D., Lvov, Y., 2014. Enhanced efficiency of antiseptics with sustained release from clay nanotubes. RSC Adv. 4, 488–494.

Yah, W.O., Yamamoto, K., Jiravanichanun, N., Otsuka, H., Takahara, A., 2010. Imogolite reinforced nanocomposites: multifaceted green materials. Materials 3, 1709–1745.

Yah, W.O., Takahara, A., Lvov, Y.M., 2012. Selective modification of halloysite lumen with octadecylphosphonic acid: new inorganic tubular micelle. J. Am. Chem. Soc. 134, 1853–1859.

Yamamoto, K., Otsuka, H., Wada, S.I., Sohn, D., Takahara, A., 2005a. Preparation and properties of [poly(methylmethacrylate)/imogolite] hybrid via surface modification using phosphoric acid ester. Polymer 46, 12386–12392.

Yamamoto, K., Otsuka, H., Wada, S.I., Sohn, D., Takahara, A., 2005b. Transparent polymer nanohybrid prepared by in situ synthesis of aluminosilicate nanofibers in poly(vinilalcohol) solution. Soft Matter 1, 372–377.

Yuan, P., Tan, D.Y., Bergaya, F., Yan, W.C., Fan, M.D., Liu, D., He, H.P., 2012a. Changes in structure, morphology, porosity, and surface activity of mesoporous halloysite nanotubes under heating. Clay Clay Miner. 60, 561–573.

Yuan, P., Southon, P.D., Liu, Z.W., Kepert, C.J., 2012b. Organosilane functionalization of halloysite nanotubes for enhanced loading and controlled release. Nanotechnology 23, 375705 (5pp).

Yuan, P., Tan, D., Bergaya, F., 2015. Properties and applications of halloysite nanotubes: recent research advances and future prospects. Appl. Clay Sci. 112–113, 75–93.

Zargarian, S., Haddadi-Asl, V., Hematpour, H., 2015. Carboxylic acid functionalization of halloysite nanotubes for sustained release of diphenhydramine hydrochloride. J. Nanopart. Res. 17, 218–231.

Zhang, Y., Chen, Y., Zhang, H., Zhang, B., Liu, J., 2013. Potent antibacterial activity of a novel silver nanoparticle-halloysite nanotube nanocomposite powder. J. Inorg. Biochem. 118, 59–64.

Zhao, Y., Wang, S., Guo, Q., Shen, M., Shi, X.J., 2013. Hemocompatibility of electrospun halloysite nanotube- and carbon nanotube-doped composite poly(lactic-co-glycolic acid) nanofibers. J. Appl. Polym. Sci. 127, 4825–4832.

Zhou, W.Y., Guo, B., Liu, M., Liao, R., Rabie, A.B.M., Jia, D.J., 2010. Poly(vinyl alcohol)/halloysite nanotubes bionanocomposite films: properties and in vitro osteoblasts and fibroblasts response. J. Biomed. Mater. Res. A 93, 1574–1587.

Current Drug Delivery, 2017, *14*, 902-903

OPINION ARTICLE

Use of Clays as Nanocarriers of First-Line Tuberculostatic Drugs

Esperanza Carazo[1,*], Ana Borrego-Sanchez[1,2], Carola Aguzzi[1], Pilar Cerezo[1] and Cesar Viseras[1,2]

[1]*Department of Pharmacy and Pharmaceutical Technology, School of Pharmacy, University of Granada, Campus of Cartuja, 18071 s/n, Granada, Spain;* [2]*Andalusian Institute of Earth Sciences, CSIC-University of Granada, Avda. de Las Palmeras 4, 18100, Armilla (Granada), Spain*

ARTICLE HISTORY

Received: February 18, 2016
Revised: April 02, 2016
Accepted: April 08, 2016

DOI:
10.2174/1567201813666160714160727

Tuberculosis (TB) is an infectious disease caused by the bacillus *Mycobacterium tuberculosis* (Mtb). TB ranks as the second leading cause of death from an infectious disease worldwide, particularly in development countries, only surpassed by the human immunodeficiency virus (HIV) [1-3]. Causing infection in one third of the world's population, TB might affect not only the lungs (pulmonary TB) but also other sites (extrapulmonary TB) [1]. Owing to its rapid spread, high morbidity and mortality rate, the development of an effective treatment for tuberculosis (TB) represents an important global health priority. "The limited effectiveness of current therapy stems largely from the lengthy and complicated nature of first-line treatment for active TB: a six- to nine month course of four drugs in combination (two months of isoniazid, rifampin, pyrazinamide and ethambutol, followed by four to seven months of isoniazid and rifampin)" [4]. On top of that, in developed nations there is likelihood to achieve a poor adherence in long-term therapies. This lack of patient compliance increases the necessity of the development of prolonged release systems in order to reduce the frequency of drug administration [5]. As if it were not enough, tuberculostatic drugs exhibit a poor/variable bioavailability and their stability might be decreased when administered in anti-tubercular fixed-dose combination (FDC) [6]. "In particular, the main stability concern with anti-TB FDC products is the interaction between rifampicin and isoniazid. Therefore, the observation of greater instability in three- or four-drug combinations lead to the conclusion that pyrazinamide and ethambutol hydrochloride are catalytic towards the reaction between rifampicin and isoniazid" [7]. Another limitation in the TB treatment is its toxicity. "A 2-month prophylactic regimen with rifampicin and pyrazinamide led to serious and fatal cases of hepatotoxicity" [8]. Likewise "combined pyrazinamide and ethambutol for latent tuberculosis infection may be associated with a high risk of hepatic toxicity, and warrants close monitoring" [9].

As previously mentioned, "patient non-compliance is the major drawback associated with the long duration chemotherapy of tuberculosis (TB); hence, reduction in dosing frequency forms an important therapeutic strategy" [10]. The information of the causes opens a few solutions that are discussed in this commentary.

As it is well documented in literature, clay minerals play a crucial role in modulating drug delivery and increasing drug stability [11-13]. Our group has a wide and long experience in the use of clays and clay-polymer nanocomposites as drug carriers not only for oral but topical and periodontal administration [14-21] as well.

The final aim of our research work in this field is to take advantage of the endless possibilities that clay minerals offer for the development of modified drug delivery systems (MDDS) of the four first-line tuberculostatic drugs (isoniazid, etambuthol, pyrazynamide and rifampicin) in order to obtain a one and only dosage form with improved stability and bioavailability and reduced adverse clinical effects. Should we succeed in fulfilling this enormous challenge, we will contribute greatly to the improvement of patient compliance, leading to increase the survival of TB patients.

Fig. (**1**) represents a posible model of the adsorption of the first-line tuberculostatic drugs in the interlayer of the laminar clay montmorillonite as an example of drug-clay interaction.

*Address correspondence to this author at the Department of Pharmacy and Pharmaceutical Technology, School of Pharmacy, University of Granada, Campus of Cartuja, 18071 s/n, Granada, Spain; Tel: +34-958243900; Fax: +34-958248958; E-mails: ecarazogil@ugr.es; cviseras@ugr.es

1875-5704/17 $58.00+.00

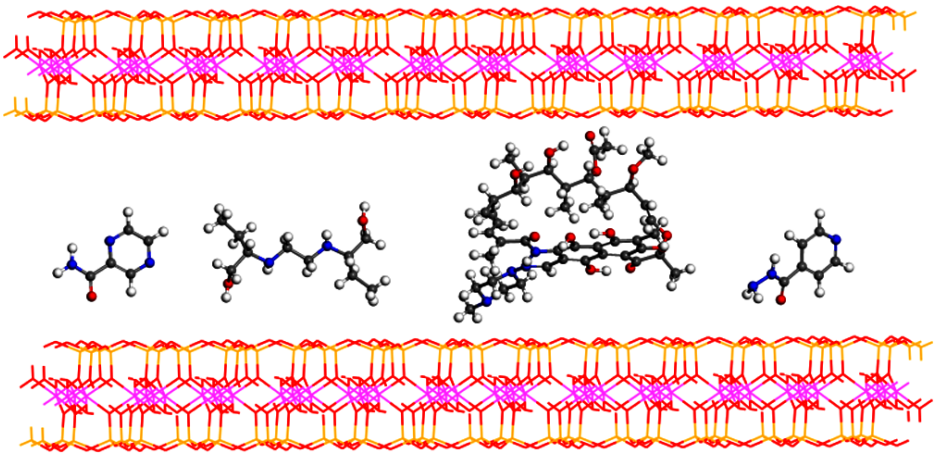

Fig. (1). Idealization of the interaction between first-line tuberculostatic drugs and montmorillonite. From left to right: isoniazid, rifampicin, ethambutol and pyrazinamide.

CONFLICT OF INTEREST

The authors declare no conflict of interest, financial or otherwise.

ACKNOWLEDGEMENTS

This study is supported by the Andalusian Project RNM-1897, the Andalusian group CTS-946 and the Ministry of Education, Culture and Sport of Spain (Predoctoral Grant FPU 13).

REFERENCES

[1] WHO Global Tuberculosis Report, **2015**.

[2] Zhang, J.; Ligu, M.; Yuanzhi, W.; Peizhi, L.; Haiyan, L.; Yi, H.; Bing, L.; Li, Y. Genotypes and drug susceptibility of *Mycobacterium tuberculosis* Isolates in Shihezi, Xinjiang Province, China. *BMC Res. Notes*, **2012**, *5*(309), 1-7.

[3] Kaewphinit, T.; Arunrut, N.; Kiatpathomchai, W.; Santiwatanakul, S.; Jaratsing, P.; Chansiri, K. Detection of *Mycobacterium tuberculosis* by using loop-mediated isothermal amplification combined with a lateral flow dipstick in clinical samples. *BioMed. Res. Int.*, **2013**, *2013*, 1-6.

[4] Ginsberg, A.M.; Spigelman, M. Challenges in tuberculosis drug research and development. *Nat. Med*., **2007**, *13*(3), 290-294.

[5] Traverso, G.; Langer, R. Perspective: Special delivery for the gut. *Nature*, **2015**, *519*(7544), S19.

[6] Saranjit, S.; Mariappan, T.T.; Sankar, R.; Sarda, N.; Baljinder, S. A critical review of the probable reasons for the poor/variable bioavailability of rifampicin from anti-tubercular fixed-dose combination (FDC) products, and the likely solutions to the problem. *Int. J. Pharm*., **2001**, *228*, 5-17.

[7] Bhutani, H.; Singh, S.; Jindal, K.C.; Chakraborti, A.K. Mechanistic explanation to the catalysis by pyrazinamide and ethambutol of reaction between rifampicin and isoniazid in anti-TB FDCs. *J. Pharm. Biomed. Anal*., **2005**, *39*, 892-899.

[8] American Thoracic Society (ATS) and the Centers for Disease Control (CDC). Update: Fatal and severe liver injuries associated with rifampin and pyrazinamide for latent tuberculosis infection, and revisions in American Thoracic Society/CDC Recommendations-United States, 2001. *Am. J. Respir. Crit. Care Med*., **2001**, *164*, 1319-1320.

[9] Younossian, A.B.; Rochat, T.; Ketterer, J.P.; Wacker, J.; Janssens, J.P. High hepatotoxicity of pyrazinamide and ethambutol for treatment of latent tuberculosis. *Eur. Respir. J.*, **2005**, *26*(3), 462-464.

[10] Pandey, R.; Zahoor, A.; Sharma, S.; Khuller, J.K. Nanoparticle encapsulated antitubercular drugs as a potential oral drug delivery system against murine tuberculosis. *Tuberculosis*, **2003**, *83*, 373-378.

[11] Aguzzi, C.; Cerezo, P.; Viseras, C.; Caramella, C. Use of clays as drug delivery systems: Possibilities and limitations. *Appl. Clay Sci*., **2007**, *36*(1), 22-36.

[12] Viseras, C.; Aguzzi, C.; Cerezo, P.; Bedmar, M.C. Biopolymer-clay nanocomposites for controlled drug delivery. *Mater. Technol*., **2008**, *24*(9), 1020-1026.

[13] Viseras, C.; Cerezo, P.; Sanchez, R.; Salcedo, I.; Aguzzi, C. Current challenges in clay minerals for drug delivery. *Appl. Clay Sci*., **2010**, *48*(3), 291-295.

[14] Viseras, C.; Aguzzi, C.; Cerezo, P. Medical and health applications of natural mineral nanotubes, natural mineral nanotubes: properties and applications, **2015**, 437.

[15] Aguzzi, C.; Capra, P.; Bonferoni, C.; Cerezo, P.; Salcedo, I.; Sanchez, R.; Caramella, C.; Viseras, C. Chitosan-silicate biocomposites to be used in modified drug release of 5-ASA. *Appl. Clay Sci*., **2010**, *50*(1), 106-111.

[16] Salcedo, I.; Aguzzi, C.; Sandri, G.; Bonferoni, M.C.; Mori, M.; Cerezo, P.; Sánchez, R.; Viseras, C.; Caramella, C. *In vitro* biocompatibility and mucoadhesion of montmorillonite chitosan nanocomposite: A new drug delivery. *Appl. Clay Sci*., **2012**, *55*, 131-137.

[17] Aguzzi, C.; Viseras, C.; Cerezo, P.; Salcedo, I.; Sanchez, R.; Valenzuela, C.; Release kinetics of 5-aminosalicylic acid from halloysite. *Colloids Surf. B. Biointerfaces*, **2013**, *105*, 75-80.

[18] Aguzzi, C.; Sandri, G.; Bonferoni, C.; Cerezo, P.; Rossi, S.; Ferrari, F.; Caramella, C.; Viseras, C. Solid state characterisation of silver sulfadiazine loaded on montmorillonite/chitosan nanocomposite for wound healing. *Colloid Surface B.*, **2014**, *113*, 152-157.

[19] Aguzzi, C.; Sandri, G.; Cerezo, P.; Ferrari, F.; Rossi, S.; Bonferoni, C.; Caramella, C.; Viseras, C. A novel bioadhesive semisolid formulation containing chitosan and tetracycline/layered clay complexes for local delivery into periodontal pockets. *Mater. Technol*., **2014**, *29*(B2), B108-B113.

[20] Salcedo, I.; Sandri, G.; Aguzzi, C.; Bonferoni, C.; Cerezo, P.; Sánchez, R.; Viseras, C. Intestinal permeability of oxytetracycline from chitosan-montmorillonite nanocomposites. *Colloids Surf. B. Biointerfaces*, **2014**, *117*, 441-448.

[21] Sandri, G.; Bonferoni, M.C.; Ferrari, F.; Rossi, S.; Aguzzi, C.; Mori, M.; Grisoli, P.; Cerezo, P.; Tenci, M.; Viseras, C.; Caramella, C. Montmorillonite-chitosan-silver sulfadiazine nanocomposites for topical treatment of chronic skin lesions: *In vitro* biocompatibility, antibacterial efficacy and gap closure cell motility properties. *Carbohyd. Polym*., **2014**, *102*(1), 970-977.

Colloids and Surfaces B: Biointerfaces 160 (2017) 337–344

Contents lists available at ScienceDirect

Colloids and Surfaces B: Biointerfaces

journal homepage: www.elsevier.com/locate/colsurfb

Full length article

Assessment of halloysite nanotubes as vehicles of isoniazid

E. Carazo[a], A. Borrego-Sánchez[a,b], F. García-Villén[a], R. Sánchez-Espejo[a], C. Aguzzi[a], C. Viseras[a,b,*], C.I. Sainz-Díaz[b], P. Cerezo[a]

[a] Department of Pharmacy and Pharmaceutical Technology, School of Pharmacy, University of Granada, Campus of Cartuja s/n, 18071, Granada, Spain
[b] Andalusian Institute of Earth Sciences, CSIC-University of Granada, Avda. de Las Palmeras 4, 18100, Armilla (Granada), Spain

ARTICLE INFO

Article history:
Received 24 May 2017
Received in revised form
11 September 2017
Accepted 13 September 2017
Available online 14 September 2017

Keywords:
Isoniazid
Halloysite
Adsorption
Thermodynamics
Molecular modeling
Nanohybrids

ABSTRACT

Equilibrium and thermodynamic aspects of the adsorption of isoniazid (INH) onto halloysite nanotubes (HLNTs) and characteristics of the resultant drug/nanocarrier systems are investigated. Equilibrium studies were performed in aqueous medium at different times, temperatures and drug concentrations. The overall adsorption process was explained as the result of two simple processes: adsorption on the activated sites of HLNTs and precipitation of INH on HLNTs surface. Formation of the INH-loaded HLNTs was spontaneous, endothermic and endoentropic, increasing the thermodynamic stability of the system ($\Delta H = 70.40$ kJ/mol; $\Delta S = 0.2519$ kJ/molK). Solid state characterization corroborated the effective interaction between the components that was also described by modeling at molecular level by quantum mechanics calculations along with empirical interatomic potentials. Transmission electron microphotographs confirmed the double allocation and homogeneous distribution of INH in the nanohybrids. FTIR spectra revealed the interaction via hydrogen bonds between the inner hydroxyl groups of HLNTs and N in INH molecules. Loading of INH in the nanohybrids was approximately 20% w/w. Effective loading of INH and activation energies of the interactions enable to propose the designed nanohybrids in the development of modified drug delivery systems.

1. Introduction

Tuberculosis (TB) ranks as the second leading cause of death worldwide from an infectious disease, particularly in development countries, only surpassed by the human immunodeficiency virus [1]. It is estimated that one third of the world's population is infected with *Mycobacterium tuberculosis*, with over 10 million new patients in 2015 and almost half a million of new cases of multidrug-resistant TB [1]. High morbidity and mortality rates make also the development of effective TB treatments an important global health priority [2]. The currently recommended treatment for new cases of TB consists on a six-month regimen of four first-line drugs (isoniazid, rifampicin, ethambutol and pyrazinamide), with a relatively low cost of about US$ 40 per person [1]. However, two factors determine a poor adherence to the therapy, especially in developed nations: its long-term duration and polymedication [3]. As a result of the low patient compliance, multidrug-resistant TB increases globally, requiring longer and more expensive treatments [1].

The design and development of new modified drug delivery systems arises as a good strategy to reduce the frequency of drug administration, increasing compliance and reducing resistant TB incidence [2,4]. A wide range of nanoparticulated systems have been proposed to modify drug delivery [5–12], even if most of them are based on expensive materials and/or technologies. The use of clay minerals as carriers for these systems appears as a low cost and biocompatible alternative [13–15]. In particular, halloysite is a multilayer nanotubular material resulting from the wrapping of 1:1 layers of kaolinite [16–18]. Halloysite nanotubes (HLNTs) have been proposed as a natural vehicle for encapsulation and modified release of several drugs [19–24].

With these premises, the aim of this work was to design INH/HLNTs hybrids useful in modified drug delivery treatment of TB. Equilibrium and thermodynamics aspects of the adsorption process between INH and HLNTs were fully investigated and the hybrid systems were then characterized by solid state techniques in order to determine the nature and degree of the interactions between the clay surfaces and the drug molecules. Complementary molecular modeling of the INH/HLNTs adsorption process was carried out in terms of quantum mechanics calculations along with empirical

* Corresponding author at: Department of Pharmacy and Pharmaceutical Technology, School of Pharmacy, University of Granada, Campus of Cartuja s/n, 18071, Granada, Spain.
E-mail address: cviseras@ugr.es (C. Viseras).

http://dx.doi.org/10.1016/j.colsurfb.2017.09.036
0927-7765/

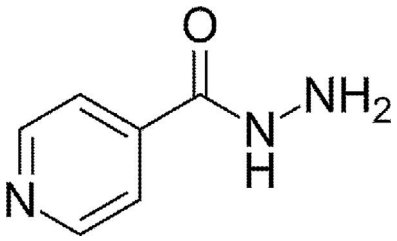

Fig. 1. INH structure.

interatomic potentials devoted to determine the most important interaction sites and to investigate mechanisms involved in the adsorption process.

2. Materials and methods

2.1. Materials

INH (Fig. 1) and HLNTs were purchased from Sigma Aldrich (Spain).

2.2. Adsorption studies

Adsorption experiments were carried out via intercalation solution technique to obtain equilibrium isotherms at different times and temperatures. 0.1 g of HLNTs were added to 20 ml of INH aqueous solutions with initial concentration (C_0) ranging from 0.05 to 0.5 M, in 25 ml Pyrex™ glass flasks and stirred (150 rpm) in a thermostated bath for different times (24 h, 48 h, one week and two weeks) at $30 \pm 0.1\,^{\circ}C$. The resulting suspensions were then centrifuged and the equilibrium concentration (C_e) of the drug in the supernatant was determined by UV spectroscopy (UV–vis spectrophotometer Lambda 25, Perkin Elmer, S) at 262 nm. The difference between the initial and equilibrium drug concentration was assumed to be due to drug adsorption onto HLNTs and the amount of INH retained per gram of clay was calculated.

One week experiments were also done at different temperatures (35, $40 \pm 0.1\,^{\circ}C$), once confirmed that this time was long enough to ensure that equilibrium was reached between INH adsorbed and INH in solution. Mathematical treatment of the data was performed [25], using the software packaging TableCurve 2D® (Systat Software Inc., UK) and the relevant adsorption parameters were obtained including monolayer adsorption capacity and equilibrium rate constants.

2.3. Solid state characterization

Hybrid systems prepared at $30\,^{\circ}C$ and initial concentration (C_0 = 0,25 mol/L) to achieve the monolayer adsorption capacity of HLNTs were characterized to determine the effective drug loading, the chemical groups involved in the adsorption process, as well as the presence and distribution of the drug in the internal lumen and/or external surface of HLNTs.

2.3.1. X-ray powder diffraction

X-Ray powder diffraction (XRPD) was done by using a Philips® X-Pert diffractometer with Cu Kα radiation, 40 kV, 40 mA, 3–70° 2θ exploration range, 6° 2θ min^{-1} scanning speed, 1×10^3 sensitivity and 2 s time constant. The diffraction data were analysed using the XPOWDER® software [26]. The experiments were run in triplicate (experimental error ±5%).

2.3.2. Electron microscopy studies

Samples were stained by drop deposition with uranyl acetate 2% (w/v) aqueous solution to achieve selective fixation of uranyl to the amino groups of the drug molecules [27]. Briefly, dehydrated samples were embedded for 2 h in a mixture of ethanol and epoxy resin for microscopy (EMbed 812, EMS Ltd., UK) and then included for 24 h in pure resin. Subsequently, polymerization was performed by heating the samples at 37 °C for 24 h and then at 70 °C for 24 h. The polymerized blocks, cut into ultrathin slices (900A° thickness) and placed on 300-mesh TEM copper grids (Neyco, France) were stained by deposition of uranyl acetate 2% (w/v) aqueous solution. The excess of the staining agent was absorbed onto filter paper and then grids were covered with a carbon film. The uranyl-stained samples were examined using a FEI Titan G2 60–300 ultra-high resolution transmission electron microscope (UHRTEM), coupled with analytical electron microscopy performed with a SUPER-X silicon-drift windowless energy-dispersive X-ray spectroscopy (EDX) detector. The AEM spectra were collected in STEM (Scaning Transmission Electron Microscopy) mode using a HAADF (High Angle Annular Dark Field) detector. X-ray chemical element maps were also collected.

2.3.3. Fourier transform infrared spectroscopy

Fourier Transform Infrared (FTIR) spectra were recorded on a FTIR spectrophotometer (JASCO 6200, with software SPECTRA MANAGER v2 and with an attenuated total reflectance (ATR) accessory). Measurements were carried out from 400 to 4000 cm^{-1} at 0.25 cm^{-1} resolution.

2.3.4. Thermal analysis

Differential scanning calorimetry (DSC) and thermogravimetric analysis (TGA) were carried out by using a METTLER TOLEDO mod. TGA/DSC1 with FRS5 sensor and a microbalance (precision 0.1 μg) (Mettler-Toledo GMBH). Samples were heated in air atmosphere at 10 °C/min. Analyses were done in triplicate.

2.4. Molecular modeling methodology and models

The INH molecule was taken from the crystallographic data of crystal form [28]. Our solid models were generated from the atomic coordinates of a slide of an HLNT from previous works [29] with the stoichiometry $Al_2Si_2O_5(OH)_4$. Periodic boundary conditions were applied to create a periodical crystal structure with the a and b cell parameters crossing the tube forming a cylinder section and the c cell parameter along the HLNT length. We established a = 50 Å, b = 50 Å large enough values for crystal lattice parameters in order to avoid interactions between vicinal tubes. However, the c cell parameter should be optimized point by point in order to connect the original slide to the next one forming a bridging O-Si distance similar of the others O-Si bonds. Then, this optimization yielded a value of c = 9.05 Å with the d(O-Si) = 1.67 Å. Hence, our unit cell of HLNT was a cylinder with an internal diameter of 27 Å formed with an external layer of Si oxide tetrahedra joined to an internal layer of aluminium hydroxide octahedral. The structure is neutral and the multilayer cylindrical structure was possible enlarging the AlOAl and OSiO angles to form the cylinder curvature. Hence, our unit cell of HLNT has the formula $Al_{76}Si_{76}O_{190}(OH)_{152}$ with 646 atoms. In some cases to avoid intermolecular interactions between adsorbates of vicinal cells a $1 \times 1 \times 2$ supercell was generated of HLNT, $Al_{152}Si_{152}O_{380}(OH)_{304}$, with 1292 atoms. In natural HLNTs the internal diameter is around 15–50 nm, nevertheless our models can represent a good scenario to reproduce the interactions at molecular level of the adsorption process.

The optimization of HLNT structure was performed with quantum mechanical calculations by using Density Functional Theory (DFT) with CASTEP code, within the generalized gradient approx-

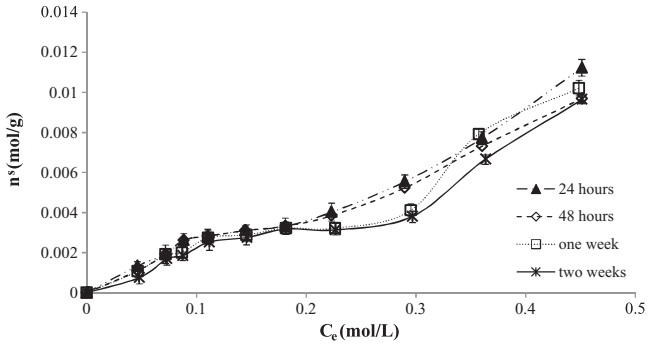

Fig. 2. Equilibrium isotherms of INH onto HLNTs at different times (mean values ± s.d.; n = 3).

imation (GGA), the Perdew–Burke–Ernzerhof (PBE) correlation exchange functional and the cut off energy of 300 eV [30]. The adsorbate was placed over the internal surface of the nanotube with the heterocycle ring in a parallel disposition with respect to surface at an average distance of 3 Å to the hydroxyl groups of the mineral surface. The adsorbed complexes were optimized maintaining the mineral structure fixed by using empirical interatomic potentials with the Compass force field that has provided good results in previous studies [30–32]. For non-bonding interactions, the coulomb and van de Waals interactions were calculated by the Ewald method with a cut-off of 12 Å.

3. Results and discussion

3.1. Equilibrium studies

The experimental equilibrium isotherms obtained at different adsorption times as n^s (moles of solute retained per gram of adsorbent) *vs* C_e are plotted in Fig. 2. The curves showed initial convex shapes, typical of L-class of Giles classification [33]. The behaviour at higher concentrations allowed further classifying the curves as L3 class, characterized by an inflection point from a plateau phase to concave profiles. This behaviour suggested possible precipitation of drug molecules on HLNTs surface. In comparison with short times (one day and two days), an enhanced delineation of the plateau phase was observed after one week, with no further improvement in equilibrium profiles at longer times. Consequently, one week was chosen as the optimal time to suitably define the adsorption curves.

Data obtained from one-week experiments were fitted to the following continuous function:

$$n^s = n_1^s + n_2^s = \sum_{i=1}^{i=2} \frac{K_i . n^s_{m(i)} . C}{K_i . C + 1} + k_f \; C^m \qquad (1)$$

where n^s = mol of sorbate adsorbed per gram of sorbent, n^s_m = monolayer retention capacity, C = equilibrium concentration, k_i = kinetic equilibrium constant, k_f = kinetic precipitation constant and m = constant.

Equation (1) suggests that the overall adsorption was the sum of two single processes: adsorption at the active surface sites of the sorbent (n^s_1) followed by precipitation of drug molecules (n^s_2) over the adsorbed monolayer [25].

The theoretical overall adsorption curves and contribution of single adsorption processes (n^s_1, n^s_2) resulting from data fitting are shown in Fig. 3.

At the studied temperatures, the initial contribution at lower drug concentrations was the n^s_1 process, whereas precipitation process (n^s_2) was significant only once the plateau phase was reached (C_e approximately 0.15 M), becoming predominant at

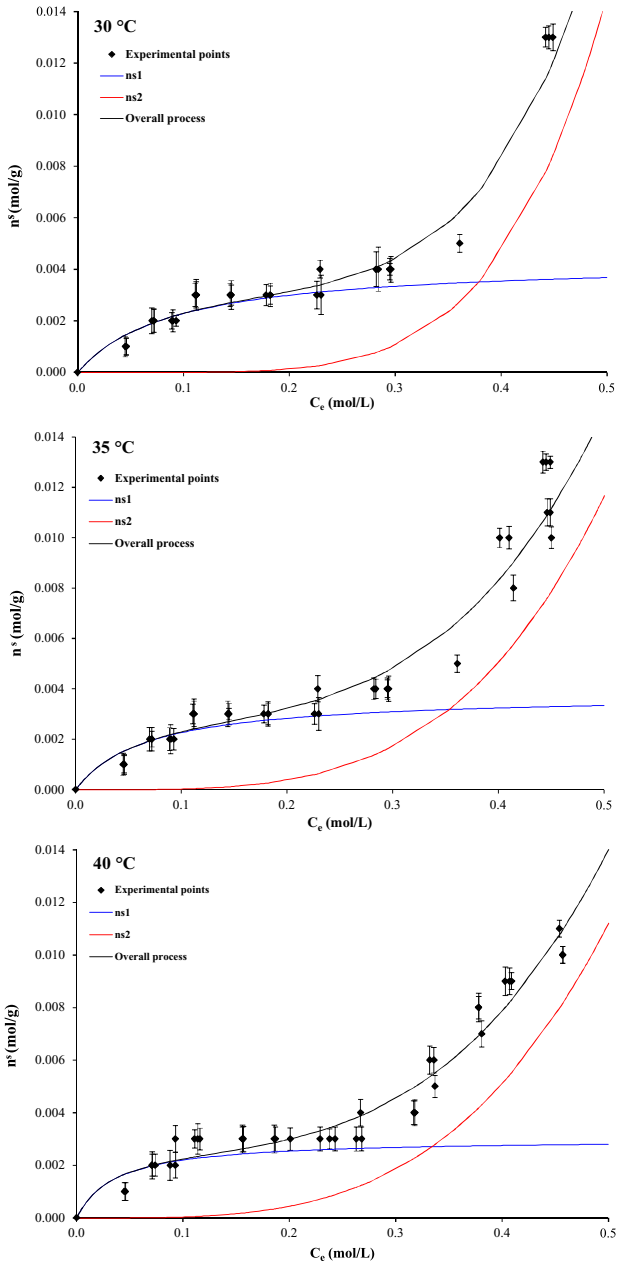

Fig. 3. Average experimental and theoretical equilibrium isotherms of INH onto HLNTs obtained at one week and three different temperatures (30 °C, 35 °C and 40 °C).

higher concentrations. The calculated parameters of Eq. (1) are shown in Table 1.

The monolayer adsorption capacity (n^s_m) increased with decreasing temperature, apparently suggesting that adsorption took place as an exothermic process. However, the trending of k_i values was compatible with an endothermic process. To elucidate the energetic behaviour of the system, k_i values were used to derive the thermodynamic activation functions by means of the following Eq. (2) [34]:

$$ln\frac{k_i}{T} = ln\frac{R}{Nh} + \frac{\Delta S^\circ}{R} - \frac{\Delta H^\circ}{R} \times \frac{1}{T} \qquad (2)$$

where k_i = kinetic equilibrium constant, R = gas constant, N = Avogadro's number, h = Planck's constant, T = temperature (K).

Table 1
Fitting parameters of Eqs. (1) and (2). for the adsorption of INH onto HLNTs at different temperatures and ΔG (activation energy) for the INH/HLNTs interaction.

	Eq. (1)				Eq. (2)		
T (°C)	n^s_m (mol/g)	$\mathbf{k}_i$	$\mathbf{k}_f$	**M**	ΔH° (kJ/mol)	ΔS° (kJ/molK)	ΔG (kJ/mol)
30	0.0025 ± 0.0002	11.271 ± 0.4865	0.508 ± 0.0245	5.116 ± 0.2147	70.40 ± 1.244	0.2519 ± 0.00127	−5.9257 ± 0.00021
35	0.0023 ± 0.0001	15.001 ± 0.3587	0.155 ± 0.0155	3.732 ± 0.1234			−7,1852 ± 0.00015
40	0.0021 ± 0.0001	27.575 ± 0.2111	0.128 ± 0.0872	3.513 ± 0.6547			−8,4447 ± 0.00071

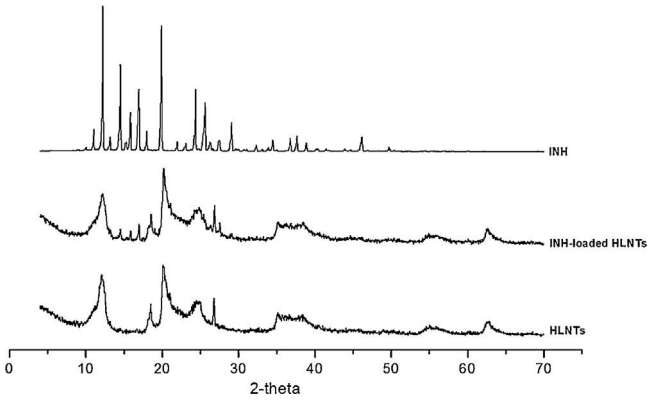

Fig. 4. XRPD patterns of INH-loaded HLNTs and their pure components (INH and HLNTs).

The calculated values are given in Table 1, which also includes ΔG (activation energy) values (calculated from the expression ΔG = ΔH-TΔS). The ΔH and ΔS values indicated that the adsorption of INH onto HLNTs was an endothermic and endoentropic process. The endothermic behaviour reflects that loss of solvation molecules (INH) is required for the incorporation of the adsorbable solute in the adsorbed phase. Otherwise, the positive ΔS value is due to the lower mobility of the adsorbed INH molecules, increasing the order of the system. Finally, the negative ΔG values revealed that at the studied conditions the adsorption process is thermodynamically spontaneous.

3.2. Solid state characterisation

3.2.1. XRPD

The powder X-ray diffraction patterns of the hybrid systems (INH-loaded HLNTs) and their individual components are given in Fig. 4.

INH showed a crystalline pattern, with main reflections at around 10°, 14°, 16° and 20° 2θ, characteristic of the drug crystals [35], whereas HLNTs showed the typical pattern of natural dehydrated halloysite, with a diffraction peak at 12.25° 2θ, corresponding to a d_{001}-spacing of 7.24 Å [36]. The dehydrated state was further confirmed by the presence of the 002 basal reflection at 24.55° 2θ [37]. INH-loaded HLNTs pattern was similar to that of HLNTs, including weak reflections coherent with the presence of crystalline INH over the adsorbed drug monolayer. This finding is in line with the beginning of the precipitation process at the plateau phase, as discussed previously (Fig. 3).

3.2.2. HREM/XEDS

Ultra-high resolution transmission electron microphotographs of the uranyl stained samples (Fig. 5) revealed the characteristic hollow tubular structure of the clay mineral both in native HLNTs (Fig. 5A1) and the hybrid system (Fig. 5B1). XEDS spectra of selected areas are also included in both cases, showing peaks of the nanotube components (O, Al and Si) and a weak Cu peak from the grids used to support the samples. The presence of uranium peaks in the nanohybrid XEDS (Fig. 5B1) allows us to confirm the effective loading of the drug. Uranyl was detected both in the interior (1) and edge (2) of halloysite tubules, which indicates the double allocation of INH molecules. X-ray maps of Si (Fig. 5A2 and B2), Al (Fig. 5A3 and B3) and U (Fig. 5A4 and B4) evidenced the elemental composition of the nanotubes as well as the homogeneous distribution of INH in the hybrid systems.

3.2.3. FTIR

FTIR spectra of the loaded nanotubes were compared to those of individual components to describe the probable interaction mechanisms (Fig. 6).

INH showed a band at 3303 cm^{-1}, due to N—H stretching vibrations. Bands at 1552 cm^{-1} and 1410 cm^{-1} corresponded to the ring C=N stretching (amide II) and the ring C=C symmetric stretching, respectively. Ring asymmetric bending were noticed twice by both bands at 1193 cm^{-1} stating for a ring C—C—H asymmetric bending and a ring C—C—C asymmetric bending with band at 745 cm^{-1}. The band observed at 886 cm^{-1} confirmed a C—N—C ring bending. The band at 1661 cm^{-1} was due to carbonyl of amide group stretching vibrations, while the one at 1631 cm^{-1} owed to the NH_2 deformation. Another band at 1331 cm^{-1} was attributed to C—N stretching vibrations, while a band at 1556 cm^{-1} was assigned to N—H bending vibrations [35,38,39].

The infrared spectrum of HLNTs showed bands at 3692 cm^{-1} and 3621 cm^{-1}, assigned to two Al_2OH-stretching bands. Band at 3670 cm^{-1}, detected under a noise level of 0.1, was attributed to the O—H stretching of inner-surface hydroxyl groups, while the one at 3545 cm^{-1} was referred to the out-of-phase vibration of the inner surface hydroxyls. The band at 1647 cm^{-1} revealed bending vibrations of the physically adsorbed water. The band at 1098 cm^{-1} was assigned to apical Si-O. Perpendicular stretching Si-O-Si vibrations were registered at 679 cm^{-1}. The peaks at 749 cm^{-1} and 796 cm^{-1} were assigned to OH translation vibration of halloysite OH units [40–42].

The INH-loaded HLNTs showed the above mentioned HLNTs Al_2OH-stretching bands at 3693 cm^{-1} and 3622 cm^{-1}, as well as those corresponding to the perpendicular Si-O-Si stretching vibrations (673 cm^{-1}), OH translation vibration of halloysite units (747 cm^{-1} and 793 cm^{-1}) and bending vibrations of the physically adsorbed water (1654 cm^{-1}). The band attributed to INH ring C—C—H asymmetric bending (1119 cm^{-1}), appeared in the INH-loaded HLNTs spectra at 1193 cm^{-1}. NH_2 deformation band which in INH spectra appeared at 1631 cm^{-1}, was also present in the spectra of the INH-loaded HLNTs but at a wavelength of 1654 cm^{-1}. However, the band at 3545 cm^{-1}, caused by the out of phase vibration of the inner surface hydroxyl in HLNTs was not observed in the spectrum of the INH-loaded HLNTs. Moreover, the little band noticeable at 3670 cm^{-1} in HLNTs spectrum, attributed to the O—H stretching of inner-surface hydroxyl groups, also disappeared in the INH-loaded HLNTs spectrum. These changes are clearly related with the interaction via hydrogen bonds between the inner hydroxyl groups of HLNTs and N in INH molecules.

3.2.4. Thermal analysis

DSC curve of INH showed an endothermic peak at 175 °C, corresponding to the melting of the drug, followed by an exothermic process beginning at 250 °C, due to decomposition (Fig. 7). DSC

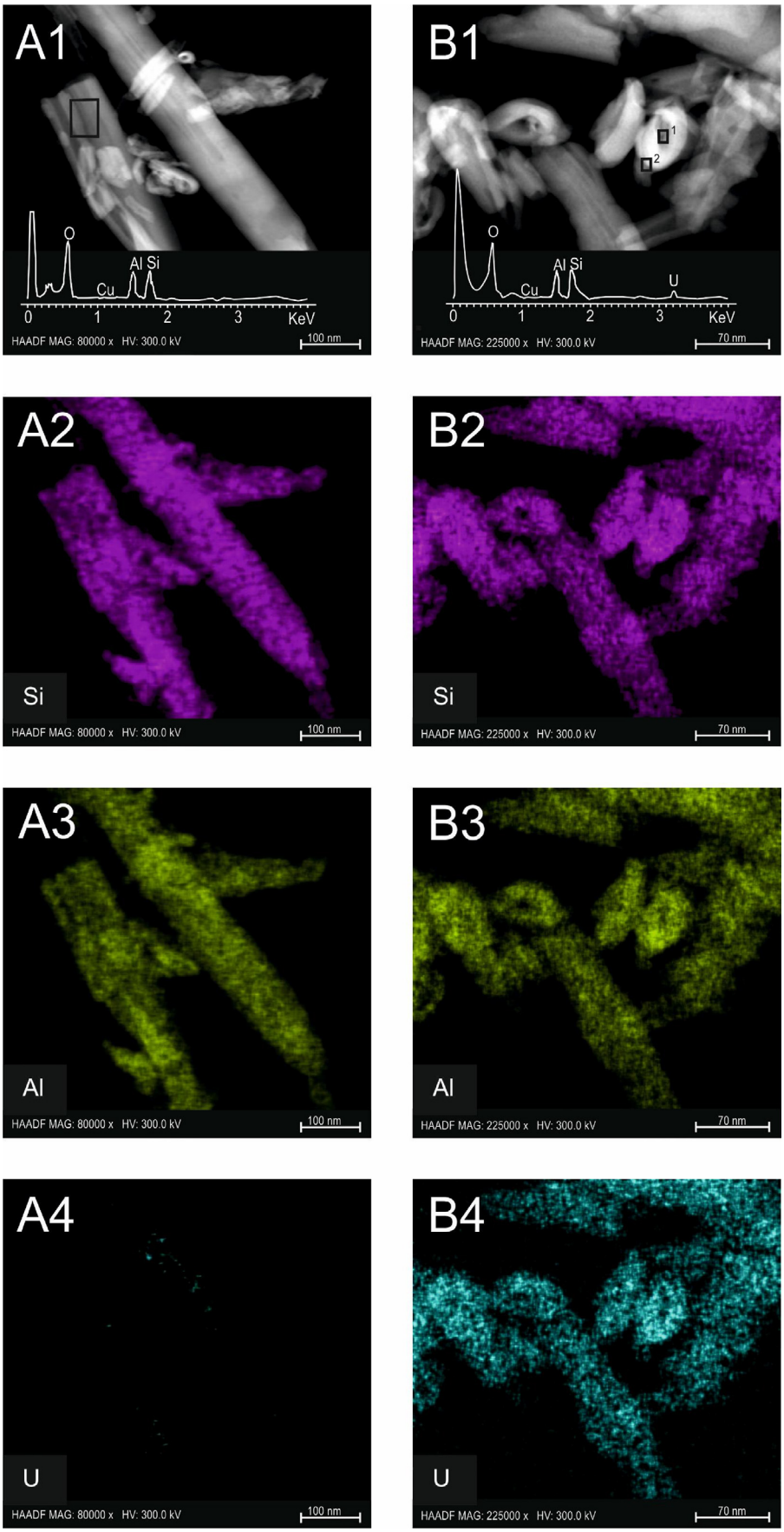

Fig. 5. UHRTEM microphotographs, XEDS analysis and elemental X-Ray maps of HLNTs (left) and INH-loaded HLNTs (right).

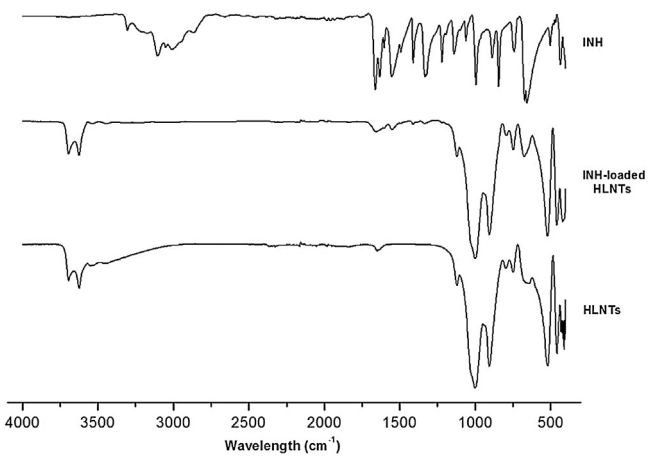

Fig. 6. FTIR spectra of INH-loaded HLNTs and their pure components (INH and HLNTs).

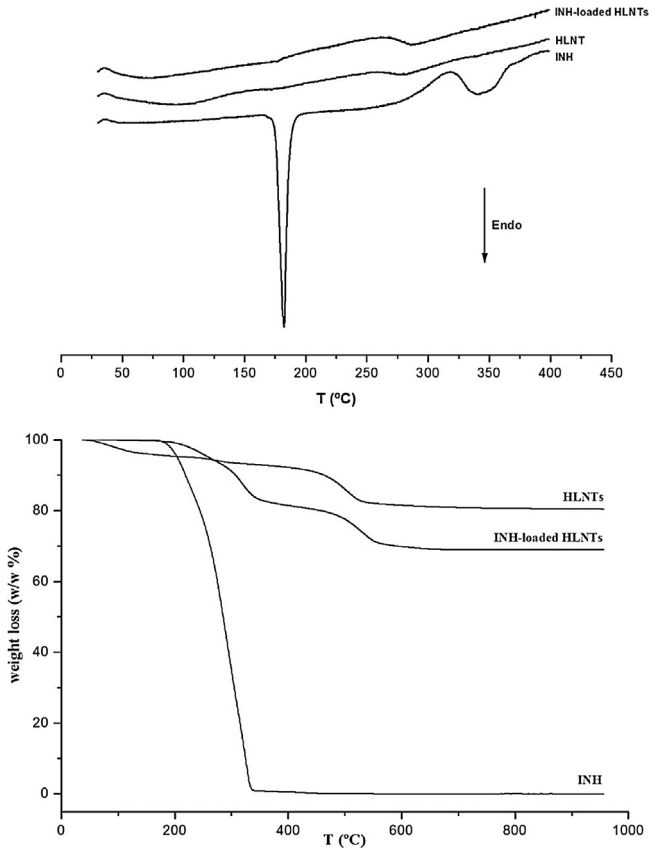

Fig. 7. DSC and TGA curves of INH-loaded HLNTs and their pure components (INH and HLNTs).

curves of HLNTs and INH-loaded HLNTs did not show any significant enthalpy changes at the studied temperature interval and conditions. TGA analysis allowed a more detailed comprehension of the thermal behaviour of the samples (Fig. 7). TGA curve of INH showed a complete loss of mass in the interval 150 °C – 350 °C, corresponding to the decomposition of the drug, and associated to the exothermic process observed in the DSC curve (Fig. 7). HLNTs exhibited two major mass losses at 100 °C approximately, attributed to dehydration of the physically adsorbed water [43] and a second loss in the interval 400 °C – 600 °C, ascribed to dehydroxylation of the structural aluminol groups (AlOH) [44]. HLNTs is an extremely thermostable material, with a solid residue of 85.2 ± 0.09% w/w% of the initial mass at 1000 °C. TGA curve of INH-loaded HLNTs showed the decomposition of the drug as well as the dehydroxylation of the clay. Weight loss ascribed to INH decomposition was calculated according to the rule of mixtures for the residual masses at 1000 °C and taking into account the water content (weight loss between 25 and 150 °C) [45]. The calculated value (18.9 ± 0.12% w/w) was in line with the theoretical amount of INH retained by the nanotubes calculated from the n^{s}_{m} at 30 °C (25.5% w/w).

3.3. Molecular modeling

The adsorption of the INH molecule in the space of HLNTs was studied to determine the most important interaction sites with the mineral. This adsorption was simulated in both of two halloysite models and one INH molecule was placed over the internal surface of HLNTs. Dry conditions without presence of water molecules

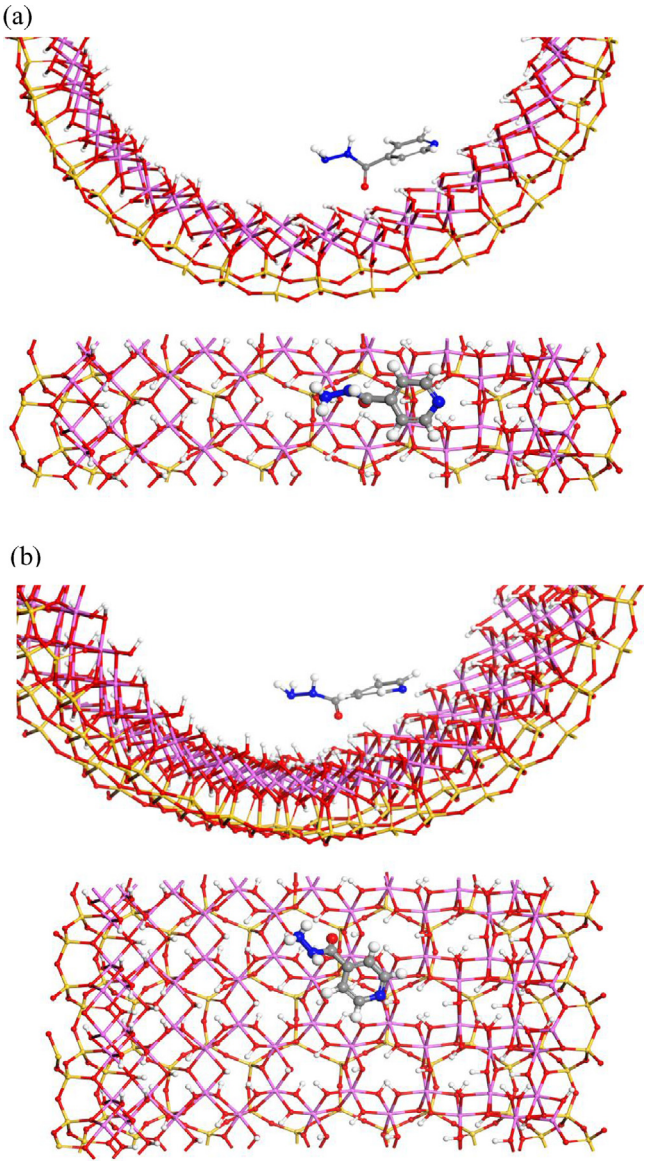

Fig. 8. Adsorption complexes H1 (a) and H2 (b) of the INH molecule adsorbed on the internal surface of HLNTs optimized with Compass FF, views from (001) and (100) planes. The atoms of silicon, aluminium, hydrogen, carbon, nitrogen and oxygen are described in yellow, pink, white, grey, blue and red, respectively. (For interpretation of the references to colour in this figure legend, the reader is referred to the web version of this article.)

were used to avoid additional interactions that can hide the actual adsorbate-surface interactions. In the $Al_{76}Si_{76}O_{190}(OH)_{152}$ model the INH molecule was orientated along the cylinder section (H1) and in the $Al_{152}Si_{152}O_{380}(OH)_{304}$ model the INH molecule was orientated along the nanotube (H2) (Fig. 8).

After the optimization, INH had similar behaviour in the adsorption of halloysite surface for both models. A conformational change was produced in the INH molecule where the carbonyl group was oriented in a perpendicular direction with respect to the heterocyclic ring. The carbonyl group and the heterocyclic N atom were approached to be coordinated with the H atoms of the OH group of HLNT surface, whereas the hydrazine moiety was oriented towards the centre of the nanotube. In both adsorption complexes the adsorbate maintained a similar orientation with respect to the HLNT with the heterocyclic ring in a parallel disposition with respect to the mineral surface. In H1 the main adsorbate-surface interactions were strong H bonds between the hydroxyl groups of mineral surface and the carbonyl and heterocyclic N atom of adsorbate with d(CO···HO) = 1.94 Å and d(N···HO) = 1.56 Å distances. Additional electrostatic interactions were detected between the N atom of the NH_2 group of INH with the H of OH groups of HLNT surface with d(HN···HO) = 3.05 Å. In H2, similar interactions were observed with d(CO···HO) = 1.69 Å, and d(N···HO) = 1.59 Å distances. Also, the N of the aromatic ring had interactions with the H of the OH group of HLNT surface, the distance is 1.59 Å. Additional electrostatic interactions were detected between the N atom of the NH group of INH with the hydroxyl H atoms of HLNT surface with d(HN···HO) = 2.89 Å.

4. Conclusions

Interaction of INH with HLNTs occurs according to two simple processes: adsorption and precipitation of drug molecules onto the nanoclay inner and outer surfaces. Formation of the INH-loaded HLNTs is a spontaneous process, endothermic and endoentropic that increases the thermodynamic stability of the system. Solid state characterization corroborates the effective interaction between the components. The adsorption of INH on the internal surface of HLNTs was possible to be modelled at molecular level with molecular modeling methods finding conformational changes in the molecule and strong hydrogen bond between the carbonyl group and heterocyclic N atom with the hydroxyl H atoms of the mineral surface. Effective loading of INH and the total amount adsorbed by the clay nanotubes as well as the measured activation energies of the interactions are promising features for the design of modified delivery systems able to promote the patient compliance in the treatment of tuberculosis. Complementary studies will be performed to assess biocompatibility and delivery release patterns of the drug from the nanotubes.

Acknowledgements

This study was supported by the Projects CGL2016-80833-R and RNM-1897, group CTS-946 and Predoctoral GrantFPU13/04765. Authors are thankful to H.A. Duarte for providing atomic coordinates of halloysite and to the CSIC Computational Center for computation facilities.

Appendix A. Supplementary data

Supplementary data associated with this article can be found, in the online version, at http://dx.doi.org/10.1016/j.colsurfb.2017.09.036.

References

[1] WHO, Global Tuberculosis Report, 2016.
[2] A.M. Ginsberg, M. Spigelman, Challenges in tuberculosis drug research and development, Nat. Med. 13 (3) (2007) 290–294.
[3] G. Traverso, R. Langer, Perspective Special delivery for the gut, Nature 519 (2015) 7544.
[4] E. Carazo, A. Borrego, C. Aguzzi, P. Cerezo, C. Viseras, Use of clays as nanocarriers of tuberculostatic drugs, Curr. Drug Deliv. 13 (2016) 1–2.
[5] X. Zhan, Y.Q. Guan, Design of magnetic nanoparticles for hepatocellular carcinoma treatment using the control mechanisms of the cell internal nucleus and external membrane, J. Mater. Chem. B 3 (2015) 4191–4204.
[6] K.P. Miller, L. Wang, B.C. Benicewicz, A.W. Decho, Inorganic nanoparticles engineered to attack bacteria, Chem. Soc. Rev. 44 (2015) 7787–7807.
[7] L. Dai, X. Cao, K.F. Liu, C.X. Li, G.F. Zhang, L.H. Deng, C.L. Si, J. He, J.D. Lei, Self-assembled targeted folate-conjugated eight-arm-polyethylene glycol–betulinic acid nanoparticles for co-delivery of anticancer drugs, J. Mater. Chem. B 3 (2015) 3754–3766.
[8] C.M.J. Hu, R.H. Fang, B.T. Luk, L. Zhang, Polymeric nanotherapeutics: clinical development and advances in stealth functionalization strategies, Nanoscale 6 (2014) 65–75.
[9] R.R. Adhikary, P. More, R. Banerjee, Smart nanoparticles as targeting platforms for HIV infections, Nanoscale 7 (2015) 7520–7534.
[10] D.J. Irvine, Drug delivery: one nanoparticle, one kill, Nat. Mater. 10 (2011) 342–343.
[11] E. Blanco, H. Shen, M. Ferrari, Principles of nanoparticle design for overcoming biological barriers to drug delivery, Nat. Biotechnol. 33 (2015) 941–951.
[12] M. Ferrari, Nanogeometry beyond drug delivery, Nat. Nanotechnol. 3 (2008) 131–132.
[13] C. Viseras, C. Aguzzi, P. Cerezo, M.C. Bedmar, Biopolymer–clay nanocomposites for controlled drug delivery, Mater. Technol. 24 (9) (2008) 1020–1026.
[14] C. Viseras, P. Cerezo, R. Sánchez, I. Salcedo, C. Aguzzi, Current challenges in clay minerals for drug delivery, Appl. Clay Sci. 48 (3) (2010) 291–295.
[15] G. Sandri, M.C. Bonferoni, S. Rossi, F. Ferrari, C. Aguzzi, C. Viseras, C. Caramella, Clay minerals for tissue regeneration, repair, and engineering, Wound Healing Biomater. Funct. Biomater. 2 (2016) 385–402.
[16] T.F. Bates, F.A. Hildebrand, A. Swineford, Morphology and structure of endellite and halloysite, Am. Mineral. 35 (7–8) (1950) 463–484.
[17] B. Singh, I.D.R. Mackinnon, Experimental transformation of kaolinite to halloysite, Clays Clay Miner. 44 (6) (1996) 825–834.
[18] P. Yuan, D. Tan, F. Annabi-Bergaya, Properties and applications of halloysite nanotubes: recent research advances and future prospects, Appl. Clay Sci. 112–113 (2015) 75–93.
[19] E. Abdullayev, Y. Lvov, Halloysite clay nanotubes for controlled release of protective agents, J. Nanosci. Nanotechnol. 11 (11) (2011) 10007–10026.
[20] E. Abdullayev, Y. Lvov, Halloysite clay nanotubes as a ceramic skeleton for functional biopolymer composites with sustained drug release, J. Mater. Chem. B 1 (2013) 2894–2903.
[21] C. Viseras, C. Aguzzi, P. Cerezo, Medical and health applications of natural mineral nanotubes, in: Natural Mineral Nanotubes: Properties and Applications, Apple Academic Press Oakville, Canada and Waretown, 2015, pp. 437–448.
[22] C. Aguzzi, G. Sandri, P. Cerezo, E. Carazo, C. Viseras, Health and medical applications of tubular clay minerals, in: P. Yuan, A. Thill, F. Bergaya (Eds.), Nanosized Tubular Clay Minerals, Elsevier, 2016, pp. 708–725.
[23] R. Yendluri, D.P. Otto, M.M. De Villiers, V. Vinokurov, Y.M. Lvov, Application of halloysite clay nanotubes as a pharmaceutical excipient, Int. J. Pharm. 521 (2017) 267–273.
[24] M. Fizir, P. Dramou, K. Zhang, C. Sun, C. Pham-Huy, H. He, Polymer grafted-magnetic halloysite nanotube for controlled and sustained release of cationic drug, J. Colloid Interface Sci. (2017), http://dx.doi.org/10.1016/j.jcis.2017.04.011.
[25] M.T. Viseras, C. Aguzzi, P. Cerezo, C. Viseras, C. Valenzuela, Equilibrium and kinetics of 5-aminosalicylic acid adsorption by halloysite, Microporous Mesoporous Mater. 108 (1–3) (2008) 112–116.
[26] J.D. Martín-Ramos, X-Powder, a software package for powder X-ray diffraction analysis, in: Legal Deposit G.R.1001/04, 2004 http://www.xpowder.com.
[27] M.T. Viseras, C. Aguzzi, P. Cerezo, G. Cultrone, C. Viseras, Supramolecular structure of 5-aminosalycilic acid/halloysite composites, J. Microencapsulation 26 (3) (2009) 279–286.
[28] G. Rajalakshmi, V.R. Hathwar, P. Kumaradhas, Topological analysis of electron density and the electrostatic properties of isoniazid: an experimental and theoretical study, Acta Crystallogr. 70 (2014) 331–341.
[29] BIOVIA Materials Studio, version 2016 (2016). Dassault Systemes.
[30] A. Borrego-Sánchez, C. Viseras, C. Aguzzi, C.I. Sainz-Díaz, Molecular and crystal structure of praziquantel: spectroscopic properties and crystal polymorphism, Eur. J. Pharm. Sci. 92 (2016) 266–275.
[31] A. Borrego-Sánchez, A. Hernández-Laguna, C.I. Sainz-Díaz, Molecular modeling and infrared and Raman spectroscopy of the crystal structure of the chiral antiparasitic drug Praziquantel, J. Mol. Model. 23 (4) (2017) 106.
[32] L. Guimarães, A.N. Enyashin, G. Seifert, H.A. Duarte, Structural, electronic, and mechanical properties of single-Walled halloysite nanotube models, J. Phys. Chem. C 114 (2010) 1358–11363.

[33] C. Hinz, Description of sorption data with isotherm equations, Geoderma 99 (3–4) (2001) 225–243.
[34] C. Valenzuela-Calahorro, A. Navarrete-Guijosa, M. Stitou, E. Cuerda-Correa, Retention of progesterone by an activated carbon: study of the adsorption kinetics, Adsorption 10 (1) (2004) 19–28.
[35] S.C. Angadi, L.S. Manjeshwar, T.M. Aminabhavi1, Interpenetrating polymer network blend microspheres of chitosan and hydroxyethyl cellulose for controlled release of isoniazid, Int. J. Biol. Macromol. 47 (2) (2010) 171–179.
[36] S. Rooj, A. Das, V. Thakur, R.N. Mahaling, A.K. Bhowmick, G. Heinrich, Preparation and properties of natural nanocomposites based on natural rubber and naturally occurring halloysite nanotubes, Mater. Des. 31 (4) (2010) 2151–2156.
[37] S.R. Levis, P.B. Deasy, Use of coated microtubular halloysite for the sustained release of diltiazem hydrochloride and propranolol hydrochloride, Int. J. Pharm. 253 (1–2) (2003) 145–157.
[38] G.A. Brewer, Isoniazid, Anal. Profiles Drug Subst. 6 (1977) 183–258.
[39] S. Gunasekaran, E. Sailatha, S. Seshadri, S. Kumaresan, FTIR, FT Raman spectra and molecular structural confirmation of isoniazid, Indian J. Pure Appl. Phys. 47 (2009) 12–18.
[40] R.L. Frost, Fourier transform Raman spectroscopy of kaolinite: dickite and halloysite, Clay Clay Miner. 43 (2) (1995) 191–195.
[41] X. Sun, Y. Zhang, H. Shen, N. Jia, Direct electrochemistry and electrocatalysis of horseradish peroxidase based on halloysite nanotubes/chitosan nanocomposite film, Electrochim. Acta 56 (2) (2010) 700–705.
[42] B. Szczepanik, P. Słomkiewicza, M. Garnuszeka, K. Czecha, D. Banaśc, A. Kubala-Kukuśc, I. Stabrawac, The effect of chemical modification on the physico-chemical characteristics of halloysite: FTIR, XRF, and XRD studies, J. Mol. Struct. 1084 (2015) 16–22.
[43] G.W. Brindley, K. Robinson, Randomness in the structures of kaolinitic clay minerals, Trans. Faraday Soc. 42 (1946) 198–205.
[44] E. Joussein, S. Petit, J. Churchman, B. Theng, D. Righi, B. Delvaux, Halloysite clay minerals–a review, Clay Miner. 40 (4) (2005) 383–426.
[45] G. Cavallaro, G. Lazzara, S. Milioto, Dispersions of nanoclays of different shapes into aqueous and solid biopolymeric matrices. Extended physicochemical study, Langmuir 27 (3) (2011) 1158–1167.

Applied Clay Science 160 (2018) 180–185

Contents lists available at ScienceDirect

Applied Clay Science

journal homepage: www.elsevier.com/locate/clay

Research paper

Adsorption and characterization of palygorskite-isoniazid nanohybrids

E. Carazo[a], A. Borrego-Sánchez[a,b], F. García-Villén[a], R. Sánchez-Espejo[a], C. Viseras[a,b,*], P. Cerezo[a], C. Aguzzi[a]

[a] Department of Pharmacy and Pharmaceutical Technology, School of Pharmacy, University of Granada, Campus of Cartuja s/n, 18071 Granada, Spain
[b] Andalusian Institute of Earth Sciences, CSIC-University of Granada, Avda. de Las Palmeras 4, 18100 Armilla, Granada, Spain

ARTICLE INFO

Keywords:
Isoniazid
Palygorskite
Adsorption
Thermodynamics
Nanohybrids

ABSTRACT

Studies of the equilibrium and thermodynamic aspects of the adsorption of isoniazid onto a pharmaceutical-grade palygorskite and features of the resultant clay drug nanohybrid systems were carried out. Equilibrium studies were performed in aqueous medium at different times and temperatures. The overall adsorption process was explained as the result of two simple processes: drug adsorption on the activated sites of palygorskite and a slight precipitation phase of drug molecules over the adsorbed monolayer. Formation of the nanohybrid was spontaneous, exothermic and exoentropic, obtaining an increase in the thermodynamic stability of the system ($\Delta H = -48{,}82$ kJ/mol; $\Delta S = -0.14$ kJ/mol K). A full and comprehensive study of the solid state characterization corroborated the effective interaction between the components. Total amount of INH loaded was about 20% w/w. FTIR spectra revealed the interaction via water bridges between the endocyclic N of the drug and surface OH groups of palygorskite. Surface charge studies confirmed the non-electrostatic nature of the interactions.

1. Introduction

Nanotechnology offers numerous possibilities in the treatment of global concern diseases as tuberculosis, the second cause of death from an infectious illness worldwide (WHO, 2015). Design of nanoparticulate drug delivery systems with the current tuberculostatic agents appears as an interesting strategy for improvement of therapy, as a result of the increase in patient compliance and decrease of drug adverse effects (Sharma et al., 2017). The use of clay minerals as nanocarriers for tuberculostatic drugs is a current matter of growing interest (Carazo et al., 2016). In particular, halloysite nanotubes (Carazo et al., 2017) and montmorillonite-polymer nanocomposites (Verma and Riaz, 2017) have been proposed as effective drug platforms in tuberculosis treatment.

Palygorskite is a fibrous clay mineral with several industrial applications (Galan, 1996) and considered a suitable candidate to vehicle bioactive molecules due to its large surface area (López-Galindo et al., 2011; Mura et al., 2016; Tenci et al., 2017). Palygorskite structure was described as a 2:1 clay mineral with tetrahedral silica sheets periodically inverted with respect to the tetrahedral bases leading to a periodically interruption in the octahedral sheets and cations occupying terminal positions must complete their coordination sphere with water molecules (Bradley, 1940). The most intense absorption sites of palygorskite with organic molecules are surface hydroxyls and Lewis acidic centers (Serratosa, 1979). Isoniazid ($C_6H_7N_3O$; 137.14 g/mol), also known as isonicotinyl hydrazine, is a first-line drug in the prevention and treatment of tuberculosis (WHO, 2015). Akyuz et al. (2010) reported changes in infrared spectrum of palygorskite after interaction with isoniazid. Nevertheless, it has not been suggested until now the potential use of this mineral in the design of modified drug delivery systems of isoniazid.

With these premises, aim of this work was the study of the thermodynamics and equilibrium features of the adsorption of the first-line tuberculostatic drug isoniazid onto palygorskite as a prior step in the development of a modified release system based on the drug-clay mineral interactions. Solid state characterization of the pure materials and the resulting hybrid system was carried out in order to confirm the effectively loading of the drug, to assess qualitative and quantitatively the different interactions involved.

2. Materials and methods

2.1. Materials

Isoniazid (INH) from Sigma Aldrich (Spain) and a pharmaceutical grade palygorskite (Pharmasorb® Colloidal) (Pal) from Basf (Germany)

* Corresponding author at: University of Granada, Instituto Andaluz de Ciencias de la Tierra, CSIC, Faculty of Pharmacy, Department of Pharmaceutical Technology, 18071, Granada, Spain.
E-mail address: cviseras@ugr.es (C. Viseras).

https://doi.org/10.1016/j.clay.2017.12.027
Received 3 October 2017; Received in revised form 11 December 2017; Accepted 14 December 2017
Available online 24 December 2017

were used as received. PAL had been fully characterized and used in previous studies (Viseras and López-Galindo, 1999, 2000; Viseras et al., 2000, 2001; Cerezo et al., 2001; Mura et al., 2016; Tenci et al., 2017).

All the reagents used were of analytical grade.

2.2. Adsorption studies

Adsorption experiments were performed following Carazo et al. (2017) to obtain equilibrium isotherms at different times and temperatures. Briefly, known amounts of Pal were dispersed into INH aqueous solutions with initial concentration (C_0) ranging from 0.05 to 0.5 mol/L, for different times (24 h, 48 h and one week) and temperatures (20, 30, 40 ± 0.1 °C). The resulting dispersions were centrifuged and the equilibrium concentration (C_e) of the drug in the supernatant was determined by UV spectroscopy (UV–Vis spectrophotometer Lambda 25, Perkin Elmer, S) at 262 nm. The difference between C_0 and C_e was used to calculate the amount of drug retained per gram of clay (expressed as n^s: mol of INH/g of Pal). Non-linear fitting of the data was performed using the software packaging TableCurve 2D® (Systat Software Inc., UK) and kinetic and thermodynamic parameters were determined.

2.3. Solid State characterization

2.3.1. Preparation of the drug-clay nanohybrids

Hybrid systems corresponding to the monolayer adsorption capacity of the clay mineral (48 h, C_0 = 0,2 mol/L) were prepared following the same procedure described above and then characterized.

2.3.2. Fourier transform infrared spectroscopy

Fourier transform infrared (FTIR) spectra were recorded on a FTIR spectrophotometer (JASCO 6200, with software SPECTRA MANAGER v2 and with an attenuated total reflectance (ATR) accessory). Measurements were carried out from 400 to 4000 cm^{-1} at 0.25 cm^{-1} resolution.

2.3.3. Thermal analysis

Thermogravimetric analysis (TGA) and Differential scanning calorimetry (DSC) were carried out by using a METTLER TOLEDO mod. TGA/DSC1 with FRS5 sensor and a microbalance (precision 0.1 μg) (Mettler-Toledo GMBH). Samples were heated in air atmosphere at 10 °C/min in the ranges 30–950 °C (TGA) and 30–400 °C (DSC).

2.3.4. X-ray powder diffraction

X-ray powder diffraction (XRPD) was done by using a Philips® X-Pert diffractometer with Cu Kα radiation. The diffraction data were analyzed using the XPOWDER® software (Ramos, 2004).

2.3.5. Surface charge

Surface charge properties of clay and drug-clay nanohybrid were determined from their zeta potential (ζ) values in aqueous suspension (0.05% w/v) on a Malvern Zetasizer Nano instrument (Malvern Instruments, USA).

3. Results and discussion

3.1. Equilibrium studies

Experimental equilibrium isotherms are plotted in Fig. 1 as n^s (moles of INH retained per gram of Pal; mol/g) vs C_e (mol/L).

The effect of time was almost negligible in the range of temperatures studied. Only a better outline of the plateau after 48 h in comparison with 24 h was observed, with no further improvement after one week of contact time. Replicates of the 48 h experiments were performed and the experimental data were collected to be mathematically treated. The isotherms fit the following equation, previously proposed to describe the adsorption of drugs to inorganic solid sorbents (Carazo et al., 2017) (Eq. 1):

$$n^s = n_1^s + n_2^s = \sum_{i=1}^{i=2} \frac{K_i.\ n^s_{m(i)}.\ C}{K_i.\ C + 1} + k_f C^m \quad (1)$$

Where n^s = moles of adsorbate adsorbed per gram of sorbent, n_1^s = adsorption at the active surface sites of the sorbent, n_2^s = precipitation of drug molecules over the adsorbed monolayer, n_m^s = monolayer retention capacity, C = equilibrium concentration, k_i = kinetic equilibrium constant, k_f = kinetic precipitation constant, n = partial order of the process respect to the concentration (C) and m = constant.

Average experimental data and theoretical calculated curves (adsorption, precipitation and the sum of both processes) are shown in Fig. 2. The global adsorption process is composed by the sum of two simple processes (adsorption of INH on the activated sites of Pal (n_1^s) followed by a slight precipitation of INH over the adsorbed monolayer (n_2^s)). The calculated fitting parameters (Table I) described adequately the experimental results with correlation coefficient ≥ 0.998. Monolayer retention capacity (n_m^s) slightly increased with temperature, whereas kinetic equilibrium constant (k_i) significantly decreased. The increase in temperature makes easier the dehydration of the drug molecules previous to their adsorption but concomitantly increase their mobility. K_f values are very low, suggesting a slight precipitation over the adsorbed drug monolayer.

K_i values obtained from Eq. (1) were used to determine the differential adsorption enthalpy ΔH° (kJ/mol) and the differential adsorption entropy ΔS° (kJ/mol K) values using the linearization of the Eyring equation (Eq. 2) by plotting ln (k/T) vs (1/T):

$$ln\frac{k_i}{T} = ln\frac{R}{Nh} + \frac{\Delta S^\circ}{R} - \frac{\Delta H^\circ}{R} \times \frac{1}{T} \quad (2)$$

(k = kinetic equilibrium constant (ki), R = gas constant, N = Avogadro's number, h = Planck's constant, T = temp (K)).

The calculated values are given in Table II, which also includes the differential activation energy ΔG° (kJ/mol) calculated via the expression: $\Delta G^\circ = \Delta H^\circ - T\Delta S^\circ$. The previous mentioned decrease of k_i values with the increase of temperature suggested an exoenergetic process that was corroborated by negative values of enthalpy (ΔH°) and activation energy (ΔG°). Adsorption of isoniazid over palygorskite was therefore an exothermic process. The thermodynamic probability of adsorption (ΔG°) revealed that the reversible adsorption-desorption process moved towards the net adsorption. Negative values of ΔS° corresponded to the reduced degree of freedom of the INH adsorbed molecules with respect to those in dissolution.

3.2. Solid State characterization

3.2.1. Fourier transform infrared spectroscopy

FTIR spectra of INH, Pal and the clay–drug nanohybrid were carried out to determine the nature of the interactions involved in the adsorption process (Fig. 3). The stretching mode of the Si–OH bond in Pal spectrum was observed as a sharp band around 3700 cm^{-1}. Some intensity and frequency changes in the OH stretching band of surface hydroxyls (Si–OH) of the Pal-INH were observed, in line with previously reported results (Akyuz et al., 2010). The band at 3612 cm^{-1}, well documented in all bibliographic references on FTIR of palygorskite (Mendelovici, 1973; Frost et al., 2001; Chahi et al., 2002; Chang et al., 2009) was related with the OH-stretching mode of structural hydroxyl groups. In the drug-clay nanohybrid, that band was detected at 3615 cm^{-1} and was assigned to coordination of INH molecules on the surface silanol (Si–OH) groups, directly or indirectly through water bridges. Bands appearing at 3543, 3400 and 3370 cm^{-1} were assigned to water molecules at terminal positions of the octahedral sheets (coordinated water) and water inside palygorskite channels (zeolitic water). Band at 3543 cm^{-1} was also ascribed to OH-stretching in

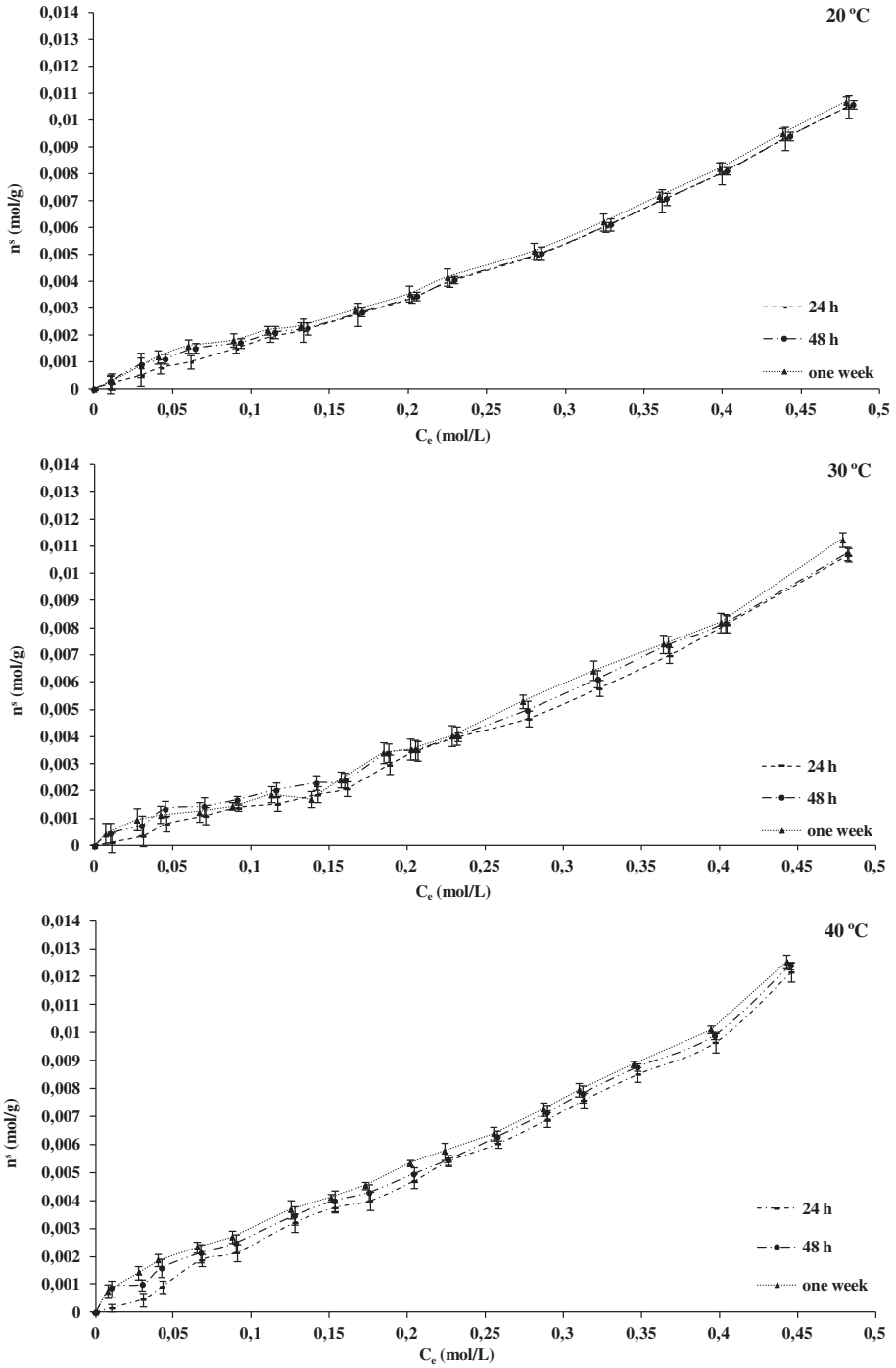

Fig. 1. Experimental adsorption isotherms of INH by Pal at different times and temperatures (mean values ± s.d.; n = 3).

Al−Mg− OH, Fe–Mg–OH and Fe_2–OH groups. Band at 1652 cm^{-1} was ascribed as bending modes of absorbed and zeolitic water (Mendelovici, 1973; Mendelovici and Portillo, 1976). This band was shifted to 1661 cm^{-1} in the nanohybrids due to the H-bonding of INH molecules with water present in the clay mineral. In the range between 1200 and 400 cm^{-1} characteristic bands of silicate was observed. Bands at 644 cm^{-1} in Pal moved to 638 cm^{-1} in the nanohybrid.

3.2.2. Thermal analysis

TGA and DSC curves of the studied samples are shown in Figs. 4 and 5. As described by Carazo et al. (2017), INH melted at ~177 °C and decomposed in the interval 250 °C–350 °C. Pal showed the previously described four stages of mass loss of this sample (Viseras and López-Galindo, 1999). The same four steps (adsorbed and zeolitic water; bound water I; bound water II; dehydroxylation) have been also discussed by other authors in palygorskite-rich samples (González et al., 1990; Frost and Ding, 2003; Ogorodova et al., 2015; Xavier et al., 2016). According to the drug clay interaction, TGA curve of the nanohybrid showed the partial removal of the water molecules placed in the structural channels or bound to the external surface of the clay mineral. Slope of drug decomposition was lower indicating a protecting effect of the clay mineral on the thermal degradation of the drug. Weight losses corresponding to water in the folded channels of the clay mineral as well as dehydroxylation were not modified in the nanohybrid TGA. According to the measured weight losses, INH in the nanohybrid was ~20% w/w.

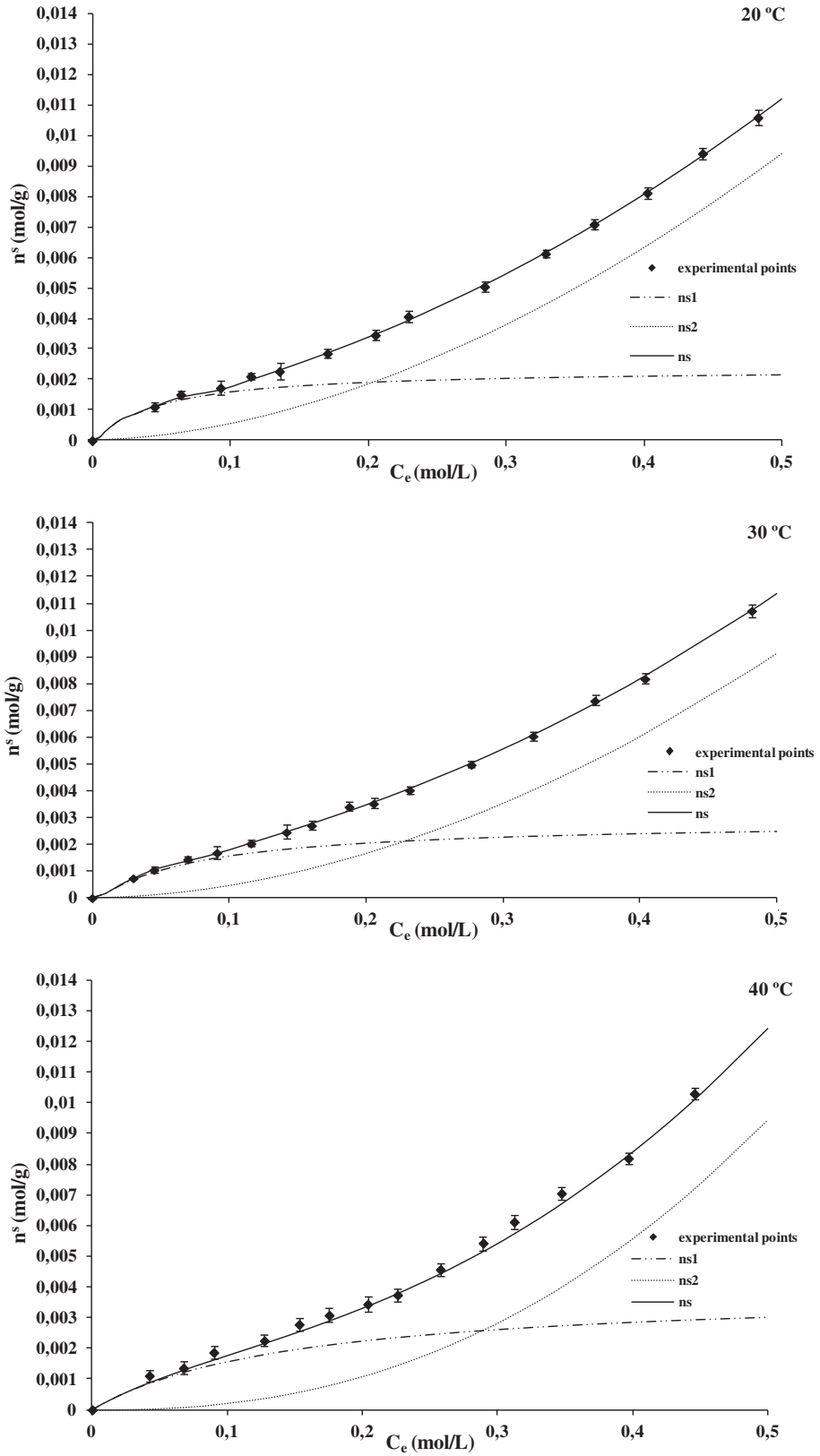

Fig. 2. Equilibrium isotherms of INH by Pal at different temperatures (mean values ± s.d.; n = 3).

3.2.3. X-ray powder diffraction

INH showed a crystalline pattern (Fig. 6), with main reflections at around 10°, 14°, 16° and 20° 2θ (Angadi et al., 2010). Pal diffraction pattern showed peaks corresponding to the mineral phases (mainly palygorskite with presence of minor quantities of quartz, Al-smectite, calcite and illite) presented in the material and quantified by Viseras and Lopez-Galindo (1999). The nanohybrid exhibited a similar diffraction pattern to the clay mineral. Disappearance of calcite and absence of INH peaks were the main differences, indicating the absence or negligible presence of precipitated crystals of the drug and the

Table I
Fitting parameters of Equation 1 for the retention of INH by Pal at different temperatures and corresponding correlation coefficients (mean values ± s.d.; n = 3).

T° (C)	n_m^s (mmol/g)	k_i	k_f	m	r^2
20	1,205 ± 0,0011	23,991 ± 0,3431	0,032 ± 0,0112	1,783 ± 0,1234	0,997
30	1,411 ± 0,0012	13,212 ± 0,4122	0,033 ± 0,0234	1,863 ± 0,2454	0,999
40	1,801 ± 0,0015	6,651 ± 0,4751	0,048 ± 0,0346	2,362 ± 0,2987	0,998

Table II
Thermodynamic functions for the Pal/INH interaction.

T (K)	ΔH° (kJ/mol)	ΔS° (kJ/mol K)	ΔG° (kJ/mol)
293	− 48,821 ± 1,7780	− 0,142 ± 0,0011	− 2,812 ± 0,0014
303			− 2,393 ± 0,0012
313			− 1,664 ± 0,0021

dissolution of the carbonate during the preparation of the hybrid.

3.2.4. Surface charge

Zeta potential of the raw clay mineral (− 15,5 ± 0,121 mV) almost remained unchanged after interaction with the drug molecules, being the ζ value of the nanohybrid − 14,9 ± 0,036 mV. The small difference was attributed to compression of the electrical double layer as a result of the coordination of the endocyclic nitrogen of INH molecules with the surface silanol (Si–OH) groups through water bridges. Similar effect with other organic molecules and palygorskite was also observed by Zeng et al. (2017). In practice, the almost absence of surface charge changes is confirming the non-electrostatic nature of the interaction.

4. Conclusions

Equilibrium isotherms fit to two simple processes: adsorption of INH on the activated sites of Pal followed by a slight precipitation of the drug on the clay mineral surface. Calculation of the fitting parameters of the equation that defines the processes and the thermodynamic functions reveals that: the INH retention capacity by the nanoclay increases with increasing temperature; the precipitation step is of low intensity and the formation of the Pal-INH nanohybrid fits to an exothermic, exoentropic and thermodynamically spontaneous process. Total amount of INH adsorbed was about 20% w/w. FTIR spectroscopy indicated that INH molecules were coordinated to surface OH groups, directly or indirectly through water bridges. It was concluded that the endocyclic nitrogen is mainly involved in the coordination. Besides, some of the adsorbed INH molecules may enter the interior channels of

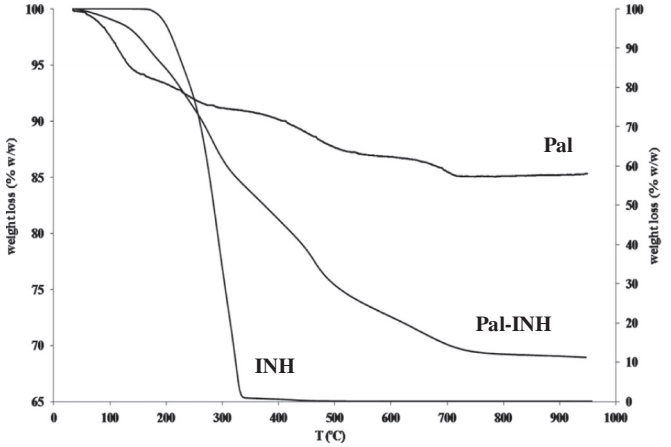

Fig. 4. TGA curves of Pal-INH nanohybrid and raw components.

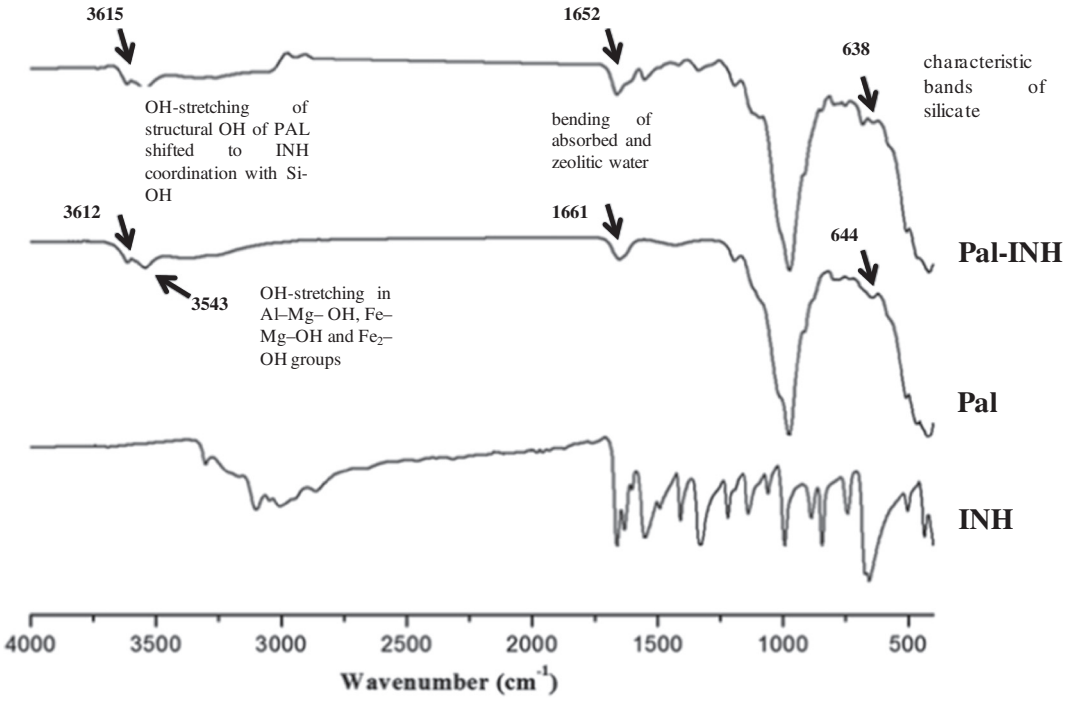

Fig. 3. FTIR spectra of Pal-INH nanohybrid and raw components.

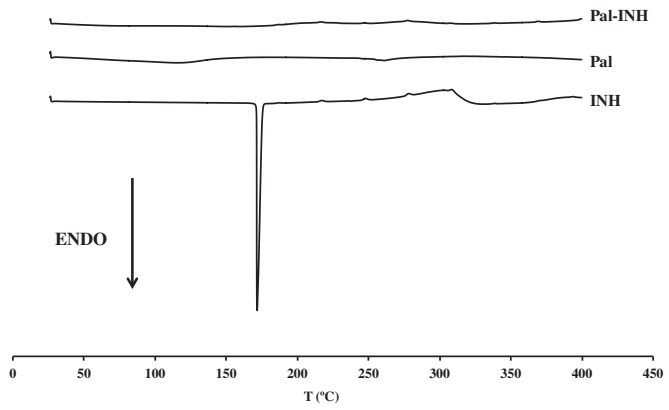

Fig. 5. DSC curves of Pal-INH nanohybrid and raw components.

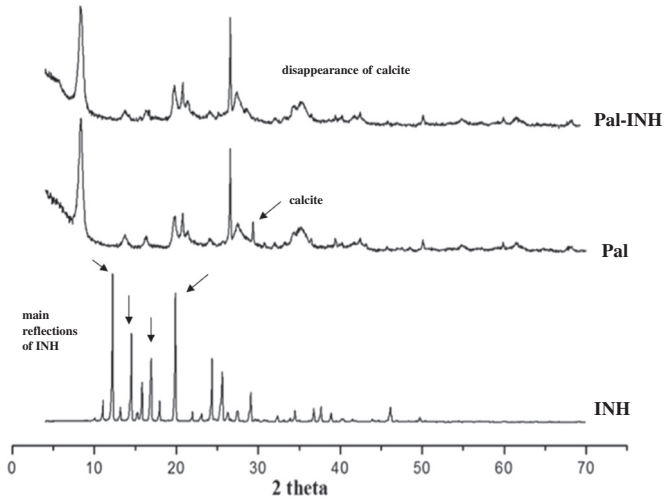

Fig. 6. XRPD patterns of Pal-INH nanohybrid and raw components.

the Pal and involve H– bonding interaction with zeolitic water. Effectively loading of INH onto Pal and a comprehensive study of the drug-clay nanohybrids structure and interactions involved in the adsorption process provided encouraging aspects to the design of modified drug delivery systems able to alleviate the struggles of the tuberculosis treatment. In particular, the low-cost of the excipients and the ease of the technique to prepare the nanosystems are important features in the development of tuberculostatic dosage forms.

Acknowledgements

This study was supported by the Projects CGL2016-80833-R and RNM-1897, group CTS-946 and Predoctoral Grant FPU13/04765.

References

Akyuz, S., Akyuz, T., Akalin, E., 2010. Adsorption of isoniazid onto sepiolite–palygorskite group of clays: an IR study. Spectrochim. Acta A Mol. Biomol. Spectrosc. 75 (4), 1304–1307.

Angadi, S.C., Manjeshwar, L.S., Aminabhavi, T.M., 2010. Interpenetrating polymer network blend microspheres of chitosan and hydroxyethyl cellulose for controlled release of isoniazid. Int. J. Biol. Macromol. 47 (2), 171–179.

Bradley, W., 1940. The structural scheme of attapulgite. Am. Mineral. 25 (6), 405–410.

Carazo, E., Borrego-Sánchez, A., Aguzzi, C., Cerezo, P., Viseras, C., 2016. Use of clays as nanocarriers of tuberculostatic drugs. Curr. Drug Deliv. 13, 1–2.

Carazo, E., Borrego-Sánchez, A., García-Villén, F., Sánchez-Espejo, R., Aguzzi, C., Viseras, C., Sainz-Diaz, C.I., Cerezo, P., 2017. Assessment of halloysite nanotubes as vehicles of isoniazid. Colloids Surf. B: Biointerfaces 160, 337–344.

Cerezo, P., Viseras, C., Lopez-Galindo, A., Ferrari, F., Caramella, C., 2001. Use of water uptake and capillary suction time measures for evaluation of the anti-diarrhoeic properties of fibrous clays. Appl. Clay Sci. 20 (1), 81–86.

Chahi, A., Petit, S., Decarreau, A., 2002. Infrared evidence of dioctahedral-trioctahedral site occupancy in palygorskite. Clay Clay Miner. 50 (3), 306–313.

Chang, P.H., Li, Z., Yu, T.L., Munkhbayer, S., Kuo, T.H., Hung, Y.C., Lin, K.H., 2009. Sorptive removal of tetracycline from water by palygorskite. J. Hazard. Mater. 165 (1), 148–155.

Frost, R.L., Ding, Z., 2003. Controlled rate thermal analysis and differential scanning calorimetry of sepiolites and palygorskites. Thermochim. Acta 397 (1), 119–128.

Frost, R.L., Locos, O.B., Ruan, H., Kloprogge, J.T., 2001. Near-infrared and mid-infrared spectroscopic study of sepiolites and palygorskites. Vib. Spectrosc. 27 (1), 1–13.

Galan, E., 1996. Properties and applications of palygorskite-sepiolite clays. Clay Miner. 31 (4), 443–453.

Gonzalez, F., Pesquera, C., Blanco, C., Benito, I., Mendioroz, S., Pajares, J.A., 1990. Structural and textural evolution under thermal treatment of natural and acid-activated Al-rich and Mg-rich palygorskites. Appl. Clay Sci. 5 (1), 23–36.

López-Galindo, A., Viseras, C., Aguzzi, C., Cerezo, P., 2011. Pharmaceutical and cosmetic uses of fibrous clays. In: In Advances in the Crystal Chemistry of Sepiolite and Palygorskite. Developments in Palygorskite–Sepiolite Research (Vol. 3). Elsevier, pp. 290–324.

Mendelovici, E., 1973. Infrared study of attapulgite and HCl treated attapulgite. Clay Clay Miner. 21 (2), 115–119.

Mendelovici, E., Portillo, D.C., 1976. Organic derivatives of attapulgite; I, Infrared spectroscopy and X-ray diffraction studies. Clay Clay Miner. 24 (4), 177–182.

Mura, P., Maestrelli, F., Aguzzi, C., Viseras, C., 2016. Hybrid systems based on “drug–in cyclodextrin–in nanoclays” for improving oxaprozin dissolution properties. Int. J. Pharm. 509 (1), 8–15.

Ogorodova, L., Vigasina, M., Melchakova, L., Krupskaya, V., Kiseleva, I., 2015. Thermochemical study of natural magnesium aluminum phyllosilicate: palygorskite. J. Chem. Thermodynamics 89, 205–211.

Ramos, J.M., 2004. XPowder. A software package for powder X-ray diffraction analysis. Legal Deposit GR 1001 (04).

Serratosa, J.M., 1979. Surface properties of fibrous clay minerals (palygorskite and sepiolite). Dev. Sedimentol. 27, 99–109.

Sharma, R., Kaur, A., Sharma, A., Dilbaghi, N., 2017. Nano-based anti-tubercular drug delivery and therapeutic interventions in tuberculosis. Curr. Drug Targets 18 (1), 72–86.

Tenci, M., Rossi, S., Aguzzi, C., Carazo, E., Sandri, G., Bonferoni, M.C., Ferrari, F., Grisoli, P., Viseras, C., Caramella, C.M., Ferrari, F., 2017. Carvacrol/clay hybrids loaded into in situ gelling films. Int. J. Pharm. 531 (2), 676–688.

Verma, A., Riaz, U., 2017. Mechano-chemically synthesized poly (o-toluidine) intercalated montmorillonite nanocomposites as anti-tuberculosis drug carriers. Int. J. Polym. Mater. Po. http://dx.doi.org/10.1080/00914037.2017.1320658.

Viseras, C., López-Galindo, A., 1999. Pharmaceutical applications of some Spanish clays (sepiolite, palygorskite, bentonite): some preformulation studies. Appl. Clay Sci. 14 (1), 69–82.

Viseras, C., López-Galindo, A., 2000. Characteristics of pharmaceutical grade phyllosilicate powders. Pharm. Dev. Technol. 5 (1), 47–52.

Viseras, C., Yebra, A., López-Galindo, A., 2000. Characteristics of pharmaceutical grade phyllosilicate compacts. Pharm. Dev. Technol. 5 (1), 53–58.

Viseras, C., Ferrari, F., Yebra, A., Rossi, S., Caramella, C., López-Galindo, A., 2001. Disintegrant efficiency of special phyllosilicates: Smectite, palygorskite, sepiolite. S.T.P. Pharma Sci. 11 (2), 137–143.

WHO Global Tuberculosis Report, 2015.

Xavier, K.C., Santos, M.S., Osajima, J.A., Luz, A.B., Fonseca, M.G., Silva Filho, E.C., 2016. Thermally activated palygorskites as agents to clarify soybean oil. Appl. Clay Sci. 119, 338–347.

Zeng, H.F., Lin, L.J., Xi, Y.M., Han, Z.Y., 2017. Effects of raw and heated palygorskite on rumen fermentation in vitro. Appl. Clay Sci. 138, 125–130.

HALLOYSITE NANOTUBES AS TOOLS TO IMPROVE THE ACTUAL CHALLENGE OF FIXED DOSES COMBINATIONS IN TUBERCULOSIS TREATMENT

Esperanza Carazo[1], Giuseppina Sandri[2], Pilar Cerezo[1], Cristina Ianni[2], Franca Ferrari[2], Cristina Bonferoni[2], Cesar Viseras[1,3,*], Carola Aguzzi[1]

1 Department of Pharmacy and Pharmaceutical Technology, School of Pharmacy, University of Granada, Campus of Cartuja, 18071 s/n, Granada, Spain, ecarazogil@ugr.es

2 Department of Drug Sciences, University of Pavia, viale Taramelli 12, 27100, Pavia, Italy

3 Andalusian Institute of Earth Sciences, CSIC-University of Granada, Avda. de Las Palmeras 4, 18100, Armilla (Granada), Spain

*Corresponding author: Cesar Viseras (cviseras@ugr.es)

ABSTRACT

Halloysite nanotubes (HLNTs) were used as nanocarriers of the tuberculostatic agent isoniazid (INH), a BCS (Biopharmaceutics Classification System) class III drug. Self-assembling nanohybrids (INH-loaded HLNTs) with an average outer diameter of 90 nm and polydispersity index of 0.7 approximately, were obtained by spontaneous adsorption of INH molecules to HLNTs powder in aqueous medium. The nanohybrids were aimed to improve oral drug bioavailability and reduce physicochemical incompatibility of INH with other concomitantly administered tuberculostatic agents. *In vitro* drug release from INH-loaded HLNTs was successfully fitted to a diffusive kinetic law founded on the adsorption-desorption equilibrium between drug molecules in solution and solid inorganic excipients. INH-loaded HLNTs showed good *in vitro* biocompatibility towards Caco-2 cells at the concentrations studied (up to 1233 μg/mL), with improved cell proliferation. Permeability tests showed that INH transport across

This article has been accepted for publication and undergone full peer review but has not been through the copyediting, typesetting, pagination and proofreading process which may lead to differences between this version and the Version of Record. Please cite this article as doi: 10.1002/jbm.a.36664

Caco-2 cellular membranes was greatly enhanced and fluorescent microscopy confirmed that the drug encapsulated into nanohybrid was effectively internalized by the cells. INH-loaded HLNTs enhanced stability of the drug in presence of other tuberculostatic agents, both in binary and quaternary combinations. It has been demonstrated that simple interaction between INH with HLNTs leads to drug permeability and stability improvements that could greatly facilitate the design of multiple drug dosage forms, an actual challenge in oral treatment of tuberculosis.

Keywords: Halloysite, Isoniazid, Cytoviability, Permeability, Stability.

INTRODUCTION

Tuberculosis (TB) is a global health priority with almost 10 million of new cases worldwide every year and first cause of death from a single infectious agent (1). TB treatment is based on a combination of four first-line tuberculostatic drugs and among them, INH is the most widely used and plays a crucial role based on its numerous advantages, as high early bactericidal activity, high selectivity to *Mycobacterium tuberculosis* and excellent bacteriostatic capacity with a minimum inhibitory concentration (MIC) of about 0.05 – 0.1 μg/mL (2,3). Despite its crucial importance (INH is included in the WHO Model List of Essential Medicines (4)), only low levels of INH gain access into plasma via oral route, due to its poor intestinal permeability, rapid and extensive hepatic metabolism and short plasma half-life (1–4 hours) (5). To achieve therapeutic effects, repetitive and high doses are therefore required, leading to severe adverse effects, such as hepatotoxicity and neuropathy (6-9).

INH possesses high aqueous solubility (140 mg/mL at 25 ºC) (10) and low permeability ((log P −0.402 at 25 ºC) (11), being considered as a class III drug of the BCS (4,12). Oral bioavailability of this class of drugs mainly depends on their permeability pattern across the enterocyte membranes (13). Any carrier which can improve the permeability of class III drugs will therefore result in improved effectiveness at lower dose with less side effects leading to improved compliance with lowered health costs (14).

The WHO Model List of Essential Drugs includes fixed-dose-combinations (FDCs) of the first-line tuberculostatic drugs (INH, Rifampicin (RIF), Pyrazinamide (PYR), and

Ethambutol dihydrochloride (ETB)) (15) with numerous advantages, as the minor risk of acquisition of drug resistance due to monotherapy and the improved patient adherence derived from the smaller number of solid dosage forms to ingest. However, the commercialized 4-FDC dosage forms exhibit severe technological problems including extensive physical changes (color fading, red bleeding) and, particularly important for therapy efficacy, significant decomposition of RIF and INH in presence of the other drug molecules (16-18).

The use of nanoparticles as vehicles for effective drug delivery in TB treatment have been proposed to increase drug bioavailability, protect from degradation and control release (14,19). A particular type of inorganic low cost nanoparticles is being proposed as potential excipients in the improvement of TB (20), and in particular some interesting hybrids have been recently designed (21-23). Halloysite is a two-layered aluminosilicate chemically similar to kaolin, with prevailing hollow tubular structure in the nanometer range (24-26). Essential features, as hollow tubular morphology and outer and inner surface charges, have made halloysite nanotubes (HLNTs) well documented carriers for encapsulation and release of drug molecules (27-35). In a previous work, it was shown that INH is spontaneously adsorbed by HLNTs, giving a self-assembled and thermodynamic stable (ΔH = 70.40 kJ/mol; ΔS = 0.2519 kJ/molK) nanohybrid (INH-loaded HNLTs), in which drug molecules were adsorbed both onto the inner and at the outer surface of the nanotubes (21).

Given these premises, aim of this work was to assess biological compatibility as well as biopharmaceutical and technological performances of INH-loaded HNLTs to effectively improve the oral bioavailability of the drug and enhance INH compatibility in presence of the other tuberculostatic drugs. Cellular biocompatibility and drug permeability were evaluated using *in vitro* approaches, in which Caco-2 cell lines were used as established models for both cytotoxicity studies and *in vitro* prediction of drug absorption through the gastrointestinal wall (36,37). Complementary fluorescent microscopy was performed to confirm cellular uptake, visualizing the presence of the nanohybrid eventually entrapped in the cells. Accelerated stability tests of pure INH and INH-

loaded HLNTs were carried out to assess the possible protective role of the nanotubes regarding INH stability as a first step aimed to design stable 4-FDC.

MATERIALS AND METHODS

Pharmaceutical-grade halloysite nanotubes (HLNTs) and isoniazid (INH) were purchased from Sigma Aldrich, (Spain). Etambuthol hydrochloride (ETB) was purchased from Hildose (India), pyrazinamide (PYR) from Calyx Chemicals and Pharmaceuticals (India) and rifampicin (RIF) from Luohe Nanjiecun (China). The purity of all drugs was >99%.

Preparation of the nanohybrid

Hybrid systems (INH-loaded HLNTs) were prepared dispersing HLNTs powder (100 mg) in 20 mL of INH aqueous solution (0.25 M) (initial drug/HLNTs ratio corresponding with the calculated monolayer adsorption capacity of the nanotubes), resulting in a drug content of 18.9 ± 0.12 % w/w (21). **Drug entrapment was calculated according both to the thermogravimetry results and by the experimental and theoretical adsorption data (21). A complete physicochemical characterization of raw materials (INH and HLNTs) and the resulting nanohybrid (INH-loaded HLNTs) has been performed (21).**

Photon correlation spectroscopy

Photon correlation spectroscopy (PCS) with low angle laser light scattering was used to determine the size distribution profile of the nanohybrid and corresponding free components. The intensity weighted mean diameter and the polydispersity index were determined using a Particle Sizer BI-90 (Brookhaven, Holtsville, USA) at 25°C under an angle of 30°. All samples were diluted with demineralized particle-free water to an adequate scattering intensity prior to the measurement. PCS run settings parameters were: diluent viscosity (0.0089 poise), diluent refractive index (1.333), tested angle (30.1461º), run time (1200 s), equilibration time (1 min). The results were average of three analyses.

Surface charge

Surface charge properties of HLNTs and INH-loaded HLNTs were determined from zeta potential (ζ) values in aqueous suspensions (0.05% w/v) on a Malvern Zetasizer Nanoinstrument (Malvern Instruments, USA).

***In vitro* release studies**

Release of INH from 150 mg of INH-loaded HLNTs was tested in the USP dissolution apparatus II (SOTAX AG, Switzerland) at 100 rpm, 37 °C and 500 mL of dissolution media: i) HCl 0.001 M (pH 3); and ii) simulated intestinal fluid (SIF) without enzymes (pH = 6.8). **pH 3 was chosen as simulated gastric environment to avoid INH degradation in more acidic conditions (38)**. At established time intervals, samples of dissolution medium (5 mL) were withdrawn and renewed with a fresh medium each time, filtered through 0.45 µm Millipore® (S) membranes and the amount of drug dissolved was measured by HPLC. A mean of six determinations were recorded. Total amounts of drug released (Q_t) were calculated as follows (Equation 1) **(27)**:

$$Q_t = V_m C_t + \sum_{i=0}^{t-1} V_a C_i \quad (1)$$

where V_m and C_t are volume and concentration of the drug at time t, V_a is the volume of the sample withdrawn and C_i is drug concentration at time i (i < t).

Drug assay

Dissolution samples were analysed using an HPLC system (Infinity II 1260, Agilent, Spain) equipped with an autosampler and a UV detector. The stationary phase was a column Agilent Infinity LabPoroshell 120 (4.6 mm×150 mm, 4µm) (Agilent, Spain) and the mobile phase was H_2O/CH_3CN (95/5, v/v). The flow rate was set at 0.8 mL/min, the injection volume was 50 µL, the detector wavelength 264 nm and the run time 5 minutes. Data were recorded using Agilent OpenLAB CDS ChemStation software package. Methods were linear in the range from 12 to 120 mg/L.

Cell cultures

Caco-2 human colorectal adenocarcinoma cell lines were obtained from the American Type Culture Collection (ATCC, USA). Cells were grown at 37°C, 5% CO_2 atmosphere (PBIinternational, Italy) in pH 7.4 Dulbecco's Modified Eagle's Medium (DMEM)

(Lonza, Italy) containing 10% v/v heat inactivated Fetal Bovine Serum (FBS) (Euroclone, Italy), penicillin (100 IU/mL), streptomycin sulphate (100 µg/mL) and 1% v/v non essential aminoacids (Sigma Aldrich, Italy). The culture medium was changed three times a week during maintenance.

Cytotoxicity measurements

Caco-2 cells were seeded in 96-well plates of area 0.35 cm^2 at density of 10^5 cells per square centimeter, resulting in approximately 35000 cells/plate. Cells were incubated at 37ºC, 5 % CO_2 for 24 h. 100 µL of suspensions of INH-loaded HLNTs containing HLNTs concentrations ranging from 1000 to 1 µg/mL in culture medium (Table I) were incubated with the cells for 24 h and then removed and washed with 100 µL of HBSS (Hank's Balanced Salt Solution). For comparison, experiments were also done on pristine halloysite and drug, according to their concentrations in the nanohybrid (Table 1). The HBSS was subsequently removed and replaced by 100 µL of HBSS and 50 µL of MTT (3-(4,5-dimethylthiazol-2-yl)-2,5-diphenyltetrazolium bromide) solution (2.5 mg/mL) in HBSS. MTT was incubated for 3 hours at 37ºC and 5% CO_2. After incubation, MTT was aspirated and 100 µL of dimethyl sulfoxide (DMSO) were added to break the cell membrane with the subsequent release of the formazan crystals. The absorbance of formazan solutions were assessed by ELISA plate reader (570 nm to 690 nm) after vigorously shaking for one minute (Microplate Absorbance Reader MARKTM, Bio-Rad Laboratories Srl, Italy).

Permeability studies

Cells were seeded on tissue-culture-treated polycarbonate filters (area 113.1 mm^2; inner diameter 13.85 mm) in 12-well plates (Greiner Bio-one, PBI international, Italy) at a seeding density of 10^5 cells/cm^2. Cell cultures were kept at 37ºC in an atmosphere of 95% air and 5% CO_2. The test was carried out as follows: 500 µL of the samples suspensions were diluted 1:1 in HBSS at pH 7.4 and were used as the apical (donor) phase of the monolayers. The basolateral (receptor) phase was 1 mL of HBSS at pH 7.4. At fixed times (0.5; 1.5; 3 and 6 h) the whole basolateral phase was collected to dose INH and fresh basolateral phase was added to the cell substrates. Drug content was assessed by HPLC as described above and the method was linear in the range from 1 to

100 mg/L. During the experiments, the integrity of the monolayers was tested by means of Transepithelial Electrical Resistance (TEER) measurements at the same times than the permeability test and after 24 h by means of a Millicell ERS-meter (Millipore Corp., Bedford, MA, USA). INH at the same concentration than that of the nanohybrid was subjected to the same assay and used as control.

Fluorescent Microscopy

Caco-2 cells grown on filters in 12-well plates and subjected to *in vitro* permeability tests were analyzed by using fluorescent microscopy to visualize INH-loaded HLNTs nanohybrids eventually entrapped in the cells. The cell substrates were fixed in ethanol by dipping for 1 h and dried overnight. Cell nuclei were stained by dipping the biological substrates into a solution (100 μg/mL) of Propidium Iodide (Sigma, Italy). A fluorescent microscope (BX51 Olympus microscope) was used to observe the cellular uptake of drug encapsulated into nanocomposites (Propidium Iodide excitation wavelength of 535 nm and an emission wavelength of 617 nm; INH excitation wavelength of 380 nm and an emission wavelength of 400 nm). The acquired images were processed by means of specific software (Olympus Image Analysis Software).

Stability Tests

Degradation of INH, loaded and unloaded in the nanohybrid, in presence of the other tuberculostatic drugs (ETB, PYR and RIF) was assessed following the ICH (International Conference on Harmonisation) guidelines for accelerated stability conditions **(39)** storing samples at 40 °C and 75% relative humidity (RH) (climatic chamber CC/HR 0/100, Uniclima, Spain). Binary physical mixtures of pure INH or INH-loaded HLNTs with each one of the other tuberculostatics as well as quaternary physical mixtures including all the drugs were assayed. Individual components were weighed in a 1:1 drug:drug ratio and gently mixed in a small glass mortar. Stability was considered in terms of % of INH remaining after 15, 30 and 90 days. INH was subjected to the same test and use as control of non self-degradation of the drug in the conditions tested. INH content was analyzed by HPLC as described above. Measurements were done in triplicate.

Statistical analysis

Statistical differences were evaluated by means of a non-parametric test: Mann Whitney (Wilcolxon) W test, using the SPSS software version 21.0 of developed by Statistical Software Package (SPSS Inc. Chicago, USA). Differences were considered significant at $P< 0.05$; only significant differences are reported in the captions of the relevant figures.

RESULTS

Photon correlation spectroscopy

The intensity weighted mean diameter and the polydispersity index obtained for both HLNTs and INH-loaded HLNTs are presented in Table II. Calculated mean diameter size of HLNTs was about 75 nm and agrees with that found in bibliography with external diameter varying from 30 to 190 nm (25). Both external diameter and polydispersity index increased in the nanohybrid in comparison with pristine HLNTs.

Surface charge

HLNTs suspension was characterized by negative zeta potential of -18.7 ± 0.21 mV, derived from the presence of hydroxyl groups in the external surface of the clay mineral (25). This value increased after loading with INH molecules, being the ζ value of the INH-HLNTs nanohybrid -14.6 ± 0.04 mV.

In vitro release studies

Drug release profiles of INH from the INH-loaded HLNTs nanohybrid in pH 3.0 and pH 6.8 are plotted in Figure 1 as w/w % of drug released *vs* time. In line with the high drug aqueous solubility, dissolution curves showed burst release and short drug delivery duration (95 w/w % of drug released in the early 15 min). A kinetic law was defined to describe the release process, following previous studies with similar inorganic carriers (27).. The calculated release parameters (Table III), **obtained using the software packaging TableCurve 2D® (Systat Software Inc., UK)**, were discussed on the basis of adsorption-desorption equilibrium between INH molecules and the nanotubular carrier. Theoretical release curves are displayed in Figure 1 (dotted lines), where the almost overlapping with experimental points, suggests high suitability of the model to fit release data. **Correlation coefficients (R^2> 0.99) confirmed that the kinetic law adequately fitted the release pattern for INH from the nanohybrid in both media**.

Calculated release rates were very high and similar in acidic and neutral pH ($k_d \approx 2000$ h^{-1}) (Table III).

Cytotoxicity measurements

Cytotoxicity was assessed for the pure materials (HLNTs and INH) and the nanohybrid (INH-loaded HLNTs) based on the percentage of viable cells in comparison with that of untreated cells grown in complete medium (positive control) (Figure 2).

Permeability studies

Permeability assays were performed on the highest concentration of INH-loaded HLNTs tested which exhibited no cytotoxic behavior on the basis of cell viability measurements (INH-loaded HLNTs 6; 1233 μg/mL). INH at the same concentration as in the nanohybrid (INH 6; 233 μg/mL) was used as control. In Figure 3, it is plotted the percentage of INH permeated to the basolateral phase *vs* time during the permeability experiments. First measured values (30 minutes) revealed no differences in % of drug permeated from the nanohybrid in comparison with pristine INH. The amount of INH permeated from the INH-loaded HLNTs tend to increase starting from 90 min., being significantly higher after 180 and 360 min., with almost 90 % of the total amount at the end of the test in comparison with the 58 % of INH alone.

Figure 4 shows the TEER profiles as a function of time for INH-loaded HLNTs nanohybrid and the same concentration of INH alone as control. The TEER profile of INH was close to the 100 % during all the experiment time. As for the INH-loaded HLNTs nanohybrid there was a reversible decrease of the TEER which becomes significant after 90 minutes. After 24 hours of the beginning of the test, TEER profile of both INH alone and INH-loaded HLNTs, returned to its primitive values assuring that the total integrity of the monolayer was recovered.

Fluorescent Microscopy

To investigate the fate of INH and the interaction with Caco-2 cell monolayers, fluorescent microscopy was performed on the substrates subjected to the permeability experiments. Microphotographs obtained at the end of the permeability experiment (6 h) between Caco-2 substrates and either INH-loaded HLNTs nanohybrid or drug alone

INH (Figure 5), showed cell nuclei (red) and INH (light blue) as free drug or loaded in nanotubes.

Stability tests

Stability results showed that only mixtures containing ETB showed significant degradation of INH compared to the pristine drug (Figure 6), whereas binary combinations of PYR and RIF with INH or INH-loaded HLNTs did not modify INH content (data not shown). Amount of INH decreased to 60 % and 25 % of the initial content after 15 and 90 days, respectively, in the binary mixtures of INH and ETB.

DISCUSSION

The increase of the polydispersity index of the nanohybrid revealed a wider variety of particle sizes after contact with INH, whereas the increase of external diameters of the hybrid was coherent with the presence of drug molecules on the outer surface of the nanotubes, as previously assessed by electron microscopy studies and theoretical computational modeling of the adsorption process (21). Moreover, the surface charge change of the nanohybrid in comparison with unloaded HLNTs, was ascribed to the adsorption of INH molecules by HLNTs, which occurred mainly by strong H bonds between the hydroxyl groups of HLNTs surfaces and the carbonyl and heterocyclic N atom of INH, as well as via electrostatic interactions between different groups of INH (-NH_2,-NH and N of the aromatic ring) with the OH groups of HLNTs surfaces (21).

Drug release profiles of INH from the INH-loaded HLNTs nanohybrid in pH 3.0 and pH 6.8 suggested that drug release was not hindered by interaction between drug molecules and HNLTs. The kinetic law governing the release process can be expressed by the following equation (Equation 2), specifically designed to describe drug release from hybrid systems based on adsorption-desorption equilibrium between drug molecules and inorganic carriers (27):

$$\frac{dC}{dt} = -k_a\, C\, (1-\theta) + k_d\, \theta \qquad (2)$$

where C is the drug concentration in solution, k_a the specific adsorption rate, k_d the specific release rate, and θ the fraction of surface active sites in the HLNTs occupied by the drug molecules.

Integration of Eq. (2) yields to:

$$F = \frac{C_t}{C_e} = 1 - e^{\left(\frac{-k_d \,.t}{C_e}\right)} \quad (3)$$

where F is the fraction of drug released, C_t is the drug concentration in solution at time t, C_e is the drug concentration in solution at the equilibrium (maximum drug released) and k_d the specific release rate.

Eq. (3) was used to fit i*n vitro* release experimental data. Theoretical release curves calculated according to Eq. (3) were assigned to desorption of INH molecules, described by the model as a solid/liquid interface process governed by diffusive transport of INH molecules from the active adsorption sites (inner and outer surfaces) of HLNTs to the surrounding liquid medium. Release rates (Table III) suggest a strong affinity of drug molecules for the surrounding media (causing very easy and quickly release process), as well as a negligible influence of pH on drug dissolution. From a practical point of view, to prevent early release of INH from HLNTs and ensure that the drug remained associated to the HLNTs at the absorption site, use of enteric coated capsules seems to be a possible strategy for oral administration.

In vitro cytotoxicity tests towards Caco-2 cell line results revealed that, except for samples 5 (100 µg/mL) and 6 (1000 µg/mL), all the HLNTs concentrations tested were biocompatible towards Caco-2 cell lines (providing viability values not lower than the positive control). These results are in agreement with previously reported literature data **(40-42)**. In addition, proliferative effects were found for concentrations 1-4, since the obtained viability values were significantly higher than the positive control. This effect was in line with previous works in which HLNTs were found to have a positive influx on cell attachment and spreading, even higher than other similar inorganic carriers due to the higher roughness of its surface in comparison with the smooth of silica or montmorillonite **(43-44)**. In case of the drug alone, none of the concentrations assayed resulted in viability values significantly lower than the untreated cells (control). Similar results were found for the nanohybrid, whose biocompatibility in the whole range of concentrations was assessed and a positive trend on cell growth was observed, being

also significant in some cases (1, 2 and 6). It is remarkable that INH-loaded HLNTs possess biocompatible behaviour even when HLNTs exhibited cytotoxic activity, so the interaction between HLNTs and INH turned to have a positive effect regarding cell viability.

Permeability tests results showed that incorporation of HLNTs significantly improved the permeation of the drug across the cellular membrane. Similar findings were observed in previous studies with similar inorganic excipients and explained as a consequence of electrostatic interactions between silanol groups in the surface of inorganic carriers and positively charged constituents of cell membranes **(45)**. Regarding the TEER results, the value of the INH-loaded HLNTs nanohybrid suffered a reversible decrease that becomes significant after 90 minutes. This behaviour suggests that the presence of nanohybrid suspension interfered with the junctional proteins, probably via H bond and/or Van der Waals interactions, causing widen of the paracellular route, in agreement with permeability results, where increased of drug permeation was observed starting from 90 minutes. After 24 hours of the beginning of the test, TEER profiles of both samples were restored to primitive values meaning the recovery of the integrity of the cell monolayer. These results supported the protective effect of silicate-based carriers in restoring the epithelial barrier of Caco-2 cells by means of TEER measurements **(46)**.

Fluorescent microphotographs revealed the internalization of INH when loaded in the nanohybrid which was non observable in the case of free INH. In the cell substrate treated with INH-loaded HLNTs, it can be noticed that there was a blue signal due to INH present in the cell substrate, to indicate an actual internalization of the drug (no blue signal was present in the control). Moreover there were some blue spots conceivably due to INH loaded nanohydrid to indicate the uptake of the system from cell substrate. In the substrate treated with INH no blue signal was visible to indicate the low propensity of the drug to be internalized by Caco-2 cells. In all cases the staining of the nuclei demonstrated that no nuclear damage occurred during the experiments and no apoptotic cell could be identified confirming the lack of cytotoxicity of the INH-loaded HLNTs nanohybrid.

Degradation of INH in presence of ETB has been explained as a result of the hygroscopic nature of ETB, which attracts moisture and creates acidic environment increasing the rate of decomposition of INH **(47)**. Inclusion of INH onto HLNTs not only did not induce INH degradation, but also protected INH from ETB-induced degradation; the amounts of INH recovered from INH-loaded HLNTs after 15 and 90 days in presence of ETB were ~80 % and 40 % (Figure 6).

Regarding the quaternary mixtures, results showed that the four first-line tuberculostatic drugs interact with each other in a multiple and complex manner leading to a significant loss of INH % in the samples, with a residual content of only ~10 % (15 days) and ~ 2% (90 days) in case of the quaternary combinations containing unloaded INH (Figure 6). In line with previous studies, isonicotinylhydrazone could be stated as the major degradation product of INH, which is formed by the interaction of the imino group of 3-formyl rifampicin of RIF with the hydrazine group of INH under acidic conditions provided by the presence of ETB **(17, 48)**. In the presence of the nanohybrid, compatibility of quaternary mixtures was enhanced, achieving residual INH contents from five to ten times higher than that found in absence of HLNTs at the same time. Assuming that INH degradation follows first order kinetics, plot of log (INH %) *vs* time allowed to calculate from the resulting straight lines the degradation rate constants (6.2×10^{-3} $days^{-1}$ for INH:ETB and 4.6×10^{-3} $days^{-1}$ for INH-loaded:HLNTs) and $t_{1/2}$ values of 38 and 65 days, respectively. Regarding the quaternary mixtures, rate constants of 15.4×10^{-3} and 7×10^{-3} $days^{-1}$ and $t_{1/2}$ of 11 and 22 days were calculated for mixtures containing unloaded and loaded INH, respectively. These findings prove that HLNTs strongly increased stability (in terms of decreasing the degradation rate) of INH in presence of the other first line tuberculostatic agents, suggesting promising application of INH-loaded HLNTs in 4-FDC treatment.

CONCLUSIONS

Major challenges of TB treatment are related with compatibility problems between first line tuberculostatic drugs when administered together in FDC dosage forms and, in particular, in the case of INH, with its low intestinal permeability requiring the administration of high doses leading to severe toxic effects. Over the past few years, it

has been shown that natural inorganic excipients as halloysite may play a leading role as affordable nanocarriers to be used in the design of advanced drug delivery systems. In this work, a novel drug-halloysite nanohybrid with significant enhancement of *in vitro* INH permeability and stability has been studied.

In vitro release measurements revealed that adsorption of INH onto HLNTs did not hinder drug dissolution, drug release being complete in the early minutes of the test both in acidic and neutral environment. The mechanism of drug release was explained on the basis of a mechanistic adsorption-desorption model, as a diffusive mass transport across the solid/liquid interface.

Cell cultures experiments confirmed that the nanohybrid was biocompatible on Caco-2 cells in the whole concentration range studied. Significant positive effects on cells proliferation were also found.

In-vitro permeability tests showed a significant increase of the drug permeation across the Caco-2 monolayer. Complementary TEER measurements suggested widen of the paracellular route. The uptake of the nanohybrid by the cells was confirmed by fluorescent microscopy.

Stability tests showed higher stability of INH-loaded HLNTs in binary and quaternary physical mixtures containing ETB, which is the principal responsible of the physical and chemical degradation of INH in 4-FDC.

ACKNOWLEDGEMENTS

This study was supported by the Projects CGL2016-80833-R and RNM-1897, group CTS-946, Predoctoral Grant FPU13/04765 and Predoctoral Mobility Grant EST15/00225 of the FPU Program (Ministerio de Educación, Cultura y Deporte, Spain).

REFERENCES

(1) WHO, Global Tuberculosis Report, 2018.

(2) Huang, D., Li, D., Wang, T., Shen, H., Zhao, P., Liu, B., Wang, S. Isoniazid conjugated poly (lactide-co-glycolide): Long-term controlled drug release and tissue regeneration for bone tuberculosis therapy. Biomaterials. 2015;52:417-425. https://doi.org/10.1016/j.biomaterials.2015.02.052.

(3) Cordes, H., Thiel, C., Aschmann, H.E., Baier, V., Blank, L.M., Kuepfer, L. A Physiologically Based Pharmacokinetic Model of Isoniazid and Its Application in Individualizing Tuberculosis Chemotherapy. Antimicrob. Agents Chemother. 2016;60(10):6134-6145. https://doi.org/10.1128/AAC.00508-16.

(4) Kasim, N. A., Whitehouse, M., Ramachandran, C., Bermejo, M., Lennernäs, H., Hussain, A. S., Amidon, G. L. Molecular properties of WHO essential drugs and provisional biopharmaceutical classification. Mol. Pharm. 2004;1(1):85-96. https://doi.org/10.1021/mp034006h.

(5) Bhandari, R., Kaur, I. P. Pharmacokinetics, tissue distribution and relative bioavailability of isoniazid-solid lipid nanoparticles. Int. J. Pharm. 2013;441(1):202-212. https://doi.org/10.1016/j.ijpharm.2012.11.042.

(6) Goldman, A. L., Braman, S. S. Isoniazid: a review with emphasis on adverse effects. Chest. 1972;62(1):71-77. https://doi.org/10.1378/chest.62.1.71.

(7) Tostmann, A., Boeree, M. J., Peters, W. H., Roelofs, H. M., Aarnoutse, R. E., van der Ven, A. J., Dekhuijzen, P. R. Isoniazid and its toxic metabolite hydrazine induce *in vitro* pyrazinamide toxicity. Int. J. Antimicrob. Agents. 2008;31(6):577-580. https://doi.org/10.1016/j.ijantimicag.2008.01.022.

(8) Maryam, S., Bhatti, A. S. A., Shahzad, A. W. Protective effects of silymarin in isoniazid induced hepatotoxicity in rabbits. Ann. King Edw. Med. Univ. 2010;16(1):43. https://doi.org/10.21649/akemu.v16i1.138.

(9) Metushi, I. G., Cai, P., Zhu, X., Nakagawa, T., Uetrecht, J. P. A Fresh Look at the Mechanism of Isoniazid Induced Hepatotoxicity. Clin. Pharmacol. Ther. 2011;89(6):911-914. https://doi.org/10.1038/clpt.2010.355.

(10) Del Río-Estrada, C., Dougherty, H.W. Profiles of Drug Substances, Excipients and Related Methodology. John Wiley and Sons. 1970. Vol 21. p. 528–533.

(11) Mariappan, T. T., Singh, S. Regional gastrointestinal permeability of rifampicin and isoniazid (alone and their combination) in the rat. Int. J. Tuberc. Lung Dis. 2003;7(8):797-803.

(12) Ramirez, E., Laosa, O., Guerra, P., Duque, B., Mosquera, B., Borobia, A. M., Lei, S. H., Carcas, A. J. and Frias, J. Acceptability and characteristics of 124 human

bioequivalence studies with active substances classified according to the Biopharmaceutic Classification System. Br. J. Clin. Pharmacol. 2010;70:694–702. https://doi.org/10.1111/j.1365-2125.2010.03757.x.

(13) Blume, H. H., Schug, B. S. The biopharmaceutics classification system (BCS): Class III drugs—Better candidates for BA/BE waiver?. Eur. J. Pharm. Sci. 1999;9(2):117-121. https://doi.org/10.1016/S0928-0987(99)00076-7.

(14) Kaur, I. P., Singh, H. Nanostructured drug delivery for better management of tuberculosis. J. Control. Release. 2014;184:36-50. https://doi.org/10.1016/j.jconrel.2014.04.009.

(15) World Health Organization (2017). The selection and use of essential medicines: report of the WHO Expert Committee, 2017 (including the 20th WHO Model List of Essential Medicines and the 6th Model List of Essential Medicines for Children).

(16) Bhutani, H., Mariappan, T. T., Singh, S. The physical and chemical stability of anti-tuberculosis fixed-dose combination products under accelerated climatic conditions. Int. J. Tuberc. Lung Dis. 2004;8(9):1073-1080.

(17) Bhutani, H., Singh, S., Jindal, K. C. Drug-drug interaction studies on first-line anti-tuberculosis drugs. Pharm. Dev. Technol. 2005;10(4):517-524.

(18) Battini, S., Mannava, M. C., Nangia, A. Improved Stability of Tuberculosis Drug Fixed-Dose Combination Using Isoniazid-Caffeic Acid and Vanillic Acid Cocrystal. J. Pharm. Sci. 2018;107(6):1667-1679.

(19) Costa-Gouveia, J., Aínsa, J. A., Brodin, P., Lucía, A How can nanoparticles contribute to antituberculosistherapy?. Drug Discov. Today. 2017;22(3):600-607. https://doi.org/10.1016/j.drudis.2017.01.011.

(20) Carazo, E., Borrego-Sánchez, A., Aguzzi, C., Cerezo, P., Viseras, C. Opinion Paper: Use of Clays as Nanocarriers of First-Line Tuberculostatic Drugs. Curr. Drug Deliv. 2017;14(7):902-903. https://doi.org/10.2174/1567201813666160714160727.

(21) Carazo, E., Borrego-Sánchez, A., García-Villén, F., Sánchez-Espejo, R., Aguzzi, C., Viseras, C., Sainz-Díaz, C.I., Cerezo, P. Assessment of halloysite nanotubes as vehicles of isoniazid. Colloids Surf. B Biointerfaces. 2017;160:337-344. https://doi.org/10.1016/j.colsurfb.2017.09.036

(22) Carazo, E., Borrego-Sánchez, A., García-Villén, F., Sánchez-Espejo, R., Viseras, C., Cerezo, P. Aguzzi, C. Adsorption and characterization of palygorskite-isoniazid nanohybrids. Appl. Clay Sci. 2018;160:180-185. https://doi.org/10.1016/j.colsurfb.2017.09.036.

(23) Carazo, E., Borrego-Sánchez, A., Sánchez-Espejo, R., García-Villén, F., Cerezo, P., Aguzzi, C., Viseras, C. Kinetic and thermodynamic assessment on isoniazid/montmorillonite adsorption. Appl. Clay Sci. 2018;165:82-90. https://doi.org/10.1016/j.clay.2018.08.009.

(24) Lvov, Y. M., Shchukin, D. G., Mohwald, H., Price, R. R. Halloysite clay nanotubes for controlled release of protective agents. ACS Nano. 2008;2(5):814-820. https://doi.org/10.1021/nn800259q.

(25) Yuan, P., Tan, D., Annabi-Bergaya, F. Properties and applications of halloysite nanotubes: recent research advances and future prospects. Appl. Clay Sci. 2015;112:75-93. https://doi.org/10.1016/j.clay.2015.05.001.

(26) Yendluri, R., Otto, D. P., De Villiers, M. M., Vinokurov, V., Lvov, Y. M. Application of halloysite clay nanotubes as a pharmaceutical excipient. Int. J. Pharm. 2017;521(1-2):267-273. https://doi.org/10.1016/j.ijpharm.2017.02.055.

(27) Aguzzi, C., Viseras, C., Cerezo, P., Salcedo, I., Sánchez-Espejo, R., Valenzuela, C. Release kinetics of 5-aminosalicylic acid from halloysite. Colloids Surf. B Biointerfaces. 2013;105:75-80. https://doi.org/10.1016/j.colsurfb.2012.12.041.

(28) Aguzzi, C., Sandri, G., Cerezo, P., Carazo, E., Viseras, C. (2016). Health and Medical Applications of Tubular Clay Minerals. In Developments in Clay Science-Volume 7: Nanosized Tubular Clay Minerals Halloysite and Imogolite. 2016. p. 708-725. https://doi.org/10.1016/B978-0-08-100293-3.00026-1.

(29) Bertolino, V., Cavallaro, G., Lazzara, G., Milioto, S., Parisi, F. Halloysite nanotubes sandwiched between chitosan layers: a novel bionanocomposite with multilayer structure. New J. Chem. 2018;42:8384. https://doi.org/10.1039/C8NJ01161C.

(30) Lvov, Y., Wang, W., Zhang, L., Fakhrullin, R. Halloysite clay nanotubes for loading and sustained release of functional compounds. Adv. Mater. 2016;28(6):1227-1250. https://doi.org/10.1002/adma.201502341.

(31) Massaro, M., Colletti, C. G., Noto, R., Riela, S., Poma, P., Guernelli, S., Lazzara, G. Pharmaceutical properties of supramolecular assembly of co-loaded cardanol/triazole-halloysite systems. Int. J. Pharm. 2015;478(2):476-485. https://doi.org/10.1016/j.ijpharm.2014.12.004.

(32) Riela, S., Massaro, M., Cavallaro, G., Colletti, C. G., Lazzara, G., Milioto, S., Noto, R Chemical modification of Halloysite nanotubes for controlled loading and release. J. Mater. Chem. B. 2018;6:3415-3433. https://doi.org/10.1039/C8TB00543E.

(33) Viseras, M. T., Aguzzi, C., Cerezo, P., Viseras, C., Valenzuela, C. Equilibrium and kinetics of 5-aminosalicylic acid adsorption by halloysite. Micropor. Mesopor. Mater. 2008;108(1):112-116. https://doi.org/10.1016/j.micromeso.2007.03.033.

(34) Viseras, C., Aguzzi, C., Cerezo, P. Medical and health applications of natural mineral nanotubes. In Natural Mineral Nanotubes: Properties and Applications. Apple Academic Press Oakville, Canada and Waretown NJ. 2015. p.437-448.

(35) Wu, Y., Yang, J., Gao, H., Shen, Y., Jiang, L., Zhou, C., Liu, M. Folate-Conjugated Halloysite Nanotubes, an Efficient Drug Carrier, Deliver Doxorubicin for Targeted Therapy of Breast Cancer. ACS Appl. Nano Mater. 2018;1(2):595-608. https://doi.org/10.1021/acsanm.7b00087.

(36) Artursson, P., Palm, K., Luthman, K. Caco-2 monolayers in experimental and theoretical predictions of drug transport1. Adv. Drug Deliv. Rev. 2001;46(1-3):27-43. https://doi.org/10.1016/S0169-409X(00)00128-9.

(37) Hubatsch, I., Ragnarsson, E. G., Artursson, P. Determination of drug permeability and prediction of drug absorption in Caco-2 monolayers. Nat. Protoc. 2007;2(9):2111-2119. https://doi.org/10.1038/nprot.2007.303.

(38) Bhutani, H., Singh, S., Vir, S., Bhutani, K. K., Kumar, R., Chakraborti, A. K., Jindal, K. C. (2007). LC and LC-MS study of stress decomposition behaviour of isoniazid and establishment of validated stability-indicating assay method. J. Pharm. Biomed. Anal. 43(4), 1213-1220.

(39) ICH Guideline Q1A(R), 2000.

(40) Vergaro, V., Abdullayev, E., Lvov, Y. M., Zeitoun, A., Cingolani, R., Rinaldi, R., Leporatti, S. Cytocompatibility and uptake of halloysite clay nanotubes. Biomacromolecules. 2010;11(3):820-826. https://doi.org/10.1021/bm9014446.

(41) Han, H. K., Lee, Y. C., Lee, M. Y., Patil, A. J., Shin, H. J. Magnesium and calcium organophyllosilicates: synthesis and *in vitro* cytotoxicity study. ACS Appl. Mater. Interfaces. 2011;3(7):2564-2572. https://doi.org/10.1021/am200406k.

(42) Sandri, G., Aguzzi, C., Rossi, S., Bonferoni, M. C., Bruni, G., Boselli, C., Ferrari, F. Halloysite and chitosan oligosaccharide nanocomposite for wound healing. Acta Biomater. 2017;57:216-224. https://doi.org/10.1016/j.actbio.2017.05.032.

(43) Kommireddy, D. S., Ichinose, I., Lvov, Y. M., Mills, D. K. Nanoparticle multilayers: Surface modification for cell attachment and growth. J. Biomed. Nanotechnol. 2005;1(3):286-290. https://doi.org/10.1166/jbn.2005.046.

(44) Lai, X., Agarwal, M., Lvov, Y. M., Pachpande, C., Varahramyan, K., Witzmann, F. A. Proteomic profiling of halloysite clay nanotube exposure in intestinal cell co-culture. J. Appl.Toxicol. 2013;33(11):1316-1329. https://doi.org/10.1002/jat.2858.

(45) Salcedo, I., Sandri, G., Aguzzi, C., Bonferoni, C., Cerezo, P., Sánchez-Espejo, R., Viseras, C. Intestinal permeability of oxytetracycline from chitosan-montmorillonite nanocomposites. Colloids Surf. B Biointerfaces. 2014;117:441-448. https://doi.org/10.1016/j.colsurfb.2013.11.009.

(46) Romero, A., Ares, I., Ramos, E., Castellano, V., Martínez, M., Martínez-Larrañaga, M. R., Martínez, M. A. Mycotoxins modify the barrier function of Caco-2 cells through differential gene expression of specific claudin isoforms: Protective effect of illite mineral clay. Toxicology. 2016;353:21-33. https://doi.org/10.1016/j.tox.2016.05.003.

(47) Bhutani, H., Singh, S., Jindal, K. C., Chakraborti, A. K. Mechanistic explanation to the catalysis by pyrazinamide and ethambutol of reaction between rifampicin and isoniazid in anti-TB FDCs. J. Pharm. Biomed. Anal. 2005;39(5):892-899. https://doi.org/10.1016/j.jpba.2005.05.015.

(48) Singh, S., Mariappan, T. T., Shankar, R., Sarda, N., Singh, B. A critical review of the probable reasons for the poor variable bioavailability of rifampicin from anti-

tubercular fixed-dose combination (FDC) products, and the likely solutions to the problem. Int. J. Pharm. 2001;228(1-2):5-17. https://doi.org/10.1016/S0378-5173(01)00754-2.

Table I. Samples tested for cytotoxicity measurements.

Sample	Concentration (μg/ml)
HLNTs 1	1
HLNTs 2	1.25
HLNTs 3	2
HLNTs 4	10
HLNTs 5	100
HLNTs 6	1000
INH-loaded HLNTs 1	1.23
INH-loaded HLNTs 2	1.54
INH-loaded HLNTs 3	2.46
INH-loaded HLNTs 4	12.3
INH-loaded HLNTs 5	123
INH-loaded HLNTs 6	1233
INH 1	0.23
INH 2	0.29
INH 3	0.46
INH 4	2.33
INH 5	23.3
INH 6	233

Table II. Average intensity weighted mean diameter and (nm) and polydispersity index for both HLNTs and INH-loaded HLNTs (mean values ± s.d.; n = 3).

Sample	Mean diameter (nm)	Polydispersity Index (PI)
HLNTs	74.864 ±0.0004	0.370 ±0.0021
INH-loaded HLNTs	89.937 ±0.0001	0.703 ± 0.0054

Table III. Values of kinetic parameters obtained from the proposed equation.

Parameters	0.001 M HCl (pH = 3)	SIF (pH = 6.8)
$k_d(h^{-1})$	1953	2167
$C_e(\%)$	95.53	94.45
R^2	0.9929	0.9934

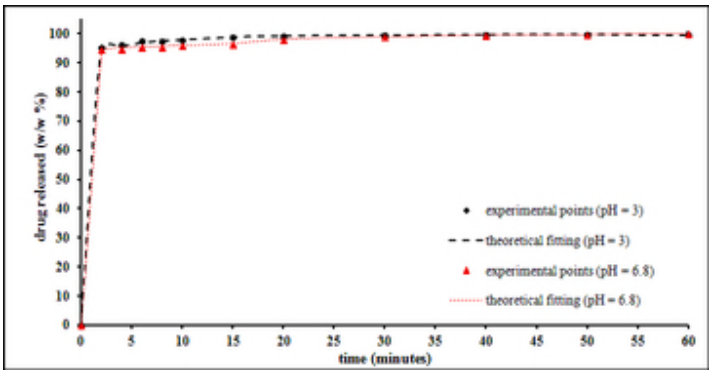

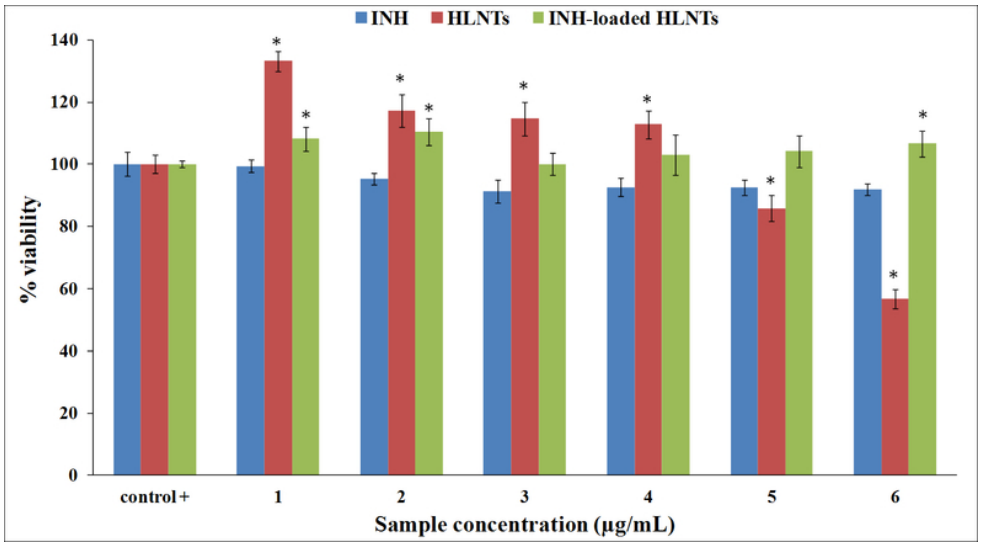

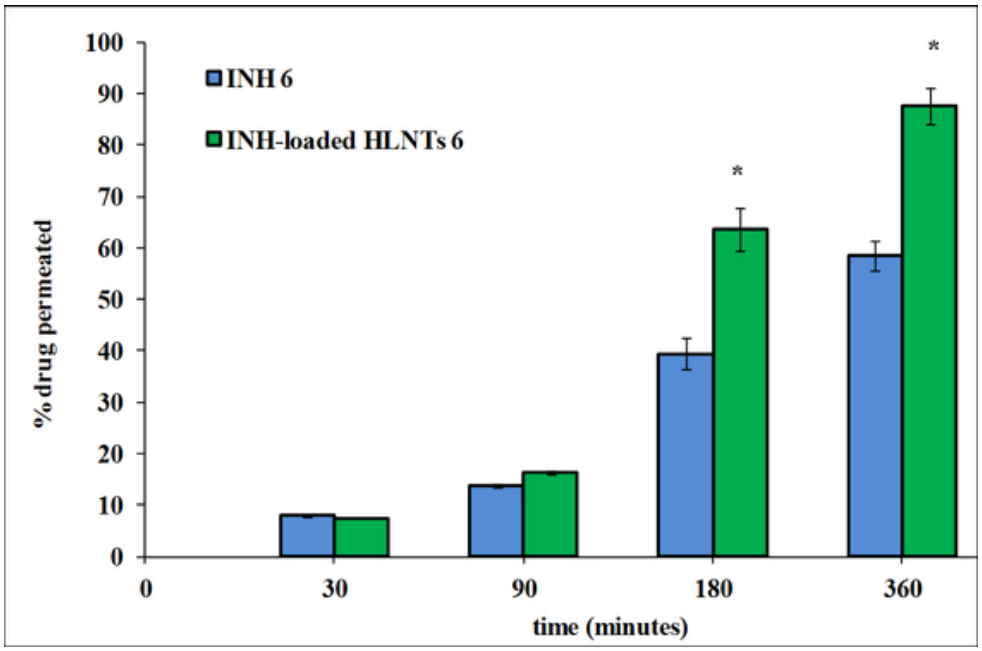

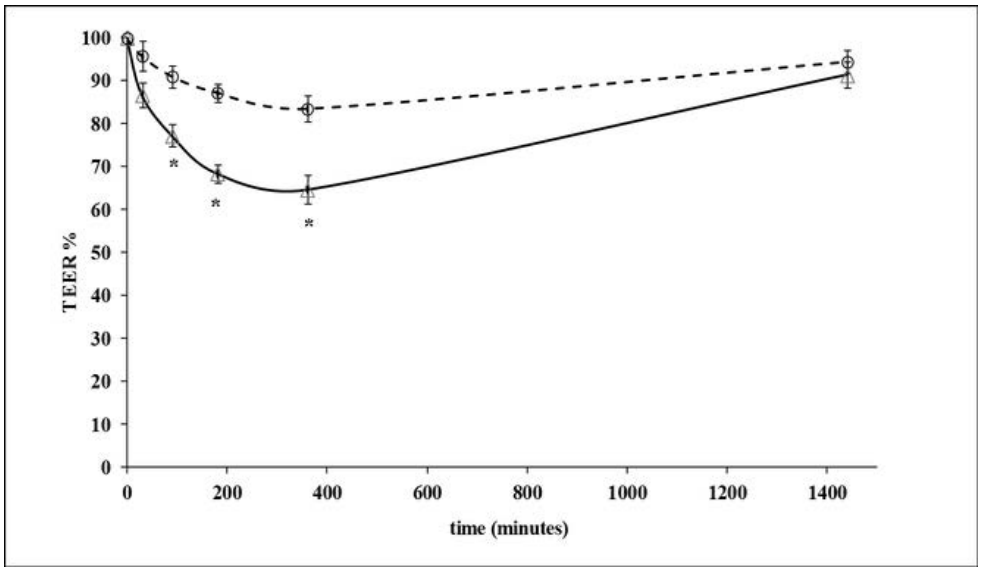

Sample	Propidium Iodide (PI)	Isoniazid (INH)	PI + INH
INH-loaded HLNTs	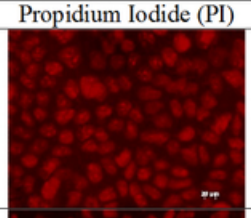		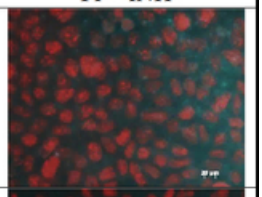
INH	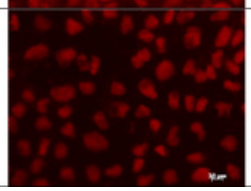	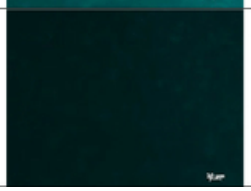	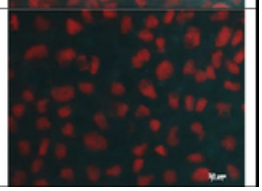

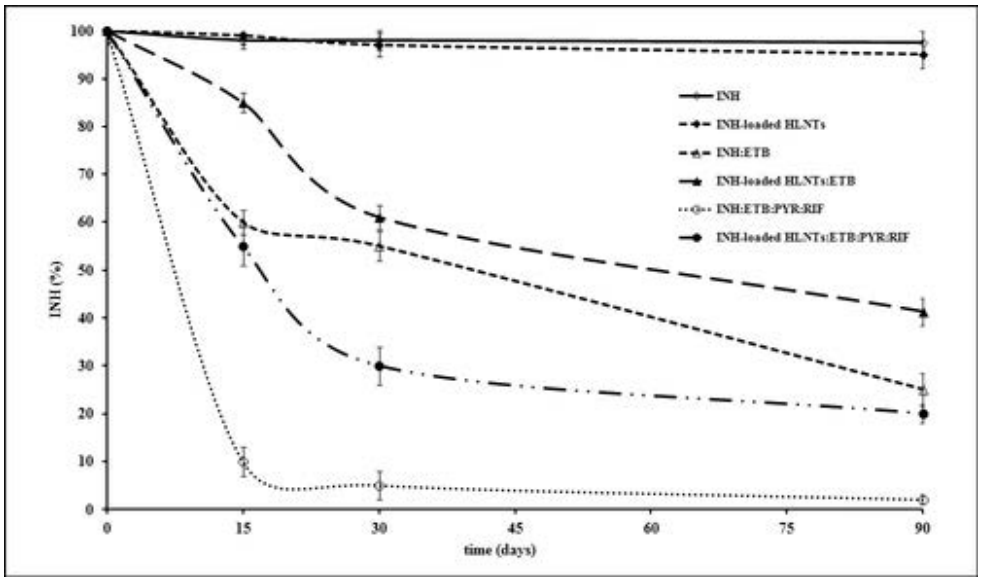

ANEXO II

Publicaciones no incluidas en la Tesis Doctoral

International Journal of Pharmaceutics 531 (2017) 676–688

Contents lists available at ScienceDirect

International Journal of Pharmaceutics

journal homepage: www.elsevier.com/locate/ijpharm

Carvacrol/clay hybrids loaded into in situ gelling films

M. Tenci[a], S. Rossi[a,b,*], C. Aguzzi[c], E. Carazo[c], G. Sandri[a,b], M.C. Bonferoni[a,b], P. Grisoli[a], C. Viseras[c,d], C.M. Caramella[a], F. Ferrari[a,b]

[a] Department of Drug Sciences, University of Pavia, v.le Taramelli 12, 27100 Pavia, Italy
[b] CHT, Centre for Health Technology, University of Pavia, 27100 Pavia, Italy
[c] Department of Pharmacy and Pharmaceutical Technology, University of Granada, Campus of Cartuja, Granada, 18071 s/n, Spain
[d] Andalusian Institute of Earth Sciences, CSIC-University of Granada, Avenida de las Palmeras, Armilla, Granada, Spain

ARTICLE INFO

Article history:
Received 23 February 2017
Received in revised form 5 June 2017
Accepted 10 June 2017
Available online 13 June 2017

Keywords:
Essential oils
Palygorskite
Carvacrol
Cytocompatibility
Antimicrobial properties
Wound healing

ABSTRACT

The aim of the present work was the development of polymer films loaded with a carvacrol (CVR)/clay hybrid (HYBD) for the delivery of CRV in infected skin ulcer treatment. Different clays were considered: montmorrilonite, halloysite and palygorskite (PHC). CRV incorporation in PHC reduced its volatility. HYBD showed 20% w/w CRV loading capacity and was able to preserve CRV antioxidant properties. HYBD was characterized by improved antimicrobial properties against *S. aureus* and *E. coli* and cytocompatibility towards human fibroblasts with respect to pure CRV.

Films were prepared by casting an aqueous dispersion containing poly(vinylalcohol) (PVA), poly (vinylpyrrolidone) (PVP), chitosan glutamate (CS), sericin and HYBD. Optimization of film composition was supported by a Design of Experiments (DoE) approach. In a screening phase, a full factorial design (FFD) was used and the following factors were investigated at two levels: PVA (12–14% w/w), PVP (2–4% w/w) and CS (0.134–0.5% w/w) concentrations. For the optimization phase, FFD was expanded to a "central composite design". The response variables considered were: elongation, tensile strength and buffer absorption of films, durability of the gels formed after film hydration. Upon hydration, the optimized film formed a viscoelastic gel able to protect the lesion area and to modulate CRV release.

1. Introduction

Chronic wounds, such as diabetic foot ulcers, pressure ulcers and venous leg ulcers represent a worldwide health problem (Boateng et al., 2008; Boateng and Catanzano, 2015). Advanced therapeutic dressings, designed to take an active role in the wound healing process, represent an interesting approach in the treatment of chronic wounds. Their biological properties are related not only to the bioactive agents loaded into dressing, but also to the presence of biomaterials able to improve tissue repair (Boateng and Catanzano, 2015). Among these biomaterials, chitosan, a linear polysaccharide obtained by chitin deacetylation, has been recognized as a biopolymer able to promote tissue repair and to avoid the onset of infections (Muzzarelli, 2009; Rossi et al., 2010, 2013; Mori et al., 2016; Tenci et al., 2016).

The association of synthetic and natural polymers in composite dressings has been recognized useful to control drug delivery in the wound site (Boateng et al., 2008). Among synthetic polymers, poly(vinylalcohol) (PVA) and poly(vinylpyrrolidone) (PVP) have been largely employed for biomedical applications, such as controlled release systems and tissue engineering (Li et al., 2010; Vicentini et al., 2010).

Carvacrol (CRV), a monoterpene phenolic compound, is the major component (up to 80%) of oregano essential oil (EO) (*Origanum vulgare*) (Burt, 2004). It possesses antioxidant, antifungal and antimicrobial properties (Ben Arfa et al., 2006; Safaei-Ghomi et al., 2009; Tunç et al., 2011).

Different strategies were proposed to reduce evaporation of EOs. One of these provides the inclusion of EOs in montmorrilonite (MMT) and halloysite (HAL). Recently, some authors proposed the use of such clays as packaging materials and demonstrated their capability to enhance the thermal stability and to preserve the antimicrobial properties of EOs (Efrati et al., 2014; Shemesh et al., 2015). Gorrasi (2015) proved that packaging hybrid/polymer films were able to control EOs release.

So far, to the best of our knowledge, no papers have been published on the use of EO/clay hybrids loaded into films for cutaneous application. Clays generally employed in the

* Corresponding author at: Department of Drug Sciences, University of Pavia, Viale Taramelli 12, 27100 Pavia, Italy.
E-mail address: silvia.rossi@unipv.it (S. Rossi).

http://dx.doi.org/10.1016/j.ijpharm.2017.06.024
0378-5173/

pharmaceutical and cosmetic fields belong to smectites, kaolin and fibrous clay groups (López-Galindo et al., 2007; Viseras et al., 2008, 2010; Sanchez-Espejo et al., 2014).

Given these premises, the aim of the present work was the preparation of CVR/clay hybrids to be loaded into gelling viscoelastic films for the treatment of infected skin lesions. Hybrids should prevent CVR evaporation and maintain its antioxidant and antimicrobial properties. Three different commercial clays have been considered: MMT, HAL and palygorskite (PHC).

In a first phase of the research, CVR and CVR/clay hybrids were prepared by using two different approaches: adsorption in saturated atmosphere and shear mixing. Hybrids were subjected to thermal analysis in order to study the effect of clay type and of preparation method on CRV volatility. On the basis of the results obtained, clay and preparation method which allowed the highest CRV loading were chosen for the continuation of the research. The chosen CRV/clay hybrid (HYBD) was investigated *in vitro* for cell viability and antioxidant activity on human fibroblasts and for antimicrobial properties on *S. aureus* and *E. coli*, in comparison with pure CRV.

A second phase of the research was devoted to the preparation and optimization of films to be used as vehicle for HYBD. Films should be characterized by suitable mechanical properties (high flexibility and resistance to rupture) and by the capability to absorb wound exudate forming a viscoelastic persistent gel, able to protect the lesion area without impairing CRV release.

Films were composed by poly(vinylalcohol) (PVA), poly(vinylpirrolidone) (PVP), chitosan glutamate (CS), sericin (SER) and glycerol. PVA was used for its excellent film-forming capacity (Guo et al., 2011; Comolli et al., 2012). PVP was combined with PVA as a controller of mechanical properties because this polymer had good aqueous solubility and extremely low cytotoxicity (Contardi et al., 2017; Sreedharan and Sujith, 2015; Seabra and De Oliveira, 2004; Singh and Pal, 2011). CS was chosen for its capability to enhance wound healing (Rossi et al., 2015). Sericin (SER) was added to improve HYBD antioxidant properties (Mori et al., 2016), while glycerol was used as plasticizing agent. To obtain films of optimized composition, a DoE approach was employed. The experimental design provided a screening and an optimization phase. In the screening phase a full factorial design (FFD) was used not only to investigate the effect of each factor (PVA, PVP and CS concentrations) on the response variables considered (flexibility, mechanical strength, hydration capability of films and gel durability), but also to individuate the main influencing factors. To find the optimal formulation, the screening design was expanded to a central composite design (CDD) (Dejaegher and Vander Heyden, 2011). The experimental results characterizing the optimized formulation were compared to those predicted by the model in order to confirm its predictive power. Moreover, film of optimized composition was subjected to rheological (viscoelastic) characterization upon hydration in a medium mimicking wound exudate and to *in vitro* CRV release measures.

2. Materials and methods

2.1. Materials

The following materials were used: antibiotic/antimycotic solution (100×), containing 10,000 units/ml penicillin, 10 mg/ml streptomycin and 25 μg/ml amphotericin B (Sigma Aldrich, Milan, I); carvacrol (natural, 99%, FG; CRV) (Sigma Aldrich, Milan, I); chitosan low MW (CS) (DD: 80%) (Sigma Aldrich, Milan, I); dimethyl sulfoxide (DMSO) (Sigma Aldrich, Milan, I); Dulbecco's Modified Eagles Medium (DMEM) (Lonza, BioWhittaker, Walkersville, MD, USA); Dulbecco's Phosphate Buffer Solution (Sigma Aldrich, Milan, I); glutamic acid (Sigma Aldrich, Milan, I); glycerol (Carlo Erba, Milan I); Hank's balanced salt solution (HBSS) (Sigma Aldrich, Milan, I); inactivated foetal calf serum (Biowest, Nuaillé, F); hydrogen peroxide (Carlo Erba, Milan, I); MTT (3-(4,5-dimethylthiazol-2-yl)-2,5-diphenyltetrazolium bromide) (Sigma Aldrich, Milan, I); $NaH_2PO_4{\cdot}H_2O$ (Carlo Erba, Milan I); $Na_2HPO_4{\cdot}H_2O$ (Carlo Erba, Milan, I); NaCl (Carlo Erba, Milan, I); *n*-hexane (Carlo Erba, Milan I); Pharmasorb© colloidal (Palygorskite, PHC) (BASF Aktiengesellschaft, Ludwigshafen, G); poly(vinylalcohol) (PVA) (Sigma Aldrich, Milan, I); poly(vinylpyrrolidone) K90 (PVP) (BASF Aktiengesellschaft, Ludwigshafen, G); trypan blue solution (Biological Industries, Beit-Haemek, IL); trypsin–EDTA solution (Sigma Aldrich, Milan, I); Veegum© HS (montmorillonite, MMT) (Vanderbilt Minerals, LLC, Norwalk, USA); Halloysite (HAL) (Sigma Aldrich, Madrid, S).

2.2. Preparation of CVR/clay hybrids

Three different clays, halloysite (HAL), montmorrilonite (MMT) and a commercial palygorskite (PHC) were considered. CVR/clay hybrids were prepared according to two different methods: adsorption in saturation conditions and shear mixing.

The first method provided to create an ambient saturated with CVR. To this aim, a beaker containing 10 ml of CVR was put in the middle of an hermetically sealed glass chamber (489 cm^3 volume). 50 mg of each clay was layered on a watch glass inside of the chamber. The chamber was thermostatated at a constant temperature (20, 40, 60, 80 and 120 °C) for a fixed time period (2 or 5 days).

Shear mixing technique provided to disperse the clay in CVR (2:1 w/w ratio) by ultra-sonication at room temperature for 1 h (Shemesh et al., 2015). CVR not adsorbed onto clay was removed by centrifugation (4218 centrifuge, ALC International s.r.l., Milan, I) at 1000*g* for 15 min and by evaporation in oven (Vismara Laseleletronics s.r.l., Lodi, I) for 24 h at 80 °C.

To assess CRV loading, CVR/clay hybrids were subjected to thermogravimetric analysis (TGA). Pure CVR and clays were used as references. TGA analysis was carried out by a Shimadzu mod. TGA-50H apparatus, in the temperature range 36–950 °C at a heating rate of 10 °C/min. The results were expressed as% mass loss as a function of temperature. From the comparison of TGA profiles of hybrids with those of pure CVR and clays, % CRV loading into hybrids was calculated (% LC) (see Eq. (1)).

$$\%LC = \frac{\text{CVR loaded (mg)}}{\text{hybrid (mg)}} \times 100 \quad (1)$$

TGA analysis was also used to assess HYBD stability upon storage for 1 month at 20 °C in a desiccator.

To confirm the data obtained from TGA analysis, the amount of CRV loaded into HYBD was assessed by an extraction method. In particular, 2 mg of HYBD was weighted and added to 10 ml *n*-hexane (Tunç and Duman, 2011). The dispersion was maintained under stirring overnight, centrifuged at 3000 rpm for 20 min and then filtered (cellulose acetate, 0.45 μm; Sartorius, Muggiò, I). The supernatant was recovered and analyzed for CRV content by means of a UV–vis spectrophotometer (Perkin Elmer, Lambda 25) at wavelengths ranging from 200 to 500 nm. A calibration curve was obtained using CRV hexane solutions having the following concentrations: 50, 25, 20, 10 and 5 μg/ml.

2.3In vitro *cytocompatibility assessment of CRV and HYBD*

NHDF (normal human dermal fibroblasts from foreskin) (Promocell GmbH, Heidelberg, G) 6th to 16th passage were used.

Cells were cultured in a polystyrene flask (Greiner bio-one, PBI International, Milan, I) with 13–15 ml of complete culture medium (CM), consisting of Dulbecco's modified Eagles medium with 4.5 g/l glucose and L-glutamine supplemented with 1% (v/v) antibiotic antimycotic solution (100×), stabilized with 10,000 units/ml penicillin, 10 mg/ml streptomycin and 25 μg/ml amphotericin B and 10% (v/v) inactivated foetal calf serum. Cells were maintained in incubator (Shellab® Sheldon® Manufacturing Inc., Oregon, USA) at 37 °C under 95% air and 5% CO_2 atmosphere. All the operations required for cell culture were carried out in a vertical laminar air flow hood (Ergosafe Space 2, PBI International, Milan, I). When cells reached 80–90% confluence, trypsinization was effected as described by Tenci et al. (2017). The amount of viable cells in the suspension after trypsinization was determined in a counting chamber (Hycor Biomedical, Garden Grove, California, USA), using 0.5% (w/v) trypan blue solution.

To assess cytocompatibility of CRV and HYBD towards human fibroblasts, cell viability tests were performed to estimate the number of viable cells after a prefixed time-contact with the samples examined.

$3.5 \cdot 10^4$ cell/well (0.35 cm^2 area) were seeded in 96-well plate (Greiner bio-one, VWR International, Milan, I) with culture medium (CM) and let growing to confluence. After medium removal, cells were put in contact for 24 h with 200 μl of CRV aqueous solutions or HYBD aqueous dispersions. In particular, a CRV aqueous solution (1 mg/ml) was diluted in CM; the final concentrations upon dilution were 5, 10, 25 and 50 μg/ml. As for HYBD, the powder was dispersed into CM in order to obtain final concentrations of CRV equal to 5, 10, 25 and 50 μg/ml. CM was used as positive control. After 24 h contact with samples, cells were washed with 100 μl of HBSS (pH 7.4) and then put in contact for 3 h with a 8 mM MTT (3-(4,5-dimethylthiazol-2-yl)-2,5-diphenyltetrazolium bromide) solution in HBSS (150 μl/well). Finally, 100 μl of dimethylsulfoxide (DMSO) was added to each well, to allow complete dissolution of formazan crystals, obtained from the reduction of MTT dye into cells by dehydrogenase enzyme. After 60 s shaking, the solution absorbance was determined at 570 nm, with a 690 nm reference wavelength, by means of an IMark® Microplate reader (Bio-Rad Laboratories S.r.l., Segrate, Milan, I). Results were expressed as % viability calculated by normalizing the absorbance measured after contact with samples with that measured after contact with pure CM, used as positive control.

2.4. In vitro *assessment of antioxidant properties of CRV and HYBD*

CVR and HYBD antioxidant properties were investigated using fibroblasts as biological substrate. NHDF fibroblasts (Promocell GmbH) from 6th to 16th passage were used. Cells were seeded (3.5×10^4 cells/cm^2) overnight into a 96-well plate (Greinerbio-one, PBI International, I) and then put in contact for 6 h with samples (200 μl). CRV and HYBD were diluted/dispersed into complete medium (CM) in order to obtain final concentrations of CRV equal to 5, 10 and 25 μg/ml. Subsequently, 10 μl of 10.5 mM H_2O_2 was added in each well (the final H_2O_2 concentration, upon dilution with 200 μl of CM or sample solution/dispersion, was equal to 1 mM) and incubated for 18 h (Mori et al., 2016; Peng et al., 2016). Then, cells were washed with HBSS (pH 7.4) and a MTT test was performed (as described in Section 2.3).

2.5In vitro *assessment of antimicrobial properties of CRV and HYBD*

To evaluate the antimicrobial properties of CRV and HYBD, the following reference bacterial strains were used: *Staphylococcus aureus* ATCC 6538 and *Escherichia coli* ATCC 10536. Before testing, bacteria were grown overnight in Tryptone Soya Broth (Oxoid, Basingstoke, UK) at 37 °C. The cultures were centrifuged at 224*g* for 20 min to separate microorganisms from culture broth and then washed with purified water. Washed cells were re-suspended in Dulbecco's PBS and optical density (OD) was adjusted to 0.1, corresponding approximately to 1×10^8 colony forming units (CFU)/ml at 650 nm wavelength.

The antimicrobial activity of CRV and HYBD was determined with the macrodilution broth method, according to Clinical and Laboratory Standards Institute guidelines (2009), with some modifications reported in this paragraph. The desired concentration of CRV was achieved through the addition in 15 mm × 100 mm test tubes of an appropriate CRV volume to 1 ml of double-concentrate isoSensitest broth (ISB, Oxoid). Bacterial suspensions were added to the test tubes.

The minimum inhibitory concentration (MIC) was evaluated after 24 h incubation at 37 °C as the lowest concentration that completely inhibited the formation of visible microbial growth. Control test tubes containing microorganisms in culture without CRV were used. The same experiment was performed suspending an appropriate quantity of HYBD in 1 ml of double-concentrated

Table 1
Experimental points of FFD and CCD.

		Experimental Points	PVA	PVP	CS
Central Composite Design	Full Factorial Design	1	+1	+1	+1
		2	+1	+1	−1
		3	+1	−1	+1
		4	+1	−1	−1
		5	−1	+1	+1
		6	−1	+1	−1
		7	−1	−1	+1
		8	−1	−1	−1
		9	0	−1.73	0
		10	0	+1.73	0
		11	+1.73	0	0
		12	−1.73	0	0
		13	0	0	+1.73
		14	0	0	−1.73
		15	0	0	0

PVA: level −1 (12%); level +1 (14%); level −1.73 (11.27%); level +1.73 (14.73%); level 0 (13%).
PVP: level −1 (2%); level +1 (4%); level −1.73 (1.27%); level +1.73 (4.73%); level 0 (3%).
CS: level −1 (0.134%); level +1 (0.5%); level −1.73 (0%); level +1.73 (0.634%); level 0 (0.317%).

isoSensitest broth (ISB, Oxoid). Test tubes containing each microorganism in culture added with unloaded clay were used as controls. MIC was detected after 24 h incubation at 37 °C.

Minimum bactericidal concentration (MBC) was evaluated by inoculating aliquots of culture medium in which the inhibition of bacterial proliferation was observed. MBC was the lowest concentration capable of killing the microbial cells (Clinical and Laboratory Standards Institute, 1999). MBC was detected after 24 h incubation at 37 °C. Bacteria-free broth was included as control.

2.6. DoE assisted approach for film formulation

2.6.1. Screening of independent variables

A screening design was used to determine which factors and which of their interactions significantly affect the response variables. Such factors would have been subsequently considered in the optimization phase. Full or fractional two-level factorial designs could have been employed for this purpose (Dejaegher and Vander Heyden, 2011).

In the present work a "2^3 full factorial design" (FFD) was chosen. Three factors, corresponding to the three polymers employed for film formulation, PVA, PVP and CS, were investigated at two different concentrations (levels). The polymer concentrations considered were: 12%, 14% w/w for PVA (x_1), 2%, 4% for PVP (x_2) and 0.134%, 0.5% w/w for CS (x_3). Eight film formulations, corresponding to the different experimental points, were prepared. In Table 1 (points 1–8) polymer concentrations employed for film preparation are reported: for each polymer the upper level is indicated as +1 and the lower one as −1. The response variables considered were: % elongation (%E), tensile strength (TS), hydration properties (buffer amount absorbed per unit weight) and gel durability. The experiments were performed in random sequence. Design generation and statistical analysis were carried out using a statistical software package (Statgraphics 5.0 Statistical Graphics Co., Rockvillle, MD, USA).

2.6.2. Optimization design

For the optimization of film formulation, a response surface design, in particular a randomized "central composite design" (CDD), was used.

Response surface designs are divided into 2 categories, symmetrical and asymmetrical designs; in particular CDD is a symmetrical response surface design and covers a symmetrical experimental domain (Dejaegher and Vander Heyden, 2011). In this type of design the dependent variables are modelled as function of the independent parameters.

CDD consists of three parts: (1) a full factorial design (2^f experiments), (2) an additional design, a star design ($2\times f$ experiments), and (3) a central point. N experiments ($N = 2^f + (2^*f) + 1$) are required to examine the most important factors (f) identified by the preliminary screening design.

In CDD, the experimental points of the full factorial design correspond to the levels −1 and +1, those of the star design at the levels 0, $-\alpha$ and $+\alpha$ ($\alpha \geq 1$), and the central point at the level 0. Depending on α value, two different CCDs exist: a face-centred CCD ($\alpha = 1$), a simplified CDD, in which three levels for each factor are considered, and a circumscribed CCD ($\alpha > 1$),examining the factors at five levels (Dejaegher and Vander Heyden, 2011).

For our purpose a CDD with $\alpha > 1$, examining five levels for each factor, was considered and seven additional dressing formulations were investigated with respect to FFD (Table 1 (points 9–15)).

The factors and the response variables considered in CDD were the same of the screening phase. The experiments were performed in random sequence. Design generation and statistical analysis were carried out using a statistical software package (Statgraphics 5.0 Statistical Graphics Co., Rockvillle, MD, USA).

In the optimization phase, experimental data obtained for each response variable of the experimental design were fitted to a multiple regression model, described below (Eq. (2)):

$$y = \beta_0 + \sum_{i=1}^{f} \beta_i x_i + \sum_{1 \leq i < f}^{f} \beta_{ij} x_i x_j + \sum_{i=1}^{f} \beta_{ii} x_i^2 \quad (2)$$

where y is the response, β_0 the intercept, β_i the main coefficients, β_{ij} the two-factor interaction coefficients, and β_{ii} the quadratic coefficients (Dejaegher and Vander Heyden, 2011).

Such model was used to predict the value of each response variable, related to any combination of factors within the experimental region, by means of a software package (Statgraphics 5.0, Statistical Graphics, Rocknille, MD). It was also possible to compare the predicted values with the experimental data by using the Analysis of Variance (ANOVA) (Dejaegher and Vander Heyden, 2009, 2011).

2.6.3. Film preparation

HYBD at 2.6% w/w concentration was dispersed into a sericin (Ser) (1.6% w/w)/glycerol (gly) (20% w/w) aqueous solution. Ser was used to strengthen CRV antioxidant properties (Mori et al., 2016), whereas gly acted as plasticizer (Rossi et al., 2013). Such a dispersion was diluted 1:1 w/w with a polymeric aqueous solution, containing PVA, PVP and CS.

The final polymer concentrations corresponded to the different points of the experimental design. After overnight stirring, 6.7 g of the diluted dispersion was layered on teflon plates (5.5 cm × 5.5 cm area) and dried for 24 h at 50 °C in oven (Vismara Laser Elettronics s.r.l., Lodi, I). After drying, films were recovered and stored in a desiccator until characterization. Dried films were characterized for CRV loading, mechanical properties, buffer absorption properties and for the durability of gel formed upon hydration in a medium mimicking wound exudate.

2.6.4. CRV loading into films

In order to quantify the amount of CRV loaded into films, 100 mg of each film was dissolved in 1 ml of distilled water. Subsequently, 10.0 ml of *n*-hexane was added. To allow the complete CRV extraction the aqueous-organic mixture was maintained under stirring overnight (Campos-Requena et al., 2015). The mixture was centrifuged at 1000*g* for 20 min to separate the organic from the aqueous phase. Finally, the organic phase recovered was filtered through a cellulose acetate membrane (cellulose acetate, 0.22 μm; Sartorius, Muggiò, I) and analyzed with a UV–vis spectrophotometer (Perkin Elmer, Lambda 25) as described in Section 2.2.

2.6.5. Assessment of film mechanical properties

Mechanical properties were measured using a TA-XT plus Texture Analyzer (ENCO, Spinea, Venice, I) equipped with a 5 kg load cell. Before testing, dried films were cut 40 mm × 20 mm and the strips obtained were clamped between tensile grips A/TG probe, setting an initial distance between the grips of 20 mm. Then, the upper grip was raised at a constant speed of 5 mm/s up to a distance equal to 20 mm, corresponding to 100% elongation. Films were visually inspected in order to observe the occurrence of a physical damage (break) during the test. % elongation corresponding to film break was recorded together with the related tensile strength applied (TS, N/mm^2). In absence of film damage, tensile strength value corresponding to 100% elongation was recorded.

TS is an index of film strength, while %E indicates film flexibility, that is the capability of the film to deform without breaking when subjected to increasing strengths (El-Malah and Nazzal, 2008).

Percent elongation was calculated as follow (Eq. (3)):

$$\%E = \frac{\text{final length} - \text{inital lenght}}{\text{initial lenght}} \quad (3)$$

2.6.6. Assessment of film hydration properties and gel durability

Films were subjected to hydration measurements at 32 °C by means of Franz diffusion cells (PermeGear, Bethlehem (PA)). A circular film, having a diameter of 20 mm and weight of 200 ± 10 mg, was layered on a pre-hydrated dialysis membrane (Mires Emanuele, MWCO 12–14000 Da; ø 36/32″–28.6 mm), used to separate the donor and the receptor chambers of the Franz cell. The receptor chamber was filled with pH 7.4 buffer (phosphate buffered saline (PBS); $NaH_2PO_4 \cdot H_2O$ 0.036% w/w, Na_2HPO_4 H_2O 0.137% w/w, NaCl 0.850% w/w), chosen to mimic wound exudate. At prefixed times (4 and 8 h), films were weighted (Tenci et al., 2017).

The PBS amount taken up by the film was normalized for dry film weight (gPBS/g) to obtain the amount of PBS uptaken/unit film weigth (gPBS/g).

The gel durability was also calculated as the amount of gel formed after 8 h of hydration; it is an index of the dressing resistance against erosion/dissolution process, upon contact with wound exudate.

2.7. Characterization of optimized film formulation

Films of optimized composition (opFILM), chosen on the basis of the results obtained by the CDD design, were prepared by casting (as described in Section 2.6.3) and subjected to the same characterization previously effected on the formulations of the full and central composite designs (Sections 2.6.5 and 2.6.6). The experimental results obtained for opFILM were compared with those provided by the model, in order to confirm its predictive power. Moreover, opFILM was characterized for CRV loading capacity, rheological and CRV release properties as hereafter described.

2.7.1. Assessment of rheological properties of opFILM after hydration

After 4 h hydration (see Section 2.6.6), opFILM was subjected to dynamic viscoelastic (stress sweep and oscillation) tests by means of a rotational rheometer (Rheostress 600, Haake, I), equipped with a cone/plate combination (C20/1: Ø 20 mm; angle = 1°) measuring system.

Stress sweep measurements provide to apply increasing shear stress values (ranging from 0.1 up to 50 Pa) at a constant frequency (0.1 Hz) and to measure the viscoelastic response of the sample, expressed as storage modulus (G′), in order to determine the linear viscoelastic region of the sample. Oscillation measurements require to apply a fixed stress chosen in the linear viscoelastic region, previously determined, at increasing frequency values (ranging from 0.1 to 10 Hz) and to measure the viscoelastic response of the sample, expressed as the ratio between loss (G") and storage (G′) moduli (loss tangent, tan delta).

2.7.2. Assessment of in vitro *CRV release from opFILM and HYBD*

CRV release from opFILM and HYBD was evaluated at 32 °C by means of Franz diffusion cells (Permeager, Bethlehem, PA, USA) having a 20 mm diameter orifice (3.14 cm^2). Dried films having a diameter of 10 mm and weighting 100 ± 5 mg were examined. For HYBD, 10.0 ± 0.5 mg of powder was layered on a filter membrane (cellulose acetate, 0.22 μm; Sartorius, Muggiò, I), separating the donor and the receptor chambers of the Franz cell (Mori et al., 2014). The receptor chamber was filled with pH 7.4 PBS. At fixed time periods (4, 8, 24 and 48 h), 1 ml of medium was collected and analyzed at 273 nm.

2.8. Statistical analysis

Whenever possible, experimental values of the various types of measures were subjected to statistical analysis. In particular, Anova one way, multiple range test (MRT) was used (Statgraphics 5.0, Statistical Graphics Corporation, Rockvillle, MD, USA).

3. Results and discussion

3.1. Choice of clay type and hybrid preparation method

Fig. 1A reports %CRV loading capacity (%LC) of the three different CVR/clay hybrids prepared by adsorption in saturated atmosphere, after 48 h storage at different temperatures. For all the three clays, an increase in % LC on increasing temperature was observed. HAL was able to adsorb CVR at temperature higher than 40 °C. Among the three clays considered, PHC was characterized by the highest% LC values. This result can be explained by the higher surface available for adsorption of PHC, being a fibrous clay. The highest %LC value was observed at 120 °C.

In Fig. 1B %LC values of the three different CRV/clay hybrids prepared by shear mixing are reported. Also for this preparation

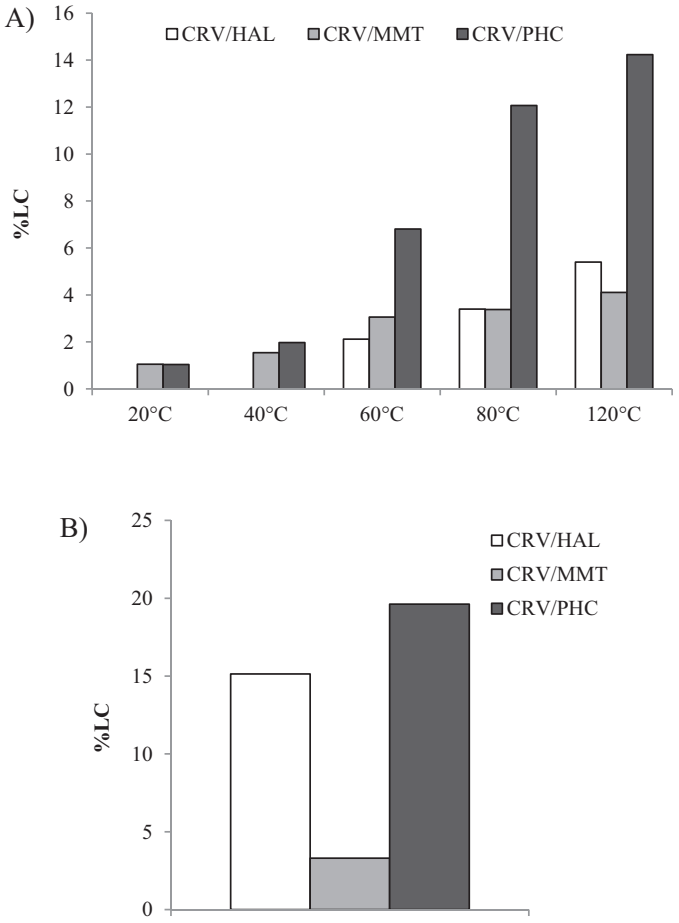

Fig. 1. %CRV loading capacity (%LC) of the three different CRV/clay hybrids prepared: A) by adsorption in saturated atmosphere technique at different temperatures (20, 40, 60, 80, 120 °C) for 48 h; B) shear mixing technique (mean values n = 3; CV% <10%).

technique, %LC was affected by clay structure: the highest value was observed for the fibrous PHC, followed, in decreasing order, by the tubular HAL and by the lamellar MMT. CVR/PHC hybrid (HYBD) prepared by shear mixing was characterized by %LC equal to 20% (w/w), greater than that determined after adsorption in saturated atmosphere technique (14% w/w). The comparison of the results obtained for the various clays with the two different techniques addressed the choice on PHC and shear mixing technique

As an example, in Fig. 2A TGA profiles of HYBD was compared with those of pure CRV and PHC. CRV shows a clear weight loss, due to CRV evaporation, starting at 36 °C and concluded at 191 °C. PHC appears as a thermostable clay, characterized by a weight loss step (150 °C), corresponding to evaporation of superficial humidity (7.6% w/w), with a solid residue at 950 °C equal to approximately 83%. In the TGA profile of HYBD three different steps can be distinguished. The first one (80–286 °C) was associated to a 17% weight loss, attributable to a 9.5% w/w CRV loss, taking into account a 7.5% w/w PHC loss (see TGA profile of pure PHC). In the second step (260–554 °C) HYBD loosed a further 16% weight, corresponding to a 7.5% w/w PHC loss and to a 8.5% w/w CRV loss (calculated as difference). Finally the increase in temperature from 505° to 708 °C produced a HYBD % weight loss equal to 5% w/w, related to a CRV loss of 2% w/w. Total % CRV loss from HYBD was about 20%, corresponding to the total %CRV loaded.

The successful loading of CRV on PHC was confirmed by UV analysis of the supernatant obtained after CRV extraction in hexane from HYBD. The supernatant showed a maximum absorption peak at 275 nm. A CRV-hexane solution, subjected to UV spectrophotometer analysis, showed a maximum absorption peak at 275 nm, which is very close to the wavelength reported by Tunç and Duman (λ_{max} in *n*-hexane∼273 nm) (Tunç and Duman, 2011).The amount of loaded CRV in 2 g of HYBD was 0.43 ± 0.02 g, corresponding to 21 ± 1% w/w.

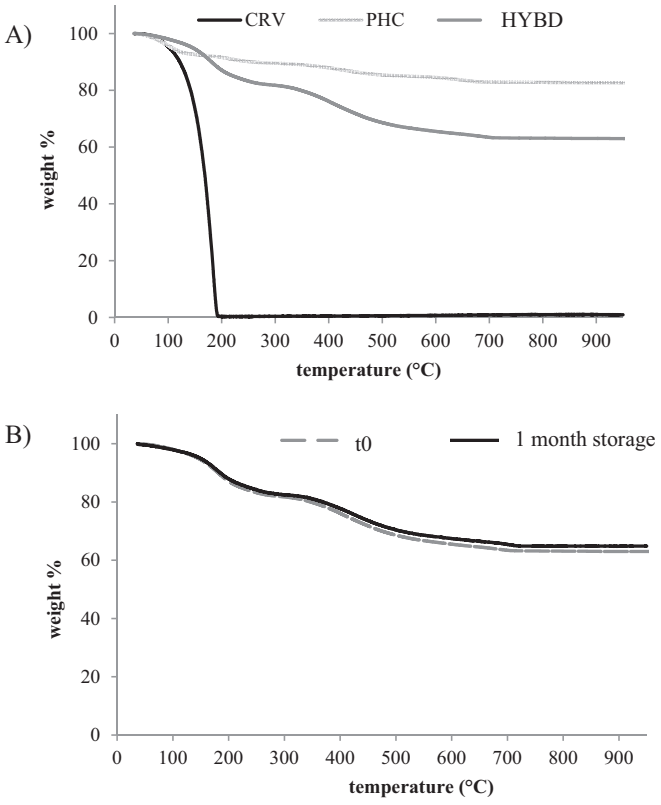

Fig. 2. Comparison of %weight *vs* temperature profiles of: A) PHC, CRV, and HYBD; B) HYBD at time 0 and after storage for 1 month in dessicator, at 20 °C.

Fig. 2B reports TGA curves of HYBD obtained at time 0 and after storage for 1 month at 20 °C in dessicator. Storage conditions did not produce any change in % weight *vs* temperature profile, indicating that in such conditions HYBD was stable: no CVR was lost during storage.

These results indicate that PHC was able to reduce CRV volatility and that HYBD is a stable composite at temperatures lower than 80 °C.

3.2. In vitro *assessment of cytocompatibility, antioxidant and antimicrobial properties of CRV and HYBD*

3.2.1. Cytocompatibility

In Fig. 3% viability values of fibroblasts treated with CRV and HYBD dissolved/dispersed in CM are reported. Different CRV concentrations, ranging from 10 to 100 μg/ml, were considered.

The results indicate that CRV is cytocompatible at low concentrations (10 and 25 μg/ml), as pointed out by % viability values not statistically different from that of the reference (CM). At CRV concentrations >50 μg/ml, a marked reduction in cell viability (76% at 50 μg/ml, and 0% at 100 μg/ml) was observed. These results confirm CVR cytotoxic effect reported by Coccimiglio et al. (2016). CVR produced a concentration-dependent decrease of cell number and total protein, accompanied by a degeneration of cell morphology. Another *in vitro* study pointed out CVR potent inhibitory effect of cell growth in A549 cell line (Koparal and Zeytinoglu, 2003). According to (Coccimiglio et al., 2016), the high CVR partition coefficient in octanol/water (3.64) is responsible for its deep partition in the cytoplasmatic membrane and a consequent alteration of cell permeability.

On the contrary, HYBD did not show any cytotoxic effect for all the concentrations investigated. These results pointed out that CRV loading in PHC is able to protect human fibroblasts against CRV cytotoxic effect. This is likely due to a slow release of CRV to cell membrane. On the basis of such hypothesis, it is necessary to verify if CVR loading in HYBD does not result in a decrease of CRV antioxidant properties.

3.2.2. Antioxidant properties

It is well known that the term oxidative stress expresses an increased formation of reactive oxygen species (ROS) and/or a decrease in their elimination. ROS are normal products of aerobic metabolism, an overproduction occurs under pathophysiological conditions. ROS damage cells, assaulting biological membrane lipids, nucleic acids, carbohydrates, and proteins (Jomova and Valko, 2011). Since H_2O_2 is produced *in vivo* by the spontaneous

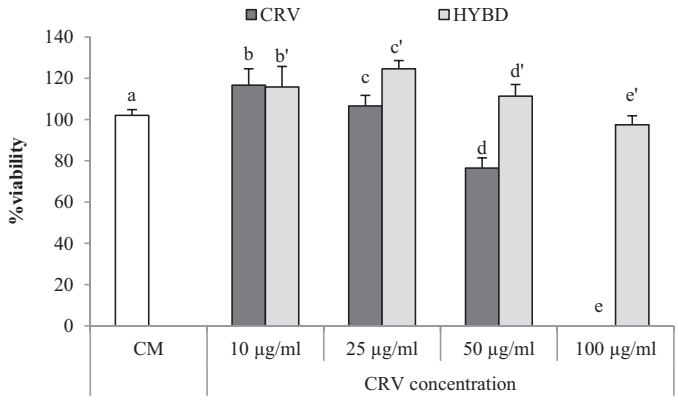

Fig. 3. Comparison of % viability values of CRV (10–100 μg/ml) and HYBD dissolved/dispersed in CM. HYBD amounts corresponding to 10–100 μg/ml CVR concentrations were considered. CM was used as reference (mean values ± s.e; n = 8). Anova one way – MRT ($p < 0.05$): a *vs* d/e; b *vs* d/e; c *vs* d/e; d *vs* e/d′; e *vs* e′; c′ *vs* e′.

and/or enzymatic dismutation of the superoxide anion radical, it was used as a model of oxidative stress.

In Fig. 4% viability values of fibroblasts treated with H_2O_2 in presence and in absence of CRV pure or loaded in HYBD, are compared. Untreated cells, cultured in CM, were used as reference. A significant decrease of % viability is observed for fibroblasts treated with H_2O_2 in comparison with untreated cells, cultured in CM. This result pointed out the suitability of the experimental conditions (H_2O_2 concentration and contact time) to produce an oxidative damage. As expected, pretreatment of fibroblasts with CRV at nontoxic concentrations (10 and 25 μg/ml) resulted in a concentration-dependent protective effect against H_2O_2. Phenols such as CRV belong to the most active natural antioxidants found in the essential oils. According to some authors, *in vitro* antioxidant properties of oregano extracts, whose main component is CRV, are due to their free radical scavenger action (Ruberto and Baratta, 2000; Yanishlieva et al., 1999)

No significant differences were observed between CRV and HYBD, when tested at the same CRV concentration. It must be underlined that % viability values of fibroblasts treated with CRV, either pure or loaded in HYBD, were not significantly different from that observed for cells not treated with the oxidative agent. It indicates CRV capability to protect human fibroblast from oxidative damage. The results obtained prove that CRV was able to protect human fibroblasts against oxidative stress and its loading in PHC did not affect such activity.

3.2.3. Antimicrobial properties

CRV antimicrobial properties are well-known. Lambert et al. (2001) attribute the antimicrobial activity of oregano essential oil and its active constituents (CVR and thymol) to interference with the pH gradient and membrane permeability. More recently, other authors have described that CVR may also be involved in inhibiting *E. coli* flagellin (Burt et al., 2004, 2007Burt et al., 2007).

In Table 2 MIC and MBC values of pure CRV and HYBD are reported. Pure clay did not show antimicrobial activity at the concentrations considered. As expected, CRV showed antimicrobial properties. CRV loading into PHC produced a decrease of MIC and MBC values with respect to pure CRV. These results indicated a higher antimicrobial activity of CRV when loaded into clay. This effect could be attributed either to a lower evaporation (i.e. loss) of CRV when loaded into clay (see Section 3.1) and to a prolonged release of CVR from HYBD.

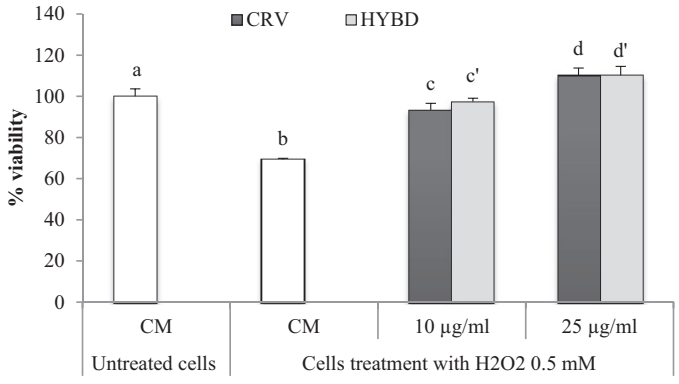

Fig. 4. %cell viability of fibroblasts subjected to oxidative damage (0.5 mM H_2O_2 for 6 h), treated or untreated with CRV (10 and 25 μg/ml), either pure or loaded in HYBD. HYBD amounts corresponding to 10 and 25 μg/ml CVR concentrations were considered. Untreated cells, cultured in CM, were used as reference (mean values ± s.e; n = 8). Anova one way – MRT ($p < 0.05$): a *vs* b; b *vs* c/d/c'/d'; c *vs* d/d'; c' *vs* d'.

Table 2
MIC (minimum inhibition concentration) and MBC (minimum bactericidal concentration) values of pure CRV and HYBD against *Escherichia coli* and *Staphylococcus aureus*. MIC and MBC are expressed as CRV concentration (mean values (s.d), n = 3).

	MIC (mg/ml)		MBC (mg/ml)	
	E. coli ATCC: 10536	*S. aureus* ATCC: 6538	*E. coli* ATCC: 10536	*S. aureus* ATCC: 6538
CRV	1.26 (0.41)	0.65 (0.27)	2.75 (0.65)	2.75 (0.65)
HYBD	0.60 (0.18)	0.26 (0.04)	1.18 (0.26)	0.49 (0.22)

3.3. DoE assisted approach for film formulation

3.3.1. Full factorial design (FFD)

A full factorial design is useful to study the effect of each factor (X) and their interactions on the response variables (Y) (Dejaegher and Vander Heyden, 2011). An analysis of variance was performed to test the statistical significance of the effects (positive or negative) of each factor and interaction on the various response parameters.

As for CRV loading into films, the supernatant (obtained after CVR extraction from film) gave a maximum peak of absorption at 275 nm, as observed for pure CRV and HYBD, confirming the presence of CRV into film. The loading amount was equal to 100 ± 9.8%, with respect to the theoretical one. Such results indicate that the method employed for film preparation did not produce CRV loss.

Fig. 5A reports the experimental results obtained for the film formulations, corresponding to the different experimental points of the FFD.

It can be observed that all films, except formulation 4 (characterized by the highest concentration of PVA and the lowest concentrations of PVP and CS) and formulation 5 (prepared with the highest PVP and CS concentrations and the lowest PVA concentration), were characterized by high elongation values. High % elongation indicates a high film deformability/flexibility, that is a high capability to deform under stress without breaking.

As for tensile stress, all the films maintained integrity when handled for mounting on the tensile apparatus. Stresses applied during such an assembly are reasonably greater than those involved during *in vivo* administration. Therefore, every film is likely to possess a mechanical resistance adequate to their use, which involves a mild manipulation. Anyway, formulations characterized by the lowest CS concentrations showed the highest strength values.

All the films prepared, with the exception of formulations 4 and 8, were able to absorb a buffer amount higher than their dry weight. Formulations 4 and 8 showed the lowest value of gel durability. Such formulations were characterized by low levels of both PVP and CS. The results demonstrate that such polymers were responsible for a slow and high hydration, corresponding to a slow erosion/dissolution and, consequently, to a high gel durability.

In Table 3, the estimated effects on each response variable and the corresponding P-values, calculated from Anova, for each factor and their interactions, are reported.

It can be observed that PVA and CS had a significant effect on % elongation, in particular an increase in PVA concentration caused an increase in such parameter; on the contrary, an increase in CS concentration determined a decrease of film elongation. Such response variable was not significantly affected by PVP concentration. All interactions between factors determined a significant effect on % elongation (see Supplementary material). As for PVA-PVP interaction, when the lowest PVA level is considered, an increase in PVP concentration would determine a decrease of % elongation, while for the highest PVA level an increase in PVP

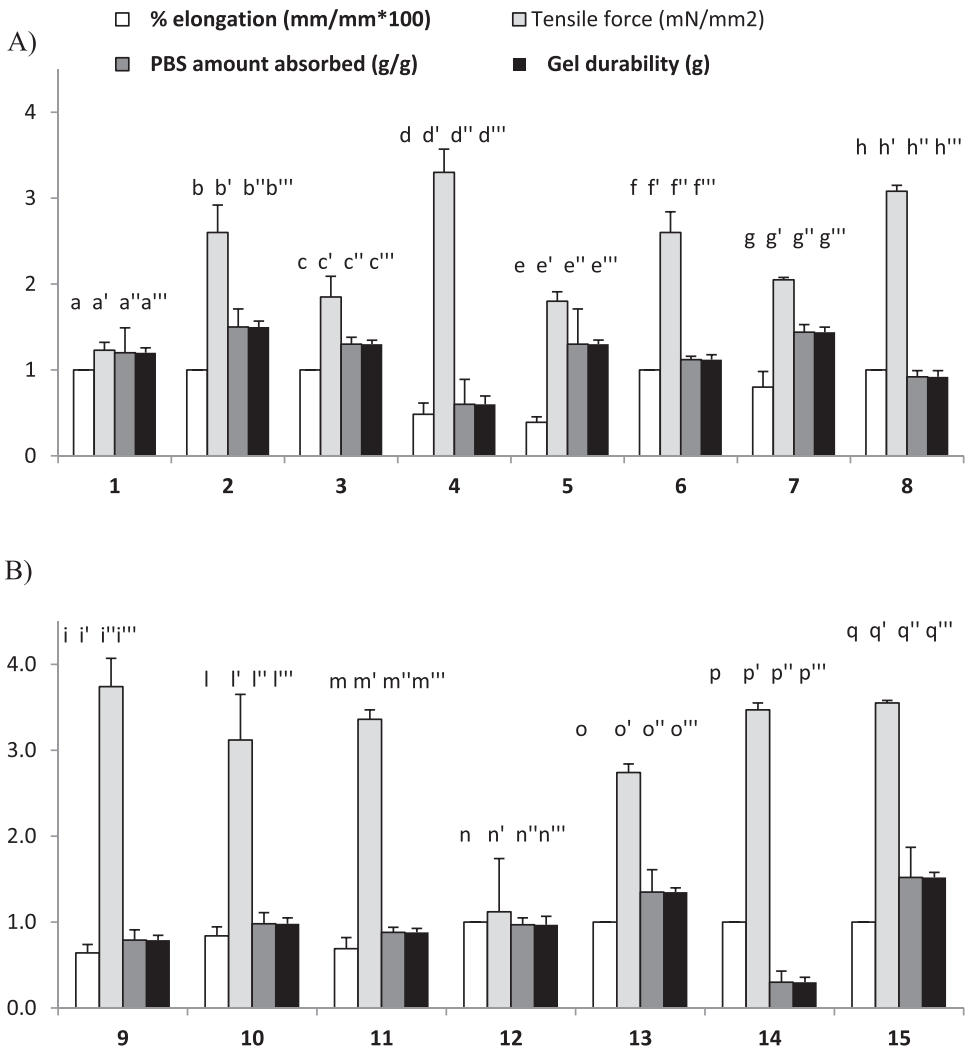

Fig. 5. Response variables of the films of FFD (A) and CCD (A + B) (mean values ± s.d.; n = 3).
Anova one way – MRT ($p < 0.05$)
a vs d/e/g/i/l/m; b vs d/e/g/i/l/m; c vs d/e/g/i/l/m; d vs f/g/h/i/l/m/n/o/p/q; e vs f/g/h/i/l/m/n/o/p/q; f vs g/I/i/m; g vs h/i/n/o/p/q; h vs i/l/m; i vs l/n/o/p/q; l vs m/n/o/p/q; m vs n/o/p/q; a′ vs b′/c′/d′/e′/f′/g′/h′/i′/l′/m′/n′/o′/p′/q′; b′ vs c′/d′/e′/g′/i′/l′/m′/n′/p′/q′; c′ vs d′/f′/h′/i′/l′/m′/n′/o′/p′/q′; d′ vs e′/f′/g′/n′/o′; e′ vs f′/h′/i′/l′/m′/n′/o′/p′/q′; f′ vs g′/i′/l′/m′/n′/p′/q′; g′ vs h′/ i′/l′/m′/n′/o′/p′/q′; h′ vs i′/n′/q′; i′ vs l′/n′/o′/p′/q′; l′ vs n′; m′ vs n′/o′; n′ vs o′/p′/q′; o′ vs p′/q′; a′′ vs d′′/i′′/p′′; b′′ vs d′′/f′′/h′′/i′′/l′′/m′′/n′′/p′′; c′′ vs d′′/h′′/l′′/m′′/p′′; d′′ vs e′′/f′′/g′′/o′′/q′′; e′′ vs h′′/i′′/m′′/p′′; f′′ vs p′′/q′′; g′′ vs h′′/i′′/l′′/m′′/n′′/p′′; h′′ vs o′′/p′′/q′′; i′′ vs o′′/p′′/q′′; l′′ vs o′′/p′′/q′′; m′′ vs o′′/p′′/q′′; n′′ vs o′′/p′′/q′′; o′′ vs p′′; p′′ vs q′′; a′′′ vs d′′′/f′′′/h′′′/i′′′/n′′′/p′′′; b′′′ vs d′′′/f′′′/h′′′/i′′′/n′′′/p′′′; c′′′ vs d′′′/ h′′′/i′′′/o′′′/p′′′; d′′′ vs e′′′/f′′′/g′′′/h′′′/ l′′′/m′′′/o′′′/p′′′; e′′′ vs h′′′/i′′′/n′′′/p′′′; f′′ vs i′′′/n′′′/p′′′; g′′′ vs h′′′/n′′′/p′′′; h′′′ vs i′′′/l′′′/m′′′/n′′′/p′′′; i′′′ vs l′′′/m′′′/n′′′/o′′′/q′′′; l′′ vs o′′′/q′′′; m′′′ vs o′′′/p′′′; n′′′ vs o′′′/p′′′/q′′′; o′′′ vs p′′′; p′′′ vs q′′′..

Table 3
-Estimated effects and their statistical significance (P-values) of each factor and their interactions on each response variable of FFD.

	% E (mm/mm)		TS (N/mm^2)		gPBS/g		Gel durability (g)	
	Estimated effect	P-value	Estimated effect	P-value	Estimated effect	P-value	Estimated effect	P-value
A: PVA	7.34667	0.0418	−0.102667	0.1689	−0.0285	0.7715	−0.00425	0.8935
B: PVP	2.42333	0.4775	−0.462833	0.0000	0.228667	0.0300	0.162083	0.0001
C: CS	−7.34667	0.0418	−1.19383	0.0000	0.259167	0.0157	0.156917	0.0001
AB	23.3583	0.0000	−0.2105	0.0090	0.197167	0.0570	0.108583	0.0029
AC	33.1283	0.0000	−0.332167	0.0002	−0.097	0.3292	0.00741667	0.8154
BC	−23.3583	0.0000	0.0193333	0.7900	−0.318833	0.0042	−0.11625	0.0017

*p-values lower than 0.05 correspond to a statistical significant effect.

concentration should produce an increase in film deformability. Conversely, for both PVA levels, an increase in CS concentration was expected to cause a decrease of % elongation value. As for PVP-CS interaction, the highest % elongation value was estimated for low levels of both PVP and CS.

As for tensile stress, PVP and CS had a significant negative effect, meaning that an increase in PVP or CS concentrations would produce a decrease of such parameter (Table 3), that is a weakening of film structure. These results are in agreement with that reported in literature. In particular, Hasan et al. (2017) observed a decrease

in mechanical properties of films based on CS and PVP on increasing PVP concentration. Yeh et al. (2007) explained similar results with the rigid and fragile nature of PVP.

As for PVA-PVP and PVA-CS interactions, the highest tensile strength values were expected for the highest PVA level associated with the lowest PVP or CS levels (see Supplementary material).

The results obtained indicate that between the two film forming polymers, PVA plays the main positive role on film mechanical properties. On the contrary, CS is responsible for film stiffening.

These results are in agreement with that recently observed by Malipeddi et al. (2017). They prepared transdermal films by dissolving PVP and PVA in distilled water and employing glycerol as plasticizer agent. They observed an increase in tensile strength on increasing PVA concentration.

Also Kim et al. (2015) prepared film based on PVP/PVA blends. They observed that films prepared at 4/10 and 6/8 w/w ratio are characterized by a lower hardness compared to that with only PVA.

Both PVP and CS concentrations would positively affect film capacity to absorb a buffer mimicking wound exudate. Such polymers were expected to cause a slow and high film hydration.

The effect of PVP level was more pronounced for the highest CS concentration (see Supplementary material). When PVP level was fixed at −1, an increase in CS concentration caused a marked decrease of PBS amount absorbed; on the contrary, in the presence of the highest PVP concentration, an increase in CS concentration determined a little decrease of such parameter. These results are in agreement with PVP high hydrophilicity (Hasan et al., 2017) and the poor CS solubility at neutral pH (Muzzarelli, 2009b).

PVP and CS concentrations also influence gel durability, that is gel capability to remain for a prolonged time at the wound site. In particular, an increase in PVP or CS concentrations would produce an increase in such parameter. PVP-CS interactions showed a significant effect. This is due to the formation of hydrogen bonds between PVP and CS, involving OH of PVP and OH or NH_2 of CS (Hassan et al., 2017; Yeh et al., 2006).

3.3.2. Central composite design (CCD)

In Fig. 5B the experimental results of the additional points investigated to expand FFD to CCD are reported.

Table 4 shows the estimated effects on each response variable and the corresponding P-values, calculated from Anova, for each factor and their interactions.

The expansion of FFD to CCD shows that no polymer concentration would individually affect film elongation. On the contrary, significant effects were determined for interactions, in particular a synergic effect for PVA-PVP and PVA-CS interactions and an antagonist one for PVP-CS interaction (see Supplementary material). As for PVA-PVP and PVA-CS interactions, for low PVP or CS concentrations, an increase in PVA concentration would cause a decrease of % elongation; on the contrary, when PVP or CS level was fixed at + 1 an increase in PVA concentration would produce an increase in such parameter. As for PVP-CS interaction, the highest % elongation value was expected for the highest PVP and CS concentrations.

As for tensile stress, the extension of FFD to CCD evidenced a significant effect only for CS. No polymer interaction had a significant effect on such parameter.

As for PBS amount absorbed, the extension of FFD to CCD did not cause changes of the effects of each factor and their interactions, with the exception of PVP concentration, that did not significantly influence film hydration properties.

Also for gel durability no difference was determined by the extension of FFD to CCD.

Based on the results of the statistical analysis (Anova), an equation of the fitted model for each response variable was obtained. In particular, for each response variable, all the factors and/or their interactions that did not significantly affect the response parameter considered were excluded from the general polynomial regression equation. These models were graphically interpreted by drawing 2D contour plots, that represent the responses as functions of the levels of two factors, and 3D response surface plots, that show the responses in three dimensions (Dejaegher and Vander Heyden, 2011).

The results of the statistical analysis (Anova) evidenced that, among the factors considered, PVA was the less influent on the response variables. For such reason, it was decided to keep the PVA level constant for the optimization procedure. To choose PVA concentration, the maximum value of each response variable predicted by the simplified fit models for each PVA level, was considered (Table 5).

Among PVA levels, only +1.73 was estimated to produce films characterized by % elongation lower than 100%. High mechanical resistance, hydration propensity and gel durability were predicted for +1, 0 and −1 levels. Among these, the lowest PVA level (-1) was chosen for the continuation of the work.

In Fig. 6A–D, bi- and tri-dimensional plots drawn according to the simplified fit model for each response variable are reported.

The model predicted that the highest value of percent elongation is obtained for PVP and CS concentrations ranging, respectively, into the intervals −0.80 (2.2% w/w)/+1.73 (4.73% w/w) and −0.67 (0.19% w/w)/+1.73 (0.634% w/w) (Fig. 6A).

As for tensile strength (Fig. 6B), counters plots evidenced the best performance for films characterized by low CS concentration (≤0.17% w/w), independently of PVP concentration.

Table 5
Maximum estimated effects of each PVA level on the response variables.

PVA level	%E	TS (N/mm^2)	gPBS/g	Gel durability (g)
−1.73	139.454	2.98	1.139	0.65
−1	131.45	3.22	1.458	0.73
0	117.97	3.22	1.578	0.73
+1	117.7	3.22	1.420	0.78
+1.73	80.8	2.98	1.074	0.68

Table 4
-Estimated effects and their statistical significance (P-values) of each factor and their interactions on each response variable of CCD.

	% E		TS (N/mm^2)		gPBS/g		Gel amount (g)	
	Estimated effect	P-value*	Estimated effect	P-value*	Estimated effect	P-value*	Estimated effect	P-value*
A: PVA	−3.43942	0.2935	−0.215376	0.2998	−0.0374002	0.6764	0.0181086	0.5219
B: PVP	6.28152	0.0598	−0.375657	0.0752	0.178422	0.0528	0.179139	0.0000
C: CS	−4.1981	0.2016	−0.837745	0.0003	0.408563	0.0001	0.222457	0.0000
AB	23.3583	0.0000	−0.2105	0.4419	0.197167	0.1028	0.108583	0.0060
AC	33.1283	0.0000	−0.332167	0.2281	−0.097	0.4150	0.00741667	0.8424
BC	−23.3583	0.0000	0.0193333	0.9434	−0.318833	0.0105	−0.11625	0.0035

* p-values lower than 0.05 correspond to a statistical significant effect.

As shown in Fig. 6C the model predicted that film formulations, prepared with PVP and CS concentrations ranging, respectively, into the intervals 2.01% w/w (−0.99)/3.93% w/w (+0.93) and 0.27% w/w (−0.25)/0.59% w/w (+1.51), were characterized by high capability to absorb PBS, mimicking wound exudate.

The model describing the gel durability response predicted the highest value of such parameter for a PVP concentration between 1.46% w/w (−1.54) and 3.37% w/w (+0.37) and a high CS concentration (≥0.431% w/w; +0.62) (Fig. 6D).

In general optimal performances do not correspond to a single point but a region of the experimental domain. For this reason, the individual 2D contour plots were superimposed in order to identify the optimal region of domain, capable of satisfying the following constraints: % elongation ≥80%; 3 N/mm^2 >tensile strength ≥2.4 N/

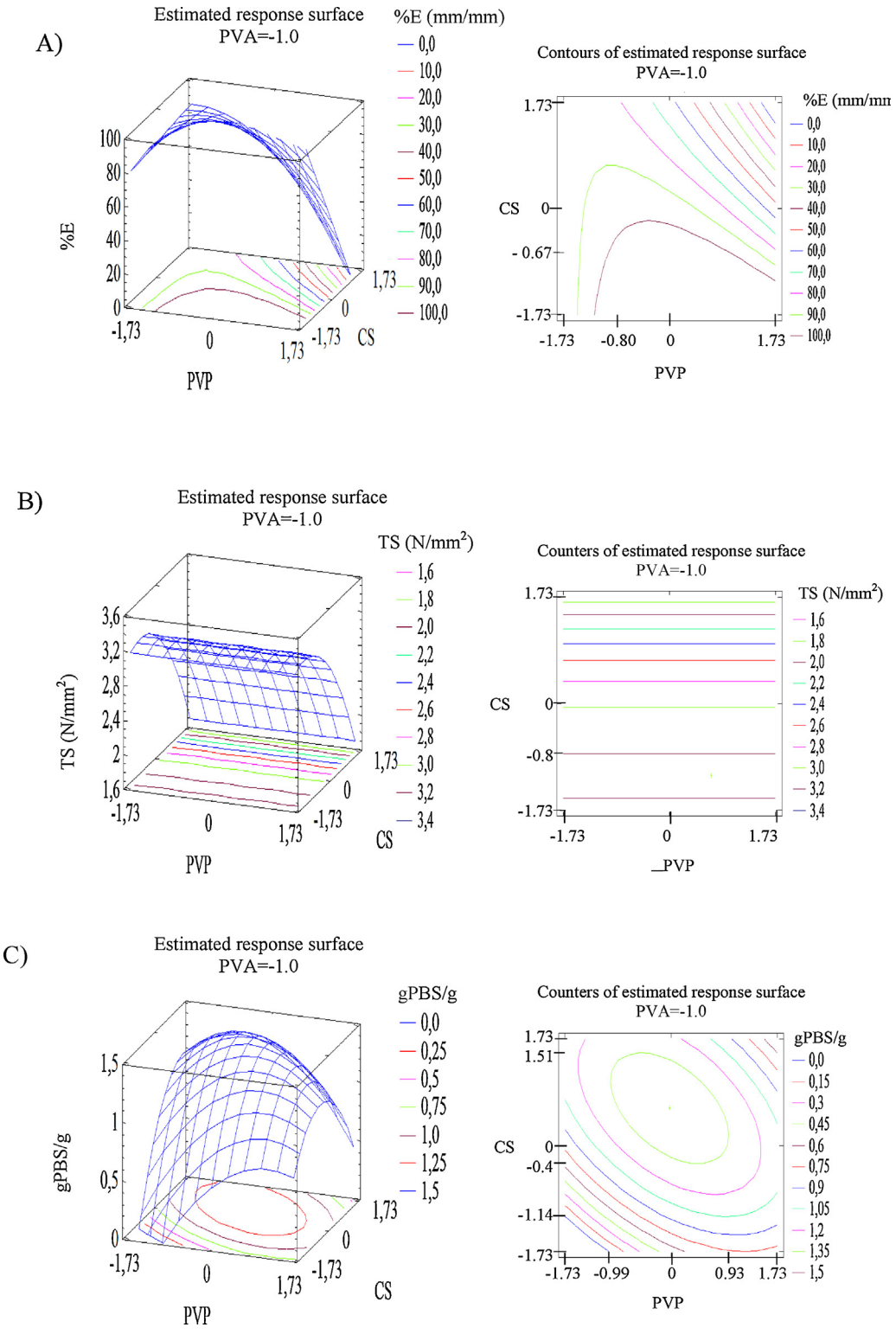

Fig. 6. Contour plots (in bi- and tri- dimensional projections) drawn according to simplified polynomial model for each response variable of CCD.

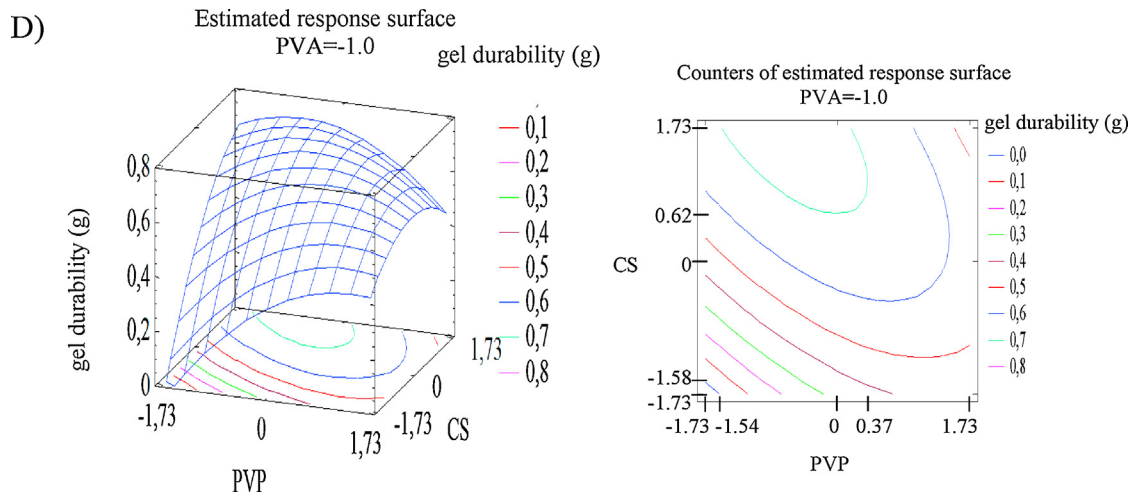

Fig. 6. (Continued)

mm^2; PBS absorbed/unit weight ≥1.0 g/g; gel durability ≥0.6 g. Such constrains characterized optimal film performance. In fact, a high film flexibility is advisable, since an easy deformation allows a comfortable and simple administration; a suitable mechanical resistance (tensile strength) is required to maintain film integrity during packaging; a good capability to absorb the excess wound exudate and a prolonged film permanence on the wound site are features useful for wound healing. In case of exudative chronic wounds, solid dressings are preferred to liquid/semisolid preparations because the formers are able to absorb the excess exudate, rich in metalloproteinases, and to maintain wetting conditions optimal for healing (Boateng and Catanzano, 2015).

The formulation of optimized composition, chosen inside the region evidenced in Fig. 7, was: PVA 11.3% w/w – PVP 2.4% w/w – CS 0.46% w/w – Ser 0.8% w/w – PHC 2% w/w – Gly 10% w/w.

Table 6 reports the predicted and experimental values obtained for the various properties of the film of optimized composition. It can be observed that the experimental values were comparable to the fitted ones at 95% confidence level. This confirms the prediction power of the regression models.

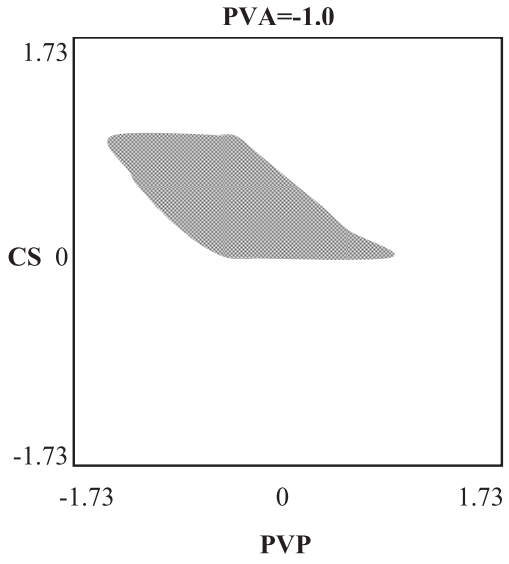

Fig. 7. Region of optimal film composition which satisfies all the constraints of the response variables.

Table 6
Predicted and experimental values of the formulation of optimized composition (mean values ± ds; n = 3).

Response	Predicted values (p<0.05)	Experimental values
%E (mm/mm)	87 ± 4.3	92 ± 11
TS (N/mm^2)	2.6 ± 0.13	2.7 ± 0.14
gPBS/g	1.44 ± 0.072	1.44 ± 0.080
Gel durability (g)	0.70 ± 0.035	0.703 ± 0.005

3.4. Characterization of optimized formulation (opFILM)

3.4.1. Rheological properties

In Fig. 8 loss tangent (tan delta) profile as a function of frequency of hydrated opFILM film is reported. It can be observed that tan delta values, independently of the frequency, were lower than 1, indicating that the gel formed after hydration was characterized by a prevalence of elastic (G′ modulus) on viscous (G″ modulus) properties (Rossi et al., 2007). High elastic properties are advisable since they are related to gel protective action towards lesion area.

3.4.2. In vitro *release properties*

In Fig. 9%CRV release profiles of opFILM and HYBD are reported. Significant ($p < 0.05$) differences are observed only at 4 and 8 h: film was characterized by lower values with respect to HYBD. This result is conceivably due to the formation of a viscoelastic gel that slowed down CRV diffusion. The superimposition of the released profiles observed after 8 h can be explained by gel dissolution: CRV release was only controlled by HYBD.

4. Conclusions

CRV loading into PHC results in maintenance of CRV antioxidant properties, improvement of its cytotoxicity towards human fibroblast and increase in antimicrobial properties. These results are due to PHC protection against CRV evaporation. Thanks to DoE approach, film characterized by optimal technological properties was determined. In particular, exploiting PVA film forming properties and CS and PVP interaction, film characterized by optimal mechanical and hydration properties was obtained. It was able upon hydration to form a viscoelastic gel capable of protecting lesion area and modulating CRV release. The overall results indicate that the optimized formulation is a promising candidate for the treatment of chronic skin ulcers. The following step of the

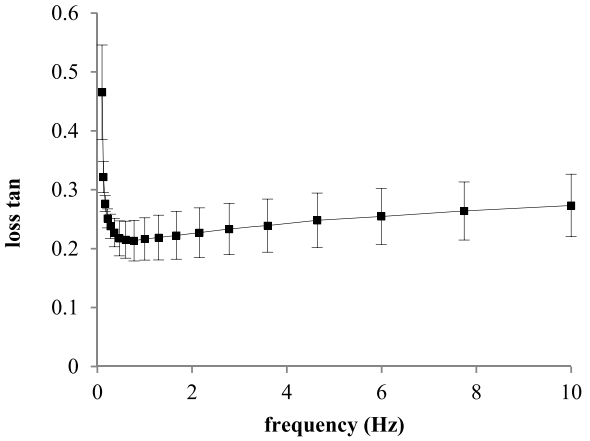

Fig. 8. Loss tangent (G″/G′) values as a function of frequency obtained for opFILM at a constant shear stress (50 Pa) (mean values ± s.d; n = 3).

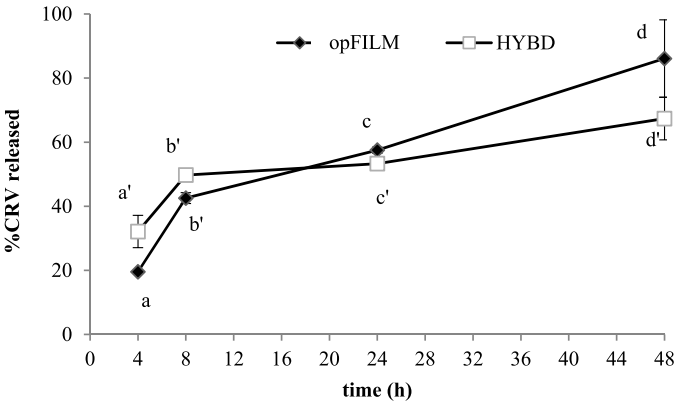

Fig. 9. % CRV released as a function of time for opFILM and HYBD (mean values ± s.e.; n = 3). T-test ($p < 0.05$): a *vs* b/c/d/a′; b *vs* c/d/b′; c *vs* d;. a' *vs* b'/c'/d'; b' *vs* c'/d′; c' *vs* d′.

research will focus on formulation performance on in vivo animal model, set up by the research group (Tenci et al., 2016, 2017), in comparison with commercial dressings.

Acknowledgements

This study was partially supported by the Spanish project CGL2016-80833-R of the Ministerio de Economía, Industria y Competitividad (MEIC).

Appendix A. Supplementary data

Supplementary data associated with this article can be found, in the online version, at http://dx.doi.org/10.1016/j.ijpharm.2017.06.024.

References

Ben Arfa, A., Combes, S., Preziosi-Belloy, L., Gontard, N., Chalier, P., 2006. Antimicrobial activity of carvacrol related to its chemical structure. Lett. Appl. Microbiol. 43, 149–154.

Boateng, J., Catanzano, O., 2015. Advanced therapeutic dressings for effective wound healing–a review. J. Pharm. Sci. 104, 3653–3680.

Boateng, J.S., Matthews, K.H., Stevens, H.N., Eccleston, G.M., 2008. Wound healing dressings and drug delivery systems: a review. J. Pharm. Sci. 97, 2892–2923.

Burt, S., van der Zee, R., Koets, A.P., de Graaff, A.M., van Knapen, F., Gaastra, W., Haagsman, H.P., Veldhuizen, E.J.A., 2007. Carvacrol induces heat shock protein 60 and inhibits synthesis of flagellin in Escherichia coli O157:H7. Appl. Environ. Microbiol. 73, 4484–4490.

Burt, S., 2004. Essential oils: their antibacterial properties and potential applications in foods – a review. Int. J. Food Microbiol. 94, 223–253.

Campos-Requena, V.H., Rivas, B.L., Pérez, M.A., Figueroa, C.R., Sanfuentes, E.A., 2015. The synergistic antimicrobial effect of carvacrol and thymol in clay/polymer nanocomposite films over strawberry gray mold. LWT-Food Sci. Technol. 64, 390–396.

Clinical and Laboratory Standards Institute, 1999. Methods for Determining Bactericidal Activity of Antimicrobial Agents: Approved Guideline M26-A. Clinical and Laboratory Standards Institute, Wayne, PA, USA.

Clinical and Laboratory Standards Institute, 2009. Methods for Dilution Antimicrobial Susceptibility Tests for Bacteria That Grow Aerobically: Approved Standard M7-A8, Eighth edition Clinical and Laboratory Standards Institute, Wayne, PA, USA.

Coccimiglio, J., Alipour, M., Jiang, Z.-H., Gottardo, C., Suntres, Z., 2016. Antioxidant, antibacterial, and cytotoxic activities of the ethanolic Origanum vulgare extract and its major constituents. Oxid. Med. Cell. Longevity (Article ID 1404505).

Comolli, N., Donaldson, O., Grantier, N., Zhukareva, V., Tom, V.J., 2012. Polyvinyl alcohol-polyvinyl pyrrolidone thin films provide local short-term release of anti-inflammatory agents post spinal cord injury. J. Biomed. Mater. Res B. Appl. Biomater. 100, 1867–1873.

Contardi, M., Heredia-Guerrero, J.A., Perotto, G., Valentini, P., Pompa, P.P., Spano, R., Goldoni, L., Bertorelli, R., Athanassiou, A., Bayer, I.S., 2017. Transparent ciprofloxacin-povidone antibiotic films and nanofiber mats as potential skin and wound care dressings. Eur. J. Pharm. Sci. 104, 133–144.

Dejaegher, B., Vander Heyden, Y., 2009. The use of experimental design in separation science. Acta Chromatogr. 21, 161–201.

Dejaegher, B., Vander Heyden, Y., 2011. Experimental designs and their recent advances in set-up, data interpretation, and analytical applications. J. Pharm. Biomed. Anal. 56, 141–158.

Efrati, R., Natan, M., Pelah, A., Haberer, A., Banin, E., Dotan, A., Ophir, A., 2014. The combined effect of additives and processing on the thermal stability and controlled release of essential oils in antimicrobial films. J. Appl. Polym. Sci. 131, 40564–40574.

El-Malah, Y., Nazzal, S., 2008. Novel use of Eudragit® NE 30D/Eudragit® L 30D-55 blends as functional coating materials in time-delayed drug release applications. Int. J. Pharm. 357, 219–227.

Gorrasi, G., 2015. Dispersion of halloysite loaded with natural antimicrobials into pectins: characterization and controlled release analysis. Carbohydr. Polym. 127, 47–53.

Guo, R., Du, X., Zhang, R., Deng, L., Dong, A., Zhang, J., 2011. Bioadhesive film formed from a novel organic-inorganic hybrid gel for transdermal drug delivery system. Eur. J. Pharm. Biopharm. 79, 574–583.

Hasan, A., Waibhaw, G., Tiwari, S., Dharmalingam, K., Shukla, I., Pandey, L.M., 2017. Fabrication and characterization of chitosan, polyvinylpyrrolidone, and cellulose nanowhiskers nanocomposite films for wound healing drug delivery application. J. Biomater. Res. doi:http://dx.doi.org/10.1002/jbm.a.3609.

Jomova, K., Valko, M., 2011. Advances in metal-induced oxidative stress and human disease. Toxicology 283, 65–87.

Kim, D.W., Kim, K.S., Seo, Y.G., Lee, B.-J., Park, Y.J., Yound, Y.S., Kim, J.O., Yong, C.S., Jin, S.G., Choi, H.-G., 2015. Novel sodium fusidate-loaded film-forming hydrogel with easy application and excellent wound healing. Int. J. Pharm. 495, 67–74.

Koparal, A.T., Zeytinoglu, M., 2003. Effects of carvacrol on a human non-small cell lung cancer (NSCLC) cell line, A549. Cytotechnology 43, 149–154.

López-Galindo, A., Viseras, C., Cerezo, P., 2007. Compositional, technical and safety specifications of clays to be used as pharmaceutical and cosmetic products. Appl. Clay Sci. 36, 51–63.

Lambert, R.J.W., Skandamis, P.N., Coote, P.J., Nychas, G.-J.E., 2001. A study of the minimum inhibitory concentration and mode of action of oregano essential oil, thymol and carvacrol. J. Appl. Microbiol. 91, 453–462.

Li, J., Zivanovic, S., Davidson, P.M., Kit, K., 2010. Characterization and comparison of chitosan/PVP and chitosan/PEO blend films. Carbohydr. Polym. 79, 786–791.

Malipeddi, V.R., Awasthi, R., Dal Molim Ghisleni, D., de Souza Braga, M., Satiko Kikuchi, I., Andreoli Pinto, T., Dua, K., 2017. Preparation and characterization of metoprolol tartrate containing matrix type transdermal drug delivery system. Drug Deliv. Transl. Res. 7, 66–76.

Mori, M., Rossi, S., Bonferoni, M.C., Ferrari, F., Sandri, G., Riva, F., Del Fante, C., Perotti, C., Caramella, C., 2014. Calcium alginate particles for the combined delivery of platelet lysate and vancomycin hydrochloride in chronic skin ulcers. Int. J. Pharm. 461, 505–513.

Mori, M., Rossi, S., Ferrari, F., Bonferoni, M.C., Sandri, G., Chlapanidas, T., Torre, M.L., Caramella, C., 2016. Sponge-like dressings based on the association of chitosan and sericin for the treatment of chronic skin ulcers. I. Design of experiments-assisted development. J. Pharm. Sci. 105, 1180–1187.

Muzzarelli, R.A.A., 2009. Chitins and chitosans for the repair of wounded skin nerve cartilage and bone. Carbohydr. Polym. 76, 167–182.

Peng, Y., Zhang, H., Liu, R., Mine, Y., McCallum, J., Kirby, C., Tsao, R., 2016. Antioxidant and anti-inflammatory activities of pyranoanthocyanins and other polyphenols from staghorn sumac (*Rhus hirta* L.) in Caco-2 cell models. J. Funct. Foods 20, 39–147.

Rossi, S., Marciello, M., Sandri, G., Ferrari, F., Bonferoni, M.C., Papetti, A., Caramella, C., Dacarro, C., Grisoli, P., 2007. Wound dressings based on chitosans and hyaluronic acid for the release of chlorhexidine diacetate in skin ulcer therapy. Pharm. Dev. Technol. 12, 415–422.

Rossi, S., Marciello, M., Bonferoni, M.C., Ferrari, F., Sandri, G., Caramella, C., Dacarro, C., Grisoli, P., 2010. Thermally sensitive gels based on chitosan derivatives for the treatment of oral mucositis. Eur. J. Pharm. Biopharm. 74, 248–254.

Rossi, S., Faccendini, A., Bonferoni, M.C., Ferrari, F., Sandri, G., Del Fante, C., Perotti, C., Caramella, C., 2013. Sponge-like dressings based on biopolymers for the delivery of platelet lysate to skin chronic wounds. Int. J. Pharm. 440, 207–215.
Rossi, S., Ferrari, F., Sandri, G., Bonferoni, M.C., Del Fante, C., Perotti, C., Caramella, C., 2015. Wound healing: biopolymers and hemoderivatives, 1st ed. In: Mishra, M. (Ed.), Encyclopedia of Biomedical Polymers and Polymeric Biomaterials, vol. 11. Taylor & Francis, New York, pp. 8280–8298.
Ruberto, G., Baratta, M.T., 2000. Antioxidant activity of selected essential oil components in two lipid model systems. Food Chem. 69, 167–174.
Safaei-Ghomi, J., Ebrahimabadi, A.H., Djafari-Bidgoli, Z., Batooli, H., 2009. GC/MS analysis and *in vitro* antioxidant activity of essential oil and methanol extracts of *Thymus caramanicus* Jalas and its main constituent carvacrol. Food. Chem. 115, 1524–1528.
Sanchez-Espejo, R., Aguzzi, C., Salcedo, I., Cerezo, P., Viseras, C., 2014. Clays in complementary and alternative medicine. Mater. Technol. 29, B78–B81.
Seabra, A.B., De Oliveira, M.G., 2004. Poly(vinyl alcohol) and poly(vinyl pyrrolidone) blended films for local nitric oxide release. Biomaterials 25, 3773–3782.
Shemesh, R., Krepker, M., Natan, M., Danin-Poleg, Y., Banin, E., Kashi, Y., Nitzan, N., Vaxmanb, A., Segal, E., 2015. Novel LDPE/halloysite nanotube films with sustained carvacrol release for broad-spectrum antimicrobial activity. RSC Adv. 5, 87108–87117.
Singh, B., Pal, L., 2011. Radiation crosslinking polymerisation of sterculia polysaccharide-PVA-PVP for making hydrogel wound dressings. Int. J. Biol. Macromol. 48, 501–510.
Sreedharan, N.R., Sujith, N., 2015. Permeation studies of captopril transdermal films through human cadaver skin. Curr. Drug Deliv. 12 (5), 517–523.
Tenci, M., Rossi, S., Bonferoni, M.C., Sandri, G., Boselli, C., Di Lorenzo, A., Daglia, M., Icaro Cornaglia, A., Gioglio, L., Perotti, C., Caramella, C., Ferrari, F., 2016. Pectin/chitosan particles for the delivery of platelet lysate and manuka honey in chronic skin ulcers. Int. J. Pharm. 509, 59–70.
Tenci, M., Rossi, S., Bonferoni, M.C., Sandri, G., Mentori, I., Boselli, C., Icaro Cornaglia, A., Daglia, M., Marchese, A., Caramella, C., Ferrari, F., 2017. Application of DoE approach in the development of mini-capsules, based on biopolymers and Manuka honey polar fraction, as powder formulation for the treatment of skin ulcers. Int. J. Pharm. 1–2, 266–277.
Tunç, S., Duman, O., 2011. Preparation of active antimicrobial methyl cellulose/carvacrol/montmorillonite nanocomposite films and investigation of carvacrol release. LWT – Food Sci. Technol. 44, 465–472.
Vicentini, D.S., Smania, A., Laranjeira, M.C.M., 2010. Chitosan/poly(vinyl alcohol) films containing ZnO nanoparticles and plasticizers. Mater. Sci. Eng. C 30, 503–508.
Viseras, C., Aguzzi, C., Cerezo, P., Bedmar, M.C., 2008. Biopolymer-clay nanocomposites for controlled drug delivery. Mater. Sci. Technol. 24, 1020–1026.
Viseras, C., Cerezo, P., Sanchez, R., Salcedo, I., Aguzzi, C., 2010. Current challenges in clay minerals for drug delivery. Appl. Clay Sci. 40, 291–295.
Yanishlieva, N.V., Marinova, E.M., Gordon, M.H., Raneva, V.G., 1999. Antioxidant activity and mechanism of action of thymol and carvacrol in two lipid systems. Food Chem. 64, 59–66.
Yeh, J.T., Chen, C.L., Huang, K., Nien, Y., Chen, J., Huang, P., 2006. Synthesis, characterization, and application of PVP/chitosan blended polymers. J. Appl. Polym. Sci. 101, 885–891.

Personal Account

DOI: 10.1002/tcr.201700061

THE CHEMICAL RECORD

Advanced Inorganic Nanosystems for Skin Drug Delivery

E. Carazo,[a] A. Borrego-Sánchez,[a, b] F. García-Villén,[a] R. Sánchez-Espejo,[b] P. Cerezo,[a] C. Aguzzi,[a] and C. Viseras[a, b]

Abstract: On/into/through the skin drug delivery represents an attractive alternative for the oral route, providing local and/or systemic drug delivery. Due to its complex and well-organised structure, most of the drugs show difficulties to penetrate the human skin. Therefore, enormous efforts have been invested to develop intelligent drug delivery systems overcoming the skin barrier with particular emphasis on increasing therapeutic activity and minimizing undesirable side-effects. Most of these strategies require the use of singular materials with new properties. In particular, and on the basis of their inherent properties, including biocompatibility, biodegradability and relative low-cost, inorganic nanoparticles are ideal candidates for the development of skin drug delivery systems. This review provides an updated and comprehensive overview of the state of the art in the trends towards skin drug delivery with a particular focus in the attractive alternative offered by inorganic-based nanosystems.

Keywords: Drug delivery, Aluminosilicates, Layered compounds, Clays, Nanoparticles

To fully understand mechanisms involved in skin delivery and, as consequence, the features expected for the optimal carriers adressed to this administration path, it is essential to be aware of the structure, composition and functions of the human skin. As largest organ of the human body, the skin is a highly complex multilayered structure that plays essential roles as the prevention of the access of microorganisms and chemicals and the control of the temperature via regulation of heat and water loss from the body. Besides, it acts as a barrier devoted to avoid physical, chemical and thermal aggressions.[1] As a result of its multistratified structure (epidermis, dermis and hypodermis) and the presence of appendages (hair follicles and sweat and sebaceous glands), human skin possesses different and interesting properties. The stratum corneum (SC) owns to the epidermis, the outermost external layer. It is the hardest barrier of the skin, comprised by rows of dead and desiccated keratinized epidermal cells, known as corneocytes. They are organized following a "brick and mortar" structure; corneocytes ("bricks") immersed in a lipid matrix ("mortar").[2] This structure is of crucial importance in terms of controlling drug penetration into the skin. Other cell populations like melanocytes and Langerhans cells are also present in the epidermis, which counts with three sublayers (stratum granulosum, stratum spinosum and stratum basale). The dermis is responsible for its excellent mechanical properties, as strength and flexibility. The appendages are deeply embedded in the dermal compartment. The hypodermis obeys the main functions of energy supply and thermal insulation. In case of diseased skin, it might present differences in structure and properties varying depending on the type and gravity of the illness.[3] Regarding drug delivery, the human skin offers an endless number of advantages such as the possibility of obtain either local or systemic actions, improve poor biopharmaceutics profiles of drugs administered via oral route (drugs suffering strong first pass hepatic metabolism or degradation by enzymes or extreme ph values of the intestinal tract) and situations in

[a] *E. Carazo, A. Borrego-Sánchez, F. García-Villén, P. Cerezo, C. Aguzzi, C. Viseras*
Department of Pharmacy and Pharmaceutical Technology, School of Pharmacy, University of Granada, Campus of Cartuja, 18071 s/n, Granada, Spain
E-mail: ecarazogil@ugr.es
[b] *A. Borrego-Sánchez, R. Sánchez-Espejo, C. Viseras*
Andalusian Institute of Earth Sciences, CSIC-University of Granada, Avda. de Las Palmeras 4, 18100, Armilla (Granada), Spain

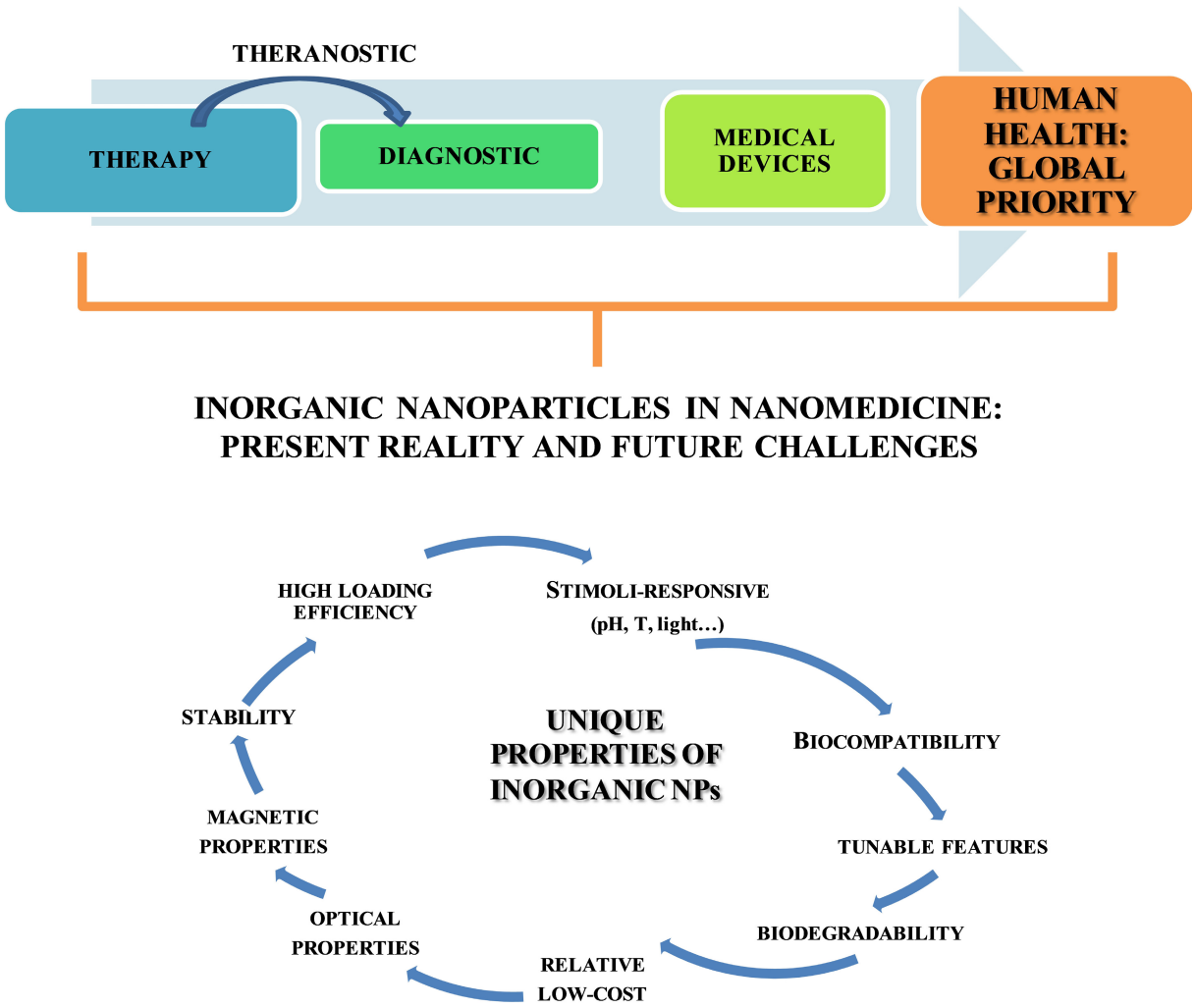

Figure 1. Present reality and future challenges of inorganic nanoparticles in nanomedicine.

which the oral administration is not possible or inadvisable.[4] With these backgrounds, the main goals of new skin drug delivery systems are improving drug biopharmaceutics and pharmacokinetics and obtaining a targeted drug delivery, without harming the protective function of the skin.[5] Their role is mainly based on an interaction with the skin appendages and skin lipids leading to a facilitated release, a sustained release caused by drug depot and/or stimuli-induced release,[6–10] as well as the use of microneedles to penetrate the skin barrier, which is another in-vogue technique.[11] In the last years, inorganic nanoparticles have achieved important success in diverse technical fields as manufacturing and materials, environment, energy, electronics[12–14] and what is more interesant for us, in the medical field. Their unique features as optical and superparamagnetic properties, biocompatibility, stability and high drug loading efficiency have caused their countless use as carriers for diverse biomolecules.[15]

Throghout the whole range of inorganic nanosystems known, in this review we focus on metallic nanoparticles (silver (AgNPs); gold (AuNPs); titanium dioxide (TiO_2), zinc oxide (ZnO), iron oxide (IONPs)), natural clay nanoparticles, mesoporous silica nanoparticles (MSNs), layered double hydroxides (LDHs) and quantum dots (QDs) as principal inorganic-based nanosystems in the dermatopharmaceutics field. (Figure 1)

2. Routes and Targets in, Into and Through Skin Drug Delivery

Skin drug delivery offers the possibility to achieve either local or systemic therapeutic effects. Addresing the diverse routes

of penetration, the two principal ones are transappendageal (transport via the pores and shafts embracing sweat glands and hair follicles with their associated sebaceous glands) and transepidermal (diffusion through the intact stratum corneum). (Figure 2)

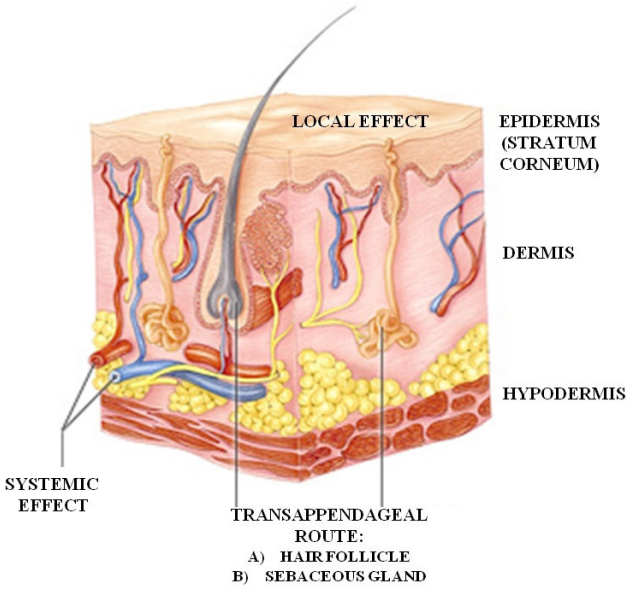

Figure 2. Skin layers and diverse routes of penetration.

The first one is minor but represents an alternative to avoid the stratum corneum, so it enables the entrance of ions and large polar molecules. The transepidermal pathway, which is the dominant one, is composed by two routes: transcellular and intercellular. Diffusion via transcellular is preferred by hydrophilic drugs. In opposition, lipophilic drugs opt for the intercellular route.[23]

2.1. Necessity of Advanced Carrier Systems

Derived from the difficulty of the majority of drugs to penetrate the human skin, the necessity of advanced carrier systems has become an important global health priority regarding skin drug administration.[24] Use of nanoparticles, liposomes and other vesicular carriers, polymeric patches, solvent-induced flexibility and microneedle technology are in-vogue strategies to handle the difficulties related with the skin drug administration pathway. Particularly, nanoparticles play a leading role in enhancing the transappendageal route; not only do they achieve a deeper penetration of the drug than drug in solution, but also are able to create depots and obtain a sustained release.[25–28] In this personal account we will discuss about recent advances in the field of inorganic-based nanoparticle drug delivery to the skin and future directions currently being explored.

3. Inorganic Nanoparticles in Skin Drug Delivery

Due to the huge amount of inorganic-based nanosystems offered to be use in skin-drug delivery it has been necessary to classify them in different groups depending on their composition. Briefly, we have made a distinction between metallic nanoparticles, mineral-based nanoparticles and quantum dots. Table 1 compiles the scope and uses of different inorganic nanoparticles administered on/into/through the skin which are further explained in the text.

3.1. Metallic Nanoparticles

3.1.1. Gold Nanoparticles (AuNPs)

Throughout the total amount of inorganic nanocarriers that have been developed, gold nanoparticles count with much positive features that make them ideal candidates to be used in the biomedical field.[29] Some of their advantages are in common with the other inorganic nanoparticles, as their stability and biocompatibility and the full range of size in which they can be developed, but there is a unique characteristic derived from the stability of the gold-sulfur bond which makes them easily tunable.[30] Several recent works deal with the possibilities offered by gold nanoparticles (AuNPs) to target skin diseases and transdermal administration of drugs. Mahmoud and coworkers have just described the preferred accumulation of AuNPs in hair follicles and their different behaviour depending on the surface charge of the nanoparticles.[31] In the last year, it has also been synthetised a AuNPs-based nanofiller for a polyelectrolyte membrane for transdermal drug delivery of the drug diltiazem hydrochloride. This novel system exhibited improved thermo mechanical properties and transparency in the visible range, which makes it attractive for cosmetical use. The AuNPs made the film resistant to microbial growth so it could be used for long term skin applications.[32] In terms of antibodies ligands conjugated with AuNPs, it was reported an increased therapeutic potential of an AuNPs-Cetuximab nanohybryd when compared with the drug alone as well as a desired alteration of the receptor recycling processes executed only by the nanohybryds leading to a an enhanced therapeutic effect with lower drug doses.[33] Not only cancer progression but also metastasis were reversed when transmembrane peptide-conjugated cationic gold nanoparticles were loaded with pDNAs for transdermal delivery.[34] Besides, melanoma tumor volume, weight and STAT3 expression were reduced after topical iontophoretic administration of AuNPs co-loaded with STAT3, siRNA and imatinib.[35] AuNPs have also been

Table 1. Types of inorganic nanosystems and their applications addressed to skin drug delivery.

1. Metallic Nanoparticles		
Type of NPs	***Application***	***Reference***
1.1. AuNPs	*Accumulation in hair follicles*	*31*
	Films resistant to bacteria long-term use for skin purposes	*32*
	Inhibition of cancer progression and metastasis via the loading of AuNPs with pDNAs	*34*
	Iontophoretic Melanoma treatment (AuNPs co-loaded with STAT3, siRNA and imatinib)	*35*
	Psoriasis treatment (AuNPs-metothrexate)	*36*
	Skin regeneration (AuNPs-VEGF)	*37*
1.2. AgNPs	*Prevent skin carcinogenesis (AgNPs against UVB radiation)*	*39*
	Antibacterial activity (dressing and coating of medical devices)	*40-41*
	Burn wounds	*42-43*
	Wound healing	*44*
1.3. TiO_2NPs	*Anti-bacteria, parasites, spore cells effects*	*45-47*
	In-vitro human colon and cervical carcinoma therapy	*48,49*
	Attenuator of UV-B radiation in sunscreens	*50-52*
1.4. ZnONPs	*Antimicrobial activity against drug-resistant bacteria*	*55, 57*
	Wound healing (Cefazolin-ZnONPs)	*56*
	Antioxidant and against Candida sp activity	*58*
	Modulate skin penetration	*59-60*
	Theranostic properties in cancer, particularly glioma and breast cancer	*61-64*
1.5. IONPs	*Facilitated skin penetration*	*67-69*
	Theranostic properties	*70*
	Surface coatings to deal with the human immune system	*71*
2. Mineral-based Nanoparticles		
2.1. Natural Clay Minerals	*Pelotherapy*	*76-79*
	Wound healing and treatment of skin lesions	*85-89*
	Skin regeneration	*90*
	Antibiotics-loaded nanoclays for acne therapy	*91-92*
	Nanocarrier of antimicrobial essential oil	*93*
	Atopic dermatitis and sensitive skin	*94*
2.2. LDHs	*Modified Drug Delivery System of Acetylsalicylic acid with increased percutaneous penetration*	*103*
	Skineven treatment (LDHs-4 hexyl resorcinol)	*104*
	Skin repair	*105*
2.3. MSNs	*MSNs-quercetin thermoresponsive delivery system*	*8*
	NH_2-MSN-quercetin topical administration and increased stability	*112*
	MSNs-trolox topical administration and increased stability	*113*
	MSNs-caffeine for topical administration	*114*
	Curcumin transdermal delivery system	*115*
	Enhancement of diverse skin cells uptake via a surface functionalization of amorphous silica particles with positively charged groups and size-dependant skin penetration of MSNs.	*116*
3. Quantum Dots		
	Photodynamic therapy of melanoma skin cancer	*120*
	Graphene oxide–iron oxide QDs for dual-modality imaging, drug delivery and photothermal therapy	*121*
	Skin mesenchymal stem cells: QD as tumour-targeted delivery	*122*
	Magnetofluorescent carbon QDs cancer theranostic (Near-infrared light triggered photo-therapy and chemo-therapy)	*123*

found to be useful for the psoriasis treatment. In particular, methotrexate-loaded AuNPs were found to be able to in-vitro penetrate keratinocytes and was also in-mouse tested the penetration of the drug through epidermis and what was more outstanding, a slight arrival to the dermis, where psoriasis inflammation occurs in mouses, suggesting that this new system would be of high value as topical therapy in psoriasis patients.[36] Not to be forgotten is the ability of different surface charges AuNPs to conjugate themselves with genes, as the vascular endothelial growth factor (VEGF), obtaining a non-invasive penetration of the VEGF without damaging its biological activity and succeed in arriving to the subcutaneous region where it is expected that the VEGF exhibits its reparative effect of the skin.[37] This kind of

delivery is interesting for cosmetics due to the role that diverse growth factors play in skin reparation.

3.1.2. Silver Nanoparticles (AgNPs)

Regarding AgNPs, several scientific works deal with the use of this kind of inorganic nanoparticles not only in basis on their inherent antimicrobial properties but also for another biomedical purpose.[38] Tyagi and coworkers have put light on the potential use of AgNPs against UVB radiation directed to prevent skin carcinogenesis, obtaining higher efficiency than titanium dioxyde nanoparticles (TiO_2NPs) and zinc oxyde nanoparticles (ZnONPs).[39] As previously stated, AgNPs possess antibacterial activity and have been worldwide used for wound dressings, coatings and impregnation of medical devices supplying a continuous release of Ag ions.[40–41] Besides, in case of burn-wounds, it has been prooved that they healed with better appearance.[42] With these backgrounds, we can understand the ancient use of this kind of nanoparticles.[43] Another work has studied the possible interactions stablished between AgNPs and keratinocytes and fibroblasts during wound healing. Results obtained stated that AgNPs increase the wound closure process via two different ways: via an enhanced proliferation and migration of keratinocytes and by promoting differentiation of fibroblasts into myofibroblasts.[44]

3.1.3. Titanium Dioxide Nanoparticles (TiO_2NPs)

The role of TiO_2NPS against drug-resistant bacteria, parasites as *leishmania spp.* and spore cells have been fully explained via ζ-Potential measurements and confocal microscopy in which were described and observed TiO_2NPs-cell membrane interactions leading to the death of the cells.[45–47] Besides, in-vitro effects in human colon[48] and cervical[49] carcinoma cells were also reported. However, the most widely known aspect related with TiO_2 is its use as attenuator of the UV–B radiation in sunscreens.[50–52] It was assessed by experimental and molecular modeling techniques the most appropriate size of this TiO_2NPs, assuming that they are spheres.[53] Finally, it has been proved that the formulation did affect the level of penetration of this kind of NPs.[54]

3.1.4. Zinc Oxide Nanoparticles (ZnONPs)

Following the antimicrobial pattern of the previous nanoparticles, ZnONPs synthesised based on aloe vera leaf extract were found to inhibit the growth of bacteria as *E. coli*, *P. aeruginosa and S. aureus* strains resilient to conventional antibiotics.[55] Cefazolin-loaded ZnONPs increased the rate of wound healing process based on a accelerated epithelial growth and improving cell adhesion.[56] Besides, the massive use of ZnONPs in medicine field based on their effective antimicrobial action and their environmentally friendly low-cost synthesis has been highlighted.[57] The green-origin and easy synthesis of colloidal ZnONPs with antimicrobial and antioxidant actions have been reported resulting of particular interest the activity against *Candida sp.* and their powerful antioxidant action preventing cellular damages produced by oxidative stress.[58] Not to be forgotten is the role of ZnONPs in skin penetration.[59–60] This kind of nanoparticles have also shown ability to induce apoptosis in cancer cells, particularly effective in glioma and breast cancer, even possessing a diagnostic role.[61–64]

3.1.5. Iron Oxide Nanoparticles (IONPs)

The use of IONPs as drug carriers has been toughly investigated.[65–66] Furthermore, remarkable foundings have been reported regarding the use of IONPs targeted to different tumors therapies based on several positive features as the facilitated skin penetration obtained when drugs are loaded onto them[67–69] providing also theranostic effects, which consisted on contemporary cancer diagnostic and treatment.[70] The effects followed by different IONPS surface coatings aimed to deal with different defense system of the body were described by Kievit and Zhang[71] that obtained different IONPs depending on the different therapeutic goals addressed. To be highlighted was also the analgesic effect of IONPs in chronic inflammatory pain which was explained to be via macrophage inhibition and free radical reduction.[72]

3.2. Mineral-based Nanoparticles

3.2.1. Natural Clay Minerals

The endless possibilities offered by clay minerals in pharmaceutics is the main topic studied by our research group. Particularly interesting for us is the use of clay minerals as drug nanocarriers alone and in combination with organic compounds[73–75] and in pelotherapy, based on the topical administration of hot-muds (peloids) consisting on inorganic gels with optimal rheological and thermal properties composed by clay minerals and mineral-medicinal water.[76–79] Other authors focus also their investigations in the use of clays as drug nanocarriers and other biological molecules such as DNA.[80–84] Regarding the use of natural clay minerals in skin-delivery, one of the most famous applications of this inorganic platforms is related with wound healing and treatment of skin lesions.[85–89] Connected with this so known wound healing application, we should also make a remark of the features presented by clay minerals to be used in skin regeneration.[90] Besides, clay minerals have also been chosen as carrier for antibiotics in acne therapy,[91–92] essential oils

with antimicrobial potential[93] and in cases of atopic dermatitis and sensitive skin.[94]

3.2.2. Layered Double Hydroxides (LDHs)

Easy obtention, biocompatibility, colloidal stability, targeted and stimoli-response release of drugs and theranostic properties, between others desirable characteristics, have become LDHs an up-to-date desired candidate to carrier drugs, genes and other active compounds, even in a co-carrier way, alone and via hybryd systems with polymers[95–102]. Focused on the main goal of this review, LDHs-based nanosystems are in-vogue addressing the skin administration. They were used as nanocarrier of acetylsalicylic acid resulting in a nanohybrid with enhanced storage and structural stability, outstanding controlled release features and in-vivo increased percutaneous penetration and efficacy than drug alone[103]. Besides, it was proved the efficacy of the nanosystem 4-hexyl resorcinol in the treatment of uneven human skin as modulator of skin pigmentation via an inhibition of the enzyme tyrosinase and melanogenesis.[104] Cunha and coworkers focused on the assessment of the activity of LDHs in skin repair by promoting both collagen deposition and renewal of the extracellular matrix as well as on their safety to be used in drug delivery even in implantable systems.[105]

3.2.3. Mesoporous Silica Nanoparticles (MSNs)

Currently, MSNs play a leading role as carrier of both cosmetics and drugs[106] based on properties as no-citotoxicity, high surface area, changeable pore size, thermal stability and well-organised mesoporous structure that can be modified by differentiating diverse subdivisions sensibles to different-stimuli response moieties (light, temperature, pH, enzymes, among others)[107–108]obtaining outstanding success as the ability to obtain an intercellular release in cells cytosol[109] or a novel tumor vascular-targeted codelivery of an antiangiogenic agent and a chemotherapeutic drug[110] or a safe and effective polypill to heart attack disease.[111].In terms of skin-directed therapies numerous scientific works have been published that deals with MSNs-based nanosystems. Ugazio and coworkers have designed a thermoresponsive MSNs-quercetin system providing controlled release of this antioxidant depending on the temperature conditions of the application place as well as a protective effect of the antioxidant molecules[8]. Besides, it was proved that MSNs act not only as efficient topical nanocarriers but also show interesting properties to increase the stability of delicate antioxidant molecules such as derivatives of flavonoids like quercetin[112] and of the vitamin E, trolox[113]. Caffeine-MSNs hybrid system obtained via ball milling was subjected to in-vitro permeation tests using newborn pig skin and vertical Franz diffusion cells[114]. Furthermore, the in-vitro penetration and in vivo anti-inflammatory and analgesic effects of curcumin-loaded MSNs were determined[115]. Regarding skin penetration, results found by Rancan and coworkers[116] gave light to the relationship stablished between positively surface charges and increased cellular uptake and the block of skin penetration of MSNs with a size greater than 75 nm.

3.3. Quantum Dots

Quantum dots (QDs) are highly tunable, fluorescent materials that possess positive features as nanometer size, biocompatibility, photostability, and high surface area that attract more and more attention in the biomedical field addressed to important global health priorities like cancer detection[117], targeted drug delivery[118] and stimoli responsive nanoplatforms for intracellular controlled release[119]. Specially interesant is their use in photodynamic skin melanoma therapies[120]. What is more, it was designed a a QDs nanosystem efficient for cancer photothermal therapy, magnetic-responsive release at desired sites and with imagin applications[121]. Skin biocompatibility of carboxyl-coated QDs with skin mesenchymal stem cells to be used in skin cancer therapies[122]. Magnetofluorescent carbon quantumdots conjugated with folic acid and riboflavin were confirmed to effectively perform chemotherapy, photodynamic and photothermal therapy associated with a diagnostic effect[123]. Finally, Yuan and coworkers have succeeded in obtaining a long-time pursued targeted-release in the nucleus of the cells using QDs-based nanoplatforms.[124]

4. Summary and Outlook

Once finished this attempt to summarise and highlight the possibilities offered by inorganic nanocarriers in terms of design and develop novel modified drug delivery systems for skin drug delivery, our final goal is to help the scientific community to take full advantage of the considerable benefits derived from both this administration path and this kind of nanosystems.

Acknowledgements

This study was supported by the Projects CGL2016-80833-R and RNM-1897, group CTS-946 and Predoctoral Grant FPU13/04765.

References

[1] K. W. Ng, W. M. Lau. Skin deep: the basics of human skin structure and drug penetration. In *Percutaneous Penetration*

Enhancers Chemical Methods in Penetration Enhancement, Springer Berlin Heidelberg, **2015**, pp. 3–11.
[2] T. W. Prow, J. E. Grice, L. L. Lin, R. Faye, M. Butler, W. Becker. , M. S. Roberts, *Adv Drug Deliv Rev.* **2011**, *63*, 470–491.
[3] A. Vogt, C. Wischke, A. Neffe, A. T. , Ma, N. , Alexiev, U. , A. Lendlein, *J. Control. Release* **2016**, *242*, 3–15.
[4] M. E. Aulton, K. M. Taylor (Eds.). *Aulton's Pharmaceutics E-Book: The Design and Manufacture of Medicines.* Elsevier Health Sciences, **2017**.
[5] M. R. Prausnitz, R. Langer, *Nat. Biotechnol.* **2008**, *26*, 1261–1268.
[6] C. Mathes, A. Melero, P. Conrad, T. Vogt, L. Rigo, D. Selzer, S.S Guterres. *J. Control. Release*, **2016**, 223, 207–214.
[7] C. O. Silva, P. Rijo, J. Molpeceres, I. V. Figueiredo, L. Ascensão, A. S. Fernandes, C. P. Reis, *493*, 271–284.
[8] E. Ugazio, L. Gastaldi, V. Brunella, D. Scalarone, S. A. Jadhav, S. Oliaro-Bosso, S. Sapino. *Int. J. Pharm.* **2016**, 446–454.
[9] S. Mitragotri. Sonophoresis: Ultrasound-Mediated Transdermal Drug Delivery. In *Percutaneous Penetration Enhancers Physical Methods in Penetration Enhancement*, Springer Berlin Heidelberg, **2017**, pp. 3–14.
[10] A. Patzelt, J. Lademann. The increasing importance of the hair follicle route in dermal and transdermal drug delivery. In *Percutaneous Penetration Enhancers Chemical Methods in Penetration Enhancement*, Springer Berlin Heidelberg, **2015**, pp. 43–53.
[11] E. Larrañeta, M. T. McCrudden, A. J. Courtenay, R. F. Donnelly, *Pharm Res.* **2016**, *33*, 1055–1073.
[12] a) E. Ruiz-Hitzky. *The Chemical Record.* **2004**, *3*, 88–100. b) E. Ruiz-Hitzky, K. Ariga, Y. M. Lvov, *Bio-inorganic Hybrid Nanomaterials: Strategies, Synthesis, Characterization and Applications.* **2008**, John Wiley & Sons.
[13] a) M. Darder, A. Isabel Ruiz, P. Aranda, H. Van Damme, E. Ruiz-Hitzky, *Curr Nanosci* **2006**, *2*, 231–241. b) M. Darder, P. Aranda, E. Ruiz-Hitzky, *Adv. Mater.* **2007**, *19*, 1309–1319.
[14] M. Akkari, P. Aranda, A. B. H. Amara, E. Ruiz-Hitzky, *Beilstein J. Nanotechnol.* **2016**, *7*, 1971.
[15] H. C. Huang, S. Barua, G. Sharma, S. K. Dey, K. Rege, *J. Control. Release* **2011**, *155*, 344–357.
[16] B. L. Cushing, V. L. Kolesnichenko, C. J. O'Connor, *Chem .Rev.* **2004**, *104*, 3893–3946.
[17] X. Liang, H. Wang, J. E. Grice, L. Li, X. Liu, Z. P. Xu, M. S. Roberts, *Nano Lett.* **2016**, *16*, 939–945.
[18] A. Baeza, D. Ruiz-Molina, M. Vallet-Regí, *Expert Opin. Drug Deliv.* **2017**, *14*, 783–796.
[19] A. C. Anselmo, S. Mitragotri, *AAPS J.* **2015**, *17*, 1041–1054.
[20] M. Henriksen-Lacey, S. Carregal-Romero, L. M. Liz-Marzán, *Bioconjug. Chem.* **2016**, *28*, 212–221.
[21] J. Conde, J. T. Dias, V. Grazú, M. Moros, P. V. Baptista, J. M. de la Fuente, *Front.Chem.* **2014**, *2*.
[22] K. P. Miller, L. Wang, B. C. Benicewicz, A. W. Decho, *Chem. Soc. Rev.* **2015**, *44*, 7787–7807.
[23] V. Planz, C. M. Lehr, M. Windbergs, *J. Control. Release* **2016**, *242*, 89–104.
[24] P. Verma, K. Pathak, *J. Adv. Pharm. Tech. Res.* **2010**, *1*, 274.
[25] A. Vogt, N. Mandt, J. Lademann, H. Schaefer, U. Blume-Peytavi, *J. Invest. Dermatol.* **2005**, *10*, 252–255.
[26] A. S. Raber, A. Mittal, J. Schäfer, U. Bakowsky, J. Reichrath, T. Vogt, C. M. Lehr, *J. Control. Release* **2014**, *179*, 25–32.
[27] a) J. Lademann, H. Richter, U. F. Schaefer, U. Blume-Peytavi, A. Teichmann, N. Otberg, W. Sterry, *Skin Pharmacol. Physiol.* **2006**, *19*, 232–236. b) J. Lademann, H. Richter, A. Teichmann, N. Otberg, U. Blume-Peytavi, J. Luengo, W. Sterry, *Eur. J. Pharm. Biopharm.* **2007**, *66*, 159–164.
[28] E. Ryan, J. E. Grice, M. S. Roberts. Nanotechnology for Topical and Transdermal Drug Delivery and Targeting in *Nanotechnology and Drug Delivery, Volume Two: Nano-Engineering Strategies and Nanomedicines against Severe Diseases*, **2016**, 75.
[29] B. Duncan, C. Kim, V. M. Rotello, *J. Control. Release* **2010**, *148*, 122–127.
[30] P. Ghosh, G. Han, M. De, C. K. Kim, V. M. Rotello, *Adv. Drug Deliv. Rev.* **2008**, *60*, 1307–1315.
[31] N. N. Mahmoud, A. M. Alkilany, D. Dietrich, U. Karst, A. G. Al-Bakri, E. A. Khalil, *J. Colloid Interface Sci.* **2017**, *503*, 95–102.
[32] T. S. Anirudhan, S. S. Nair, *J. Membr. Sci.* **2017**.
[33] L. García-Fernández, J. Garcia-Pardo, O. Tort, I. Prior, M. Brust, E. Casals, V. F. Puntes, *Nanoscale* **2017**, *9*, 6111–6121.
[34] J. Niu, Y. Chu, Y. F. Huang, Y. S. Chong, Z. H. Jiang, Z. W. Mao, J. Q. Gao, *ACS Appl. Mater. Interfaces* **2017**, *9*, 9388–9401.
[35] S. Labala, A. Jose, S. R. Chawla, M. S. Khan, S. Bhatnagar, O. P. Kulkarni, V. V. K. Venuganti, *Int. J. Pharm.*, **2017**, *525*, 407–417
[36] H. Bessar, I. Venditti, L. Benassi, C. Vaschieri, P. Azzoni, G. Pellacani, A. Costanzo, *Colloids Surf. B Biointerfaces* **2016**, *141*, 141–147.
[37] Y. Chen, Y. Wu, J. Gao, Z. Zhang, L. Wang, X. Chen, J. Dai, *ACS Appl. Mater. Interfaces* **2017**, *9*, 5173–5180.
[38] K. Chaloupka, Y. Malam, A. M. Seifalian, *Trends Biotechnol.* **2010**, *28*, 580–588.
[39] N. Tyagi, S. K. Srivastava, S. Arora, Y. Omar, Z. M. Ijaz, A. G. Ahmed, S. Singh, *Cancer Lett.* **2016**, *383*, 53–61.
[40] J. Tian, K. K. Wong, C. M. Ho, C. N. Lok, W. Y. Yu, C. M. Che, P. K. Tam, *ChemMedChem* **2007**, *2*, 129–136.
[41] K. H. Kwan, X. Liu, M. K. To, K. W. Yeung, C. M. Ho, K. K. Wong, *Nanomed.-Nanotechnol.* **2011**, *7*, 497–504.
[42] B. S. Atiyeh, M. Costagliola, S. N. Hayek, S. A. Dibo, *Burns* **2007**, *33*, 139–148.
[43] M. Rai, A. Yadav, A. Gade, *Biotechnol. Adv.* **2009**, *27*, 76–83.
[44] X. Liu, P. Y. Lee, C. M. Ho, V. C. Lui, Y. Chen, C. M. Che, K. K. Wong, *ChemMedChem* **2010**, *5*, 468–475.
[45] P. K. Stoimenov, R. L. Klinger, G. L. Marchin, K. J. Klabunde, *Langmuir* **2002**, *18*, 6679–6686.
[46] A. M. Allahverdiyev, E. S. Abamor, M. Bagirova, M. Rafailovich, *Future Microbiol.* **2011**, *6*, 933–940.

[47] E. S. Abamor, A. M. Allahverdiyev, M. Bagirova, M. Rafailovich, *Acta Trop.* **2017**, *169*, 30–42.
[48] A. P. Zhang, Y. P. Sun, *World J. Gastroenterol.* **2004**, *10*, 3191.
[49] M. Pandurangan, G. Enkhtaivan, J. A. Young, H. J. Hoon, H. Lee, S. Lee, D. H. Kim, *Biol. Trace Elem. Res.* **2016**, *171*, 293–300.
[50] M. P. Abuçafy, E. B. Manaia, R. C. K. Kaminski, V. H. Sarmento, L. A. Chiavacci. *J. Nanomater.*, **2016**, *73*.
[51] S. G. Coelho, A. K. Patri, A. M. Wokovich, S. E. McNeil, P. C. Howard, S. A. Miller, *JAMA Dermatol.* **2016**, *152*, 470–472.
[52] M. Morsella, N. d'Alessandro, A. E. Lanterna, J. C. Scaiano, *ACS Omega* **2016**, *1*, 464–469.
[53] A. P. Popov, A. V. Priezzhev, J. Lademann, R. Myllylä, *J. Phys. D: Appl. Phys.* **2005**, *38*, 2564.
[54] H. A. E. Benson, Y. Mohammed, J. E. Grice, M. S. Roberts, *Nanosci. Dermatol.* **2016**, *115*.
[55] K. Ali, S. Dwivedi, A. Azam, Q. Saquib, M. S. Al-Said, A. A. Alkhedhairy, J. Musarrat, *J. Colloid Interface Sci.* **2016**, *472*, 145–156.
[56] G. Rath, T. Hussain, G. Chauhan, T. Garg, A. K. Goyal, *Mater. Sci. Eng. C* **2016**, *58*, 242–253.
[57] H. Mirzaei, M. Darroudi, *Ceram. Int.* **2017**, *43*, 907–914.
[58] S. Sonia, K. Ruckmani, M. Sivakumar, *Mater. Sci. Eng. C* **2017**, *79*, 581–589.
[59] A. M. Holmes, Z. Song, H. R. Moghimi, M. S. Roberts, *ACS nano* **2016**, *10*, 1810–1819.
[60] V. R. Leite-Silva, W. Y. Sanchez, H. Studier, D. C. Liu, Y. H. Mohammed, A. M. Holmes, J. E. Grice, *Eur. J. Pharm. Biopharm.* **2016**, *104*, 140–147.
[61] M. V. Yezhelyev, X. Gao, Y. Xing, A. Al-Hajj, S. Nie, R. M. O'Regan, *Lancet Oncol.* **2006**, *7*, 657–667.
[62] C. Hanley, J. Layne, A. Punnoose, K. M. Reddy, I. Coombs, A. Coombs, D. Wingett, *Nanotechnology* **2008**, *19*, 295103.
[63] S. Ostrovsky, G. Kazimirsky, A. Gedanken, C. Brodie, *Nano Res.* **2009**, *2*, 882–890.
[64] M. J. Akhtar, M. Ahamed, S. Kumar, M. M. Khan, J. Ahmad, S. A. Alrokayan, *Int. J. Nanomedicine* **2012**, *7*, 845.
[65] M. Mahmoudi, S. Sant, B. Wang, S. Laurent, T. Sen, *Adv. Drug Deliv. Rev.* **2011**, *63*, 24–46.
[66] S. A. Wahajuddin, *Int. J. Nanomedicine* **2012**, *7*, 3445.
[67] B. Chertok, B. A. Moffat, A. E. David, F. Yu, C. Bergemann, B. D. Ross, V. C. Yang, *Biomaterials* **2008**, *29*, 487–496.
[68] Y. F. Rao, W. Chen, X. G. Liang, Y. Z. Huang, J. Miao, L. Liu, Z. Chen, *Small* **2015**, *11*, 239–247.
[69] Z. Bakhtiary, A. A. Saei, M. J. Hajipour, M. Raoufi, O. Vermesh, M. Mahmoudi, *Nanomed.-Nanotechnol.* **2016**, *12*, 287–307.
[70] H. L. Xu, K. L. Mao, Y. P. Huang, J. J. Yang, J. Xu, P. P. Chen, J. Xiao, *Nanoscale* **2016**, *8*, 14222–14236.
[71] F. M. Kievit, M. Zhang, *Acc. Chem. Res.* **2011**, *44*, 853–862.
[72] P. C. Wu, H. T. Hsiao, Y. C. Lin, D. B. Shieh, Y. C. Liu, *Nanomed.-Nanotechnol.* **2017**, *13*, 1975–1981.
[73] a) C. Aguzzi, P. Cerezo, C. Viseras, C. Caramella, *Appl.Clay Sci.* **2007**, *36*, 22–36. b) C. Aguzzi, P. Capra, C. Bonferoni, P. Cerezo, I. Salcedo, R. Sánchez, C. Viseras, *Appl.Clay Sci.* **2010**, *50*, 106–111. c) C. Aguzzi, P. Cerezo, G. Sandri, F. Ferrari, S. Rossi, C. Bonferoni, C. Viseras, *Mater. Technol.* **2014**, *29*, B96-B99. d) C. Aguzzi, G. Sandri, P. Cerezo, E. Carazo, C. Viseras. Health and Medical Applications of Tubular Clay Minerals in *Developments in Clay Science*, **2016**, Vol. 7, 708–725.
[74] a) C. Viseras, C. Aguzzi, P. Cerezo, A. Lopez-Galindo, *Appl. Clay Sci.* **2007**, *36*, 37–50. b) C. Viseras, C. Aguzzi, P. Cerezo, M. C. Bedmar, *Mater. Sci.Technol.* **2008**, *24*, 1020–1026. c) C. Viseras, P. Cerezo, R. Sanchez, I. Salcedo, C. Aguzzi, *Appl. Clay Sci.* **2010**, *48*, 291–295.
[75] E. Carazo, A. Borrego, C. Aguzzi, P. Cerezo, C. Viseras, *Curr. Drug Deliv.* **2016**, *13*, 1–2.
[76] M. T. Baschini, G. R. Pettinari, J. M. Vallés, C. Aguzzi, P. Cerezo, A. López-Galindo, C. Viseras, *Appl. Clay Sci.* **2010**, *49*, 205–212.
[77] C. Aguzzi, R. Sánchez-Espejo, P. Cerezo, J. Machado, C. Bonferoni, S. Rossi, C. Viseras, *Int. J. Pharm.* **2013**, *453*, 473–479.
[78] a) R. Sánchez-Espejo, C. Aguzzi, P. Cerezo, I. Salcedo, A. López-Galindo, C. Viseras, *J. Ethnopharmacol.* **2014**, *155*, 810–814. b) R. Sánchez-Espejo, P. Cerezo, C. Aguzzi, A. López-Galindo, J. Machado, C. Viseras, *Appl. Clay Sci.* **2015**, *116*, 1–7.
[79] C. Pesciaroli, C. Viseras, C. Aguzzi, B. Rodelas, J. González-López, *Appl. Clay Sci.* **2016**, *132*, 59–67.
[80] a) E. Ruiz-Hitzky, P. Aranda, J. M. Serratosa. Clay-organic interactions: Organoclay complexes and polymer-clay nanocomposites. In *Handbook of Layered Materials*, **2004**, pp.91-154. b) E. Ruiz-Hitzky, P. Aranda, M. Darder, G. Rytwo, *J. Mater. Chem.* **2010**, *20*, 9306–9321.
[81] M. Ghadiri, W. Chrzanowski, R. Rohanizadeh, *RSC Adv.* **2015**, *5*, 29467–29481.
[82] F. A. Castro-Smirnov, O. Piétrement, P. Aranda, J. R. Bertrand, J. Ayache, E. Le Cam, B. S. Lopez, *Sci. Rep.* **2016**, *6*, 36341.
[83] M. Hun Kim, G. Choi, A. Elzatahry, A. Vinu, Y. Bin Choy, J. H. Cho, *Clays Clay Miner.* **2016**, *64*, 115–130.
[84] G. Lazzara, S. Riela, R. F. Fakhrullin, *Ther. Deliv.* **2017**.
[85] G. M. Dário, G. G. da Silva, D. L. Gonçalves, P. Silveira, A. T. Junior, E. Angioletto, A. M. Bernardin, *Mater. Sci. Eng. C* **2014**, *43*, 109–116.
[86] E. E. Gaskell, A. R. Hamilton, *Future* **2014**, *6*, 641–655.
[87] a) M. Ghadiri, W. Chrzanowski, W. H. Lee, R. Rohanizadeh, *RSC Adv.* **2014**, *4*, 35332–35343. b) M. Ghadiri, W. Chrzanowski, R. Rohanizadeh, *J. Mater. Sci.* **2014**, *25*, 2513–2526.
[88] G. Sandri, M. C. Bonferoni, F. Ferrari, S. Rossi, C. Aguzzi,, M. Mori, C. Caramella, *Carbohyd. Polym.* **2014**, *102*, 970–977.
[89] A. Karimi, W. M. A. W. Daud, *JOM* **2017**, *69*, 1213–1220.
[90] G. Sandri, M. C. Bonferoni, S. Rossi, F. Ferrari, C. Aguzzi, C. Viseras, C. Caramella. Clay minerals for tissue regeneration, repair, and engineering. In *Wound Healing Biomaterials-Volume 2:Functional Biomaterials*, **2016**, 385.
[91] G. Cerri, M. De'Gennaro, M. C. Bonferoni, C. Caramella, *Appl. Clay Sci.* **2004**, *27*, 141–150.

[92] M. C. Bonferoni, G. Cerri, M. de'Gennaro, C. Juliano, C. Caramella, *Appl. Clay Sci.* **2007**, *36*, 95–102.
[93] M. Tenci, S. Rossi, C. Aguzzi, E. Carazo, G. Sandri, M. C. Bonferoni, F. Ferrari, *Int. J. Pharm.* **2017**.
[94] Y. Ohara, M. Suzuki, N. Takano, S. Mitsuyama. *U. S. Patent No. 8,741,323.* **2014**, Washington, DC: U. S. Patent and Trademark Office.
[95] M. Darder, M. López-Blanco, P. Aranda, F. Leroux, E. Ruiz-Hitzky, *Chem. Mater.* **2005**, *17*, 1969–1977.
[96] a) K. Ladewig, Z. P. Xu, G. Q. Lu, *Expert Opin. Drug Deliv.* **2009**, *6*, 907–922. b) K. Ladewig, M. Niebert, Z. P. Xu, P. P. Gray, G. Q. M. Lu, *Appl. Clay Sci.* **2010**, *48*, 280–289.
[97] K. Zhang, Z. P. Xu, J. Lu, Z. Y. Tang, H. J. Zhao, D. A. Good, M. Q. Wei, *Int. J. Mol. Sci* **2014**, *15*, 7409–7428.
[98] B. Balcomb, M. Singh, S. Singh, *ChemistryOpen* **2015**, *4*, 137–145.
[99] Y. Kuthati, R. K. Kankala, C. H. Lee, *Appl. Clay Sci.* **2015**, *112*, 100–116.
[100] G. Choi, H. Piao, Z. A. Alothman, A. Vinu, C. O. Yun, J. H. Choy, *Int. J. Nanomedicine* **2016**, *11*, 337.
[101] L. Li, Z. Gu, W. Gu, J. Liu, Z. P. Xu, *J. Colloid Interface Sci.* **2016**, *470*, 47–55.
[102] G. Huang, K. L. Zhang, S. Chen, S. H. Li, L. L. Wang, L. P Wang, H. H. Yang, *J. Mater. Chem. B* **2017**, *5*, 3629–3633.
[103] D. Mosangi, L. Moyo, S. K. Pillai, S. S. Ray, *RSC Adv.* **2016**, *6*, 105862–105870.
[104] D. Mosangi, S. K. Pillai, L. Moyo, S. S. Ray, *RSC Adv.* **2016**, 6, 77709–77716.
[105] V. R. R. Cunha, R. B. De Souza, I. H. J. Koh, V. R. L. Constantino, *Scientific reports* **2016**, *6*, 30547.
[106] Y. Li, N. Li, W. Pan, Z. Yu, L. Yang, B. Tang, *ACS Appl. Mater.Interfaces* **2017**, *9*, 2123–2129.
[107] D. Chang, Y. Gao, L. Wang, G. Liu, Y. Chen, T. Wang, X. Zeng, *J. Colloid Interface Sci.* **2016**, *463*, 279–287.
[108] J. Liu, Z. Luo, J. Zhang, T. Luo, J. Zhou, X. Zhao, K. Cai, *Biomaterials* **2016**, *83*, 51–65.
[109] V. Weiss, C. Argyo, A. A. Torrano, C. Strobel, S. A. Mackowiak, A. Schmidt, T. Bein, *Microporous Mesoporous Mater.* **2016**, *227*, 242–251.
[110] X. Li, M. Wu, L. Pan, J. Shi, *Int. J. Nanomedicine* **2016**, *11*, 93.
[111] A. L. Doadrio, J. M. Sánchez-Montero, J. C. Doadrio, A. J. Salinas, M. Vallet-Regí, *Eur. J. Pharm. Sci.* **2017**, *97*, 1–8.
[112] S. Sapino, E. Ugazio, L. Gastaldi, I. Miletto, G. Berlier, D. Zonari, S. Oliaro-Bosso, *Eur. J. Pharm. Biopharm* **2015**, *89*, 116–125.
[113] L. Gastaldi, E. Ugazio, S. Sapino, P. Iliade, I. Miletto, G. Berlier, *Phys. Chem. Chem. Phys.* **2012**, *14*, 11318–11326.
[114] M. Pilloni, G. Ennas, M. Casu, A. M. Fadda, F. Frongia, F. Marongiu, C. Sinico, *Pharm. Dev. Technol.* **2013**, *18*, 626–633.
[115] F. Hamam, M. Al-Remawi, *J. Funct. Foods* **2014**, *8*, 87–99.
[116] F. Rancan, Q. Gao, C. Graf, S. Troppens, S. Hadam, S. Hackbarth, A. Vogt, *ACS Nano* **2012**, *6*, 6829–6842.
[117] N. Bajwa, N. K. Mehra, K. Jain, N. K. Jain, *Artif. Cell Nanomed. Biotechnol.* **2016**, *44*, 758–768.
[118] V. Mishra, E. Gurnany, M. H. Mansoori, Quantum Dots in Targeted Delivery of Bioactives and Imaging. In *Nanotechnology-Based Approaches for Targeting and Delivery of Drugs and Genes*, **2017**, 427.
[119] X. Cai, Y. Luo, W. Zhang, D. Du, Y. Lin, *ACS applied materials & interfaces* **2016**, *8*, 22442–22450.
[120] S. Beack, W. H. Kong, H. S. Jung, I. H. Do, S. Han, H. Kim, S. K. Hahn, *Acta Biomater.* **2015**, *26*, 295–305.
[121] R. Justin, K. Tao, S. Román, D. Chen, Y. Xu, X. Geng, S. MacNeil, S. *Carbon*, **2016**, *97*, 54–70.
[122] L. Saulite, D. Dapkute, K. Pleiko, I. Popena, S. Steponkiene, R. Rotomskis, U. Riekstina. *Beilstein J. Nanotechnol.* **2017**, *8*, 1218–1230.
[123] M. Zhang, W. Wang, N. Zhou, P. Yuan, Y. Su, M. Shao, F. Pan, *Carbon* **2017**, *118*, 752–764.
[124] Y. Yuan, B. Guo, L. Hao, N. Liu, Y. Lin, W. Guo, B. Gu, *Colloids Surf. B: Biointerfaces.* **2017**

Received: September 14, 2017
Accepted: December 22, 2017
Published online on ■■ ■■, ■■■■

PERSONAL ACCOUNT

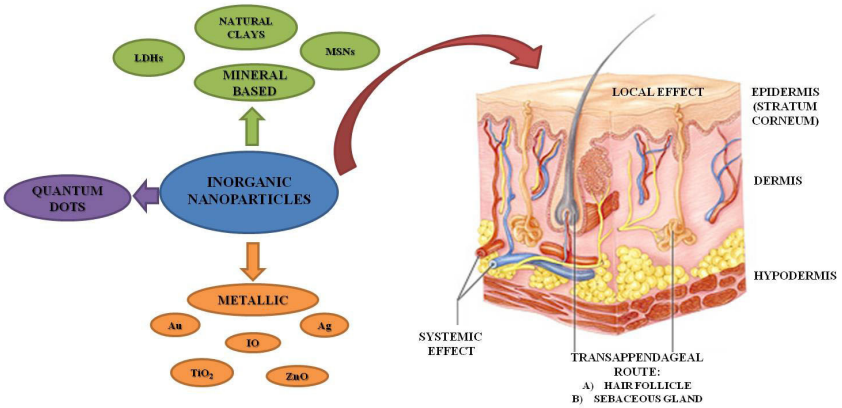

E. Carazo, A. Borrego-Sánchez, F. García-Villén, R. Sánchez-Espejo, P. Cerezo, C. Aguzzi, C. Viseras

1 – 10

Advanced Inorganic Nanosystems for Skin Drug Delivery

On the basis of their inherent properties, including biocompatibility, biodegradability and relative low-cost, inorganic nanoparticles are ideal candidates for the development of skin drug delivery systems. This review provides an updated and comprehensive overview of the state of the art in the trends towards skin drug delivery with a particular focus in the attractive alternative offered by inorganic-based nanosystems.

Applied Clay Science 160 (2018) 173–179

Contents lists available at ScienceDirect

Applied Clay Science

journal homepage: www.elsevier.com/locate/clay

Research paper

Biopharmaceutical improvement of praziquantel by interaction with montmorillonite and sepiolite

Ana Borrego-Sánchez[a,b], Esperanza Carazo[b], Carola Aguzzi[b], César Viseras[a,b,*], C. Ignacio Sainz-Díaz[a]

[a] Instituto Andaluz de Ciencias de la Tierra, CSIC-University of Granada, Av. de las Palmeras 4, 18100 Armilla, Granada, Spain
[b] Department of Pharmacy and Pharmaceutical Technology, Faculty of Pharmacy, University of Granada, Campus de Cartuja s/n, 18071 Granada, Spain

ARTICLE INFO

Keywords:
Praziquantel
Clay minerals
Montmorillonite
Sepiolite
Schistosomiasis
Bioavailability

ABSTRACT

Praziquantel is the drug of first choice for the treatment of the human schistosomiasis. It is administered orally, requiring high doses to overcome adverse biopharmaceutical properties, including high lipophilia and intense hepatic first pass metabolism. According to its biopharmaceutical profile, praziquantel has very low water solubility and high permeability. Therefore, dissolution is the limiting factor for absorption in the gastrointestinal tract. Improvement of the aqueous solubility of the drug would reduce the currently high oral doses. Meanwhile, montmorillonite and sepiolite are clay minerals, with a high adsorption and swelling properties, potentially useful as a low-cost nanocarrier to design praziquantel delivery systems. In this work, the interactions between the drug and clay minerals are studied experimentally, with the aim of improving the biopharmaceutical profile of the drug. The results showed the effective loading of the drug in the clay minerals as well as the significant increase of the dissolution rate and the dissolved amount of praziquantel, potentially improving the bioavailability of the drug.

1. Introduction

Clay minerals, in particular montmorillonite and sepiolite, are widely used pharmaceutical excipients in different pharmaceutical dosage forms, designed for oral and topical administration (López-Galindo and Viseras, 2004; Viseras et al., 2010). Besides their classic pharmaceutical uses, clay minerals may be effectively used in the development of modified drug delivery systems (Aguzzi et al., 2007; Viseras et al., 2010).

Montmorillonite is a dioctahedral 2:1 phyllosilicate with one octahedral sheet and two tetrahedral sheets (T:O:T). An interlayer nanospace exists between each triple-sheet-layer. These layers have isomorphic substitutions of Si^{4+} by Al^{3+} in the tetrahedral sheet and Al^{3+} by Mg^{2+} in the octahedral layer. An important part of the physicochemical properties of montmorillonite depends on the isomorphic substitutions that confer a negative residual charge compensated by cations in the interlayer space. These interlayer spaces represent about 90% of the mineral total surface and are accessible to water molecules and other compounds, yielding a high adsorption capacity for polar molecules (Bergaya and Lagaly, 2006; Aguzzi et al., 2007).

On the other hand, sepiolite is a non-planar phyllosilicate with fibrous morphology. The basal oxygen layer is continuous but the apical oxygens undergo a periodic inversion every 8 octahedral positions. This inversion causes a discontinuous octahedral layer forming long channels, where the water and organic molecules can be adsorbed (Guggenheim et al., 2006).

Because of their high adsorption and cation exchange capacities, both montmorillonite and sepiolite are peculiar nanostructurated material. These solids can retain organic molecules in their structures and after administration release the retained active compounds under controlled conditions, being good candidates for the design of modified delivery systems of several drugs (Viseras et al., 2010). Besides the above mentioned clay minerals, halloysite nanotubes have been also exploited as nanocarriers for several applications (Massaro et al., 2016; Makaremi et al., 2017).

Praziquantel is the drug of choice for an extended parasitic disease, schistosomiasis that it is a parasitic disease caused by *Schistosoma*. The infection is caused by the parasite penetration through the skin of individuals, in contact with contaminated water. It is widely extended, mainly in at least 74 developing countries, in the tropics and subtropics (Chitsulo et al., 2000) and it affects 250 million people approximately, causing over half a million of deaths every year (Steinmann et al., 2006). Behind of malaria, the Schistosomiasis is the second of the most prevalent diseases that affects African children (WHO, 2017).

* Corresponding author at: Instituto Andaluz de Ciencias de la Tierra, CSIC-University of Granada, Av. de las Palmeras 4, 18100 Armilla, Granada, Spain.
E-mail address: cviseras@ugr.es (C. Viseras).

https://doi.org/10.1016/j.clay.2017.12.024
Received 16 October 2017; Received in revised form 6 December 2017; Accepted 13 December 2017
Available online 19 December 2017

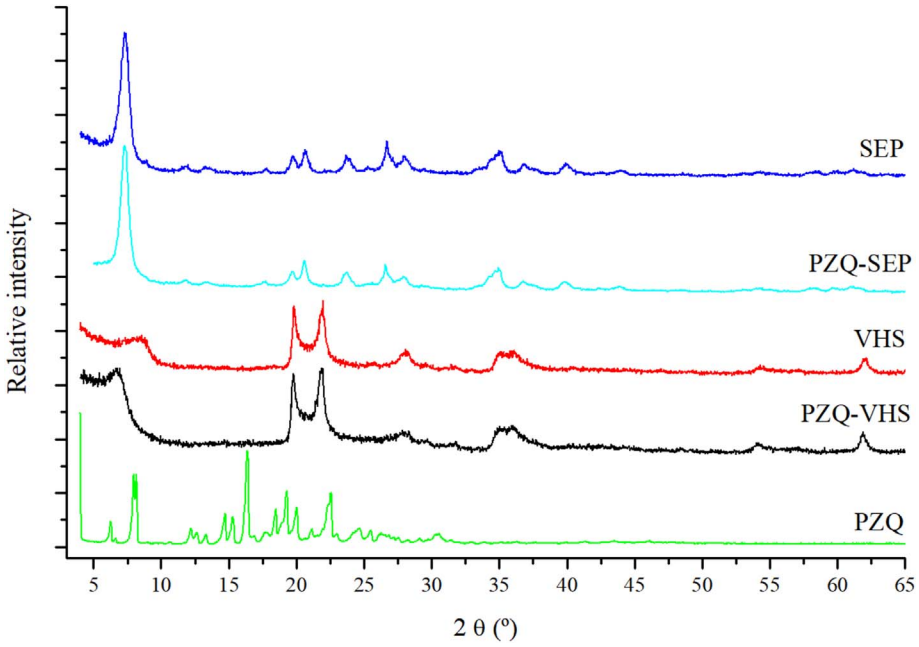

Fig. 1. XRPD patterns of the studied samples.

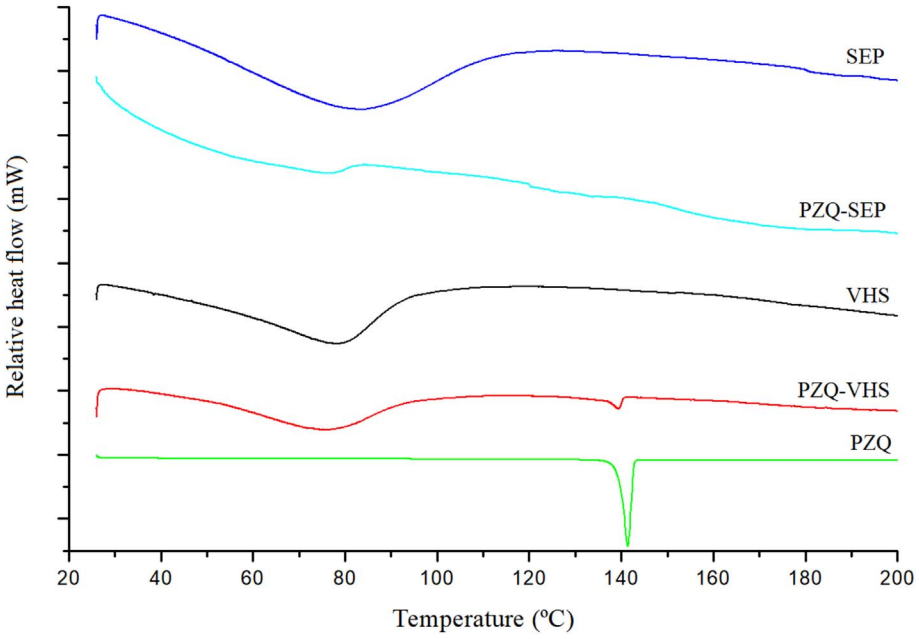

Fig. 2. DSC profiles of the studied samples.

The prevention of the Schistosomiasis is difficult and there is no effective vaccine against the disease. Praziquantel is the most used drug for the treatment of Schistosomiasis (WHO, 2017). However, its extensive use and the lack of compliance during the treatment is causing drug resistance (Wang et al., 2012).

Praziquantel has a chiral center and only the R-(-)-enantiomer possesses anthelmintic activity (Andrews, 1985) even if the actual treatments use a racemic mixture. It is classified in Class II in Biopharmaceutics Classification System (BCS) (FDA, 2017; González-Esquivel et al., 2005), due to its low aqueous solubility and high permeability, and has low absorption in the gastrointestinal tract (GIT) (Amidon et al., 1995). For these reasons, high oral doses are required to treat schistosomiasis. The interaction of praziquantel with montmorillonite in aqueous medium was studied by El-Feky et al. (2015). However, the resultant interaction products did not improve *in vitro* dissolution rates neither *in vivo* absorption rates. Probably, as a result of the presence of water molecules in the interlayer space of the montmorillonite, the entry of praziquantel was hindered and the drug was only absorbed on the external surface, resulting in the absence of relevant biopharmaceutical improvements.

With these premises, aim of this work was to obtain praziquantel/clay mineral interaction products in absence of water as a strategy to improve the effective entrapment of the drug molecules. The potential increase in praziquantel solubility was a rational approach to the improvement of drug bioavailability.

2. Materials and methods

2.1. Materials

Praziquantel (PZQ) was purchased from Sigma Aldrich (S). Ethanol of 99% of purity was used as solvent. Purified pharmaceutical degree

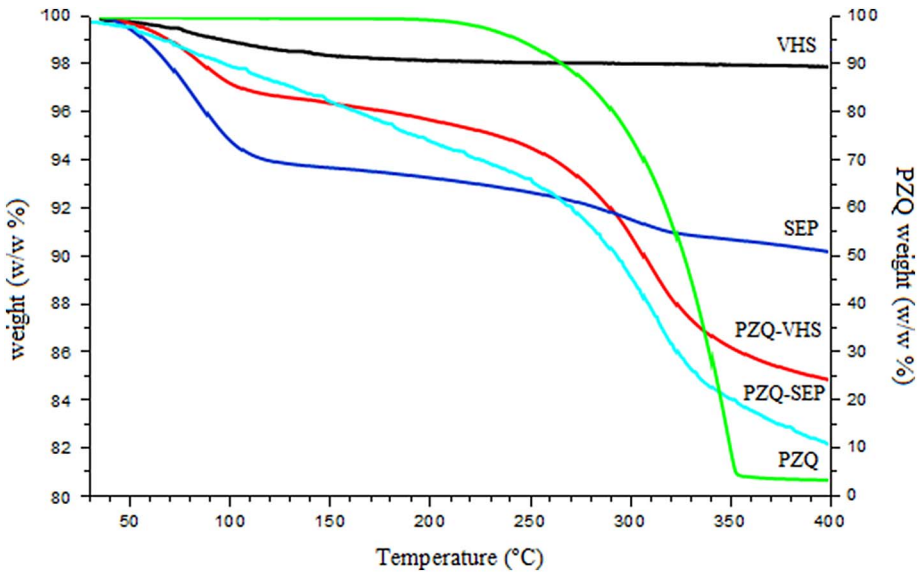

Fig. 3. TGA profiles of the studied samples.

Montmorillonite (Veegum HS®, VHS) was purchased from Vanderbilt Company (USA). The Sepiolite samples from Vicálvaro (Madrid) (SEP) were kindly gifted by TOLSA (S). These solids were used without any pretreatment and were characterized elsewhere (Torres-Ruíz et al., 1994; Viseras and López-Galindo, 1999; Aguzzi et al., 2005).

2.2. Methods

2.2.1. Preparation of praziquantel/clay minerals interaction products

Clay powders were dispersed in 100 mL of ethanolic solution of PZQ under magnetic stirring at room temperature for 24 h, in such way that the clay/drug ratio was 5:1 w/w in order to ensure complete interaction between the components. After 24 h, the solvent was evaporated at 40 °C by means a rotary evaporator (Buchi® R II, CH) and the solid residue (PZQ-VHS or PZQ-SEP prepared with VHS or SEP, respectively) was stored in a desiccator at room temperature with freshly activated silica-gel grafted with a moisture indicator of Co salt.

2.2.2. X-ray diffraction

Powder X-ray diffraction was performed with a Philips®X-Pert diffractometer with the CuKa wavelength. The information of diffraction was analyzed using XPOWDER® software (Martín-Ramos, 2005).

2.2.3. Thermal analysis

Differential Scanning Calorimetric analysis (DSC) and thermogravimetric analysis (TGA) were performed with a Mettler Toledo mod. TGA/DSC1 calorimeter, equipped with sensor and FRS5 microbalance (precision 0.1 μg) and FP89 software package, using a heating rate of 5 °C/min in the 30–400 °C temperature range for TGA and DSC runs and a rate of 2 °C/min for additional specific DSC runs. Nitrogen was used as purge gas in DSC under flows of 100 and 15 mL/min.

2.2.4. Scanning electron microscopy (SEM)

Microphotographs of the samples were performed using a Hitachi S-510 scanning electron microscope (voltage 25 kV, secondary electron images) (Hitachi Scientific Instruments Ltd., Tokyo, Japan). The samples were mounted on adhesive paper, fixed with colloidal gold and metallized with gold in two orientations (20–30°). The images were captured digitally using the program ScanVision, Version 1.2.

2.2.5. Fourier transform infrared (FTIR) and Raman spectroscopies

FTIR spectra were recorded in the range 4000–600 cm^{-1} with a 0.5 cm^{-1} resolution and a well-plate sampler (JASCO 6200 spectrophotometer with Spectra Manager II software). Raman spectra were recorded in the range 3500–800 cm^{-1} with a 6.48 cm^{-1} resolution using a Micro-Raman dispersive JASCO NRS-5100 spectrophotometer, with laser light source VIS-NIR with red diode at 785 nm with 500 mW of power (TorsanaStarbright) and refrigeration by air and a KnowItAll JASCO Edition for Raman software.

2.2.6. In vitro release studies

Hard gelatine capsules containing 600 mg of each PZQ, PZQ-VHS and PZQ-SEP, in which 100 mg correspond to PZQ, were prepared. Similarly, hard gelatine capsules containing 100 mg of PZQ were elaborated as reference. The capsules were subjected to *in vitro* release studies following the European Pharmacopoeia procedure for dissolution test of solid oral dosage forms. Experiments were carried out using European Pharmacopoeia apparatus 2 with sinkers (Sotax AT7, CH) at 150 rpm, 37 °C, 1 L of dissolution medium (no sink conditions). Two dissolution media were used: i) HCl 0.001 M simulating the stomach physiological fluid; and ii) a simulated intestinal fluid (pH = 6.8) (SIF) without enzymes. At established time intervals, samples of dissolution medium (5 mL) were withdrawn, filtered through 0.45 μm Millipore® (S) membranes and the amount of drug dissolved measured by high-performance liquid chromatography (HPLC), using a 1260 Infinity II Agilent equipment (G) with quaternary pump, autosampler, column oven and UV-VIS diode-array spectrophotometer. The stationary phase was a column Kromasyl® C18, 5 μm, 250 × 4.6 mm (Teknokroma, S) and the mobile phase was a mixture of H_20 and CH_3CN (35:65 v/v). The flow rate was set at 0.8 mL/min with an injection volume of 10 μL. A detector with a wavelength of 225 nm was used and the run time for each analysis was 5 min. Data were recorded and analyzed by using LC Open LAB HPLC 1260 software (Agilent, G). The analytical method was linear in the concentration range 10–50 mg/L of PZQ in both media, resulting in correlation coefficients of 0.9994 (HCl 0.001 M) and 0.9992 (SIF).

3. Results and discussion

3.1. X-ray diffraction

The powder XRD patterns of raw components and interaction products are shown in Fig. 1. PZQ showed the most intense reflection at around 16.5° 2θ and other intense reflections at approximately 8.0°, 19.1° and 23.3° 2θ according with that previously reported (El-Subbagh and Al-Badr, 1998). After interaction with the clay minerals, complete

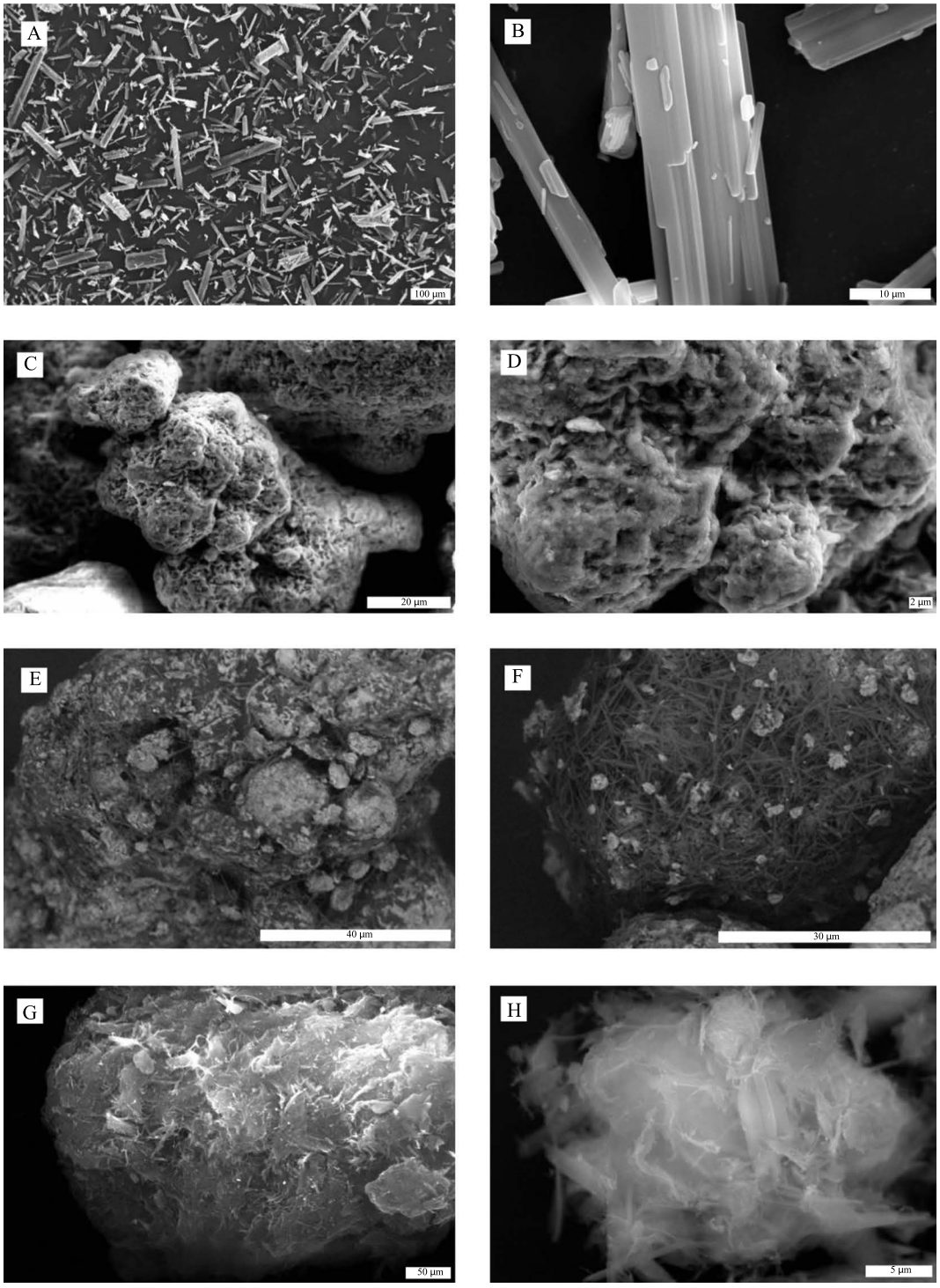

Fig. 4. SEM microphotographs of PZQ (A–B), VHS (C–D), PZQ-VHS (E–F) and PZQ-SEP (G–H).

absence of drug reflections was probably due to a loss of crystallinity of PZQ. In previous works a similar behavior of PZQ was observed in the formation of a solid dispersion with PVP (polyvinylpyrrolidone) (De la Torre et al., 1999) and with sodium starch glycolate (Chaud et al., 2013).

As a result of the interaction with the drug, diffraction patterns of SEP did not show changes, whereas VHS patterns evidenced significant changes in some reflections. In particular, reflection corresponding to *d* (001) of VHS shifted to lower angles after interaction with the drug. The resultant interlayer spaces changed from 12.32 Å in the pristine VHS to 16.05 Å in PZQ-VHS, clearly suggesting the effective inclusion of drug molecules in the clay mineral interlayer.

3.2. Thermal analysis

The DSC profiles of PZQ showed a strong endothermic peak at 144 °C with enthalpy $\Delta H = -90.41\ Jg^{-1}$, corresponding to the melting of the (RS)-PZQ crystals (Fig. 2) and with no loss of weight in TGA curve (Fig. 3). Calorimetric profiles of VHS and SEP showed broad endothermic peaks in the range 50–90 °C, corresponding to the evaporation of water. As a result of interaction, DSC curve of PZQ-SEP showed only a very low intensity peak corresponding to water

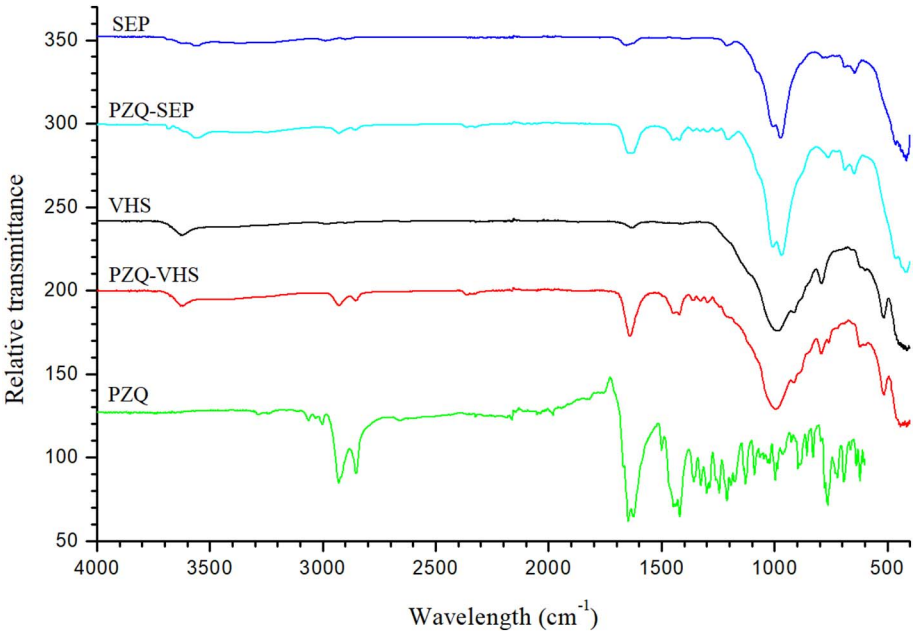

Fig. 5. FTIR spectra of the studied samples.

evaporation and complete disappearance of melting peak of the drug. In PZQ-VHS curve water evaporation was also evident as well as a small peak corresponding to the melting of the drug, with $\Delta H = 1.86\ Jg^{-1}$. The crystallinity degree of the drug in the interaction product, calculated as ΔH melting(PZQ/VHS)/ΔH melting(pure PZQ), was approximately 2%. Similar approach was proposed by Cavallaro et al. (2013), studying the amorphization of polyethylene glycol in polymer/clay composites. The obtained results showed that amorphization of the PZQ occurs in the prepared interaction products, justifying the lack of the PZQ reflections in the PZQ-VHS and PZQ-SEP powder XRD patterns. This amorphization is slightly higher in PZQ-SEP product.

Thermogravimetric profiles of the clay minerals showed a weight loss (2% w/w and 10% w/w), corresponding to evaporation of adsorbed water molecules from VHS and SEP surfaces, respectively (Fig. 3). Second weight loss of the sepiolite sample in the interval 250–350 °C corresponded to loss of zeolitic water (Viseras and López-Galindo, 1999). In the interaction products, thermal decomposition of the drug resulted in weight losses in the range between 200 and 400 °C, corroborating the adsorption of the PZQ in these mineral solids.

3.3. Electron microscopy

The microphotographs of the praziquantel (Fig. 4A–B) presented elongated prismatic morphology and crystal sizes > 100 μm, similar to those of PZQ racemic mixtures previously observed (Liu et al., 2004; Espinosa-Lara et al., 2013).

SEM microphotographs of montmorillonite (Fig. 4C–D) showed grains with different particle sizes. Particles associated with any impurities were not detected, corroborating the XRD results. In the SEM microphotographs of the PZQ-VHS interaction product, significant changes of texture and morphology were observed (Fig. 4E–F). Filamentous particles of praziquantel were observed between the montmorillonite particles, as well as, the amorphization and the loss of the crystalline structure of praziquantel. The initial PZQ particles disappeared and PZQ formed aggregates in the montmorillonite particles during the dispersion and solvent evaporation process. The amorphization of a portion of the praziquantel and the formation of these small size crystalline fibers may also justify the low crystallinity and the previous lack of XRD reflections in this IP mixture (PZQ-VHS), corroborating XRD diffraction and the DSC results.

Sepiolite morphologies were described previously as being constituted by grains with different particle sizes formed by fibrous particles (Viseras and López-Galindo, 1999; Suárez and García-Romero, 2012). In PZQ-SEP microphotographs, these well-known characteristics were observable, as well as the absence of crystalline praziquantel, due to the total amorphization of the drug, corroborating the DSC and the XRD results (Fig. 4G–H).

3.4. Fourier transform infrared spectroscopy

FTIR spectra of the racemic PZQ, sepiolite, montmorillonite and the interaction products (PZQ-VHS and PZQ-SEP) are compared in Fig. 5. PZQ showed two main characteristic bands in the range 2960–2840 cm^{-1} assigned to stretching vibration modes ν(CH) of CH and CH_2 groups (Rodrigues et al., 2010). Two bands corresponding to the ν(C═O) vibration mode were observed at 1665–1621 cm^{-1} (Rodrigues et al., 2010), which were assigned to each carbonyl group with different local environment in the crystal packing (Borrego-Sánchez et al., 2017). The δ(C—H) and ν(C—N) modes were observed around 1350–1021 cm^{-1} (Passerini et al., 2006). These experimental values coincide with previous theoretical data that completed the infrared spectra of praziquantel, assigning new bands not identified experimentally, both in the molecule (Borrego-Sánchez et al., 2016) and in the crystalline structure of praziquantel (Borrego-Sánchez et al., 2017).

The spectra of montmorillonite and sepiolite showed characteristic bands of the clay minerals at 3700–3600 cm^{-1} of the octahedral OH groups, ν(AlOHAl) ν(AlOHMg), ν(MgOHMg), 1680–1600 cm^{-1} (δ(OH water)) and 1200–1000 cm^{-1} (ν(Si—O)) (Frost et al., 2001; Ortega-Castro et al., 2009). In PZQ-VHS and PZQ-SEP, the bands of PZQ were detected which means that the drug was present in the interaction product, although no clear differences could be observed due to the high proportion of clays, whose bands overlap those of PZQ.

3.5. In vitro release studies

Drug release profiles of PZQ and the two interaction products are shown in Fig. 6. PZQ dissolution rate was higher in acidic medium (Fig. 6 up) than in intestinal fluid (Fig. 6 down), in concordance with its pH dependent solubility. As it was reported by Chaud et al. (2010), solubility of PZQ was 0.735 mg/mL and 0.454 mg/mL in HCl and phosphate buffer, respectively. Interaction of the drug with the clay

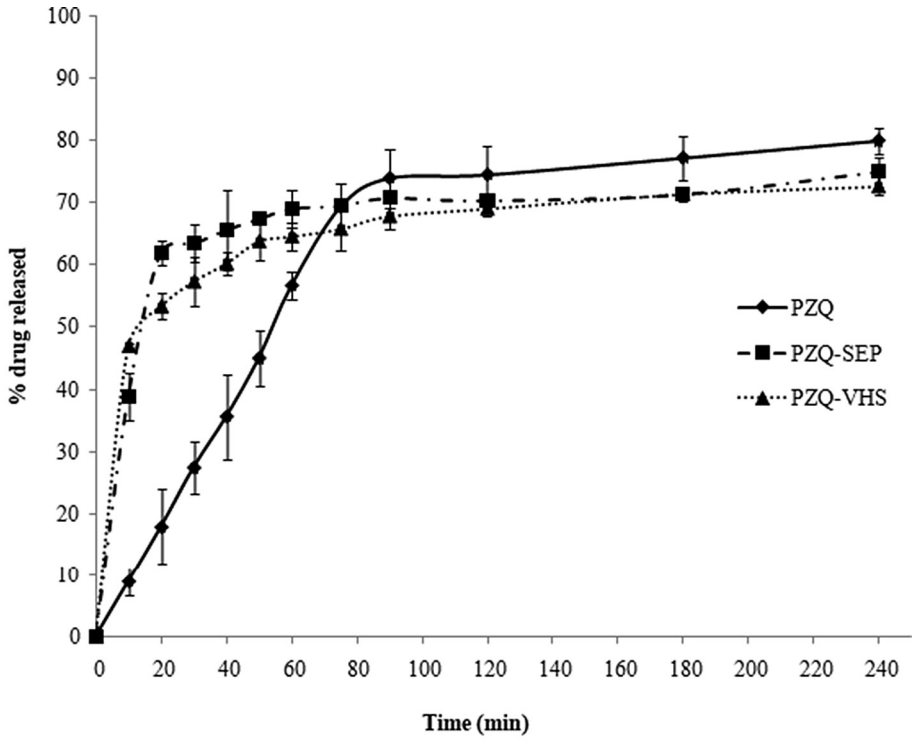

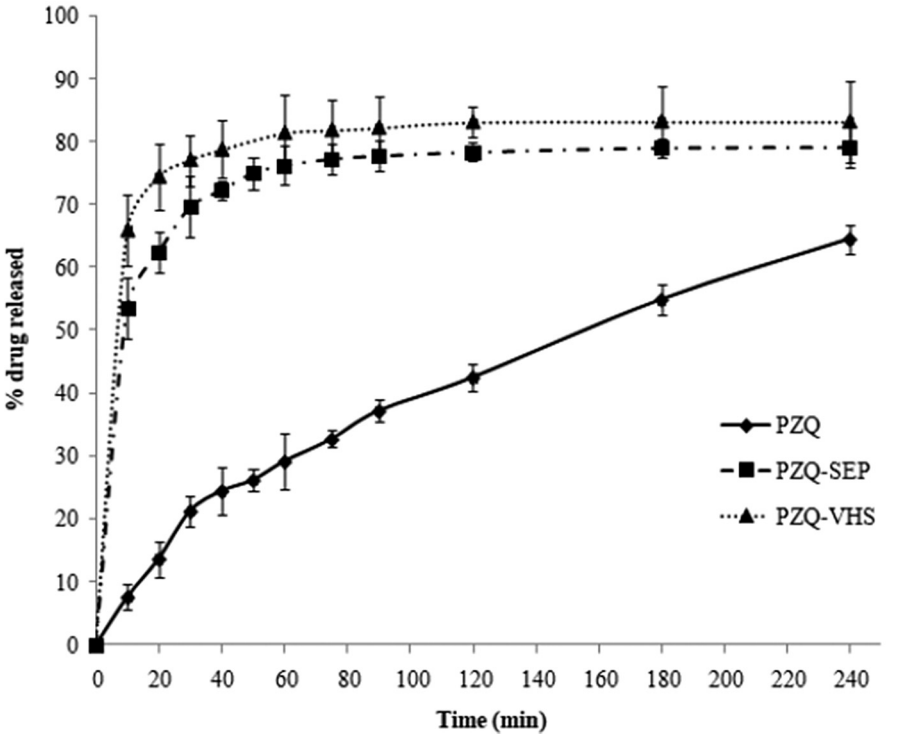

Fig. 6. *In vitro* drug release profiles in HCl 0.001 M. (up) and simulated intestinal fluid (down); (mean values ± s.d.; n = 6).

minerals induced an increase in dissolution rates with independence of pH. This improvement is particularly important in phosphate buffer (Fig. 6 down), being the intestinal environment the preferential site of absorption of orally administered drugs. The final amount of drug dissolved from the interaction products increased approximately a 20% in simulated intestinal fluid with respect to the pure PZQ. Therefore, PZQ-VHS and PZQ-SEP interaction products might improve oral bioavailability of the drug by increasing both dissolution rate and amount of drug dissolved in FIS.

4. Conclusions

The antihelmintic drug PZQ was easily intercalated in montmorillonite interlayer space and sepiolite channels by using a non-aqueous polar medium (ethanol), which allowed overcoming the water barriers for low-water soluble organic compounds. This method can be extended to any short-chain alcohols where PZQ is soluble. These solvents can be easily eliminated after the preparation process.

PZQ-VHS and PZQ-SEP increased dissolution rates and global amount of drug dissolved. These kinds of interaction products can be

considered as promising alternatives to improve bioavailability of water low-soluble drugs like praziquantel.

Acknowledgements

Authors are thankful to MINECO projects (FIS2013-48444-C2-2-P and CGL2016-80833-R) and Andalusian projects (RNM363 and RNM1897) for financial support.

References

Aguzzi, C., Viseras, C., Cerezo, P., Rossi, S., Ferrari, F., López-Galindo, A., Caramella, C., 2005. Influence of dispersion conditions of two pharmaceutical grade clays on their interaction with some tetracyclines. Appl. Clay Sci. 30, 79–86. http://dx.doi.org/10.1016/j.clay.2005.03.007.

Aguzzi, C., Cerezo, P., Viseras, C., Caramella, C., 2007. Use of clays as drug delivery systems: possibilities and limitations. Appl. Clay Sci. 36 (1–3). http://dx.doi.org/10.1016/j.clay.2006.06.015.

Amidon, G.L., Lennernäs, H., Shah, V.P., Crison, J.R., 1995. A theoretical basis for a biopharmaceutic drug classification: the correlation of in vitro drug product dissolution and in vivo bioavailability. Pharm. Res. 12, 413–420. http://dx.doi.org/10.1023/A:1016212804288.

Andrews, P., 1985. Praziquantel: mechanisms of anti-schistosomal activity. Pharmacol. Ther. 29, 129–156. http://dx.doi.org/10.1016/0163-7258(85)90020-8.

Bergaya, F., Lagaly, G., 2006. Chapter 1 general introduction: clays, clay minerals, and clay science. Dev. Clay Sci. 1, 1–18. http://dx.doi.org/10.1016/S1572-4352(05)01001-9.

Borrego-Sánchez, A., Viseras, C., Aguzzi, C., Sainz-Díaz, C.I., 2016. Molecular and crystal structure of praziquantel. Spectroscopic properties and crystal polymorphism. Eur. J. Pharm. Sci. 92, 266–275. http://dx.doi.org/10.1016/j.ejps.2016.04.023.

Borrego-Sánchez, A., Hernández-Laguna, A., Sainz-Díaz, C.I., 2017. Molecular modeling and infrared and Raman spectroscopy of the crystal structure of the chiral antiparasitic drug praziquantel. J. Mol. Model. 23 (106). http://dx.doi.org/10.1007/s00894-017-3266-3.

Cavallaro, G., De Lisi, R., Lazzara, G., Milioto, S., 2013. Polyethylene glycol/clay nanotubes composites. Thermal properties and structure. J. Therm. Anal. Calorim. 112, 383–389.

Chaud, M.V., Tamascia, P., de Lima, A.C., Paganelli, M.O., Gremião, M.P.D., de Freitas, O., 2010. Solid dispersions with hydrogenated castor oil increase solubility, dissolution rate and intestinal absorption of praziquantel. Braz. J. Pharm. Sci. 46, 473–481. http://dx.doi.org/10.1590/S1984-82502010000300010.

Chaud, M.V., de Lima, A.C., Vila, M.M.D.C., Paganelli, M.O., Paula, F.C., Pedreiro, L.N., Gremião, M.P.D., 2013. Development and evaluation of praziquantel solid dispersions in sodium starch glycolate. Trop. J. Pharm. Res. 12, 163–168. http://dx.doi.org/10.4314/tjpr.v12i2.5.

Chitsulo, L., Engels, D., Montresor, A., Savioli, L., 2000. The global status of schistosomiasis and its control. Acta Trop. 77, 41–51. http://dx.doi.org/10.1016/S0001-706X(00)00122-4.

De la Torre, P., Torrado, S., Torrado, S., 1999. Preparation, dissolution and characterization of Praziquantel solid dispersions. Chem. Pharm. Bull. 47, 1629–1633. http://dx.doi.org/10.1248/cpb.47.1629.

El-Feky, G.S., Mohamed, W.S., Nasr, H.E., El-Lakkany, N.M., Seif El-Din, S.H., Botros, S.S., 2015. Praziquantel in a clay nanoformulation shows more bioavailability and higher efficacy against murine Schistosoma mansoni infection. Antimicrob. Agents Chemother. 59, 3501–3508. http://dx.doi.org/10.1128/AAC.04875-14.

El-Subbagh, H.I., Al-Badr, A.A., 1998. Praziquantel. In: Florey (Ed.), Analytical Profiles of Drug Substances and Excipients. vol. 25. Academic Press Inc., New York, pp. 463–500.

Espinosa-Lara, J.C., Guzmán-Villanueva, D., Arenas-García, J.I., Herrera-Ruiz, D., Rivera-Islas, J., Román-Bravo, P., Morales-Rojas, H., Höpfl, H., 2013. Cocrystals of active pharmaceuticals ingredients-praziquantel in combination with oxalic, malonic, succinic, maleic, fumaric, glutaric, adipic and pimelic acids. Cryst. Growth Des. 13, 169–185. http://dx.doi.org/10.1021/cg301314w.

FDA, 2017. U.S. Food and Drug Administration. Recovered February. https://www.fda.gov/AboutFDA/CentersOffices/OfficeofMedicalProductsandTobacco/CDER/ucm128219.htm.

Frost, R.L., Locos, O.B., Ruan, H., Kloprogge, J.T., 2001. Near-infrared and mid-infrared spectroscopic study of sepiolites and palygorskites. Vib. Spectrosc. 27, 1–13. http://dx.doi.org/10.1016/S0924-2031(01)00110-2.

González-Esquivel, D., Rivera, J., Castro, N., Yepez-Mulia, L., Helgi, J.C., 2005. In vitro characterization of some biopharmaceutical properties of praziquantel. Int. J. Pharm. 295, 93–99. http://dx.doi.org/10.1016/j.ijpharm.2005.01.033.

Guggenheim, S., Adams, J.M., Bain, D.C., Bergaya, F., Brigatti, M.F., Drits, V.A., Formoso, M.L.L., Galán, E., Kogure, T., Stanjek, H., 2006. Summary of recommendations of nomenclature committees relevant to clay mineralogy: report of the association internationale pour l'etude des argiles (aipea) nomenclature committee for 2006. Clay Clay Miner. 54, 761–772. http://dx.doi.org/10.1346/CCMN.2006.0540610.

Liu, Y., Wang, X., Wang, J.K., Ching, C.B., 2004. Structural characterization and enantioseparation of the chiral compound praziquantel. J. Pharm. Sci. 93, 3039–3046. http://dx.doi.org/10.1002/jps.20211.

López-Galindo, A., Viseras, C., 2004. Pharmaceutical and cosmetic applications of clays. Interface Sci. Technol. 1, 267–289. http://dx.doi.org/10.1016/S1573-4285(04)80044-9.

Makaremi, M., Pasbakhsh, P., Cavallaro, G., Lazzara, G., Aw, Y.K., Lee, S.M., Milioto, S., 2017. Effect of morphology and size of halloysite nanotubes on functional pectin bionanocomposites for food packaging applications. ACS Appl. Mater. Interfaces 9, 17476–17488. http://dx.doi.org/10.1021/acsami.7b04297.

Martín-Ramos, J.D., 2005. XPowder software. http://www.xpowder.com.X-Power.

Massaro, M., Amorati, R., Cavallaro, G., Guermelli, S., Lazzara, S., Milioto, S., Noto, R., Poma, P., Riela, S., 2016. Direct chemical grafted curcumin on halloysite nanotubes as dual-responsive prodrug for pharmacological applications. Colloids Surf. B: Biointerfaces 140, 505–513. http://dx.doi.org/10.1016/j.colsurfb.2016.01.025.

Ortega-Castro, J., Hernández-Haro, N., Muñoz-Santiburcio, D., Hernández-Laguna, A., Sainz-Díaz, C.I., 2009. Crystal structure and hydroxyl group vibrational frequencies of phyllosilicates by DFT methods. Theochem. J. Mol. Struct. 912, 82–87. http://dx.doi.org/10.1016/j.theochem.2009.02.013.

Passerini, N., Albertini, B., Perissutti, B., Rodriguez, L., 2006. Evaluation of melt granulation and ultrasonic spray congealing as techniques to enhance the dissolution of praziquantel. Int. J. Pharm. 318, 92–102. http://dx.doi.org/10.1016/j.ijpharm.2006.03.028.

Rodrigues, S.G., Chaves, I.S., Melo, N.F.S., de Jesus, M.B., Fraceto, L.F., Fernandes, S.A., de Paula, E., de Freitas, M.P., Pinto, L.M.A., 2010. Computational analysis and physico-chemical characterization of an inclusion compound between praziquantel and methyl-β-cyclodextrin for use as an alternative in the treatment of schistosomiasis. J. Incl. Phenom. Macrocycl. Chem. 70, 19–28. http://dx.doi.org/10.1007/s10847-010-9852-y.

Steinmann, P., Keiser, J., Bos, R., Tanner, M., Utzinger, J., 2006. Schistosomiasis and water resources development: systematic review, meta-analysis, and estimates of people at risk. Lancet Infect. Dis. 6, 411–425. http://dx.doi.org/10.1016/S1473-3099(06)70521-7.

Suárez, M., García-Romero, E., 2012. Variability of the surface properties of sepiolite. Appl. Clay Sci. 67-68, 72–82. http://dx.doi.org/10.1016/j.clay.2012.06.003.

Torres-Ruíz, J., López-Galindo, A., González-López, J.M., Delgado, A., 1994. Geochemistry of Spanish sepiolite-palygorskite deposits: genetic considerations based on trace elements and isotopes. Chem. Geol. 112, 221–245. http://dx.doi.org/10.1016/0009-2541(94)90026-4.

Viseras, C., López-Galindo, A., 1999. Pharmaceutical applications of some spanish clays (sepiolite, palygorskite, bentonite): some preformulation studies. Appl. Clay Sci. 14, 69–82. http://dx.doi.org/10.1016/S0169-1317(98)00050-7.

Viseras, C., Cerezo, P., Sánchez, R., Salcedo, I., Aguzzi, C., 2010. Current challenges in clay minerals for drug delivery. Appl. Clay Sci. 48, 291–295. http://dx.doi.org/10.1016/j.clay.2010.01.007.

Wang, W., Wang, Li., Liang, Y.-S., 2012. Susceptibility or resistance of praziquantel in human schistosomiasis: a review. Parasitol. Res. 111, 1871–1877. http://dx.doi.org/10.1007/s00436-012-3151-z.

WHO, 2017. World Health Organization. Recovered February. http://www.who.int/schistosomiasis/en/.

Applied Clay Science 160 (2018) 201–205

Contents lists available at ScienceDirect

Applied Clay Science

journal homepage: www.elsevier.com/locate/clay

Research paper

Characterisation of Andalusian peats for skin health care formulations

Fátima García-Villén[a], Rita Sánchez-Espejo[b], Esperanza Carazo[a], Ana Borrego-Sánchez[c], Carola Aguzzi[a], Pilar Cerezo[a], César Viseras[a,c,*]

[a] Department of Pharmacy and Pharmaceutical Technology, University of Granada, Campus of Cartuja, s/n, 18071 Granada, Spain
[b] Aguas Termales de Graena, S.A. C/San Antonio, 5, 18517 Cortes y Graena, Granada, Spain
[c] Andalusian Institute of Earth Sciences, CSIC-University of Granada, Avda. de Las Palmeras 4, 18100 Granada, Spain

ARTICLE INFO

Keywords:
Peats
Clay minerals
Pelotherapy
Rheology

ABSTRACT

Composition and properties of three different peat strata from "El Padul" peatbog have been studied and peat pastes have been formulated to prepare skin health care products. As for composition, the main phase of each stratum was constituted of smectites (outer stratum), organic matters (intermediate) or carbonates (inner). Pristine strata and their aqueous dispersed systems were characterized for such properties (pH, rheology and cooling kinetics) that are considered determinant in view of their topical application. Main phases of each stratum influenced pH and rheology but not cooling kinetics. Combination of the strata in different w/w ratios led to peat pastes with improved performance for skin administration.

1. Introduction

Peat pastes are semisolid systems used in medical hydrology and cosmetic treatments on the basis of chemical and physical mechanisms derived from their composition (Dudare and Klavins, 2013; Gomes de Melo et al., 2015). Typical peat pastes applications imply temperatures between 42 and 44 °C for 15–30 min (Flaig, 1992). Peats have demonstrated adsorptive, estrogenic, astringency, antioxidant and revulsive actions (Beer et al., 2000, 2001, 2002, 2003; Suárez et al., 2011). Fungicidal, antibacterial and antiviral properties, UV absorption as well as influences on smooth muscles and prostaglandin synthesis are also been reported (Klöcking and Helbig, 2005; Fioravanti et al., 2007; Sławinska et al., 2007; Khil'ko et al., 2011; Gomes de Melo et al., 2015).

Peats are complex mixtures of organic and inorganic components. Organic fraction comes from vegetable wastes transformed under anaerobic and waterlogged conditions for extended periods and includes humic acids, humin and fulvic acids as principal compounds. Organic compounds have demonstrated biologic activities, which make them potentially useful in topical health care and cosmetology (Summa and Tateo, 1999; Beer et al., 2003). Mineral fraction of peats is composed of clay minerals such as illite and chlorite as well as gypsum, muscovite and quartz (Summa and Tateo, 1999; Romão et al., 2007; Orru et al., 2011). The presence and the type of minerals in peats hugely depend on the deposit location (Summa and Tateo, 1999). Inorganic components, and in particular clay minerals, may greatly influence the technological and biopharmaceutical properties of peats, as for example, stability and rheology of the solid/water systems or bioavailability of the organic actives (Aguzzi et al., 2007; Viseras et al., 2007). Consequently, detailed identification of the mineral phases associated with organic substances in peat deposits must be considered in the design of semisolid health care formulations with these materials.

With these premises, the aims of the present study were i) to characterise three different peat strata from a deposit located in El Padul (Granada), ii) to prepare dispersed systems with the aforementioned strata in order to determine the technological properties and iii) to study dispersed systems feasibility as potential semisolid health care formulations.

2. Materials and methods

2.1. Materials

Peat samples were extracted from the peatbog "Turbera del Agia" located in El Padul (Granada, Spain). Peat is currently extracted from an area of approximately 20,000 m2 (Fig. 1). The actually exploited peat (P2), mainly commercialized as fertilizer, is characterized by deep black chrome and appears as a stratum of ~5 m thickness, delimitated by two other non-commercialized peat strata (P1 and P3). Details of sample position and depth are included in Fig. 1. Each stratum was separately extracted and hermetically sealed to prevent loss of natural moisture and preserved at room temperature.

* Corresponding author at: Department of Pharmacy and Pharmaceutical Technology, University of Granada, Campus of Cartuja, s/n, 18071 Granada, Spain.
E-mail address: cviseras@ugr.es (C. Viseras).

https://doi.org/10.1016/j.clay.2017.12.017
Received 10 October 2017; Received in revised form 7 December 2017; Accepted 10 December 2017

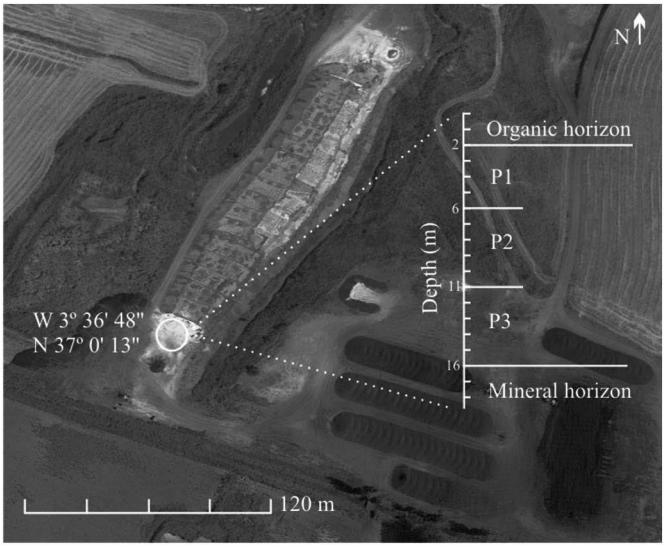

Fig. 1. Location of sampling position in "Turbera del Agia" and vertical-cross section of the samples (Photo from Google©2017).

2.2. Methods

2.2.1. X-ray powder diffraction

Peat samples were dried at 40 °C for 24 h and grounded previous X-ray powder diffraction analysis (XRPD). Mineralogical study was carried out using a PANalytical X'Pert Pro diffractometer equipped with an X'Celerator solid-state detector and a sample holder spinning. X-ray powder diffraction patterns were recorded using random oriented mounts with CuKα radiation, at 45 kV, 40 mA, in the range 3 to 50°2θ. The estimation of the solid composition in crystalline phases was obtained by X'Pert HighScore Plus (PANalytical, 2005). Chemical analysis by X-Ray fluorescence (XRF) was performed using a Bruker® S4 Pioneer equipment working at 60 kV and 150 mA.

2.2.2. Elemental analysis

Elemental analyses (EAN) were performed in order to determine the content of carbon, hydrogen, nitrogen and sulfur in P1, P2 and P3. These determinations were carried out once samples were dried after 24 h at 40 °C. Elemental analyser used was THERMO SCIENTIFIC, Flash 2000 model, equipped with a thermal conductivity detector and a precision microbalance (precision 0.01).

2.2.3. Thermal analysis

Thermogravimetric Analysis (TGA and DTG) of peat samples was carried out by using a METTLER TOLEDO mod. TGA/DSC1 with FRS5 sensor and a microbalance (precision 0.1 μg) (Mettler-Toledo GMBH). Samples were heated in air atmosphere at 10 °C/min, in the range of temperature 30–950 °C. All the experiments were run in triplicate.

2.2.4. Preparation of peat dispersed systems

Raw peats and their mixtures in different w/w ratios were dispersed in purified water to obtain a final solid concentration of 60% (w/w) (Table 1). The systems were manually homogenized until the disappearance of heavy lumps and then by a high speed agitation of 3000 rpm for 10 min by using a Silverson® L4RT (Silverson Machines, UK). All systems were packed inside hermetic containers and preserved at room temperature.

Table 1
Composition of dispersed systems.

Dispersed system	S1	S2	S3	S4	S5	S6	S7
Solid phase (60% w/w)	P1	P2	P3	P1:P2 (20:80)	P1:P2 (30:70)	P2:P3 (80:20)	P2:P3 (70:30)

2.2.5. Determination of pH

Values of pH for each peat strata and the aforementioned dispersed systems were determined by using a Crison 25 + pH-meter, equipped with a solid electrode (code 5053T), with a pH tolerance range between 2 and 11.

2.2.6. Rheological properties

Rheological analysis was carried out by means a viscometer (Thermo Scientific HAAKE, RotoVisco 1; HAAKE RheoWin software) with a plate/plate combination (Plate Ø 20 mm serrated PP20/S sensor) as measuring system. Measurements were carried out at 25 °C (TCP/P, HAAKE unit control temperature system), 90 s of rest time and 0–800 s^{-1} of shear rate. Six replicates were performed on each sample.

2.2.7. Cooling kinetics

Cooling curves were obtained following the procedure described by Sánchez-Espejo et al. (2015). Experimental cooling data were fitted by using the Newton law, describing thermal exchange between two bodies in contact at different temperatures:

$$(T - T_{min}) = (T_{max} - T_{min})e^{-kt} \quad (1)$$

where T_{min} was the room temperature (25 °C), T_{max} was the initial temperature (50 °C), t was the time in minutes and k was a constant that depends on the material and apparatus, given by:

$$k = \frac{P}{C} = \frac{P}{mC_p} \quad (2)$$

where P is the instrumental constant of the apparatus, C the heat capacity of the heated material, m the heated mass and C_p the specific heat. The apparatus constant was obtained by fitting of cooling data obtained with a known amount of a reference water dispersion of TiO_2. Experimental thermal parameters of the studied samples were then obtained by using the aforementioned equations.

3. Results and discussion

3.1. X-ray powder diffraction

X-powder diffractograms and X-ray fluorescence results were used to identify the mineral composition of the samples. Main mineral phases in sample P1 were smectites, quartz and mica (Fig. 2). Other minerals presented were calcium carbonates (calcite and aragonite) as well as pyrite in minor proportion. The studied samples came from a sedimentary basin and the minor presence of pyrite was ascribed to microbial sulphate reduction. The presence of smectites is positive in terms of technological properties due to their swelling and rheological properties in water dispersions (Viseras et al., 2007). Presence of calcium carbonate must be considered in the interpretation of EAN results. Sample P2 contained high amounts of amorphous organic matter, causing a lower crystallinity pattern. Nevertheless, presence of quartz, mica and pyrite was clearly stated. The presence of pyrite (FeS_2) in higher amount than P1 confirmed its biogenic origin. Sample P3 was mainly constituted by calcium carbonates with absence of quartz, smectites and organic matter.

3.2. Elemental analysis

P2 presented high amounts of carbon and nitrogen, clear indicators of its organic composition (Table 2). Sulfur content was in agreement with the pyrite presence discussed previously. The C/N ratio is used to measure the degree of decomposition of the organic matter in peat. During the evolution of peat, the organic matter suffers a mineralization

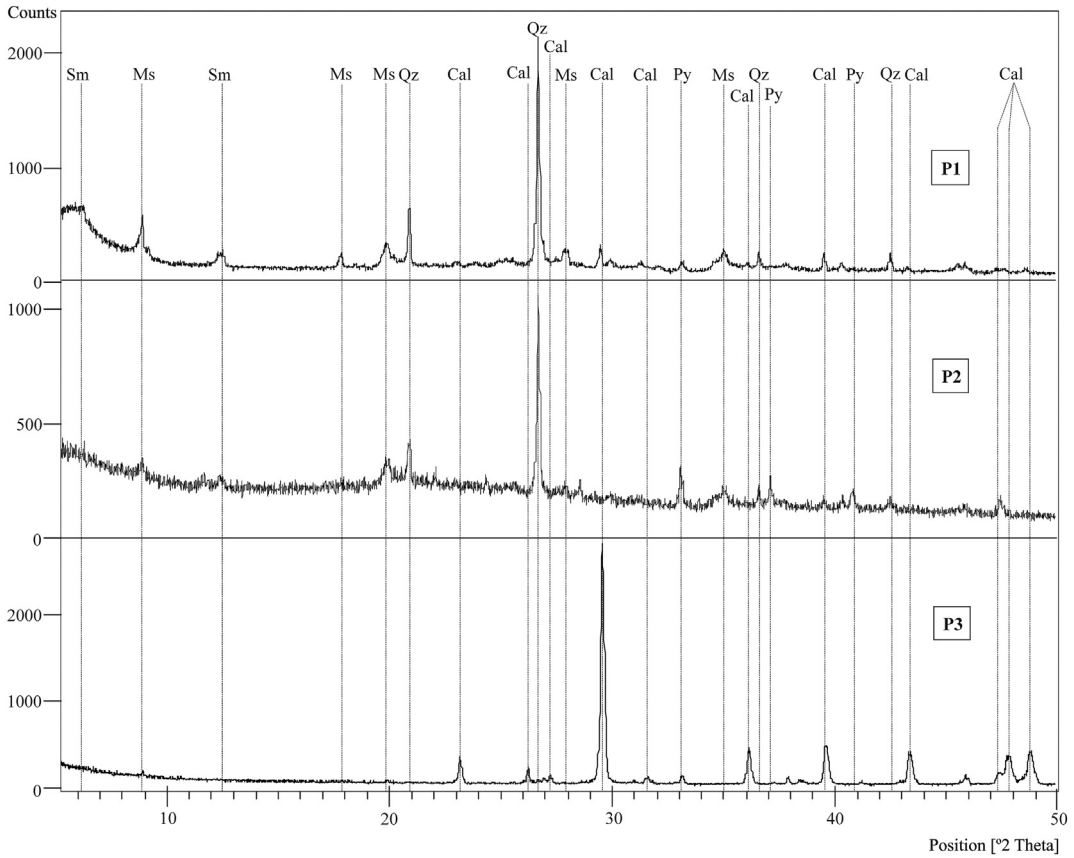

Fig. 2. X-ray powder diffraction patterns for peat strata. *Sm*: smectite; *Ms.*: muscovite; *Qz*: quartz; *Cal*: calcite; *Arg*: aragonite; *Py*: Pyrite.

Table 2
Elemental analysis results for each sample.

Stratum	N	C	H	S	C/N
P1	0.12	1.85	1.08	–	15.42
P2	1.01	36.90	4.96	3.72	36.53
P3	0.12	12.95	0.41	–	107.92

process marked by a nitrogen enrichment relative to carbon (Kuhry and Vitt, 1996; Gandois et al., 2013; Biester et al., 2014). Nitrogen in samples P1 and P3 revealed the presence of minor amounts of organic matter. Sample P3 showed a carbon content higher than expected, in view of its low organic matter content. Microbes responsible for peat decay are more active in more oxygenated and dryer conditions (Scott et al., 2001; Biester et al., 2014). Depth of P2 is higher than P1, causing that the organic matter of P2 suffered higher anoxic and watery conditions, which favoured a slower rate of decay with increasing depths. In sample P3, the high content in carbonates is responsible for the measured C value that distorted the C/N ratio.

3.3. Thermal analysis

Fig. 3 shows TGA results of peat strata studied. Total average weight losses were 46, 92 and 61% (w/w) for P1, P2 and P3, respectively. In P1, loss of hydration and interlayer water (~40% w/w) was mainly ascribed to organic matter and smectite hydration water and occurred at temperatures lower than 130 °C. Dehydroxylation of biotite and organic carbon decarboxylation occurred at ~500 °C (~6% w/w). Final ~1% w/w of weight loss at ~885 °C was ascribed to the trioctahedral smectites (the smectite content of this sample based on dehydroxylation was ~20% w/w). P2 showed intense weight loss due to hydration of the organic matter (75% w/w). Then, oxidative pyrolysis and

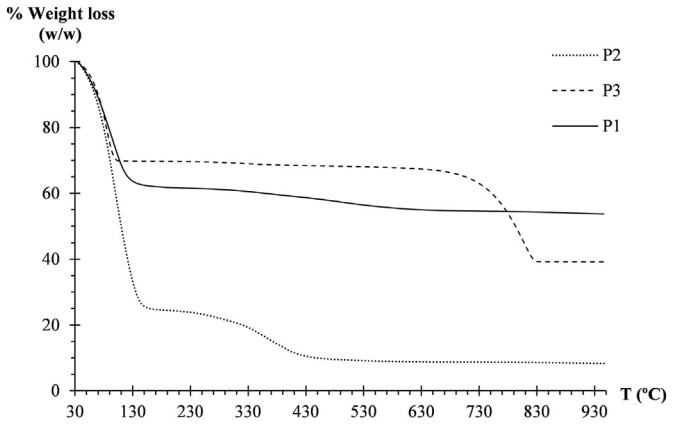

Fig. 3. Thermogravimetric curves of the peats.

subsequent carbonization in the interval 260–340 °C accounted for a 17% w/w of the total weight loss. This second interval included thermal degradation of organic compounds typically present in peats, including hemicellulose, cellulose and lignine derivatives such as humic and fulvic acids (Schnitzer and Hoffman, 1965; Aho et al., 1989; Romão et al., 2007). P3 presented a first weight loss corresponding to hydration water (the samples were assayed without any previous drying). Once dried, the TGA curve of P3 solely corresponded to typical thermal decomposition of carbonates (~20% w/w; ~800 °C).

3.4. pH

Values of pH of the raw samples and the dispersed systems in purified water are shown in Table 3. The measured pH of distilled water was 5.50 (± 0.012). pHs of the pure samples (P1–P3) were not

Table 3
pH values of natural peat strata (P1–P3) and dispersed systems (S1–S7).

	pH ± s.e.; n = 8
P1	7.29 ± 0.053
P2	3.10 ± 0.114
P3	7.82 ± 0.059
S1	7.62 ± 0.030
S2	5.03 ± 0.023
S3	7.76 ± 0.017
S4	5.62 ± 0.013
S5	5.23 ± 0.061
S6	6.22 ± 0.017
S7	5.91 ± 0.038

physiologically adequate, as none of them were in the optimal tolerated interval (4.5–6.0) required for skin formulations (Pons and Parra, 1995; Sánchez-Espejo et al., 2014). P1 and P3 showed very similar pH values, proximal to neutrality. On the other hand, stratum P2 presented acidic character due to the presence of humic substances. Particularly, the basic nature of P3 stratum is justified by the presence of carbonate minerals, previously identified by XRD and TGA analyses.

Dispersed systems S1 and S3 showed non-significant changes in pH values compared to the pH of the corresponding peat strata used for their preparation (P1 and P3), probably due to the presence of carbonates acting as buffers. On the other hand, S2 experimented an increase of two units in the pH value compared to that of P2 stratum. Suspensions from S4 to S7 showed acidic pH values since in all of them, stratum P2 prevailed as the main ingredient. Dispersed systems S4 and S5, which contain strata P1 and P2, showed pH values between those of S1 and S2 due to the mixture of the strata. The presence of P3 stratum in systems S6 and S7 could be noted by a slight increase on pH values (~6) ascribable to the amphoteric nature of carbonate minerals.

S1, S3 and S6 showed pH values which were above the tolerance range of the skin (4.5–6). Dispersions S2, S4, S5 and S7 possessed pH values that could allow their topical application in terms of pH tolerability. In particular, pH of S2 and S5 were closer to the most healthy human skin pH (approximately 4.7) which favours the skin microflora (Lambers et al., 2006) and prevents the growth of pathogenic bacteria (Fluhr and Elias, 2002).

3.5. Rheological properties

The studied dispersed systems showed non-Newtonian viscoplastic flow curves with spur points at low shear stress values (Fig. 4). This behaviour has been described for high concentrated suspensions used in pelotherapy (Aguzzi et al., 2013). S1 exhibited rheopectic behaviour, ascribable to the smectitic content of P1 stratum. Smectite suspensions are often thixotropic (shear thinning), although rare cases of rheopectic (shear thickening) behaviour have also been reported (Abu-Jdayil, 2011). S2 and S3 did not show any hysteresis areas, according to the absence of clay minerals in their compositions.

The influence exerted by stratum P1 was noticeable in systems S4 and S5, showing rheopectic behaviour. In these dispersions, although P2 was the main ingredient, clear hysteresis areas were observed.

Apparent viscosities and the yield values of the systems are shown in Table 4. Viscosity was calculated at a shear value (250 s^{-1}) representative of the stress produced by skin spreading during application (Schott, 1995). Yield stresses were obtained according to the experimental spur points (Barry, 1974) and represent the shear stress necessary to break particle attractions in the dispersed systems.

S2 showed very high viscosity and yield stress values, as a result of the interconnections between the lignin and other organic fibres (Hendry et al., 2012). These values could make difficult spreading of S2 suspension over the skin surface. On the other hand, S3 did not show suitable viscosity and yield values to ensure the permanence of the

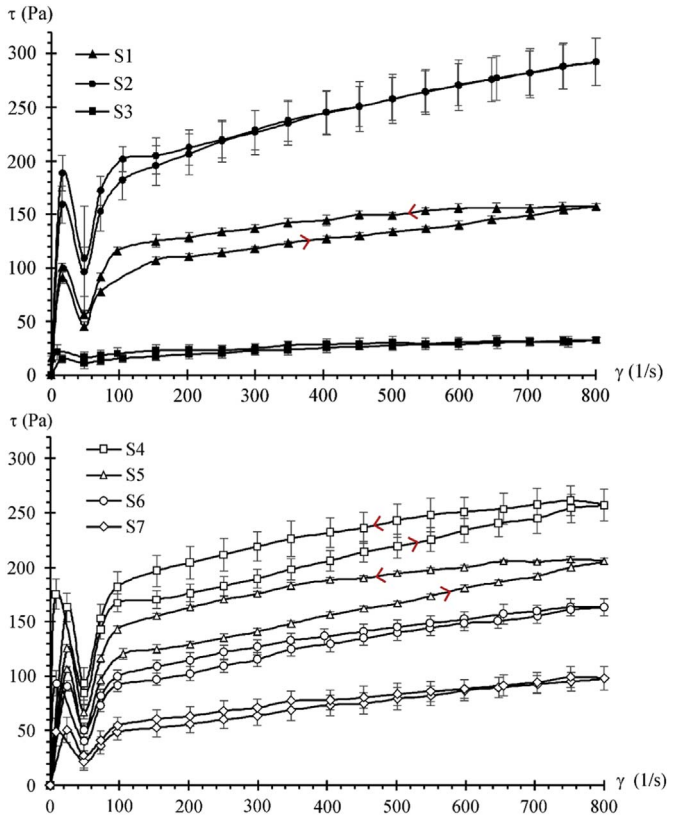

Fig. 4. Flow curves (shear stress (τ) vs shear flow (γ)) of the dispersed systems (mean values ± s.d.; n = 6).

Table 4
Apparent viscosities (250 s^{-1}; 25 °C) and yield values of the samples (mean values ± s.d.; n = 6).

	Viscosity (Pa·s)	Yield value (Pa)
S1	0.46 ± 0.016	90.83 ± 5.000
S2	0.88 ± 0.068	188.50 ± 14.164
S3	0.09 ± 0.020	14.79 ± 3.809
S4	0.74 ± 0.013	175.18 ± 13.907
S5	0.54 ± 0.017	106.77 ± 2.600
S6	0.44 ± 0.022	93.59 ± 11.816
S7	0.24 ± 0.034	46.00 ± 11.599

product during application. Intermediate behaviour was observed in the case of S1. In comparison with S2, viscosity and yield stress values decreased by mixing P1 and P2 strata (samples S4 and S5). In the case of S5, containing higher amount of P1, values were very similar to those observed for S1. Dispersed systems S6 and S7 (composed of P2 and P3 stratum) presented the lowest viscosities and yield points due to the influence of P3 stratum.

3.6. Cooling kinetics

Results of cooling kinetic studies are shown in Table 5. Linear regression of Eq. (1) was used to calculate the time required for each dispersed system to achieve 32 °C (t_{32}) and the temperature after 20 min (T_{20}), which is within the time range for traditional peat pastes application. Experimental specific heats (C_p) are homogeneous and similar to other systems used in pelotherapy (Sánchez-Espejo et al., 2014). In all samples, the temperature after 20 min (T_{20}), were around 36 °C and t_{32} values were around 30 min. These values assured heat transfer during the normal application of peat pastes which corresponds to treatments of 15–30 min with a paste temperature around 42–44 °C.

Table 5
Thermal studies: experimental specific heats (C_p), temperature after 20 min (T_{20}) and time until reaching 32 °C (t_{32}).

	C_p (J/g·K) ± s.d. (n = 3)	T_{20} (°C) ± s.d. (n = 3)	t_{32} (min) ± s.d. (n = 3)
S1	3.05 ± 0.048	35 ± 1.0	29 ± 1.3
S2	3.26 ± 0.087	36 ± 1.2	30 ± 1.2
S3	3.04 ± 0.065	35 ± 1.0	28 ± 1.1
S4	3.12 ± 0.029	36 ± 1.2	30 ± 1.3
S5	3.31 ± 0.023	36 ± 0.9	31 ± 1.1
S6	3.86 ± 0.045	36 ± 0.8	32 ± 0.9
S7	3.81 ± 0.075	36 ± 1.1	33 ± 0.9

The homogeneity of the values in Table 5, despite the compositional differences of samples, confirmed that thermal behaviour of peat pastes mainly depends on water content, as previously observed (Sánchez-Espejo et al., 2015).

4. Conclusions

Composition and properties of three different peat strata from "El Padul" peatbog greatly vary, making necessary their combination to formulate health care peat pastes with adequate features. Stratum P2 should always be present in the systems since it possessed the highest amount of organic matter, which are responsible for therapeutic effects of peat pastes. The addition of P1 allowed to control final pH and to modify rheological properties, although the addition of P3 stratum produced an undesirable decrease in viscosity. On the other hand, dispersed systems S2 and S4 possessed proper viscosities for topical applications, similar to pelotherapy formulations previously studied (Aguzzi et al., 2013). Thermal behaviours of dispersed systems greatly depended on water content and, in all cases, the results showed that heat transfer during peat paste treatment was assured.

Acknowledgements

This study was supported by the Projects CGL2016-80833-R and RNM-1897, group CTS-946, Predoctoral Grant FPU15/01577 and Torres Quevedo contract PTQ-15-07625.

References

Abu-Jdayil, B., 2011. Rheology of sodium and calcium bentonite–water dispersions: effect of electrolytes and aging time. Int. J. Miner. Process. 98, 208–213.
Aguzzi, C., Cerezo, P., Viseras, C., Caramella, C., 2007. Use of clays as drug delivery systems: possibilities and limitations. Appl. Clay Sci. 36, 22–36.
Aguzzi, C., Sánchez-Espejo, R., Cerezo, P., Machado, J., Bonferoni, C., Rossi, S., Salcedo, I., Viseras, C., 2013. Networking and rheology of concentrated clay suspensions "matured" in mineral medicinal water. Int. J. Pharm. 453, 473–479.
Aho, M., Tummavuori, J., Hämäläinen, J., Saastamoinen, J., 1989. Determination of heats of pyrolysis and thermal reactivity of peats. Fuel 68, 1107–1111.
Barry, B.W., 1974. Rheology of pharmaceutical and cosmetic semisolids. In: Bean, H.S., Beckett, A.H., Carless, J.E. (Eds.), Advances in Pharmaceutical Sciences. Academic Press Inc., London, pp. 1–72.
Beer, A.M., Lukanov, J., Sagorchev, P., 2000. The influence of fulvic and humic acids from peat, on the spontaneous contractile activity of smooth muscles. Phytomedicine 7, 407–415.
Beer, A.M., Fey, S., Walch, S., Lüthgens, K., Ostermann, T., Lukanov, J., 2001. The effect of peat components on endocrine and immunological parameters and on trace elements—results of two pilot studies. Clin. Lab. 47, 161–167.
Beer, A.M., Sagorchev, P., Lukanov, J., 2002. Isolation of biologically active fractions from the water soluble components of fulvic and ulmic acids from peat. Phytomedicine 9, 659–666.
Beer, A.M., Grozeva, A., Sagorchev, P., Lukanov, J., 2003. Comparative study of the thermal properties of mud and peat solutions applied in clinical practice. Biomed Tech (Berl) 48, 301–305.
Biester, H., Knorr, K.H., Schellekens, J., Basler, A., Hermanns, Y.M., 2014. Comparison of different methods to determine the degree of peat decomposition in peat bogs. Biogeosciences 11, 2691–2707.
Dudare, D., Klavins, M., 2013. Complex-forming properties of peat humic acids from a raised bog profiles. J. Geochem. Explor. 129, 18–22.
Fioravanti, A., Perpignano, G., Tirri, G., Cardinale, G., Gianniti, C., Lanza, C.E., Loi, A., Tirri, E., Sfriso, P., Cozzi, F., 2007. Effects of mud-bath treatment on fibromyalgia patients: a randomized clinical trial. Rheumatol. Int. 27, 1157–1161.
Flaig, W., 1992. Humic substances and associated small molecules from peats in balneology. Sci. Total Environ. 117/118, 561–567.
Fluhr, J.W., Elias, P.M., 2002. Stratum corneum pH: formation and function of the "acid mantle". Exog. Dermatol. 1, 163–175.
Gandois, L., Cobb, A.R., Hei, I.C., Lim, L.B.L., Salim, K.A., Harvey, C.F., 2013. Impact of deforestation on solid and dissolved organic matter characteristics of tropical peat forests: implications for carbon release. Biogeochemistry 114, 183–199.
Gomes de Melo, B.A., Lopes Motta, F., Andrade Santana, M.H., 2015. Humic acids: structural properties and multiple functionalities for novel technological developments. Mater. Sci. Eng. C 62, 967–974.
Hendry, M.T., Sharma, J.S., Martin, C.D., Barbour, S.L., 2012. Effect of fibre content and structure on anisotropic elastic stiffness and shear strength of peat. Can. Geotech. J. 49, 403–415.
Khil'ko, S.L., Efimova, I.V., Smirnova, O.V., 2011. Antioxidant properties of humic acids from brown coal. Solid Fuel Chem. 45, 367–371.
Klöcking, R., Helbig, B., 2005. Medical aspects and applications of humic substances. In: Steinbüchel, A., Marchessault, R.H. (Eds.), Biopolymers for Medical and Pharmaceutical Applications. WILEY-VCH Verlag GmbH & Co. KGaA, Weinheim.
Kuhry, P., Vitt, D.H., 1996. Fossil carbon/nitrogen ratios as a measure of peat decomposition. Source. Ecology 77, 271–275.
Lambers, H., Piessens, S., Bloem, H., Pronk, H., Finkel, P., 2006. Natural skin surface pH is on average below 5, which is beneficial for its resident flora. Int. J. Cosmet. Sci. 28, 359–370.
Orru, M., Übner, M., Orru, H., 2011. Chemical properties of peat in three peatlands with balneological potential in Estonia. Est. J. Earth Sci. 60, 43–49.
Pons, L.G., Parra, J.L., 1995. Ciencia cosmética. Bases fisiológicas y criterios prácticos, first ed. Heliotipia Artistica S.L, Madrid.
Romão, L.P.C., Lead, J.R., Rocha, J.C., de Oliveira, L.C., Rosa, A.H., Mendonça, A.G.R., de Ribeiro, A.S., 2007. Structure and properties of brazilian peat: analysis by spectroscopy and microscopy. J. Braz. Chem. Soc. 18, 714–720.
Sánchez-Espejo, R., Aguzzi, C., Cerezo, P., Salcedo, I., López-Galindo, A., Viseras, C., 2014. Folk pharmaceutical formulations in western Mediterranean: identification and safety of clays used in pelotherapy. J. Ethnopharmacol. 155, 810–814.
Sánchez-Espejo, R., Cerezo, P., Aguzzi, C., López-Galindo, A., Machado, J., Viseras, C., 2015. Physicochemical and in vitro cation release relevance of therapeutic muds "maturation". Appl. Clay Sci. 116–117, 1–7.
Schnitzer, M., Hoffman, I., 1965. Thermogravimetry of soil humic compounds. Geochim. Cosmochim. Acta 29, 859–870.
Schott, H., 1995. Reología. In: Gennaro, A.R. (Ed.), Remington Farmacia. MedicaPanamericana, Buenos Aires, vol. I. pp. 426–455.
Scott, M.J., Jones, M.N., Woof, C., Simon, B., Tipping, E., 2001. The molecular properties of humic substances isolated from a UK upland peat system: a temporal investigation. Environ. Int. 27, 449–462.
Sławinska, D., Polewski, K., Rolewski, P., Sławiński, J., 2007. Synthesis and Properties of Model Humic Substances Derived from Gallic Acid. vol. 21. pp. 199–208.
Suárez, M., González, P., Domínguez, R., Bravo, A., Melián, C., Pérez, M., Herrera, I., Blanco, D., Hernández, R., Fagundo, J.R., 2011. Identification of organic compounds in San Diego de los Baños peloid (Pinar del Río, Cuba). J. Altern. Complement. Med. 17, 155–165.
Summa, V., Tateo, F., 1999. Geochemistry of two peats suitable for medical uses and their behaviour during leaching. Appl. Clay Sci. 15, 477–489.
Viseras, C., Aguzzi, C., Cerezo, P., López-Galindo, A., 2007. Uses of clay minerals in semisolid health care and therapeutic products. Appl. Clay Sci. 36, 37–50.

European Journal of Pharmaceutics and Biopharmaceutics 132 (2018) 180–191

Contents lists available at ScienceDirect

European Journal of Pharmaceutics and Biopharmaceutics

journal homepage: www.elsevier.com/locate/ejpb

Conformational polymorphic changes in the crystal structure of the chiral antiparasitic drug praziquantel and interactions with calcium carbonate

Ana Borrego-Sánchez[a,b], Esperanza Carazo[b], Beatrice Albertini[c], Nadia Passerini[c], Beatrice Perissutti[d], Pilar Cerezo[b], César Viseras[a,b], A. Hernández-Laguna[a], Carola Aguzzi[b,*], C. Ignacio Sainz-Díaz[a]

[a] Instituto Andaluz de Ciencias de la Tierra (CSIC-University of Granada), Av. de las Palmeras 4, 18100 Armilla, Granada, Spain
[b] Department of Pharmacy and Pharmaceutical Technology, Faculty of Pharmacy, University of Granada, Campus de Cartuja s/n, 18071 Granada, Spain
[c] Department of Pharmacy and BioTechnology, University of Bologna, Via S. Donato 19/2, 40127 Bologna, Italy
[d] Department of Chemical and Pharmaceutical Sciences, University of Trieste, P.le Europa 1, 34127 Trieste, Italy

ARTICLE INFO

Keywords:
Praziquantel
Calcium carbonate
Solid state characterization
DFT calculations
IR spectroscopy
Molecular modeling

ABSTRACT

Praziquantel is an antiparasitic drug used for decades. Currently, the praziquantel commercial preparation is a racemic mixture, in which only the levo-enantiomer possesses anthelmintic activity. The knowledge of its properties in the solid state and other chemical-physical properties is necessary for improving its efficacy and applications. Drug solid dispersions were prepared with calcium carbonate at 1:5 drug to excipient weight ratio by solvent evaporation method. Then, the modification of the crystal structure of the racemic polymorph of praziquantel in presence of calcium carbonate has been studied by means of several analytical techniques (DSC, TGA, XRD, SEM, FTIR, Raman spectroscopy and chiral liquid chromatography). This study has been completed with atomistic calculations based on empirical interatomic force fields and quantum mechanics methods applied to the crystal structure of praziquantel and of intermolecular interactions. The results evidenced that calcium carbonate provoked a conformational change in the praziquantel molecule yielding the formation of different polymorphs of praziquantel crystal. These alterations were not observed replacing calcium carbonate with colloidal silica as excipient in the solid dispersion.

1. Introduction

Schistosomiasis is a parasitic disease caused by *Schistosoma*. It is widely extended, mainly in 78 developing countries in the tropics and subtropics [1–3], and it affects 210 million people approximately, causing two hundred thousand deaths every year. Moreover, at least 92% of people who need treatment for schistosomiasis live in Africa and, behind of malaria, is the second of the most prevalent diseases that affects African children [4].

The infection is caused by the parasite penetration through the skin of healthy individuals, who are in contact with contaminated water. The Schistosomiasis treatment consists in three drugs (oxamniquine, albendazole and praziquantel), due to the fact that prevention is difficult and there is no vaccine. Praziquantel (PZQ) is the most used drug, considering that it has several advantages: i) being active against every Schistosomas species [5] ii) its administration is orally, iii) it produces few side effects, iv) it has a high efficiency, and v) it has low toxicity. For all of these reasons, World Health Organization considers PZQ to be an essential drug [4]. However, its extensive use might produce drug resistance. Another factor, which contributes to drug resistance, is that the drug is only effective against parasite adult forms [6].

PZQ, (RS)-2-(cyclohexylcarbonyl)-1,2,3,6,7,11b-hexahydro-4H-pyrazin[2,1a]-isoquinolin-4-one) [7,8], is a molecule that contains an oxo group in position 4, which is very important for drug activity (Fig. 1). Moreover, if this group is modified, the activity gets suppressed. Furthermore, PZQ has a chiral center in position 11b, therefore, it has two enantiomers with different properties, where only the R-(-)-enantiomer possesses anthelmintic activity [9,10]. However, commercial preparation is a racemic mixture. The process which is the most widely used to obtain enantiomers is the crystallization [11]. The PZQ enantiomeric system behavior was studied at different temperatures and several enantiomer mixtures of PZQ were obtained [12]. Likewise, thermodynamic and solubility properties of PZQ enantiomers were characterized and compared with those of the commercial racemic product [13]. Enantiomers crystals showed different thermal properties relative to the racemic drug and the results of Differential Scanning Calorimetry

* Corresponding author.
E-mail address: carola@ugr.es (C. Aguzzi).

https://doi.org/10.1016/j.ejpb.2018.09.028
Received 2 July 2018; Received in revised form 14 September 2018; Accepted 26 September 2018
Available online 26 September 2018

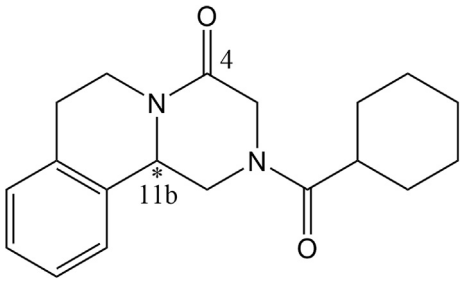

Fig. 1. Molecular structure of PZQ.

(DSC) indicated that the PZQ used is a racemic compound rather than a racemic mixture. Consequently, it is difficult to separate mechanically both enantiomers, unless crystallization and chromatography processes would be used [14]. Moreover, it was possible to combine the racemic PZQ, (RS)-PZQ, with aliphatic dicarboxylic acids to form different co-crystals which differ in their properties, making possible to overcome some of the restrictions on the use of this drug in humans and animals [15]. In addition, PZQ is classified in Class II in Biopharmaceutics Classification System (BCS) [16]. Therefore, the improvement of PZQ dissolution rate and/or solubility has an important technological interest [17]. Solid dispersions prepared by melt granulation and spray congealing showed their efficacy in enhancing the PZQ dissolution rate [18]. Recently, clay minerals as montmorillonite and sepiolite were studied as nanocarrier with the aim of improving the biopharmaceutical profile of the drug [19]. More recently, a new PZQ polymorphic phase, called Form B, has been discovered and fully characterized demonstrating better bioavailability in term of intrinsic dissolution and solubility [20].

Ground calcium carbonate (GCC) is a pharmaceutical excipient widely used as a diluent in solid dosage forms, as an adjuvant in dissolution for dispersible tablets, as a food additive and calcium supplement [21]. GCC is a natural and economic component for pharmaceutical and veterinary drugs with an interesting potential use in developing countries. Therefore, calcium carbonate has been proposed as excipient for a new delivery system of low soluble drugs, e.g. praziquantel. In particular PZQ-GCC solid dispersions were prepared by solvent evaporation method and then characterized to detect possible drug solid state modifications or interactions with the excipient. This is important because the characterization and stability of chiral drugs properties in solid state are critical for their development, manufacturing and applications. Previous solubility studies of PZQ reported ambiguous behavior due particularly to the existence of crystal polymorphism [11,12,14]. Thus, the main aims of this work were to investigate the physico-chemical characteristics of the racemic crystal form of PZQ once in contact with powdered calcium carbonate, by means of DSC, TGA, XRD, SEM, FTIR, Raman spectroscopy and chiral chromatography. Finally, the relationships between the different crystal forms of PZQ at molecular scale were discussed.

2. Experimental section

2.1. Materials

Praziquantel (PZQ) was kindly donated by Fatro S.p.A. (Bologna, Italy). Calcium carbonate, as Ground Calcium Carbonate Calcitec Pure PH V/40S (GCC), was purchased from Italy (Company “Mineraria Sacilese”). The Calcium Carbonate Calcitec Pure PH is used in the food industry and in industries where a low content of heavy metals is requested as well as in the pharmaceutical industry, since it was accepted in the latest edition of the European Pharmacopoeia and the USP. Colloidal silica (Aerosil® 200) was purchased to Degussa AG (Frankfurt). Ethanol of 96% and 99% of purity were used as PZQ solvents.

2.2. Preparation of the PZQ and GCC interaction product (IP)

An amount of GCC was dispersed in an ethanolic solution of PZQ under magnetic stirring at room temperature and protected from light to obtain a drug/calcium carbonate ratio of 1:5 w/w. After 24 h, the solvent was evaporated at 40 °C with a rotary evaporator (Buchi® R II) at reduced pressure. The solid residue was dried in a desiccator and then it was pulverized. The obtained solid dispersions were stored in a desiccator at room temperature. As a control experiment, comercial PZQ was treated without GCC following the same procedure (PZQ_c). Colloidal silica was also used instead of GCC in the same way for comparison purposes.

2.3. Powder X-ray diffraction

Powder X-ray diffraction was performed with a Philips® X-Pert diffractometer with Cu Kα radiation. The information of diffraction was analyzed using XPOWDER® software [22].

2.4. Thermal analysis

Differential Scanning Calorimetric analysis (DSC) and thermogravimetric analysis (TGA) were performed with a Mettler Toledo mod. TGA/DSC1 calorimeter, equipped with sensor, a FRS5 microbalance (precision 0.1 µg) and the FP89 software package. A heating rate of 5 °C/min was used in the 30–400 °C temperature range for TGA and DSC runs. Additionally, a rate of 2 °C/min was used for some specific DSC runs. Nitrogen was used as purge gas in DSC under flows of 15 mL/min^{-1}.

2.5. Scanning electron microscope (SEM)

Microphotographs of the samples were performed using a Hitachi S-510 scanning electron microscope (voltage 25 kV, secondary electron images) (Hitachi Scientific Instruments Ltd, Tokyo, Japan). The samples were mounted on adhesive paper, fixed with colloidal gold and metallized with gold in two orientations (20–30°). The images were captured digitally using the program ScanVision 1.2 attached to the microscope.

2.6. Fourier Transform Infrared (FTIR) and Raman spectroscopies

Fourier Transform Infrared Spectroscopy (FTIR) spectra were recorded in the range 4000–600 cm^{-1} with a 0.5 cm^{-1} resolution and a well-plate sampler (JASCO 6200 spectrophotometer with Spectra Manager II software). Raman spectra were recorded in the range 3500–800 cm^{-1} with a 6.48 cm^{-1} resolution using a Micro-Raman dispersive JASCO NRS-5100 spectrophotometer, with laser light source VIS-NIR, red diode at 785 nm with 500 mW of power (*TorsanaStarbright*), refrigeration by air and a KnowItAII JASCO Edition for Raman software.

2.7. High-performance liquid chromatography (HPLC)

The chirality of drug in the interaction product was measured by high-performance liquid chromatography (HPLC), using a 1260 Infinity II Agilent equipment (G) with quaternary pump, autosampler, column oven and UV-VIS diode-array spectrophotometer. The stationary phase was a column Chiralpak® IC, 5 µm, 150 × 4.6 mm (Daicel Corporation), and the mobile phase was a mixture of H_2O and CH_3CN (35:65 v/v). The flow rate was set at 0.8 mL/min with an injection volume of 10 µL. A detector with a wavelength of 225 nm was used and the run time for each analysis was 5 min. Data were recorded and analyzed by using LC Open LAB HPLC 1260 software (Agilent, G).

3. Computational section

The Compass FF [23] based on empirical interatomic potentials was used within the Discover program of the Materials Studio package on the periodical crystal models [24]. This FF was used previously to describe PZQ molecules and crystal structure with satisfactory results [25]. An atomic interactions cut-off of 18.5 Å was used for calculating Van der Waals and Coulomb interactions.

Additional DFT calculations of the periodic racemic crystal of PZQ were also performed with the SIESTA program [26] using the generalized gradient approximation (GGA) with the Perdew–Burke–Ernzerhof (PBE) [27] correlation exchange functional, and norm-conserving pseudopotentials [28]. Preliminary calculations were set up to explore different values of mesh cut-off energy and different numbers of *k*-points in the irreducible wedge of the Brillouin zone to optimize the calculations level. A wide range of mesh cut-off energy values in steps of 50 Ry was explored according to previous work [29,30], finding a suitable cut-off energy of 800 Ry and two *k*-points in the Brillouin zone in this work.

Powder XRD patterns were simulated from crystal structures by using the Reflex code implemented in Materials Studio package [24].

4. Results

4.1. Physico-chemical evaluation of PZQ-GCC interaction product

Possible interactions between PZQ and GCC were first explored by powder XRD on pristine PZQ, GCC and the IP obtained by solvent evaporation using ethanol 96% (Fig. 2). The pristine PZQ was solved and recrystallized through the same procedure evaporation of ethanol 96%, as a control experiment without GCC, and its XRD pattern showed a crystalline PZQ according with that previously reported [31] (Fig. 2a). GCC shows a typical pattern of calcite with reflections at 23.0°, 29.4° (the most intense), 39.5° and 43.1° (2Θ units).

The IP mixture showed reflections of mainly calcium carbonate crystals. Reflection peaks of PZQ crystals in IP had very low intensity and resolution probably due to the amorphization of PZQ or several changes in the crystallinity of the PZQ crystals with GCC as explained later. In previous works a similar behavior of PZQ was observed in the formation of a solid dispersion with polyvinylpyrrolidone (PVP) [32], sodium starch glycolate [33] and clay minerals [19]. The powder XRD pattern of a physical mixture (PM) of PZQ with GCC showed that the crystallinity of PZQ was maintained corroborating that the treatment of GCC and ethanol 96% affects the crystallinity of PZQ (Fig. 2b).

Thermogravimetric profiles of the samples studied are shown in the Fig. 3. GCC shows a slight weight loss (0.34% w/w) at 40 °C approximately, corresponding to the surface humidity evaporation. PZQ weight loss occurs in the range between 200 and 422 °C (97.64% w/w) due to the decomposition of PZQ. The IP showed similar profiles with the decomposition of the PZQ fraction at 250–300 °C, indicating the PZQ is remained in the IP, although the thermal range is narrower than the pure PZQ. This range can be due to a different crystallinity of PZQ in the IP.

The DSC profiles of these samples are reported in Fig. 4. PZQ showed a strong endothermic peak at 142–144 °C corresponding to the melting of the (RS)-PZQ crystal. GCC showed no significant peak in the DSC profile at T < 200 °C. The IP profile was completely different that pure PZQ and GCC, displaying two small peaks at 110–112 °C and around 133–144 °C. Since no weight loss was observed by TGA at this temperature range, the peak at about 110–112 °C could be attributable to the melting of either the monoenantiomeric crystals or of the new polymorph (Form B) described recently by Zanolla et al. [20], both reported at around 111 °C. The second endothermic peak at higher temperature could be ascribed to possible agglomerate or pseudoracemate crystals (134–138 °C) according to a previous work [11]. Finally, the broad and weak shoulder around 142–143 °C corresponded to the initial racemic (RS)-PZQ crystals. Therefore, the formation of a disordered mixture of several crystal forms in IP could justify the low resolution of the PZQ reflections in the XRD pattern.

In order to obtain better DSC profiles with more accurate melting points and for comparisons with previous studies [14], a lower temperature rate (2 °C/min) and gas flow (15 mL/min) was used confirming the above profiles. An experimental control of pristine PZQ treated was performed with ethanol 96% following the same procedure as the IP. The treated PZQ showed its endothermic peak at 142 °C (Fig. 5a) with a melting enthalpy of $\Delta H = 90.4$ J/g according to previous work [32]. On the contrary, the IP mixture showed endothermic peaks at 112 °C, 134 °C and 138 °C (Fig. 5b). Similar DSC profile was found by De la Torre et al. [32] in IP of PZQ with PVP. The peak at 134 °C disappeared after 3 months from preparation, increasing the area of the peak at 138 °C. This can indicate that the crystal form with the melting point at 134 °C was metastable and transformed slowly to the form which melted at 138 °C. Therefore, we can conclude that the alteration of PZQ solid state within the IP mixture was not due to the dissolution-evaporation process, but it is due the direct interaction of PZQ with GCC.

SEM microphotographs of GCC (Fig. 6A) showed a grain size lower than 10 μm, with typical morphologies of GCC of high purity for pharmaceutical use previously reported [21]. Particles associated with any impurities were not detected, corroborating the XRD results. The micropictures of the racemic (RS)-PZQ (Fig. 6B) presented elongated prismatic morphology and sizes superior to 100 μm, similar to those observed for drug racemic mixture previously [11,15].

In the SEM micropictures of the IP, significant changes of size, texture and morphology were observed (Fig. 6C and D). Filamentous particles interconnecting the GCC particles were observed along with some wider needles. The initial particles of PZQ disappeared and PZQ formed aggregates on the GCC particles during the dispersion and solvent evaporation process and the filaments grew inside these aggregates. This small crystal size of these disordered fibers can justify the low crystallinity and the above lack of XRD reflections in this IP mixture. A similar behavior was observed in previous works when PZQ is mixed with PVP in a solid dispersion [32], with sodium starch glycolate [33], and with clay minerals [19], where the formation of similar fibers was observed after preparation of IP. Recently this formation of fibers of PZQ was also observed after neat grinding without additives, and it was attributed to the new PZQ polymorphic form (Form B) [20], which can be in agreement with the 112° peak of our DSC analysis. However, in our experimental control the PZQ recrystallized in EtOH 96% in the same conditions as IP showed a similar crystal shape and morphology that the pristine PZQ in the SEM micropictures (Fig. 6E and F). This corroborates the effect of water and GCC on the crystallinity of PZQ.

FTIR spectra of the racemic PZQ, calcium carbonate (GCC) and the IP are compared in Fig. 7. PZQ shows two main characteristic bands in the range 2960–2840 cm^{-1} assigned to stretching vibration modes ν(CH) of CH and CH_2 groups [18]. Two bands corresponding to the ν(C═O) vibration mode are observed at 1665–1621 cm^{-1} [18], which can be assigned to each carbonyl group with different local environment in the crystal packing. The δ(C—H) and ν(C—N) modes are observed around 1350–1021 cm^{-1} [34]. The spectrum of GCC shows characteristic bands of the carbonate group (CO_3^{2-}) at 1453, 875 and 712 cm^{-1} [35,36]. In the IP, the bands of PZQ were detected with lower intensity than in the pure product, but most of them overlap with the bands of Ca carbonate due to the high proportion of GCC. However, slight differences can be distinguished in the ν(C═O) bands. In PZQ, two ν(C═O) bands appear with maxima at 1647 and 1624 cm^{-1}, corresponding to the syn relative conformation of the carbonyl groups in the (RS)-PZQ crystal. The shoulders observed at higher frequency are assigned to the syn conformation in twisted planes of each C═O group, according to previous work [37]. On the contrary, in IP these bands are broader with maxima at 1644 and 1634 cm^{-1}. These frequency shifts could also be assigned to the conformation change of the C═O groups in an anti conformer whose frequencies are closer according our

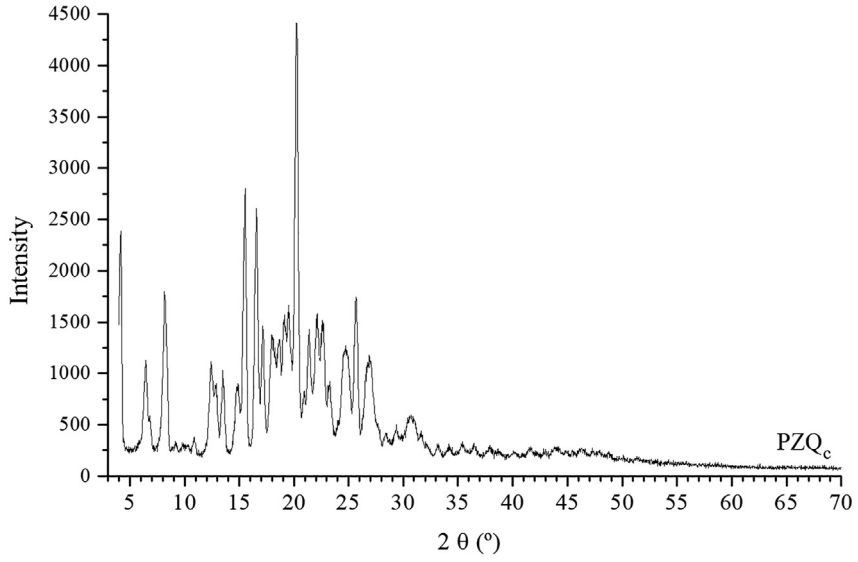

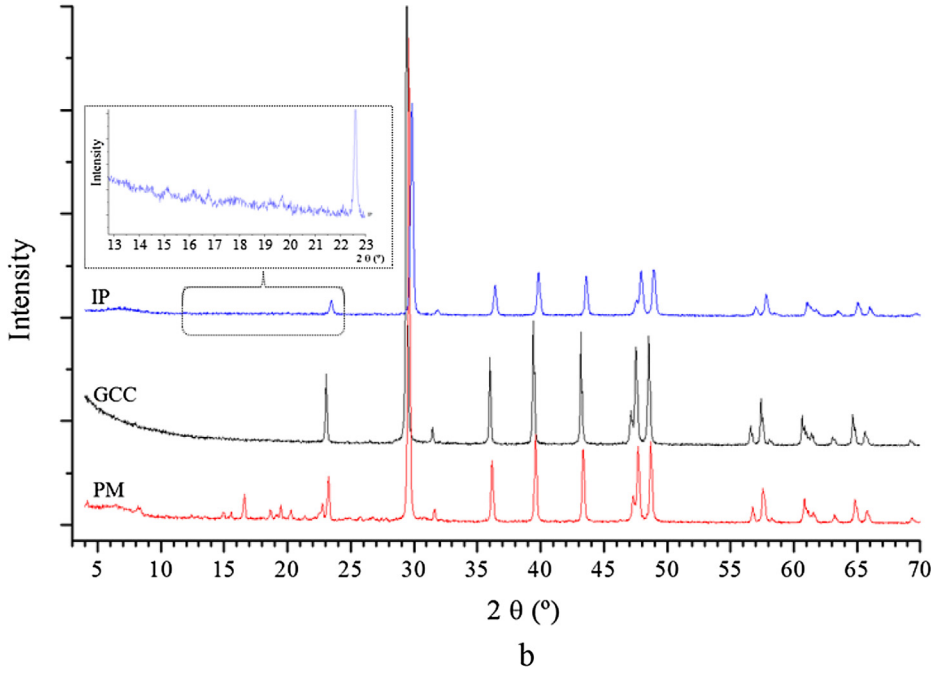

Fig. 2. Powder XRD patterns of the studied samples, PZQ obtained crystalized through ethanol 96% evaporation (a), IP, GCC, and PM samples (b).

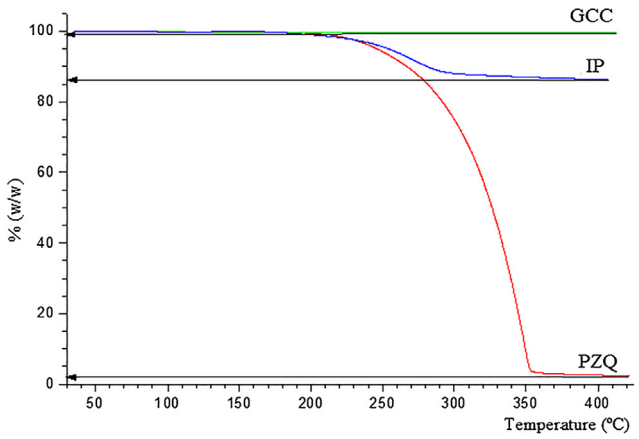

Fig. 3. TGA profiles of the studied samples.

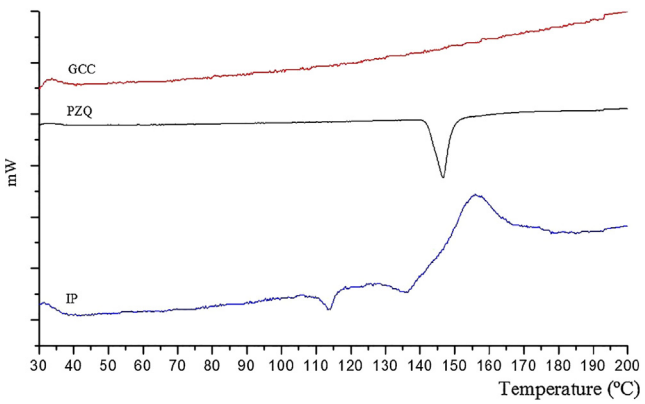

Fig. 4. DSC profiles of GCC, PZQ, and the IP.

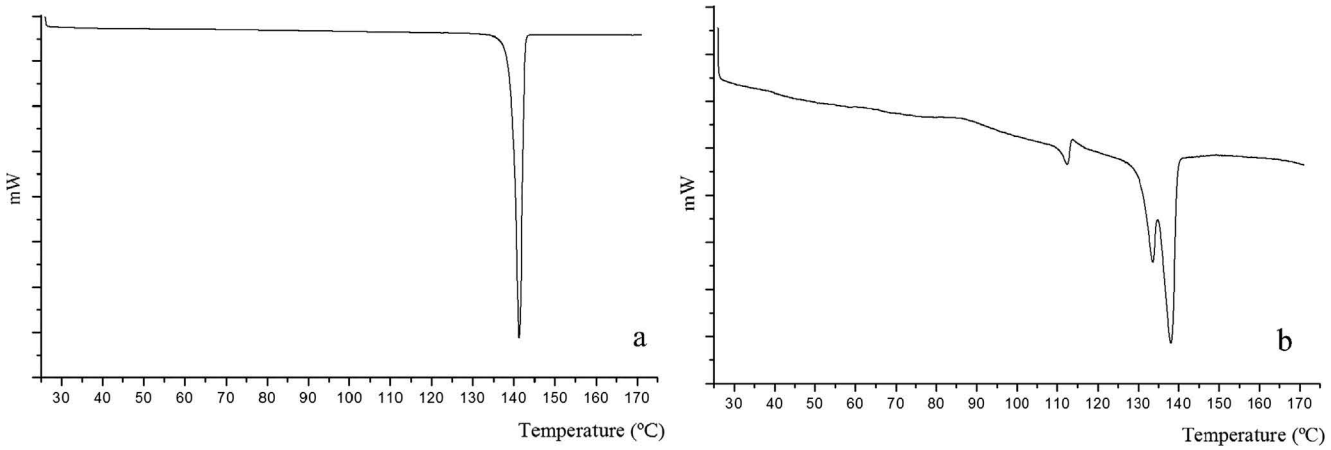

Fig. 5. DSC profiles of PZQ treated with ethanol 96% (PZQ_c) (a), and the IP (b).

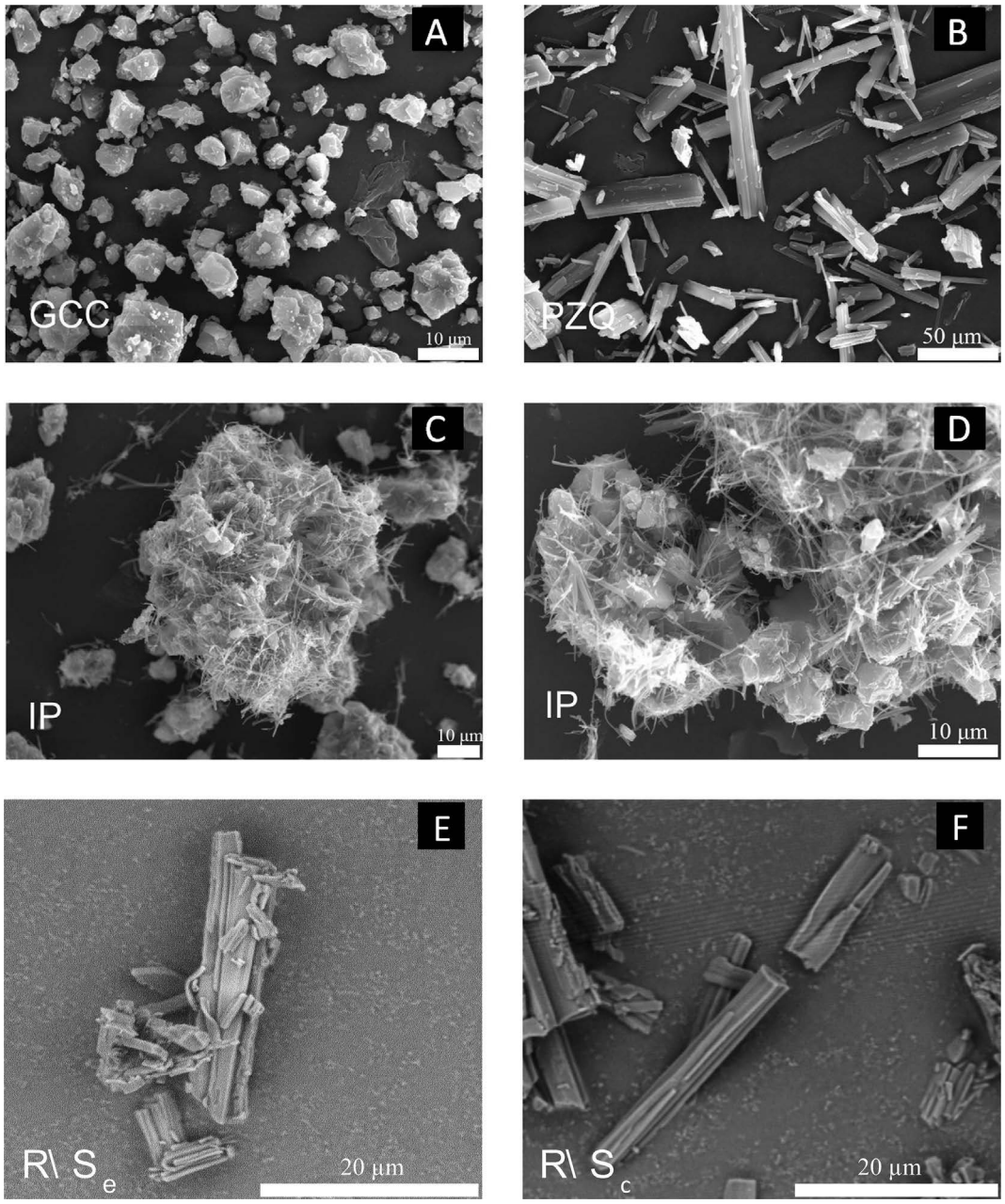

Fig. 6. SEM microphotographs of studied samples at different magnifications.

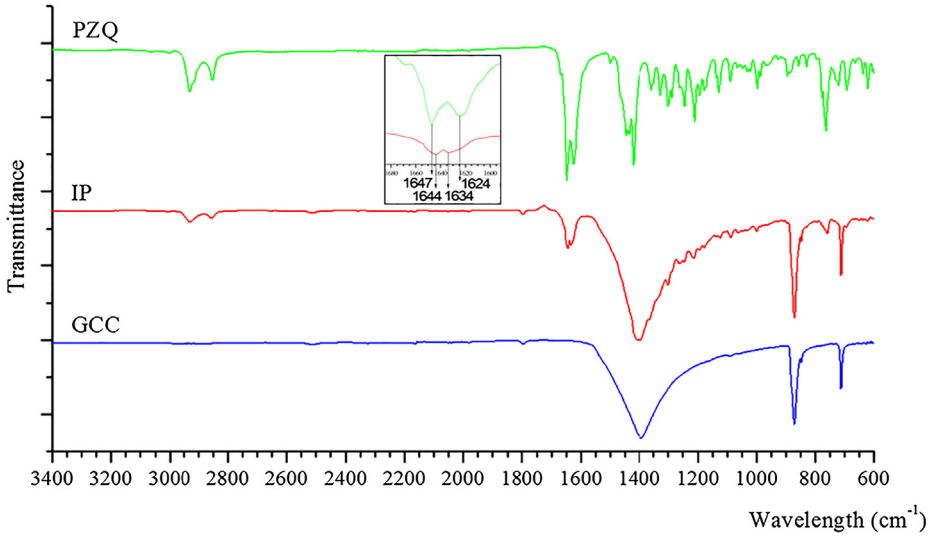

Fig. 7. FTIR spectra of PZQ, the IP, and GCC.

previous calculations [37]. This frequency shifts were also previously observed for the Form B phase [20]. These bands are broader due to the co-existence of several conformations, syn and anti, confirming the mixture of crystal forms detected above.

In addition, the Raman spectra of PZQ (Fig. 8) shows a high intensity band at 1044 cm^{-1} that can be assigned to a symmetric deformation vibration mode of C-N, $\delta(CN)_s$. Whereas the most intense band of the calcium carbonate (GCC) spectra appears at 1085 cm^{-1}, that corresponds to the symmetric ν(C—O) stretching [38–40]. The intensities of the PZQ fraction of the IP mixture are very low indicating the possible formation of different PZQ crystal forms. Nevertheless, the main bands of PZQ can be weakly observed in the IP spectrum. However, slight differences can be detected in the ranges of 1150–1250 cm^{-1}, and 1280–1360 cm^{-1} where the profiles are different and closer to the calculated anti conformer of PZQ [37]. Hence this enforces the existence of other crystal forms with different conformer mixture.

In addition, the chirality of the drug in the IP was measured by high-performance liquid chromatography (HPLC), obtaining the same proportion of each enantiomer in pure PZQ and IP, which means that the IP obtained was still a racemic product (Fig. 9). Taking into account the melting point observed at 111 °C in DSC, we tried to separate this melted phase from the rest of crystal form and observe possible changes in the enantiomer proportion by HPLC. Then, we placed an IP solid sample on a mesh and heated it for 3 h at 125 °C. No melted material was observed with shorter heating time. The melted part was absorbed by an absorbent paper placed below the mesh. Subsequently, this paper was treated with ethanol 96% to extract the melted compound and this dissolution was analyzed by HPLC. The chromatogram showed (Fig. 9c) a greater proportion of the area of peak that appeared at a time of retention of 6 min, approximately. However, this peak appeared as a double peak, suggesting the overlapping of two compounds formed during the heating of the IP at 125 °C. Other peaks with low retention time are observed, indicating other different compounds formed during

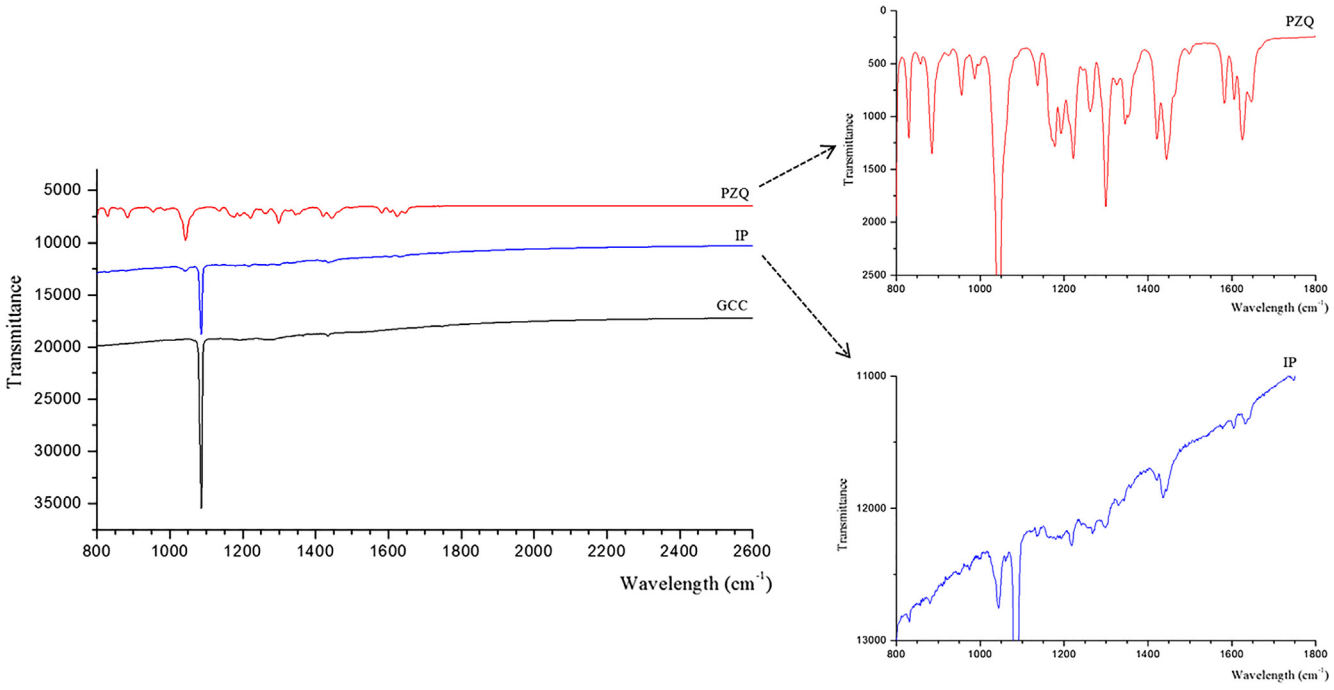

Fig. 8. Raman spectra of PZQ, the IP, and GCC.

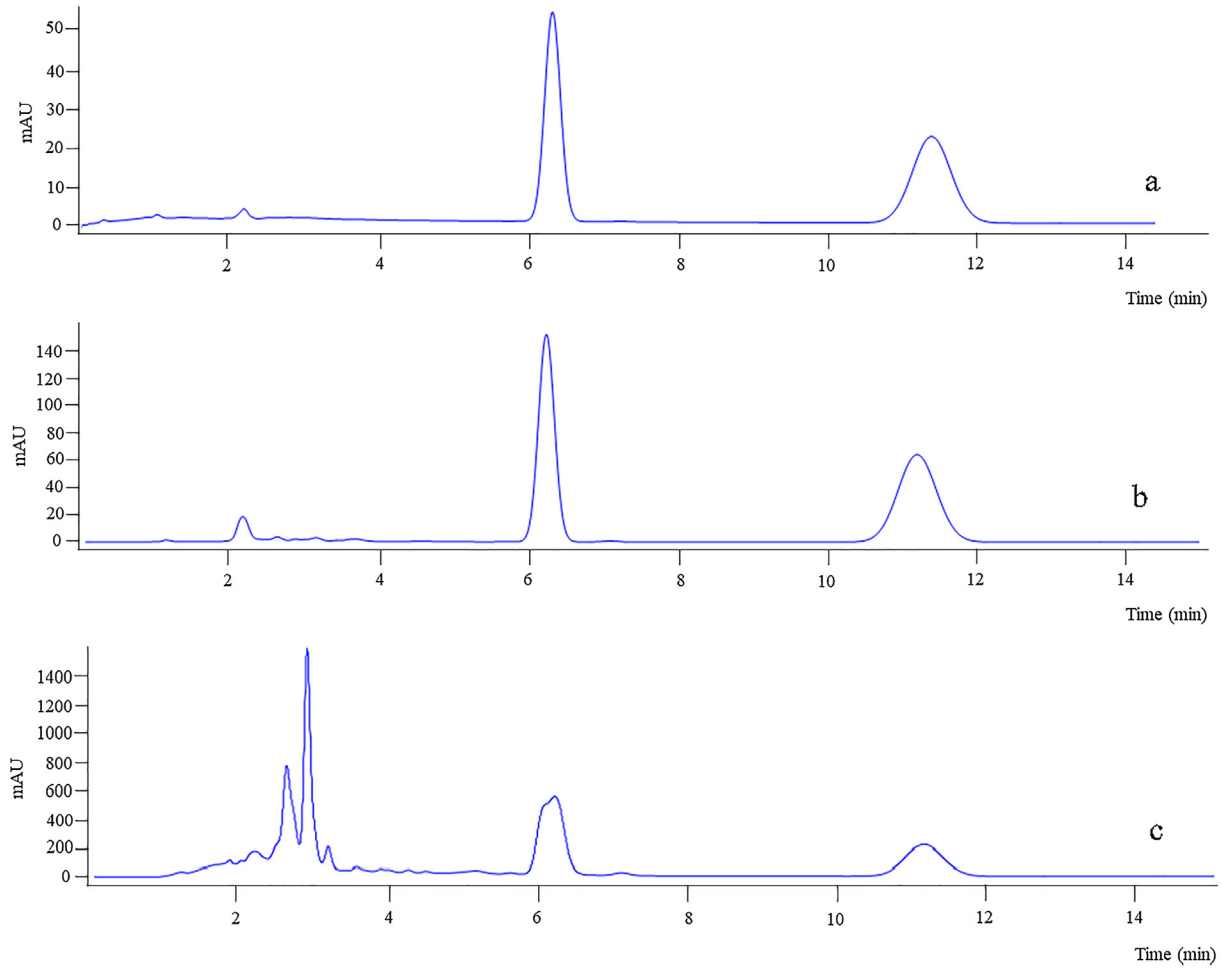

Fig. 9. HPLC chromatograms of the pure PZQ (a), IP (b), and the melted part of the IP after 3 h at 125 °C (c).

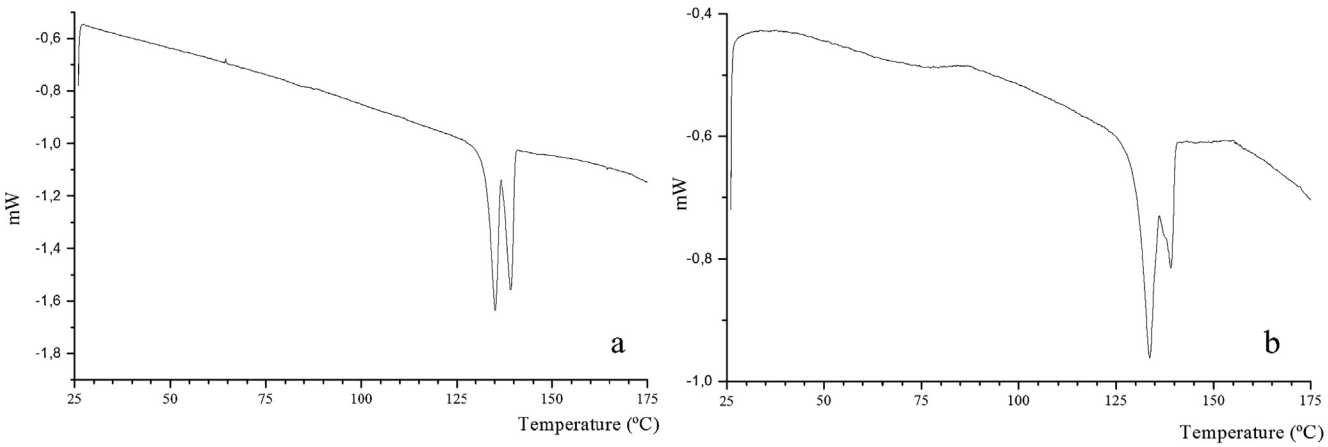

Fig. 10. DSC profiles of PZQ treated with ethanol 99% in GCC during 24 h of agitation (a), in GCC during 72 h of agitation (b).

the heating process.

To confirm this hypothesis, this experiment was repeated by using DSC, treating the IP at 125 °C for 3 h. After that process, the DSC profile was gone on by heating up to 400 °C, then a subsequent cooling process up to room temperature was followed (Fig. S1). An exothermic peak was observed at 110–125 °C corresponding to the decomposition of the compound instead of the melting endothermic peak of Form B crystal phase (Fig. S1a and S1b). The shoulder at 111 °C could indicate a balance between the melting and decomposition of the Form B. This degradation was small maintaining the main molecular structure, because the main degradation occurred at 210–310 °C. In N_2 atmosphere, the degradation decreased, the melting peak of (RS)-PZQ crystal was observed at 134–140 °C and the main thermal degradation occurred at a higher temperature range, 270–350 °C. As a result, the degradation of the drug was observed (Fig. S1). Therefore, the alteration of the HPLC chromatogram of the IP treated at 125 °C was due to the PZQ degradation. By performing the DSC scan of the pristine PZQ sample no degradation of the drug was observed (Fig. S1c). No peak was observed during the cooling process indicating no recrystallization of the initial compound confirming the total degradation of PZQ. Therefore, this

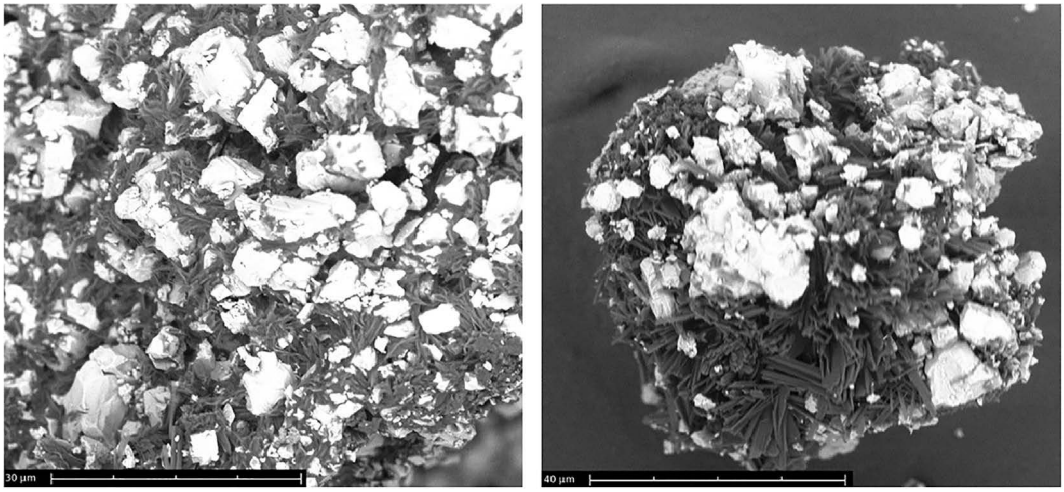

Fig. 11. SEM microphotographs of the PZQ treated with ethanol 99% in GCC during 24 h of agitation and afterwards solvent evaporation.

means that when the IP was maintained at 125 °C for 3 h, the crystal form, which has a melting peak of 112 °C, degrades under these conditions, while the rest of the sample does not degrade until T > 210 °C.

4.2. Interaction products of PZQ in other conditions

Other experimental conditions have been explored, such as the influence of a more pure ethanol to minimize the presence of water and contact time in the formation of IP in the same conditions as in the above experiments. The DSC profile of the PZQ treated with ethanol 99% and GCC showed endothermic peaks only at 134 °C and 138 °C (Fig. 10a). Therefore, the peak at 112 °C only appears with ethanol 96% (with 4% of water). On the other hand, the contact time was also explored considering 24 and 72 h with ethanol 99%. The same behavior was observed. The DSC profile showed endothermic peaks only at 134 °C and 138 °C (Fig. 10b). The peak at 134 °C was more intensive than the other peak, and no peak at 112 °C was found.

In the micropictures (SEM) of PZQ treated with ethanol 99% in GCC for 24 h and afterwards solvent evaporation, the crystal particles were different and smaller than those of pristine PZQ (Fig. 11 and Fig. 6B, respectively). No filamentous fibers, similar to those found in the IP obtained with ethanol 96% (Fig. 6C and 6D), were observed. Therefore, the presence of water resulted fundamental for the formation of the crystal forms with melting point at 112 °C.

The behavior of PZQ in interaction with a less reactive compound like colloidal silica was tested in the same conditions that with GCC. PZQ was treated with colloidal silica in ethanol 99% and ethanol 96% during 24 h of agitation and afterward ethanol evaporation. DSC profiles showed a single melting peak at 140 °C, without splitting of peaks (Fig. 12). The peak is typical of pure PZQ. No formation of the crystal form with melting point at 112 °C was observed. Therefore, the presence of GCC is critical for the change in the crystallinity of PZQ.

5. Discussion

5.1. Interactions between PZQ and calcium carbonate at molecular level

Our experiments described above indicated that the interaction of the (RS)-PZQ solid with calcium carbonate affects the crystallization process and crystallinity of PZQ, forming other different crystal forms. No chemical decomposition of PZQ was observed, but only alterations of the ordering in the packing of PZQ molecules and a conformational change in the PZQ molecule. In the (RS)-PZQ crystal the carbonyl groups are oriented to the same direction, *syn* conformation (Fig. 13a). During the nucleation step, the calcium carbonate can interact with these carbonyl groups of PZQ. This interaction can be enhanced with the presence of a small amount of residual water coming from the ethanol (96%) solvent during the treatment. Previous calculations showed that the *syn* conformation of PZQ is the more polar than the *anti* one [37] (Fig. 13b) and it is likely to be present in an ethanol/water solution during the formation of the solid dispersion. Then, both conformers can be present in the solution and form different crystal nuclei. Our FTIR analysis indicates the presence of several conformers in the broadening of the stretching C═O bands in IP sample (Fig. 7).

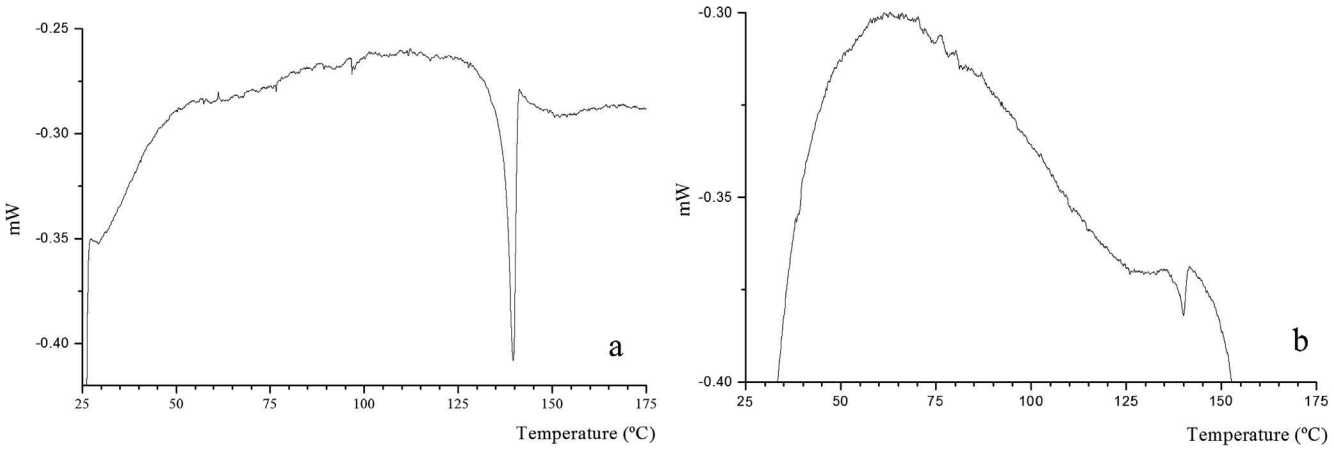

Fig. 12. DSC profiles of PZQ treated in colloidal silica with ethanol 99% (a) and in colloidal silica with ethanol 96% (b).

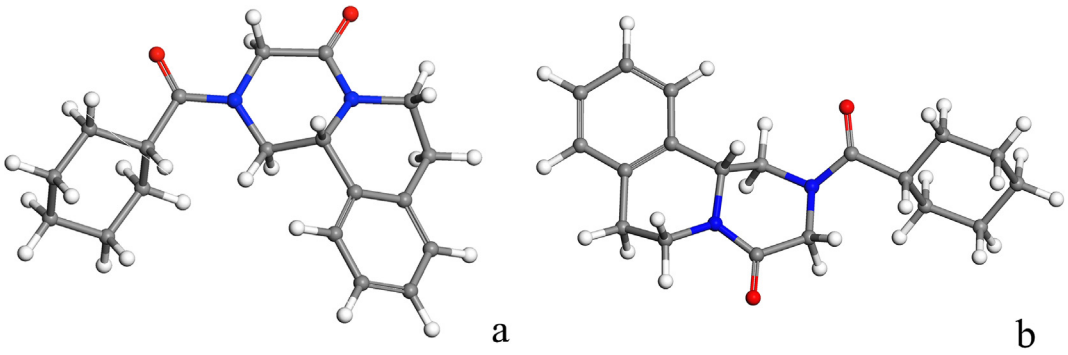

Fig. 13. Conformations *syn* (a) and *anti* (b) of PZQ. The C, H, N, and O atoms are in grey, white, blue, and red color. (For interpretation of the references to color in this figure legend, the reader is referred to the web version of this article.)

Our above experiments indicate that the interaction of PZQ with water and GCC is critical for the crystallinity alteration in the IP samples. The presence of water/carbonate alters definitely the recrystallization of PZQ. Possibly, a local zone of high pH aqueous conditions could affect in this recrystallization during the nucleation and ordering of the PZQ units. However, we cannot measure the pH at nanoscale level. Nevertheless, we include here this idea as a hypothesis and as a starting point for future investigations. Definitely the actual effect will be the interactions at molecular level in a PZQ/water/$CaCO_3$ complex. In order to explore these interactions, we can create small models to describe this complex system with only one PZQ molecule, one water molecule and one GCC salt complex. We understand that these models can be considered too small. But these models do not pretend to reproduce exactly the experimental scenario, that would be too complex and difficult to calculate. Our models represent the minimal expression to describe the formation of interatomic interactions between PZQ/water/$CaCO_3$. Of course this complex will be surrounded by more water molecules and $CaCO_3$ species but they will be in outer coordination spheres.

Then, two possible complexes can be considered: PZQCCw1, where the Ca^{2+} cation is coordinated with both carbonyl groups in a equidistant distance of 2.9 Å; and PZQCCw2, where the water molecule interacts directly with both carbonyl groups by means of hydrogen bonds at 2.3 Å. Both models were generated and the geometry was optimized with Compass FF calculations, using the SPC water model. In both models the coordination changed to only one carbonyl group during the optimization process. In PZQCCw1, the Ca^{2+} cation is coordinated at 2.30 Å to only one carbonyl O atom, which is joined to the cyclohexyl ring, leaving free the other carbonyl group; and the water H atoms form hydrogen bonds with the carbonate O atoms at 1.48–1.52 Å (Fig. 14a). Similarly in PZQCCw2, one water H atom is coordinated at 1.73 Å to only one carbonyl O atom, which is joined to the cyclohexyl ring, leaving also free the other carbonyl group (belonged to the heterocyclic ring), and the water O atom is coordinating the Ca^{2+} cation *d* (O···Ca) = 2.25 Å (Fig. 14b).

In both models the Ca^{2+} cation is coordinated to two carbonate O atoms at 1.87–1.91 Å. It is remarkable that in both complexes the heterocyclic carbonyl moiety is not coordinated being more free for rotating to the *anti* conformation facilitating the formation of other crystal forms as observed experimentally.

5.2. Molecular interactions in the conformational changes of PZQ in the crystal forms

In the above experiments the racemic crystal of (RS)-PZQ was partially decomposed on other crystal forms owing to the interaction with GCC during the nucleation and recrystallization of PZQ. The molecular interactions in the different crystal forms can be explored at molecular level by means of molecular modeling simulations to explain this experimental behavior. In this work, the intermolecular interactions within the different crystal forms are analyzed more exhaustively. The crystal structures of the R enantiomer of PZQ, the commercial racemic (RS)-PZQ and the new polymorph of (RS)-PZQ, form B proposed by Zanolla et al. [20], were calculated at molecular level and compared. All details of these calculations are described in the Supplementary material.

The crystal lattice of (RS)-PZQ is formed by enantiomer pairs and the molecular packing is due to the electrostatic interactions of the carbonyl groups with the H atoms of the heterocycles and π-π interactions between aromatic and heterocyclic rings (Fig. 15a). The difference between the (R)-PZQ and (RS)-PZQ crystals is not only the proportion of enantiomers, but they are different crystal forms, with

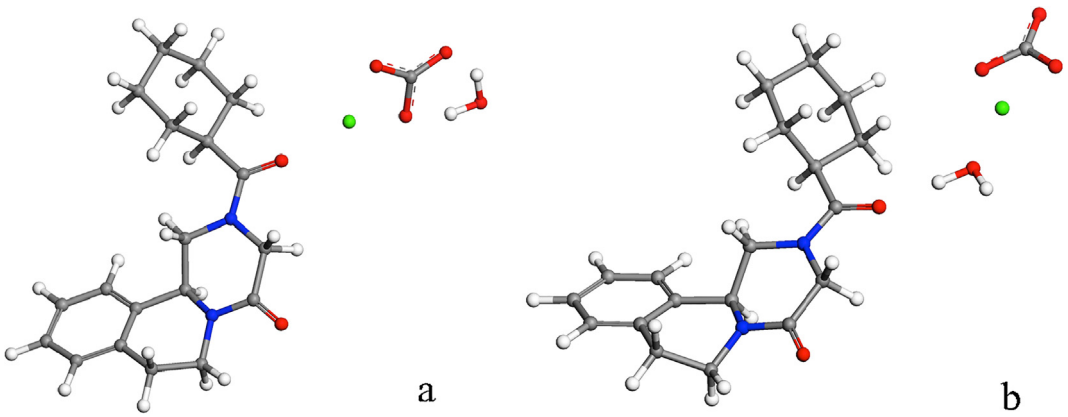

Fig. 14. Models of PZQCCw1 (a), and PZQCCw2 (b) complexes optimized with Compass. The C, Ca, H, N, and O atoms are in grey, green, white, blue, and red color. (For interpretation of the references to color in this figure legend, the reader is referred to the web version of this article.)

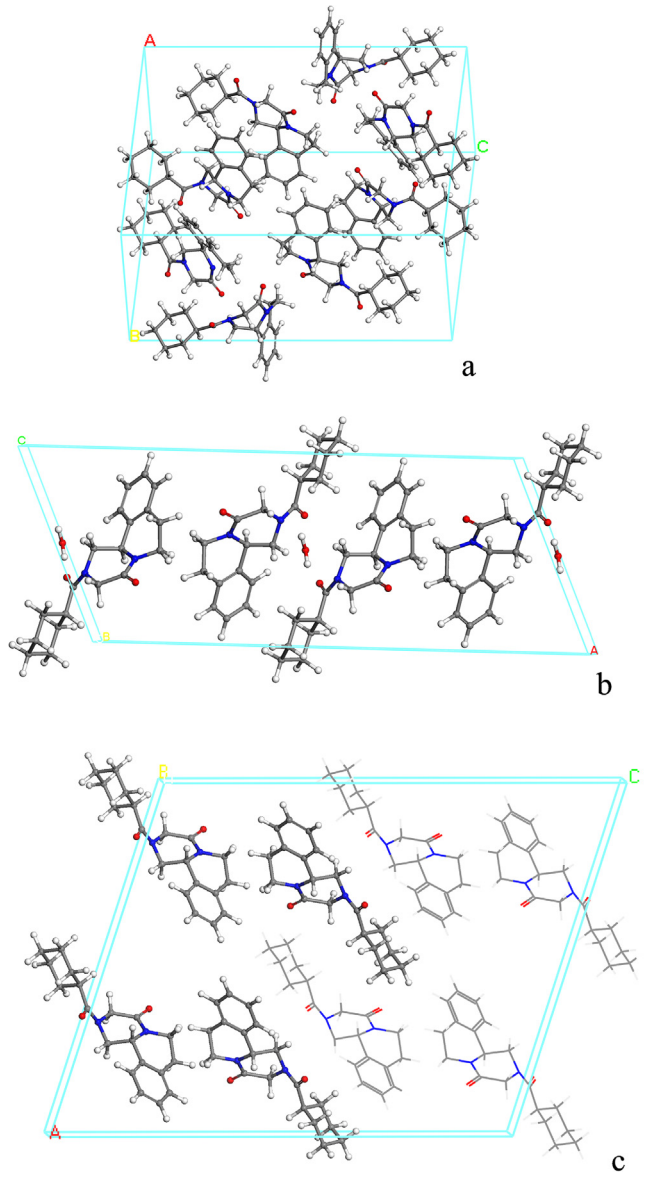

Fig. 15. Intermolecular interactions in the optimized crystal lattice of (RS)-PZQ (a), (R)-PZQ (b), the new RS polymorph (Form B) (The enantiomer S is highlighted with the atoms represented as balls) (c).

different molecular conformations, different intermolecular interactions and the presence of water molecules. In the (RS)-PZQ crystal both carbonyl groups are oriented to the same direction, conformation *syn*, whereas in the R-enantiomer hemihydrate crystal these carbonyl groups are oriented to opposite directions, conformation *anti*. In the crystal of the hemihydrate of the enantiomer (R)-PZQ (Fig. 15b), the crystallization water provides hydrogen bonds to connect the carbonyl groups.

In the crystal structure of the new RS polymorph (Form B), all PZQ molecules are in the anti conformation and the main intermolecular interactions are electrostatic between the carbonyl O atoms and the surrounding alkyl H atoms at d(CO···HC) = 2.6–2.9 Å. The unit cell is a racemic mixture with 4 molecules of each enantiomer per unit cell (Fig. 15c). However, the relative distribution of enantiomers is different from that of the pristine (RS)-PZQ. The enantiomers R are separate from the S ones forming clusters that form alternate slabs of each enantiomer in a tridimensional supercell structure, whereas in the initial pristine (RS)-PZQ the molecules are forming pairs of R and S enantiomers. The cohesion energy (−41.42 kcal/mol per PZQ molecule) of this new RS polymorph (Form B) is similar to the initial pristine (RS)-PZQ crystal form, −39.78 kcal/mol per PZQ molecule. This small energy difference can indicate a similar probability for nucleating both polymorphs.

The IUPAC definition of the term “racemic mixture” in the solid state refers to a heterogeneous mixture of two separate solid phases, while the term “racemate” refers to a homogeneous single phase [41]. Pseudoracemate is other possible solid structure that can be defined in chiral compounds. When one enantiomer has a greater affinity for molecules of its own kind than for those of the other enantiomer, both enantiomers crystallize in separate phases forming a racemic mixture. On the contrary, one enantiomer can have greater affinity for molecules of the opposite enantiomer than for its own kind and form a racemic compound. In both cases, the unit cell of the crystal lattice contains an equal number of molecules of each enantiomer and the product is a true addition compound. When there is little difference in the affinity between enantiomers of like or opposite configuration, both enantiomers exist in a disordered manner in the crystal forming a racemic solid solution or pseudoracemate [41]. In this work, one additional difference exists, that is, pure enantiomers form a different crystal polymorph with respect to the racemate. Liu et al. [11] studied several mixtures of PZQ enantiomers finding different melting points and concluded that the direct transformation between racemic mixture and racemic compound was not possible. However, in this work we conclude the opposite way. In the experimental crystallographic CIF file of (RS)-PZQ crystal (TELCEU, CCDC-896767), four PZQ molecules (two enantiomers pairs) per unit cell are disordered in the atomic positions of the aromatic-heterocyclic moiety of the molecule [15]. This mobility of the molecules could favor the easy polymorphic change in this system. Zanolla et al. [20] obtained the new polymorph just by milling physically without dissolution-recrystallization process. The conformer *anti* is less polar than the *syn* one, and the *anti* one is more stable than *syn* without polar interactions [37]. The mechanical energy during the grinding process can provoke a disorder in the molecules and a conformational change obtaining the most stable conformer. However, the ordering of this system did not produce a racemate, like in the initial (RS)-PZQ, but a pseudoracemate or racemic mixture where each enantiomer of the same sign is clustered.

After the dissolution of PZQ and treatment with GCC, both enantiomers precipitate forming a mixture of a solid solution of PZQ enantiomers (pseudoracemate) showing a melting point at 134–137 °C and some crystals of PZQ with a melting point at 111–113 °C. Previous authors [11] found a melting point at 111 °C of the crystal form of the enantiomer (-)-(R)-PZQ and a melting point at 134–138 °C for a 50:50 mixture of enantiomers of PZQ, indicating that this mixture was a racemate and not a conglomerate of enantiomers. In our work, the hemihydrate crystals of the separate enantiomers have the same melting point that the Form B. This can confuse in the interpretation of the polymorphic changes. In our experiments, the interaction of the calcium carbonate provokes the alteration of the pristine (RS)-PZQ that is not observed with a more inert excipient like colloidal silica. However, the presence of water is also critical for this alteration to form crystals that melt at 111–112 °C. This water content cannot be detected in our thermal analysis because it is embedded in the hemihydrate crystals. Therefore, we can conclude that these formed crystals, with melting point at 111–112 °C, could be assigned to the polymorph of hemihydrate of (R) and (S)-PZQ in separate crystals, instead of the anhydrous RS polymorph, Form B, reported by Zanolla et al. [20]. Nevertheless, DSC analysis did not distinguish the presence between the enantiomers and Form B crystals, or the formation of both polymorphs.

Besides, the DSC experiments of this work can identify clearly the melting points of the monoenantiomeric crystal or the Form B [20] (110–112 °C) and the pure racemic crystals (142–144 °C). However, new solid forms have been detected with intermediate melting points (134–138 °C), which cannot be clearly assigned. This happened only with the presence of calcium carbonate and can be produced also with and without the presence of water, indicating that could correspond to anhydrous forms. The solid phase with a melting point at 134 °C could

be assigned to another pseudoracemate or (RS)-racemate with defects and we cannot know its crystal structure. On the other hand, the solid phase with melting point at 138 °C could be another solid solution of enantiomers. Any of these phases could correspond tentatively to the initial racemate where the presence of defects or disordered PZQ could decrease its melting point. However, the phase with melting point at 134 °C is metastable and is transformed slowly to the phase whose melting point is 138 °C.

6. Conclusions

Our experiments conclude that the GCC used as excipient of the PZQ through the formation of a solid dispersion affected the crystal structure of the PZQ and modified the pristine PZQ solid state. This effect was enhanced with the presence of residual water molecules from the solvent. A crystal form change occurred along with conformational changes in the molecules. These modifications of the crystal forms could correspond either to monoenantiomeric forms or to the (RS)-Form B (melting point at 112 °C) and other phases (melting point at 134–138 °C) that could be tentatively assigned to a disordered pseudoracemate solid phases. These crystallographic changes were not observed using colloidal silica as solid excipient.

This phenomenon is due to the interaction of calcium carbonate with the carbonyl groups of PZQ, which are in the *syn* conformation. The presence of water is critical in the formation of the crystals with melting point at 111–112 °C. Probably the solvation water of Ca^{2+} cation forms hydrogen bonds with the carbonyl group joined to the cyclohexyl group. The PZQ molecule can adopt an *anti* conformation, which is energetically more stable than the syn one, like in the enantiomeric crystal. Then, the hydrated cyclohexyl-carbonyl group can interact with another PZQ molecule forming the hemihydrate enantiomer crystal (either the same enantiomer or a pseudoracemate crystal, if it is the other enantiomer) in a solid solution of mixed enantiomers.

Computational modeling, with classical FF and at quantum mechanical level, has been a useful tool for understanding the molecular interactions in the crystal structures and the effect of GCC on PZQ and the PZQ conformational changes in the crystal structures experimentally observed.

Acknowledgments

Authors are thankful to the regional Andalusian projects (RNM363 and RNM1897) and national MINECO project (FIS2016-77692-C2-2-P and CGL2016-80833-R) for financial support and to the Supercomputational Center of Universidad de Granada and CSIC for computing facilities.

Appendix A. Supplementary material

Supplementary data to this article can be found online at https://doi.org/10.1016/j.ejpb.2018.09.028.

References

[1] L. Chitsulo, D. Engels, A. Montresor, L. Savioli, The global status of schistosomiasis and its control, Acta Trop. 7 (2000) 41–51.
[2] P. Steinmann, J. Keiser, R. Bos, M. Tanner, J. Utzinger, Schistosomiasis and water resources development: systematic review, meta-analysis, and estimates of people at risk, Lancet Infect. Dis. 6 (2006) 411–425.
[3] R. Trastullo, L.S. Dolci, N. Passerini, B. Albertini, Development of flexible and dispersible oral formulations containing praziquantel for potential schistosomiasis treatment of pre-school age children, Int. J. Pharm. 495 (2015) 536–550.
[4] WHO, WHO Schistosomiasis, World Health Organization, http://www.who.int/es/news-room/fact-sheets/detail/schistosomiasis, 2018 (accessed 29 June 2018).
[5] D. Cioli, L. Pica-Mattoccia, S. Archer, Antischistomal drugs: past, present…and future? Pharmacol. Ther. 68 (1995) 35–85.
[6] D. Cioli, L. Pica-Mattoccia, Praziquantel, Parasitol. Res. 90 (2003) 3–9.
[7] EP 7.0. European Pharmacopoeia Seventh Edition. Directorate for the Quality of Medicines of the Council of Europe, Strasbourg, France, 2011.
[8] USP 36-NF31. United States Pharmacopoeia 36 and National Formulary 31. US Pharmacopoeial Convention, Rockville, MD USA, 2013.
[9] P. Andrews, Praziquantel: mechanisms of anti-schistosomal activity, Pharmacol. Ther. 29 (1985) 129–156.
[10] R. Pax, J.L. Bennett, R. Fetterer, A benzodiazepine derivative and praziquantel: effects on musculature of Schistosoma mansoni and Schistosoma japonicum, Naanyn-Schmiedeberg's Arch. Pharmacol. 304 (1978) 309–315.
[11] Y. Liu, X. Wang, J.K. Wang, C.B. Ching, Structural characterization and enantioseparation of the chiral compound praziquantel, J. Pharm. Sci. 93 (2004) 3039–3046.
[12] B.G. Lim, R.B.H. Tan, S.C. Ng, C.B. Ching, Solubility phase-diagram of praziquantel enantiomeric system, Chirality 7 (1995) 74–81.
[13] S.K. El-Arini, D. Giron, H. Leuenberg, Solubility properties of racemic praziquantel and its enantiomers, Pharm. Dev. Techn. 3 (1998) 557–564.
[14] Y. Liu, X. Wang, J.K. Wang, C.B. Ching, Investigation of the phase diagrams of chiral praziquantel, Chirality 18 (2006) 259–264.
[15] J.C. Espinosa-Lara, D. Guzmán-Villanueva, J.I. Arenas-García, D. Herrera-Ruiz, J. Rivera-Islas, P. Román-Bravo, H. Morales-Rojas, H. Höpfl, Cocrystals of active pharmaceuticals ingredients-praziquantel in combination with oxalic, malonic, succinic, maleic, fumaric, glutaric, adipic and pimelic acids, Cryst. Growth. Des. 13 (2013) 169–185.
[16] M. Lindenberg, S. Kopp, J.B. Dressman, Classification of orally administered drugs on the World Health Organization Model list of essential medicines according to the biopharmaceutics classification system, Eur. J. Pharm. Biopharm. 58 (2004) 265–278.
[17] D. González-Esquivel, J. Rivera, N. Castro, L. Yepez-Mulia, J.C. Helgi, In vitro characterization of some biopharmaceutical properties of praziquantel, Int. J. Pharm. 295 (2005) 93–99.
[18] N. Passerini, B. Albertini, B. Perissutti, L. Rodriguez, Evaluation of melt granulation and ultrasonic spray congealing as techniques to enhance the dissolution of praziquantel, Int. J. Pharm. 318 (2006) 92–102.
[19] A. Borrego-Sánchez, E. Carazo, C. Aguzzi, C. Viseras, C.I. Sainz-Díaz, Biopharmaceutical improvement of praziquantel by interaction with montmorillonite and sepiolite, Appl. Clay. Sci. 160 (2018) 173–179.
[20] D. Zanolla, B. Perissutti, N. Passerini, M.R. Chierotti, D. Hasa, D. Voinovich, L. Gigli, N. Demitri, S. Geremia, J. Keiser, P.C. Vioglio, B. Albertini, A new soluble and bioactive polymorph of praziquantel, Eur. J. Pharm. Biopharm. 127 (2018) 19–28.
[21] R.C. Rowe, P.J. Sheskey, P.J. Weller, Handbook of Pharmaceutical Excipients, sixth ed., Pharmaceutical Press, London, 2009.
[22] J.D. Martín-Ramos, XPowder software, http://www.xpowder.com, 2005 (accessed 29 June 2018).
[23] H. Sun, COMPASS: an ab initio force-field optimized for condensed-phase applications-overview with details on alkane and benzene compounds, J. Phys. Chem. B 102 (1998) 7338–7364.
[24] Accelrys Materials Studio, version v 6.0. Accelrys Inc., San Diego, USA, 2012.
[25] A. Borrego-Sánchez, C. Viseras, C. Aguzzi, C.I. Sainz-Díaz, Molecular and crystal structure of praziquantel. Spectroscopic properties and crystal polymorphism, Eur. J. Pharm. Sci. 92 (2016) 266–275.
[26] J.M. Soler, E. Artacho, J.D. Gale, A. García, J. Junquera, P. Ordejón, D. Sánchez-Portal, The Siesta method for ab initio order-N materials simulation, J. Phys. Condens. Matter. 14 (2002) 2745–2779.
[27] J.P. Perdew, K. Burke, M. Ernzerhof, Generalized gradient approximation made simple, Phys. Rev. Lett. 77 (1996) 3865–3868.
[28] N. Troullier, J.L. Martins, Efficient pseudopotentials for plane-wave calculations, Phys. Rev. B 43 (1991) 1993–2006.
[29] C.I. Sainz-Díaz, E. Escamilla-Roa, A. Hernández-Laguna, Quantum mechanical calculations of trans-vacant and cis-vacant polymorphism in dioctahedral 2:1 phyllosilicates, Am. Miner. 90 (2005) 1827–1834.
[30] R. Martos-Villa, M. Francisco-Márquez, M.P. Mata, C.I. Sainz-Díaz, Crystal structure, stability and spectroscopic properties of methane and CO_2 hydrates, J. Mol. Graph. Model. 44 (2013) 253–265.
[31] H.I. El-Subbagh, A.A. Al-Badr, Praziquantel, in: Florey (Ed.), Analytical Profiles of Drug Substances and Excipients, Academic Press Inc., New York, 1998, pp. 463–500.
[32] P. De la Torre, S. Torrado, S. Torrado, Preparation, dissolution and characterization of praziquantel solid dispersions, Chem. Pharm. Bull. 47 (1999) 1629–1633.
[33] M.V. Chaud, A.C. Lima, M.M.D.C. Vila, M.O. Paganelli, F.C. Paula, L.N. Pedreiro, M.P.D. Gremião, Development and evaluation of praziquantel solid dispersions in sodium starch glycolate, Trop. J. Pharm. Res. 12 (2013) 163–168.
[34] S.G. Rodrigues, I.S. Chaves, N.F.S. Melo, M.B. De Jesus, L.F. Fraceto, S.A. Fernandes, E. De Paula, M.P. De Freitas, L.M.A. Pinto, Computational analysis and physico-chemical characterization of an inclusion compound between praziquantel and methyl-β-cyclodextrin for use as an alternative in the treatment of schistosomiasis, J. Incl. Phenom. Macrocycl. Chem. 70 (2010) 19–28.
[35] F.B. Reig, J.V. Gimeno-Adelantado, M.C.M. Moya-Moreno, FTIR quantitative analysis of calcium carbonate (calcite) and silica (quartz) mixtures using the constant ratio method. Application to geological samples, Talanta 58 (2002) 811–821.
[36] N.V. Vagenas, A. Gatsouli, C.G. Kontoyannis, Quantitative analysis of synthetic calcium carbonate polymorphs using FT-IR spectroscopy, Talanta 59 (2003) 831–836.
[37] A. Borrego-Sánchez, A. Hernández-Laguna, C.I. Sainz-Díaz, Molecular modeling and infrared and Raman spectroscopy of the crystal structure of the chiral anti-parasitic drug praziquantel, J. Mol. Model. 23 (2017) 106.
[38] H.G.M. Edwards, S.E.J. Villar, J. Jehlicka, T. Munshi, FT–Raman spectroscopic study of calcium-rich and magnesium-rich carbonate minerals, Spectrochim. Acta A

61 (2005) 2273–2280.
[39] S.M. De Paula, M.F.G. Huila, K. Araki, H.E. Toma, Confocal Raman and electronic microscopy studies on the topotactic conversion of calcium carbonate from Pomacea lineate shells into hydroxyapatite bioceramic materials in phosphate media, Micron 41 (2010) 983–989.
[40] G.P.S. Smith, K.C. Gordon, S.E. Holroyd, Raman spectroscopic quantification of calcium carbonate in spiked milk powder samples, Vib. Spectrosc. 67 (2013) 87–91.
[41] A. Mitchell, Racemic drugs: racemic mixture, racemic compound, or pseudoracemate? J. Pharm. Pharm. Sci. 1 (1998) 8–12.

CHAPTER

Clay minerals in drug delivery systems

6

Fátima García-Villén[1], Esperanza Carazo[1], Ana Borrego-Sánchez[2], Rita Sánchez-Espejo[3], Pilar Cerezo[1], César Viseras[1,2] and Carola Aguzzi[1]

[1]Department of Pharmacy and Pharmaceutical Technology, University of Granada, Granada, Spain [2]Andalusian Institute of Earth Sciences, CSIC-University of Granada, Granada, Spain [3]Aguas Termales de Graena, Granada, Spain

6.1 INTRODUCTION

Drug delivery is the first step occurring once a medicine is administered to the body, and must guarantee the maintenance of a safe and effective drug concentration in the site of action during the treatment. Drug bioavailability, i.e., the rate and fraction at which the administered dose reaches the site of action, greatly depends on the design of the drug delivery system (DDS). All pharmaceutical dosage forms may be considered DDS, as they transport, protect and deliver a drug through the proper route of administration to obtain a therapeutic effect. Conventional dosage forms lead to possible overdosing or underdosing periods in plasma concentrations (Fig. 6.1).

Modified drug delivery systems (MDDSs) are designed to improve drug bioavailability and/or minimize adverse effects, by changing the rate and/or time and/or site of drug release in comparison with conventional dosage forms. MDDSs are considered as useful strategies to ameliorate patient compliance (Sastry et al., 2000), and MDDSs include prolonged-release systems, delayed-release systems, and site-specific systems (Council of Europe & Convention on the Elaboration of a European Pharmacopoeia, 2017). Prolonged-release systems are those in which the drug is released within a more extended period, compared with conventional dosage forms. Delayed-release systems are able to delay drug release for a certain time lapse, after which it occurs in a conventional way. Site-specific dosage forms perform drug delivery at the diseased tissue/organ or in the physiological drug receptor location.

The design of an MDDS depends as much on the method of preparation as on the excipients employed. In this regard, clay minerals have been proposed as useful MDDS excipients, due to their effective interactions with drug molecules, inertness, swelling capacity, abundance, and low toxicity (Aguzzi et al., 2007; Viseras et al., 2010, 2015; Rodrigues et al., 2013; Fakhrullina et al., 2015; Sandri et al., 2016; Jafarbeglou et al., 2016; Yang et al., 2016a; Carazo et al., 2018). In certain cases it may be necessary to improve some clay properties, such as

Modified Clay and Zeolite Nanocomposite Materials. DOI: https://doi.org/10.1016/B978-0-12-814617-0.00010-4

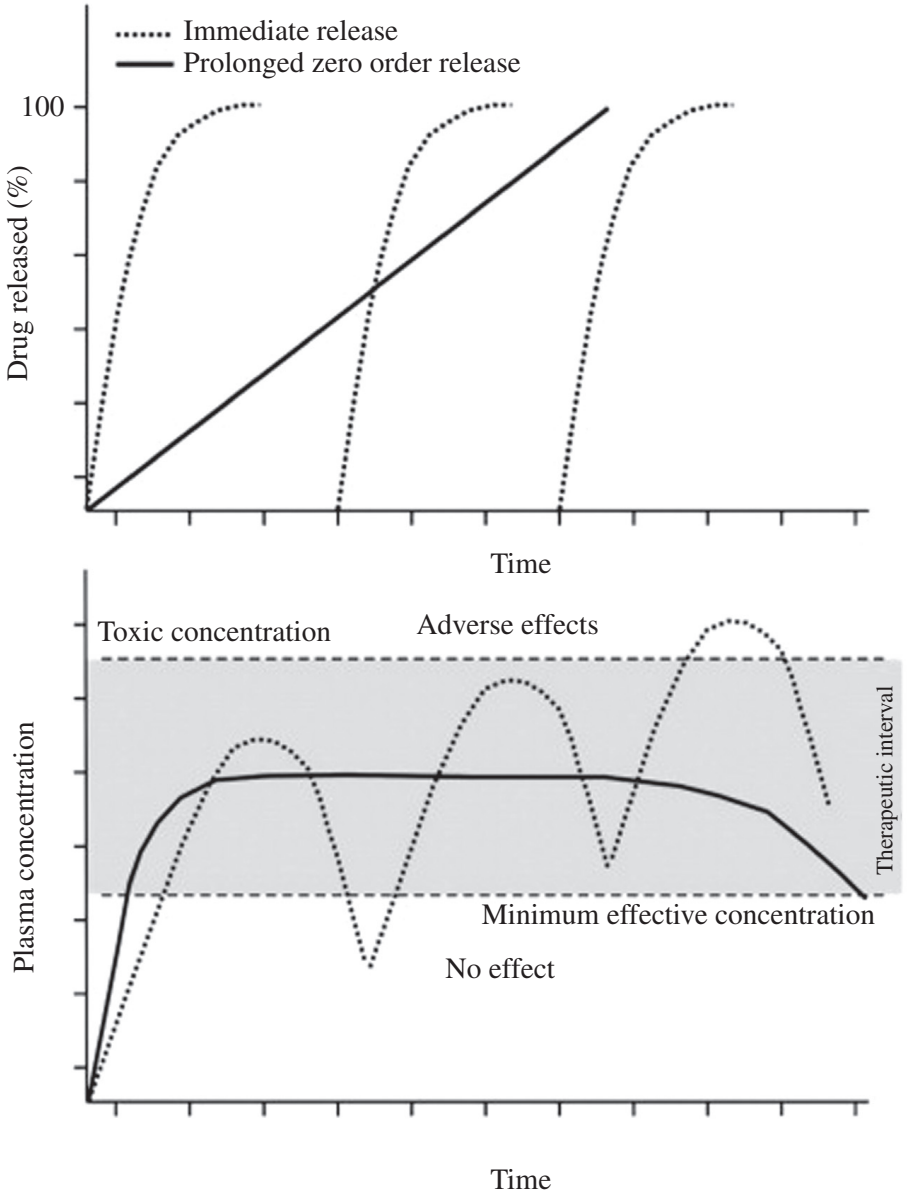

FIGURE 6.1

Schematic representation of correlation established between drug release profiles and plasma concentrations.

Figure extracted from Viseras, C., et al., 2010. Current challenges in clay minerals for drug delivery. Appl. Clay Sci. 48(3), 291–295.

specific surface area, type of exchangeable cations, hydrophilic nature, zeta potential, interlayer space, or porosity, to engineer their performance as drug carriers and delivery systems. Raw clay minerals are usually treated to eliminate

impurities and/or obtain homoionic clay minerals (i.e., sodium derivates). These are frequently named as natural excipients in contrast to those prepared by more specific treatments. In this regard, organic functionalization of clays, pillarization, or combination with polymers are highlighted as the most used clay modification strategies (Aguzzi et al., 2007; Viseras et al., 2008, 2010, 2015; Rodrigues et al., 2013; Liu et al., 2014; Nazir et al., 2016; Yang et al., 2016a; Meirelles and Raffin, 2017). This chapter focuses on the last decade's advances in the use of natural and functionalized clay minerals as well as clay/polymer nanocomposites in drug delivery.

6.2 LAYERED CLAY MINERALS

Two groups of layered clay minerals are frequently used as MDDS excipients: smectites (2:1 phyllosilicates) and kaolin (1:1 phyllosilicate).

Smectites are a group of layered clay minerals including montmorillonite (MMT), saponite, hectorite, beidellite, and nontronite, among others. As pharmaceutical excipients, these minerals are included in two pharmacopeial monographs: bentonite (mainly composed of MMT) and magnesium aluminum silicate (mainly composed of saponite and MMT) (Council of Europe & Convention on the Elaboration of a European Pharmacopoeia, 2017). Other smectites are used in the design of MDDS once modified (e.g., disteardimonium hectorite, stearalkonium hectorite, quaternium-18hectorite).

MMT is the most commonly used smectite in pharmaceutical applications. It possesses a dioctahedral structure in which Si(IV) atoms coordinate with oxygen, thus forming tetrahedral sheets that confine an octahedral sheet formed by Al(III) atoms also coordinated with oxygen. Typical Al isomorphic substitutions include Mg(II) and Fe(II), thus giving the structure a negative charge that is compensated by metal cations in the interlayer space. Ideal chemical structure of MMT has been defined as $Si_8Al_{3.5}Mg_{0.5}O_{20}(OH)_4$ (Schoonheydt and Johnston, 2006). The incorporation of a drug between MMT interlayers, which sometimes can even produce clay mineral exfoliation, can be easily detected by X-ray diffraction (XRD) analysis by observing a characteristic shift in the *d*-001 value of the mineral. Both natural and functionalized MMT have been widely used in drug delivery (Aguzzi et al., 2007; Park et al., 2016). However, the combination of MMT with polymers is one of the most currently extended strategies, leading to MMT-polymer nanocomposites (Viseras et al., 2008).

Kaolinite is the most common clay mineral of the kaolin group. It possesses a 1:1 structure, and it is composed of repetitive units of SiO_4 tetrahedral layers bonded to $Al(O,OH)_6$ octahedral layers through apically shared oxygen atoms. In relation to DDSs, and compared with other types of clay minerals, kaolinite is not as widely used as MMT or palygorskite. Nevertheless, studies performed with kaolinite on drug delivery issues showed promising results, and have been focused on basic drugs (Holešová et al., 2014).

6.2.1 NATURAL LAYERED CLAY MINERALS

Table 6.1 summarizes examples of some most recent clay-based MDDS. In most cases, MMT, sometimes activated or functionalized or in combination with saponite, was used.

Diclofenac sodium is one of the most prescribed nonsteroidal antiinflammatory (NSAID) drugs, though extensive side effects are reported due to the frequent doses needed and short half-life of the active ingredient. Prolonged-release systems would help to minimize such problems with diclofenac sodium. MMT demonstrated an effective control of diclofenac release [76% (w/w) of loaded drug was dissolved in phosphate buffer medium (pH 7.4) after 8 h] (Kaur and Datta, 2014).

Chlorhexidine is a bacteriostatic and bactericidal agent widely used for sterilizing purposes since it is active against Gram-positive and Gram-negative bacteria, molds, yeasts, and viruses. Chlorhexidine dosage forms usually show erratic release profiles, and may result in toxicity to human dermal fibroblasts when topically applied. Na^+-MMT was chosen as a chlorhexidine carrier in systems intended to be used as topical DDS with improved release properties (Saha et al., 2014).

Na^+-MMT was also demonstrated to be able to protect labile molecules from external agents such as light. Promethazine is a photolabile antihistamine topically administered to treat insect bites and erythema. Its degradation, when exposed to light, could cause cutaneous photoreactions. After MMT intercalation, photostability and diffusion-prolonged release of promethazine in *in vitro* Franz cell tests were accomplished (Ambrogi et al., 2014). The authors attributed the enhanced photostability to the confined space in which the drug was located after intercalation within MMT. This formulation consequently reduced the mobility of free electrons and oxygen species, avoiding drug alterations.

Intercalation of anticancer drug paclitaxel in a Na^+-MMT was optimized by Bothiraja et al. (2014). Subsequently, the resultant system was coated with a natural polysaccharide (chitosan, CS). Results showed a controlled release of paclitaxel and an improvement of its *in vitro* anticancer activity.

Gallic acid is a natural molecule extracted from gallnut, tea, cherries, and other plants. It is widely known by its antioxidant activity and also some antimutagenic, anticarcinogenic, antiinflammatory, and antimicrobial activities. Nevertheless, it is also a molecule with poor solubility, permeability, high instability, and fast metabolism. Rabiei et al. (2016) suggested the necessity of an MDDS to overcome these problems. They recently loaded gallic acid into MMT, and the adsorption/desorption of the active substance was evaluated in terms of pH and contact time. The measured lower loading capacity of MMT in neutral pH was ascribed to the formation of gallate anions. The authors claimed that, according to thermogravimetric analyses, stronger linkages existed between gallic acid adsorbed at neutral pH than acidic pH. On the other hand, release studies were conducted in simulated human cell fluid at pH 7.4, and no differences were found: ~70% (w/w) of gallic acid was released in 1 h, and total dissolution was obtained after 6 h for both the drug/clay hybrids prepared at acidic and neutral pH values.

Table 6.1 Most Recent Layered Clay/Drugs Combinations as Drug Delivery Systems

	Clay Mineral	Interaction Methodology	Drug	References
Natural MMT	MMT	Intercalation solution	Diclofenac sodium	Kaur and Datta (2014)
			Chlorhexidine	Saha et al. (2014)
			Promethazine	Ambrogi et al. (2014)
			Paclitaxel	Bothiraja et al. (2014)
			Gallic acid	Rabiei et al. (2016)
			Silver, lidocaine	Rangappa et al. (2017)
			Praziquantel	Borrego-Sánchez et al. (2017)
			Metformin	Rebitski et al. (2018)
		Intercalation solution + thermal treatment	Silver and titanium dioxide	Krishnan and Mahalingam (2017)
		Intercalation solution + ALG coating	Mesalazine	Hong et al. (2017)
	Acid-treated MMT	Intercalation solution	Ciprofloxacin	Wu et al. (2017)
			Silver nanoparticles	Phukan et al. (2017)
			Silver nanoparticles	Roy et al. (2017)
Others	MMT-Saponite	Intercalation solution	Tetracycline	Aguzzi et al. (2014a, 2014b)
			Gentamicin	Rapacz-Kmita et al. (2017a, 2017b)
			Theophylline	Trivedi et al. (2018)
	Kaolinite		Ciprofloxacin	Hamilton et al. (2014)
Functionalized	Pillared MMT	Intercalation solution	Nitric oxide	Fernandes et al. (2013)
	Silica pillared MMT		Acetylsalicylic acid	Mao et al. (2014)
			Ibuprofen	Mao et al. (2016)
	Functionalized kaolinite		Doxorubicin	Zhang et al. (2017)

Treatment of first grade burn wounds should be addressed by antibacterial, moisturizing, and analgesic compounds. With this objective, dermal patches made of Na^{+}-MMT, silver, lidocaine, and betaine hydrochloride were prepared (Rangappa et al., 2017). Silver would act as a prophylactic antimicrobial agent, and lidocaine would minimize the pain. MMT would act as a skin smoothening agent and control the release of the drug. *In vitro* results showed that lidocaine was released in considerable and gradual amounts, and was also able to penetrate

the skin due to its lipophilic nature. Nevertheless, the authors claimed that the *in vivo* model used in the study was limited, and further studies are needed to confirm the effectiveness of the clay-based dermal patch (Rangappa et al., 2017).

Metformin, an oral antidiabetic drug, has been recently intercalated in Na^+-MMT to evaluate the usefulness of the resultant system in the control release of the drug (Rebitski et al., 2018). The authors aimed to create a dosage form able to maintain effective doses over prolonged periods to reduce doses and, therefore, side effects. *In vitro* release results showed that drug release depended highly on the pH of the medium, although authors stated the necessity of further studies since the amount of drug released in an acidic environment (pH 1.2) was too high and fast (40%−50% (w/w) total metformin amount released in 2 h).

Silver and titanium dioxide were proposed as useful antibacterial agents with low toxicity levels. These two agents were loaded onto Na^+-MMT by a thermal decomposition method (Krishnan and Mahalingam, 2017). On this occasion, *Staphylococcus aureus* and *Escherichia coli* were chosen as Gram-positive and Gram-negative bacteria, respectively. MMT-Ag-TiO_2 possessed an enhanced antibacterial activity, and the material was more intense against *E. coli* than *S. aureus.*

5-Aminosalicylic acid (mesalazine) is widely used for treating Crohn's disease and ulcerative colitis. Therapeutic amounts of the drug should reach the colon for the treatment to be effective. However, 5-aminosalicylic acid is mainly absorbed in the upper part of the gastrointestinal tract. MMT was used as a mesalazine carrier to prolong the drug release, and the system was then encapsulated in alginate (ALG) beads able to further reduce the drug dissolution in the acidic environment of the stomach (Hong et al., 2017). The MMT-mesalazine system immediately released more than 25% (w/w) of mesalazine in the gastric solution, while ALG-MMT-mesalazine beads released $<5\%$ (w/w) of the total amount of drug in the same medium (Hong et al., 2017).

Acid activation of Na^+-MMT generates pores and discontinuities on the clay layered structure, which effectively improves the clay surface area, along with interlayer charge modifications. MMT, treated with HCl at different concentrations, was evaluated as a ciprofloxacin carrier (Wu et al., 2017). Results showed that acidic treatment allowed a significant reduction of the drug release rate, being slower at a higher HCl concentration during the acid treatment of MMT. This effect was due to the amount of charges in the MMT interlayer spaces: a stronger interaction with ciprofloxacin molecules was established at a higher concentration of HCl, thus retarding the drug release process (Wu et al., 2017). Consequently, this study demonstrated the possibility to control drug release rates by defining the interlayer charge behaviors of a smectite clay (Wu et al., 2017).

In a recent work, silver nanoparticles were loaded in an activated Na^+-MMT by an intercalation process (Phukan et al., 2017). According to the authors, silver nanoparticles were loaded inside the newly formed pores by acid activation of Na^+-MMT. No *in vitro* release studies were performed for this system, although the antibacterial activity was tested against *S. aureus* (Gram-positive) and *Proteus vulgaris* (Gram-negative) bacteria. Bigger inhibition zones were found in the case

of *S. aureus* than for *P. vulgaris*, which led the authors to think a stronger activity of the clay hybrid against Gram-positive bacteria. A similar recent study by Roy et al. (2017) compared the loading capacity and the antibacterial activity of the resultant MMT-silver hybrids by using both non−acid activated Na^+-MMT and acid-activated one. Silver nanoparticle loading capacity of acid-activated MMT was higher than non−acid activated MMT due to an improved cation exchange capacity (CEC) of the acid-activated material. Moreover, in comparison with the non−acid activated system, the acid activated MMT-silver system showed a more effective antibacterial activity against *E. coli* and *S. aureus*, ascribable to the smaller sized silver nanoparticles obtained in the MMT-silver hybrid.

Veegum® HV is a pharmaceutical excipient made of pharmaceutical grade MMT and saponite, and has been used as a tetracycline (antibiotic drug) carrier (Aguzzi et al., 2014a). Successful intercalation of the drug was achieved in the clay minerals. The drug release rate in simulated gingival fluid could allow the use of the resultant drug/clay hybrid as a periodontal extended release system. Chitosan gel was used as mucoadhesive base for application of the hybrid into the periodontal pocket, and the drug release results were compatible with a once-weekly administration regimen (Aguzzi et al., 2014b).

Veegum F is also a pharmaceutical excipient composed of a mixture of natural smectites, specifically saponite and MMT. It was used to load gentamicin, an aminoglycoside antibiotic. Rapacz-Kmita et al. (2017a) studied the intercalation of gentamicin in Veegum F by a solution intercalation method at different temperatures (20°C, 50°C, and 80°C) for 24 h to establish the optimum intercalation conditions. Moreover, they evaluated the antibacterial activity of the resultant composite against *E. coli*. Temperature was demonstrated to have influence on the drug loading efficiency, with 50°C being optimal. All systems provided a sustained release of the drug up to 8 days, and thus high antibacterial effects, according to inhibitory zone tests (Rapacz-Kmita et al., 2017a). The subsequent release study of gentamicin loaded onto Veegum F composite at 50°C showed a fast release within the first 12 h followed by a sustained release until reaching a plateau after 2 days (Rapacz-Kmita et al., 2017b).

Theophylline is a drug used in the treatment of asthma and chronic obstructive pulmonary disease due to its bronchodilator activity. The acidic environment of the stomach induces premature drug absorption and produces variable plasmatic drug levels and undesirable gastric side effects. Theophylline was loaded into Veegum® F with two objectives: avoid gastric drug absorption and perform a sustained drug release once in the intestine (Trivedi et al., 2018). The protonated cationic form of theophylline established electrostatic interactions with the anionic clay layers, which was improved with a drop in pH of the environment. Because of that, no detectable amount of drug was released at pH 1.2 during 72 h. On the other hand, in an alkaline environment, the drug was released in a sustained manner during the whole period (Trivedi et al., 2018).

Kaolin−ciprofloxacin systems showed higher *in vitro* antibacterial activity against *Staphylococcus epidermidis* and *Propionibacterium acnes* compared with

similar ciprofloxacin systems prepared with two synthetic clays (MMT-K10 and Laponite) (Hamilton et al., 2014). The authors ascribed this effect to weaker drug−clay interactions, which allowed easier ciprofloxacin release. No antibacterial effect was shown by kaolinite itself, thus guaranteeing that the antibacterial activity was solely due to the drug.

6.2.2 FUNCTIONALIZED LAYERED CLAY MINERALS

Organic functionalization of smectites is usually carried out by grafting the clay mineral with cationic surfactants (i.e., exchanging the interlayer cations with a quaternary ammonium compound). Another type of functionalization to which Na^+-MMT can be subjected includes the exchange between interlayer Na^+ cations by monomeric cations such as 4-(dimethylamino)-1-(4-vinylbenzyl) pyridinium chloride and 1-methyl-3-(4-vinylbenzyl) imidazolium chloride (Mahkam et al., 2015). These functionalized layered clay minerals have been proposed in MDDS (Table 6.1).

Pillared clays are a type of functionalized layered phyllosilicates characterized by an increased permanent porosity. They are obtained by exchanging interlayered cations by bulky inorganic compounds, which are subsequently calcinated. This technique allows to increase the interlayer space of the clay as well as to create micro and mesoporosity. Consequently, pillarization produces specific surface area enlargement and potential drug adsorption, thus the pillared minerals could hold bulky molecules. A pillared interlayered MMT was synthesized by different procedures and their nitric oxide adsorption/desorption studied (Fernandes et al., 2013). Results claimed that simple MMT pillarization procedures were a promising alternative for nitric oxide storage and release. Pillarization of Ca^{2+}-MMT in the presence of Fe^{2+} and Fe^{3+} led to a product with mesoporous structure and magnetic properties, and the system was loaded with acetylsalicylic acid (Mao et al., 2014). The investigators claimed a sustained release of the drug, which reached its maximum at about 20 h. Magnetic properties of this kind of nanocomposite would permit site-specific releases.

Natural MMT was magnetically functionalized with Fe_3O_4 to create a silica-pillared clay, and ibuprofen was loaded into the composite (Mao et al., 2016). Release profiles under magnetic field influence were compared with release profiles of the corresponding nanocomposites without magnetic influence (Mao et al., 2016). A clear delay in ibuprofen release was measured under magnetic field. This effect was related to the aggregation of the composite under magnetic influence.

Natural kaolin platelets were functionalized with different products to increase the interlayer space of the kaolinite: dimethyl sulfoxide, methanol, 3-aminopropyltriethoxy silane (APTES), medium-chain hexylamine, and long-chain dodecylamine. Then, doxorubicin was loaded by an intercalation method in a phosphate buffer solution (Zhang et al., 2017). All the functionalized kaolinites

loaded over 87% (w/w) of the drug and showed pH-responsive release behavior and therapeutic effect against 10 different cancer cell lines.

6.2.3 LAYERED CLAY/POLYMER NANOCOMPOSITES

Examples of some most recent layered clay mineral/polymer nanocomposites are summarized in Table 6.2. In most nanocomposites, MMT (natural or functionalized) was combined with both natural and synthetic polymers.

Veegum® HS (pharmaceutical excipient made of MMT) was combined with CS as a potential MDDS of 5-aminosalicylic acid (Aguzzi et al., 2010). Results showed an effective interaction between the clay and the polymer. Both components showed to have a synergistic effect over 5-aminosalicylic acid loading and release control (higher loading capacity and slower drug release rate), compared with the corresponding CS/drug and MMT/drug interaction products.

Veegum® HS was also combined with CS to prepare an oxytetracycline carrier (Salcedo et al., 2014). Oxytetracycline is a broad-spectrum bacteriostatic agent that should be administered in high doses to compensate its oral absorption variations. The study by Salcedo et al. (2014) aimed to improve oral bioavailability of the drug. The authors found that permeation rate of the drug through Caco-2 cell cultures proceeded linearly and constantly. Moreover, cellular internalization of the nanocomposite was found, which suggested that the absorbed drug was able to elude the efflux transporter P-glycoprotein system, thus improving oxytetracycline oral bioavailability.

CS/Na^+-MMT films were proposed as chlorhexidine release systems (Ambrogi et al., 2017). The authors studied how to reduce chlorhexidine cytotoxicity to human fibroblasts and to perform a topical controlled release of the drug. Prepared films performed a sustained release. MMTs presence in clay−polymer composites induced a reduction of the drug release profile and burst release step. Cytotoxicity results were in agreement with the dissolution profile, and sustained release composites were not cytotoxic. Moreover, toxicity was correlated with the amount of loaded drug in the system.

Silver sulfadiazine is the main drug to treat topical burns. Nonetheless, cytotoxicity was reported, which delays the wound healing processes. In an attempt to reduce this drawback, silver sulfadiazine was successfully loaded into Veegum©HS/CS glutamate composites (Aguzzi et al., 2014a). Electrostatic interactions between the cationic polymer and MMT were reported. The presence of the drug in the nanocomposite was confirmed by high-resolution transmission electron microscopy (TEM) and elemental analysis. Both biocompatibility and *in vitro* wound healing properties of this nanocomposite were assessed and confirmed (Sandri et al., 2014). Additionally, antimicrobial activity of the drug was not affected but actually improved against *Pseudomonas aeruginosa*.

Guar gum, a galactomannan biopolymer extracted from the guar plant's seeds, was proposed as a nanocomposite ingredient with MMT to control the delivery of ibuprofen (Dziadkowiec et al., 2017). Nanocomposites provided a slow release

Table 6.2 Most Recent Layered Clay/Polymer Nanocomposites Used in Drug Delivery

	Components	Interaction Methodology	Drug	References
Natural MMT	MMT/CS	Intercalation solution	Mesalazine	Aguzzi et al. (2010)
			Oxytetracycline	Salcedo et al. (2014)
			Chlorhexidine	Ambrogi et al. (2017)
	MMT/CS-glutamate		Silver sulfadiazine	Aguzzi et al. (2014a)
			Silver sulfadiazine	Sandri et al. (2014)
	MMT/Guar gum		Ibuprofen	Dziadkowiec et al. (2017)
	MMT/ALG	Ionotropic gelation	Venlafaxine	Jain and Datta (2016)
	MMT/ALG/XG	Intercalation solution	Olanzapine	Oliveira et al. (2017)
	MMT/CMC		Curcumin	Madusanka et al. (2015)
	MMT/PC/MC		Ketorolac	Saha et al. (2016)
	MMT/PLLA		6-Mercaptopurine	Kevadiya et al. (2013)
	MMT/P(AAm-MA)		Caffeine	Dadkhah et al. (2014)
	MMT/polyamide		Diazoles	Salahuddin et al. (2014)
	MMT/silica based copolymers		Doxorubicin, methotrexate, ciprofloxacin	Bazmi-Zeynabad et al. (2015)
	MMT/PLGA	Emulsion solvent evaporation	Dexamethasone	Jain and Datta (2015)
			Atenolol	Lal and Datta (2015)
			Insulin	Lal et al. (2017)
	MMT/PCLA-PEG-PCLA	Intercalation solution	Gemcitabine	Phan et al. (2016)
	MMT/PLA	Nanoprecipitation	Paracetamol	Othman et al. (2016)
	MMT/HEMA	*In situ* radical polymerization	Paracetamol	Bounabi et al. (2016)
	MMT/PEG750/5000-PE	Intercalation solution	Doxorubicin	Kohay et al. (2017)

Functionalized MMT	Organomodified MMT/Epoxy resin	*In situ* reduction	Copper nanoparticles	Das et al. (2014)
	Organomodified MMT/MAA	Intercalation solution	Naproxen	Mahkam et al. (2015)
	Organomodified MMT/PCL	Nanoprecipitation	Curcumin	Bakre et al. (2016)
	Organomodified MMT/PVP K30	Intercalation solution	Copaiba oil resin	de Almeida-Borges et al. (2016)
Others	MMT-Saponite/CS	Casting/solvent evaporation	Nicotine	Pongjanyakul et al. (2013)
	Kaolinite/urea/chlorhexidine	Intercalation solution	Chlorhexidine	Holešová et al. (2014)
	Kaolinite/PVP/sodium lauryl sulfate	Intercalation solution	Heteropolyoxometalate of tungsten	Bayaumy and Darwish (2016)
	HNT/PVA/CS	Swelling	5-Fluorouracil	Reddy et al. (2016)

rate of the drug, which could be useful in reducing ibuprofen side effects in the intestinal tract. Burst releases were also reduced by these formulations.

Sodium ALG was crosslinked with venlafaxine and MMT in $CaCl_2$ to obtain beads (Jain and Datta, 2016). Venlafaxine is a third generation antidepressive drug. The posology involves the administration of 2–3 daily doses, compromising patient compliance. MMT/ALG provides no more than 25% of venlafaxine released within 30 h in both media. Prolonged release was definitely obtained, although the amounts of drug released could be considered to be low.

ALG and xanthan gum (XG) were used to entrap sodium Cloisite®/olanzapine hybrids (Oliveira et al., 2017). Olanzapine is a poorly water soluble and highly permeable drug used in schizophrenia and bipolar disorder. Release profile of the drug was compared with a commercial tablet, ALG–XG/olanzapine beads, and ALG–XG/Cloisite/olanzapine beads at different pHs (Fig. 6.2). Commercial tablet showed a fast and complete release of drug within 30 min at acidic pH. ALG–XG/olanzapine beads showed remarkable olanzapine controlled release, reaching 100% (w/w) at 6 h. The addition of Cloisite allowed an even more marked control of drug release. This complex material utilizes the Cloisite-OLZ and the biopolymer blend of ALG–XG to produce a more controlled release of OLZ.

Curcumin, extracted from the rhizome of *Curcuma longa*, is widely used as a food spice. It was demonstrated to have antibacterial, antioxidant, antiinflammatory, and anticancer properties. Curcumin aqueous solubility in acidic/neutral pH

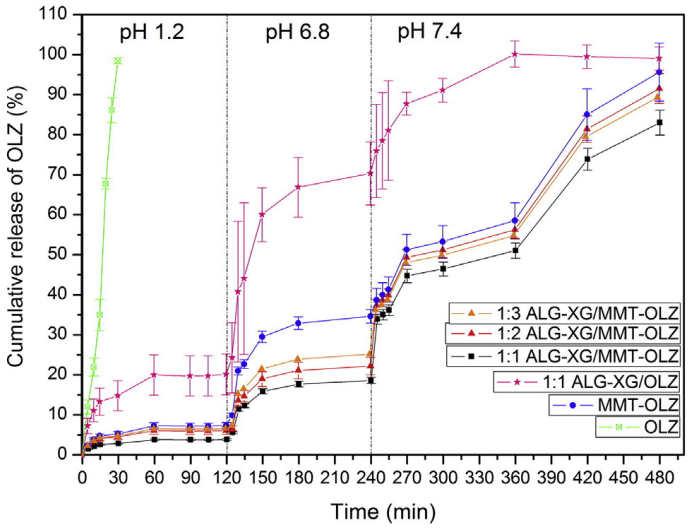

FIGURE 6.2

Cumulative release of olanzapine from hybrid materials at different pH values.

Figure extracted from Oliveira, A.S., Alcântara, A.C.S., Pergher, S.B.C., 2017. Bionanocomposite systems based on montmorillonite and biopolymers for the controlled release of olanzapine. Mater. Sci. Eng. C, 75, 1250–1258.

is remarkably low. Curcumin dispersed in carboxymethyl cellulose (CMC) was intercalated in MMT (Madusanka et al., 2015). The presence of CMC improved the dispersion of curcumin in aqueous environments prior to its intercalation into MMT. Despite curcumin's low solubility in acidic medium, the release rate of the drug in acidic pH conditions was significantly increased from the MMT/CMC nanocomposite.

Nanocomposite films made of MMT, methyl cellulose and pectin in different proportions were prepared by Saha et al. (2016). Ketorolac (an NSAID) was loaded on these films aiming to prepare a transdermal DDS. All the formulations performed ketorolac burst releases ascribable to the amount of drug located on the surface of the nanocomposite films. Nevertheless, the release rate decreased as the amount of MMT increased, thus demonstrating the useful effect of the clay mineral in terms of controlled release.

The anticancer drug 6-mercaptopurine was successfully intercalated into Na^+-MMT prior to the formation of poly(L-lactide) acid (PLA) microspheres (Kevadiya et al., 2013). Microspheres containing MMT performed faster and had higher release rate of 6-mercaptopurine in comparison with microspheres prepared without MMT. The authors ascribed this behavior to the low permeability of the polymer and low water solubility of the drug. Moreover, the presence of the clay mineral controlled drug release, as well as improved 6-mercaptopurine water solubility.

Poly(acrylamide-*co*-maleic acid) is a synthetic polymer considered to have a pH-dependent swelling behavior (higher swelling at higher pH). This system would allow pH-dependent drug release when used as a drug carrier. Drug release mechanism was sensitive to hydrogel composition and was swelling-controlled for low concentrations of poly(acrylamide-*co*-maleic acid) and showed Fickian diffusion for high concentrations of the polymer (Thakur et al., 2012). In an attempt to improve poly(acrylamide-*co*-maleic acid) performance, MMT was added during *in situ* polymerization and caffeine loading/release was evaluated (Dadkhah et al., 2014). The authors claimed that the addition of small amounts of MMT ($<5\%$, w/w) exerted a significant control during caffeine release, especially when pH of the release medium was changed from gastric to intestinal conditions. Burst release effect during pH change was also reduced.

1,3,4-Oxa(thia)diazoles were loaded into polyamide, and subsequently intercalated into Na^+-MMT by ion exchange process (Salahuddin et al., 2014). Diazole derivatives are very versatile molecules in terms of therapeutic activities, since they can act as antibiotic, vasodilator, antifungal, cytotoxic, antiinflammatory, and analgesic agents. *In vitro* release studies indicated that the resultant nanocomposites could be used as prolonged oral DDSs. Antimicrobial activity results were contradictory since no antimicrobial activity was detected *in vitro*, while *in vivo* experiments produced good results (Salahuddin et al., 2014).

Two anticancer drugs, doxorubicin and methotrexate, together with the antibacterial molecule ciprofloxacin were combined with a silica based polymer/Na^+-MMT to create a nanocomposite able to perform a site-specific release, mainly

determined by the acidic pH of tumors (Bazmi-Zeynabad et al., 2015). Burst releases were minimal in all *in vitro* release tests performed. Methotrexate and doxorubicin performed similar release profiles at pH 4 and 5.8 reaching ~80%–100% w/w of drug release within 25 days. In this period, the three drugs evaluated performed a prolonged release at pH 7.4, and ~20% (w/w) of total amount of drug was released. The difference between ciprofloxacin release profile at pH 5.8 and 4 was very distinct: at pH 5.8, the total amount of drug released within the total time lapse was less than 40% (w/w), whereas at pH 7.4 was less than 20% (w/w), and at pH 4 was close to 100% (w/w).

Poly(lactic-*co*-glycolic) acid (PLGA) is a safe, biodegradable, and biocompatible polymer extensively used and approved by the Food and Drug Administration. PLGA/MMT were used as carriers of both dexamethasone (Jain and Datta, 2015) and atenolol (Lal and Datta; 2015). Atenolol molecule has short half-life and low intestinal permeability leading to low oral bioavailability and variable plasma concentrations during long-term treatments. An MDDS able to maintain effective doses of the drug for longer time would minimize the aforementioned problems. Atenolol was emulsified with PLGA, and then added to MMT to form a double emulsion (w/o/w) followed by solvent evaporation (Lal and Datta, 2015). Results showed the effective intercalation of PLGA-atenolol inside MMT layers in combination with a partial MMT exfoliation. In comparison with pure atenolol and commercial formulation, the MMT-PLGA-atenolol nanocomposites reduced the dissolution rate of the active substance in both acidic and alkaline media. In particular, the strongest change occurred in the acidic medium, where no burst release was reported (4% (w/w) of atenolol released within 30 min) (Lal and Datta, 2015). The authors postulated that the presence of MMT imposed a longer path through which drug molecules should migrate before their release, thus explaining the modification in release profiles (Lal and Datta, 2015). Dexamethasone is a hydrophobic molecule, which clearly hinders its aqueous solubility. High doses are therefore required to achieve effective plasma concentration, and side effects such as osteoporosis can be encountered during long-term treatments of rheumatoid arthritis or bronchospasm. Emulsion solvent evaporation was used to intercalate the drug within MMT interlayer spaces in MMT/PLGA nanocomposites (Jain and Datta, 2015). *In vitro* drug release studies showed a high influence of the clay mineral during the dissolution of the active substance. The drug released steadily at acidic pH values, with a less remarkable burst effect in comparison with the pure drug, and reached 100% (w/w) before 25 h. Dissolution profile in simulated intestinal fluid reached approximately 60% (w/w) of total release in 30 h. No burst release was observed under these conditions, which strongly contrasted with pure dexamethasone (Jain and Datta, 2015).

The acid stability of MMT and its mucoadhesive properties could be useful to protect labile molecules such as proteins. A double emulsion solvent evaporation procedure was used to load insulin in MMT/PLGA nanocomposites (Lal et al., 2017). Successful intercalation of the drug was obtained according to XRD results, and the loaded nanocomposites did not influence the normal growth on

HEK-293 cells. *In vitro* release studies showed that the presence of the clay mineral induced more sustained release profiles: insulin should travel a longer path before its dissolution. The amount of insulin released was higher in simulated intestinal fluid than in simulated gastric fluid, demonstrating the potential protective role of MMT (Lal et al., 2017).

Gemcitabine is an anticancer drug widely used in the treatment of solid tumors. It possesses a short half-life due to a fast metabolism, meaning frequent and high doses were needed. Among all strategies proposed within the past few years, intercalation of gemcitabine into MMT was found to be an effective way to control the drug release. In particular, a gemcitabine-MMT composite was combined with PCLA−PEG−PCLA triblock copolymer hydrogel to make it compatible with intravenous administration as well as to reduce side effects (Phan et al., 2016). The presence of MMT in the nanocomposite significantly controlled the release of the anticancer drug by reducing burst release. *In vivo* experiments showed that therapeutic concentrations were maintained for several days, and this suppressed tumor growth without remarkable side effects.

Commercial organomodified MMT Cloisite 30B was combined with poly(D,L-lactide) to form nanoparticles able to carry and release paracetamol. During this synthesis, microfluidic mixing/precipitation was used (Othman et al., 2016). PLA is considered to be biodegradable and bioresorbable inside the human body. This composite was synthesized by mixing aqueous and organic phase in a glass capillary device. The inclusion of MMT increased the size of the resulting nanoparticles and improved the amount of drug encapsulated. In all cases, a burst release occurred, due to the high solubility of the drug in aqueous solution, followed by a very slow release, which was more pronounced as a higher proportion of clay was added (Othman et al., 2016).

Paracetamol dissolution profile was also intended to be modified by Na^+-MMT/poly(2-hydroxyethyl methacrylate) (HEMA) nanocomposite (Bounabi et al., 2016). Combination of HEMA with MMT significantly decreased the burst release in comparison with the HEMA/paracetamol formulation.

PEG750/5000-PE polymer was combined with doxorubicin and then loaded over Na^+-MMT (Kohay et al., 2017). As these nanocomposites were thought to be site-specific release systems, nanocomposite cellular internalization was tested. Polymers delayed the internalization but improved cytotoxicity due to the interruption of the P-gp pumps, which expel the drug outside of the cell.

Nanocomposites prepared with octadecylamine functionalized MMT and an epoxy resin were coated with copper nanoparticles by Das et al (2014). Enhanced antibacterial activity of the obtained material was thus reported.

Functionalized MMT was polymerized with methacrylic acid, and naproxen was chosen as a drug model to evaluate drug loading capacity and release profiles. In acidic pH, all composites prepared showed a naproxen release $<30\%$ (w/w). On the other hand, at pH 7.4, the nanocomposite acquired a deprotonated stage, which generated electrostatic repulsions with the drug, thus explaining a higher release rate (Mahkam et al., 2015).

A organomodified MMT (*n*-cetyl-*N,N,N*-trimethylammonium bromide) was combined with PCL to obtain a nanocomposite. Curcumin was included, and release studies were done in simulated intestinal fluid (Bakre et al., 2016). The MMT ratio in the nanocomposite influenced the amount of drug released in an indirect manner (the higher the MMT proportion, the lower the amount of curcumin released).

Copaiba oleoresin (COPA) is a natural molecule obtained from *Copaifera langsorffi* able to reduce cyst size and increase apoptosis in endometrial explants. It is widely used in Brazil to treat endometriosis. Organomodified commercial MMT was combined with polyvinylpyrrolidone (PVP) K-30 to encapsulate COPA (de Almeida-Borges et al., 2016). Nanocomposites showed a burst release profile, ascribable to the presence of adsorbed COPA to the nanocomposite surface. At acidic pH (1.2), the amount of COPA dissolved was ~60% (w/w) within 15 min, and increased progressively during the rest of the test.

Veegum® HV was used to obtain nanocomposites with CS (Pongjanyakul et al., 2013). A direct relationship between the amount of clay and the nicotine loading capacity of the composites was found. Moreover, the presence of the clay was the main factor controlling the release profile of the drug. More particularly, as the ratio of clay increased in the composite, the mucosal permeation rate of the drug decreased.

One of the kaolinite optimization strategies to intercalate bulky substances inside kaolinite platelets is the use of polar molecules to expand the clay, and therefore, break the interlayer hydrogen bonds. With this method Holešová et al. (2014) prepared an antibacterial kaolinite/urea/chlorhexidine system. Minimum inhibitory concentration after antibacterial tests revealed that the hybrid provided an improved antibacterial effect: less concentration of chlorhexidine was needed to produce the same growth inhibition in comparison with the pure drug.

PVP and sodium lauryl sulfate were used to exfoliate and functionalize kaolinite clay platelets. Then, heteropolyoxometalate of tungsten (HPW) was added as an active substance to treat schistosomiasis (Bayaumy and Darwish, 2016). *In vitro* HPW release occurred in a sustained manner and pilot *in vivo* studies results were also promising.

5-Fluorouracil is a rapidly metabolized drug and its oral absorption is very variable. 5-Fluorouracil was recently encapsulated in a polymeric composite made of polyvinyl alcohol (PVA), CS, and MMT (Reddy et al., 2016). Results indicated that the higher was the amount of clay in the composite, the higher was the loading efficiency and the fraction of drug released.

6.3 TUBULAR AND FIBROUS CLAY MINERALS

Halloysite (Hal) is a clay mineral of the kaolin group, with dioctahedral 1:1 structure. In terms of chemistry, halloysite composition is the same as kaolinite though

water is present between halloysite monolayers, thus it is known as the hydrated kaolinite phase (Brigatti et al., 2006). Hal particles can adopt different morphologies such as tubes, fibers, spheres, plates, laths, etc. The tubular morphology of halloysite is the most common one. Tube dimensions range from 0.2 to 2 μm in length; inner and outer diameters range from 10 to 40 nm and 40 to 70 nm (Liu et al., 2014). They are considered biocompatible, naturally abundant, and environmentally friendly materials. Tubular conformation causes aluminols (Al-OH) groups normally located in the interior of the tubes, while most of the silanols (Si-O-Si) are located in the outer part. This particularity explains why the outer surface of halloysite nanotubes is negatively charged and the inner surface is positive. The charges maintain at physiological pH (>2) (Qi et al., 2013; Tu et al., 2013). Hal nanotubes (HNTs) shape and properties make them very versatile in terms of drug carrying and drug release applications, including proteins as active substances (Lvov et al., 2014, 2016a,b; Aguzzi et al., 2016; Ariga et al., 2017; Minullina et al., 2017; Yendluri et al., 2017a). These substances can also be loaded into the lumen of HNTs under vacuum or using immersion techniques. HNTs have numerous advantages benefiting their interactions with chemically and biologically active molecules. Nevertheless, functionalizing HNTs could exert a huge difference to enhance their final properties, making them even able to interact with polymers and to form diverse nanocomposites. Functionalization processes could, however, reduce the biocompatibility, something that should be checked before human administration.

Besides HNTs, some other ribbon-shaped clay minerals are also used in drug delivery. In particular, fibrous phyllosilicates [palygorskite (Pal) and sepiolite (Sep)] show inverted tetrahedral arrangements that form ribbons and discontinuous octahedral sheets (Guggenheim and Krekeler, 2011). The resultant zeolitic channels are 3.7×6.4 Å (Pal) and 3.7×10.6 Å (Sep) in diameter. Their use in drug delivery was reviewed previously (López-Galindo et al., 2011; Viseras et al., 2015).

In the following sections, the most recent progress in the use of tubular and fibrous clay minerals as advanced excipients in MDDS will be reviewed (Table 6.3) along with the nanocomposites prepared with these clay minerals (Table 6.4).

6.3.1 NATURAL TUBULAR AND FIBROUS CLAY MINERALS

5-Amino salicylic acid was encapsulated inside HNTs and over the nanotube surfaces (Viseras et al., 2008, 2009). The release of the drug was fitted to a novel kinetic model based on drug adsorption−desorption equilibrium. The superficially adsorbed drug released faster, while the drug located in the lumen of the tubes performed a more controlled and progressive release (Aguzzi et al., 2013).

Wang et al. (2014a) evaluated the effect of acid and heat treatment of HNTs and the influence of these treatments over ofloxacin loading and release behaviors. Under acidic conditions, HNTs maintained their crystallinity, though

Table 6.3 Most Recent Tubular and Fibrous Clays/Drugs Combinations as Drug Delivery Systems

	Clay Mineral	Methodology	Active Pharmaceutical Ingredient	References
Natural	HNT	Intercalation solution	5-Aminosalycilic acid	Viseras et al. (2008, 2009) and Aguzzi et al. (2013)
			Ofloxacin	Wang et al. (2014a)
			Tetracycline, ciprofloxacin, chlorpheniramine, diphenhydramine	Jiang et al. (2016)
			Isoniazid	Carazo et al. (2017b)
			Binase	Khodzhaeva et al. (2017)
		Vacuum cycle	Breviscapine	Gao et al. (2017)
		Intercalation solution, vacuum cycle	Vancomicin	Pan et al. (2017)
		Vacuum cycle + PLGA coating	Tetracycline hydrochloride	Qi et al. (2010, 2013)
		Vacuum cycle + CS/PLGA coating	Amoxicillin	Tohidi et al. (2016)
		Vacuum cycle + PMMM coating	Paclitaxel	Yendluri et al. (2017a)
	Pal	Intercalation solution	Ofloxacin	Wang et al. (2014b)
			Isoniazid	Carazo et al. (2017c)
		Vapor intercalation	Carvacrol	Tenci et al. (2017)
	Sep	Intercalation solution	Praziquantel	Borrego-Sánchez et al. (2017)
	Pal or Sep	Melting intercalation + CD coground	Oxaprozin	Mura et al. (2016)

Functionalized	Triazole-functionalized HNT	Intercalation solution	Curcumin	Riela et al. (2014)
	APTES-functionalized HNT		Silver	Zhang et al. (2013)
			Silver nanoparticles	Jana et al. (2017)
			Ibuprofen	Tan et al. (2014)
			Vancomycin	Kurczewska et al. (2017)
		Vacuum cycle	Metronidazole	Xue et al. (2015)
	APTES-functionalized HNT/ALG/CS	Vacuum cycle	Ibuprofen	Li et al. (2016b)
	Thiol-functionalized HNT	Vacuum cycle, intercalation solution	Silibin, curcumin	Massaro et al. (2016a)
	Cysteamine hydrochloride-functionalized HNTs	Chemical reactions	Curcumin	Massaro et al. (2016b)
	AZPES-functionalized HNT	Condensation, vacuum cycle	Trolox, quercetin	Massaro et al. (2016c)

Table 6.4 Most Recent Tubular and Fibrous Clay/Polymer Nanocomposites Used in Drug Delivery

	Clay Mineral	Interaction Methodology	Drug	References
Natural	HNT/CS	Intercalation solution	Doxorubicin	Yang et al. (2016b)
			Aspirin	Li et al. (2016a)
			Chitosan	Sandri et al. (2017)
	HNT/Cellulose		Curcumin	Huang et al. (2017)
	HNT/ALG, HNT/ALG/Gelatin		Vancomycin	Kurczewska et al. (2017)
	HNT/PEGm		Hydrocortisone	Ghebaur et al. (2016)
	HNT/PEGdm		Hydrocortisone	Ghebaur et al. (2016)
	HNT/PC	Vacuum cycle	Rosemary essential oil	Gorrasi (2015)
	HNT/hyaluronate/poly(HEMA)		5-Fluorouracil	Rao et al. (2014)
	HNT/PLL/PAA	Intercalation solution and vacuum cycle	Curcumin	Dionisi et al. (2016)
	HNT/PVA		Sodium D-pantothenate	Lee et al. (2016)
	HNT/HPMCAS	Immersion	Atorvastatin	Li et al. (2017)
			Celecoxib	Li et al. (2017)
	HNT/ SBMP resin	Vacuum cycle	Doxycycline	Feitosa et al. (2014) and Palasuk et al. (2017)
	HNT/PEI	Self-assembly	pDNA	Long et al. (2017)
	HNT/LIP	Intercalation solution	Doxorubicin	Li et al. (2018)
	Pal/CS	Adsorption/entrapment	Diclofenac sodium	Wu et al. (2014)
		Intercalation solution	5-Aminosalicylic acid	Santana et al. (2017)
	Pal/PPy	*In situ* electropolymerization	Aspirin	Kong et al. (2014)
	Sep/CS	Intercalation solution	Tetracycline	Gür et al. (2015)
	Sep/CS/PVA		Cefazolin	Mahdavinia et al. (2016)
Functionalized	APTES-functionalized HNT/CS		Curcumin	Liu et al. (2016)
	AZPES-functionalized HNTs/Fmoc-F	Vacuum cycle	Camptothecin	Rizzo et al. (2017)

exchangeable cations were leached as HCl concentration increased. This caused weaker electrostatic interactions with ofloxacin, which led to a faster drug release. Temperatures higher than 400°C caused dehydroxylation of aluminol groups, leading to a decrease in the drug adsorption capacity and faster drug release.

Drug loading capacities of HNTs and the mechanisms influencing drug loading processes of tetracycline, ciprofloxacin, chlorpheniramine, and diphenhydramine were investigated by Jiang et al. (2016). CEC was determined to be the main factor controlling the drug loading. The pH of the medium influenced the drug loading process since it determined the ionization of the active substances (Jiang et al., 2016).

Recent studies performed by Carazo et al. (2017a,b) explored the equilibrium and thermodynamic aspects of isoniazid adsorption onto HNTs. Isoniazid is one of the first-line drugs used to treat tuberculosis. Its presence on HNTs was confirmed by a fully comprehensive TEM study coupled with energy dispersive X-ray analysis (Fig. 6.3). It was also shown that the isoniazid loading process occurred spontaneously since it increased the thermodynamic stability of the resultant system.

Specific anticancer treatments are focused on genetic treatments. Binase is an RNase enzyme of *Bacillus pumilus*, which triggers apoptosis in cancer cells expressing rat sarcoma oncogene. The inmobilization of the enzyme in HNT and the resultant activity were studied by Khodzhaeva et al. (2017). Optimal HNT−binase ratio was worked out and the resultant anticancer activity reported to be enhanced by the complex.

Unmodified HNTs were proposed as a potential sustained DDS of breviscapine, a short half-life, natural cerebrovascular drug extracted from *Erigeron breviscapinus*. The drug was loaded inside HNTs lumen by vacuum cycles, and *in vitro* phosphate buffer release was tested (Gao et al., 2017). HNT-breviscapine nanocomposite showed a slight reduction of the initial burst effect. Another drug vancomycin was loaded within the lumen of HTNs applying vacuum cycles (Pan et al., 2017). The resultant system released drug during a period of 33 days (a burst release occurred within the first 3 days). High antibacterial activity was also reported during the whole period against *S. aureus* and *B. streptococcus* (Pan et al., 2017).

A double drug loading process involving vacuum was used to load tetracycline and amoxicillin on HNTs, which were then coated with PLGA and CS polymers by electrospun technique (Qi et al., 2010, 2013; Tohidi et al., 2016). Qi et al. (2010, 2013) reported that the cationic form of the drug, tetracycline hydrochloride, in solution interacted with the negative outer surface of HNTs, but it could also enter within the positively charged lumen of HNTs due to the applied vacuum during the drug loading process. The influence of the dissolution medium in which the drug and the clay mineral interacted with each other was crucial in terms of drug loading efficiency and release kinetics. In both experiments, the combination of PLGA and HNT allowed a sustained drug release since the initial burst weakened and no plateau was reached during the

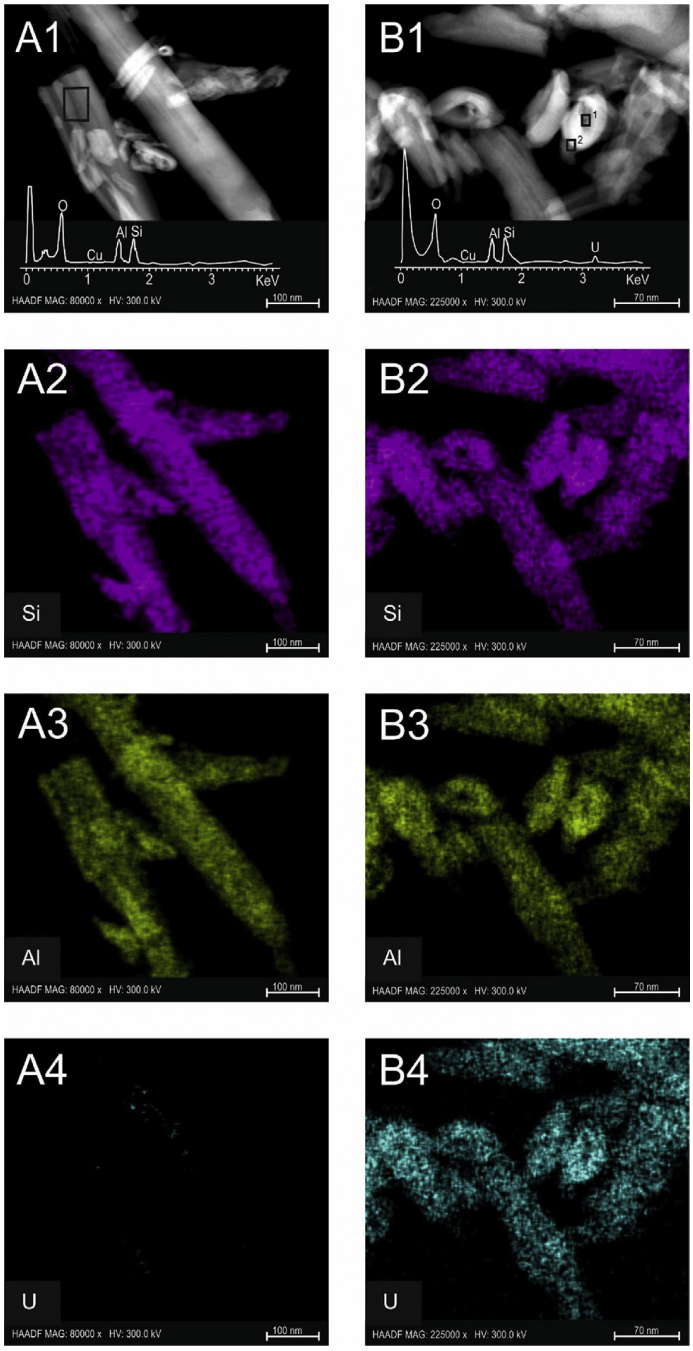

FIGURE 6.3

Ultrahigh-resolution transmission electron microscopy, energy dispersive X-ray spectroscopy (XEDS), and X-ray maps of unloaded HNTs (A) and HNTs loaded with isoniazid (B).

Figure extracted from Carazo, E., et al., 2017b. Assessment of halloysite nanotubes as vehicles of isoniazid. Colloids Surf. B Biointerfaces, 160, 337–344.

experiment (Qi et al., 2010, 2013). The combination of PLGA and CS with HNT-amoxicillin achieved via electrospun technique supported the aforementioned results in terms of controlled release behavior (Tohidi et al., 2016). The authors highlighted the performance of HNT during amoxicillin release: CS and PLGA released amoxicillin faster than HNT-amoxicillin and HNT−CS−PLGA formulations. Burst release was remarkably prevented with the two latter formulations, confirming the importance of the clay mineral in the controlled delivery system.

Paclitaxel-loaded HNTs were coated with poly(methyl methacrylate-*co*-methacrylic acid) as a pH-responsive polymer (Yendluri et al., 2017b). An increase in pH produced a triggered drug release, and a high therapeutic anticancer effect was observed for the aforementioned hybrid.

Palygorskite (Pal) particles interact with each other due to van der Waals forces (interparticle forces) forming aggregates. This property could limit Pal's usefulness in drug delivery due to a reduction of the effective surface available to interact with organic molecules. Freeze-drying was proposed to reduce such particle aggregation problems (Wang et al., 2014b).

Adsorption of isoniazid active substance onto Pal was performed by Carazo et al. (2017c). The antimicrobial molecule interacted through hydrogen bonds with superficial OH groups on the clay mineral surface and zeolitic water inside Pal channels. Isoniazid retention capacity in Pal increased as intercalation temperature increased.

Carvacrol is a natural, volatile, phenolic compound extracted from *Origanum vulgare* essential oil. Its antioxidant, antifungal, and antimicrobial properties make it useful for the treatment of infected skin lesions. To prevent carvacrol evaporation, its adsorption into MMT, HNT, and Pal was evaluated, and Pal showed the highest drug loading and prevented its evaporation without hindering its therapeutic activities (Tenci et al., 2017).

Praziquantel is used as a first-line drug in the treatment of schistosomiasis, and it possesses low water solubility and high permeability. Veegum HS and sepiolite were combined with praziquantel by Borrego-Sánchez et al. (2017). The resultant hybrids improved drug dissolution profiles both in acidic and basic environments (Fig. 6.4). The total amount of drug dissolved increased by 20% (w/w) with respect to the pristine praziquantel phosphate buffer dissolution profile. In acidic medium, the total amount of drug dissolved did not improve, although a high dissolution rate was found: ∼50% (w/w) of total amount of drug was dissolved in less than 20 min compared with ∼20% (w/w) in the case of pure praziquantel (Borrego-Sánchez et al., 2017).

Oxaprozin is an NSAID molecule used in the treatment of inflammatory disorders, typically osteoarthritis and rheumatoid arthritis. Oxaprozin bioavailability is hindered by its low solubility and permeability. Hybrids of Pal or Sep with modified cyclodextrins were proposed by Mura et al. (2016) as dissolution enhancers of oxaprozin. The combination of cyclodextrin with the clay minerals allowed to achieve higher oxaprozin dissolution rates.

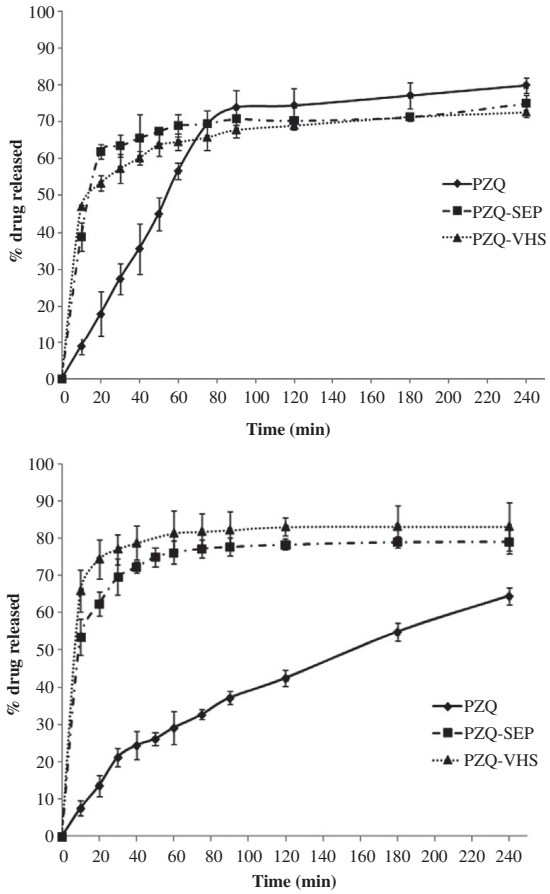

FIGURE 6.4

Praziquantel *in vitro* drug release profiles in HCl (up) and simulated intestinal fluid (down) from sepiolite, Veegum HS composites, and pure praziquantel.

Figure extracted from Borrego-Sánchez, A., et al., 2017. Biopharmaceutical improvement of praziquantel by interaction with montmorillonite and sepiolite. Appl. Clay Sci.

6.3.2 FUNCTIONALIZED TUBULAR AND FIBROUS CLAY MINERALS

HNTs functionalized with triazolium salts were proved to perform site-specific drug delivery of curcumin (Riela et al., 2014). Results demonstrated that curcumin was preferentially adsorbed over functionalized HNT surfaces, though small amounts were also detected inside the nanotube lumen. The release highly depended on the pH: higher and faster release at lower pH of the medium. In acidic environment, both curcumin and triazolium-functionalized HNTs acquired positive charges, which caused repulsion and promoted curcumin release (Riela et al., 2014).

Trimethoxy(propyl)silane and triethoxy(octyl)silane were used to functionalize HNTs (Sánchez-Fernández et al., 2014). Biocompatibility and cytotoxicity were

tested on C6 Rat glioblastoma cells. HNTs were biocompatible, but functionalized materials induced cell apoptosis, probably due to the nature of the functionalizing organosilanes selected. Consequently, functionalization conditions should be carefully selected to obtain the desired HNT performances, and further studies are needed in this area.

HNT modified with [3-(2-aminoethyl) aminopropyl] trimethoxysilane was used to carry and release silver nanoparticles by electrostatic interactions over the surface of the clay mineral (Zhang et al., 2013). The higher antibacterial activity of Ag loaded HNTs compared with pure Ag nanoparticles could be related to the homogeneous dispersion of Ag particles over halloysite surfaces, which led to superior specific surface area, hence better antibacterial properties (Zhang et al., 2013). APTES allowed to immobilize silver nanoparticles over the surface of HNTs, giving resultant antibacterial activity against *E. coli*, as reported by Jana et al. (2017). APTES-modified HNTs also carried ibuprofen drug, which was located both in the lumen and onto the external surface of nanotubes, in its crystalline form (Tan et al., 2014). In unmodified HNTs, ibuprofen established hydrogen bonds; while in APTES-HNT the drug interacted stronger due to electrostatic bonds. These divergences explained the slow release rate performed for ibuprofen from APTES-HNTs (up until 50 h) (Tan et al., 2014). Coating through layer-by-layer technique of drug-APTES-HNT hybrids with CS and ALG extended ibuprofen release for longer than 110 h with a first-order release kinetic (Li et al., 2016b). Xue et al. (2015) also functionalized HNT with APTES to be used as an ingredient in the formulation of guided tissue regeneration/guided bone regeneration membranes. Electrospinning technique was used to synthesize the membrane, and metronidazole was selected as an antibacterial drug aiming to prevent infections of anaerobic microorganisms. Hal improved the mechanical properties of the film, allowed further sustained release and reduced the initial burst (Xue et al., 2015).

Vancomycin was also loaded on HNTs previously functionalized with APTES (Kurczewska et al., 2017). In comparison with nonmodified HNT and acid-activated HNT carrying vancomycin, the APTES-functionalized clay mineral avoided burst release effect and provided a prolonged release of drug for more than 70 h. This result could be justified by the strong electrostatic interactions established between vancomycin and functionalized-HNT.

Cyclodextrins, cyclic oligosaccharides composed of α-D-glucopyranose units, and functionalized HNTs were combined as dual drug-loaded systems for silibinin and curcumin. Both drugs are anionic molecules, and silibinin was loaded inside HNTs, while curcumin was located inside the cyclodextrin to improve its water solubility. The complex nanohybrid showed antiproliferative activity as well as high propensity to cross the cell membranes and performed a site-specific release (Massaro et al., 2016a). Curcumin was also bonded to HNT surfaces, thanks to HNTs functionalized with cysteamine hydrochloride, thus providing imine bonding with curcumin molecules (Massaro et al., 2016b). HNTs increased curcumin stability in alkaline/basic environment and lowered drug release rates. Due to the disulfide bond established between HNTs and curcumin, the drug release

significantly increased in acidic and glutathione rich environments. These latter conditions corresponded to the typical microenvironment of cancer cells (Massaro et al., 2016b).

Trolox and quercetin, typically used as potent antioxidants, were loaded into HNT after surface functionalization of the clay nanotubes (Massaro et al., 2016c). Particularly, functionalization was started by 3-azidopropyltrimethoxysilane reaction (AZPES). Once the functionalization was performed, trolox reacted by condensation and formed an amide bond in the external surface of HNTs. Subsequently, quercetin was loaded into the clay lumen by vacuum cycles (Massaro et al., 2016c). The antioxidant activity improved significantly due to synergistic effects between trolox and quercetin. Moreover, the presence of quercetin in HNT lumens implied a controlled release of this substance, hence a prolonged antioxidant activity.

6.3.3 TUBULAR AND FIBROUS CLAY–POLYMER NANOCOMPOSITES

CS-grafted HNTs were loaded with doxorubicin (Yang et al., 2016b) and curcumin (Liu et al., 2016). The functionalization of HNTs with APTES and its combination with CS allowed higher adsorption capacities of hydrophobic drugs such as curcumin (Liu et al., 2016). Moreover, they showed specific toxicity toward cancer cells. HNT loaded with curcumin was covered with poly-L-lysine as positive electrolyte and poly-acrilic-acid as negative electrolyte using layer-by-layer technique, thus creating three layers of polymers. Polymer coated HNT-curcumin nanocomposite showed a much more slow release ($<20\%$ (w/w) of drug in 24 h) in comparison with free curcumin ($>90\%$ (w/w) of curcumin in 24 h) and uncoated HNT-curcumin ($>40\%$ (w/w) in 24 h) (Dionisi et al., 2016). CS-grafted HNTs with doxorubicin were internalized by human breast cells and effectively induced cell apoptosis (Yang et al., 2016b).

Physical adsorption between curcumin and cellulose-modified MMT also showed good biocompatibility, thus demonstrating the promising applications in cancer DDSs and wound dressings (Huang et al., 2017).

Crosslinked PVA nanofibers with HNTs were prepared as a sodium D-pantothenate DDS (Lee et al., 2016). Significant changes occurred in drug release patterns due to the presence of the clay mineral. Burst releases were not avoided, although the second step of release occurred more slowly and total amount of drug release was smaller in comparison with the corresponding PVA-sodium D-pantothenate fibers.

Hydroxypropyl methylcellulose acetate succinate (HPMCAS) is insoluble in acidic conditions but highly soluble in neutral–alkaline conditions. Colon cancer is mainly treated with drugs such as atorvastatin and celecoxib, which are administered together due to their synergistic action. These drugs were loaded in HNT-HPMCAS microspheres prepared by a microfluidic flow-focusing oil-in-water emulsion technique, schematically represented in Fig. 6.5. In comparison with pure celecoxib and atorvastatin, HNT-HPMCAS loaded microspheres did not

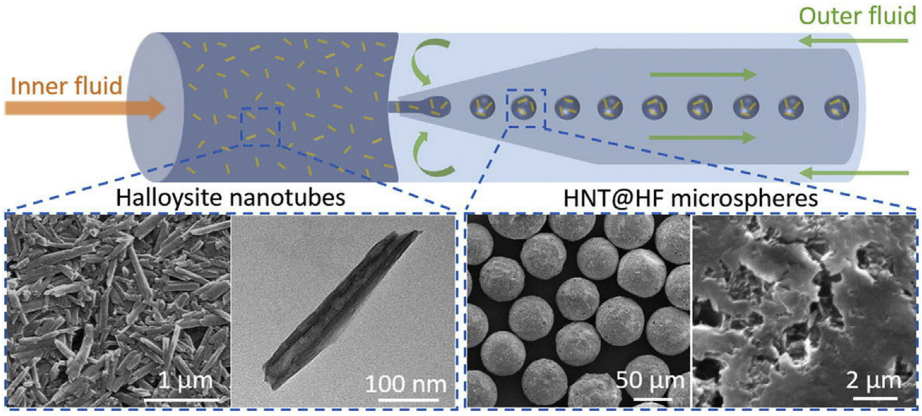

FIGURE 6.5

Preparation of pH-responsive nanocomposite of HNT and HPMCAS.

Figure extracted from Li, W., et al., 2017. Microfluidic assembly of a nano-in-micro dual drug delivery platform composed of halloysite nanotubes and a pH-responsive polymer for colon cancer therapy. Acta Biomater. 48, 238–246.

release any drug at pH $\leq$6.5, while a complete release occurred within 30 min at pH $>$6.8. The immediate and complete release of both the drugs increased their permeability across the intestinal membranes inhibiting colon cancer cell proliferation in a more effective way (Li et al., 2017).

HNTs functionalized with AZPES were condensed with fluoromethoxycarbonyl-L-phenylalanine (Fmoc-F) (Rizzo et al., 2017). Fmoc-F is able to create high density hydrogels. Camptothecin was loaded by intercalation solution and vacuum cycles. Oral administration of the drug is hindered by low solubility and low stability. AZPES-functionalized HNTs/Fmoc-F nanocomposites allowed the total dissolution of the drug in phosphate buffer solution.

Vacuum method was also used to prepare HNTs/pectin nanocomposites to carry rosemary essential oil (Gorrasi, 2015). The aim of the study was to obtain a nanocomposite film with biodegradable and antibacterial properties in which the release of the active substance proceeded in a sustained manner.

HNTs were combined with CS to prepare microspheres. Both materials were kept in contact for 12 h right after their dispersion/dissolution. Microspheres were prepared through an emulsification process with oleic acid (Li et al., 2016a). Aspirin was selected as a model drug. The partial dissolution of aspirin in the acidic environment of the stomach produces the adhesion of aspirin crystals over the gastric mucosa, which can pose gastric diseases. To minimize this problem, Li et al. (2016a) proposed the preparation of the aforementioned microspheres to control aspirin release. The encapsulation efficiency was improved by HNT/CS microspheres, and the dissolution profile showed a lower release of aspirin in simulated gastric fluid, leading to a reduction of accumulation of the drug, and consequently minimizing the possible gastric side effects.

CS oligosaccharides, homo- or heterooligomers of *N*-acetylglucosamine and D-glucosamine, accelerate wound healing by enhancing the activity of inflammatory and repairing cells. Sandri et al. (2017) used these oligomers and HNTs to obtain nanocomposites able to enhance healing in the treatment of chronic wounds. The results showed good *in vitro* biocompatibility with normal human dermal fibroblasts and enhanced *in vitro* fibroblast motility, promoting both cellular proliferation and migration. The HTNs/chitosan oligosaccharide nanocomposites allowed better skin reepithelization and reorganization than HNTs or CS, separately (Fig. 6.6).

HNTs embedded inside hydrogels sensitive to pH changes were demonstrated to be a good strategy for the encapsulation of the anticancer drug 5-fluorouracil (Rao et al., 2014). This drug is used in colon cancer therapies, although its intravenous administration poses remarkable side effects. An oral dosage form would be a more convenient one for these kind of treatments. In this case, sodium hyaluronate and poly(HEMA) were crosslinked by free radical redox polymerization with and without the presence of HNTs (Rao et al., 2014). Vacuum cycles were performed to entrap the drug both inside the hydrogel network and in HNT lumen. The resultant nanocomposites practically avoided drug release in acidic pH (<10% (w/w) when HNTs were added), while in neutral environment 5-fluorouracil was successfully released.

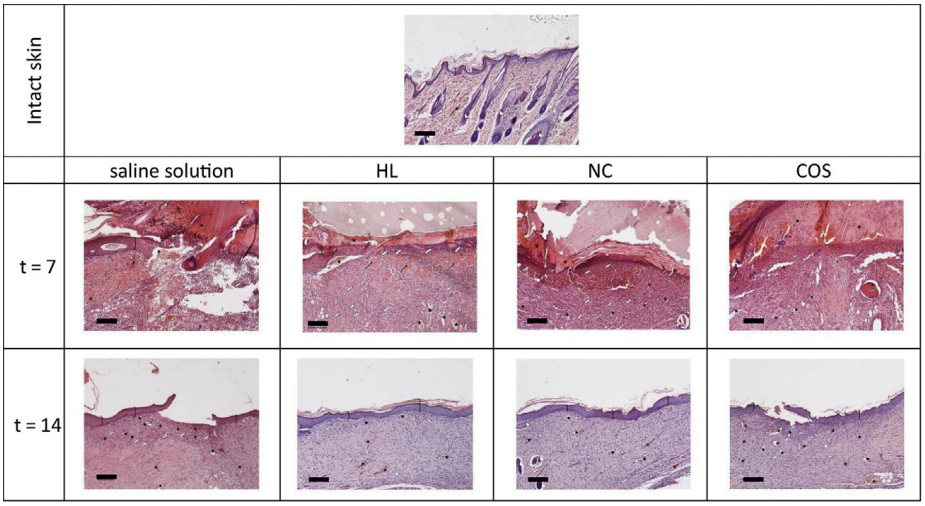

FIGURE 6.6

Light microphotographs of hematoxylin and eosin stained skin sections after 7 and 18 days of treatment with saline solution (negative control), HNTs, chitosan oligosaccharide/HTNs nanocomposite, and chitosan oligosaccharide. Intact tissue section is also reported. Skin structures are labeled as follows: epidermis = bracket; vessel = star; granulation tissue = pentagons; hair follicle = triangle; platelets = white arrow; necrotic tissue = asterisk, muscular fibers = arrow. Scale bar = 200 μm (Sandri et al., 2017).

A commercial adhesive resin used in dentin implants was modified by including HNTs loaded with doxycycline, a matrix metalloproteinases-inhibiting drug. Metalloproteinases are enzymes able to destroy connective tissue during certain issues such as periodontitis, hepatitis, atherosclerosis, asthma, skin and dental photoaging. The incorporation of HNTs and doxycycline inside dental resin (Scotchbond Multi-Purpose) was proposed to improve the adhesively bonded resin composite restorations (Feitosa et al., 2014; Palasuk et al., 2017). Doxycycline was successfully encapsulated within the system, and released in such a controlled manner that metalloproteinases were inhibited in subantimicrobial concentrations. Additionally, the biocompatibility of the system was not compromised.

Polyethylene glycol methacrylate (PEGm) and polyethylene glycol dimethacrylate (PEGdm) were proposed as HNT pH-sensitive modifying polymers (Ghebaur et al., 2016). The drug/clay ratio was the only factor influencing the adsorption of hydrocortisone, while polymers exerted a negligible impact on drug loading. Sustained releases were found in all cases, even with the absence of polymers (HNT/hydrocortisone).

APTES-functionalized HNTs were combined with ALG and gelatin, and vancomycin as an antibacterial drug was loaded to design a wound healing nanocomposite (Kurczewska et al., 2017). Nanocomposites showed sustained release of the drug in phosphate buffer medium, without any burst release.

HNT/cellulose-curcumin nanocomposite was tested and compared with a cellulose−curcumin system (Huang et al., 2017). HNTs improved the amount of drug loaded and provided sustained release of curcumin without burst releases: ∼15% (w/w) of drug in approximately 2.5 h reaching more than ∼50% (w/w) after 20 h during *in vitro* release study.

APTES-HNTs were grafted with polyethyleneimine (PEI) to load pDNA and create a nonviral vector able to deliver pDNA into determined cells as a strategy to treat diseases such as cancer (Long et al., 2017). The complex with HNTs showed less *in vitro* toxicity than the one without HNTs. Likewise, the transfection efficiency of the clay-based nanocomposite was higher, being able to deliver the pDNA into the cellular nucleus (Long et al., 2017).

Doxorubicin loading efficiency increased by increasing HNT proportion in HNT/soybean phospholipid nanocomposites (Li et al., 2018). At neutral pH, doxorubicin was released in a sustained way, without burst release and reaching approximately 15% (w/w) of drug after 4 days. On the other hand, at acidic pH (5.4), the release profile possessed two stages: a burst release step in which 20% (w/w) of drug was released within the first 10 min followed by a more sustained and prolonged release to 25% (w/w) of total amount of drug released in 4 days.

Pal was mixed with polypyrrole (PPy) to improve physicochemical properties of the polymer as a drug carrier (Kong et al., 2014). Polypyrrole is a biocompatible polymer able to change its oxidation state under electrical potential, thus promoting drug release. In comparison with polypyrrole alone, Pal-polypyrrole composites showed higher drug loading capacities ascribable to the presence of

the clay mineral. Pal-PPy-aspirin composites were demonstrated to be a promising implantable DDS, which could help to release drugs according to patient convenience under electric stimulus (Kong et al., 2014).

Organomodification of Pal with hexadecyl betaine was combined with CS through crosslinking reaction to create beads able to carry drugs such as diclofenac sodium (Wu et al., 2014). The organomodification of the clay mineral improved chemical interactions with the polymer. Additionally, the presence of the clay mineral increased the swelling properties of the beads and modified drug release. Beads with 10%−20% (w/w) of organomodified Pal showed slower drug release and burst release reduction. Beads with 30% (w/w) of palygorskite performed faster release, even higher than pure CS-diclofenac beads.

Pal/CS as drug carrier was recently addressed (Santana et al., 2017). The model drug chosen in this study was 5-aminosalicylic acid. CS and Pal interacted through electrostatic interactions and intermolecular hydrogen bonds. The use of basic pH during Pal/CS interaction highly influenced the interactions between these components and influenced the drug loading capacity. At pH 11, the CS protonation decrease favored the interaction with Pal but contributed to reduce 5-aminosalicylic acid adsorption due to low available drug interaction sites.

Sep and CS were combined by Gür et al. (2015) to form a nanocomposite carrying tetracycline drug. A clear dependence of Sep ratio on the amount of drug released was found. Burst releases were also found in all the *in vitro* release studies performed, and were attributed to a fast swelling of the gel.

Sep was also combined with CS and PVA, and loaded with cefazolin, a broad-spectrum antibacterial drug (Mahdavinia et al., 2016). Drug release profile and antibacterial activity (*Bacillus cereus*, *Proteus* bacteria, and *E. coli*) were evaluated. CS improved swelling capacity of the nanocomposite. PVA decreased the amount of drug released since higher crosslinking occurred, consequently creating smaller hydrogel pore sizes that could hinder the diffusion of cefazolin. Effective growth inhibition areas were found except for the nanocomposite without cefazolin. The highest antimicrobial activity was reported against *B. cereus*.

6.4 FUTURE TRENDS

Ten years have passed since Aguzzi et al. (2007) published their review article titled "Use of clays as drug delivery systems: Possibilities and limitations." During this time span the number of studies focused on this subject have increased exponentially. In this chapter, current advances are addressed, MMT and halloysite being the main clay minerals used in the design of new DDS. Recent results confirm that the usefulness of clay minerals will go beyond their conventional uses in pharmaceutical applications, thanks to multidisciplinary research efforts. The developments in biotechnology and nanomedicine research make us think that a possible future use of clay minerals would be focused on MMDS of biopharmaceuticals,

including gene and protein delivery. Consequently, the number of patents and commercial pharmaceutical products will be increased, ultimately improving many pharmacological therapies.

ACKNOWLEDGMENTS

This study was supported by the Projects CGL2016-80833-R and RNM-1897, group CTS-946, and Predoctoral Grant FPU15/01577.

ABBREVIATIONS

AMP clay	3-aminopropyl functionalized magnesium phyllosilicate
APTES	3-aminopropyltriethoxysilane
APMES	amino-propyldimethylethoxysilane
ALG	alginate
AZPES	3-azidopropyltrimethoxysilane
CMC	carboxymethylcellulose
CS	chitosan
CTAB	*n*-cetyl-*N*,*N*,*N*-trimethylammonium bromide
FGF2	fibroblast growth factor 2
Fmoc-F	fluoromethoxycarbonyl-L-phenylalanine
HPMCAS	hydroxypropyl methylcellulose acetate succinate
HNT	halloysite nanotubes
LDH	layered double hydroxides
LIP	soybean phospholipid
MAA	methacrylic acid
MC	methylcellulose
MMT	montmorillonite
Na^+-MMT	sodium montmorillonite
PAA	poly-acrilic-acid
P(AAm-MA)	poly(acrylamide-*co*-maleic acid)
PAH	poly(allylamine) hydrochloride
PC	pectin
PCL	poly(ε-caprolactone)
PCLA	poly(ε-caprolactone-*co*-lactide)
PEG	poly(ethylene glycol)
PEGdm	polyethylene glycol dimethacrylate
PEGm	polyethylene glycol methacrylate
PMMM	poly(methyl methacrylate-*co*-methacrylic acid)
PEG750/5000-PE	1,2-distearoyl-sn-glycero-3-phosphoethanolamine-*N*-[methoxy (polyethylene glycol)-750/5000] (ammonium salt)
PEI	polyethyleneimine
PLA	poly(D,L-lactide)
PLGA	poly(lactic-*co*-glycolic acid)

PLLA	poly (L-lactide)
PLL	poly-L-lysine
PSS	poly(sodium styrene) sulfonate
Poly(HEMA)	poly(hydroxyethyl methacrylate)
PPy	polypyrrole
PVA	polyvinyl alcohol
rhBMP-2	bone morphogenetic protein-2
SBMP	commercial dental resin Scotchbond Multi-Purpose
TPT	oligo(trimethylene carbonate)−poly(ethylene glycol)−oligo (trimethylene carbonate) diacrylate
VEGF	vascular endothelial growth factors

REFERENCES

Aguzzi, C., et al., 2007. Use of clays as drug delivery systems: possibilities and limitations. Appl. Clay Sci. 36 (1−3), 22−36.

Aguzzi, C., et al., 2010. Chitosan−silicate biocomposites to be used in modified drug release of 5-aminosalicylic acid (5-ASA). Appl. Clay Sci. 50 (1), 106−111.

Aguzzi, C., et al., 2013. Release kinetics of 5-aminosalicylic acid from halloysite. Colloids Surf. B Biointerfaces 105, 75−80.

Aguzzi, C., et al., 2014a. Intercalation of tetracycline into layered clay mineral material for drug delivery purposes. Mater. Technol. 29 (Suppl. 3), B96−B99.

Aguzzi, C., et al., 2014b. Solid state characterisation of silver sulfadiazine loaded on montmorillonite/chitosan nanocomposite for wound healing. Colloids Surf. B Biointerfaces 113, 152−157.

Aguzzi, C., et al., 2016. Health and medical applications of tubular clay minerals. In: Yuan, P., Bergaya, F., Thill, A. (Eds.), Nanosized Tubular Clay Minerals. Elsevier, pp. 708−725.

Ambrogi, V., Nocchetti, M., Latterini, L., 2014. Promethazine−montmorillonite inclusion complex to enhance drug photostability. Langmuir 30 (48), 14612−14620.

Ambrogi, V., et al., 2017. Montmorillonite−chitosan−chlorhexidine composite films with antibiofilm activity and improved cytotoxicity for wound dressing. J. Colloid Interface Sci. 491, 265−272.

Ariga, K., et al., 2017. Halloysite and related mesoporous carriers for advanced catalysis and drug delivery. In: Lvov, Y., Guo, B., Fakhrullin, R. (Eds.), Functional Polymer Composites with Nanoclays. Royal Society of Chemistry, Cambridge, pp. 207−222.

Bakre, L.G., Sarvaiya, J.I., Agrawal, Y.K., 2016. Synthesis, characterization, and study of drug release properties of curcumin from polycaprolactone/organomodified montmorillonite nanocomposite. J. Pharm. Innovat. 11 (4), 300−307.

Bayaumy, F.E.A., Darwish, A.S., 2016. Exfoliated Egyptian kaolin immobilized heteropolyoxotungstate nanocomposite as an innovative antischistosomal agent: in vivo and in vitro bioactive studies. Mater. Sci. Eng. C 59, 717−730.

Bazmi-Zeynabad, F., et al., 2015. pH-Controlled multiple-drug delivery by a novel antibacterial nanocomposite for combination therapy. R. Soc. Chem. Adv. 5 (128), 105678−105691.

Borrego-Sánchez, A., et al., 2017. Biopharmaceutical improvement of praziquantel by interaction with montmorillonite and sepiolite. Appl. Clay Sci. 160, 173−179.

Bothiraja, C., et al., 2014. Chitosan coated layered clay montmorillonite nanocomposites modulate oral delivery of paclitaxel in colonic cancer. Mater. Technol. 29 (3), 120–126.
Bounabi, L., et al., 2016. Development of poly(2-hydroxyethyl methacrylate)/clay composites as drug delivery systems of paracetamol. J. Drug Deliv. Sci. Technol. 33, 58–65.
Brigatti, M.F., Galan, E., Theng, B.K.G., 2006. Structures and mineralogy of clay minerals. In: Bergaya, F., Theng, B.K., Lagaly, G. (Eds.), Handbook of Clay Science. Elservier, pp. 19–86.
Carazo, E., et al., 2017a. Use of clays as nanocarriers of first-line tuberculostatic drugs. Curr. Drug Deliv. 14 (7), 902–903.
Carazo, E., et al., 2017b. Assessment of halloysite nanotubes as vehicles of isoniazid. Colloids Surf. B Biointerfaces 160, 337–344.
Carazo, E., et al., 2017c. Adsorption and characterization of palygorskite-isoniazid nanohybrids. Appl. Clay Sci. 160, 180–185.
Carazo, E., et al., 2018. Advanced inorganic nanosystems for skin drug delivery. Chem. Rec. 18, 1–10.
Council of Europe & Convention on the Elaboration of a European Pharmacopoeia, 2017. European Pharmacopoeia, ninth ed. Maisonneuve, Sainte-Ruffine, France.
Dadkhah, D., et al., 2014. Application of Taguchi method to investigate the drug release behavior of poly(acrylamide-co-maleic acid)/montmorillonite nanocomposite hydrogels. Adv. Polym. Technol. 33 (4).
Das, G., et al., 2014. Antibacterial activities of copper nanoparticle-decorated organically modified montmorillonite/epoxy nanocomposites. Appl. Clay Sci. 90, 18–26.
de Almeida-Borges, V.R., et al., 2016. Development and pharmacological evaluation of in vitro nanocarriers composed of lamellar silicates containing copaiba oil-resin for treatment of endometriosis. Mater. Sci. Eng. C 64, 310–317.
Dionisi, C., et al., 2016. Halloysite clay nanotubes as carriers for curcumin: characterization and application. IEEE Trans. Nanotechnol. 15 (5), 720–724.
Dziadkowiec, J., et al., 2017. Preparation, characterization and application in controlled release of ibuprofen-loaded guar gum/montmorillonite bionanocomposites. Appl. Clay Sci. 135, 52–63.
Fakhrullina, G.I., et al., 2015. Toxicity of halloysite clay nanotubes in vivo: a *Caenorhabditis elegans* study. Environ. Sci. Nano 2 (1), 54–59.
Feitosa, S.A., et al., 2014. Doxycycline-encapsulated nanotube-modified dentin adhesives. J. Dent. Res. 93 (12), 1270–1276.
Fernandes, A.C., et al., 2013. Clay based materials for storage and therapeutic release of nitric oxide. J. Mater. Chem. B 1, 3287–3294.
Gao, M., et al., 2017. Preparation of a novel breviscapine-loaded halloysite nanotubes complex for controlled release of breviscapine. Mater. Sci. Eng. 265, 1–8.
Ghebaur, A., et al., 2016. pH-sensitive clays as drug delivery carriers for controlled release of hydrocortisone. Mater. Plast. 53 (3), 419–423.
Gorrasi, G., 2015. Dispersion of halloysite loaded with natural antimicrobials into pectins: characterization and controlled release analysis. Carbohydr. Polym. 127, 47–53.
Guggenheim, S., Krekeler, M.P.S., 2011. The structures and microtextures of the palygorskite–sepiolite group minerals. In: Galán, E., Singer, A. (Eds.), Developments in Clay Science. Elsevier, pp. 3–32.
Gür, E., Altinisik, A., Yurdakoc, K., 2015. Preparation and characterization of chitosan/sepiolite bionanocomposites for tetracycline release. Polym. Polym. Compos. 38 (9), 1810–1818.

Hamilton, A.R., et al., 2014. Formulation and antibacterial profiles of clay−ciprofloxacin composites. Appl. Clay Sci. 87, 129−135.
Holešová, S., et al., 2014. Antibacterial kaolinite/urea/chlorhexidine nanocomposites: experiment and molecular modelling. Appl. Surf. Sci. 305, 783−791.
Hong, H.J., et al., 2017. pH-sensitive mesalazine carrier for colon-targeted drug delivery: a two-fold composition of mesalazine with a clay and alginate. Macromol. Res. 25 (11), 1145−1152.
Huang, B., Liu, M., Zhou, C., 2017. Cellulose−halloysite nanotube composite hydrogels for curcumin delivery. Cellulose 24 (7), 2861−2875.
Jafarbeglou, M., et al., 2016. Clay nanocomposites as engineered drug delivery systems. RSC Adv. 6 (55), 50002−50016.
Jain, S., Datta, M., 2015. Oral extended release of dexamethasone: montmorillonite−PLGA nanocomposites as a delivery vehicle. Appl. Clay Sci. 104, 182−188.
Jain, S., Datta, M., 2016. Montmorillonite-alginate microspheres as a delivery vehicle for oral extended release of Venlafaxine hydrochloride. J. Drug Deliv. Sci. Technol. 33, 149−156.
Jana, S., et al., 2017. Halloysite nanotubes with immobilized silver nanoparticles for antibacterial application. Colloids Surf. B Biointerfaces 151, 249−254.
Jiang, W.T., et al., 2016. Halloysite nanotubes as a carrier for the uptake of selected pharmaceuticals. Micropor. Mesopor. Mater. 220, 298−307.
Kaur, M., Datta, M., 2014. Diclofenac sodium adsorption onto montmorillonite: adsorption equilibrium studies and drug release kinetics. Adsor. Sci. Technol. 32 (5), 365−387.
Kevadiya, B.D., et al., 2013. Evaluation of clay/poly (L-lactide) microcomposites as anticancer drug, 6-mercaptopurine reservoir through in vitro cytotoxicity, oxidative stress markers and in vivo pharmacokinetics. Colloids Surf. B Biointerfaces 112, 400−407.
Khodzhaeva, V., et al., 2017. Binase immobilized on halloysite nanotubes exerts enhanced cytotoxicity toward human colon adenocarcinoma cells. Front. Pharmacol. 8, 1−10.
Kohay, H., et al., 2017. PEG-PE/clay composite carriers for doxorubicin: effect of composite structure on release, cell interaction and cytotoxicity. Acta Biomater. 55, 443−454.
Kong, Y., et al., 2014. Palygorskite polypyrrole nanocomposite: a new platform for electrically tunable drug delivery. Appl. Clay Sci. 99, 119−124.
Krishnan, B., Mahalingam, S., 2017. Ag/TiO_2/bentonite nanocomposite for biological applications: synthesis, characterization, antibacterial and cytotoxic investigations. Adv. Powder Technol. 28 (9), 2265−2280.
Kurczewska, J., et al., 2017. Halloysite nanotubes as carriers of vancomycin in alginate-based wound dressing. Saudi Pharm. J. 25 (6), 911−920.
Lal, S., Datta, M., 2015. In vitro prolonged gastric residence and sustained release of atenolol using novel clay polymer nanocomposite. Appl. Clay Sci. 114, 412−421.
Lal, S., et al., 2017. Design and development of a biocompatible montmorillonite PLGA nanocomposites to evaluate in vitro oral delivery of insulin. Appl. Clay Sci. 147, 69−79.
Lee, I.W., et al., 2016. Electrospun poly(vinyl alcohol) composite nanofibers with halloysite nanotubes for the sustained release of sodium D-pantothenate. J. Appl. Polym. Sci. 133 (4), 1−11. 42900.
Li, X., et al., 2016a. Chitosan modified halloysite nanotubes as emerging porous microspheres for drug carrier. Appl. Clay Sci. 126, 306−312.
Li, H., et al., 2016b. The combination of adsorption by functionalized halloysite nanotubes and encapsulation by polyelectrolyte coatings for sustained drug delivery. RSC Adv. 6 (59), 54463−54470.

Li, W., et al., 2017. Microfluidic assembly of a nano-in-micro dual drug delivery platform composed of halloysite nanotubes and a pH-responsive polymer for colon cancer therapy. Acta Biomater. 48, 238–246.
Li, K., et al., 2018. Enhanced antitumor efficacy of doxorubicin- encapsulated halloysite nanotubes. Int. J. Nanomed. 13, 19–30.
Liu, M., et al., 2014. Recent advance in research on halloysite nanotubes-polymer nanocomposite. Prog. Polym. Sci. 39 (8), 1498–1525.
Liu, M., et al., 2016. Functionalized halloysite nanotube by chitosan grafting for drug delivery of curcumin to achieve enhanced anticancer efficacy. J. Mater. Chem. B 4 (13), 2253–2263.
Long, Z., et al., 2017. Polyethyleneimine grafted short halloysite nanotubes for gene delivery. Mater. Sci. Eng. C 81, 224–235.
López-Galindo, A., et al., 2011. Pharmaceutical and cosmetic uses of fibrous clays. In: Galán, E., Singer, A. (Eds.), Developments in Clay Science. Elsevier, pp. 299–324.
Lvov, Y., Aerov, A., Fakhrullin, R., 2014. Clay nanotube encapsulation for functional biocomposites. Adv. Colloid Interface Sci. 207, 189–198.
Lvov, Y.M., DeVilliers, M.M., Fakhrullin, R.F., 2016a. The application of halloysite tubule nanoclay in drug delivery. Expert Opin. Drug Deliv. 13 (7), 977–986.
Lvov, Y., et al., 2016b. Halloysite clay nanotubes for loading and sustained release of functional compounds. Adv. Mater. 28 (6), 1227–1250.
Madusanka, N., de Silva, K.M.N., Amaratunga, G., 2015. A curcumin activated carboxymethyl cellulose–montmorillonite clay nanocomposite having enhanced curcumin release in aqueous media. Carbohydr. Polym. 134, 695–699.
Mahdavinia, G.R., et al., 2016. The release of cefazolin from chitosan/polyvinyl alcohol/sepiolite nanocomposite hydrogel films. Iran. Polym. J. 25 (11), 933–943.
Mahkam, M., et al., 2015. Preparation of montmorillonite-pH-sensitive positive charges nanocomposites as a drug delivery system. Int. J. Polym. Mater. Polym. Biomater. 64 (1), 32–37.
Mao, H., et al., 2014. Fabrication of magnetic silica-pillared clay (SPC) nanocomposites with ordered interlayer mesoporous structure for controlled drug release. Micropor. Mesopor. Mater. 184, 169–176.
Mao, H., et al., 2016. Facile synthetic route to Fe_3O_4/silica nanocomposites pillared clay through cationic surfactant-aliphatic acid mixed system and application for magnetically controlled drug release. Micropor. Mesopor. Mater. 225, 216–223.
Massaro, M., et al., 2016a. Dual drug-loaded halloysite hybrid-based glycocluster for sustained release of hydrophobic molecules. RSC Adv. 6 (91), 87935–87944.
Massaro, M., et al., 2016b. Direct chemical grafted curcumin on halloysite nanotubes as dual-responsive prodrug for pharmacological applications. Colloids Surf. B Biointerfaces 140, 505–513.
Massaro, M., et al., 2016c. A synergic nanoantioxidant based on covalently modified halloysite–trolox nanotubes with intra-lumen loaded quercetin. J. Mater. Chem. B 4 (13), 2229–2241.
Meirelles, L.M.A., Raffin, F.N., 2017. Clay and polymer-based composites applied to drug release: a scientific and technological prospection. J. Pharm. Pharm. Sci. 20, 115–134.
Minullina, R., et al., 2017. Halloysite clay nanotubes for long acting controlled release of drugs and proteins. In: Lvov, Y., Guo, B., Fakhrullin, R.F. (Eds.), Functional Polymer Composites with Nanoclays. Royal Society of Chemistry, Cambridge, pp. 354–378.

Mura, P., et al., 2016. Hybrid systems based on "drug − in cyclodextrin − in nanoclays" for improving oxaprozin dissolution properties. Int. J. Pharm. 509 (1−2), 8−15.

Nazir, M.S., et al., 2016. Characteristic properties of nanoclays and characterization of nanoparticulates and nanocomposites. In: Jawaid, M., Qaiss, A., Bouhfid, R. (Eds.), Nanoclay Reinforced Polymer Composites. Springer, Singapore, pp. 35−55.

Oliveira, A.S., Alcântara, A.C.S., Pergher, S.B.C., 2017. Bionanocomposite systems based on montmorillonite and biopolymers for the controlled release of olanzapine. Mater. Sci. Eng. C 75, 1250−1258.

Othman, R., et al., 2016. Fabrication of composite poly(D,L-lactide)/montmorillonite nanoparticles for controlled delivery of acetaminophen by solvent-displacement method using glass capillary microfluidics. Colloids Surf. B Biointerfaces 141, 187−195.

Palasuk, J., et al., 2017. Doxycycline-loaded nanotube-modified adhesives inhibit MMP in a dose-dependent fashion. Clin. Oral Investig. 1−10.

Pan, Q., et al., 2017. Halloysite clay nanotubes as effective nanocarriers for the adsorption and loading of vancomycin for sustained release. RSC Adv. 7, 21352−21359.

Park, J.H., et al., 2016. Application of montmorillonite in bentonite as a pharmaceutical excipient in drug delivery systems. J. Pharm. Investig. 46 (4), 363−375.

Phan, V.H.G., et al., 2016. Pancreatic cancer therapy using an injectable nanobiohybrid hydrogel. RSC Ad. 6 (47), 41644−41655.

Phukan, A., Bhattacharjee, R.P., Dutta, D.K., 2017. Stabilization of SnO_2 nanoparticles into the nanopores of modified Montmorillonite and their antibacterial activity. Adv. Powder Technol. 28 (1), 139−145.

Pongjanyakul, T., et al., 2013. Characterization of chitosan−magnesium aluminum silicate nanocomposite films for buccal delivery of nicotine. Int. J. Biol. Macromol. 55, 24−31.

Qi, R., et al., 2010. Electrospun poly(lactic-co-glycolic acid)/halloysite nanotube composite nanofibers for drug encapsulation and sustained release. J. Mater. Chem. 20 (47), 10622.

Qi, R., et al., 2013. Controlled release and antibacterial activity of antibiotic-loaded electrospun halloysite/poly(lactic-co-glycolic acid) composite nanofibers. Colloids Surf. B Biointerfaces 110, 148−155.

Rabiei, M., Sabahi, H., Rezayan, A.H., 2016. Gallic acid-loaded montmorillonite nanostructure as a new controlled release system. Appl. Clay Sci. 119, 236−242.

Rangappa, S., et al., 2017. Evaluation of lidocaine loaded clay based dermal patch systems. J. Drug Deliv. Sci. Technol. 39, 450−454.

Rao, K.M., et al., 2014. pH sensitive halloysite-sodium hyaluronate/poly(hydroxyethyl methacrylate) nanocomposites for colon cancer drug delivery. Appl. Clay Sci. 97−98, 33−42.

Rapacz-Kmita, A., et al., 2017a. Characterisation, in vitro release study, and antibacterial activity of montmorillonite-gentamicin complex material. Mater. Sci. Eng. C 70, 471−478.

Rapacz-Kmita, A., et al., 2017b. Magnesium aluminium silicate−gentamicin complex for drug delivery systems: preparation, physicochemical characterisation and release profiles of the drug. J. Therm. Anal. Calorim. 127 (1), 871−880.

Rebitski, E.P., et al., 2018. Intercalation of metformin into montmorillonite. Dalton Trans. 47 (9), 3185−3192. Available from: https://doi.org/10.1039/c7dt04197g.

Reddy, A.B., et al., 2016. 5-Fluorouracil loaded chitosan−PVA/Na^+MMT nanocomposite films for drug release and antimicrobial activity. Nano-Micro Lett. 8 (3), 260−269.

Riela, S., et al., 2014. Development and characterization of co-loaded curcumin/triazole-halloysite systems and evaluation of their potential anticancer activity. Int. J. Pharm. 475 (1−2), 613−623.
Rizzo, C., et al., 2017. Hybrid supramolecular gels of Fmoc-F/halloysite nanotubes: systems for sustained release of camptothecin. J. Mater. Chem. B 5 (17), 3217−3229.
Rodrigues, L.A., de, S., et al., 2013. The systems containing clays and clay minerals from modified drug release: a review. Colloids Surf. B Biointerfaces 103, 642−651.
Roy, A., Butola, B.S., Joshi, M., 2017. Synthesis, characterization and antibacterial properties of novel nano-silver loaded acid activated montmorillonite. Appl. Clay Sci. 146, 278−285.
Saha, K., Butola, B.S., Joshi, M., 2014. Drug release behavior of polyurethane/clay nanocomposite: film vs. nanofibrous web. J. Appl. Polym. Sci. 131 (19), , p. n/a-n/a.
Saha, N.R., et al., 2016. Studies on methylcellulose/pectin/montmorillonite nanocomposite films and their application possibilities. Carbohydr. Polym. 136, 1218−1227.
Salahuddin, N., et al., 2014. Polyamide-montmorillonite nanocomposites as a drug delivery system: preparation, release of 1,3,4-oxa(thia)diazoles, and antimicrobial activity. J. Appl. Polym. Sci. 131 (23).
Salcedo, I., et al., 2014. Intestinal permeability of oxytetracycline from chitosan-montmorillonite nanocomposites. Colloids Surf. B Biointerfaces 117, 441−448.
Sánchez-Fernández, A., et al., 2014. Synthesization, characterization, and in vitro evaluation of cytotoxicity of biomaterials based on halloysite nanotubes. Materials 7 (12), 7770−7780.
Sandri, G., et al., 2014. Montmorillonite-chitosan-silver sulfadiazine nanocomposites for topical treatment of chronic skin lesions: in vitro biocompatibility, antibacterial efficacy and gap closure cell motility properties. Carbohydr. Polym. 102, 970−977.
Sandri, G., et al., 2016. Clay minerals for tissue regeneration, repair, and engineering. In: Ågren, M.S. (Ed.), Wound Healing Biomaterials. Elsevier, pp. 385−402.
Sandri, G., et al., 2017. Halloysite and chitosan oligosaccharide nanocomposite for wound healing. Acta Biomater. 57, 216−224.
Santana, A.C.S.G.V., et al., 2017. Preparation and physicochemical characterization of binary composites palygorskite−chitosan for drug delivery. J. Therm. Anal. Calorim. 128 (3), 1327−1334.
Sastry, S.V., Nyshadham, J.R., Fix, J.A., 2000. Recent technological advances in oral drug delivery − a review. Pharm. Sci. Technol. Today 3 (4), 138−145.
Schoonheydt, R.A., Jonhston, C.T., 2006. Surface and interface chemistry of clay minerals. In: Bergaya, F., Lagaly, G. (Eds.), Handbook of Clay Science. Elservier, pp. 87−113.
Tan, D., et al., 2014. Loading and in vitro release of ibuprofen in tubular halloysite. Appl. Clay Sci. 96, 50−55.
Tenci, M., et al., 2017. Carvacrol/clay hybrids loaded into in situ gelling films. Int. J. Pharm. 531 (2), 676−688.
Thakur, A., Wanchoo, R.K., Singh, P., 2012. Hydrogels of poly(acrylamide-co-acrylic acid): in-vitro study on release of gentamicin sulfate. Chem. Biochem. Eng. Quart. 25 (4), 471−482.
Tohidi, S., Ghaee, A., Barzin, J., 2016. Preparation and characterization of poly(lactic-co-glycolic acid)/chitosan electrospun membrane containing amoxicillin-loaded halloysite nanoclay. Polym. Adv. Technol. 27 (8), 1020−1028.
Trivedi, V., et al., 2018. Intercalated theophylline-smectite hybrid for pH-mediated delivery. Drug Deliv. Translat. Res. 1−9.

Tu, J., et al., 2013. Halloysite nanotube nanocomposite hydrogels with tunable mechanical properties and drug release behaviour. Compos. Sci. Technol. 85, 126–130.
Viseras, C., et al., 2008. Biopolymer–clay nanocomposites for controlled drug delivery. Mater. Sci. Technol. 24 (9), 1020–1026.
Viseras, C., et al., 2010. Current challenges in clay minerals for drug delivery. Appl. Clay Sci. 48 (3), 291–295.
Viseras, C., Aguzzi, C., Cerezo, P., 2015. Medical and health applications of natural mineral nanotubes. In: Pasbakhsh, P., Churchman, G.J. (Eds.), Natural Mineral Nanotubes: Properties and Applications. Apple Academic Press, Inc, Oakville, pp. 437–448.
Viseras, M.T., et al., 2009. Supramolecular structure of 5-aminosalycilic acid/halloysite composites. J. Microencapsul. 26 (3), 279–286.
Wang, Q., et al., 2014a. Adsorption and release of ofloxacin from acid- and heat-treated halloysite. Colloids Surf. B Biointerfaces 113, 51–58.
Wang, Q., Zhang, J., Wang, A., 2014b. Freeze-drying: a versatile method to overcome re-aggregation and improve dispersion stability of palygorskite for sustained release of ofloxacin. Appl. Clay Sci. 87, 7–13.
Wu, J., et al., 2014. Preparation and drug release properties of chitosan/organomodified palygorskite microspheres. Int. J. Biol. Macromol. 68, 107–112.
Wu, L., et al., 2017. Drug release material hosted by natural montmorillonite with proper modification. Appl. Clay Sci. 148, 123–130.
Xue, J., et al., 2015. Electrospun microfiber membranes embedded with drug-loaded clay nanotubes for sustained antimicrobial protection. ACS Nano 9 (2), 1600–1612.
Yang, J.H., et al., 2016a. Drug–clay nanohybrids as sustained delivery systems. Appl. Clay Sci. 130, 20–32.
Yang, J., et al., 2016b. Enhanced therapeutic efficacy of doxorubicin for breast cancer using chitosan oligosaccharide-modified halloysite nanotubes. ACS Appl. Mater. Interfaces 8 (40), 26578–26590.
Yendluri, R., et al., 2017a. Application of halloysite clay nanotubes as a pharmaceutical excipient. Int. J. Pharm. 521 (1–2), 267–273.
Yendluri, R., et al., 2017b. Paclitaxel encapsulated in halloysite clay nanotubes for intestinal and intracellular delivery. J. Pharm. Sci. 106 (10), 3131–3139.
Zhang, Y., et al., 2013. Potent antibacterial activity of a novel silver nanoparticle-halloysite nanotube nanocomposite powder. J. Inorg. Biochem. 118, 59–64.
Zhang, Y., et al., 2017. Intercalated 2D nanoclay for emerging drug delivery in cancer therapy. Nano Res. 10 (8), 2633–2643.

FURTHER READING

Joshi, G.V., et al., 2009. Montmorillonite as a drug delivery system: intercalation and in vitro release of timolol maleate. Int. J. Pharm. 374 (1–2), 53–57.